

**Dynamic Testing of In-Situ Composite Floors and
Evaluation of Vibration Serviceability Using the Finite Element Method**

By

Anthony R. Barrett

Dissertation submitted to the Faculty of
Virginia Polytechnic Institute and State University
in partial fulfillment for the requirements of the degree of

Doctor of Philosophy

in

Civil Engineering

Thomas M. Murray, Chair

Finley A. Charney

W. Samuel Easterling

Raymond H. Plaut

Mehdi Setareh

Alfred L. Wicks

21 August 2006

Blacksburg, VA

Keywords: vibration, floor, serviceability, walking, modal analysis, fundamental frequency, mode shape, resonance, damping, acceleration response, finite element

Report Documentation Page				Form Approved OMB No. 0704-0188	
Public reporting burden for the collection of information is estimated to average 1 hour per response, including the time for reviewing instructions, searching existing data sources, gathering and maintaining the data needed, and completing and reviewing the collection of information. Send comments regarding this burden estimate or any other aspect of this collection of information, including suggestions for reducing this burden, to Washington Headquarters Services, Directorate for Information Operations and Reports, 1215 Jefferson Davis Highway, Suite 1204, Arlington VA 22202-4302. Respondents should be aware that notwithstanding any other provision of law, no person shall be subject to a penalty for failing to comply with a collection of information if it does not display a currently valid OMB control number.					
1. REPORT DATE 21 AUG 2006		2. REPORT TYPE N/A		3. DATES COVERED -	
4. TITLE AND SUBTITLE Dynamic Testing of In-Situ Composite Floors and Evaluation of Vibration Serviceability Using the Finite Element Method				5a. CONTRACT NUMBER	
				5b. GRANT NUMBER	
				5c. PROGRAM ELEMENT NUMBER	
6. AUTHOR(S)				5d. PROJECT NUMBER	
				5e. TASK NUMBER	
				5f. WORK UNIT NUMBER	
7. PERFORMING ORGANIZATION NAME(S) AND ADDRESS(ES) Virginia Polytechnic Institute and State University				8. PERFORMING ORGANIZATION REPORT NUMBER	
9. SPONSORING/MONITORING AGENCY NAME(S) AND ADDRESS(ES)				10. SPONSOR/MONITOR'S ACRONYM(S)	
				11. SPONSOR/MONITOR'S REPORT NUMBER(S)	
12. DISTRIBUTION/AVAILABILITY STATEMENT Approved for public release, distribution unlimited					
13. SUPPLEMENTARY NOTES The original document contains color images.					
14. ABSTRACT					
15. SUBJECT TERMS					
16. SECURITY CLASSIFICATION OF:			17. LIMITATION OF ABSTRACT UU	18. NUMBER OF PAGES 451	19a. NAME OF RESPONSIBLE PERSON
a. REPORT unclassified	b. ABSTRACT unclassified	c. THIS PAGE unclassified			

**Dynamic Testing of In-Situ Composite Floors and
Evaluation of Vibration Serviceability Using the Finite Element Method**

Anthony R. Barrett

Dr. Thomas M. Murray, Chairman

Civil Engineering

(ABSTRACT)

The presented research examined three areas: best practices in high quality dynamic testing of in-situ floor systems, extensive dynamic testing of three bare (non-fit out) in-situ multi-bay steel composite floors to estimate their dynamic parameters/response and to identify trends in dynamic behavior, and development of a set of fundamental finite element (FE) modeling techniques to adequately represent the dynamic response of steel composite floors for the purpose of evaluating vibration serviceability. The measurement, analysis, and computation of a floor's accelerance frequency response function (FRF) is the core premise linking all areas of the presented research.

The burst chirp signal using an electrodynamic shaker is recommended as the most accurate and consistent source of excitation for acquiring high quality measurements suitable for use in parameter estimation, operating deflection shape animation, and calibration/validation of FE models. A reduced mid-bay testing scheme is recommended as a time-saving alternative to modal testing over a full coverage area, provided the only desired estimated parameters are frequencies, damping, and mid-bay acceleration response.

Accelerance FRFs were measured with an electrodynamic shaker located within 23 unique bays on the three tested floors. Dominant frequencies ranged from 4.85 Hz to 9 Hz and measured estimates of damping varied considerably, ranging from 0.44% to 2.4% of critical (0.5%-1.15% was typical). Testing showed several mode shapes were localized to just a few bays and not all modes were adequately excited by forcing at a single location. The quality of the estimated mode shapes was significantly improved using multi-reference modal testing.

FE models for the tested floors were developed based on high quality measured data and were shown to provide adequate representations of measured floor behavior. Fundamental techniques are presented for modeling mass, stiffness, boundary conditions, and performing dynamic analysis. A method of evaluating vibration serviceability was proposed using the FE model's computed accelerance FRF for comparison with a *design accelerance curve* that represents an acceleration response threshold in the frequency domain. An example design accelerance curve is presented based on current serviceability guidelines for acceleration tolerance and effective harmonic forces due to human activities such as walking.

DISCLAIMER: The views expressed in this article are those of the author and do not reflect the official policy or position of the United States Air Force, Department of Defense, or the U.S. Government.

ACKNOWLEDGEMENTS

I would like to sincerely thank my advisor and chair of my committee, Dr. Murray, for introducing me to the subject of floor vibrations leading me through my research endeavors. Never mind that I received a B- in structural dynamics at Illinois and the graduate school wouldn't accept the transferred credit hours, your valuable mentorship allowed me to make up for a little lost ground. Thank you for all of the once-in-a-lifetime opportunities and adventures that took us from the Verrazano-Narrows Bridge in New York to the Arizona Cardinals Stadium in Phoenix to the vineyards of Bordeaux, France. I came to Virginia Tech to work with you, and I could not have made a better choice that will forever guide my future.

I would also like to thank my committee members Dr. Setareh and Dr. Wicks for providing me such a strong foundation in modal testing that was invaluable to my research. I appreciate all the guidance and encouragement from the other members of my committee: Dr. Charney, Dr. Easterling, and Dr. Plaut. It was a pleasure working with you and I learned a tremendous amount from your classes.

I would like to thank members of Lefrak (Nick and Scott) and Branch (Pat) for granting access to test such outstanding buildings and their great support on site.

Thanks to my friends John Ryan and Troy Twesme, who were great wing-men as we traveled together through the trials and tribulations of a Ph.D. program. I'd also like to thank all the folks at the Structures and Materials Lab: Clark Brown for his mastery of the sorcery and witchcraft involved with electronics; Brett Farmer and Dennis Huffman for their help, great company, and motivational questions such as "Tell us again why you have an office out here?" Thanks to other friends that also supported me in my studies: Onur Avci, David Martin, Chuck Newhouse, Craig Favor, Devin Harris, Kirsten Baldwin-Metzger, and Brad Davis. You all rock.

I am grateful for my family and their support, or mockery, or sometimes both. Now when they ask me, "Are you done yet?" I can say, "Yes, yes I am." A big thank you my wife, who was a "dissertation widow" for way too long and, quite frankly, is SO AWESOME!!!

I am very thankful to the Via Department of Civil and Environmental Engineering for offering such a great graduate program and for the generous Via Fellowship in my last year of studies. Lastly, I would especially like to thank the United States Air Force Academy's Department of Civil and Environmental Engineering for their confidence in my abilities and providing wonderful opportunity in all of my educational endeavors.

TABLE OF CONTENTS

ABSTRACT.....	i
ACKNOWLEDGEMENTS.....	iii
TABLE OF CONTENTS.....	iv
LIST OF FIGURES	vii
LIST OF TABLES.....	xiii
CHAPTER 1 Introduction and Literature Survey.....	1
1.1 Introduction.....	1
1.2 Scope of Research.....	2
1.3 Literature Survey	4
1.3.1 Background	4
1.3.2 AISC/CISC Steel Design Guide Series 11: Vibrations Due to Human Activity	5
1.3.3 Floor Vibration Experimental Testing and Finite Element Modeling	10
1.4 Need for Research	18
CHAPTER 2 Experimental Modal Analysis of Floor Systems	20
2.1 Objectives	20
2.2 Modal Testing Theory	21
2.2.1 Analytical Modal Analysis	21
2.2.2 Digital Signal Processing	24
2.2.3 Parameter Estimation	27
2.3 Dynamic Testing Equipment	30
2.3.1 Electrodynamic Shaker	31
2.3.2 Measurement of Input Force - Force Plate.....	32
2.3.3 Measurement of Acceleration Response – Accelerometers.....	34
2.3.4 Cables.....	35
2.3.5 Multi-Channel Spectrum Analyzer	37
2.3.6 Single-Channel Spectrum Analyzer.....	39
2.4 Experimental Testing Methods.....	41
2.4.1 Chirp Signals.....	42
2.4.2 Instrumented Heel Drop.....	53
2.4.3 Driving Point Accelerance Frequency Response Functions	55

2.4.4 Sinusoidal Driving Functions	58
2.4.5 Unreferenced Measurements	62
2.4.6 Damping Estimates	65
2.4.7 Floor Test Area	74
2.4.8 Measurement Quality and Other Behavioral Investigations	76
2.4.9 Summary of Experimental Testing Methods	80
2.5 Classification of Floor Vibration Testing	83
 CHAPTER 3 Dynamic Testing and Behavior of In-Situ Floor Systems	87
3.1 In-Situ Floor Systems	87
3.2 Tested Floors #1 and #2 - New Jersey Office Building, NOC VII (24 th & 18 th Floors).....	88
3.2.1 Description of Tested Floors #1 and #2	88
3.2.2 Measurement Coverage of Tested Floors #1 and #2.....	94
Tested Floor #1 (NOC VII-24) Measurement Coverage	94
Tested Floor #2 (NOC VII-18) Measurement Coverage	100
3.2.3 Measured Floor Behavior – NOC VII (Tested Floors #1 and #2)	109
Measured Floor Behavior - NOC VII 24 (Tested Floor #1)	113
Measured Floor Behavior - NOC VII-18 (Tested Floor #2).....	125
3.3 Tested Floor #3 – VT KnowledgeWorks 2 Building, VTK2 (2 nd Floor)	161
3.3.1 Description of Tested Floor #3	161
3.3.2 Measurement Coverage of Tested Floor #3	165
3.3.3 Measured Floor Behavior – VTK2 (Tested Floor #3)	174
3.4 Summary and Implications of Observed In-situ Floor Behavior.....	211
 CHAPTER 4 Finite Element Modeling of Composite Floors for Vibration Serviceability	222
4.1 Finite Element Modeling of Composite Floors for Vibration Serviceability	222
4.1.1 Representing Mass, Stiffness, and Boundary Conditions	225
Mass & Materials	225
Stiffness.....	228
End Releases, Partial Fixity, and Boundary Conditions	232
4.1.2 Dynamic Finite Element Analysis Techniques for Floor Systems	237
Modal Analysis	237
Damping.....	240

Time-History Analysis and Steady State Analysis	242
4.2 Finite Element Analysis of Tested Floors.....	252
4.2.1 New Jersey Office Building, NOC VII.....	252
4.2.2 VT KnowledgeWorks 2 Building, VTK2	269
4.3 Summary of Recommended FE Modeling Techniques for Composite Floors.....	282
4.4 Floor Vibration Serviceability Evaluation Using the Finite Element Method	285
 CHAPTER 5 Conclusions and Recommendations for Future Research	296
5.1 Conclusions.....	296
5.1.1 Dynamic Testing of In-Floor Systems	297
5.1.2 Dynamic Behavior of In-Situ Floor Systems	298
5.1.3 Fundamental Modeling Techniques for Composite Floors	302
5.1.4 Evaluation of Vibration Serviceability of Floor Systems	304
5.2 Recommendations for Future Research	305
 REFERENCES	308
 APPENDIX A In-Situ Floor Framing Plans and Slab Details.....	313
APPENDIX B Design Guide 11 Analyses – FloorVibe Analysis Reports	316
APPENDIX C Single Channel Handheld Analyzer Measurements – NOC VII-24.....	332
APPENDIX D Single Channel Handheld Analyzer Measurements – VTK2.....	337
APPENDIX E Driving Point Accelerance Frequency Response Functions – NOC VII	344
APPENDIX F ME’scopeVES Modal Parameter Estimation – NOC VII.....	362
APPENDIX G Decay Measurements and Decay Curve Fit Analyses – NOC VII-18	374
APPENDIX H Driving Point Accelerance Frequency Response Functions – VTK2	387
APPENDIX I ME’scopeVES Modal Parameter Estimation – VTK2.....	402
APPENDIX J Decay Measurements and Decay Curve Fit Analyses – VTK2	411
APPENDIX K Example Composite Section Calculations	422
APPENDIX L Partial Fixity Curve for Assumed Moment-Rotation Relationship.....	425
APPENDIX M NOC VII – Composite Section Calculations & FE Model Input Values	427
APPENDIX N VTK2 – Composite Section Calculations & FE Model Input Values.....	431
VITA.....	436

LIST OF FIGURES

Figure 1.1: Recommended Peak Accelerations for Human Comfort due to Human Activities (Allen and Murray 1993; ISO 2631-2 1989)	6
Figure 2.1: Example Accelerance Frequency Response Function Plot	29
Figure 2.2: Modal Testing Schematic	30
Figure 2.3: Electrodynamic Shaker and Amplifier	31
Figure 2.4: Force Plate	32
Figure 2.5: Force Plate Calibration	34
Figure 2.6: PCB Model 393C Seismic Accelerometer	35
Figure 2.7: Accelerometer Cables – Coaxial (above) and Microdot (below)	36
Figure 2.8: Model 20-42 SigLab Digital Signal Processor	37
Figure 2.9: Ono Sokki CF-1200 Handheld FFT Analyzer	40
Figure 2.10: Typical 4-12 Hz Continuous Chirp Force Input Signal	43
Figure 2.11: Typical 4-12 Hz Chirp Signal Acceleration Response	44
Figure 2.12: Typical 4-12 Hz Continuous Chirp FRF Magnitude and Coherence (0-20 Hz)	45
Figure 2.13: Typical 4-12 Hz Continuous Chirp FRF Magnitude, Phase, and Coherence	45
Figure 2.14: Typical 4-12 Hz Burst Chirp Force Input Signal	47
Figure 2.15: Typical 4-12 Hz Burst Chirp Acceleration Response	48
Figure 2.16: Typical 4-12 Hz Burst Chirp Magnitude and Coherence (0-20 Hz)	49
Figure 2.17: Typical 4-12 Hz Burst Chirp Magnitude, Phase, and Coherence	50
Figure 2.18: Coherence Comparison of Continuous Chirp & Burst Chirp Excitation Signals	50
Figure 2.19: Armature Acceleration and Force Plate Autospectra for 5-10 Hz Burst Chirp	51
Figure 2.20: Driving Point Accelerance FRF Magnitude and Phase from Different References.	52
Figure 2.21: Instrumented Heel Drop	53
Figure 2.22: Instrumented Heel Drop Time Histories and Autospectra	54
Figure 2.23: Comparison of Chirp & Instrumented Heel Drop Force Input Autospectra	55
Figure 2.24: 35 Driving Point Accelerance FRFs (Magnitude, Phase, and Coherence)	57
Figure 2.25: Example Sinusoidal Excitation Force Time History & Autospectrum	59
Figure 2.26: Example Sinusoidal Acceleration Response Time History & Autospectrum	60
Figure 2.27: Comparison of Force and Acceleration Time Histories	61
Figure 2.28: Accelerance FRF Magnitude and Phase for a Sinusoidal Measurement	61
Figure 2.29: Sample Acceleration Time History to Unreferenced Heel Drop Excitation	63
Figure 2.30: Autospectra of Unreferenced Heel Drop and Chirp Measurements	64

Figure 2.31: Accelerance FRF – Driving at Point 281	69
Figure 2.32: Point 281 – Response Decay from 5.025 Hz.....	70
Figure 2.33: Point 281 – Decay Curve Fit, $\beta = 0.70\%$ at 5.025 Hz.....	70
Figure 2.34: Point 281 – Response Decay from 4.725 Hz.....	71
Figure 2.35: Accelerance FRF – Driving at Point 21	71
Figure 2.36: Point 21 – Response Decay from 4.875 Hz.....	71
Figure 2.37: Example Analytical Decay Curves with Multiple Frequencies	72
Figure 2.38: Accelerance FRF – Driving at Point 125	73
Figure 2.39: Point 125 – Response Decay from 5.05 Hz.....	73
Figure 2.40: Point 125 – Misinterpreted Curve Fit Decay.....	74
Figure 3.1: Newport Office Center (NOC) VII, Jersey City, New Jersey	88
Figure 3.2: NOC VII Floor Framing Layout (18 th and 24 th Floors).....	89
Figure 3.3: NOC VII General Layout of Tested Floors.....	90
Figure 3.4: Conditions of Tested Floor #1, NOC VII-24	91
Figure 3.5: Installation of Raised Flooring on NOC VII 24 th Floor	92
Figure 3.6: Conditions of Tested Floor #2, NOC VII-18	93
Figure 3.7: Chevron Bracing at End of Interior Core Partitions.....	93
Figure 3.8: NOC VII General Test Grid Point Numbers (Tested Floors #1 and #2).....	94
Figure 3.9: NOC VII-24 Excitation Locations	95
Figure 3.10: NOC VII-24 Shaker at Excitation Locations	96
Figure 3.11: NOC VII-24 Measurement Coverage - Shaker at Point 73.....	97
Figure 3.12: NOC VII-24 Measurement Coverage - Shaker at Point 69.....	98
Figure 3.13: NOC VII-24 Measurement Coverage - Shaker at Point 25.....	99
Figure 3.14: NOC VII-18 Excitation Locations	100
Figure 3.15: NOC VII-18 Shaker Located at Point 281	102
Figure 3.16: NOC VII-18 Burst Chirp Measurement Coverage (Forcing at Point 281)	102
Figure 3.17: NOC VII-18 Sinusoidal Measurement Coverage (Point 281 at 5.025 Hz).....	103
Figure 3.18: NOC VII-18 Shaker Located at Point 73	104
Figure 3.19: NOC VII-18 Measurement Coverage (Forcing at Point 73)	105
Figure 3.20: NOC VII-18 Burst Chirp Measurement Coverage.....	105
Figure 3.21: NOC VII-18 Shaker Located at Point 69 and Point 65	106
Figure 3.22: NOC VII-18 Reciprocal Measurement Coverage	107

Figure 3.23: NOC VII-18 Reciprocal Measurement Coverage	108
Figure 3.24: NOC VII-24 ME'scope Model of Full Coverage (Forcing at Point 73)	110
Figure 3.25: NOC VII-24 Driving Point Accelerance FRFs and Coherence (Point 73)	113
Figure 3.26: NOC VII-24 Driving Point FRFs with Curve Fit Overlay (Point 73).....	114
Figure 3.27: NOC VII-24 Driving Point Accelerance FRF (Point 69).....	115
Figure 3.28: NOC VII-24 Driving Point Accelerance FRF (Point 25).....	116
Figure 3.29: NOC VII-24 ME'scope Models	118
Figure 3.30: NOC VII ME'scope 3-Bay Centerline Model.....	119
Figure 3.31: NOC VII-24 3-Bay Centerline ODSs (Forcing at Point 73)	120
Figure 3.32: NOC VII ME'scope 10-Bay Centerline Model.....	121
Figure 3.33: NOC VII-24 10-Bay Centerline ODSs (Forcing at Point 73)	122
Figure 3.34: NOC VII-24 10-Bay Centerline ODS (magnified) at 5.80 Hz.....	123
Figure 3.35: NOC VII-24 End-Bay Area ODSs (Forcing at Point 73).....	124
Figure 3.36: NOC VII-18 Driving Point Accelerance FRFs (All Excitation Points).....	125
Figure 3.37: NOC VII-18 Driving Point Accelerance FRFs (6-Bay Strip)	126
Figure 3.38: NOC VII-18 Driving Point Accelerance FRFs and Coherence (Point 281)	128
Figure 3.39: NOC VII-18 10-Bay Strip ODSs (Forcing at Point 281)	129
Figure 3.40: NOC VII-18 Exterior Bay ODSs (Forcing at Point 281)	129
Figure 3.41: NOC VII-18 10-Bay Centerline ODSs (Forcing at Point 281)	130
Figure 3.42: NOC VII-18 Stepped Sine Sweep Linearity Investigation (Point 281)	131
Figure 3.43: NOC VII-18 Chirp Accelerance FRF Linearity Investigation (Point 281).....	132
Figure 3.44: NOC VII-18 3-Bay ODS Shape Comparison (Forcing at Point 281)	134
Figure 3.45: NOC VII-18 Driving Point Accelerance FRFs (Point 73)	135
Figure 3.46: NOC VII-18 End-Bay Area ODS at 5.05 Hz (Forcing at Point 73).....	136
Figure 3.47: NOC VII-18 End-Bay Centerline ODS at 5.05 Hz (Forcing at Point 73).....	137
Figure 3.48: NOC VII-18 End-Bay ODSs (Forcing at Point 73)	138
Figure 3.49: NOC VII-18 7-Bay ODS Shape Comparison (Forcing at Point 73)	139
Figure 3.50: NOC VII-18 Driving Point Accelerance FRFs (Point 69)	140
Figure 3.51: NOC VII-24 Driving Point Accelerance FRFs (Point 69)	140
Figure 3.52: NOC VII-18 Driving Point Accelerance FRFs (Point 65)	142
Figure 3.53: NOC VII-18 3-Bay Strip Accelerance FRFs (Multiple References)	143
Figure 3.54: NOC VII-18 3-Bay Centerline ODSs (Multiple References)	144
Figure 3.55: NOC VII-18 Driving Point Accelerance FRFs (Point 25)	146

Figure 3.56: NOC VII-24 Driving Point Accelerance FRFs (Point 25)	147
Figure 3.57: NOC VII-18 Driving Point Accelerance FRFs (Point 21)	148
Figure 3.58: NOC VII-18 Driving Point Accelerance FRFs (Point 117)	149
Figure 3.59: NOC VII-18 Driving Point Accelerance FRFs (Point 125)	150
Figure 3.60: NOC VII-18 Driving Point Accelerance FRFs (Point 177)	151
Figure 3.61: NOC VII-18 Driving Point Accelerance FRFs (Point 216)	153
Figure 3.62: NOC VII-18 Partially Open Bay F/G-4/5 (Adjacent to Point 333).....	153
Figure 3.63: NOC VII-18 Driving Point Accelerance FRFs (Point 333)	154
Figure 3.64: NOC VII-18 Reciprocal Accelerance FRF Comparison (Barrett et al. 2006)	155
Figure 3.65: VT KnowledgeWorks 2 Building (VTK2), Blacksburg, Virginia	161
Figure 3.66: VTK2 Floor Framing Layout	161
Figure 3.67: VTK2 Exterior Conditions of Tested Floor	163
Figure 3.68: VTK2 Exterior Wall Framing Attached to Tested Floor and Vertical Clip	163
Figure 3.69: VTK2 Surface Conditions of Tested Floor	164
Figure 3.70: VTK2 Stacked Construction Materials in Bays C/D-1/3 and D/E-1/3	164
Figure 3.71: VTK2 Underside Conditions of Tested Floor	165
Figure 3.72: VTK2 B-Wall Partition Framing on Underside of Tested Floor.....	165
Figure 3.73: VTK2 Test Grid Point Numbers (Tested Floor #3)	166
Figure 3.74: VTK2 Excitation Locations.....	166
Figure 3.75: VTK2 Mid-Bay Investigations and Reciprocal Measurement Coverage.....	168
Figure 3.76: VTK2 Measurement Coverage of Modal Sweep (Forcing at Point 126).....	170
Figure 3.77: VTK2 Shaker Located at Point 126 for Modal Sweep of 9-Bay Area.....	171
Figure 3.78: VTK2 Measurement Coverage of Modal Sweep (Forcing at Point 134).....	172
Figure 3.79: VTK2 Measurement Coverage of Modal Sweep (Forcing at Point 130).....	173
Figure 3.80: VTK2 Driving Point Accelerance FRFs (All Excitation Points)	174
Figure 3.81: VTK2 Driving Point Accelerance FRFs (By Bay Type)	175
Figure 3.82: VTK2 Driving Point Accelerance FRFs (Point 21)	177
Figure 3.83: VTK2 Driving Point Accelerance FRFs (Point 25)	179
Figure 3.84: VTK2 Driving Point Accelerance FRFs (Point 74)	180
Figure 3.85: VTK2 Driving Point Accelerance FRFs (Point 78)	181
Figure 3.86: VTK2 Driving Point Accelerance FRFs (Point 82)	182
Figure 3.87: VTK2 Multiple Day Driving Point Accelerance FRFs (Point 126).....	184
Figure 3.88: VTK2 Driving Point Accelerance FRFs (Point 126 Modal Coverage)	184

Figure 3.89: VTK2 Driving Point Accelerance FRFs (Point 126 Modal Coverage)	186
Figure 3.90: VTK2 Driving Point Accelerance FRFs (Point 130)	187
Figure 3.91: VTK2 Driving Point Accelerance FRFs (Point 134)	188
Figure 3.92: VTK2 Driving Point Accelerance FRFs (Point 178)	189
Figure 3.93: VTK2 Driving Point Accelerance FRFs (Point 182)	190
Figure 3.94: VTK2 Driving Point Accelerance FRFs (Point 186)	191
Figure 3.95: VTK2 Driving Point Accelerance FRFs (Point 230)	192
Figure 3.96: VTK2 9-Bay Area Multi-Reference FRFs (Forcing at Points 126 and 134)	194
Figure 3.97: VTK2 9-Bay Area ODSs from Forcing at Points 126 and 134.....	195
Figure 3.98: VTK2 9-Bay Area Curve Fit Mode Shapes	198
Figure 3.99: VTK2 Comparison of ODS at Strong Reference to Curve Fit Mode Shapes	199
Figure 3.100: VTK2 3-Bay Strip Multi-Reference FRFs (Points 126, 130 and 134).....	201
Figure 3.101: VTK2 3-Bay Strip ODS at 7.95 Hz (Forcing at Point 130)	201
Figure 3.102: VTK2 3-Bay Strip Curve Fit Mode Shapes	202
Figure 3.103: VTK2 Comparison of Reference Specific ODS & Curve Fit Mode Shapes.....	203
Figure 3.104: Comparison of Tested Bay's Driving Point FRFs (NOC VII-18 and VTK2).....	212
Figure 3.105: VTK2 Mid-Bay Accelerance FRFs (Forcing at Point 78)	219
Figure 3.106: VTK2 Example Shape Evaluation Using Mid-Bay Accelerance FRFs	220
Figure 3.107: VTK2 Curve Fit Mode Shape at 7.97 Hz (Max Response at Point 78)	220
Figure 4.1: 8-Bay Floor Model Example – Framing Member Layout	225
Figure 4.2: 8-Bay Floor Model Example – Plate Area Element Layout and Mesh.....	228
Figure 4.3: Representations of Composite Slab and Framing Members	229
Figure 4.4: 8-Bay Floor Model Example – End-Release and Partial Fixity	234
Figure 4.5: 8-Bay Floor Model Example – Pinned Supports Representing Interior Restraints .	236
Figure 4.6: 8-Bay Floor Example – Computed Frequencies and Mode Shapes	238
Figure 4.7: 8-Bay Floor Example – Applied Unit Load (1 lb) for Forced Response Analysis ..	243
Figure 4.8: 8-Bay Floor Example – Time History Response to Sinusoidal Load	245
Figure 4.9: 8-Bay Floor Example – Driving Point Accelerance FRF (Real and Imaginary)	247
Figure 4.10: 8-Bay Floor Example – Driving Point Accelerance FRF and Phase	248
Figure 4.11: 8-Bay Floor Example – Other Representations of Response	249
Figure 4.12: 8-Bay Floor Example – Examples Using Interpolated Hysteretic Damping	250
Figure 4.13: NOC VII – Floor Layout and Full Floor FE Model	253

Figure 4.14: NOC VII – Full Floor Model Moment End Releases and Partial Fixities	255
Figure 4.15: NOC VII – Full Floor Model Interior Restraints	255
Figure 4.16: NOC VII – Full Floor Model Computed Mode Shapes (Modes 1-12)	256
Figure 4.17: NOC VII – Full Floor Model Computed Mode Shapes (Modes 13-24)	257
Figure 4.18: NOC VII – Full Floor Model Mode Shape and ODS Comparison	258
Figure 4.19: NOC VII – Constant Damping Ratios Used in Steady State Analysis	260
Figure 4.20: NOC VII – Full Floor Accelerance FRFs (Points 21, 25, 69, 73).....	261
Figure 4.21: NOC VII – Full Floor Accelerance FRFs (Pts 65,117,125,177,216,281, & 333)..	262
Figure 4.22: NOC VII – 10-Bay Strip FE Model	263
Figure 4.23: NOC VII – 10-Bay Strip Model Computed Mode Shapes.....	265
Figure 4.24: NOC VII – 10-Bay Strip Model Mode Shape and ODS Comparison (Point 281)	265
Figure 4.25: NOC VII – 10-Bay Strip Model Mode Shape and ODS Comparison (Point 65) ..	266
Figure 4.26: NOC VII – 10-Bay Strip Model Accelerance FRFs.....	267
Figure 4.27: VTK2 – Floor Layout and FE Model.....	270
Figure 4.28: VTK2 – Moment End Releases and Partial Fixities.....	271
Figure 4.29: VTK2 – Interior Pinned Restraints.....	271
Figure 4.30: VTK2 – Computed Mode Shapes 1-7 (Tested Area of Floor)	272
Figure 4.31: VTK2 – Computed Mode Shapes 8-20 (Tested Area of Floor)	273
Figure 4.32: VTK2 – FE Mode Shape and Curve Fit Mode Shape Comparison	274
Figure 4.33: VTK2 – Dominant Mode Shapes (Points 25, 230, 21)	275
Figure 4.34: VTK2 – Computed Modes (Non-Tested Area of Floor and Double Curvature) ...	275
Figure 4.35: VTK2 – Constant Damping Ratios Used in Steady State Analysis	276
Figure 4.36: VTK2 – Accelerance FRFs (Points 21, 25, 230).....	277
Figure 4.37: VTK2 – Accelerance FRFs (Points 74, 78, 82).....	278
Figure 4.38: VTK2 – Accelerance FRFs (Points 126, 130, 134).....	279
Figure 4.39: VTK2 – Accelerance FRFs (Points 178, 182, 186).....	280
Figure 4.40: Proposed DG11 Design Accelerance Curves for Different Reduction Factors	288
Figure 4.41: FE Serviceability Evaluation Example – Accelerance FRFs and Design Curve ...	291
Figure 4.42: FE Serviceability Evaluation Example – All Bays	293

LIST OF TABLES

Table 1.1: Common Forcing Frequencies and Dynamic Coefficients (Murray et al. 1997)	8
Table 2.1: Digital Signal Processor Settings.....	39
Table 3.1: Summary of Test Settings and Parameters of Tested Floor #1, NOC VII-24	97
Table 3.2: Summary of Test Settings and Parameters of Tested Floor #2, NOC VII-18	101
Table 3.3: NOC VII-24 Pt 73 – Driving Point Curve Fit Estimated Frequencies & Damping ..	114
Table 3.4: NOC VII-24 Pt 69 – Driving Point Curve Fit Estimated Frequencies & Damping ..	116
Table 3.5: NOC VII-24 Pt 25 – Driving Point Curve Fit Estimated Frequencies & Damping ..	116
Table 3.6: NOC VII-24 Global Curve Fit Estimated Frequencies and Damping (Point 73).....	117
Table 3.7: NOC VII-18 Pt 281–Driving Point Curve Fit Estimated Frequencies & Damping ..	128
Table 3.8: NOC VII-18 Parameter Estimates at Various Excitation Levels (Point 281)	132
Table 3.9: NOC VII-18 Pt 73–Curve Fit Estimated Frequencies & Damping	136
Table 3.10: NOC VII-18 Pt 69–Driving Point Curve Fit Estimated Frequencies & Damping ..	141
Table 3.11: NOC VII-18 Pt 65–Driving Point Curve Fit Estimated Frequencies & Damping ..	142
Table 3.12: NOC VII-18 Multi-Reference Curve Fitting Shape Strengths	145
Table 3.13: NOC VII-18 Multi-Reference Curve Fit Estimated Frequencies and Damping	145
Table 3.14: NOC VII-18 Pt 25–Driving Point Curve Fit Estimated Frequencies & Damping ..	147
Table 3.15: NOC VII-18 Pt 21–Driving Point Curve Fit Estimated Frequencies & Damping ..	148
Table 3.16: NOC VII-18 Pt 117–Driving Point Curve Fit Estimated Frequencies & Damping ..	149
Table 3.17: NOC VII-18 Pt 125–Driving Point Curve Fit Estimated Frequencies & Damping ..	150
Table 3.18: NOC VII-18 Pt 177–Driving Point Curve Fit Estimated Frequencies & Damping ..	152
Table 3.19: NOC VII-18 Pt 216–Driving Point Curve Fit Estimated Frequencies & Damping ..	153
Table 3.20: NOC VII-18 Pt 333–Driving Point Curve Fit Estimated Frequencies & Damping ..	154
Table 3.21: NOC VII-18 Summary of Decay Curve Fit Damping Estimates	157
Table 3.22: NOC VII-18 Summary of Dominant Frequency & Damping Estimates (All Bays).....	158
Table 3.23: NOC VII - DG11 Predicted Beam/Girder/System Frequencies (Hz).....	159
Table 3.24: Summary of Test Settings and Parameters of Tested Floor #3, VTK2	167
Table 3.25: VTK2 Point 21 – Driving Point Curve Fit Estimated Frequencies and Damping...	178
Table 3.26: VTK2 Point 25 – Driving Point Curve Fit Estimated Frequencies and Damping...	179
Table 3.27: VTK2 Point 74 – Driving Point Curve Fit Estimated Frequencies and Damping...	181
Table 3.28: VTK2 Point 78 – Driving Point Curve Fit Estimated Frequencies and Damping...	182
Table 3.29: VTK2 Point 82 – Driving Point Curve Fit Estimated Frequencies and Damping...	183

Table 3.30: VTK2 Point 126 – Driving Point Curve Fit Estimated Frequencies and Damping.	185
Table 3.31: VTK2 Point 130 – Driving Point Curve Fit Estimated Frequencies and Damping.	187
Table 3.32: VTK2 Point 134 – Driving Point Curve Fit Estimated Frequencies and Damping.	188
Table 3.33: VTK2 Point 178 – Driving Point Curve Fit Estimated Frequencies and Damping.	190
Table 3.34: VTK2 Point 182 – Driving Point Curve Fit Estimated Frequencies and Damping.	191
Table 3.35: VTK2 Point 186 – Driving Point Curve Fit Estimated Frequencies and Damping.	192
Table 3.36: VTK2 Point 230 – Driving Point Curve Fit Estimated Frequencies and Damping.	193
Table 3.37: VTK2 9-Bay Area Multi-Reference Curve Fitting Shape Strengths and Estimated Frequencies and Damping.....	198
Table 3.38: VTK2 3-Bay Area Multi-Reference Curve Fitting Shape Strengths and Estimated Frequencies and Damping.....	202
Table 3.39: VTK2 Consolidated Summary of Curve Fit Estimated Frequency & Damping	204
Table 3.40: VTK2 Summary of Decay Curve Fit Estimates of Damping	206
Table 3.41: VTK2 Summary of Dominant Frequency and Damping Estimates – Part 1.....	207
Table 3.42: VTK2 Summary of Dominant Frequency and Damping Estimates – Part 2.....	208
Table 3.43: VTK2 - DG11 Predicted Beam/Girder/System Frequencies (Hz)	210
Table 4.1: NOC VII – Composite Slab Parameters & Slab Area Element/Material Properties.	253
Table 4.2: NOC VII – Computed Modes for Full Floor Model.....	256
Table 4.3: NOC VII – Computed Modes for 10-Bay Strip Model	264
Table 4.4: VTK2 – Composite Slab Parameters and Slab Area Element/Material Properties ...	269
Table 4.5: VTK2 – Computed Modes.....	272
Table 4.6: FE Serviceability Evaluation Example – Change in Computed Frequencies.....	290

CHAPTER 1

INTRODUCTION AND LITERATURE SURVEY

1.1 Introduction

Low-frequency floor vibration serviceability problems typically arise when a floor is excited in resonance due to a walking excitation and the resulting accelerations exceed human comfort levels (Murray et al. 1997). Excessive discomfort of occupants can result in complaints or even loss of productivity. If the discomfort of the affected personnel becomes overwhelming, the occupants may opt for extreme measures such as litigation or relocation to another facility, and consequently the unoccupied structure will no longer fulfill its intended purpose. While most floor vibration problems are not this extreme, the scenario highlights the potential significance of this serviceability problem. The measures required to resolve an annoying floor vibration problem after the building is constructed can be very difficult and expensive to implement. In most cases, the costs of fixing the problem in-situ are much greater than tackling the problem in the design phase prior to the floor's construction, which doesn't even include the potential cost to building owners from legal expenses, loss of rental revenue, or consultation fees (Hanagan 2005). The easiest "fix" for a floor vibration problem is avoidance: simply designing a floor such that it's unlikely to experience a vibration serviceability problem. Avoidance becomes particularly important in the design of tall buildings, which can have the same floor framing plan for 20+ stories at a time. The key to avoidance is the ability to predict the dynamic behavior of the floor in the design stage and to determine if it will be a problem under service conditions, a task much easier said than done, and the subject of much of the floor vibration research to date.

The popularity of open office plans has led to the specification of larger bay sizes and longer spans in floor systems. In such cases, the economical floor of choice is typically a steel composite floor design that includes concrete on metal deck supported by steel framing members. Unfortunately, despite satisfying strength requirements and traditional live load stiffness criteria, this floor type coupled with the fit out (or lack thereof) of open office floor

plans can be quite susceptible to annoying floor vibration problems due to walking excitation and consequently is the subject of this research effort.

Various design guides and codes around the world address vibration serviceability in the same general manner: outline simplified hand calculation methods for estimating the dynamic properties of a floor system, estimate an applied dynamic load that simulates walking forces, and finally compute the dynamic response of the system to the applied loads for comparison with an established level of acceptability. Although the current design guidance is generally acceptable, it is filled with generalizations for application to the widest variety of floor layouts, and thus predictions of frequency or other dynamic properties may differ considerably from the actual properties of the floor. Unique or non-standard framing, different beam sizes between columns, moment connections, and interior floor-to-ceiling partitions are all examples of common deviations not typically accounted for in the simplified design methods. However, such deviations can be addressed when floors are modeled in a finite element (FE) analysis program. Unfortunately, the simple mention of a finite element model of a floor system elevates the level of effort for checking floor vibration serviceability well beyond “a simplified hand calculation method.”

Finite element modeling for vibration serviceability is not meant to be a replacement for standard evaluation methods, but a specialized approach to be used when needed. A good analogy of this approach is current practices in seismic analysis, where lower levels of analysis such as the Equivalent Lateral Force procedure satisfy most requirements, but further interest in the response of a structure may call for a more advanced inelastic response history analysis. The development of finite element models of any level of complexity is fairly involved and requires some amount of experience. However, despite the level of experience of the individual creating the model, the one thing that holds true is that the model is only as good as the assumptions and parameters used in its creation. Research in developing FE models of floor systems validated by high-quality experimental measurements provides the best way for identifying fundamental modeling techniques, including the validation of assumptions, and paves the way for advanced vibration serviceability evaluation using the finite element method.

1.2 Scope of Research

The purpose of this study is to examine the dynamic behavior of in-situ composite steel floors and to generate a set of general FE modeling techniques for modeling these floor systems

using a commercially available FE analysis program, where the resulting dynamic analysis yields an acceptable prediction of response for evaluation of vibration serviceability. The desired goals of the research are as follows:

- Identify and summarize best practices in dynamic testing of in-situ floor systems, including comments on equipment, experimental techniques, and measurement analysis. Develop a classification system for floor vibration testing for use by researchers, consultants, and building owners, broken down by equipment and techniques employed, as well as the information available from each class of testing.
- Conduct experimental dynamic testing of in-situ multi-bay steel composite office floors using an electrodynamic shaker to identify general trends in dynamic behavior of the floor system. Directly measure response of the floor system to steady-state and broadband excitation and determine the dynamic properties of frequencies, damping, and mode shapes.
- Create finite element models of the tested floors and use the experimentally measured dynamic properties to validate each floor's corresponding FE model. From the validated FE models, the identified fundamental modeling techniques include methods for representing the mass, stiffness, and boundary conditions of the floor, as well as incorporating an assumed (or measured) level of damping into the model for use in dynamic response analysis.
- Propose a method for floor vibration serviceability evaluation using the finite element method.

Chapter 2 provides background theory on experimental modal analysis and highlights the testing techniques employed to identify the dynamic properties and behavior of the floor systems. Besides describing some best practice techniques for testing floor systems, Chapter 2 also provides a classification system for different levels of dynamic floor testing as described above. A data set of high quality dynamic measurements was obtained through experimental testing of three in-situ steel composite office floors, as summarized in Chapter 3. Measurements from these in-situ floors provide an adequate sample of stiffness, geometry, and boundary conditions for identification of the FE modeling trends required to bring experimental and analytical results into agreement. Although three in-situ floors may seem to be a low number of test specimens, additional samples come from bays of variable geometry and boundary conditions within each floor's own assemblage. The parameters and validation of the tested floor systems' FE models are presented in Chapter 4. The fundamental techniques used in

creating the models are a product of validation using the high quality dynamic measurements described in Chapter 3. Chapter 4 also includes a proposed method for using the results of the finite element analysis as a tool for floor vibration serviceability evaluation due to walking excitation. Finally, Chapter 5 summarizes the results from the entirety of the presented research and provides recommendations for future endeavors in the topic.

1.3 Literature Survey

Structures susceptible to vibration serviceability problems include floors, footbridges, stadia, and even stairs, among others. The available literature on vibration serviceability is vast when considering the multidisciplinary aspects of the subject, which includes the physical components and properties of the structure, the biomechanics of the imperfect and probabilistic nature of human walking, the dynamic response of the structures to such loads, and even identifying the actual level of dynamic response that is unacceptable to the human receptor. The information presented in the following literature survey does not cover all aspects of vibration serviceability; it only focuses on summarizing the state of the practice as it pertains to the presented research. Additionally, some summaries presented in the literature survey are cursory, as more detailed coverage of the subject is more appropriately presented in the chapters that delve deeper into that topic.

1.3.1 Background

Vibration serviceability is by no means a new issue for designers to tackle, as indicated by Tredgold (1828), who published one of the first known stiffness criteria with the intent of avoiding vibration problems. This criterion simply suggested sufficient depth of girders with long spans to avoid “shaking everything in the room.” Nearly 40 years ago, Lenzen (1966) noticed that advances in technology and materials led to lighter types of floors with little decrease in factors of safety. As a result, the economical floor systems occasionally resulted in noticeable floor vibrations caused by human impact even though the designs satisfied code stiffness criteria. As such, the Steel Joist Institute sponsored its first initiative to research the vibration of steel joist-concrete slab floor systems (Lenzen 1966). Research in the subject persisted in the following years and continues today.

While not listed here in detail, the subsequent research studied and refined techniques for evaluating the two most basic components of the vibration serviceability issue (1) the dynamic

response of a floor system subject to human excitation and (2) the tolerance levels of human subject to the dynamic response. Presently in North America, the design guidance most often used for composite steel framed floor systems is the *AISC/CISC Steel Design Guide Series 11: Floor Vibrations Due to Human Activity* (Murray et al. 1997).

1.3.2 AISC/CISC Steel Design Guide Series 11: Vibrations Due to Human Activity

Design Guide 11 (DG11) contains simplified hand calculation methods for evaluating the vibration serviceability of floors. In short, each bay (as defined as a generally rectangular area between four or more columns) within the floor system that has unique framing is evaluated using DG11's procedures for walking excitation. Each evaluation involves two sets of calculations: one to compute the fundamental frequency of the bay and another to compute the maximum amplitude of acceleration. Evaluation results from comparing the predicted peak acceleration with human tolerance levels. The following inequality represents the comparison:

$$\frac{a_o}{g} \geq \frac{a_p}{g} = \frac{P_o e^{-0.35 f_n}}{\beta W} \quad (1.1)$$

where

- a_o/g = human tolerance level of peak acceleration (as a fraction of gravity)
- a_p/g = estimated peak acceleration due to walking excitation (as a fraction of gravity)
- P_o = a constant force
- f_n = fundamental natural frequency of the system
- β = modal damping ratio
- W = effective weight of the system

The left side of Inequality (1.1) represents the human tolerance level of peak acceleration, expressed as a fraction of gravity. The right side of the inequality represents the computed peak acceleration within the bay due to walking excitation, expressed as a fraction of gravity. The individual parameters involved in the evaluation are discussed further in the remainder of this section but will not be expanded upon beyond the extent that they relate to the presented research. Detailed treatises of the parameters can be found either directly within DG11 or the corresponding references listed in DG11. The topics that are of particular interest are the human perception limits due to walking excitation, the representation of stiffness in steel composite floor systems (for use in determining natural frequency), and the dynamic forces involved with walking excitation.

Human Perceptibility

The human response to floor motion is a complex perception issue that involves a variety of environmental factors, most notably the magnitude and duration of the motion, visual or audible cues, and activity (or lack thereof) of the affected person (Hanes 1970). In general, studies of human perception and tolerance of vibrations indicate that acceleration is the best overall indicator of potential discomfort of humans due to floor motion (Ellingwood 1989). DG11 acceleration criteria are based on the chart shown in Figure 1.1, which was developed using baseline acceleration limits recommended by the International Standards Organization (ISO 2631-2 1989) that were adjusted for intended occupancy and experience (Allen and Murray 1993).

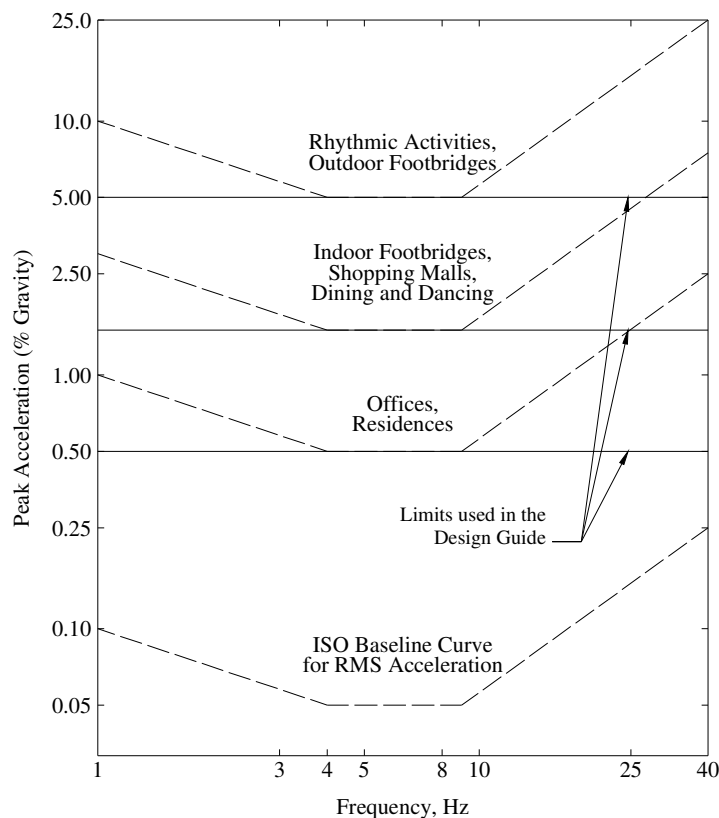


Figure 1.1: Recommended Peak Accelerations for Human Comfort due to Human Activities (Allen and Murray 1993; ISO 2631-2 1989)

DG11 suggests the peak acceleration used as the threshold for human comfort in offices or residences subjected to vibration frequencies between 4 Hz and 8 Hz is 0.005g, or 0.5% of gravity. The lower threshold within the frequency range of 4 to 8 Hz can be explained by studies showing humans are particularly sensitive to vibrations with frequencies in the 5-8 Hz range,

corresponding with typical natural frequencies of many of the main organs in the body (Griffin 1990, Murray 1991).

The 0.5%g acceleration limit within a range of 4 to 8 Hz is highlighted because it represents the frequency range that may be excited with the second or third harmonic of walking, where a harmonic is defined as an integer multiple of the step frequency. Under normal walking, human footfalls average about 2 steps per second, but can get up to about 2.4 steps per second. If each downward step is seen as an input force, then for instance, the second and third harmonic of the 2.4 Hz input force are 4.8 Hz and 7.2 Hz, respectively. Floors that have a natural frequency at or near one of these harmonics may exhibit an excessive response because the input force component of the harmonic may coincide with the resonant frequency of the floor (Bachmann 1995).

Acceleration Response

The expression for estimated peak acceleration shown in Inequality (1.1) was determined by modeling the floor (or more appropriately one bay of a floor system with some corresponding effective weight) as a simplified spring-mass-damper system driven at its natural frequency by an effective harmonic force due to walking, resulting in a resonant response.

The effective harmonic force term $P_o e^{-0.35 f_n}$ of Inequality (1.1) is based on representing the time-dependent repeated force of a person walking across a floor, $F(t)$, as a Fourier series, or combination of sinusoidal forces, comprised of the harmonics of the walking pace:

$$F(t) = P \left[1 + \sum_i \alpha_i \cos(2\pi i f_{step} t + \phi_i) \right] \quad (1.2)$$

where P = person's weight (taken as 157 lbs in DG11)

α_i = dynamic coefficient for the i^{th} harmonic force component

i = harmonic multiple of the step frequency

f_{step} = step frequency of the person walking

t = time

ϕ_i = phase angle for the harmonic

DG11 assumes that only one of the harmonic components of Equation (1.2) will be associated with the floor's natural frequency, inciting resonant response of that mode, and that the response due to all other harmonics of the step frequency will be small in comparison. Thus, the time-dependent harmonic force component corresponding to the natural frequency of the floor is:

$$F_i(t) = P\alpha_i \cos(2\pi i f_{step} t) \quad (1.3)$$

DG11 suggests the dynamic coefficients for walking excitation shown in Table 1.1. This stepped relationship for the dynamic coefficients was simplified by approximating the steps at the various frequency ranges by the term $\alpha = 0.83e^{-0.35f_n}$.

Table 1.1: Common Forcing Frequencies and Dynamic Coefficients (Murray et al. 1997)

Harmonic i	Person Walking	
	f (Hz)	α_i
1	1.6 - 2.2	0.5
2	3.2 - 4.4	0.2
3	4.8 - 6.6	0.1
4	6.4 - 8.8	0.05
α is the peak sinusoidal force divided by the weight of the person(s)		

Pernica (1990) also computed the dynamic coefficients from measured forces of individuals performing rhythmic activities, including walking, which fell within the range of those suggested in Table 1.1. Kerr (1998) conducted an extensive experimental study on vertical footfall forces. Young (2001) analyzed the harmonic components of each of Kerr's 882 single step force time histories and developed a similar table of dynamic coefficients for the first four harmonics of walking. Rather than constant values for the dynamic coefficient for frequencies that fell within a particular harmonic range, he developed linear functions within the ranges. Although not shown here, they are in general agreement with the values suggested by Table 1.1. They are similarly stepped in nature within various frequency ranges, although Young's steps have a slight upward slope.

The resonant response function presented in DG11, resulting from the single harmonic force component causing the resonant response, is in the form:

$$\frac{a}{g} = \frac{R\alpha_i P}{\beta W} \cos(2\pi i f_{step} t) \quad (1.4)$$

where a/g is the floor acceleration, expressed as a fraction of gravity. R is a reduction factor taken as 0.5 for floor structures with two-way mode shape configurations to account for the fact that "full steady-state motion is not achieved for walking and that the walking person and the person annoyed are not simultaneously at the location of maximum modal displacement." This expression for steady-state acceleration due to harmonic resonance is given by Rainer et al. (1988) and Allen and Murray (1993). For evaluation purposes, Equation (1.4) reduces to the

peak acceleration expression on the right side of Inequality (1.1), where the numerator, $P_o e^{-0.35 f_n}$ is just a simplified expression containing the 157 lb person's weight, the 0.5 reduction factor mentioned above, and the dynamic coefficient in the form $\alpha = 0.83 e^{-0.35 f_n}$, and can be viewed as the effective harmonic force applied at the midpoint of the bay that represents the forces generated by a person walking.

Frequency and Effective Weight Estimation

DG11 procedures for predicting the natural frequency of a floor system for use in Inequality (1.1) consists of a series of calculations for the simply supported beam/joist and girder panel frequencies and ultimately a combination of these to represent the system frequency, f_n , using Dunkerly's relationship:

$$\frac{1}{f_n^2} = \frac{1}{f_j^2} + \frac{1}{f_g^2} \quad (1.5)$$

where f_j, f_g = fundamental frequency of the joist and girder panel, respectively

Although the equations are not shown here for the individual panel frequencies, the procedure involves computing the maximum static deflection of the beam/joist or girder panel assuming it is uniformly loaded, simple supported, and exhibits composite action between the deck/slab system and the steel framing member, provided they are in continuous contact, regardless of whether or not the floor was designed with composite connectors. The latter assumption is based on the extremely small displacements involved with floor vibrations, in which the resulting shear forces at the slab/member interface are resisted by construction spot welds or friction.

The DG11 recommendations for computation of the beam/joist and girder panel stiffness are noted because the methods for computing stiffness are applied to the framing members in the finite element models of the presented research. DG11 recommends that when calculating the transformed moment of inertia for the beam/joist or girder panel, the modulus of elasticity of concrete is taken as 1.35 times the current structural standard, as shown in Equation (1.6), to account for the greater stiffness of concrete on metal deck under dynamic loading.

$$E_c = w^{1.5} \sqrt{f_c'} \quad (1.6)$$

where E_c = modulus of elasticity of concrete (ksi)

w = unit weight of concrete (lb/ft³)

f_c' = compressive strength of concrete (ksi)

There are additional recommended limitations on effective width of the concrete slab that differ from those currently used for strength design. For beam and girders, the effective slab width is taken as the member spacing, but not greater than 0.4 of the member span. This limitation is cut in half for spandrel members, where the effective slab width is half the adjacent spacing (plus spandrel edge overhang), but not more than 0.2 of the member span. Stiffness adjustments are recommended for open web joists and joist girders to account for the effects of joist seats, web shear deformation, and eccentricity or joints.

The final two parameters required for the right side of Inequality (1.1) to estimate the peak acceleration response are the effective panel weight, W , and the modal damping, β . DG11 outlines a series of calculations used to determine the effective panel weight of the system as a function of relative stiffness of components, continuity factors, and floor geometry. Unless otherwise measured, the modal damping parameter must be estimated based on experience and recommended values for the expected final condition (office fit out) of the evaluated floor. For offices (the type of floor use of this research), DG11 recommends the following values for damping ratios: 0.02 for floors with few non-structural components (ceilings, ducts, partitions, etc.), 0.03 for floors with non-structural components and furnishings, but with only small demountable partitions, and 0.05 for full height partitions between floors.

1.3.3 Floor Vibration Experimental Testing and Finite Element Modeling

The following is a survey of the literature with particular regard to experimentally tested steel composite floor systems (or similar), measurement comparison of finite element models with tested systems, and general steel composite floor finite element modeling techniques. Note that the phrase “unreferenced measurement” used throughout is meant to describe vibration response measurements taken outside the traditional experimental modal analysis setup whereby the input force is explicitly measured simultaneously with the response. This typically applies where just the acceleration response from heel drop and walking excitations were measured, unless expressly noted as an instrumented heel drop. A more detailed explanation of experimental modal testing is presented in Chapter 2; however a brief summary of experimental modal testing as it applies to floor structures is presented, as this is the basis of the experimental work in the presented research.

Modal Testing

In contrast to response-only dynamic measurements, modal testing offers an expanded capability to characterize the dynamic properties of a floor by measuring both the input force and output response and forming a frequency response function (FRF) between the excitation and measurement locations. The advantage of knowing this relationship for a set of points on a structure is that in addition to frequency and damping estimates, the mode shapes can be estimated from the magnitude and phase information contained in the complex frequency domain FRFs (Ewins 2000). Hanagan et al. (2003) noted the ability to express the behavior of a floor system in terms of its modal properties provides a consistent baseline for comparing the results of finite element analysis and actual measured behavior.

A “heel drop” refers to an impulse load excitation frequently used to evaluate floors. A heel drop is an impact force caused by a person assuming a natural stance, maintaining straight knees, shifting their weight to the balls of the feet, rising approximately 2.5 in. on their toes, and then suddenly relaxing to allow their full weight to freefall and strike the floor with their heels. The force-time relationship of the resulting impulse load is normally approximated by a triangular pulse load with an initial magnitude of 600 lbs. decreasing to zero over 0.05 seconds (Ohmart 1968). An obvious advantage of this type of impulse excitation is how easy it is to perform and that it does not require any equipment other than what is needed to measure the response (Blakeborough and Williams 2003). Unfortunately, no matter how consistent experimentalists are in performing heel drops, it still remains an unmeasured input unless conducted on an instrumented device. To that end, Blakeborough and Williams (2003) evaluated the use of an instrumented heel drop test as an alternative source of excitation for performing modal analysis on floor systems. They concluded the instrumented heel drop was a more effective modal testing technique than an instrumented impact hammer because it gave better results at lower frequencies, while sufficiently exciting the structures with frequencies in the range of 1 to 15 Hz, which is the range of interest for floor vibration problems due to walking excitation. Hanagan et al. (2003) also concluded the instrumented heel drop yielded high quality data and served as a good alternative to an electrodynamic shaker when cost and portability are an issue.

The literature covering the techniques and application of the different methods of modal testing to obtain quality and consistent measurements is quite vast as it mostly spans the

automotive and aerospace industries. Ewins (2000) text is a very comprehensive source on modal testing theory, practice, and application. A few researchers in floor vibration research have published works evaluating the most common techniques for testing floors and procedures for ensuring quality and consistent measurements. Most notably, Pavic and Reynolds published a series of articles on experimental assessment of office floors using modal testing, impact hammer versus shaker excitation, and quality assurance procedures for modal testing of building floors (Pavic and Reynolds 1999, Reynolds and Pavic 2000a, 2000b). Hanagan et al. (2003) expanded on the articles by applying the different modal testing techniques and quality control procedures to a steel composite laboratory floor with the intent of characterizing the best technique and providing a set of guidelines for others performing future research. Pavic, Reynolds, and Hanagan all agreed that modal testing using an electrodynamic shaker yielded the highest quality experimental data, albeit at a much higher equipment cost.

Laboratory/In-situ Floor Testing and Finite Element Modeling Techniques

The following is a chronological survey of the selected literature involving experimental testing and modeling of floor systems. The topics of experimental testing of laboratory floors, in-situ floors, and finite element modeling are presented in a single section because most of the literature found contained all three topics, and it would be difficult or repetitive to discuss separately.

Pernica and Allen (1982) tested several floor areas of a shopping center of steel beam composite deck construction. Dynamic properties, including peak accelerations, were determined from un-measured heel drop and walking input excitations.

Rainer and Swallow (1986) tested a very long span (105 ft) steel-joist concrete-slab gymnasium floor using two electrodynamic shakers to drive the floor sinusoidally at varying frequencies to determine the floor's frequencies, mode shapes, and damping. Although peak acceleration levels were reported for various rhythmic activities, the peak acceleration levels and corresponding input forces from the steady-state shaker excitation were not.

Eriksson (1994) investigated the behavior of in-situ low-frequency floors constructed of prestressed concrete elements. He performed experimental modal analysis on six in-situ floors and performed analytical studies on three of the floors using finite element analysis.

Shope and Murray (1994) recorded accelerations on a laboratory test floor and an in-situ long span (52 ft) steel joist composite floor identified from occupant complaints of excessive levels of vibrations. The authors presented unreferenced acceleration time histories of both structures from heel drop and walking excitations, and the study included the successful implementation of tuned-mass dampers to reduce the acceleration response.

Kitterman (1994) investigated several vibration characteristics of steel member supported floors, particularly the effective width of one-way steel joist and steel beam-concrete slab floors and the effective moments of inertia of steel joist and joist-girder members. The author created finite element models of numerous theoretical floors and performed a dynamic response analyses to synthesized heel drop impacts. The only experimental work conducted was on an atypical steel joist and joist-girder laboratory floor, investigating the ability of joist seats to transfer shear from the supporting girder to the overlying slab. The experimental work included finite element modeling and frequency measurements. Finite element modeling techniques recommended by Kitterman were incorporated in the presented research.

Pavic et al. (1995) performed impact hammer modal testing of a large concrete parking garage floor and performed finite element modeling. Although his investigation involved a concrete structure and not a steel composite structure, Pavic concluded that using significantly higher values for modulus of elasticity of concrete was needed to bring computed results into agreement with measured frequencies. This agreed with the DG11 recommendation of using 1.35 times the computed modulus of elasticity for concrete (Murray et al. 1997).

Rottmann (1996) investigated the use of tuned mass dampers to control annoying floor vibrations in steel composite floor systems, which involved experimental measurements of a laboratory test floor and multiple bays of an in-situ office floor found to have problems. The study included acceleration time history response measurements due to heel drop and walking excitation, as well as the Fast Fourier Transform (FFT) of the time history data to examine frequency content and determine the floor's frequencies (response measurements only, not input force). The author created finite element models of the tested structures and used explicit springs at the boundaries to account for support flexibility and to bring computed frequencies into agreement with those measured. Dynamic response analysis due to a synthesized heel drop function was conducted on the FE model.

Band (1996) investigated the vibration characteristics of long span composite joist floors. He tested four in-situ floors with spans ranging from 45 ft to 117 ft by measuring the time history acceleration response due to heel drop impact and performing an FFT to evaluate the frequency content. He chose to report all response measurements in terms of peak displacement, which was derived from integrating the acceleration response. A test floor was constructed with the intent of evaluating modification techniques to joist floors for increasing floor frequency.

The research conducted by Khoncarly (1997) most closely follows the presented research. The objective of his study was to develop practical guidelines, in the form of simplified response spectra, for use in the evaluation and design of steel composite office floor systems subject to walking excitation. The researcher measured the response due to unreferenced heel drop and walking excitation of one in-situ steel joist composite office floor identified to have problems with annoying floor vibrations. Khoncarly identified that loads from footfall excitation should be modeled within a dynamic finite element analysis by taking into account the time-dependent spatial variability of each footfall as the repeated footfalls move across a floor (i.e. applying footfall pulse loads at different stride locations in sequence at their respective arrival times). The response measurements taken from the in-situ floor were used to calibrate his finite element model. From this single floor test and model, he expanded the modeling technique to a variety of “ideal” office floor models and computed the dynamic response from walking excitation, which was used to generate the response spectra for evaluating acceptability. Like most floor vibration researchers, he had no way to directly measure the spatially varying footfall forces on the in-situ floor at the same time the response measurements were obtained. The calibration of his finite element model of the in-situ floor (and all subsequent models) was based on the comparison of the computed response due to a simulated load to an unreferenced measured response of the in-situ floor due to an actual walking load. In reality, the actual load may have varied more significantly than the assumed simulation. To account for this, the simulated load was based on his research that included measuring the actual force-time history records of different individuals walking at various paces to model the magnitude, duration, stride length, and overlap of the footfall forces. It is this writer’s opinion that the reference “ideal” floors the author modeled and used to develop the design/evaluation response spectra were overly simplified for use with many floor systems of different geometry,

although the response spectra approach may be worthwhile for future research provided a valid modeling technique is used.

Beavers (1998) investigated the most effective way of finite element modeling steel joist supported floors to predict the first natural frequency. His models were compared to the experimentally measured natural frequencies of six concrete slab steel joist floors: four laboratory test floors and two in-situ office floors. His modeling technique explicitly defined each of the joist web and chord members and used rigid links to position the plate elements at the slab centroid to the proper distance above the centerline of the top joist chords. With this technique, he successfully matched the first natural frequency. Beavers reported measured and modeled first natural frequencies, but did not include any force-response measurements or analyses.

Falati (1999) mainly investigated the effects of non-structural components on the dynamic behavior of concrete floors using a slender one-way span, 50% scaled post-tensioned concrete slab, although his research also included testing of an in-situ steel composite concrete floor subject to various excitations. He recorded the acceleration response to unreferenced heel drop and walking excitations as well as measured forced-vibration testing using a shaker, allowing him to estimate frequencies, mode shapes, and damping. Shaker testing only included measurements from the mid-bay location of one bay on one in-situ occupied floor. Accelerance frequency response functions (acceleration response per unit of input force) from the modal testing were reported, as were the acceleration response time histories from the unreferenced excitations. He reported the quality of the accelerance frequency response function measurements were much higher for an in-situ floor using shaker excitation than for impact hammer excitation due to the shaker's ability to provide more energy to the larger system.

Sladki (1999) used finite element modeling of steel composite floors to predict the fundamental frequency of vibration and the peak acceleration due to walking excitation as given in DG11. He concluded his modeling techniques were able to predict the fundamental frequency of the floor more accurately than DG11, but were unable to accurately predict the acceleration response of the floor to a given dynamic load. He concluded the inaccurate predictions were the result of applying dynamic loads to the models that were not measured values, but were estimations of the applied force.

Alvis (2001) used finite element modeling of steel composite floors to predict peak

accelerations due to sinusoidal loads with magnitudes suggested by DG11. He conducted experimental modal analysis on several laboratory test floors to obtain their dynamic properties, and applied known (measured) sinusoidal loads to measure peak response. While the frequency and mode shapes of the FE models matched well, he concluded the computed peak accelerations did not match well with the measured values, and speculated the value of damping used in the FE model was the source of the discrepancy. Alvis also compared peak accelerations predicted by the FE method and DG11, which did not correlate well. He concluded the source of discrepancy between the two was that the modeling technique did not account for the effective area of the floor system that actually vibrates due to energy dispersion and frictional damping.

El-Dardiry et al. (2002) conducted a vibration study on the long span (25 ft) flat plate concrete floor of a full-scale laboratory test building and calibrated a finite element model on the floor from only natural frequency measurements of unreferenced heel drop excitations. The researchers concluded that to match natural frequencies, the FE models had to include column elements at the supports to account for the rotational restraint provided to the slab at its boundaries. Reynolds et al. (1999) and Pavic et al. (2001) also suggested to explicitly include columns when modeling reinforced concrete and post-tensioned concrete floors.

Warmoth (2002) investigated the effect of joist seats on effective girder moment of inertia and girder frequency of steel joist composite systems. The frequency spectra of several laboratory test floors were measured. He proposed a method for calculating the effective moment of inertia based on the type of joist seats used in the composite construction, which is insightful for use of the presented research techniques for FE modeling of the stiffness of steel joist floor systems.

Boice (2003) evaluated different methods for predicting the fundamental frequency for a bay as well as the predicted acceptability of a floor system based on computed peak accelerations. He evaluated the different methods by comparing measured fundamental frequencies and subjective floor evaluations with the corresponding values predicted by four commonly used methods: AISC/CISC Design Guide 11, Steel Construction Institute (SCI) *Design Guide for Vibrations of Long Span Composite Floors* (UK standard, Hicks et al. 2000), Murray Criterion (Murray 1979), and the Modified Reiher-Meister scale (Lenzen 1966; Murray 1975). He concluded that the SCI procedure most accurately predicted the fundamental

frequency of the bay, but overall DG11 most accurately evaluated a floor's acceptability based on comparison to 78 existing in-situ floor case studies.

Ritchey (2003) investigated the use of specialized tuned-mass dampers to reduce floor vibrations. His research included experimental modal testing of a one-way steel composite laboratory test floor both with and without the device installed. The experimental testing he accomplished was conducted with the same test equipment as the presented research.

Like the presented research, Perry (2003) studied computer modeling techniques using commercially available finite element software to evaluate the acceptability of floors. His research objective was to model floors in a way that computed an acceleration response (due to walking excitation) that matched the response predicted by DG11. He calibrated his modeling techniques by analyzing ideal floor systems (both partial and full floor models) and adjusting parameters and loading protocols until the fundamental frequencies and computed accelerations approached those predicted by the DG11 techniques. Perry applied the same modeling techniques to case study floors and compared the computed frequencies and accelerations to the measured frequencies and subjective evaluations. He found that while his techniques gave a better prediction of fundamental frequency than the DG11 techniques, the computed accelerations were not an accurate way to predict the acceptability of a floor system because they did not correlate well with the subjective evaluations of the tested floors. It should be noted that Perry's techniques never included matching actual measured acceleration response to a measured input force. Perry attributed the error in response prediction to the inability of the computer model to adequately represent the effective mass of the floor in its fundamental mode. Perry recommended future research on in-situ floors to include experimental measurement of response to known dynamic loads and the discrepancies between measured and predicted results to be resolved.

Salyards and Hanagan (2005) presented research on modeling a stadium facility for evaluation and prediction of dynamic response. The research included incremental FE modeling of the stadium and tuning based on experimental modal measurements taken by others. The researchers also used SAP2000 (CSI 2004) to create the FE models, the same program used in the presented research. While the structure differed considerably from the type of structure in this research, a particular observation demonstrated a similar phenomenon found in floor testing. It was noted by the researchers that the cantilever mode of the roof structure was the lowest

frequency mode computed by the FE model and was not found in the experimental data. They stated that because the shaker excitation was applied to the seating areas, the vertical force likely did not excite this particular mode. Additionally, only modes that show considerable response in occupied areas of the seating should be considered critical, even if these are not the lowest (fundamental) frequency modes of the structure.

El-Dardiry et al. (2006) investigated the finite element modeling of profiled composite floors. The detailed methods for creating equivalent isotropic and orthotropic shell sections to represent the composite steel deck concrete slab are insightful; however the application of their methods to experimental data is rather sparse. The only experimental measurements for comparison were from a three-bay by five-bay composite steel test floor within a full scale multi-story building built in 1994 for the exclusive purpose of research for the construction industry. However, only a single bay was dynamically tested by an unreferenced response to a person jumping, which yielded a single frequency measurement of 8.50 Hz. The researchers constructed a detailed FE model of the entire floor and found that the corresponding frequency of the excited bay was actually the fourth mode of the floor, computed as 8.17 Hz, not as close as one may hope for with such detailed modeling techniques. The researchers chose to explicitly model the steel columns for the floor system, citing previous research they conducted with FE modeling of a concrete floor (El-Dardiry et al. 2002). However, the obvious differences between the column-floor boundary of a monolithically cast concrete floor plate-column system and steel column and composite floor system are quite substantial. It is this writer's opinion that the method for modeling the composite slab is too intricate for the degree of accuracy it provides, and it is not conducive for automation.

1.4 Need for Research

The reviewed literature documents that dynamic testing of in-situ office building floors and development of FE model representations of their dynamic properties has been accomplished several times before. However, despite the numerous studies, there is an obvious lack of published cases involving the development of calibrated finite element models of in-situ steel composite floors based on extensive, high quality modal testing measurements. In some cases in the reviewed literature, limited unreferenced measurements became the cornerstone on which elaborate FE models and analyses were based, making huge leaps of faith with models validated

by only the most basic of the measured dynamic properties. Hanagan et al. (2003) succinctly summarized the need for the presented research:

“Fundamentally, modal analysis provides a basis for comparing analytical predictions of dynamic behavior to experimental results from actual in-place floors. A comparison might be used to evaluate the success of a finite-element model in predicting floor behavior. A successful analytical modeling approach, verified from experimental modal data, can be used to evaluate structures before they are built. Collecting high-quality experimental data on a floor is essential to developing better analytical techniques.”

As stated above, calibration of dynamic FE models to actual structures is best achieved using high quality modal data as well as a good understanding of the tested structure, which is why a large number of laboratory test floor cases are found in the literature.

The number of case studies involving in-situ floors are limited and the quality of measurements is questionable because opportunities to test large, in-situ, floor systems without the presence of occupants, construction materials, office furniture, or non-structural fit out are rare. Even rarer are studies that include testing in-situ floors using equipment with the capability to capture high-quality modal measurements. Experimental testing of relatively “clean” floor systems is part of the included research, as such floors serve as valuable test specimens when developing valid computational models under dynamic loadings.

Validated computational models of in-situ floors give researchers a method of predicting the response of the floor to dynamic loads, and consequently the ability to evaluate the performance due to human activities such as walking. If a set of general modeling techniques for steel composite floor systems can be developed from the calibrated FE models such that they adequately predict response to dynamic excitation, designers will have a better tool to evaluate proposed floor designs and avoid potential serviceability issues.

CHAPTER 2

EXPERIMENTAL MODAL ANALYSIS OF FLOOR SYSTEMS

2.1 Objectives

The basis for accurately characterizing the dynamic behavior of an in-situ floor, and validating the ability of FE models to represent that behavior, relies solely on the acquisition of high quality dynamic measurements. Thus, it is important to first outline the fundamental theory of modal analysis that allows experimentalists to estimate the dynamic properties of a floor through testing. It is also important to discuss the equipment and techniques used for testing floor systems because the acquisition of high quality modal data is a product of the available equipment and its effective employment. Lastly, it would be beneficial to researchers, consultants, and building owners if there were a common language, or classification system, for floor vibration testing that allowed all parties to understand the limitations on the type, quality, and accuracy of the data obtained using the various methods for testing floors. All too often, excellent opportunities for testing floors that would contribute to the current state of knowledge of in-situ floor behavior is met with the lack of proper equipment to acquire high quality results. Equally as often, ornate FE models are presented that were “validated” using only the most basic or minimal amount of dynamic testing.

The objectives of this chapter are to address all of the above listed issues. The following sections outline the theory of modal analysis and the processing of dynamic measurements, the equipment used to acquire dynamic measurements, a description of the applied and recommended experimental modal testing techniques for floor systems, and finally a classification system for floor vibration testing is presented to aid researchers, consultants, and building owners in understanding the advantages, disadvantages, and limitations of the various methods and equipment used for investigating floor behavior. It should be noted that many of the techniques used in testing the in-situ floors in this research were based on recommendations outlined by Hanagan et al. (2003) and others (Pavic and Reynolds, 1999; Reynolds and Pavic, 2000a, 2000b) from their experiences testing in-place steel composite floors and concrete floors,

respectively; however in many cases, the recommended techniques are improved or expanded upon based on the experiences of testing the in-situ floors of the presented research.

2.2 Modal Testing Theory

Important information about the behavior of the floor can be achieved through a simple measurement of the time history response. The spectral analysis of the time history response to yield its autospectrum shows the frequency content of the response. The time history response yields important indicators of peak accelerations due to various types of unmeasured excitation such as a heel-drop impulse load or walking parallel or perpendicular to the joists, a good demonstration of the floor's behavior in service. Examination of the decay from the heel-drop or a bouncing excitation can be useful in providing limited estimates of the damping in the system, however there are certain limitations to the usefulness of such "unreferenced" response measurements. Modal testing offers an expanded capability to characterize the dynamic properties of a floor by measuring both the input force and output response and forming a frequency response function (FRF) between the excitation and measurement locations. These dynamic properties (frequencies, damping, and modes shapes) estimated from experimental measurements can be used to validate analytical models that represent the dynamic behavior of the floor, usually formulated with finite element analysis. The actual process through which the FRF is computed using experimental measurements and digital signal processing requires a bit more explanation, but only in general terms as needed to explain how the process pertains to the presented research, because much more comprehensive texts are available on the subject (Ewins 2000). Before the theory behind the experimental computations is presented, a brief explanation of the theoretical analysis is warranted.

2.2.1 Analytical Modal Analysis

Ewins (2000) used three phases to describe theoretical multi-degree-of-freedom (MDOF) vibration analysis, which is based on the premise that the response of a structure is just a combination of the responses of its individual modes of vibration. The first stage is to compute the spatial properties of the model (mass, stiffness, and damping) to use in setting up the governing equations of motion. The second phase is performing a free vibration analysis to compute the modal properties of the model. The solution to the free vibration analysis yields the eigenvalues and eigenvectors of the system of equations, which correspond to the modal

properties of natural frequencies and damping, and mode shapes, respectively. The last stage is a forced vibration analysis where the applied force is harmonic excitation, and the solution is a frequency response function, $H(\omega)$. The frequency response function is a complex frequency domain function that when multiplied by the frequency domain harmonic forcing function yields the steady-state frequency domain response. Alternatively, the frequency response function can be defined as the response divided by the input force,

$$H(\omega) = \frac{X(\omega)}{F(\omega)} \quad (2.1)$$

Note that ω is the circular frequency in units of radians/second and is used simply for convenience; it is interchangeable with the cyclical frequency representation, f , in units of cycles/second, or Hz.

The term $H(\omega)$ in Equation (2.1) is a general term often used to annotate a frequency response function. Using the same notation as Ewins (2000), a more specific designation for the quantity described in Equation (2.1) is $\alpha(\omega)$, the *displacement* response per input force, which is known as the “receptance” or “compliance.” It is quite literally the ratio of the harmonic steady-state displacement response to the harmonic input force, preserving both the amplitude ratio between the two harmonic signals and the difference in phase, and thus is a complex function. Alternate forms of this are based on the response quantity used in its formulation. If the *velocity* response per input force is used, this is called the “mobility,” and the notation $Y(\omega)$ is used. Similarly, if the *acceleration* response per input force is used, this is called the “inertance” or more often the “accelerance,” and the notation used is $A(\omega)$. Displacement, velocity, and acceleration can all be defined by derivatives or integrals of one another, and they can all be related as follows:

$$\begin{aligned} \alpha(\omega) &= \frac{X(\omega)}{F(\omega)} && \text{RECEPTANCE} \\ Y(\omega) &= \frac{\dot{X}(\omega)}{F(\omega)} = (j\omega)\alpha(\omega) && \text{MOBILITY} \\ A(\omega) &= \frac{\ddot{X}(\omega)}{F(\omega)} = (j\omega)^2\alpha(\omega) = -\omega^2\alpha(\omega) && \text{ACCELERANCE} \end{aligned} \quad (2.2)$$

Note that $j = \sqrt{-1}$ and the $j\omega$ terms in the mobility and accelerance expressions in Equation (2.2) are derived from the complex representation of the harmonic forcing function, $f(t) = Fe^{j\omega t}$, and the harmonic displacement response, $x(t) = Xe^{j\omega t}$. Thus, the harmonic velocity and acceleration responses are $\dot{x}(t) = (j\omega)Xe^{j\omega t}$ and $\ddot{x}(t) = (j\omega)^2 Xe^{j\omega t} = -\omega^2 Xe^{j\omega t}$, respectively.

In a multi-degree-of-freedom system like floors, not just one frequency response function is computed, but an entire matrix called the frequency response function matrix, $[H(\omega)]$. Each term of the FRF matrix is a complex function in the frequency domain representing the force/response relationship between two degrees of freedom on a structure for a given frequency, ω . Thus, the accelerance FRF matrix is an assemblage of terms $A_{ik}(\omega)$, which relate the acceleration response of a particular location on the floor, i , to an input force at another location, k , as shown:

$$[A(\omega)] = \frac{\ddot{X}_i(\omega)}{F_k(\omega)} = \frac{a_i(\omega)}{F_k(\omega)} = \begin{matrix} & \text{Forcing Location, } k \\ \begin{bmatrix} A_{11}(\omega) & A_{12}(\omega) & \cdots & A_{1k}(\omega) \\ A_{21}(\omega) & A_{22}(\omega) & \cdots & \vdots \\ \vdots & \vdots & \ddots & \vdots \\ A_{i1}(\omega) & A_{i2}(\omega) & \cdots & A_{ik}(\omega) \end{bmatrix} & \begin{matrix} \text{Response} \\ \text{Location, } i \end{matrix} \end{matrix} \quad (2.3)$$

While the derivation of the harmonic acceleration response of a MDOF system from the uncoupled equations of motion is straight forward, it is not presented here for brevity. The fundamentally important solution is shown in Equation (2.4), which is a single term from the accelerance FRF matrix:

$$A_{ik}(\omega) = \frac{a_i(\omega)}{F_k(\omega)} = \sum_{r=1}^R \frac{-\omega^2 (\phi_{ir})(\phi_{kr})/m_r}{(\omega_r^2 - \omega^2) + j(2\beta_r \omega_r \omega)} \quad (2.4)$$

where

R = the number of modes

ω_r = the circular natural frequency of the r^{th} mode

m_r = the modal mass of the r^{th} mode

β_r = the modal damping ratio of the r^{th} mode

ϕ_{ir}, ϕ_{kr} = the corresponding i or k DOF term of the the r^{th} mode shape

$[\Phi] = [\{\phi\}_1 \quad \{\phi\}_2 \quad \cdots \quad \{\phi\}_R] = \text{matrix of } R \text{ mode shapes}$

Note the expression is in a form that assumes viscous damping, and although not shown here, there are more general forms that accommodate other damping models such as proportional or hysteretic damping (Ewins 2000). The denominator of Equation (2.4) holds the global properties of the structure, the resonant frequencies and damping ratios, and does not hold any information pertaining to the location of excitation or response. This information is contained in the numerator, which holds terms from the mode shape that scales the response. This fundamental analytical expression of the accelerance FRF is the basis from which all experimentally determined dynamic properties of the system are derived, as it is a mathematical expression of these quantities of interest (frequencies, damping, and mode shapes) in a formulation directly related to quantities that are measured during modal testing (acceleration response and input force).

2.2.2 Digital Signal Processing

As stated previously, the frequency response function goes by many names, but it is simply a transfer function, which is a general term for a function that describes the relationship between two simultaneously measured signals, an input signal and an output signal. For modal testing of a structure, this is generally set up with the input signal as the excitation of the structure, such as an applied force or support excitation, and the output signal as the physical response of the structure, such as displacement, velocity, or acceleration. It is the accelerance FRF between an applied force and the acceleration response of floor structures that is of interest in the presented research.

The basis of the whole process relies on the accurate measurement of signals in the time domain and Fourier analysis of those signals to transform them into the frequency domain. Fourier analysis simply states that a function in time can be written as an infinite series of sines and cosines with varying amplitudes and frequencies. Obviously anything involving infinity is fairly difficult to deal with, so several assumptions and simplifications are made along the way to make this process manageable. Rather than infinite time, only a block of time is analyzed. The signal within the time block is assumed to be periodic and is sampled a finite number of times at discrete increments, which can then be analyzed using a simplified Discrete Fourier Transform (DFT) analysis. This whole process is accomplished using a spectrum analyzer (also called a spectral analyzer, signal analyzer, or digital signal processor), a piece of equipment that receives

the analog signals from the force and accelerometer transducers and immediately digitizes the signals using an analog-to-digital converter. It is this digitization that creates a discretely sampled time record of the signals, which the spectrum analyzer uses to perform a Fast Fourier Transform (FFT) on the time domain data to transform it into the frequency domain. The FFT is a very efficient algorithm for computing the DFT when the digital time record is set up in a specific way, namely the time record length must be a power of 2, such as 128, 512, 1024, 2048, 4096, or 8192. Virtually all modern day spectrum analyzers are set up this way to take advantage of the speed of the FFT (Ewins 2000). Each spectral value of the FFT is a complex number, as it represents the corresponding Fourier coefficients that belong to the sine and cosine terms of the Fourier series at the given frequency. Thus, for the two types of measured signals of interest in modal testing of floor systems, the input force $f(t)$ and the acceleration response $\ddot{x}(t)$, the spectrum analyzer computes $FFT_f(\omega)$ and $FFT_x(\omega)$, respectively. It is at this point, with the simultaneously measured force input signals and acceleration response signals digitized in the time domain and their respective FFTs computed, where the frequency domain functions used in modal testing to describe the dynamic properties of the floor are captured.

From the FFTs of the digitized time history records, the first frequency domain function computed is the cross-spectrum of the acceleration response signal and the input force signal, $G_{xf}(\omega)$, which is a measure of the correlation between the two signals:

$$G_{xf}(\omega) = FFT_f^*(\omega) * FFT_x(\omega) \quad (2.5)$$

where

$FFT_x(\omega)$ = the FFT of the acceleration response

$FFT_f(\omega)$ = the FFT of the input force

$FFT_f^*(\omega)$ = the complex conjugate of $FFT_f(\omega)$

Because the values of the FFTs are complex numbers, the cross-spectra are complex as well, and the phase information represents the relative shift between the two signals.

The next frequency domain function computed is the autospectrum of each signal, $G_{ff}(\omega)$ for the input force and $G_{xx}(\omega)$ for the acceleration response,

$$G_{ff}(\omega) = FFT_f^*(\omega) * FFT_f(\omega) \quad (2.6)$$

$$G_{xx}(\omega) = FFT_x^*(\omega) * FFT_x(\omega)$$

where

$FFT_x^*(\omega)$ = the complex conjugate of $FFT_x(\omega)$

The autospectrum, which is the cross-spectrum of a signal with itself, can be seen as just a measure of the relative strength of the signal at each of the spectral frequencies at which it is computed. Note that this is a real valued function, as there is no phase shift between a function and itself (also because the product of a complex number and its complex conjugate is a real number). The autospectrum can be displayed in several formats, such as units²/Hz (commonly called the Power Spectral Density, or PSD), but the one used in the presented research is in root-mean-squared (RMS) units, which is actually the square root of the values that are computed by $G_{ff}(\omega)$ and $G_{xx}(\omega)$. This simply puts the units of the autospectrum back into the intuitive units of the original measured signal (lbs RMS or g RMS).

Making a few assumptions on whether the uncorrelated content is on the input or on the output, the computation of the frequency response function (FRF) in its general form is:

$$H(\omega) = \frac{G_{xf}(\omega)}{G_{ff}(\omega)} \quad (2.7)$$

Equation (2.7) states that the FRF is computed by dividing the cross-spectrum of the response and excitation signal (a complex valued function that holds the phase information between the signals as well as the general correlation) by the autospectrum of the excitation signal (a real valued function that simply scales the correlation in cross-spectrum). This makes the FRF a complex valued function, complete with magnitude and phase information (or real and imaginary parts) at each spectral frequency in the units of response per unit of input excitation. For floor vibrations (including the presented research), the FRF measured is the accelerance, the acceleration response per unit of input force, and is displayed in units of in/s²/lb for convenience of presenting the measured values, which generally have a magnitude ranging from 0 to 2 in the presented research. Other units, such as g/lb or m/s²/N are acceptable, but they lead to much smaller values that can be difficult to work with (1 in/s²/lb = 2.59x10⁻³ g/lb = 5.71x10⁻³ m/s²/N).

It should be noted that while the cross-spectra and autospectra that formulate the FRFs are computed between two signals each time a measurement is taken, it is the averaging of repeated measurements that allows a level of confidence that the computed spectral values are well correlated (or not well correlated, an indicator of either high levels of noise or very little response or excitation). Thus, the coherence function is computed with each average, providing a quality check on the correlation of all of the measured data. This computation is:

$$\gamma^2(\omega) = \frac{|G_{xf}(\omega)|^2}{G_{xx}(\omega)G_{ff}(\omega)} \quad (2.8)$$

This function shares a very similar form to the correlation coefficient between two random variables, as it should, because the coherence function gives a measure of the linear dependence between the input excitation signal and the acceleration response (Formenti 1999). The coherence function is a real valued function because the autospectrum terms in the denominator are real valued, and the magnitude of the complex valued cross-spectrum in the numerator is also real valued. The values of the coherence function lie between 0 and 1. A coherence of 0 indicates absolutely no correlation, and a coherence of 1 indicates the two signals are perfectly correlated. It is this end of the range of coherence values, very close to 1, that the experimentalist strives for. Diligent care was taken in the presented research to ensure the highest quality measurements were obtained whenever possible.

2.2.3 Parameter Estimation

In general, modal testing can either be classified as gathering a set of *fixed-input, roving-response* measurements (one column of the accelerance FRF matrix shown in Equation (2.3), and restated for convenience in Equation (2.9)), or conversely a *fixed-response, roving-input* set of measurements (one row of the FRF matrix).

$$[A(\omega)] = \frac{\ddot{X}_i(\omega)}{F_k(\omega)} = \frac{a_i(\omega)}{F_k(\omega)} = \begin{matrix} & \text{Forcing Location, } k \\ \begin{bmatrix} A_{11}(\omega) & A_{12}(\omega) & \cdots & A_{1k}(\omega) \\ A_{21}(\omega) & A_{22}(\omega) & \cdots & \vdots \\ \vdots & \vdots & \ddots & \vdots \\ A_{i1}(\omega) & A_{i2}(\omega) & \cdots & A_{ik}(\omega) \end{bmatrix} & \begin{matrix} \text{Response} \\ \text{Location, } i \end{matrix} \end{matrix} \quad (2.9)$$

If done properly, each yields the same information for the system. The former is typically accomplished using a shaker excitation in a fixed location while accelerometers are swept across the area of interest at measurement points. The latter is usually accomplished with an accelerometer placed in a fixed position while an impulse excitation is provided across the area of interest. In this scenario, an instrumented impact hammer is traditionally used for the impulse excitation in the fixed-response, roving-input test protocol. One should note the two testing techniques are not limited to the described set-ups, but it is much less common to use an impulse excitation in the fixed-input, roving-response setup. An alternative to shaker excitation

in the fixed-input, roving-response set-up is using an instrumented heel-drop on a force plate at a fixed location, which is an attractive alternative provided the same high quality data can be obtained.

Analysis of a set of measurements, the experimentally measured accelerance FRFs (one or multiple columns or rows of the accelerance FRF matrix), is the final step in the process of experimental modal analysis. These measurements are used to extract the dynamic properties of frequencies, damping, and mode shapes. This process is called parameter estimation. The different methods for conducting parameter estimation, and the theory behind the mathematics for each of the methods, is also quite vast and is better left to texts devoted to the subject. Again, a comprehensive source for parameter estimation is also found in the text by Ewins (2000), and a paper by Avitabile (2005) gives a brief overview and history of the development and implementation of the various methods of parameter estimation. Only a few comments on parameter estimation are noted in this section, as the methods used in the presented research will be addressed in the sections dedicated to presenting the experimental results or testing techniques.

Each term in Equation (2.9), $A_{ik}(\omega)$, represents the accelerance FRF of one location on the floor with respect to an input force at another location. An example accelerance FRF trace is shown in Figure 2.1. In the example shown, the accelerometer is located at the same point on the floor as the input force, thus it is known as a driving point measurement. Plotted separately are the accelerance FRF's magnitude and phase, although an alternative representation of the FRF would be plots of the real and imaginary parts. The process of parameter estimation is based on relating these FRF measurements to the mathematical formulation of the accelerance in Equation (2.4). In the most basic of terms, the peaks in the FRF indicate the presence of at least one mode, and the sharpness of the peaks indicates the level of damping of that mode. The relative magnitude and phase between the measurement shown in Figure 2.1 to accelerance FRFs of other locations around the floor characterize the mode shapes. While various methods are used for parameter estimation, they all essentially formulate a mathematical expression simulating the *measured accelerance* in terms of estimated parameters (frequencies, damping, and mode shape terms) that would closely approximate the *analytical expression of the accelerance* in Equation (2.4). This is why the term *parameter estimation* is synonymous with the term *curve fitting*. Specific methods used for curve fitting and estimating the dynamic properties of the floor are

presented elsewhere in this dissertation. With a cursory review of the theoretical basis of modal analysis, the fundamentals of the digital signal processing, and parameter estimation, it is important to describe the equipment used in modal testing that enables estimates of the floor's dynamic properties.

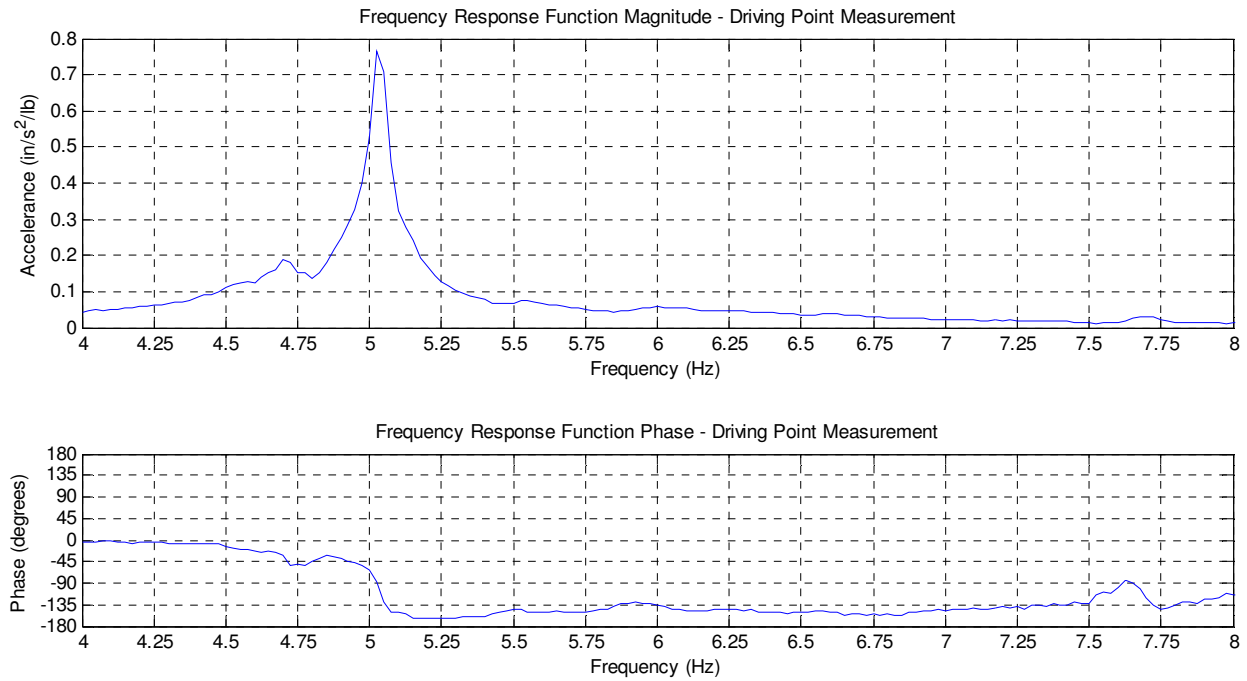


Figure 2.1: Example Accelerance Frequency Response Function Plot

2.3 Dynamic Testing Equipment

The tested floors were loaded dynamically in the fixed-input, roving response setup using an electrodynamic shaker inputting various excitation functions. A force plate beneath the shaker was used to measure the input force to the floor system and an array of accelerometers was used to measure the acceleration response. Figure 2.2 shows a schematic of the test setup.

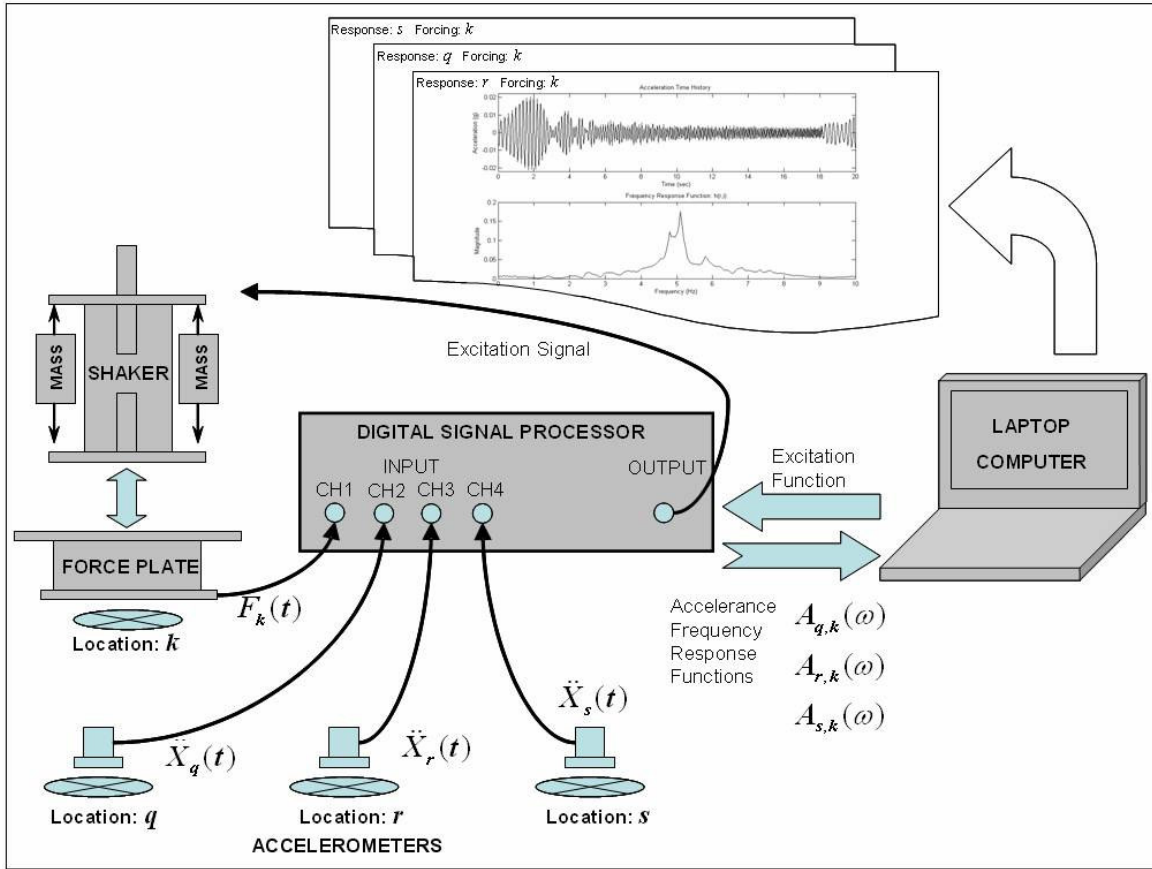


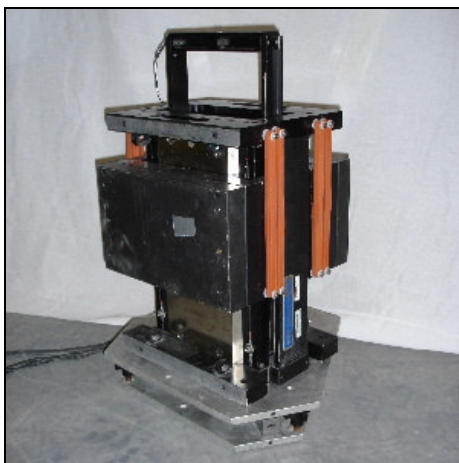
Figure 2.2: Modal Testing Schematic

To briefly summarize, the laptop computer interfaces with the digital signal processor (a multi-channel spectrum analyzer) to generate the excitation signal that is sent to the shaker. The excitation signal sent to the shaker is amplified to drive the shaker's armature and reaction mass, which in turn generates a force through the base of the shaker to the force plate and ultimately the floor system. The force plate measures the excitation force applied to the floor and sends the information back to the digital signal processor as a voltage signal. As the floor responds to the excitation force, the accelerations at various points on the floor are measured with accelerometers, which also send their signals back to the digital signal processor. With the simultaneously measured force and acceleration response signals, the digital signal processor can

compute all of the various autospectra, cross-spectra, and accelerance FRFs, all of which are sent back to the laptop computer to be stored for future analysis. Outside of the traditional modal testing setup described above, unreferenced measurements from heel drop excitation were also recorded for each floor. Detailed descriptions of the testing equipment used are presented in the following sections.

2.3.1 Electrodynamic Shaker

The shaker used is an APS Electro-Seis Model 400 shaker produced by APS Dynamics, Inc. (Figure 2.3(a)), which has a frequency range of 0 to 200 Hz and a rated peak sinusoidal force of 100 lbs from 2.2 Hz to 12 Hz (APS Dynamics 400). The shaker is comprised of a stationary main core with a moving armature and suspended reaction mass blocks that have a weight of 67.4 lbs (armature and reaction mass) per the manufacturer's specifications. The entire shaker assembly static weight is 236 lbs. The shaker induces a load by taking a time-varying voltage signal and driving the reaction mass up and down to generate the applied dynamic force. A laptop computer interfacing with the digital signal processor was used to generate the excitation function as a voltage signal to send to the APS Dual-Mode Model 144 Amplifier (Figure 2.3(b)), which would send it to the shaker at an amplified level (APS Dynamics 144).



(a) APS Model 400 Shaker on Force Plate



(b) APS Dual-Mode 144 Amplifier

Figure 2.3: Electrodynamic Shaker and Amplifier

Although the rated peak sinusoidal force of the shaker is 100 lbs, the typical peak magnitude of the sinusoidal driving force applied during testing was much lower than that to be commensurate with expected magnitudes of applied force to simulate walking excitation (sinusoidal signals less than 25 lbs). A constant compromise was necessary, however, because it

was also important to be able to introduce a large enough force into the system to incite a measurable response and to help maximize the signal-to-noise ratio by having a strong response signal.

By far, the electrodynamic shaker and amplifier are the most costly pieces of equipment used for floor testing. However, the advantages of shaker excitation over the various forms of impulse excitation, like a force hammer or instrumented heel-drop, far outweigh the high cost. More specifically, shaker excitation allows better signal-to-noise ratio throughout the time sample, it can produce controlled excitation within a specified frequency range of interest, and its variety of forcing inputs such as steady-state sinusoidal, chirp, and random is unparalleled (Mayes and Gomez 2005). With the Model 400 shaker weighing in at 236 lbs, it was fairly hefty for the individuals moving it to different locations around the floor, however its localized mass was considered negligible to the system as the tested floors had a total weight nearly four orders of magnitude larger.

2.3.2 Measurement of Input Force - Force Plate

A force plate was placed between the shaker and the floor to measure the time history of input force. The force plate used was the only non-commercial piece of equipment, and it was specifically fabricated for floor vibration testing. The force plate consists of three Nikkei Model NSB-500 shear beam load cells, rated at 500 lbs each, mounted in a triangular orientation to support a 1-in. thick triangular aluminum plate (Figures 2.4(a) and (b)). A summing amplifier was used to collect the voltage output of the three individual load cells, integrate and amplify the signal, and pass it along to the digital signal processor as a single voltage signal representing the total input force on the force plate (Howard et al. 1998). This force input signal served as the reference signal from which all accelerance FRF measurements were based.



(a) Force Plate Shear Beam Load Cells



(b) Force Plate with Top Plate

Figure 2.4: Force Plate

The force plate was used to measure the force as opposed to monitoring the shaker voltage signal or placing an accelerometer on the armature of the shaker and using an acceleration computation. Because the shaker itself is a mass-spring-damper system, it has inherent dynamic properties that affect the output force for a given input voltage (Hanagan et al. 2003). An accelerometer attached to the moving armature of the shaker measures an *absolute* acceleration, but it is the *relative* acceleration between the floor and the reaction mass that induces the dynamic load. A force plate directly measuring the input force at the shaker-floor interface avoids these issues.

The force plate signal output is a measured voltage, thus a calibration factor was determined to convert the voltage into physical force units. This voltage-to-force calibration factor, C , has the units of lbs/volt and was multiplied by the voltage time history to convert it into physical force units. It was also used in the conversion of the accelerance FRFs from the measured units of volts/volt to physical units of in/s²/lb. The following is a brief derivation of how this calibration factor C was determined:

$$\begin{aligned}
 F_{(lbs)} &= F_{v(volts)} \cdot C_{(lbs/volt)} = mass \cdot acceleration = \frac{W_{(lbs)}}{g} \cdot a_{(g)} \\
 C_{(lbs/volt)} &= \frac{W_{(lbs)}}{g} \cdot \frac{a_{(g)}}{F_{v(volts)}} = W_{(lbs)} \cdot \frac{a}{F_{v(volts)}} \\
 S_{(1/volts)} &= \frac{a}{F_{v(volts)}} \\
 C_{(lbs/volt)} &= W_{(lbs)} \cdot S_{(1/volts)} = 67.4_{(lbs)} \cdot S_{(1/volts)}
 \end{aligned} \tag{2.10}$$

where

C = voltage-to-force calibration value ($lbs / volt$)

S = ratio (or spectral value) of armature acceleration to force plate output voltage ($1 / volts$)

W = 67.4 lbs , the weight of the shaker armature and reaction mass (lbs)

F_v = measured force plate output voltage ($volts$)

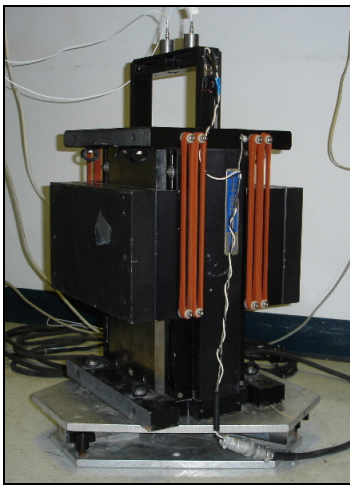
F = computed force plate output in physical force units (lbs)

a = measured armature acceleration in units of g or $volts$, since $1 g = 1 volt (g)$

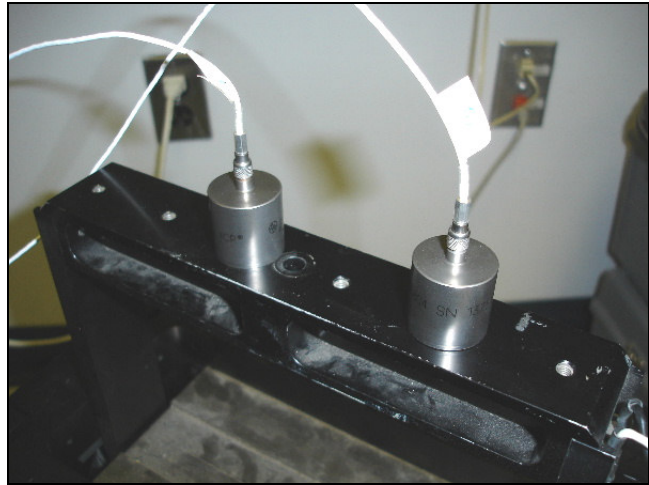
g = acceleration of gravity (in / s^2)

Derivation (2.10) states that the applied force is simply equal to the mass of the moving part of the shaker (the armature and attached reaction blocks) multiplied by the acceleration of

the moving part of the shaker. The mass (or weight) of the armature assembly is known as 67.4 lbs. By mounting an accelerometer to the armature assembly, the acceleration time history of the mass was recorded. This acceleration time history was multiplied by the armature mass to serve as the baseline force time history. Note that the shaker and force plate must be on a rigid surface, such as a slab on grade or adjacent to a column, to measure (as closely as possible) the true acceleration of the armature and not the relative acceleration between the armature and a moving structure (such as a floor). The applied force of the moving mass was measured by the force plate output voltage, and thus a calibration factor, C , was determined by dividing the computed force (mass times acceleration) by the measured force voltage. From this method of calibration testing, the calibration value C used for the presented research was 240 lbs/volt. Figure 2.5 shows a calibration test performed on a slab on grade with the shaker on the force plate and accelerometers mounted to the armature of the shaker.



(a) Shaker/Force Plate on Rigid Surface



(b) Accelerometers Mounted on Shaker Armature

Figure 2.5: Force Plate Calibration

2.3.3 Measurement of Acceleration Response – Accelerometers

Acceleration response measurements were taken using PCB Model 393C seismic accelerometers produced by PCB Piezotronics (Figure 2.6). The 393C accelerometer has a frequency range of 0.025–800 Hz and a sensitivity of 1.0 volt/g, which made it easy to judge real-time accelerations as a percentage of gravity. Depending on the number of digital signal processing units utilized, arrangements of three to seven accelerometers were used to simultaneously capture multiple response measurements. Each accelerometer weighs 31.2 ounces, and with measured peak accelerations less than 0.10g, the effect of gravity prevented the

need for any mechanical fastening of the accelerometers to the floor structure, although Hanagan et al. (2003) recommends fixing accelerometers to the structure using beeswax or clay.



Figure 2.6: PCB Model 393C Seismic Accelerometer

While testing the in-situ floors, accelerometers were placed on very thin and stiff rubber bearing pads to minimize the possible rattling effect due to small debris or imperfections in the unfinished concrete surface (Figure 2.6). The stiffness and small thickness of the pad were such that measured accelerations were not affected. This was verified from tests run on a laboratory test floor. In these tests, the laboratory test floor was driven sinusoidally at acceleration levels ranging from 1% of gravity to 10% of gravity with the accelerometer either resting on the bare steel floor surface, resting on a stiff rubber bearing pad, or fastened to the floor using removable putty adhesive. Nearly identical acceleration values were recorded for each case. The large flat base of the accelerometer also alleviated the need for any additional leveling devices to ensure the measurements were taken perpendicularly to the floor surface.

2.3.4 Cables

One aspect to modal testing large in-situ structures that is often overlooked in the literature is the cable requirements for connecting the components of the test setup. The higher the channel count (i.e. the more channels used in the modal test) and the larger the test area, the more cables are required. Hunt and Brillhart (2005) claim that accelerometer cables are often the weakest link in the modal test setup, especially microdot, which can be easily broken if they are bent or kinked into sharp angles. The PCB 393C accelerometers required microdot connections, and the digital signal processors had BNC connector inputs, thus a microdot-to-BNC cable was required. Microdot cable is the most expensive cable type, and as stated above, likely the most

fragile (Hunt and Brillhart 2005). Because of the long cable runs and austere conditions of the tested floor systems that were under construction, heavier and more rugged coaxial cables with BNC connectors were fabricated for the long runs to the accelerometers. Short 10-ft lengths of microdot cable (with microdot/BNC connections) were hooked up to the accelerometers and left coiled to protect the fragile cables from wear and kinks. Figures 2.6 and 2.7 show the microdot cable in its coiled position. Heavier and more durable coaxial cable was connected to the microdot for the long cable runs. These cables were assembled from combinations of 50-ft, 75-ft, and 100-ft lengths, typically running for 150-ft to 200-ft total length. Whenever possible, the number of splices was kept to a minimum to reduce the locations where a malfunction could occur.

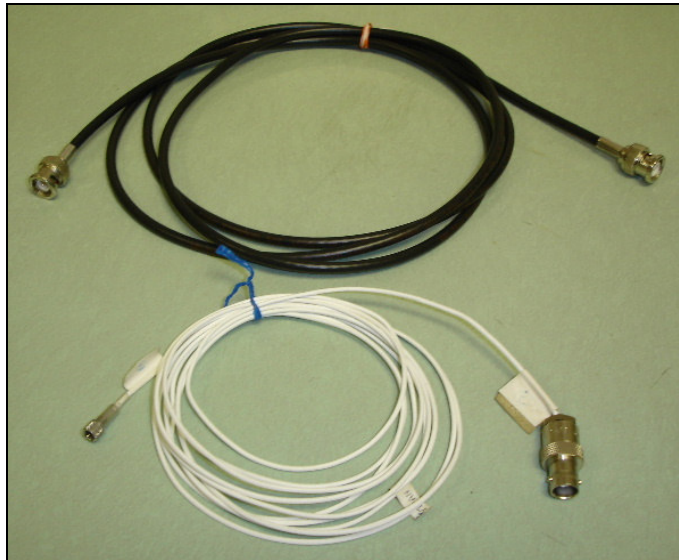


Figure 2.7: Accelerometer Cables – Coaxial (above) and Microdot (below)

The majority of the time required to test a floor system is the time required for taking actual dynamic measurements, however a close second is cable management, especially when long cable runs are involved and a high channel count is used. In one of the floor systems tested, a total of 1700 ft of cable was moved around the floor for each measurement (seven accelerometers with 200-ft cables and two 150-ft cables for the shaker and force plate). In performing a modal sweep across an area of the floor, the accelerometers are constantly moved from one response point to another for the next measurement. Extreme care was taken to ensure the cables were laid out in a fashion so that they would not tangle each time the accelerometers were moved.

2.3.5 Multi-Channel Spectrum Analyzer

The digital signal processing (DSP) equipment consisted of Model 20-42 SigLab units produced by Spectral Dynamics, Inc. (Figure 2.8). These multi-channel DSP units are fully functioning spectral analyzers and have the ability to record and compute the full suite of dynamic measurements, including (but not limited to) the time history response, autospectrum, cross-spectrum, frequency response function, and coherence. These devices have four input and two output channels per unit, with the capability of being connected in series to provide up to 16 input channels. A standard laptop computer running SigLab v3.28, a front-end program driven by MATLAB, was used to control the DSP unit to generate the output excitation signal for the shaker and process the input measurements from the force plate and accelerometers. The SigLab units have a frequency bandwidth of 5 Hz to 20 kHz, although for floor vibration testing only the 10 Hz and 20 Hz bandwidth selections were used. The units are capable of generating a variety of output excitation signals for the shaker, including sine, square, sawtooth, triangle, impulse, random, and chirp. Only the steady-state sine and chirp functions were used in the presented research.



(a) Four-Channel DSP Unit



(b) Two DSP Units in Series and Laptop

Figure 2.8: Model 20-42 SigLab Digital Signal Processor

For most test setups in the presented research, two SigLab DSP units were connected in series to provide eight input channels (Figure 2.8(b)). The advantage of a higher channel count was that more response measurements could be taken simultaneously, reducing the time to test a given area of the floor. The only disadvantage was that there were more measurements to keep track of and an increased difficulty in keeping the cables untangled, however the advantages far outweighed the disadvantages. During modal testing using the shaker, input Channel 1 was always designated as the reference channel for the FRF measurements and was connected to the

force plate. The remaining input channels were connected to the array of accelerometers, and thus the accelerance FRFs were computed.

Despite having the capability to compute the FRF, a multi-channel spectrum analyzer does not have to be used in this capacity and can easily serve as simply a multi-channel response-only measurement tool. While not as sophisticated as true modal test measurements (i.e. referenced), simple unreferenced response-only measurements can be useful in evaluating floor systems and their dynamic properties. In some testing situations, response-only measurements may be the only measurements available because capturing the input force is not practical or possible; such is the case for walking excitation. In this situation, an array of accelerometers simultaneously measuring the response of an area of interest from an unreferenced walking excitation can still yield important information about the in-service behavior of the floor.

If a multi-channel spectrum analyzer is available but there is no way to measure an input force (i.e. no force plate or shaker with mounted accelerometer), all hope is not lost if there is still an interest in quantifying the general shape(s) of the floor when excited dynamically. Although not used in the presented research, there is a measurement type called an Operating Deflection Shape (ODS) FRF, which is simply an FRF taken with the reference signal being an acceleration measurement rather than a force measurement (Richardson 1997). While not nearly as fully descriptive as a force-referenced FRF, the result is a relative magnitude and phase difference between two responses on a floor. This could potentially be used in floor testing by conducting unreferenced heel drops at the middle of a bay next to the reference accelerometer, while the roving accelerometers are placed in the middle of adjacent bays (or other locations). The ODS FRF should reflect the relative magnitude of the responses in reference to the response at the excitation location, as well as the difference in phase. It should be stressed that this would only yield information about the frequencies and relative shape, and no information about the acceleration response per input force, which is key in validating FE models.

The available record lengths of the DSP units used in the research ranged from 64 samples to 8192 samples over the time block. A selection of DSP settings and the resulting time and frequency domain resolutions are presented in Table 2.1. The frequency domain resolution and time domain resolution of the measurements were products of the selected frequency bandwidth and record length. A fine frequency domain resolution comes at a cost of a longer

time record. The entries of Table 2.1 in bold print represent settings used at various times for the floors tested in the presented research.

Table 2.1: Digital Signal Processor Settings

Bandwidth (Hz)	Record Length (samples)	Frequency Resolution Δf (Hz)	Record Length (sec)	Time Resolution Δt (sec)
10	512	0.05	20	0.0390625
20	512	0.10	10	0.01953125
50	512	0.25	4	0.0078125
100	512	0.50	2	0.00390625
10	1024	0.025	40	0.0390625
20	1024	0.05	20	0.01953125
50	1024	0.125	8	0.0078125
100	1024	0.25	4	0.00390625
10	2048	0.0125	80	0.0390625
20	2048	0.025	40	0.01953125
50	2048	0.0625	16	0.0078125
100	2048	0.125	8	0.00390625
10	4096	0.00625	160	0.0390625
20	4096	0.0125	80	0.01953125
50	4096	0.03125	32	0.0078125
100	4096	0.0625	16	0.00390625
10	8192	0.003125	320	0.0390625
20	8192	0.00625	160	0.01953125
50	8192	0.015625	64	0.0078125
100	8192	0.03125	32	0.00390625

2.3.6 Single-Channel Spectrum Analyzer

An extensive database of problem floors has been accumulated over the years for which only subjective analysis exists. In many of the floors evaluated, the only measured data are acceleration response time histories from unreferenced heel drop, bouncing, and/or walking excitations. In such cases, as well as the tested floors in the presented research, the response-only measurements were taken using a single-channel spectrum analyzer, the Ono Sokki CF-1200 Handheld FFT Analyzer, and a PCB 393C seismic accelerometer (Figure 2.9).



Figure 2.9: Ono Sokki CF-1200 Handheld FFT Analyzer

The CF-1200 has an available frequency bandwidth of 100 Hz to 20 kHz and a maximum time record length of 1024 samples. For all measurements in the presented research, the handheld analyzer was set to its finest resolution, a 100 Hz bandwidth with record length of 1024 samples, resulting in a four second acceleration time history block, a time domain resolution of 0.003906 sec., and a frequency domain resolution of 0.25 Hz (i.e. a frequency accuracy of ± 0.125 Hz). Although unparalleled in its portability and ease of use, the only weakness of the handheld analyzer for use in capturing unreferenced response measurements is its coarse frequency resolution.

2.4 Experimental Testing Methods

Almost every aspect of experimental dynamic testing of in-situ floor systems is a compromise. The compromises are based on a variety of influences, most notably the time and equipment available for testing. Limitations on the types of information achievable based on the available equipment are obvious, however the time allowed for testing is the critical factor because time has the greatest influence on the quality, quantity, and level of detail of the dynamic measurements. In many cases, the desired test areas are large, with perhaps hundreds of test points. A fine frequency resolution is often critical, particularly when damping values are very low, and an accurate representation of the peak magnitudes of the accelerance FRF is required. Fine frequency resolution comes at the cost of longer record lengths. A common trait of in-situ structures is the presence of extraneous noise, which may require a higher number of averages during testing to improve the quality of FRF measurements. Large test areas, numerous test points, long record lengths, and high number of averages all take time. Thus, with a limited amount of time to test a floor system, these are all aspects of testing that lend themselves to compromise. In most cases, compromise is made by reducing the area to be tested, using a coarser grid of test points, and finding a balance between frequency resolution, time record length, and the number of averages that will provide a set of measurements of an acceptable quality.

The best way to address the inevitable compromise is by clearly defining the overall objectives of the dynamic testing of the floor system and match those objectives with the time available for testing. If the objective of the testing is to provide a reasonable estimate of frequencies and to capture behavior under service conditions from individuals walking, bouncing, or performing heel drops, then perhaps simple unreferenced (response-only) measurements are needed. On the other end of the spectrum, the objective may be to gather a set of high quality measurements for a fine mesh of test points over an area, perhaps for developing a detailed model for use in extensive response simulation. This would require extensive modal testing with an electrodynamic shaker, and plenty of time. In most cases, such as the presented research, the objectives lie somewhere in between. The objectives were to capture enough measurements to adequately estimate the modal properties for use in validating an FE model of the floor. This translates into identifying the resonant frequencies, estimating the level of

damping in the floor, and determining the mode shapes for a reasonable comparison with the ones generated by an FE model.

While all measurements satisfy the overall objective of quantifying the dynamic behavior of the floor to some degree, different types of measurements and methods of testing have different goals. In the traditional modal testing setup using a shaker, the chirp signal (swept sine) or other types of broadband excitation (instrumented heel drop) is used to measure the accelerance FRF over a certain frequency range of interest. Steady state sinusoidal excitation is used primarily to verify the accelerance FRF values at specific spectral lines (frequencies) and also serve as the initial excitation for decay measurements, useful for damping estimates. Unreferenced response-only measurements have their place in measuring in-service accelerations or the autospectrum of response, which in some cases can capture low frequencies of a structure that are not possible with a shaker due to its own limiting dynamics. Any of the above listed measurement types can be used to measure the response, referenced or unreferenced, at long distances from the point of excitation. The following sections describe the acquisition and use of the different types of measurements for testing floors, including best practice techniques recommended by others and expanded upon from the experiences of testing the in-situ floors in the presented research.

2.4.1 Chirp Signals

The chirp signal, also known as a swept sine, is a sinusoidal function driving at a changing frequency over time to provide force input to the floor system over a range of frequencies. This is a quick and controlled method to get the frequency response, whereas other broadband methods such as impulse excitation can create measurement difficulties by exciting a wider range of frequencies. The chirp signals can sweep from lower frequencies to higher frequencies, or vice versa. Theoretically the resulting accelerance FRF should be identical for either direction of the sweep; however the most common arrangement is to sweep from a lower to higher frequency because lower frequencies generally take longer to die out. This maximizes the chances that all the response will be captured within the time record. The goal of a chirp signal measurement is to provide a controlled excitation within a specific frequency band so that the accelerance FRF can be clearly defined within this range of frequencies without the effect of out-of-range frequencies. The controlled level of excitation and limited range of frequency make

it much easier to capture well correlated accelerance FRFs with high coherence, indicating quality measurements. Two types of chirp excitation were used to derive the accelerance FRFs in the presented research, a continuous chirp signal and a burst chirp signal. The type of chirp signal, the sweep frequency range, and the chirp duration were varied for each of the three tested floors in the presented research and will be discussed later.

Continuous Chirp - A continuous chirp signal is where the signal sweeps between two frequencies over a period of time and continuously repeats itself without pause. Hanagan et al. (2003) points out that if the chirp sweep cycle matches the data acquisition time, there is a decrease in signal processing errors. A typical time history and autospectrum of a 4-12 Hz continuous chirp excitation signal is shown in Figure 2.10. As suggested, the duration of the chirp exactly matches the time block. The average peak magnitude of force was around 25 lbs, with an occasional surge when the continuous chirp cycle would reinitialize to 4 Hz. As the chirp cycle finished its sweep to 12 Hz, it would immediately start the cycle over at 4 Hz, as shown in Figure 2.10 at the 18-second point.

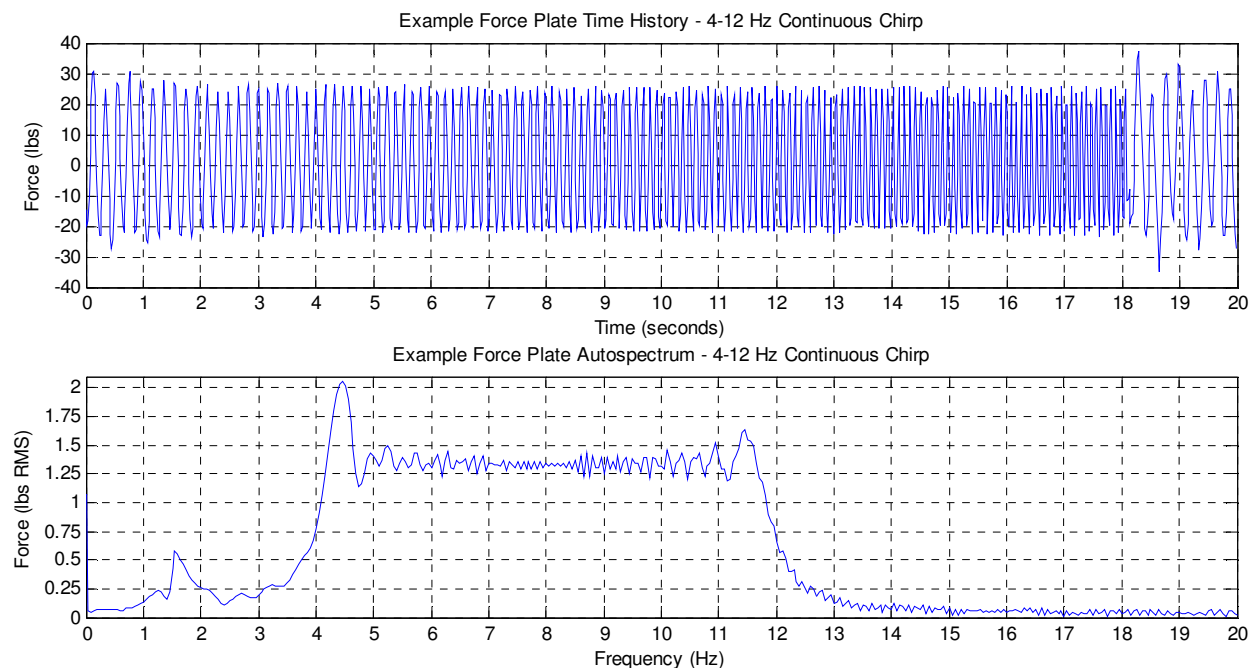


Figure 2.10: Typical 4-12 Hz Continuous Chirp Force Input Signal

The start of a measurement was manually controlled and an attempt was made to initialize at the beginning of the measurement to coincide with the chirp cycle starting over at 4 Hz. Despite the best efforts to start the measurement right at the transition, most measurements started around two seconds after reinitializing, highlighting one disadvantage of the continuous

chirp measurement. Although various measurement trigger methods are available in the spectrum analyzer to correct this, they were not employed in the above measurement. Figure 2.10 also shows the autospectrum of the chirp signal time history, as noted by the roughly constant level of energy introduced into the system within the 4-12 Hz frequency range of the chirp. The choice of the chirp frequency range was based on previous unreferenced response-only measurements that indicated all frequencies of the floor were greater than 4 Hz. The 12 Hz upper end of the sweep was used because there was no significant response around that frequency and natural frequencies above 10-12 Hz are not typically of interest for walking induced vibrations as they are unlikely to be excited by one of the higher harmonics of walking.

Figure 2.11 is the time history and the autospectrum of the acceleration response of the floor at the driving point (response at location of excitation) and is typical of the floor response at other locations. The time history shows the varying response as the floor is excited by the sweeping frequencies, and the autospectrum of the acceleration response clearly shows the vast majority of the response to a chirp signal is within the targeted 4-12 Hz frequency range of interest and very little at other frequencies. The autospectrum in Figure 2.11 also highlights the frequency of the tested bay from the dominant peak response at 5.05 Hz.

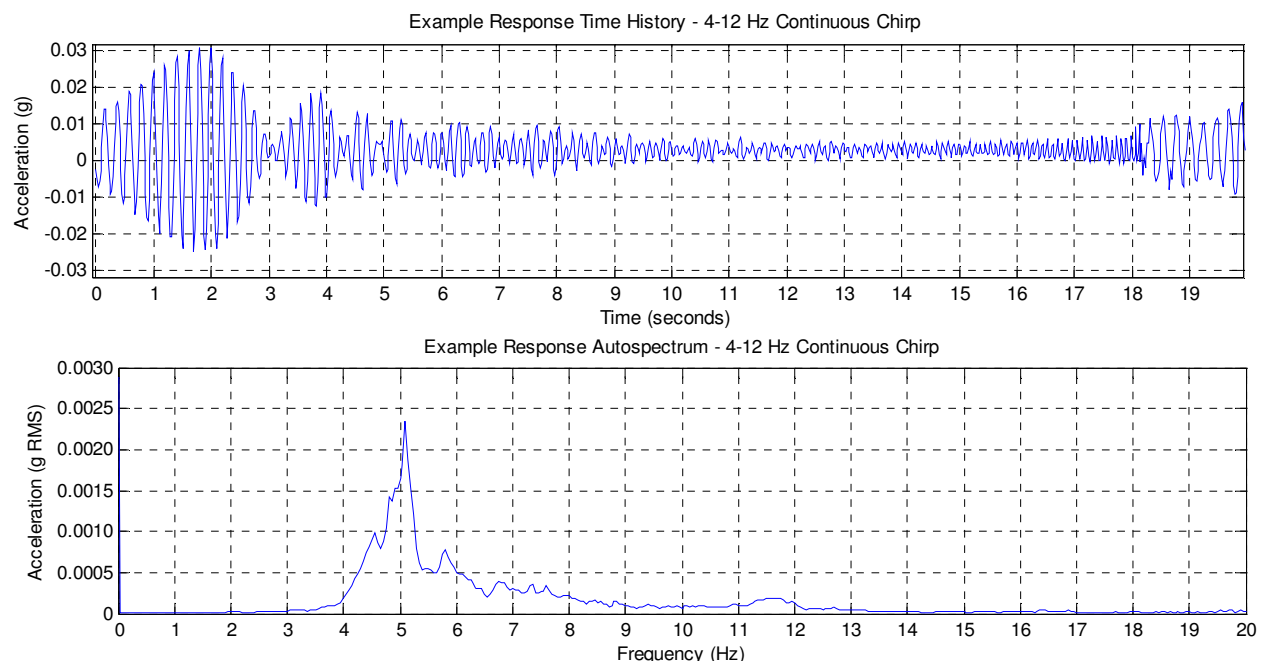


Figure 2.11: Typical 4-12 Hz Chirp Signal Acceleration Response

With the input force and acceleration response of the system concentrated within the 4-12 Hz chirp sweep, it was expected to have well correlated data within this range and not much

elsewhere. Because there is negligible force input and acceleration response outside the range of the chirp signal frequencies, poor correlation for acceleration FRF measurements is expected in these areas, as indicated by the poor coherence outside 4-12 Hz in Figure 2.12, and good coherence within 4-12 Hz as shown in Figures 2.12 and 2.13.

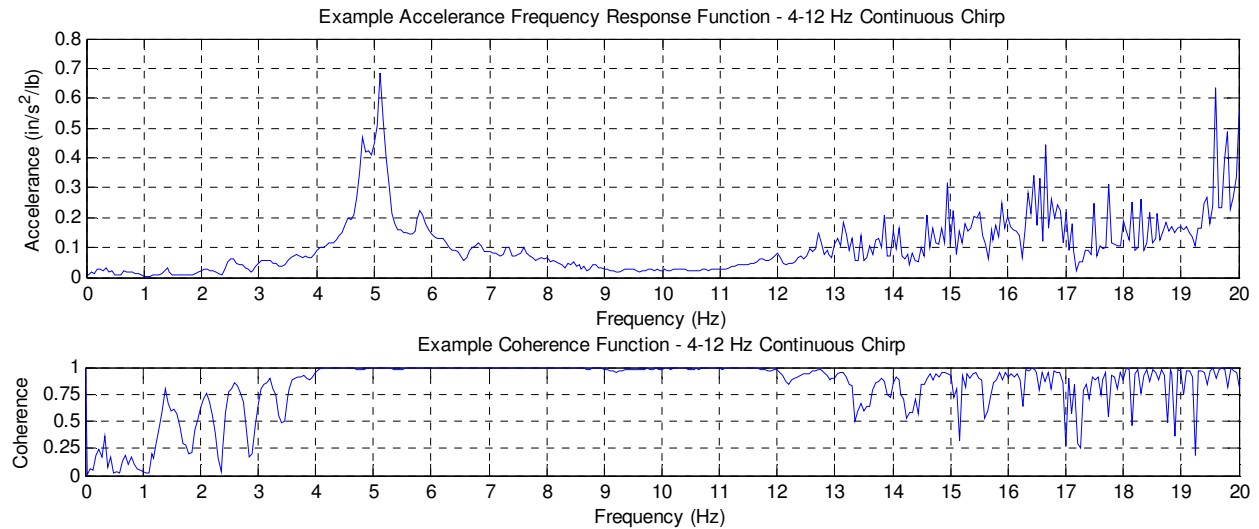


Figure 2.12: Typical 4-12 Hz Continuous Chirp FRF Magnitude and Coherence (0-20 Hz)

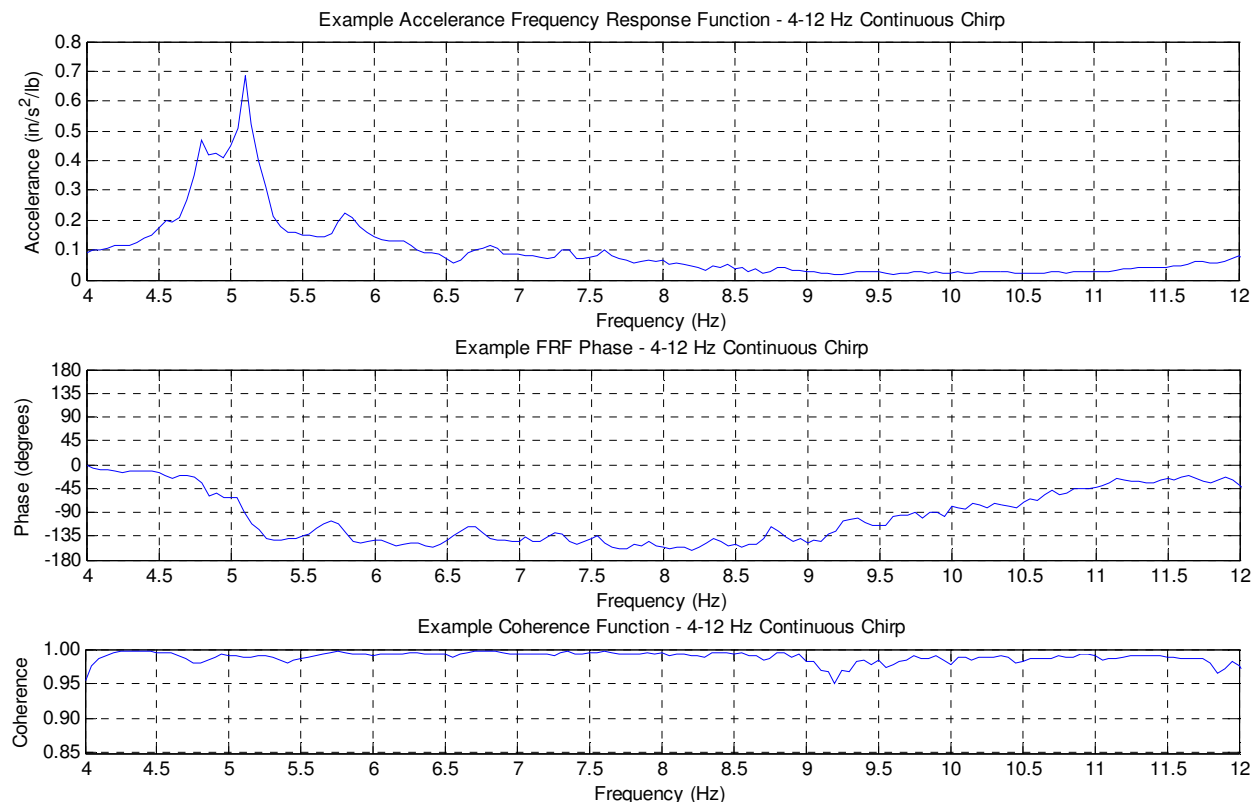


Figure 2.13: Typical 4-12 Hz Continuous Chirp FRF Magnitude, Phase, and Coherence

With poorly correlated data outside the 4-12 Hz range, future frequency domain plots (autospectra, accelerance FRF magnitude and phase, and coherence) resulting from chirp signal excitation will display just the usable frequency range of interest, unless otherwise noted. The accelerance FRF magnitude, phase, and coherence for the example driving point measurement are presented within the chirp frequency range in Figure 2.13.

It should be noted that the nature of obtaining accelerance FRFs is based on averaging measurements; more specifically, the cross-spectra and autospectra are updated with each average using the most recently recorded input force and acceleration response measurements. When frequency domain plots are presented (autospectra, accelerance FRFs), they reflect the averaged functions. When time domain measurements (force and acceleration time histories) are presented, they reflect the last of the averaged measurements that were recorded. The number of averages needed for a measurement is a product of the compromise noted earlier, but the minimum number should be whatever ensures quality (well correlated) measurements as indicated by good coherence. From preliminary measurements with the equipment, it was determined only three averages of each chirp cycle were needed to ensure the quality of the measurement within the frequency range of interest, and a higher number of averages did not improve the coherence, only lengthened the time required to take the measurement.

While the continuous chirp excitation signal seemed to produce accelerance FRF measurements of acceptable quality, it is not recommended for testing floors. As recommended by Hanagan et al. (2003), the duration of the chirp sweep was 20 seconds, equal to the time record length. Even though the continuous nature of the excitation and response is intuitively suspect in the computation of the FRF, the assumptions made in the digital signal processing make it possible to achieve measurements of acceptable quality. Specifically, the input force and acceleration response are assumed to be periodic within the time window, which occurs if the chirp duration exactly matches the time record length because consecutive time records should be identical. Secondly, well correlated measurements are assumed to be a product capturing the entire force input and the entire acceleration response. In the continuous chirp signal, the response at the beginning of the time record is due to the previous input force (not measured), and the force at the end of the time block produces response that occurs after the end of the time block, which intuitively suggests the measurement should be poor. However, the periodicity of the force and response time blocks help because the FRF is based on *frequency domain*

representations of the signals, which are not concerned with the actual order of the input and response signals in the *time domain*. Again, despite the capability to produce acceptable quality FRF measurements, the continuous chirp signal is not recommended for testing floors. A better alternative for measuring accelerance FRFs of floor systems is a burst chirp excitation signal, which takes advantage of all the chirp signal concepts and has proven to provide superior quality measurements.

Burst Chirp Signal – For a burst chirp signal, the floor system initially starts at rest and is excited as the chirp signal sweeps between two frequencies over a period of time. The duration of the chirp is shorter than the overall length of the time record, allowing the floor to come to rest before the end of the record. In this manner, the entire force and response time histories are captured within each time record, maximizing the chances of computing high quality and well correlated FRFs within the chirp frequency range. While adjustments of the chirp duration and sweep frequency range must be made to accommodate the frequency range of interest and selected record lengths, the burst chirp signal is a highly recommended method of excitation for floor vibration testing due to its flexibility and superior quality measurements. A typical time history and autospectrum of a 4-12 Hz burst chirp excitation signal is shown in Figure 2.14.

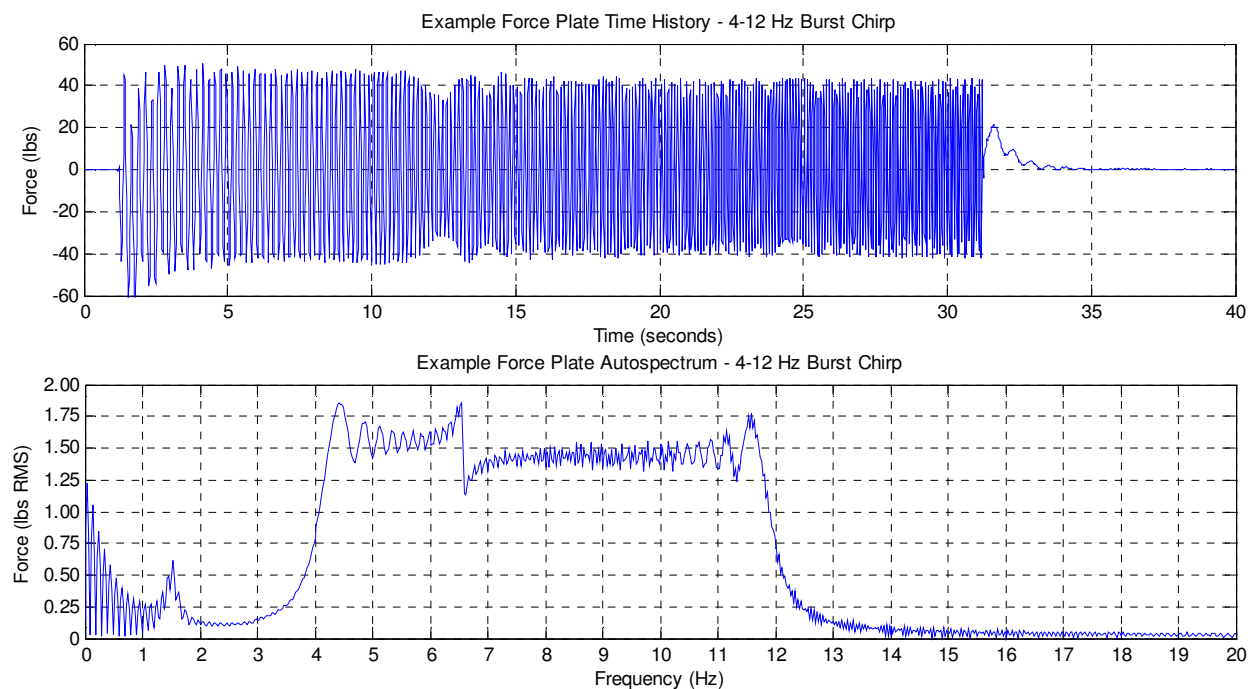


Figure 2.14: Typical 4-12 Hz Burst Chirp Force Input Signal

The small peak in the force input autospectrum around 1.5 Hz corresponds to the natural frequency of the shaker's reaction mass and suspension bands. This force input is visible at the 31-second point of the time history in Figure 2.14, where the chirp signal ends and the shaker's reaction mass comes to rest over a few seconds. This has no effect on the measurement. The measurement was set up with a 40-second time record, and the duration of the chirp sweep was 30 seconds, with a 15-second idle period before the next burst chirp signal, allowing the floor to come to rest before the next measurement. Note that the 30 seconds of chirp signal and 15 seconds of off time are longer than the 40-second time record length. This technique served two purposes. First, it enabled the use of the triggering mechanisms in the SigLab DSP units. The triggers are cues for starting a measurement and are based on the signal from an input or output channel. For the burst chirp measurement, the trigger for every average was set to start a measurement when the output channel providing the signal to the shaker started the chirp. Additionally, the SigLab DSP unit has the capability for positive or negative delays with the use of the trigger. In the chirp signal of Figure 2.14, a negative 2.5% delay was used. This informed the DSP unit that the start of a time block to be recorded was 2.5% of the total time record length prior to the trigger mark (1 second for a 40-second record).

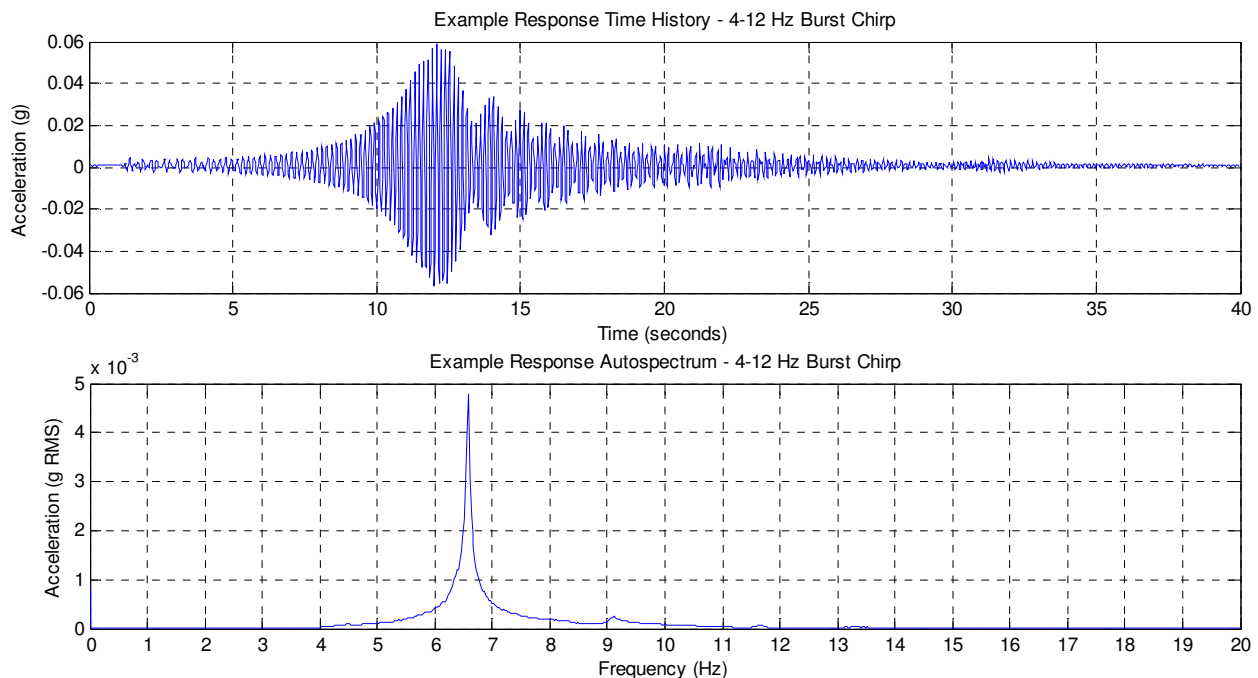


Figure 2.15: Typical 4-12 Hz Burst Chirp Acceleration Response

Using this burst chirp technique, as shown for the input force of Figure 2.14 and the corresponding acceleration response of Figure 2.15, the measurement has one full second of no

input or response, 30 seconds of a burst chirp signal sweeping from 4 to 12 Hz, followed by no input force and decaying response for the remainder of the 40-second record. Note that both the input force and acceleration response are completely captured within the time record block. Nothing is measured during the extra five seconds the shaker is off, which gives the floor additional time to come to rest before the next record. The driving point accelerance FRF magnitude and coherence for the full 20 Hz bandwidth is shown in Figure 2.16. Note the impeccable coherence within the 4-12 Hz frequency range of the burst chirp signal and a clearly dominant peak at the bay's resonant frequency of 6.575 Hz.

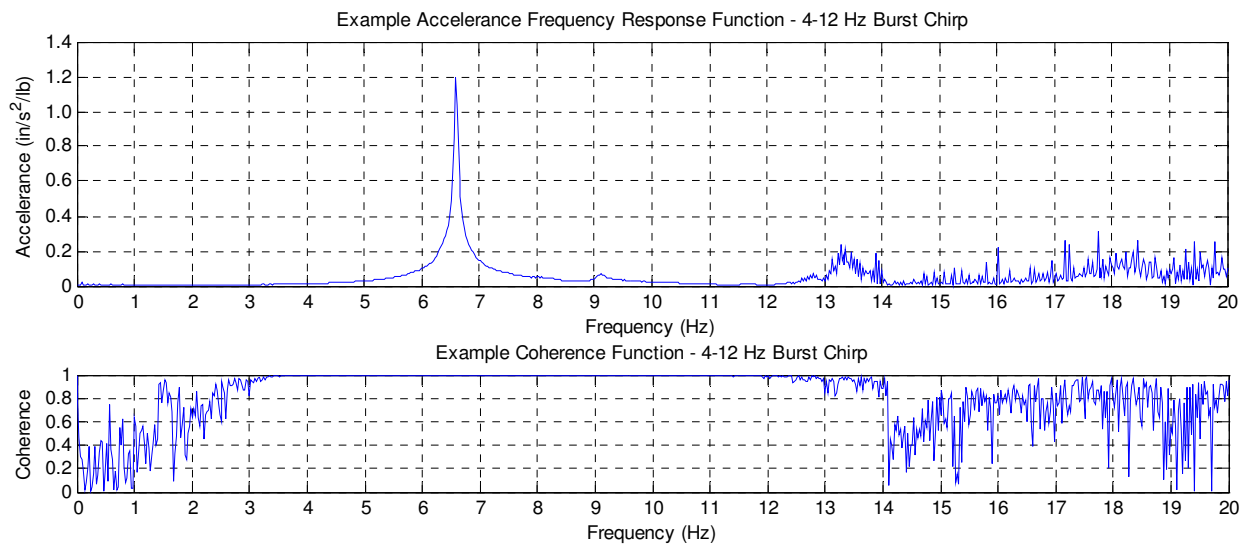


Figure 2.16: Typical 4-12 Hz Burst Chirp Magnitude and Coherence (0-20 Hz)

The accelerance FRF magnitude, phase, and coherence for the example driving point measurement within the 4-12 Hz range are shown in Figure 2.17. Again, the superior coherence achieved with only three averages of the burst chirp signal is apparent, particularly considering the vertical axis scale. For comparison of quality, the coherence from the previous continuous chirp is shown with the burst chirp at a similar scale in Figure 2.18.

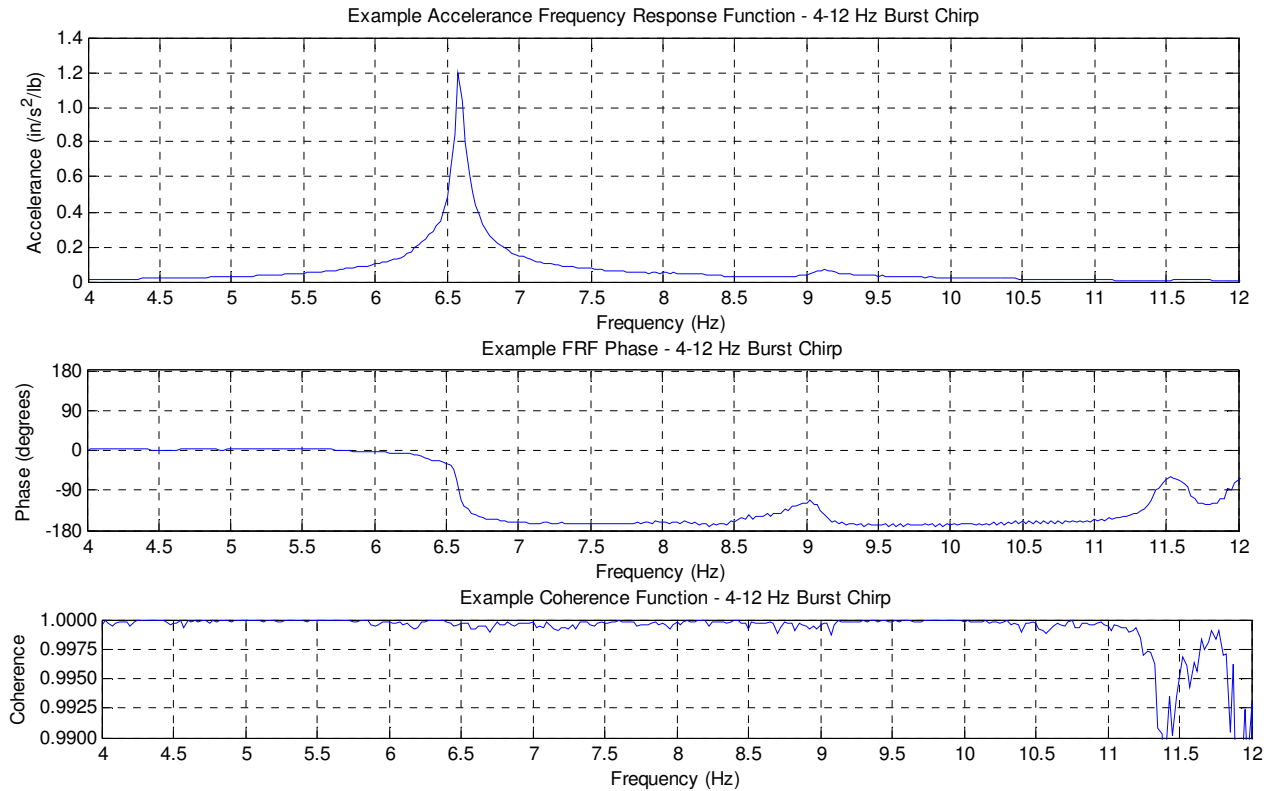


Figure 2.17: Typical 4-12 Hz Burst Chirp Magnitude, Phase, and Coherence

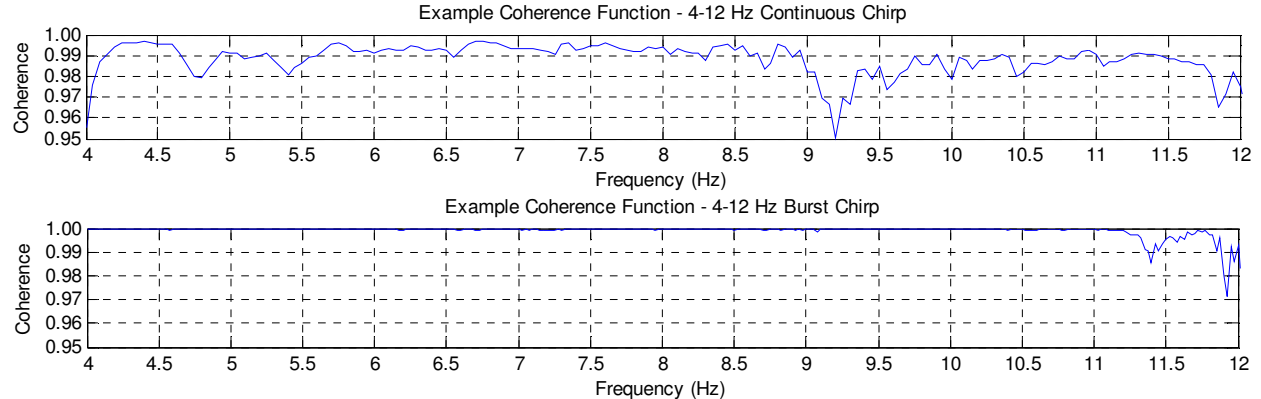


Figure 2.18: Coherence Comparison of Continuous Chirp & Burst Chirp Excitation Signals

One last item worth mentioning is the use of an accelerometer mounted to the armature of the shaker as a measure of the input force. In the autospectrum of this example's force input shown in Figure 2.14, note the dip or hitch of the measurement at 6.575 Hz, which corresponds to the resonant frequency of the tested floor for this measurement. This is also noticeable in the force plate time history of this example as a dip in input force around the 12-second point. This occurs when driving the floor because it takes very little force to achieve very large amplitude response at the resonant frequency. This dip in force is not captured when accelerance FRFs are

derived using an accelerometer mounted to the armature of the shaker and not a force plate. The actual force applied to the floor is due to the *relative* acceleration between the armature and the floor, which at resonance are 90 degrees out-of-phase from one another, and not the absolute acceleration of just the armature. Because the absolute acceleration is measured on the armature, this dip in the reference signal (i.e. the armature acceleration) at resonance is not captured. For example, Figure 2.19 shows the autospectra of a measurement taken on a flexible structure (i.e. a floor) subjected to a 5-10 Hz burst chirp signal. For comparison, both the armature acceleration and the force plate voltage were measured simultaneously and used as reference channels for a driving point acceleration FRF measurement.

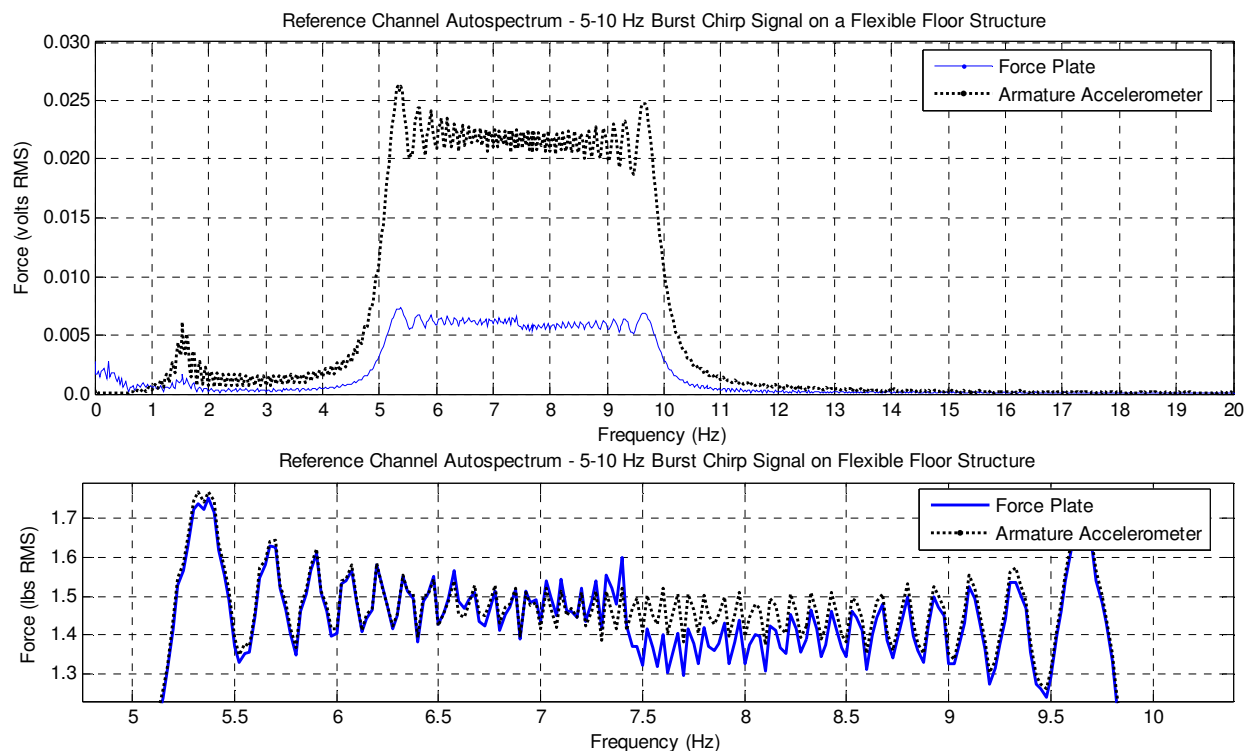


Figure 2.19: Armature Acceleration and Force Plate Autospectra for 5-10 Hz Burst Chirp

The first set of input force autospectra in Figure 2.19 is in raw voltage units. In the second set of autospectra, the two signals are converted into pound units for direct comparison by multiplying the armature acceleration by 67.4 lbs (the weight of armature) and multiplying the force plate signal by its calibration value, 240 lbs/volt. There is a noticeable deviation at and after 7.45 Hz, the resonant frequency of the tested floor in this example. Although the difference is slight in the provided example, it becomes worse as the tested floor accelerations are greater. The overestimation of force by the armature acceleration leads to an underestimation of the

accelerance value. The deviations only occur where accelerations are high, such as at the resonant frequencies, but these are the most critical areas of the accelerance FRF for analysis, which is why the use of an armature accelerometer for estimating force is discouraged.

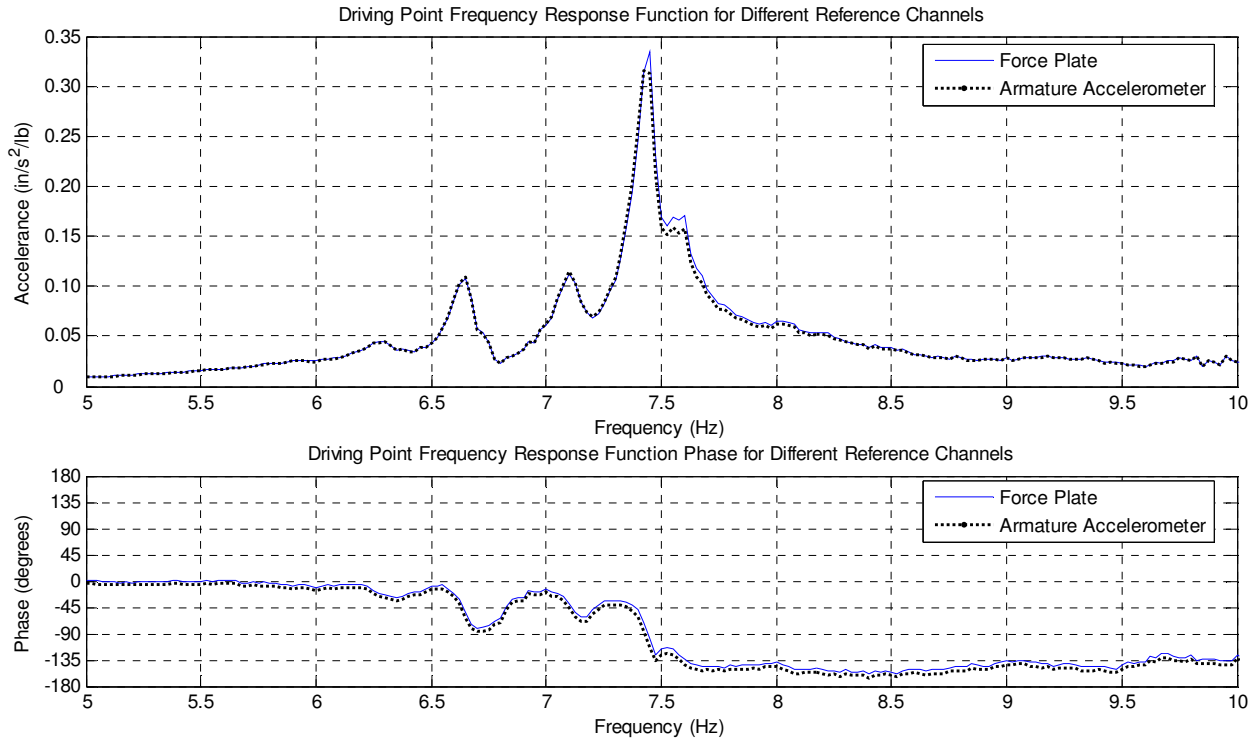


Figure 2.20: Driving Point Accelerance FRF Magnitude and Phase from Different References

The differences in measured accelerance FRF magnitude and phase are shown in Figure 2.20. While the two FRFs are nearly identical, they deviate at the most critical areas, the peaks. At the 7.45 Hz resonant frequency, the peak magnitude is underestimated by 6.6% by the armature accelerometer accelerance FRF, which may or may not be considered negligible depending on the desired accuracy and the application of the measurement. It should be noted that the provided example had relatively low peak accelerance values compared to the tested floors of the presented research, which had peak values often exceeding $1.0 \text{ in/s}^2/\text{lb}$, three times the magnitude of the example accelerance FRF. If at all possible, the use of a force plate is recommended as the best practice, and the use of an armature accelerometer is discouraged unless no other means for measuring the force is possible. Even then, the presented data should include a qualifying statement reflecting the possibility of underestimated accelerance FRF magnitudes around the resonant peaks.

2.4.2 Instrumented Heel Drop

Like the chirp signal, another form of broadband excitation that may be useful for efficiently deriving the accelerance FRFs during modal testing is the instrumented heel drop, where a heel drop impulse excitation is performed on a force plate. Blakeborough and Williams (2003) evaluated the use of an instrumented heel drop test for performing modal analysis on floor systems. They concluded the instrumented heel drop was a more effective modal testing technique than an instrumented impact hammer because it gave better results at lower frequencies, while sufficiently exciting the structures with frequencies in the range of 2 to 15 Hz, which is the range of interest for floor vibration problems due to walking excitation. Hanagan et al. (2003) also concluded the instrumented heel drop yielded high quality data and served as a good alternative to a shaker when cost and portability are an issue. The instrumented heel drop was not used extensively on the floors in the presented research; however this technique for testing floors is described because it could be used efficiently in the absence of a shaker device.

A heel drop is an impact force caused by a person assuming a natural stance, maintaining straight knees, shifting their weight to the balls of the feet, rising approximately 2.5 in. on their toes, and then suddenly relaxing to allow their full weight to freefall and strike the floor with their heels. A demonstration of this technique on a force plate is illustrated in Figure 2.21.

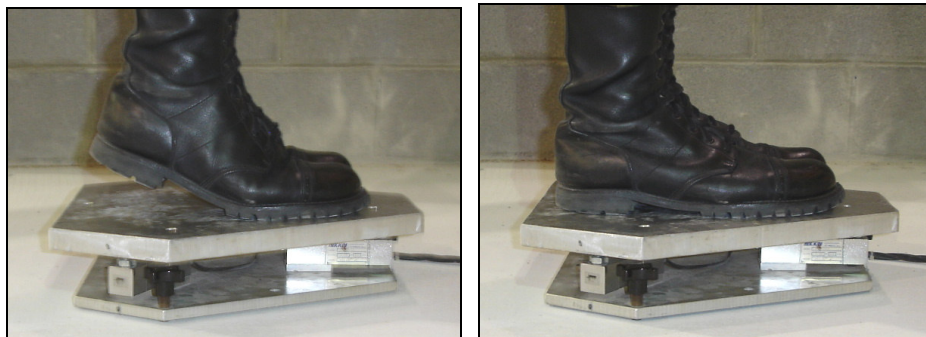


Figure 2.21: Instrumented Heel Drop

An obvious advantage of this type of impulse excitation is how easy it is to perform and that it does not require any equipment other than what is needed to measure the response. Figure 2.22 includes the time histories and autospectra for instrumented heel drops conducted on a rigid surface (slab-on-grade) and a flexible floor structure. The measurements were taken using three heel drop averages from a 245-lb individual wearing rubber heeled boots (Figure 2.21). It is difficult to achieve exactly the same heel drop multiple times, even when they are conducted

consecutively by the same individual; thus averages were taken, which had the effect of smoothing out the autospectra to the form shown in Figure 2.22.

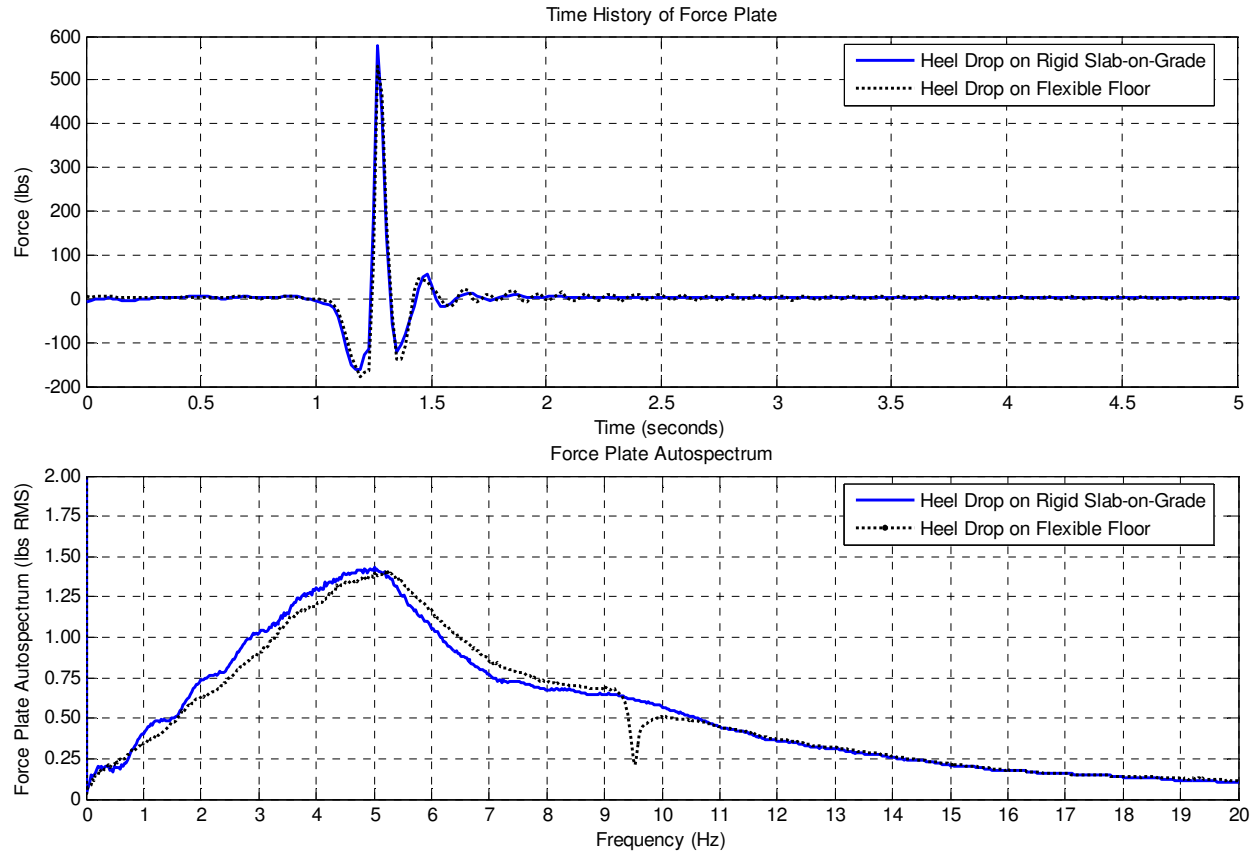


Figure 2.22: Instrumented Heel Drop Time Histories and Autospectra

The impulse loads of the time histories in Figure 2.22 line up because the same trigger settings were used for both the rigid and flexible surface measurements (trigger on input of the force plate with a -2.5% delay). Note that both the time histories and the autospectra are very similar, with the exception of a dip in the input force autospectrum for the flexible floor measurement at 9.55 Hz. Again, like the autospectrum of the force input for a burst chirp measurement, this force drop off is typical at the resonant frequencies of the structure.

Figure 2.23 is a comparison of the force input autospectra for instrumented heel drop excitation and the example 4-12 Hz burst chirp signal discussed in the previous section, which was a different flexible floor system but is still valid for general comparison (Figure 2.14, dominant frequency at 6.575 Hz). One advantage of the instrumented heel drop over the shaker is the ability to excite the lower frequencies that may not be reachable with a shaker due to its internal dynamics. Although concentrated more in the 2-7 Hz range, the instrumented heel drop

does seem to provide a reasonable amount of energy over the general frequency range of interest for floor vibration serviceability.

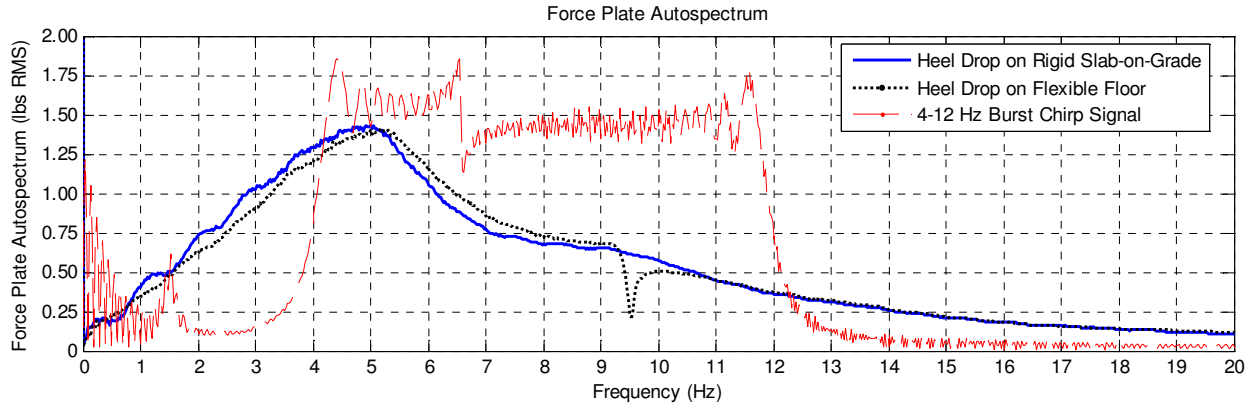


Figure 2.23: Comparison of Chirp & Instrumented Heel Drop Force Input Autospectra

As mentioned previously by Hanagan et al. (2003) and Blakeborough and Williams (2003), the instrumented heel drop could serve as an inexpensive and portable method for conducting rough modal testing, however it should be noted that the quality, consistency, and control offered by modal testing using an electrodynamic shaker cannot be replaced by the instrumented heel drop. Unlike the instrumented heel drop, the electrodynamic shaker has the ability to input concentrated excitation at resonance. It is also worth mentioning that in practice the instrumented heel drop requires the individual to remain on the force plate, likely located in the middle of a bay, for the duration of the measurement. The presence of the individual on the floor will add some amount of damping to the system, particularly at a location of large response. For floor structures with very low levels of damping to begin with, the effects on damping by the individual may be considerable, although this was not studied in this research effort.

2.4.3 Driving Point Accelerance Frequency Response Functions

A driving point measurement is taken by an accelerometer located next to the force plate at the point of excitation and is the key measurement for defining mode shapes. Whether measuring a row or a column of the accelerance FRF matrix of Equation (2.3), this measurement represents a diagonal term, where the input force location, k , is the same as the acceleration response location, i , and thus $A_{ik}(\omega) = A_{ii}(\omega) = A_{kk}(\omega)$. More importantly, it is the datum measurement used by modal analysis software from which responses at all other locations on the floor are scaled. For testing floor systems, the driving point measurement has additional significance. Because most of the current design guidance for floor vibration serviceability is

based on the response at the middle of a bay, this is typically where the shaker is located during modal testing for a direct comparison of experimental response to the response predicted by other hand calculation methods. Typically, this mid-bay location also corresponds with the anti-node of response over a tested area, or the point with the greatest level of response. This makes the driving point measurement ideal for parameter estimation because it will typically have the highest signal-to-noise ratio, the best coherence, and the most consistency between repeated measurements of any location on the floor.

By looking at the accelerance FRFs for the driving point measurements of an excited bay, the “dominant frequency” can be visually identified as the frequency with the largest magnitude peak. Most driving point FRFs for the numerous bays tested had several peaks, usually closely spaced with some larger than others. Therefore, “dominant frequency” is used rather than “fundamental frequency” because this term is typically reserved to describe the lowest frequency of a structure. The intent of the investigation was not to determine the lowest frequency of the floor, but the frequency of excitation that would create the greatest response at the center of a bay within a certain bandwidth. This is a logical approach because it is the center of the bay that will experience the greatest response due to one of the harmonics of walking exciting the dominant frequency.

Figure 2.24 shows 35 driving point accelerance measurements overlaid on one another. These 35 measurements were taken over roughly a three hour period during a modal test of a floor system. An accelerometer was left with the shaker throughout testing to record the driving point accelerance FRFs shown as well as the accelerance FRFs for the other locations of the floor where the roving accelerometers were placed (not shown). While there are a couple of things to note, the first is the consistency and quality of the measurements, even though 35 traces are plotted together. Secondly, each peak on the accelerance FRF indicates the presence of at least one mode, of which there are several, but clearly the dominant frequency is 7.20 Hz.

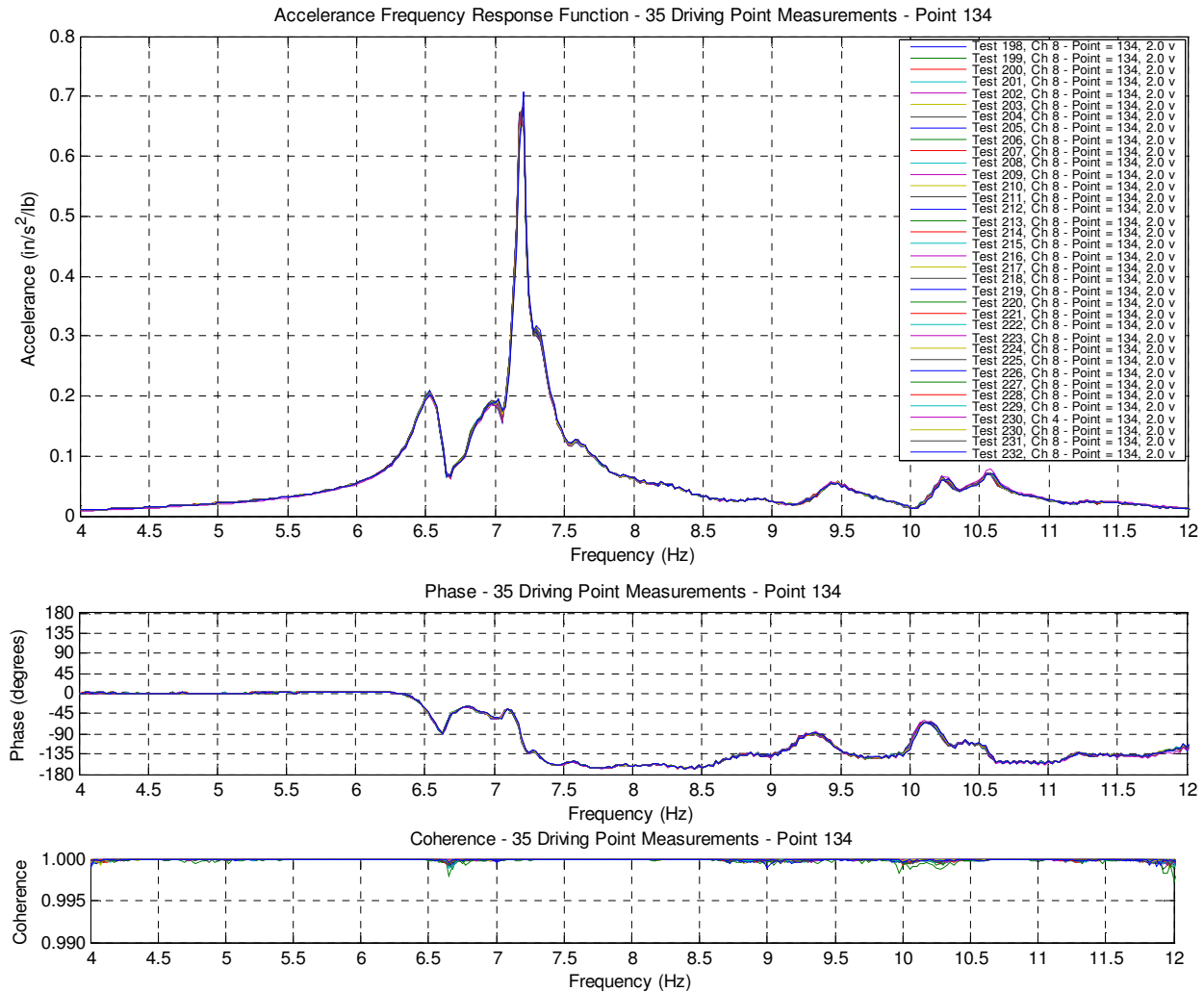


Figure 2.24: 35 Driving Point Accelerance FRFs (Magnitude, Phase, and Coherence)

Most modal analysis software only needs one driving point measurement for scaling mode shapes and performing parameter estimation; however there is a practical reason for always reserving one channel of a multi-channel spectrum analyzer to record the driving point measurement, which is to build an additional level of quality assurance into the modal test. Having an accelerometer with the shaker for every measurement to record the driving point accelerance is a way to identify equipment malfunctions, monitor any change in the floors response over the long periods of time that it may take to sweep the modal coverage area, and simply for redundancy of this key measurement. Although the driving point measurements of Figure 2.24 are very consistent, this may not always be the case, particularly if the sweep over the modal test area is large and takes a long period of time (possibly over multiple days of testing). The consistency of a driving point measurement is an assumption, and given the means

of a free channel on the multi-channel DSP unit, this assumption should constantly be validated. If the driving point measurements do change over time, having the redundant measurements provides an opportunity to identify how they have changed, and possible ways to adjust for it.

2.4.4 Sinusoidal Driving Functions

In the interest of time, certain assumptions must be made by the experimentalist; however it is also the responsibility of the experimentalist to validate those assumptions. Forming the accelerance FRF over a specific frequency range by using a burst chirp excitation is an assumption that claims each FRF spectral value computed has the same magnitude and phase as a measurement where the structure is driven sinusoidally at that spectral frequency and allowed to achieve steady state conditions. Fortunately, with an electrodynamic shaker, this assumption is easily validated. This manual verification of the accelerance measurements derived from the burst chirp signal is a good technique to ensure the quality and consistency of the modal test, and to build confidence that the measured response of the structure corresponds to measured forces, an important part of validating the computed response from FE models.

In a steady state sinusoidal excitation, there is virtually no input force or response at any other frequency besides the driving frequency. Consequently, the accelerance FRF computed for a steady state sinusoidal measurement is completely invalid except for the single spectral value at the driving frequency because the response and force computations at other frequencies are based purely on measured noise. The magnitude of the accelerance for a driving frequency f can be computed by dividing the amplitude of the acceleration response by the amplitude of the input force as shown in Equation (2.11), which is just a single driving frequency representation of the accelerance between two points previously expressed by Equation (2.3).

$$A(\omega) = A(f) = \frac{a_{peak}(f)}{F_{peak}(f)} \quad \text{or} \quad \frac{a_{rms}(f)}{F_{rms}(f)} \quad (2.11)$$

The second expression in Equation (2.11) is valid because the relationship between peak and root-mean-square (RMS) values for a sinusoidal function is simply the constant $\sqrt{2}$. Equations (2.12) are a short derivation of this relationship in terms of $a(t)$, a steady state sinusoidal acceleration function with amplitude a_{peak} :

$$a(t) = a_{peak} \sin \omega t \quad \text{and} \quad T = \frac{2\pi}{\omega} \quad (2.12)$$

$$a_{rms} = \sqrt{\frac{1}{T} \int_0^T a(t)^2 dt} = \frac{a_{peak}}{\sqrt{2}} \quad \text{and} \quad a_{peak} = a_{rms} \sqrt{2}$$

This relationship is convenient because the autospectrum values of input force and acceleration response are usually expressed in terms of RMS voltage by the spectrum analyzers and can easily be extracted from the data at a specified frequency for the spectral value computation using Equation (2.11).

Using the 7.20 Hz dominant frequency identified in the previous example of driving point accelerance FRFs (Figure 2.24), an example steady state sinusoidal measurement is shown in Figures 2.25 and 2.26. For this example measurement, the floor was excited with a 7.20 Hz sinusoidal forcing function with a magnitude of approximately 20 lbs. The resulting driving point acceleration response had a magnitude of approximately 0.035g (3.5%g). Note there are two channels measuring the driving point response at Point 134 (Channels 4 and 8) for this example measurement, and the other accelerometers are located at the middle of other bays on the floor, which is why some are in-phase and others are out-of-phase with the driving point response. The autospectra for both the input force and acceleration response are also included in the figures.

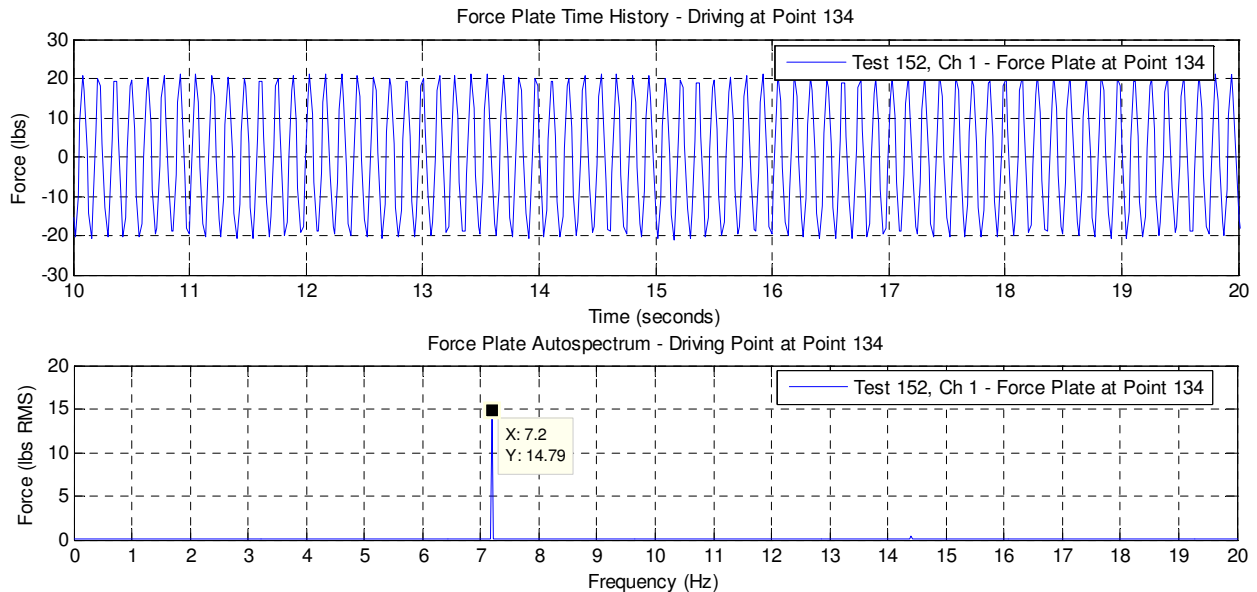


Figure 2.25: Example Sinusoidal Excitation Force Time History & Autospectrum

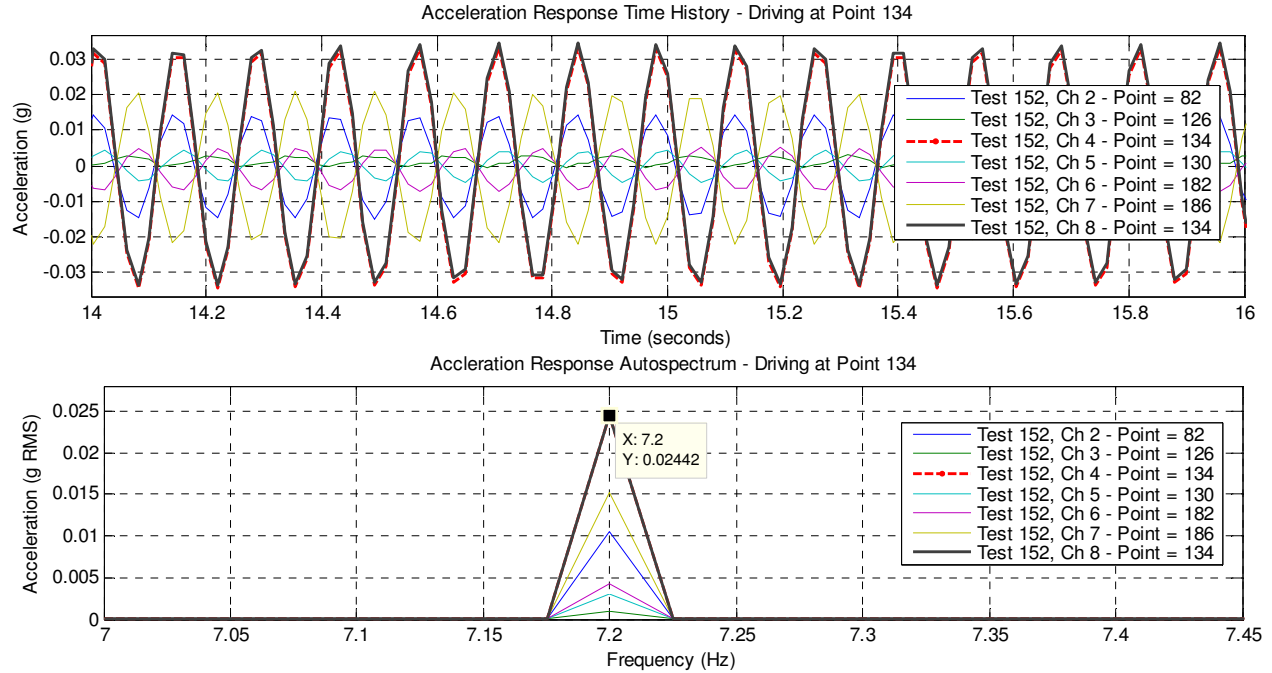


Figure 2.26: Example Sinusoidal Acceleration Response Time History & Autospectrum

The RMS acceleration and force values at the 7.20 Hz driving frequency are highlighted in the autospectra of Figure 2.25 and Figure 2.26. Equation (2.11) can be applied to compute an acceleration of $0.6375 \text{ in/s}^2/\text{lb}$ of input force, that is

$$A(f = 7.20 \text{ Hz}) = \frac{a_{rms}(f)}{F_{rms}(f)} = \frac{(0.02442 \text{ g RMS}) * (386 \text{ in/s}^2 / \text{g})}{(14.7871 \text{ lbs RMS})} = 0.6375 \left(\frac{\text{in/s}^2}{\text{lb}} \right)$$

The average peak magnitude of the 35 driving point accelerance FRFs in Figure 2.24 was $0.67 \text{ in/s}^2/\text{lb}$ at 7.20 Hz, which is in excellent agreement with the manually derived value of $0.64 \text{ in/s}^2/\text{lb}$ ($< 5\%$ difference). Using the RMS values from the autospectra rather than estimated peak values from the time history functions gives a better representation of the accelerance for several reasons. First, there may be some DC offset in the accelerometer or force plate signals, thus requiring an average of the positive and negative peaks to account for the offset. The computation of the autospectrum automatically removes the average of the signal, which for a sinusoidal function is either zero or the amount of the DC offset. Secondly, the time history shown is the last of the measured time block(s), whereas the autospectrum reflects the updated average of all time blocks included in the measurement.

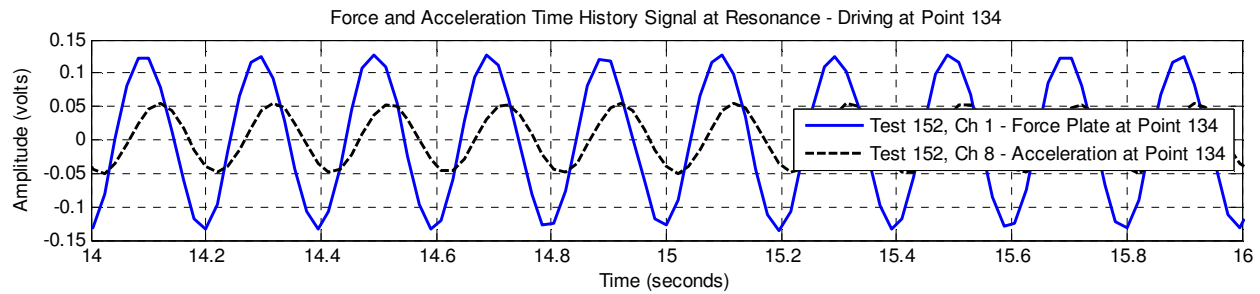


Figure 2.27: Comparison of Force and Acceleration Time Histories

Because the autospectra do not carry any phase information, a different approach is needed if there is an interest in the phase between the excitation and response signals for a sinusoidal measurement. For the example provided, the difference in phase is quite noticeable (especially because it is being driven at resonance) as shown in Figure 2.27.

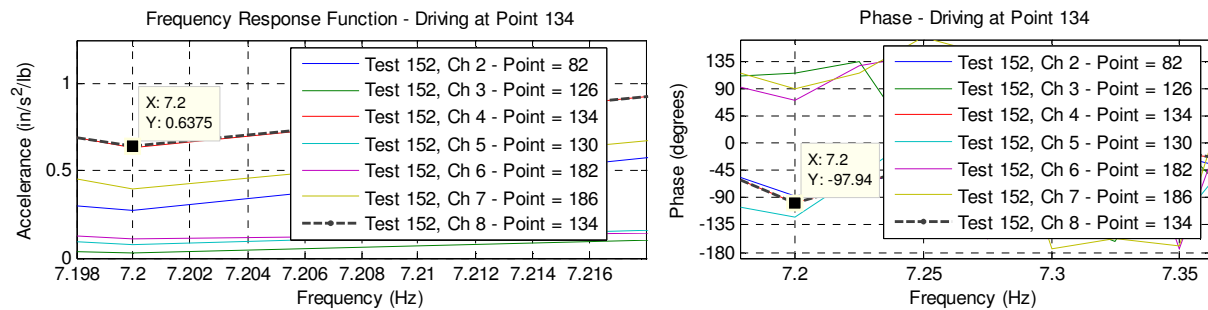


Figure 2.28: Accelerance FRF Magnitude and Phase for a Sinusoidal Measurement

One method to estimate the phase would be the visual evaluation of the phase shift of the two signals; however there is a much easier and more accurate way to measure this quantity. If one or multiple averages are taken of the sinusoidal measurement, the computation of Equation (2.11) is automatically performed by the spectrum analyzer and given as the magnitude of the accelerance FRF at that frequency. Additionally, the phase is computed in this manner. If more than one average is used, then a coherence function is computed, providing a tangible representation of the measurement quality. Figure 2.28 shows the computed accelerance FRF magnitude and phase values for the provided example, demonstrating that by taking an average during a steady state sinusoidal measurement, the hand calculations for accelerance and phase can be avoided by relying on the computation by the spectrum analyzer. Additionally, because more than one average was taken in the example, a coherence of 0.99995 was computed at the 7.20 Hz driving frequency, providing additional confidence in the measurement quality.

The most useful application of the sinusoidal measurement is not simply to verify the accelerance values computed by an accelerance FRF derived from burst chirp excitation, but the

verification of the location of the peak frequency. As a manual check to ensure the dominant frequency (i.e. the frequency of peak accelerance) was correctly located using burst chirp excitation, the shaker can be run sinusoidally at frequency increments above and below the identified dominant frequency. This must be accomplished only at frequency increments that correspond to computed spectral lines, which are based on the chosen frequency resolution, otherwise the estimated values will be invalid (underestimated, actually). In some instances, the actual peak accelerance from steady state sinusoidal excitation may be at a frequency that is one or two spectral lines different from the one identified from the chirp derived accelerance FRF (0.025 Hz to 0.05 Hz for the tested floors). Although not strictly required for every modal test, this is another example of checking the assumptions often taken for granted during modal testing so that the experimentalist has confidence in the quality of the modal measurements.

2.4.5 Unreferenced Measurements

The easiest dynamic measurement to take when testing a floor system is the unreferenced response-only measurement because it requires the least amount of equipment and technique. Handheld single-channel spectrum analyzers are much less expensive and more portable than their multi-channel counterparts that have the ability to conduct the referenced modal testing measurements previously discussed. Examining the acceleration levels from various types of unreferenced excitation can indicate a lot about the behavior of the floor under service conditions. As previously shown in the autospectrum of a heel drop in Figure 2.22, despite whether the input force of the heel drop is measured or not, it can still provide adequate excitation to a floor system within the frequency range of interest for floor vibration serviceability. Thus, analysis of the frequency content of the response from an unmeasured heel drop excitation can give insight into the active frequencies of the floor. Arguably, the only drawback to unreferenced measurements is when too much is interpreted from the limited information they provide. The only information a single-channel unreferenced measurement can provide is an accurate measure of the acceleration over a period of time, and the frequency content of that acceleration time history. Given certain types of excitation, dynamic properties of the floor can be estimated to a limited degree from the unreferenced measurement; however it should be understood that only modal testing provides the accuracy typically needed for any detailed characterization of the behavior of a floor system. As long as this limitation is

understood, then the unreferenced measurement is an effective tool that has its place in dynamic testing of floor systems.

Unreferenced heel drop measurements are most effective for indicating the lower frequency content of the floor system. Previously, Figure 2.23 showed the autospectrum of an instrumented heel drop compared to the autospectrum of a chirp signal. The heel drop has a noticeable advantage at lower frequencies because the shaker is limited by its internal dynamics and is limited in its ability to excite these lower frequencies. This is why it is good practice to conduct several heel drop measurements prior to the start of modal testing to identify the active frequencies of the floor system, which are crucial for choosing the parameters for the chirp signal. Figure 2.29 shows an example acceleration time history for a heel drop measurement using a single-channel Ono Sokki CF-1200 Handheld FFT Analyzer.

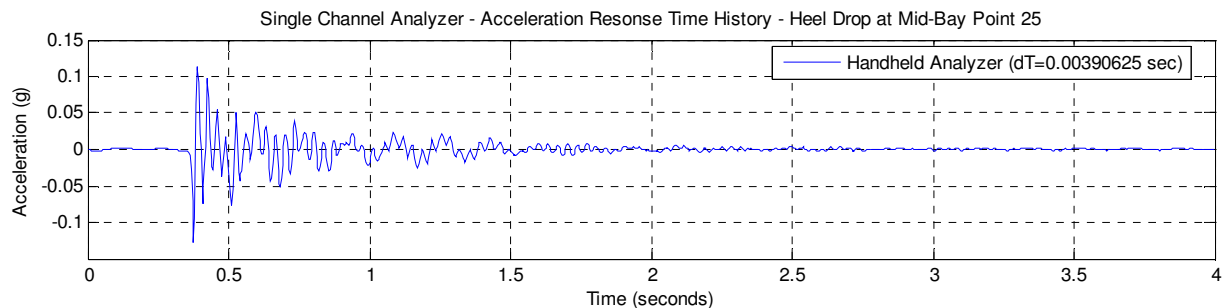


Figure 2.29: Sample Acceleration Time History to Unreferenced Heel Drop Excitation

Note that the unreferenced time history measurement has excellent time domain resolution, which is a product of 1024 samples taken over the four second time record. Unfortunately, a byproduct of the shorter time history is a loss in frequency domain resolution, which for measurements using the Handheld FFT Analyzer was 0.25 Hz (+/- 0.125 Hz) as shown in Figure 2.30. This frequency domain resolution is in stark contrast with the autospectrum of the response at the same location on the floor due to a 4-12 Hz chirp signal (Figure 2.30). The chirp signal autospectrum was taken using the multi-channel SigLab spectrum analyzer set at a frequency domain resolution of 0.05 Hz.

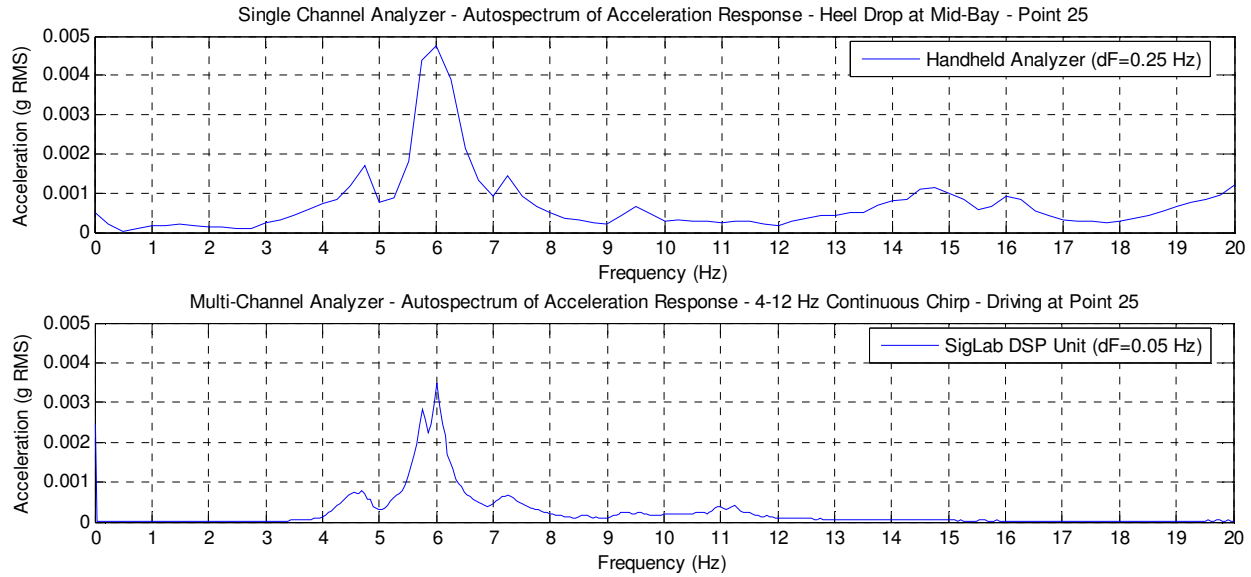


Figure 2.30: Autospectra of Unreferenced Heel Drop and Chirp Measurements

The first three significant frequencies of the heel drop autospectrum of Figure 2.30 are 4.75 Hz, 6.00 Hz, and 7.25 Hz. The respective peaks in the autospectrum of the chirp signal (with much finer frequency domain resolution), are 4.70 Hz, 6.00 Hz, and 7.25 Hz; however the peak at 5.75 Hz is completely missed by the poor resolution of the heel drop autospectrum. If only the unreferenced autospectra were available, the wide peak at 6.00 Hz may be misunderstood as a large amount of damping at this frequency, rather than the presence of the two closely spaced peaks shown in chirp autospectrum. It should be stressed that this was not a weakness of the unreferenced measurement, but a weakness of the equipment that could not provide adequate frequency domain resolution for low frequencies and low levels of damping. It is also worth mentioning that for all but the strongest of frequencies, the peaks of the autospectrum may not be the exact peak frequencies of the accelerance FRF, should it be measured. The magnitude of the accelerance FRF can be interpreted as the autospectrum of the response divided by the autospectrum of the force. Unless the autospectrum of the force is a constant value across all frequencies, which it is not even for a chirp signal, the magnitude of the peaks in the accelerance FRF may not be the same as those in the response autospectrum. Although not shown, the peaks of the accelerance FRF computed for the chirp signal shown in Figure 2.30 are 4.75 Hz, 5.80 Hz, 6.00 Hz, and 7.25 Hz, two of which differ from the autospectrum by one spectral line. The difference may be slight in this instance, but the nuance should not be overlooked when interpreting data from unreferenced measurements. It should

also be noted that for heel drop measurements, the shape of the autospectrum is definitely not constant across the frequency range, as shown in Figure 2.23. Because of this, extra caution should be exercised when attempting any comment on the relative strengths of modes from the relative size of the peaks of the autospectrum. These discrepancies highlight the need for using a referenced modal testing setup for floor systems if it is desired to accurately characterize their dynamic behavior.

Several different types of unreferenced measurements are available. Some examples include measurements from ambient conditions and various human excitations, including heel drops, walking parallel and perpendicular to the floor framing, and bouncing at harmonics of the bay's dominant frequency. One technique is to attempt to excite the floor by bouncing at a harmonic of the resonant frequency in an attempt to achieve steady-state resonant response. The bouncing excitation can then be suddenly stopped and the resulting response decay recorded for the purpose of estimating damping in the system. While this method provides a crude estimate of damping, it is typically higher than actual values due to the damping that the human body introduces into the system. Additionally, closely spaced modes can create a beating effect in the decay that makes the estimate difficult. More accurate methods exist for estimating damping of the system, such as the half-power bandwidth method using the accelerance FRF, or multi-degree-of-freedom curve fitting methods of a set of accelerance FRFs, which are discussed later.

As previously mentioned, unreferenced measurements have their advantages, but high quality referenced modal data is a better indicator of the dynamic behavior of a structure, particularly if it is to be used to validate FE models. Much of the previous research and FE modeling of steel composite floors have been based on frequency content of unreferenced measurements. As demonstrated in the unreferenced heel drop example, the frequency content and/or damping of a system can be misinterpreted or overlooked by poor frequency domain resolution or other misguided assumptions about the autospectrum of response.

2.4.6 Damping Estimates

Although it is commonly known that the actual mechanism of energy dissipation of an in-situ floor system (or any large structure for that matter) is much more complicated than simple viscous damping used for mathematical convenience, the equivalent modal viscous damping ratio, β_r , is still the most common value used for expressing the damping behavior of the floor.

Unlike mass and stiffness, damping cannot be determined by the materials and layout of the structure other than in the most general estimated terms (Clough and Penzien 1993). It is a value that must be estimated from measurements, and several methods are available for this process. Some of these methods (as used in the presented research) are presented in this section along with their advantages and disadvantages.

The half-power method, also known as the bandwidth method or half-power bandwidth method, is the most straightforward of the methods for estimating damping and is based on the properties of the frequency response function of a system at resonance. The half-power bandwidth of a resonant peak is defined as the width of the frequency response function at $1/\sqrt{2}$ of the peak amplitude at resonant frequency f_r . Equation (2.13) shows the computation of the damping ratio, where f_a and f_b are the frequencies on either side of the resonant frequency that mark the half power width.

$$\beta_r = \frac{f_b - f_a}{2f_r} \quad (2.13)$$

A derivation of Equation (2.13) can be found in the text by Chopra (2001). The advantage of this method is the ability to compute damping directly from the peaks of the measured accelerance FRFs. This simple computation can be done in the field or in post processing. The driving point measurements are typically the best measurements to use for the computation, as the peaks of the accelerance FRFs are generally much more defined than measurements at other locations of the floor. Theoretically, the estimated damping should be the same regardless of the chosen measurement; however the peaks in measurements that are far away from the driving point can sometimes be poorly defined if at a boundary or other location not significantly excited by the frequency. As a cautionary note, it was previously discussed that the autospectrum of response can share a similar shape as the accelerance FRF, but it is not the same. The half-power method is derived from a forced-vibration frequency response curve, and not the autospectrum, which is simply a response-only measurement. Although the computed damping values may seem reasonable, the half-power method is not suitable for unreferenced response autospectra. A potential disadvantage of the half-power method is that the frequency response must be accurate at and around the resonant peak (Clough and Penzien 1993). At the low levels of damping typically found in bare floor systems ($< 2\%$), the peaks of the accelerance FRFs are quite sharp. Not only does this highlight the need for good quality control of the accelerance measurements,

it also demonstrates how the choice of frequency domain resolution can affect the ability to adequately estimate the damping of the system using the half-power method. Another disadvantage of the method, as with all the methods for estimating damping, is the difficulty of properly estimating damping in system with closely spaced modes (peaks). If two peaks of the accelerance FRF are close, the half-power estimate may be skewed by the presence of the other peak, which has the effect of widening the accelerance FRF and increasing the computed estimate of damping.

To verify the measured accelerance FRFs adequately capture the resonant peak(s), it may be worthwhile to perform sinusoidal measurements to manually compute the accelerance values at frequencies around the peak. If steady state sinusoidal measurements are taken at enough frequency increments on either side of the resonant frequency (i.e. out to frequencies with accelerance values less than $1/\sqrt{2}$ of the peak accelerance), the accelerance FRF may be defined enough to perform a half-power damping calculation on the manually derived values. The advantage of this stepped sine sweep approach is that it provides an additional level of verification of both the accelerance FRF values and the estimated damping. The disadvantage of this approach is the time required to perform the measurements, and if it is determined that the accelerance FRF measurements from chirp excitation are of a high enough quality, it may be unnecessary or redundant.

Driving the floor sinusoidally is also useful as an initial part of capturing the time history of the response decay, another limited method for estimating damping. While the time history of decay of the response from any type of excitation demonstrates the floor's ability to dissipate energy, impact excitation using a heel drop or instrumented impact hammer tends to excite a wide range of frequencies, thus the response decay to these types of excitations may include response from several excited modes. If there is only one very dominant mode of vibration, however, the resulting decay trace may be very smooth. Unfortunately, there is typically more than one participating mode for this type of excitation on in-situ floor systems. Additionally, an individual performing the heel drops adds damping to the system, as does an individual with instrumented impact hammer. With closely spaced modes, or several strong modes, there will not be a clean decay trace if multiple modes are participating in the response. One method of attempting to minimize the effect of other modes is to drive the floor sinusoidally at the resonant frequency of the mode of interest, and then shut off the sinusoidal excitation to record the time

history of response decay. To estimate the damping of the mode, the resulting decay trace can be analyzed by either the logarithmic decrement method or by curve fitting the decay with an analytical expression. The equation for the logarithmic decrement is not shown here, but it is a method that uses the magnitude of the response peaks over several decay cycles to estimate the damping in the system. A brief derivation of the analytical expression of decay that is used to curve fit the response is:

The displacement free decay of a SDOF oscillator in terms of initial conditions is:

$$u(t) = e^{-\beta\omega_n t} \left[u(0) \cos(\omega_d t + \phi) + \left[\frac{\dot{u}(0) + u(0)\beta\omega_n}{\omega_d} \right] \sin(\omega_d t + \phi) \right]$$

where

$$\omega_d = \omega_n \sqrt{1 - \beta^2} = \text{the damped natural frequency}$$

For $u(0) = 0$ (i.e. initial velocity only): (2.14)

$$u(t) = e^{-\beta\omega_n t} \left[\left[\frac{\dot{u}(0)}{\omega_d} \right] \sin(\omega_d t + \phi) \right]$$

\therefore The acceleration free decay of a SDOF oscillator from an initial velocity is:

$$\ddot{u}(t) = \left[\frac{\dot{u}(0)}{\omega_d} \right] e^{-\beta\omega_n t} \left[(\beta^2 \omega_n^2 - \omega_d^2) \sin(\omega_d t + \phi) + (2\beta\omega_n \omega_d) \cos(\omega_d t + \phi) \right]$$

The natural frequency, ω_n , should equal to (or be very near) the driving frequency prior to decay. The initial velocity term, $\dot{u}(0)$, is arbitrary and just scales the magnitude of the decay curve. The only two terms in the expression that define the curve fit decay are the natural frequency ω_n and the damping ratio β (the damped natural frequency is defined using those terms). Thus, the analytical decay trace can be defined exclusively by these two estimated values and shifted along the time axis until it visually overlays the measured response decay. It is worth mentioning that the logarithmic decrement method is frequency independent, whereas the analytical expression in (2.14) accounts for a decay frequency that may be slightly different than the driving frequency. This may occur because the applied frequency is usually at a spectral frequency increment and the actual frequency of the floor may fall between spectral lines.

The theory of why the decay from resonance should work is based on the orthogonality of mode shapes and the principle that if a structure is initially displaced in the exact shape of a

mode shape, then the resulting free decay response will only be in that mode of vibration. Because it is impossible to place an in-situ floor in an initial displaced shape by static methods, driving the floor at resonance theoretically produces a standing wave of the floor in the shape of that mode of vibration and stopping the excitation should result in free decay in that mode. Theoretically, this is a great method for estimating the damping of a mode. In practice, however, there are a lot of assumptions in the preceding statement and *this method of estimating damping only has limited application and is likely not as efficient as other methods*. Ensuring that the exact resonant frequency is achieved is difficult, thus it is assumed that the floor is being driven only very near resonance. More importantly, shutting off the excitation at exactly the right instant so that the floor does not undergo a step function is not possible. As a result of the step function, however small it may be, the floor is excited in other frequencies than just the targeted resonant frequency. The resulting response decay trace may not be a single mode function and the resulting damping estimates of the analytical decay expression (or the logarithmic decrement method) may be skewed. These same limitations apply when the response decay is achieved from an impulse load like a heel drop, because the impulse load excites multiple frequencies.

To demonstrate the limitations of this method, a few examples are presented of actual measured accelerance FRFs for an in-situ floor system and the corresponding decay analysis that was performed as described above. The first example is where the decay curve fit is an effective method for estimating damping, at least for modes that are clearly dominant and separated from other modes. An accelerance FRF for a driving point measurement is presented in Figure 2.31.

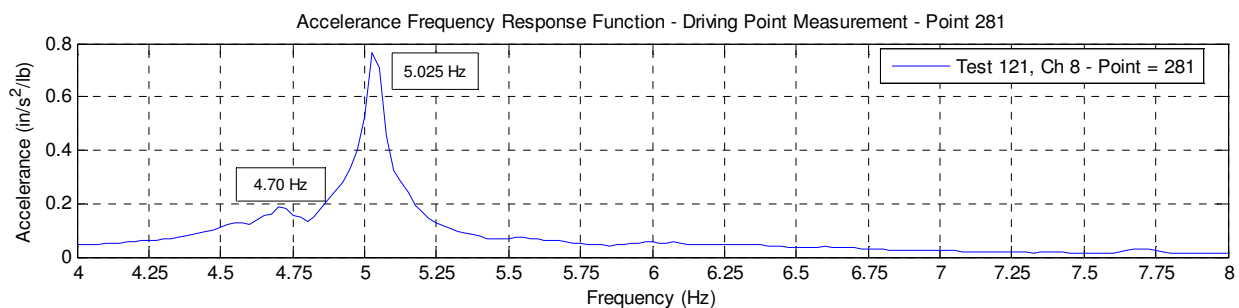


Figure 2.31: Accelerance FRF – Driving at Point 281

The dominant frequency is clearly 5.025 Hz, and the floor was excited to steady state conditions at this frequency before the shaker was shut off to allow free decay. The resulting decay trace is shown in Figure 2.32 and the corresponding analytical decay curve fit is shown in Figure 2.33 for the entire time record as well as a representative time segment. The curve fit

estimated a damping ratio of 0.70%, which was in excellent agreement with the corresponding half-power method estimate of 0.65% from the 5.025 Hz peak in Figure 2.31.

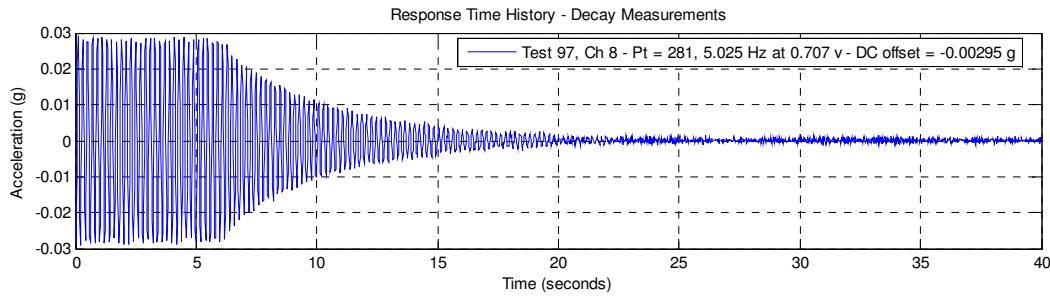


Figure 2.32: Point 281 – Response Decay from 5.025 Hz

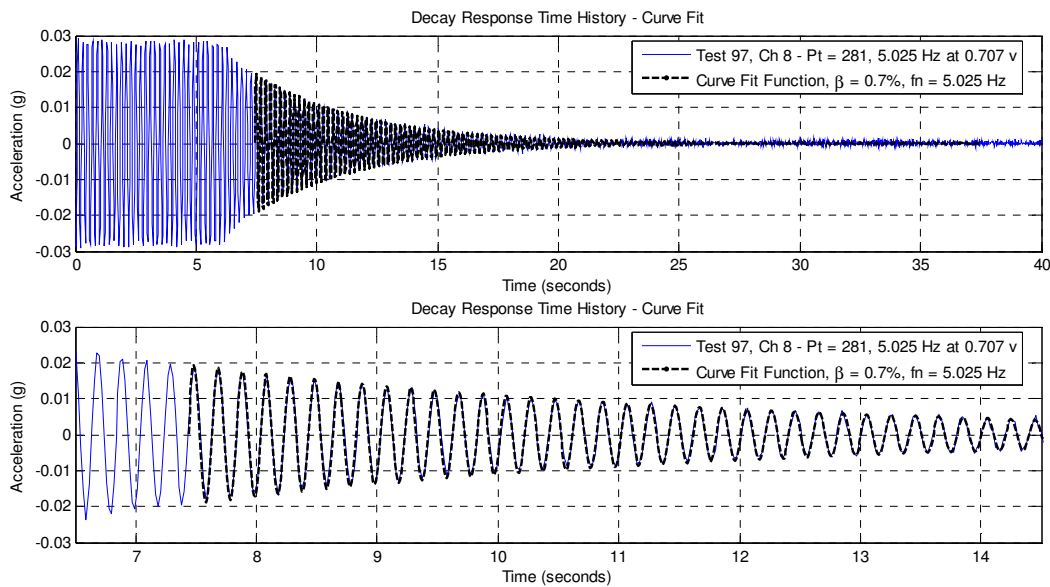


Figure 2.33: Point 281 – Decay Curve Fit, $\beta = 0.70\%$ at 5.025 Hz

For contrast, Figure 2.34 shows the decay from steady state at 4.70 Hz, the other peak frequency of the accelerance FRF of Figure 2.31. This is a clear demonstration of the limitations of the decay curve fit method, as the decay response is obviously not a single frequency response. In fact, the clear beating phenomenon indicates a significant contribution from another frequency, which in this case is the 5.025 Hz dominant frequency of the bay. If two sinusoids with slightly different frequencies are added together, the resulting beating phenomenon is a product of the signals going in and out of phase with one another, alternately adding and canceling, respectively. The period of the resulting beat is equal to the difference in the two frequencies. In Figure 2.34, the period of the beat is approximately 3.2 seconds, indicating a

difference in frequency of $1/3.2 \approx 0.31$ Hz. The difference between the actual peaks of the accelerance FRF (5.025 Hz and 4.70 Hz) is 0.325 Hz.

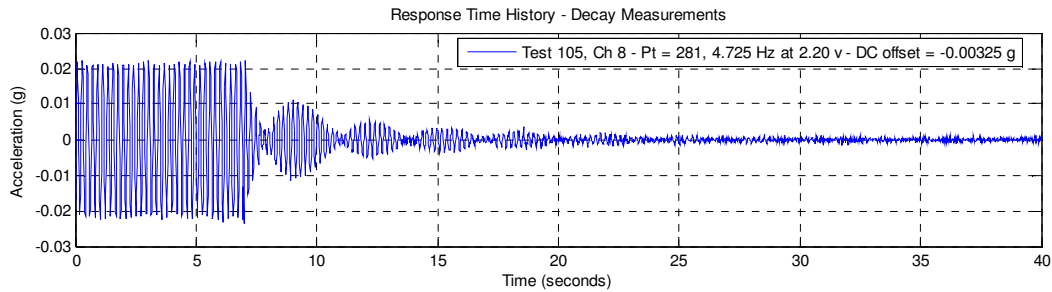


Figure 2.34: Point 281 – Response Decay from 4.725 Hz

The beat of Figure 2.34 is very obvious because of the significant contribution of the other frequency, and the effects of smaller contributions may not always be as clear. For example, Figure 2.35 shows the accelerance FRF for another bay on the floor with several closely spaced frequencies of similar magnitude. The resulting decay from driving at its dominant frequency of 4.875 Hz is shown in Figure 2.36.

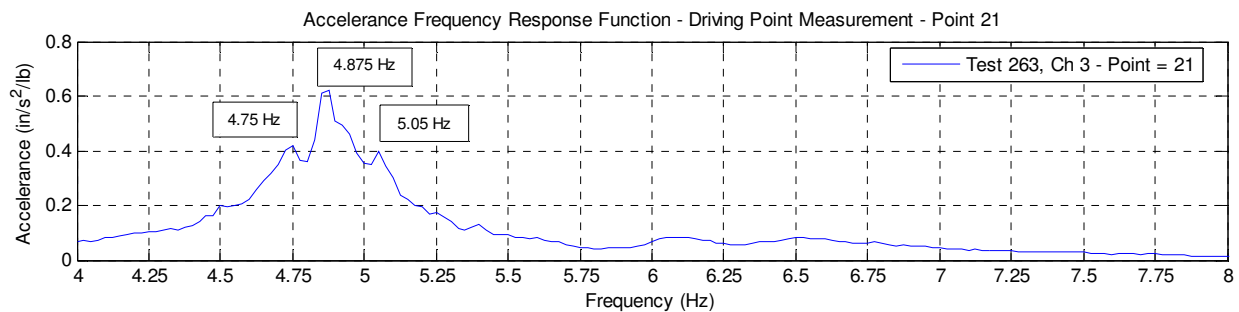


Figure 2.35: Accelerance FRF – Driving at Point 21

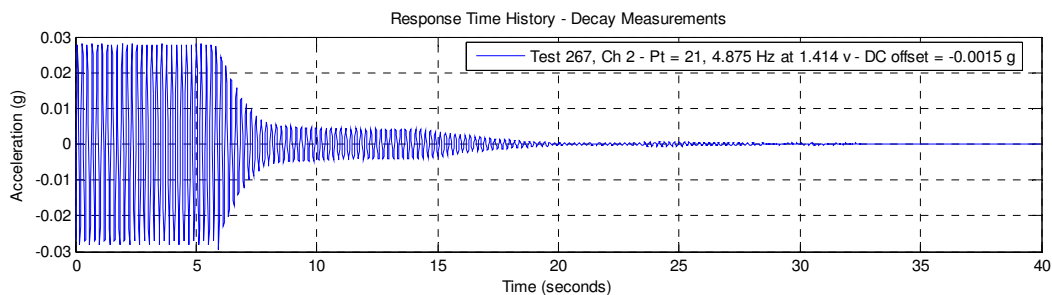


Figure 2.36: Point 21 – Response Decay from 4.875 Hz

While the shape of the decay trace is obviously quite unexpected, it may not be clear that this is the beating phenomenon previously described and a result of the contribution of the other modes. In fact, using only the driving frequencies and one additional frequency in decay

expressions (not shown), it did not take much effort to reproduce the same general unexpected shapes of the previous two decay traces as shown in Figure 2.37.

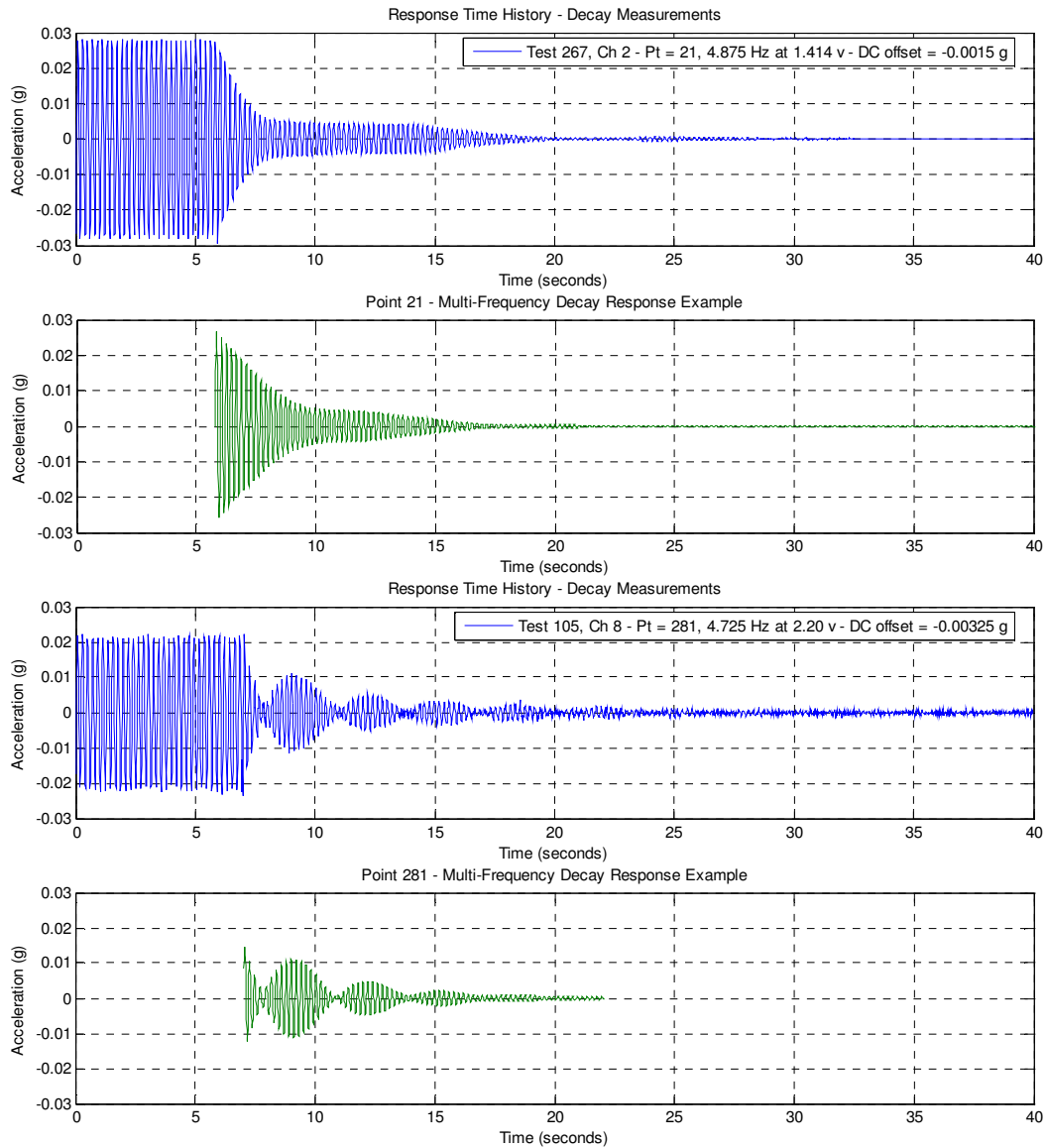


Figure 2.37: Example Analytical Decay Curves with Multiple Frequencies

Obviously, trying to reproduce a series of non-intuitively-shaped decay traces using analytical expressions is not an efficient use of time, especially considering there are other methods of estimating damping for systems with closely spaced modes, namely MDOF curve fitting of the accelerance FRFs using modal analysis software. The previous examples were presented as a cautionary note and to demonstrate the limitations of the decay curve fitting method.

Although it was demonstrated the analytical decay curve fitting technique is a valid method for estimating damping for systems with well-defined dominant modes, a final example is presented to show another situation where the method could be misinterpreted. Figure 2.38 is an accelerance FRF for another bay on the floor, with a clearly dominant peak at 5.075 Hz and a much smaller, but closely spaced, peak at 4.90 Hz. A half-power method estimate of the peak may be skewed due to the contribution of the closely spaced mode, so a response decay from resonance was performed and is shown in Figure 2.39.

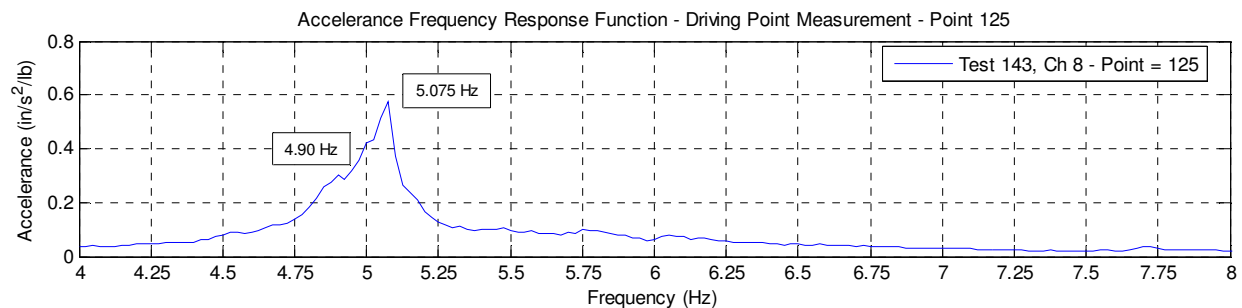


Figure 2.38: Accelerance FRF – Driving at Point 125

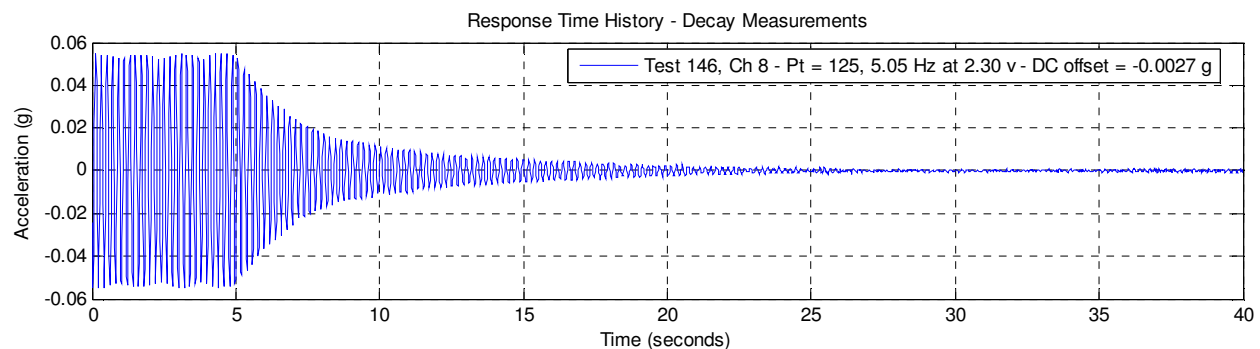


Figure 2.39: Point 125 – Response Decay from 5.05 Hz

At first glance, the decay trace in Figure 2.39 may seem accommodating to an analytical curve fit, however attempts would prove difficult as there seem to be very different decay properties for the first three seconds of decay and the remaining portion of the decay. Again, the beating phenomenon (contributions from multiple frequencies) is the cause, and without an understanding of this the decay of Figure 2.39 could easily be mistaken for amplitude dependent damping, which does often occur (Clough and Penzien 1993). In Figure 2.40, two portions of the curve seemed to be fit well by two different damping values, an initial level of 1.2% over the first three seconds of decay, and a final level of 0.5% starting at an acceleration amplitude of 0.02g. However, this is an incorrect assessment, and although not shown, the actual shape of the

decay can be expressed as a combination of the driving frequency of 5.05 Hz and a small contribution from the closely spaced peak frequency 4.90 Hz.

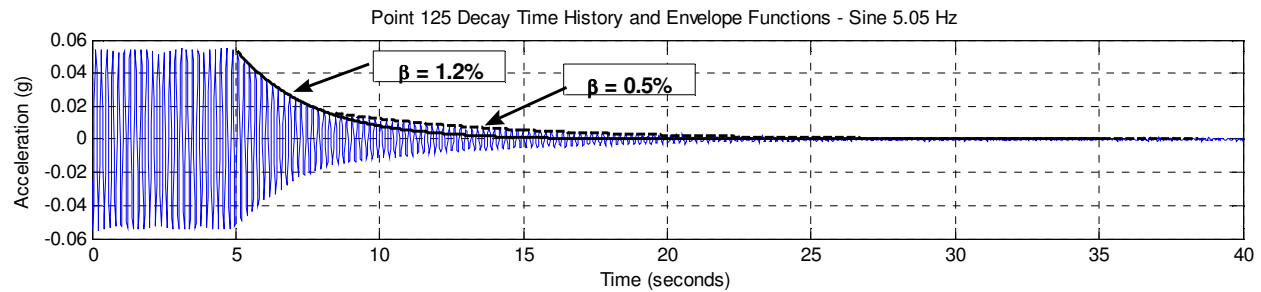


Figure 2.40: Point 125 – Misinterpreted Curve Fit Decay

To summarize the different methods for estimating damping, the half-power method using the driving point accelerance FRFs is the quickest, easiest, and most reliable in the field. Additional verification that the peak of the accelerance FRF is correctly captured may be accomplished through steady-state sinusoidal measurements. Using any method of analysis on the decay response should be approached with caution because it is very difficult to capture a pure single mode response. This applies for using the logarithmic decrement method or curve fitting with a single frequency analytical expression. It should also be noted that this also applies to decay response to impulse loads, such as instrumented or unreferenced heel drops, as well as decay from steady state sinusoidal excitation. Overall, the most reliable method for estimating the damping of a system is the MDOF curve fitting of a set of accelerance FRFs using modal analysis software, and a manual check using the half-power method is a good quality check to ensure that realistic values are computed.

2.4.7 Floor Test Area

As previously stated, the test area of a floor may be quite large, and the time available for testing is typically limited. If the tested floor is within a building under construction, testing may be limited to evenings or weekends due to the extraneous noise in the building during construction activities. The rapidly changing conditions of a building under construction may also pose problems, particularly if the work being done affects the boundaries of the tested floor. If the tested floor is within an occupied office building, similar problems arise due to working hours and the presence of cubicle partitions or other office fit out that can make testing difficult. Thus, the “ideal area to be tested” and the “actual area to be tested” are typically quite different. Within the actual area to be tested, the number and location of test points must be determined on

a case-by-case basis, resulting in a compromise based on test objectives, access to test areas, available equipment, and available time to test.

For a modal sweep of a floor area (i.e. measuring the accelerance FRFs over an area to extract the mode shapes), a grid of quarter points within a bay is recommended. For a rectangular bay, the quarter point grid has 25 points, including the middle of the bay where the shaker is typically located and all boundaries of the rectangular area including the columns. Although this may seem like a coarse test grid, it has the ability to capture both single and double curvature of the rectangular floor panel. For a perfectly symmetric rectangular panel, the midpoint is a node for the higher modes with double curvature; however the different boundaries of a real floor system place the node slightly off center. Although the mode shapes of double curvature within a bay are almost always beyond the frequencies of interest for floor vibrations, a shaker located at the middle of the bay is still capable of exciting these higher modes provided the chirp signal covers the frequency range.

One method for reducing the number of measurements on a floor is to not test certain areas based on the assumption of little or no response, like some types of boundaries. Columns, exterior walls, interior full height partitions above and below the tested floor, and shear walls are all locations where the response will likely be small, but may or may not be negligible. Not taking extensive measurements at these locations is acceptable, provided the assumptions are validated by a few measurements.

When testing time is limited but the behavior over a larger area is of interest, a reduced testing protocol consisting of just the centerline measurements or the three interior quarter point measurements over a strip of bays may be used. While not as detailed as a full area set of measurements, this reduced set of measurements can still provide enough resolution to animate the mode shapes and describe the general behavior of the floor along the length or width of the building. The shapes from a centerline set of measurements are essentially 2-D cross-sections of the floor sliced down the centerline. Floor systems are plate structures in two-way bending, so even though a cross-section through the middle of the plate maximizes the chances of capturing the overall behavior of the floor, it may still lead to misinterpretations. Measuring the interior three quarter points along a strip rather than just the centerline takes advantage of a reduced set of measurements, but also provides the ability to capture the two-way behavior.

A minimal reduced set of measurements consists of just measuring the mid-bay accelerance FRFs of all other bays while forcing at the middle of one bay. What this method provides is a point-to-point comparison of the magnitude and phase for the middle of two bays at frequencies of interest. The difference in accelerance magnitude at a dominant frequency gives an indication of the relative acceleration response between the two points in that mode, and the phase will give an indication whether the response is in-phase, out-of-phase, or somewhere in between with the excited bay. Because the lowest frequency modes of a floor system are generally a combination of single curvature in each bay, this comparison can give an idea of the rough shape of the mode by indicating which bays are concave up or concave down with respect to the excited bay. It is recommended that for characterizing the general behavior of the floor over a large area, this is the absolute minimum set of measurements.

2.4.8 Measurement Quality and Other Behavioral Investigations

The text by Ewins (2000) provides general recommendations for checking and maintaining the quality of measured data, and many of those techniques were applied when testing the in-situ floors of the presented research. He recommends five components of a modal test that should be monitored throughout: signal quality, signal fidelity, measurement repeatability, measurement reliability, and measured data consistency, including reciprocity. These components of the test protocol apply to any type of structure to be tested, however they are described in the following section as they apply to the modal testing of in-situ floor systems. Besides describing methods to ensure the quality of the measurements through proper techniques and use of the equipment, other methods are described for checking the behavior of the floor for nonlinearities that would excessively degrade the quality of the measurement. While most of the recommended techniques in this section should be accomplished at all times during testing, others (linearity and reciprocity) are reserved for more detailed investigation of floor behavior or to serve as additional levels of quality assurance if time permits.

Signal quality is a product of the testing technique and use of the equipment, and a good way to monitor the signal quality of modal measurements is the coherence function. Poor signal quality may be the result of extraneous noise, which translates into uncorrelated content and poor coherence. For in-situ floors, the greatest source of extraneous noise is building occupancy; thus it is important to try and conduct modal testing on floors at times when extraneous noise is

minimized, such as nights or weekends. Poor signal strength can also cause degraded signal quality because the noise is a much larger part of the measured signal. Poor signal strength often occurs at areas with little response, such as boundaries or long distances from the point of excitation (more than three bays away from the location of the shaker). Measurements of these areas with degraded coherence may not be invalid, they may just have verified a location of little response. Care must be taken, however, to make the distinction between a valid measurement with poor coherence due to minimal response, and just a bad measurement. Increasing the level of excitation to increase the response may force the floor to vibrate at amplitudes well outside the range that is generated by walking excitation, so it becomes a constant balancing act to determine a level of excitation and response useful for the test objectives. For a given choice of excitation level, the only way to accommodate signal quality is to ensure the dynamic range of the measurement channel is saturated as much as possible with the signal. This requires constant monitoring of all accelerometers for each modal measurement and new accelerometer location. As the amplitude of response changes for each sequential measurement, the range of the channel should be adjusted accordingly. Additionally, the coherence should be constantly monitored for each channel and each measurement. *Signal fidelity* refers to the truth of a measurement (Ewins 2000). For example, consider two accelerometers located at the same point on the floor (such as a redundant driving point measurement). If the two accelerometers are recording very different responses, then there is obviously something wrong with one of the channels. By constantly monitoring the response of all channels for each measurement, malfunctions or misrepresentative measurements can be identified during the test, rather than afterwards when it may be too late.

The *repeatability of measurements* was discussed in a previous section and refers to the ability of the same type of excitation to produce the same response each time. It is recommended to always leave one accelerometer with the shaker and force plate while conducting a modal sweep over a test area to record the driving point accelerance FRF. This serves as an additional level of quality assurance because the driving point measurement can be monitored throughout the test. A modal sweep of a large floor area may take a long time and include many sets of measurements; constantly measuring the driving point response can give an indication if the floor is changing over time, which may have a significant effect on the analysis of the measurements (Ewins 2000). Additionally, the *reliability of the measurement* can be checked by applying a different type of excitation signal to the floor to ensure the same accelerance values

are obtained. For floor testing, the reliability is checked with manual validation of accelerance FRF measurements using sinusoidal steady state testing, or could even be accomplished by performing instrumented heel drop measurements.

The *measured data consistency* described by Ewins (2000) refers to the assumption that the tested structure will reflect the same frequencies, damping, and mode shapes in the measured FRFs, even though many measurements may be taken sequentially over a long period of time due to the large number of test points. A check of this consistency is the theoretical reciprocity of accelerance FRF measurements. The idea of reciprocity comes from a property of the accelerance FRF matrix, in which the same dynamic properties can be defined from either a row or a column of the matrix. Dynamic reciprocity between two points on the floor shares the same relationship as its static counterpart, although instead of relating the static deflection between two points, a dynamic response is related. This property states $A_{ik}(\omega) = A_{ki}(\omega)$, which means the accelerance FRF measured from forcing at point k on the floor and measuring the response at point i should theoretically be the same as the accelerance FRF measured from forcing a point i on the floor and measuring the response at point k . From experiences testing in-situ floor systems, this property holds well for test locations that are close together and does not hold well for long distances away from the point of excitation (greater than three bays away). It should be noted, however, that this is more likely a result of poor signal quality at those long distances than an indication of nonlinear behavior of the floor. Although a check for reciprocity is typically not conducted as a stand-alone investigation, reciprocity tests can be run simultaneously while gathering other sets of measurements. For example, if a reduced testing scheme is used and just the mid-bay accelerance FRFs are measured for direct comparison with one another, the measurement set can be used for reciprocal comparison when the shaker is moved to all the other bays for a similar set of measurements.

As a final recommendation in regard to measurement consistency, if a set of measurements is acquired with the purpose of extracting mode shapes, it is recommended to gather the entire set of accelerance FRFs at one time, preferably within the same day. Gathering the set of measurements in the least amount of time minimizes the effects of any changing conditions of the floor, which was occasionally observed testing the floors in the presented research. Shutting down the test equipment for the day and starting again the next, which theoretically should not have any effect on the consistency of the measurements, may

inadvertently introduce some small amount of inconsistency in the measurements that may not be acceptable. Taking the measurements in one day, in the least amount of time, minimizes any of these unknowns.

One of the fundamental assumptions in modal analysis is that the structure is linear, which means it will exhibit the same dynamic properties and response at all levels of excitation. If the level of excitation doubles, the response should double, and the other dynamic properties (frequencies, damping, and mode shapes) should stay the same. This is another example of an assumption that should be validated at a cursory level when testing in-situ floors, if not validated extensively. Extensive linearity tests can take a lot of time, especially if entire sets of data are acquired multiple times at different levels of excitation for comparison. Thus, the extent of linearity checks should be determined as part of the overall objectives of the test beforehand. The most straightforward method for checking linearity of floor systems is to run a burst chirp signal at different levels of excitation to measure the accelerance FRFs and compare the peak frequencies and the magnitudes/phases at those peak frequencies. Large differences in either the frequencies or the magnitudes of the peaks will give an indication of any gross nonlinearity in the floor system. Another method of checking for nonlinearities is using the coherence function. It should be noted that the coherence function is simply the measure of linear dependence between the input force and the acceleration response as a function of frequency, and has nothing directly to do with level of applied force. For example, two sets of measurements taken with two different levels of excitation, each using multiple averages, may both have excellent coherence because the input force and acceleration response was well correlated for each given force level. Formenti (1999, 2000) suggested taking averages with *varying* force levels between averages to determine any force nonlinearities. His example for this technique was an FRF measured using three averages with a force hammer. The first two averages were taken with the same force level, but for the third average a much larger or smaller level of force was applied. Any degradation of the coherence between the second and third averages would be an indication of force nonlinearity. Extending this technique to in-situ floor testing, a floor could be tested in this manner using a strong/weak instrumented heel drop. For shaker excitation, the approach is a bit more complicated, but possible if the amplifier could be manually adjusted *between* averages to vary the chirp signal input force from the shaker. It should be noted that this type of testing for nonlinearities was not conducted in this research and is only included here for reference.

2.4.9 Summary of Experimental Testing Methods

The previous sections provided detailed descriptions of the various experimental testing methods and measurement types available for dynamic testing of in-situ floor systems. The availability of testing equipment significantly limits the ability to perform several of the described techniques or capture certain types of measurements, but these limitations are second only to those created by the time available to test a floor. However, simply having the appropriate equipment and ample time to conduct testing does not guarantee high quality measurements; this is a product of the proper application of the equipment and continuous monitoring of the data throughout testing to ensure quality measurements are acquired. The following is an outline of a recommended approach to planning and conducting any level of in-situ floor vibration testing and investigation, so that the previously discussed compromises can be efficiently resolved before testing, and the recommended techniques can be applied to ensure quality measurements:

- 1) Clearly identify the overall objectives of the investigation. The objective may be to simply get a rough idea of the floor's frequencies, or the objective may be to gather a detailed set of high quality measurements for modeling and response simulation. Regardless, these objectives must be identified up front, and may even be determined by a building owner, consultant, or researcher. Note that the original and the final objectives may change based on available equipment, or more likely, the available time to test, which is the greatest limitation on the feasibility to perform the objectives.
- 2) Establish rough test parameters based on test objectives and allotted time. Various test parameters affect the ability to conduct a test in the allotted time and virtually all require some degree of compromise.
 - Determine the desired measurement types to be gathered for the tested floor (accelerance FRFs, referenced/unreferenced time histories, decay from resonance, autospectra, etc.).
 - Identify the area to be tested and plan out a test grid for that area.
 - Identify digital signal processor settings of frequency bandwidth, frequency domain resolution, time record lengths, etc.
 - Determine the types of excitation to be applied based on the desired measurement types (chirp signals, sinusoidal, instrumented/unreferenced heel drops, etc.).

The term “rough test parameters” is used because pre-test parameters must be flexible and accommodating to the unexpected, such as equipment malfunctions, differing site conditions, odd floor behavior, etc. It is wise to have several contingency plans for the unexpected, including a “core” or minimal set of measurements, and an “ideal” set of measurements that would be useful to gather if time permits.

- 3) Establish the level of additional behavioral investigation to be accomplished. Although technically this may fall under establishing test parameters, it is mentioned separately here to refer to checks on linearity and reciprocity, or perhaps investigations using decay or testing boundary behavior, which can take a significant amount of time if not planned for accordingly.
- 4) Conduct floor vibration testing using recommended best practice techniques, and adjust test parameters to accommodate the actual conditions of the tested floor. For example, to acquire high quality accelerance FRFs, it is recommended to use an electrodynamic shaker on a force plate using a burst chirp signal for excitation; however the parameters of the chirp signal (frequency range, duration) can typically only be determined from preliminary measurements on site. Other test parameters are also determined on site, like the number of averages required to achieve acceptable coherence. Very low levels of damping may require a finer frequency resolution to adequately define the peaks of the FRFs, resulting in longer time record lengths. The rough test parameters, and perhaps even the feasibility to achieve all of the overall objectives, may change based on actual behavior of the floor. Again, it is recommended to be flexible and have contingency plans.
- 5) Constantly apply recommended techniques for checking the quality of measured data. Example recommended techniques include constant monitoring of the coherence function, acquiring redundant driving point accelerance FRFs, and saturating the dynamic range with the measured signal. Ensuring quality measurements in the field is critical as it is usually impossible to get a second chance to re-test an in-situ floor under the same conditions.
- 6) Post process measurements. The last step in the process, and not expanded on here, is post processing the data from a set of measurements to meaningful results. Depending on the overall objectives and the types of measurements acquired, this may range from a report detailing levels of acceleration and comments on frequency, to a full array of parameter estimation including frequencies, damping, and visually displayed mode shapes.

As previously stated, almost every aspect of testing floors is a compromise, and the choices of techniques, test settings, and measurement types have a significant effect on the time and effort required to test as well as the quality of the acquired data. The experimental testing methods and recommendations presented in this section provide a fundamental set of best practice techniques for the dynamic testing of in-situ floor systems.

2.5 Classification of Floor Vibration Testing

The previous sections in this chapter provided some theory behind modal testing, the different types of equipment available for conducting dynamic testing, the types of information available using modal testing and other types of dynamic measurements, and a set of recommended best practice testing techniques to ensure the quality of the acquired data. The presented information ranged from broad philosophy (setting overall test objectives) down to tedious techniques (choosing specific settings or types of measurements), creating numerous items for consideration when planning and conducting any level of floor vibration test. With that in mind, it may be beneficial to classify floor testing into specific categories, thus establishing a common language for building owners, engineering consultants, experimentalists, and academics intent on troubleshooting, designing, evaluating, or researching the floor vibration performance of in-situ structures.

The idea of classifying certain levels of dynamic investigation is not new. The United Kingdom's Dynamic Testing Agency (DTA) previously classified five different Levels of Test in its *Handbook of Modal Testing* (DTA 1993), each of which describes the level of detail/accuracy required for application. They are as follows:

Level 0: Estimation of natural frequencies and damping factors; response levels measured at few points; very short test times.

Level 1: Estimation of natural frequencies and damping factors; mode shapes defined qualitatively rather than quantitatively.

Level 2: Measurements of all modal parameters suitable for tabulation and mode shape display, albeit un-normalized.

Level 3: Measurements of all modal parameters, including normalized mode shapes; full quality checks performed and model usable for model validation.

Level 4: Measurements of all modal parameters and residual effects for out-of-range modes; full quality checks performed and model usable for all response-based applications, including modification, coupling, and response predictions.

The Levels of Test described by the DTA are purposely vague, as they apply to the full range of modal testing and are not tied to any specific structure being tested nor equipment employed. Another noteworthy attribute is that they apply to modal testing, which implies the traditional setup of simultaneously measuring both the input force and corresponding response.

In floor vibration testing, it is very common to take more generic response-only dynamic measurements and much less common to have the standard input-response modal testing setup. In terms of the detail/accuracy outlined in the DTA's Levels of Test, the accuracy of any floor testing measurements is a product of the quality/capability of the available equipment and experience of the experimentalist (which is arguably of equal importance). The application of the extracted information is subject to its availability; only certain types of measurements can quantify certain information. Stated differently, *only certain types of equipment and testing methods can take certain types of measurements and can quantify certain information...*so in this respect, not all dynamic measurements are created equal. Thus, a common ***Classes of Floor Testing*** classification system is defined here in terms of:

- 1) the methods and equipment used (or required) for testing
- 2) the extent of the useful information that can be extracted from the tests

A standard classification such as the ***Classes of Floor Testing*** will benefit all of the above mentioned parties, as there will not be any false expectations in the capabilities of the reportable results, nor in the equipment, time, and cost required to obtain the desired results. Below are the proposed ***Classes of Floor Testing*** in order of increasing levels of detail, complexity of testing, and most certainly increasing cost in terms of equipment, time, and testing/analysis effort:

Class-I Testing: Single Channel Response Testing

Equipment: Single channel spectrum analyzer.

Extent of Useful Information: Single point acceleration response time history, autospectrum for estimating frequency content, limited estimates of damping using decay of heel drops or from bouncing excitation.

Class-II Testing: Multi-Channel Response Testing

Equipment: Multi-channel spectrum analyzer.

Extent of Useful Information: Multi-channel (multi-location) acceleration response time histories, autospectra of acceleration response for estimating frequency content, limited estimates of damping using decay of heel drops or from bouncing excitation. The multi-channel response gives the ability to compute an operating deflection shape frequency response function between two response locations, in which the response of one location on the floor is used as a reference channel to compute the FRF between the responses at the

other locations. This gives the capability to roughly define shapes using the magnitude and phase information, although this is not a true measure of accelerance.

Class-III Testing: Impact Induced Modal Testing

Equipment: Multi-channel spectrum analyzer. Force transducer for recording impact force such as a force plate for performing instrumented heel drops or a large instrumented impact hammer.

Extent of Useful Information: Simultaneous input force and multi-channel response time histories, autospectra of input force and acceleration responses, accelerance FRF measurements and all the associated benefits of that data, such as the ability to perform curve fitting operations for parameter estimation. The minimum level of testing for detailed estimates of damping, accelerance values, and scaled mode shapes. In general, this is the minimum set-up required for full modal analysis, although not the most reliable method for achieving high quality data due to the potential inconsistency of the applied impact force.

Class-IV Testing: Shaker Induced Limited Modal Testing

Equipment: Multi-channel spectrum analyzer. Electrodynamic shaker. Force transducer for recording shaker force, such as a force plate.

Extent of Useful Information: Simultaneous input force and multi-channel response time histories, autospectra of input force and acceleration responses, accelerance FRF measurements of generally higher quality than achieved through impact testing. The higher quality measurements provide more reliability for parameter estimation (frequencies, damping, general mode shapes). While this set-up is capable of full modal analysis, it only involves minimal or limited area testing for characterizing specific information. Examples of limited modal testing would be centerline or mid-bay accelerance FRFs, enough to perform MDOF parameter estimation for multiple response/reference locations and to display basic mode shape information due to the limited measurements.

Class-V Testing: Shaker Induced Full Modal Testing

Equipment: Multi-channel spectrum analyzer. Electrodynamic shaker. Force transducer for recording shaker force, such as a force plate.

Extent of Useful Information: Every capability of Class-IV testing, however one step further to include full modal analysis to experimentally quantify the shapes over a full area.

Note: For each Class, it is assumed that the response measurements are taken with accelerometers, either one or many, as is typical for floor testing. These accelerometers and the required cabling are not reported under the equipment heading. It should also be noted that any Class automatically includes the capability to perform all lower Classes of testing by the nature of the equipment. The only exception to this is Class-III testing cannot be performed without a force transducer (i.e. force plate), which may not be available if shaker testing (Class-IV and Class-V) is accomplished by attaching an accelerometer to the shaker armature as a means for computing input force. This method of force measurement is discouraged for floor system testing.

For the tested in-situ floors in the presented research, the Class of Testing fell somewhere between Class-IV and Class-V, in which modal sweeps were made over various areas of the floors to define mode shapes, but there were also many behavioral investigations that did not necessarily involve the full area (linearity, reciprocity, decay investigations). Hopefully, this classification system can establish a common language and understanding of the capabilities (and limitations) of the different types and techniques for floor testing. A potential application of the classification system would be to help consultants explain the different options of testing to their clients, allowing for a better understanding of the effort (and cost) of the proposed Class of Testing.

As a final comment, it should be noted that none of the described theory, digital signal processing, equipment, or techniques presented in this chapter were specific to the steel composite office floors of the presented research. In fact, the techniques also extend themselves to testing other types of large in-situ structures such as footbridges or stadia, which share similar behavior of low frequencies and damping and have the potential vulnerability for excessive vibration due to resonant response.

CHAPTER 3

DYNAMIC TESTING AND BEHAVIOR OF IN-SITU FLOOR SYSTEMS

3.1 In-Situ Floor Systems

Within the floor vibration literature, case studies involving modal testing of multi-bay in-situ floors are limited, particularly studies of steel composite floor systems that are the focus of the presented research. A steel composite floor, as referred to in the presented research, is meant to describe a floor constructed with concrete on steel deck as the slab system that is supported by steel framing members. The previous chapter described the theory, equipment, and methods involved with testing virtually any type of in-situ floor system, not just steel composite floors. Considering the numerous pieces of equipment and testing techniques described, the chapter indirectly demonstrated the likely reason for the limited number of case studies, particularly due to the complexity and compromise necessary for the process of obtaining high quality modal data for use in characterizing a floor's dynamic behavior.

Laboratory floor systems typically differ considerably from in-situ floor systems, mainly due to idealized boundary conditions and the finite space available to construct a full scale multi-bay setup. Generally, laboratory floors are limited to just one or two bays and rarely see the two-way bending action that dominates an in-situ floor system with a large number of bays. In-situ floor systems commonly differ from the idealizations used in the current design guidance such as Design Guide 11. Unique or non-standard framing, different beam sizes between columns, moment connections, and interior floor-to-ceiling partitions are all examples of common deviations to the assumptions of simplified design methods as well as many laboratory test floors. It is these differences that prompt the need for the testing of multi-bay in-situ floor systems to better characterize their dynamic behavior. Unfortunately, opportunities to test large in-situ floor systems, particularly in the level of detail desired, are rare as demonstrated by the lack of published cases in the literature. Even rarer are opportunities to test floor systems without the presence of occupants, excessive construction materials, office furniture, or non-structural fit out of partitions and cubicles. Other challenges of testing in-situ floor systems, as noted in the previous chapter, include limited equipment, large test areas, extraneous noise, and

possible changing conditions of the floor. The presented research includes the extensive modal testing of three relatively “clean” large scale in-situ steel composite floor systems and the characterization of the floors’ dynamic properties. These floors served as valuable test specimens and provide significant insight into the behavior of multi-bay floor systems, as well as the best methods for characterizing their dynamic properties.

The following chapter details the experimental testing and the characterization of dynamic behavior of three large multi-bay in-situ steel composite floor systems. Presented first are descriptions of the tested structures, followed by a description of the dynamic measurement coverage of each floor. The notable measurements and behavior of each of the tested floor systems are summarized, including driving point accelerance FRFs and dynamic properties of frequency, damping, and mode shapes. Finally, some generalizations on the overall behavior of this type of floor system are presented, including commentary on how certain characteristics of floor behavior can be used to accommodate future testing and finite element modeling in further research endeavors.

3.2 Tested Floors #1 and #2 - New Jersey Office Building, NOC VII (24th & 18th Floors)

3.2.1 Description of Tested Floors #1 and #2



Figure 3.1: Newport Office Center (NOC) VII, Jersey City, New Jersey

The first two in-situ steel composite floor systems tested were the 24th floor and 18th floor of a 31-story high-rise office building located in Jersey City, New Jersey (Figure 3.1). These two tested floors are presented together as they are nearly identical floors located within the

same building; however they were tested at different times using different techniques and exhibited slightly different behavior. During construction, the building was commonly referred to as NOC VII, short for Newport Office Center VII. The designations NOC VII-24 and NOC VII-18 are used in the presented research to identify the 24th and 18th floors tested, respectively. NOC VII-24 was the first floor tested in the presented research, followed by NOC VII-18. Although the layouts of the partitions within the interior bays differ slightly, the two floors share the common floor framing layout shown in Figure 3.2. A full framing plan for the floor(s), including designated sections, is found in Appendix A

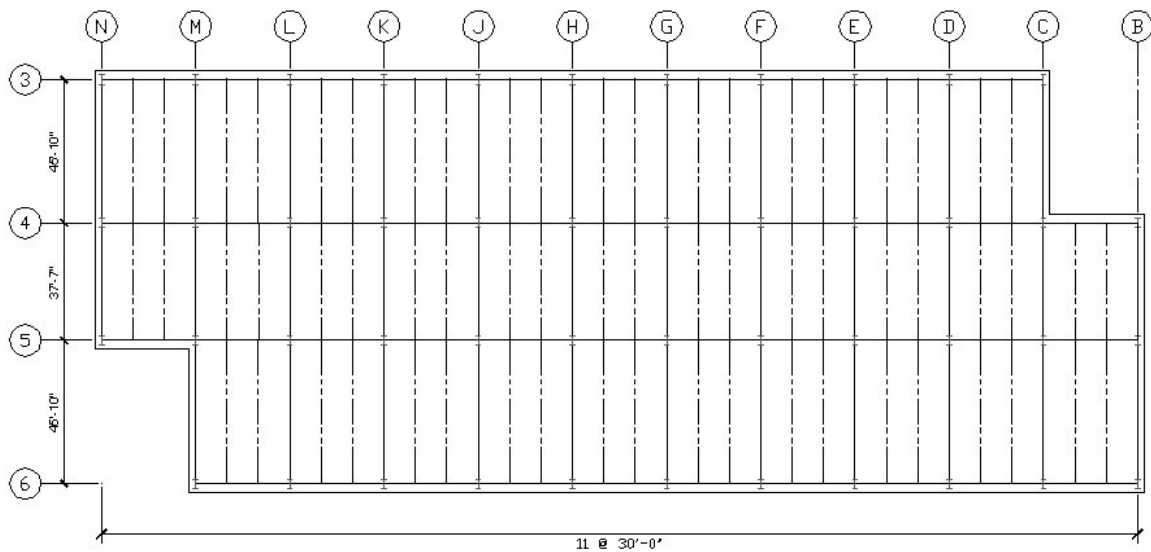
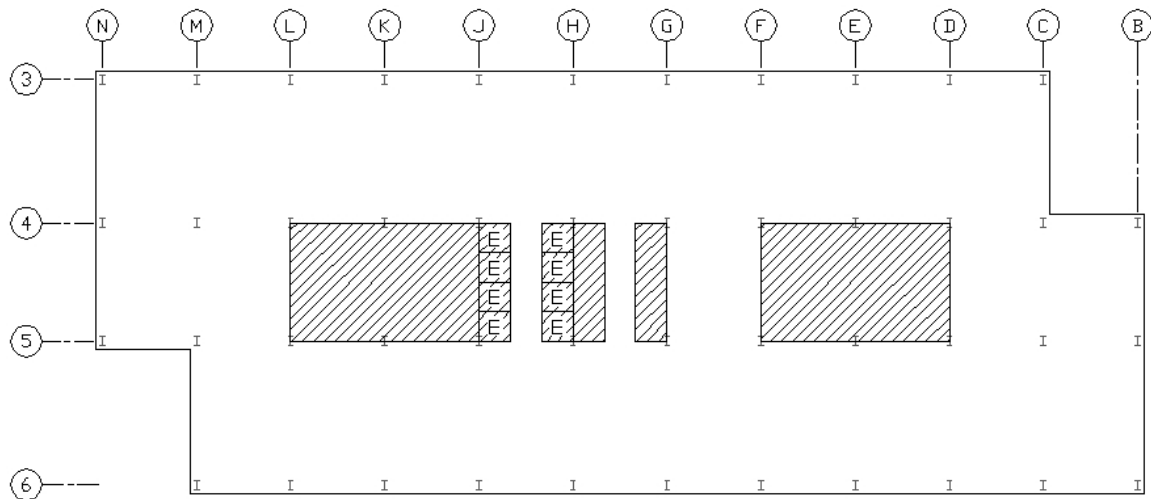
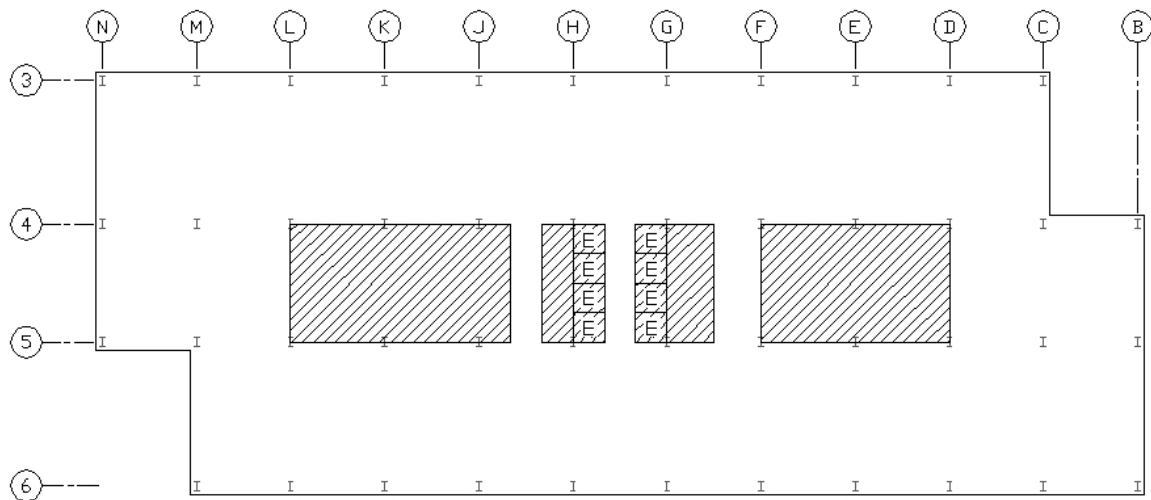


Figure 3.2: NOC VII Floor Framing Layout (18th and 24th Floors)

The 330-ft building length consisted of eleven bays with “executive corners” on opposite ends of the building, creating an asymmetric layout. The floor beams span in the short direction of the building, that is, the three unequal-span bays that comprise the building’s 129-ft width. A “bay,” as referenced in the presented research, is considered the rectangular floor area between four (or more) columns and is specified by a letter-number combination representing the outermost grid lines bounding the bay. For example, a bay designated L/M-5/6 is bound by grid lines L and M in the north-south directions and grid lines 5 and 6 in the east-west directions. The “length” of a bay is the dimension in the direction parallel to the floor beams, whereas the “width” is perpendicular to the beams. While all bays have a width of 30 ft, the exterior bays have a length 45 ft-10 in., and the lengths of the interior bays are 37 ft-7 in. The floor beams are spaced 10 ft on center. The different partition layouts of each of the two tested floors in the NOC VII building are shown in Figure 3.3.



(a) NOC VII - 24th Floor Partition Layout (Tested Floor #1)



(b) NOC VII - 18th Floor Partition Layout (Tested Floor #2)

Figure 3.3: NOC VII General Layout of Tested Floors

With the exception of occupant fit out, the building was complete including a fully clad non-structural glass façade. The shaded areas in Figure 3.3 designate the central bays or portions of a bay that are encased in full height floor-to-ceiling partition (dry-wall) walls. The configurations vary slightly between the two tested floors due to the termination of the low and mid-rise elevator banks. One condition not evident in Figure 3.3(b) is the entire bay beneath Bay F/G-4/5 is enclosed by full-height partitions housing the elevator equipment for the low-rise bank of elevators that terminated service on the 15th floor. This was evident during testing due to the lack of response in this seemingly open area. The “E” in Figure 3.3 represents the active bank of elevators that services the floors.

As shown in Figure 3.4(a), the tested portion of the floor was very “clean” at the time of testing due to the lack of any construction materials, office furniture, demountable partitions, installed partition walls, or raised flooring. The full height partitions enclosed the interior bays containing mechanical rooms, restrooms, stairwells, and elevator banks and were installed both above and below the tested floor (Figures 3.4(a), 3.4(c) and 3.4(d)). All columns were encased with dry-wall for fireproofing, with the exterior dimensions of the encasement measuring approximately 28-30-in. square. On the underside of the floor tested there was no mechanical ductwork, lighting, cable track, or acoustical suspended ceiling. The only items attached beneath the tested floor were spray-on fireproofing and the fire sprinkler piping (Figure 3.4(b)).



(a) Bare Conditions of Tested Floor



(b) Spray-On Fireproofing, Underside of Floor



(c) Full-Height Partitions Above Tested Floor



(d) Full-Height Partitions Below Tested Floor

Figure 3.4: Conditions of Tested Floor #1, NOC VII-24

The floor system was designed for composite action and consists of 3.25-in. lightweight concrete over 2-in. steel deck for a total composite depth of 5.25-in. The lightweight concrete

has a specified unit weight of 115 pcf and a specified compressive strength of 4000 psi. The slab/deck spans the 120-in. beam spacing and is supported by hot-rolled beams and girders. The floor beams are not continuous over the girders and are connected to the girder webs with simple shear connections. All beam-to-column and girder-to-column connections are moment connections.

The 24th floor of NOC VII was the first in-situ floor tested in the presented research; however it served as a more useful specimen for learning how to test floors rather than to determine the actual dynamic behavior of these floor systems. Only one day was available for testing and thus only a very limited area of the floor was covered. Furthermore, many of the quality testing techniques described in the previous chapter were based on experiences testing this initial floor and efforts to refine the quality of the measurements. Access to test such a large, fully enclosed multi-bay floor system was a fortunate opportunity; hence a return trip to Jersey City was made to perform further testing on the 24th floor and/or another available floor within the NOC VII building. Upon arrival, the 24th floor was no longer available to test because contractors had begun installation of 8-in. raised computer flooring as shown in Figure 3.5.



Figure 3.5: Installation of Raised Flooring on NOC VII 24th Floor

Although there were a number of other unoccupied floors in NOC VII for testing, the 18th floor was chosen as the second test floor because it was several levels away from the work taking place in the building, minimizing potential noise in the test measurements, and because it had the same type of fireproofing both above and below the floor. Although the fireproofing in the floor above the 18th floor was not an important consideration, it seemed convenient to have as much continuity as possible for comparison to the previous measurements of the 24th floor. With the exception of a slight difference in the full-height partition framing around the interior bays as

shown in Figure 3.3, the conditions were the same as for the previously tested floor. Conditions of the second tested floor (NOC VII-18) are shown in Figure 3.6.



Figure 3.6: Conditions of Tested Floor #2, NOC VII-18

According to the building drawings, concentrically braced frames are located in the interior bays running in the short direction of the building at grid lines F, G, H, and J, although these braces were not visually verified on site. These braces have alternating chevrons on each floor, so they appear as an X-brace over a two-floor elevation. Each is encased in the full height partition walls surrounding the three core bays housing elevator banks. Additional concentrically braced frames are located along grid lines L (with chevrons pointing down on all floors) and D (chevrons pointing up on all floors) as shown by the photos in Figure 3.7(a), (b). These frames add considerable stiffness to the beam spanning between the two interior columns as shown by very small measured response along these walls.



(a) Grid line L Brace (all floors)



(b) Grid line D Brace (all floors)

Figure 3.7: Chevron Bracing at End of Interior Core Partitions

3.2.2 Measurement Coverage of Tested Floors #1 and #2

For each of the tested floors, measurements within a bay were taken at the quarter points, both on the interior of the bay as well as around the perimeter boundaries. Although a coarse testing grid, the quarter point grid of testing locations within a bay seemed a reasonable compromise and provided enough points to describe the shape of the response across the testing area. When measurements were taken at the boundaries, accelerometers were placed as close as possible to the columns and along the centerline of the spandrel beams and girders (or interior members if next to partition walls). Because the columns were completely encased, the measurements at these boundaries were 12 to 18 in. from the column centerline, which is likely the greatest source of the minimal response measured at the columns. Similarly, site conditions prevented placing accelerometers directly on the centerline of perimeter beams and girders. On average, the accelerometers on these boundaries were 12 in. from their respective centerlines. The entire floor grid of interior and boundary locations was numbered sequentially to track measurements, regardless of whether a measurement was taken at that point. These grid numbers, shown in Figure 3.8, are used in the remainder of the presented research to designate shaker and accelerometer locations. Because of the same general floor layout for both NOC VII-24 and NOC VII-18, the same grid of numbers was used to track each set of measurements. In presenting the measurement coverage and experimental results, care is taken to distinguish which tested floor system is being discussed.

	N			M			L			K			J			H			G			F			E			D			C			B														
3	1	10	19	28	37	50	63	76	89	102	115	128	141	154	167	180	193	206	219	232	245	258	271	284	297	310	323	336	349	362	375	388	401	414	427	440	453	466	479	492	505	3						
	2		11	20	29	38	51	64	77	90	103	116	129	142	155	168	181	194	207	220	233	246	259	272	285	298	311	324	337	350	363	376	389	402	415	428	441	454	467	480	493		506	3				
	3		12	21	30	39	52	65	78	91	104	117	130	143	156	169	182	195	208	221	234	247	260	273	286	299	312	325	338	351	364	377	390	403	416	429	442	455	468	481	494		507		3			
	4		13	22	31	40	53	66	79	92	105	118	131	144	157	170	183	196	209	222	235	248	261	274	287	300	313	326	339	352	365	378	391	404	417	430	443	456	469	482	495		508			3		
4	5	14	23	32	41	54	67	80	93	106	119	132	145	158	171	184	197	210	223	236	249	262	275	288	301	314	327	340	353	366	379	392	405	418	431	444	457	470	483	496	509	518	527				536	545
	6	15	24	33	42	55	68	81	94	107	120	133	146	159	172	185	198	211	224	237	250	263	276	289	302	315	328	341	354	367	380	393	406	419	432	445	458	471	484	497	510	519	528	537			546	4
	7	16	25	34	43	56	69	82	95	108	121	134	147	160	173	186	199	212	225	238	251	264	277	290	303	316	329	342	355	368	381	394	407	420	433	446	459	472	485	498	511	520	529	538	547		4	
	8	17	26	35	44	57	70	83	96	109	122	135	148	161	174	187	200	213	226	239	252	265	278	291	304	317	330	343	356	369	382	395	408	421	434	447	460	473	486	499	512	521	530	539	548	4		
5	9	18	27	36	45	58	71	84	97	110	123	136	149	162	175	188	201	214	227	240	253	266	279	292	305	318	331	344	357	370	383	396	409	422	435	448	461	474	487	500	513	522	531	540	549			
					46	59	72	85	98	111	124	137	150	163	176	189	202	215	228	241	254	267	280	293	306	319	332	345	358	371	384	397	410	423	436	449	462	475	488	501	514	523	532	541	550			5
					47	60	73	86	99	112	125	138	151	164	177	190	203	216	229	242	255	268	281	294	307	320	333	346	359	372	385	398	411	424	437	450	463	476	489	502	515	524	533	542	551		5	
					48	61	74	87	100	113	126	139	152	165	178	191	204	217	230	243	256	269	282	295	308	321	334	347	360	373	386	399	412	425	438	451	464	477	490	503	516	525	534	543	552	5		
6					49	62	75	88	101	114	127	140	153	166	179	192	205	218	231	244	257	270	283	296	309	322	335	348	361	374	387	400	413	426	439	452	465	478	491	504	517	526	535	544	553			
	N	M			L			K			J			H			G			F			E			D			C			B																

Figure 3.8: NOC VII General Test Grid Point Numbers (Tested Floors #1 and #2)

Tested Floor #1 (NOC VII-24) Measurement Coverage

All measurements for NOC VII-24 were taken in a single day, thus the limitations on testing time and equipment only allowed measurements over a portion of the floor. With only

partial coverage of the floor, an attempt was made to capture enough useful data for the research. The primary goal was to characterize the floor's response in orthogonal directions of each bay tested. Overall, 184 measurements were taken while the shaker was positioned at the middle of three different bays (Points 73, 69, and 25), as shown in Figure 3.9. These three excitation locations were specifically chosen to correspond with locations from a previous investigation of this floor using a single-channel Ono Sokki CF-1200 Handheld Analyzer. This response-only investigation included a variety of heel drop, bouncing, and walking measurements. Select measurements from that investigation are presented in Appendix C for comparison with measurements taken with the SigLab DSP units used in this research.

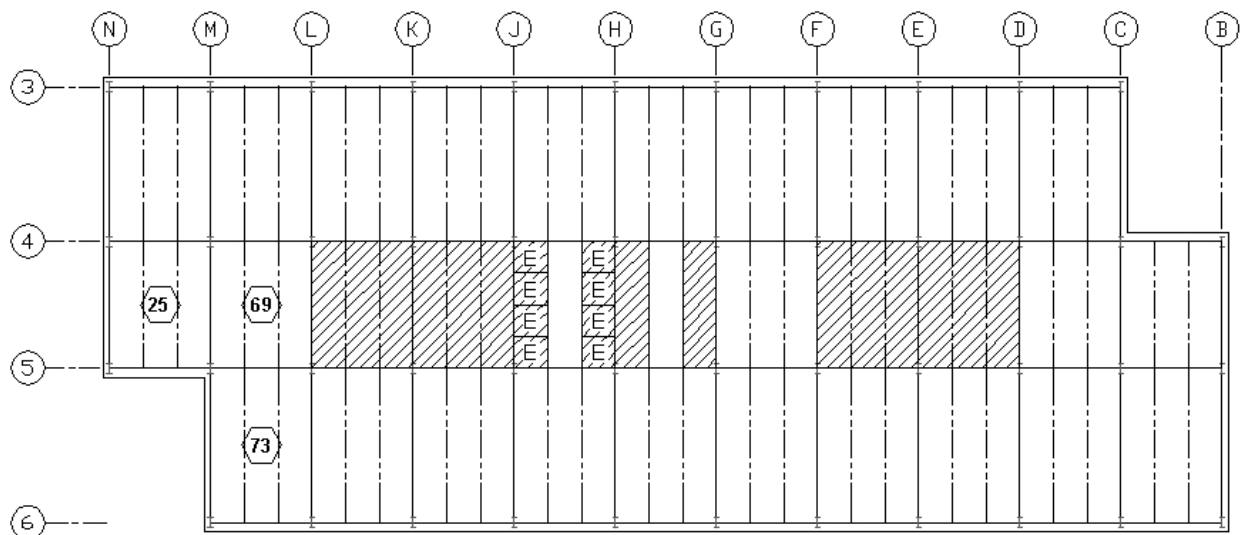


Figure 3.9: NOC VII-24 Excitation Locations

Each measurement taken with the SigLab DSP units included the response of either three or six accelerometers, depending on the number of units used. Initially, two SigLab DSP units were used for testing with six roving accelerometers and one driving point accelerometer. Unfortunately, a problem with the communication between the two DSP units forced the use of a reduced configuration using only one unit for the bulk of the measurements. Using only one SigLab DSP unit reduced the capability for taking extensive measurements, as only three roving accelerometers were used without the redundant driving point measurement. A total of 184 measurements were taken, including 55 chirp signal measurements to acquire accelerance FRFs and 129 steady-state sinusoidal measurements. Figure 3.10 shows the shaker located at each of the three excitation locations used for NOC VII-24.



(a) Shaker Located at Point 73



(b) Shaker Located at Point 69



(c) Shaker Located at Point 25

Figure 3.10: NOC VII-24 Shaker at Excitation Locations

A summary of the test settings and signal parameters used for testing NOC VII-24 is presented in Table 3.1. The settings used for measurements with the SigLab DSP unit included a 20 Hz bandwidth and 1024 samples over a 20-second time record, which resulted in a frequency domain resolution of 0.05 Hz. The chirp signal used for measuring the accelerance FRFs was a three-average continuous chirp sweeping from 4 Hz to 12 Hz over the 20-second time record. The sweep frequency was determined from the frequency content identified from the previous investigation of the floor using the handheld analyzer (Appendix C). The steady-state sinusoidal measurements used the same DSP settings, but only took one average of the 20-second time record. This allowed the computation of the accelerance at the specific frequency but without a computation of the coherence. No decay measurements were taken for NOC VII-24. Descriptions of the measurement coverage for each shaker location are presented below.

Table 3.1: Summary of Test Settings and Parameters of Tested Floor #1, NOC VII-24

Chirp Measurements:									
DSP Settings					Signal Settings				
Bandwidth	Record Length	Δf	Record Length	Δt	Chirp Type	Frequency Range	On Time	Off Time	# of Avgs
20 Hz	1024 samples	0.05 Hz	20 sec	0.01953125 sec	Continuous	4-12 Hz	20-sec	0-sec	3 avgs

Sinusoidal Measurements:						
DSP Settings					Signal Settings	
Bandwidth	Record Length	Δf	Record Length	Δt	Sine Frequency	# of Avgs
20 Hz	1024 samples	0.05 Hz	20 sec	0.01953125 sec	specified	1 avg

Decay Measurements:						
DSP Settings					Signal Settings	
Bandwidth	Record Length	Δf	Record Length	Δt	Sine Frequency	# of Avgs
-	-	-	-	-	-	-

NOC VII-24, Point 73 - Mid-Bay L/M-5/6

The most extensive testing of the floor was conducted with the shaker located in the middle of Bay L/M-5/6 (Point 73). With the shaker in this location, the accelerance FRFs for 167 different locations were obtained from a three-average continuous chirp signal sweeping from 4 Hz to 12 Hz. Besides the chirp measurements, steady-state sinusoidal measurements at 5.05 Hz, the bay's dominant frequency, were measured at each of these locations. The coverage of the measurements taken for the shaker located in Bay L/M-5/6 is shown in Figure 3.11. Note that an effort was made to capture the response around the end bays of the floor as well as along the centerline of bays in the long direction of the building, perpendicular to the direction of the floor framing.

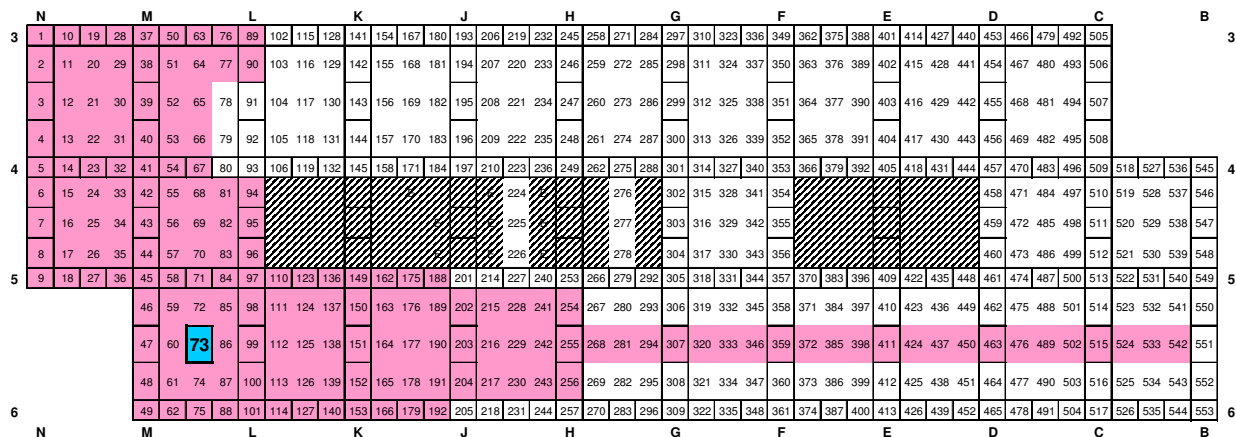


Figure 3.11: NOC VII-24 Measurement Coverage - Shaker at Point 73

NOC VII-24, Point 69 - Mid-Bay L/M-4/5

The bulk of the measurements with the shaker located in the middle of Bay L/M-4/5 (Point 69) were sinusoidal steady-state measurements, and only one chirp measurement was taken to identify the dominant frequency. Two sets of steady-state measurements at 55 locations were taken when forcing sinusoidally at 6.55 Hz, the identified dominant frequency. The accelerance FRFs from chirp excitation provide more useful information for the behavior of the floor than just sinusoidal measurements at a single frequency, but this was a lesson learned testing this floor. The coverage of the two sets of steady-state sinusoidal measurements taken is shown in Figure 3.12. The first set of sinusoidal measurements was taken to obtain the steady-state acceleration response along the centerline of the bays in orthogonal directions from the one tested (Figure 3.12(a)). The second set of measurements was taken to obtain the acceleration response along a three-bay strip running the short direction of the building (Figure 3.12(b)).

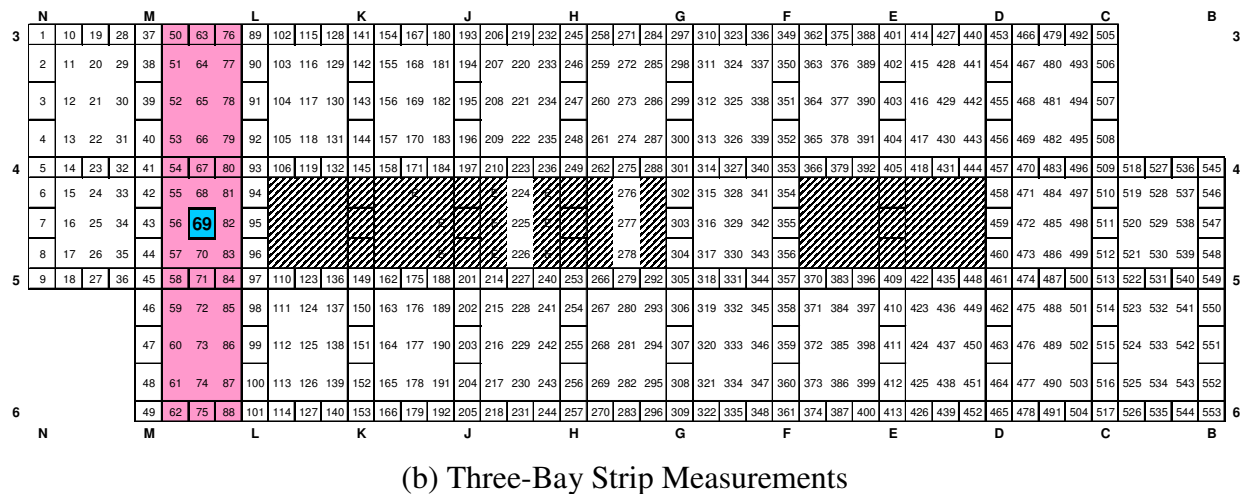
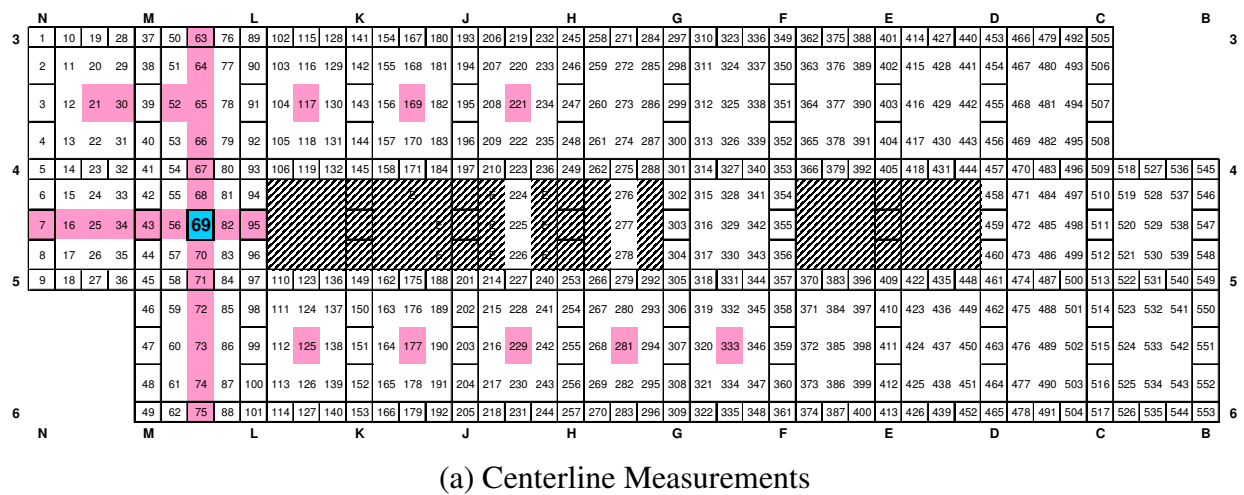
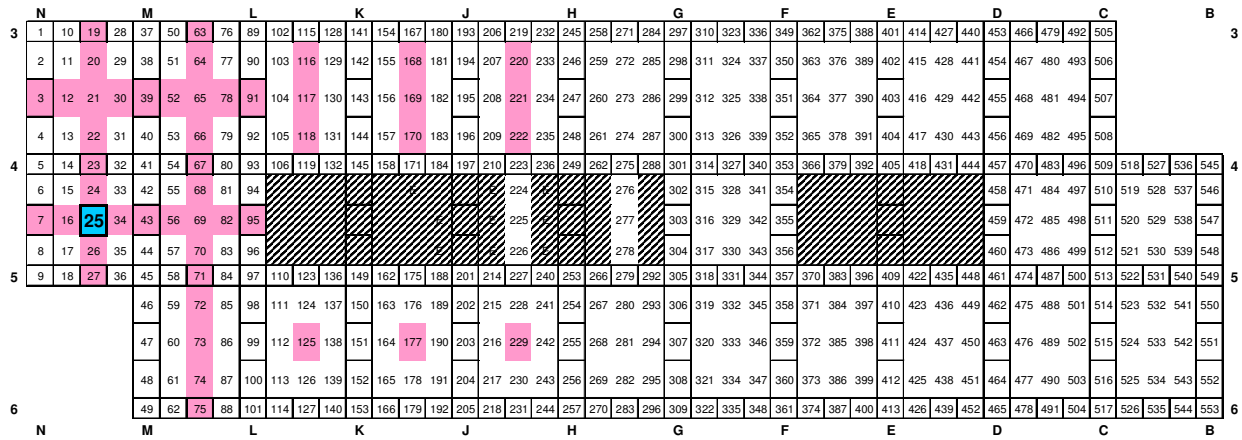


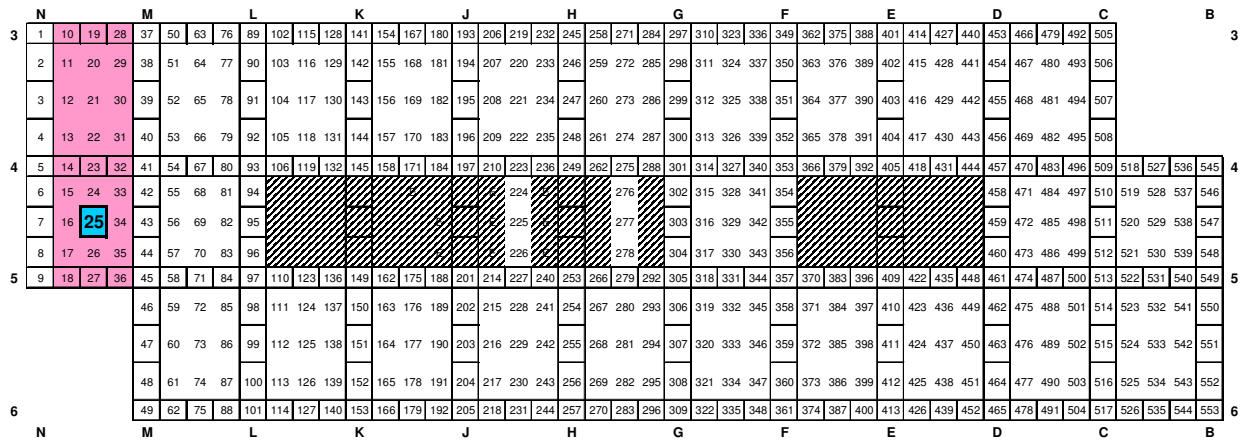
Figure 3.12: NOC VII-24 Measurement Coverage - Shaker at Point 69

NOC VII-24, Point 25 - Mid-Bay M/N-4/5

Similar to tests at the previous location, only one chirp measurement was taken to capture the acceleration FRF and identify the dominant frequency with the shaker located in the middle of Bay MN-45 (Point 25). At 62 different locations, two sets of steady-state measurements were taken when driving the shaker sinusoidally at 6.00 Hz, the identified dominant frequency. The coverage of these two sets of measurements taken for excitation at Point 25 is shown in Figure 3.13. As with the previous measurements, the first set captured the steady-state acceleration response along the centerline of the bays in orthogonal directions from the point of excitation (Figure 3.13(a)); the second set measured the steady-state acceleration response along the two-bay strip spanning the last two bays of the building (Figure 3.13(b)).



(a) Centerline Measurements



(b) Two-Bay Strip Measurements

Figure 3.13: NOC VII-24 Measurement Coverage - Shaker at Point 25

While the coverage areas, measurement types, and methods employed on the first tested floor seem a bit rudimentary, they are included to provide some contrast with more effective and

higher quality measurements and testing techniques achieved with the other two tested floors. The other two tested floors took advantage of the lessons learned, including using an increased frequency domain resolution, burst chirp signals, capturing redundant driving point measurements, taking fewer sinusoidal measurements and more chirp measurements, and exciting a greater number of bays on a tested floor whenever possible.

Tested Floor #2 (NOC VII-18) Measurement Coverage

Measurements for the second tested floor, NOC VII-18, were taken over five days of testing, a considerable amount of time for access to such a valuable test specimen. Despite the ample time, only a limited amount of measurements was taken over a portion of the floor. One reason for this was the use of an increased frequency domain resolution, which came at the cost of doubling the time to take a measurement compared to the previously tested floor. Overall, 274 measurements were taken while the shaker was positioned within 11 different bays as shown in Figure 3.14. All excitation locations were at the middle of the bays with the exception of Point 216, which is at the short direction quarter point of Bay H/J-5/6. The excitation locations were chosen for comparison with the previously tested floor and for capturing the behavior of the bays along the length of the floor.

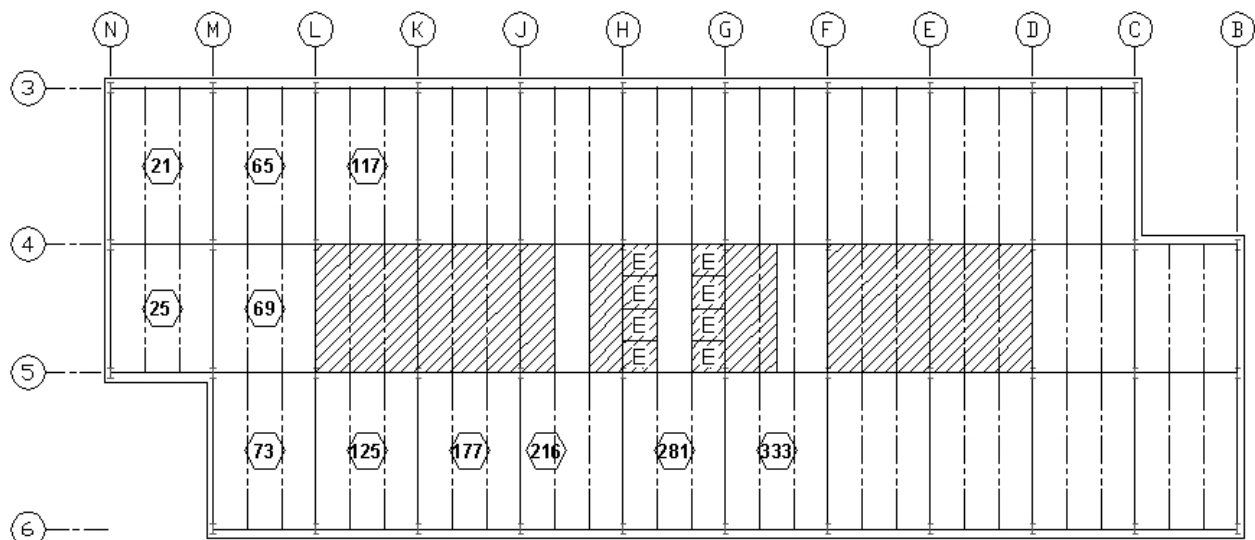


Figure 3.14: NOC VII-18 Excitation Locations

Each of the 274 measurements were taken with the two SigLab DSP unit setup using up to eight channels (seven for the accelerometers, one for the force plate). With this setup, redundant driving point measurements were taken. The 274 measurements recorded over the

five days of testing included 133 burst chirp signal measurements for capturing the accelerance FRFs, 115 steady-state sinusoidal measurements, 25 decay measurements, and one ambient measurement. A summary of the test settings used for the various chirp, sine, and decay measurements is presented in Table 3.2.

Table 3.2: Summary of Test Settings and Parameters of Tested Floor #2, NOC VII-18

Chirp Measurements:									
DSP Settings					Signal Settings				
Bandwidth	Record Length	Δf	Record Length	Δt	Chirp Type	Frequency Range	On Time	Off Time	# of Avgs
10 Hz	1024 samples	0.025 Hz	40 sec	0.0390625 sec	Burst	4-8 Hz	30-sec	15-sec	3 avgs

Sinusoidal Measurements:									
DSP Settings					Signal Settings				
Bandwidth	Record Length	Δf	Record Length	Δt	Sine Frequency	# of Avgs			
20 Hz	2048 samples	0.025 Hz	40 sec	0.01953125 sec	specified	3 avgs			

Decay Measurements:									
DSP Settings					Signal Settings				
Bandwidth	Record Length	Δf	Record Length	Δt	Sine Frequency	# of Avgs			
20 Hz	2048 samples	0.025 Hz	40 sec	0.01953125 sec	specified	1 avg			

The 10 Hz frequency bandwidth and 4-8 Hz burst chirp signal frequency range was used because it encompassed the frequency range of interest and the active frequency content of the floor, which was verified with several instrumented heel drop measurements. This was the first floor tested using the burst chirp signal, which produced higher quality measurements compared to the first tested floor using a continuous chirp signal. The various chirp, sine, and decay measurements were taken to investigate different aspects of the floor's behavior. Although eleven different bays were excited with the shaker, only four different bays (bays including Points 281, 73, 69, and 65) were excited with the intent of defining the mode shapes over a substantial area of the floor. The other excited points on the floor were generally excited with the intent of obtaining their accelerance FRFs, damping estimates, and/or investigating reciprocity between excitation locations. In many cases, the same chirp or sinusoidal signal was used at different levels of excitation to investigate the linearity of response of the floor. Results of such investigations are presented in the next section, and descriptions of the measurement coverage for each shaker location are presented below. In some instances, the identified dominant frequency of a tested bay is reported, however they are only mentioned to describe the frequencies of the steady-state sinusoidal and decay measurements. Discussions of the dominant

frequencies are not covered in as much detail as in the next section dedicated to describing the experimental results and behavior of the floor.

NOC VII-18, Point 281 - Mid-Bay G/H-5/6

The shaker was placed in the middle of bay G/H-5/6 (Point 281) with the intention of sweeping along the entire length of the floor in both directions to capture its behavior perpendicular to the floor framing (Figure 3.15). The greatest number of measurements for the tested floor were taken with the shaker in this location, mainly due to the large area covered along the length of the building, which included measurements from more than 150 ft away from the point of excitation. With the shaker located at Point 281 in bay G/H-5/6, the acceleration FRFs were obtained from burst chirp measurements for the coverage area shown in Figure 3.16, which includes a total of 175 different locations on the floor. The measurements were taken over two days of testing.



Figure 3.15: NOC VII-18 Shaker Located at Point 281

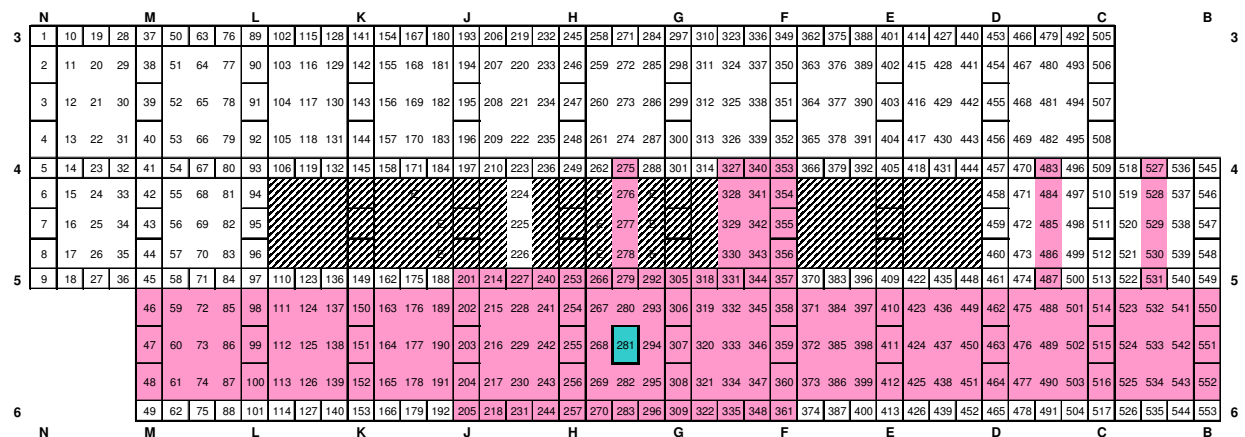


Figure 3.16: NOC VII-18 Burst Chirp Measurement Coverage (Forcing at Point 281)

As shown in Figure 3.16, the burst chirp coverage area included all points within the excited bay and the adjacent bays on either side (up to grid lines F and J). Beyond these bays, a reduced measurement configuration was used to capture only the interior three quarter point response along the remaining distance to the ends of the building on either side. Other areas within the measurement coverage included the centerline of the two interior end bays (B/C-4/5 and C/D-4/5) and the partially open bay F/G-4/5, which lies directly over the fully enclosed elevator mechanical room for the low rise elevator. Measurements were taken to investigate the response along the centerline of the active bank of elevators in bay G/H-4/5, which was in the bay adjacent to the point of excitation in the direction of the floor framing. These measurements were taken with the accelerometers on top of the installed raised computer flooring.

In addition to the burst chirp measurements, a series of steady-state sinusoidal measurements was made over the 65 point area of the floor shown in Figure 3.17 at the identified dominant frequency of 5.025 Hz. Note the coverage area for these measurements was not as extensive as for the accelerance FRF measurements. The target level of excitation used for the sinusoidal measurements was more commensurate with the magnitude of the walking function computed using DG11, which was considerably lower than the level used for burst chirp excitation. Too large a force at resonance may produce excessive response beyond the limits of interest for serviceability. At longer distances from the source of excitation, it becomes difficult to distinguish between ambient noise and the signal, even for the larger magnitude chirp excitation. Thus, with the small level of sinusoidal excitation and the limits of accelerometer sensitivity, the steady-state response was only measured in the immediate vicinity of the shaker (i.e. one bay to either side) as shown in Figure 3.17.

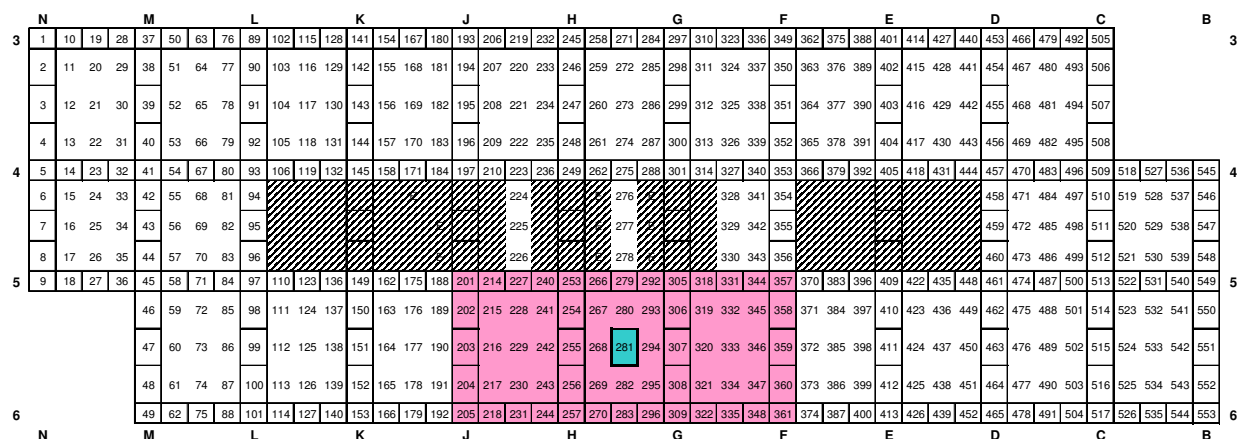


Figure 3.17: NOC VII-18 Sinusoidal Measurement Coverage (Point 281 at 5.025 Hz)

As with all of the excitation locations, other investigations of the floor behavior were more specific to the driving point measurement rather than measurements over a coverage area. They are mentioned here to summarize the extent in which a bay was investigated. These include such measurements as stepped sine sweep sinusoidal measurements for verifying the location and magnitude of the identified dominant peak (or manual half power damping estimates), linearity checks by repeating different measurements at different levels of excitation, and decay measurements. For Point 281, these additional measurements included a stepped sine sweep at three different levels of excitation about the 5.025 Hz dominant frequency, taking care that enough spectral lines were measured on either side of 5.025 Hz to accommodate a half power method damping calculation from the manual accelerance FRF values. Decay measurements from resonance were made at four different levels of excitation.

NOC VII-18, Point 73 - Mid-Bay L/M-5/6

The second greatest number of measurements for the tested floor were taken with the shaker located at the middle of bay L/M-5/6 (Point 73) as shown in Figure 3.18. The intent of these measurements was to capture the response of the end-bay area of the floor. This also corresponded to the same excitation location and area investigated in the first tested floor, NOC VII-24, for comparison.



Figure 3.18: NOC VII-18 Shaker Located at Point 73

The measurement coverage with the shaker located at Point 73 is shown in Figure 3.19. For the coverage area shown, the floor was excited with both the standard 4-8 Hz burst chirp signal to obtain the accelerance FRF as well as the low amplitude sinusoidal signal at 5.025 Hz to manually measure the spectral value at the identified dominant frequency. A total of 130

different locations on the floor were covered with the shaker at this excitation location. Besides the burst chirp and sinusoidal measurements over the coverage area shown in Figure 3.19, a stepped sine sweep around the dominant frequency of 5.025 Hz was made to accommodate a half power method damping calculation, and decay measurements from resonance were taken at three different levels of excitation.

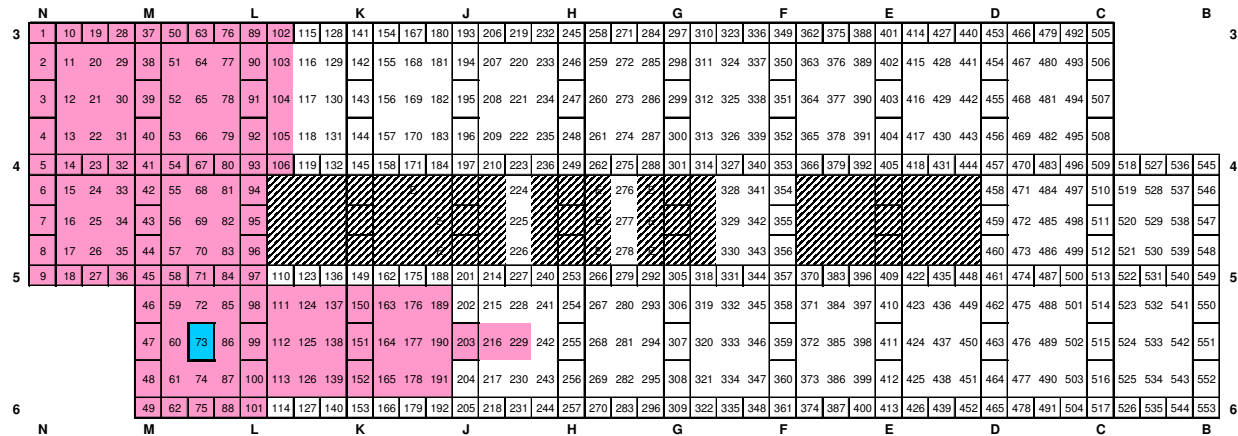
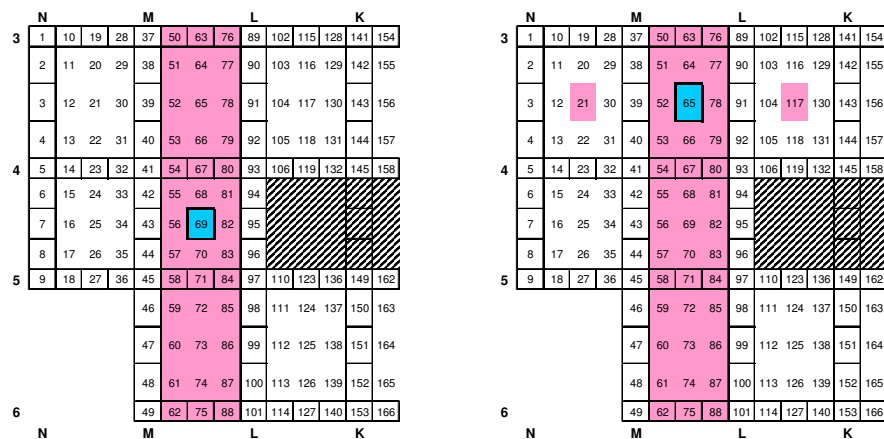


Figure 3.19: NOC VII-18 Measurement Coverage (Forcing at Point 73)

NOC VII-18, Point 69 (Mid-Bay L/M-4/5) and Point 65 (Mid-Bay L/M-3/4)

The measurement coverages for excitations at Point 69 and Point 73 are presented together because they are the only other area measurements on NOC VII-18. They also represent the other two bays of the three-bay strip running in the short direction of the building between grid lines L and M. The third bay in the three-bay strip is the previously described bay that includes Point 73. With the shaker located at each of these two locations, the acceleration FRFs were obtained for the coverage areas shown in Figure 3.20 from burst chirp excitation.



(a) Forcing at Point 69

(b) Forcing at Point 65

Figure 3.20: NOC VII-18 Burst Chirp Measurement Coverage

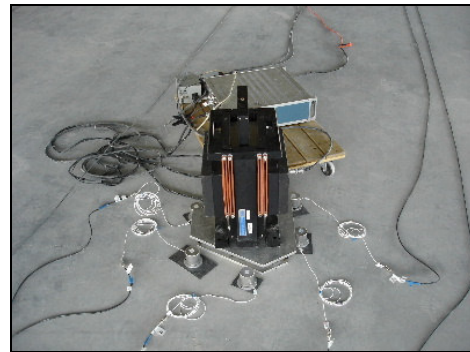
The intent of these measurements was to capture the response along the interior three quarter points of the three-bay strip shown in Figure 3.20. The same three-bay strip of measurements was also covered within the area while forcing at Point 73, allowing a direct comparison of the frequencies and mode shapes of the strip using three different excitation locations within that area. With the shaker at the middle of bay L/M-4/5 (Point 69), the only measurements taken were burst chirp signals to obtain the accelerance FRFs (i.e. no sinusoidal measurements). Unfortunately, due to time constraints, no dominant frequency sinusoidal excitation and/or decay measurements were taken for this forcing location. With the shaker moved to the middle of bay L/M-3/4 (Point 65), another set of burst chirp measurements captured the accelerance FRFs of the interior three quarter points along the three-bay strip. Additional measurements were taken at this excitation location, including a stepped sine sweep across the identified dominant frequency of 4.85 Hz to accommodate a half power method damping calculation, and decay measurements from resonance were taken at three different levels of excitation. Figure 3.21 shows the shaker and force plate at both excitation locations, including the multiple driving point measurements taken with the shaker at Point 65.



(a) Shaker Located at Point 69



(b) Shaker Located at Point 65



(c) Point 65 Redundant Driving Point Measurements

Figure 3.21: NOC VII-18 Shaker Located at Point 69 and Point 65

NOC VII-18, Other Points of Excitation (Point 21, 25, 117, 125, 177, 216, 333)

At various times while testing the NOC VII-18 floor, the shaker was located within seven different bays other than the four locations previously discussed. These locations were Points 21, 25, 117, 125, 177, 216, and 333 previously shown in Figure 3.9. Measurements at these locations were taken for a variety of purposes. In Figure 3.22, a series of measurements was set up to measure the driving point response and roving response with the shaker located at each of the locations highlighted, which includes Points 125, 177, 216, and 333 as well as the previously discussed Points 73 and 281. This investigation examined several characteristics of the floor, namely the driving point acceleration FRFs and damping estimates, but it also investigated the reciprocity of FRF measurements across the long distances of the floor. The reciprocal measurements between points in Figure 3.22 allow direct comparison of two acceleration FRFs that theoretically should be identical: forcing at point A and measuring response at point B, and forcing at point B and measuring the response at point A. While the shaker was located at each of the locations indicated in Figure 3.22, the bay was excited with a burst chirp signal to record the acceleration FRFs and sinusoidal signals to determine the steady state response at its dominant frequency, but no stepped sine sweep. Each location also included measurements of decay from resonance (one level of excitation only).

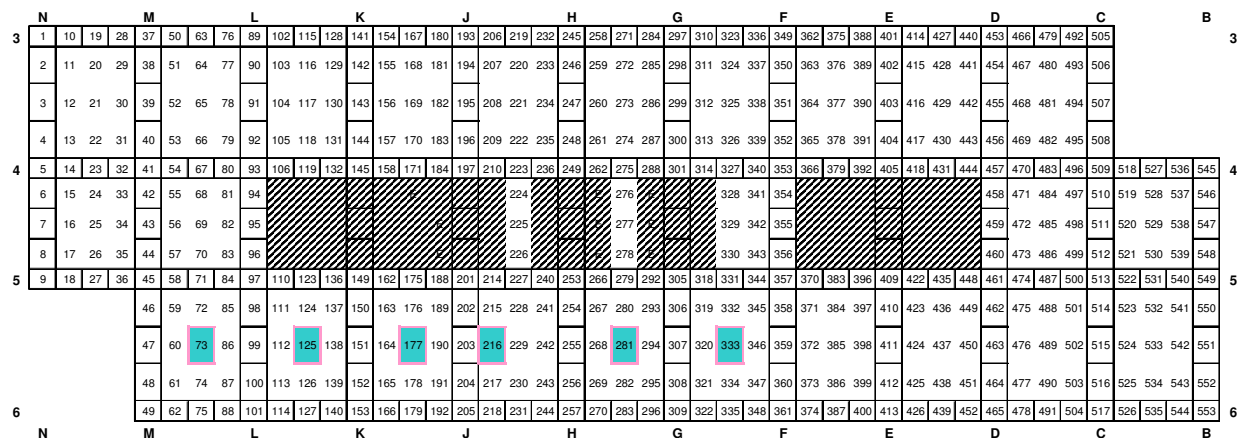


Figure 3.22: NOC VII-18 Reciprocal Measurement Coverage

The final three locations of excitation were Points 21, 25, and 117. The coverage of these measurements is shown in Figure 3.23. The measurements for these excitation locations investigated the driving point response as well as the response in select adjacent bays for use in reciprocal acceleration FRF comparison. With the shaker in the middle of bay K/L-3/4 (Point 117) and the coverage area shown in Figure 3.23(a), the measurements included burst chirp

signals to capture the accelerance FRFs, sinusoidal steady state measurements at the dominant frequency of 4.975 Hz, and decay measurements at two different levels of excitation. With the shaker in the middle of bay M/N-3/4 (Point 21) and the coverage area shown in Figure 3.23(b), the measurements included burst chirp signals to capture the accelerance FRFs, sinusoidal steady state measurements at the identified dominant frequency of 4.875 Hz, and decay measurements at two different levels of excitation. Measurements investigated the mid-bay response of M/N-4/5 (Point 25) and the coverage area shown in Figure 3.23(c). The measurements included burst chirp signals to capture the accelerance FRFs, which indicated dual peaks (and oddly enough great coherence) at both 6.00 Hz and 5.75 Hz. Sinusoidal steady state measurements were taken at 6.00 Hz and 5.75 Hz, as well as decay measurements at two different levels of excitation.

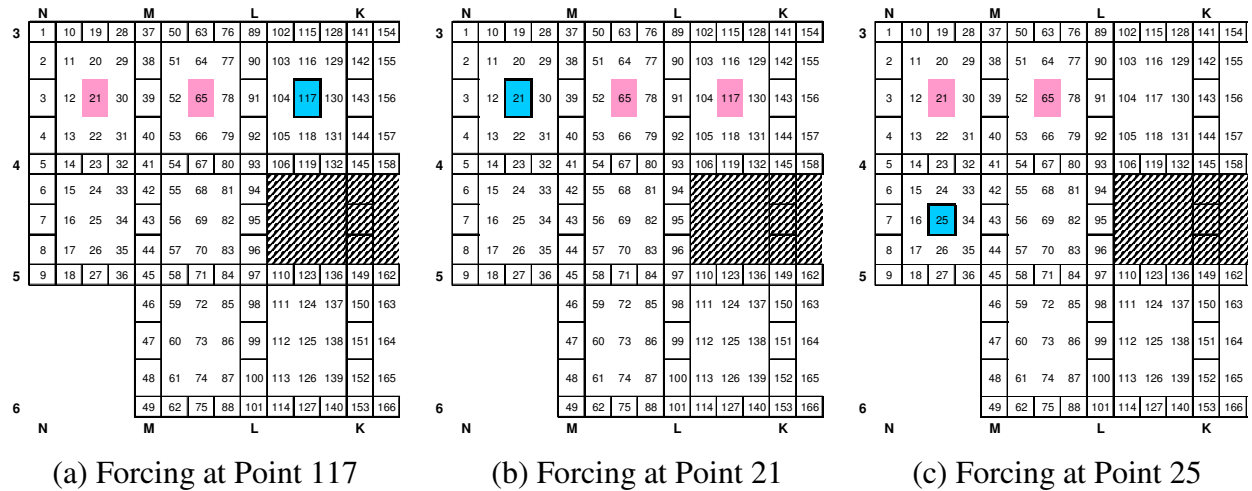


Figure 3.23: NOC VII-18 Reciprocal Measurement Coverage

3.2.3 Measured Floor Behavior – NOC VII (Tested Floors #1 and #2)

This section presents the results of testing NOC VII-24 (Tested Floor #1) and NOC VII-18 (Tested Floor #2) and discussion on the behavior of these floors implicated by the measurements. Limited results from testing NOC VII-24 are presented first, followed by results from testing NOC VII-18. Only limited results are presented for the first tested floor because of the lower quality of the measurements and limited measurement coverage. As previously stated, more information about the methods for testing floors was obtained from this specimen than valuable experimental results. As such, the limited results better serve as contrast for the measurements of NOC VII-18, the second tested floor. Also included in this section is a discussion of the modal analysis software used for modal parameter estimation and the methods used for estimating the frequencies, damping, and mode shapes.

For each of the tested floors, the driving point accelerance FRFs are presented first. These are the key measurements for dynamic testing of in-situ floor systems and provide the strongest measurements for estimating frequencies and damping. The participating frequencies, including the identified dominant frequency, are listed for each of the excitation locations. Each peak on the accelerance FRF is evidence of at least one mode (Vibrant Technology 2003); however, some are clearly more significant than others. As such, only the most clearly defined peak frequencies are remarked upon in the presented research. Estimates of damping using the half power bandwidth method on the identified dominant frequency of the driving point accelerance FRFs are presented. For comparison of manually identifying peak frequencies and damping from the accelerance FRFs, results from MDOF curve fitting using modal analysis software are presented. For area coverage of the floor, the visual operating deflection shapes or mode shapes are presented. Finally, this section covers various other investigations and remarks of measured floor behavior, such as damping estimates using decay from resonance, linearity, and reciprocity of measurements.

Modal Parameter Estimation Software

The modal analysis software used in this research was ME'scopeVES Version 3.0, which is a series of modal testing analysis tools that allows the user to observe, analyze, and document the dynamic behavior of tested structures (Vibrant Technology 2003). The software allows the user to construct 3-D models of the tested floor, import multi-channel frequency domain accelerance FRF measurements, and display the spatially acquired vibration data on the floor

model surface in the form of mode shapes or operating deflected shapes (ODS). Additionally, manually defined shapes (such as those derived from steady-state sinusoidal measurements over an area) can be imported, animated, and compared with other shapes. The software has the capability to perform modal parameter estimation by curve fitting a set of imported FRF measurements. Although several curve fitting techniques were available in the software, the chosen technique was the MDOF rational fraction polynomial curve fitting algorithm. The advantage of MDOF curve fitting operations rather than SDOF or manual methods is the ability to identify and estimate the frequencies and damping of closely spaced modes.

The basic elements available for constructing the visual model were points, lines, and four node surfaces. The FRF measurements were assigned to the points on the model that spatially corresponded with the measured points on the floor. The points in the model, numbered in the same fashion as in Figure 3.8, were connected to one another using either line elements or surface elements, which provided the ODS when animated at a given frequency. Figure 3.24 shows an example of the ME'scope 3-D model of the entire coverage area of NOC VII-24 with accelerance FRF measurements from excitation at Point 73 in the middle of Bay L/M-5/6 (measurement coverage shown in Figure 3.11). For both floors, smaller models were constructed to observe more localized behavior, such as reduced area coverage, centerlines, and interior quarter points of a strip of bays.

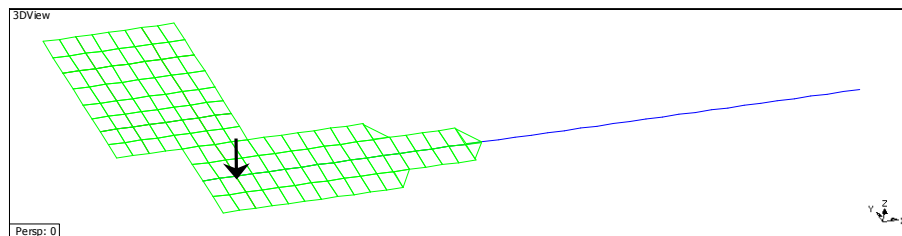


Figure 3.24: NOC VII-24 ME'scope Model of Full Coverage (Forcing at Point 73)

Once imported into the software, the accelerance FRF measurement for each DOF was assigned to its corresponding DOF in the ME'scope model. By definition, each spectral value of the imported FRF is a complex value representing the magnitude and phase of the accelerance at a particular frequency. The most important accelerance FRF measurement assigned to the model is the driving point measurement because it is the one from which all the other accelerance FRFs are referenced. After assigning all the FRF measurements to the ME'scope models, the vibration responses at specified frequencies were displayed as static or animated shapes. Note that this also applied to accelerance FRFs from steady-state sinusoidal excitation, which are valid only for

the driving frequency. Using ME'scope's curve fitting applications on the imported chirp derived accelerance FRFs, estimates were made on frequencies, damping, and mode shapes. Specific applications of the above listed capabilities to the models and measurements of the tested in-situ floors are described in the following sections.

Mode Shapes and Operating Deflection Shapes

Before continuing any further with the presentation of experimental results, it is important to point out the difference and/or relationship between an operating deflection shape (ODS) and a mode shape. A paper by Richardson (1997) is an excellent reference for explaining the relationship between the two, which is summarized here. Richardson states that mode shapes are basically structural resonances, which are a product of the elastic, inertial, and possibly even the energy dissipation properties of a structure. They are load independent, their amplitudes are arbitrary, and they are associated with their specific respective resonant frequencies. An ODS, on the other hand, can be defined at any frequency. An operating deflection shape is defined as the shape at a specific time or frequency from forced vibration, such as the experimental testing in the presented research. The amplitude and shape of the forced response is dependent on the magnitude and location of the force. A gathered set of accelerance FRFs, such as those presented in this research, are the ODS's of the structure over the measured frequency range, any of which can be animated in a program such as ME'scope. Mode shapes are obtained from these measurements through post processing using modal analysis software or other manual methods. In short, the analytical expression of a single term in the accelerance FRF matrix shown in Equation 2.4 is "fit" with estimated parameters, which includes terms from the mode shape vectors of the excitation and response DOFs in the numerator. Each of the summation terms in Equation 2.4 is a resonance curve for one mode, and thus the summation of each of those resonance curves is the accelerance FRF. Curve fitting is simply backing out the terms that form the resonance curves (modal frequency, damping, and mode shape). If a set of accelerance FRFs are curve fit in this manner, the mode shape terms are estimated over the coverage area.

Note that if either the excitation location or the response location is on a nodal line of a mode shape, there will not be a measured response in the accelerance FRF (the ODS) at that frequency. Consequently, that particular mode shape cannot be estimated from this measurement. A corollary to this problem is that if the shaker is located in an area that does not have much participation in a given mode, such as *near* a nodal line, then the resulting

accelerance FRFs may be weakly represented, potentially to the point that an accurate estimate of the modal properties is degraded due to lack of fidelity. The weaker the mode represented in a set of accelerance FRFs, the more difficult (and less accurate) it is to estimate the modal parameters from that set of FRFs.

The distinctions between a mode shape and an ODS are highlighted in such detail because many of the shapes presented in this research are displayed as operating deflection shapes and not the curve fit mode shapes. There are two main reasons for this. First, at a resonant frequency, the ODS will closely approximate the mode shape if the ODS is dominated by a single mode (Richardson 1997). Secondly, the ODSs are true forced-response measured shapes from the accelerance FRFs, and the quality of the displayed shape is a direct result of the quality of the measurements. On the other hand, the curve fit mode shapes are subject to error in the curve fitting process and can be misleading, particularly when trying to distinguish from an unexpected mode shape and a poorly curve fit set of data.

If the ODS has significant contributions from multiple closely spaced modes at a particular frequency, then the resulting shape is not invalid, it is simply the summation of the response of multiple modes. This can be seen in decay from resonance measurements when driving the floor at a peak frequency that has significant contribution from other modes. The end goal of the research must be kept in mind, which is characterizing the behavior of these in-situ floor systems with the intent of evaluation of vibration serviceability. An individual annoyed by excessive vibration is not concerned with the number of participating modes, just the overall acceleration causing the annoyance. All floor systems have multiple modes, thus it is the multi-mode response from an individual walking that causes excessive vibration, not a single mode (although technically the contribution from the other modes may be very small). For development of a modal model for use in forced-response simulations, an accurate estimation of the mode shapes is critical; however this application was not used in this research. For visual display of the shapes, however, the ODS is often a better representation of the floor's behavior as it applies to evaluation to vibration serviceability because the portions of the floor participating in the response (and subject to excitation and annoyance) are clearly evident.

Measured Floor Behavior - NOC VII 24 (Tested Floor #1)

With the shaker at Point 73 (mid-bay LM-56), a total of 12 driving point measurements were taken from the continuous chirp signals. Figure 3.25 contains the accelerance FRF magnitude, phase, and coherence for nine driving point measurements (three traces are not included due to poor quality). Note that the traces are very consistent between each of the measurements and there is good coherence at the peaks. The only noticeable dip in coherence is around the 9 Hz range, which corresponds to the dip in the FRF and occurs due to a lack of response at these frequencies. For the driving point accelerance FRFs when forcing at Point 73, the three significant peaks are at 4.80 Hz, 5.10 Hz, and 5.80 Hz, with 5.10 Hz identified as the dominant frequency, or the one that would generate the most response per input sinusoidal force at this frequency. Although presented in smaller format within the following section, the driving point accelerance FRFs (including magnitude, phase, and coherence) of all three excitation locations for NOC VII-24 are presented in larger format in Appendix E.

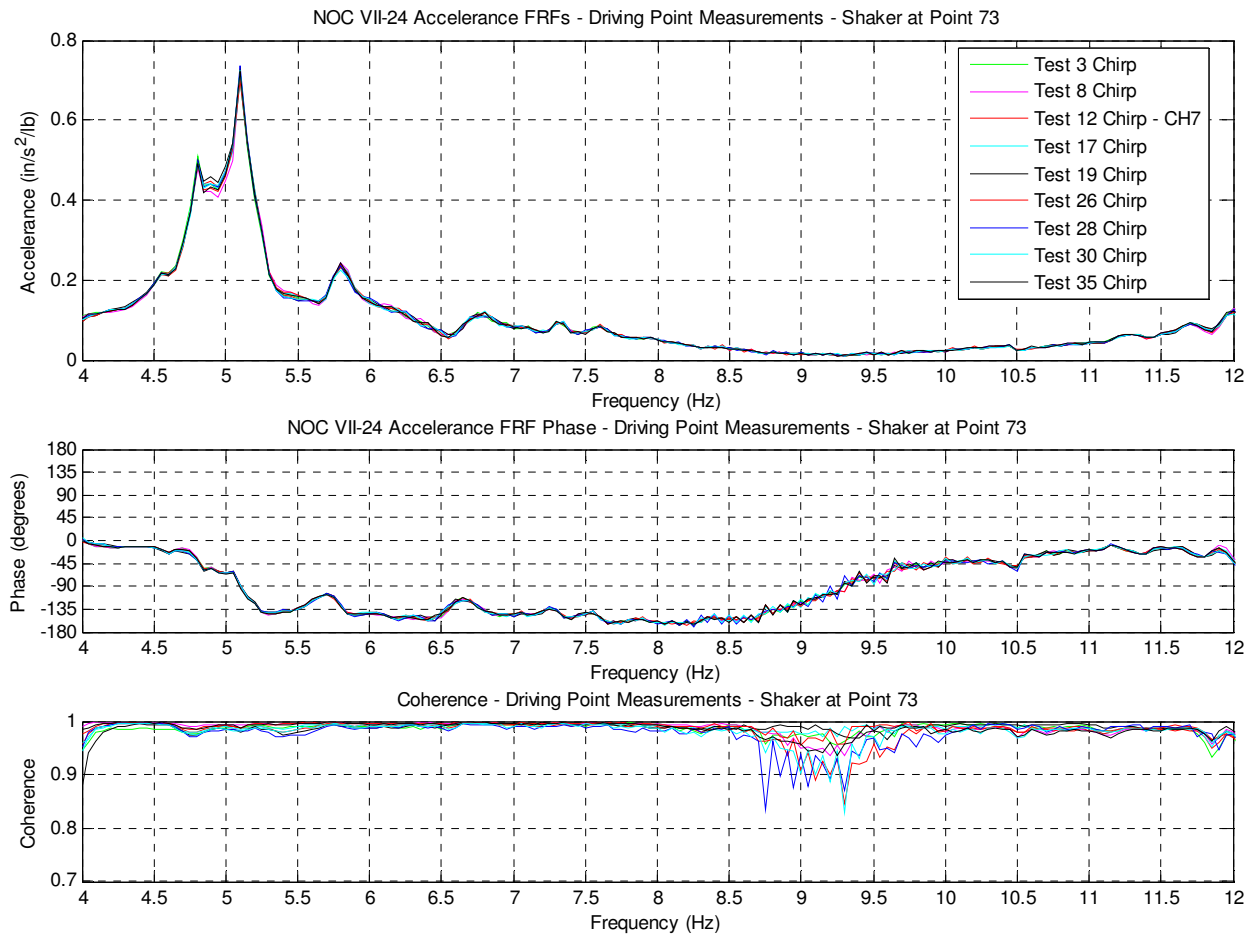


Figure 3.25: NOC VII-24 Driving Point Accelerance FRFs and Coherence (Point 73)

The half power bandwidth estimates of damping for the 5.10 Hz peak on the individual driving point measurements in Figure 3.25 ranged from 0.99% to 1.4% of critical. Given the consistency and apparent quality of the driving point measurements, the wide range of values was not expected, and suggested future measurements should use an increased frequency domain resolution in the hopes of adequately defining the shape in the immediate vicinity of the peak. MDOF curve fitting of just the driving point measurements of Figure 3.25 resulted in the estimated frequencies and damping values of Table 3.3 and show agreement with previously identified frequencies at 4.80 Hz, 5.10 Hz, and 5.80 Hz. Several frequencies other than the ones identified visually from the FRFs were used to achieve the best fit possible. The estimated damping value for the dominant frequency of the curve fit data (5.09 Hz) is 1.00%. Overall, these low estimated values of damping are reasonable considering the bare condition of the floor.

Table 3.3: NOC VII-24 Pt 73 – Driving Point Curve Fit Estimated Frequencies & Damping

Frequency (Hz)	Damping (%)
4.57	2.00
4.81	1.60
4.91	1.80
5.09	1.00
5.79	1.01
6.72	2.00

The driving point accelerance FRF traces were curve fit using the polynomial function of ME'scope. While not described here in detail, the general process of curve fitting a set of FRFs involves three basic steps: selecting a frequency bandwidth in which to identify one or more modes, estimating the frequencies and damping of the identified modes within that bandwidth (i.e. the global parameters in the denominator of Equation 2.4), and lastly estimating the mode shapes by fitting a curve to the FRF data (i.e. estimating the numerator for each of the summation terms of Equation 2.4 and plotting). The curve fit data overlaid on the driving point FRFs of Figure 3.25 is shown in Figure 3.26.

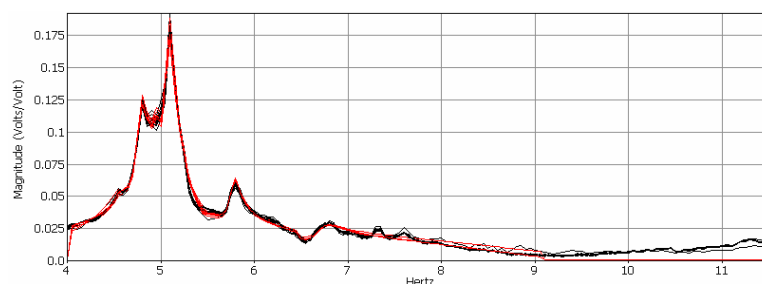


Figure 3.26: NOC VII-24 Driving Point FRFs with Curve Fit Overlay (Point 73)

It should be noted that the process of curve fitting is a subjective task that requires a fair amount of engineering judgment. At each step in the process (bandwidth selection, frequency and damping estimation, and curve fit), the parameters may be manually changed to get a better visual fit of the FRF data. Thus, the resulting frequency and damping estimates of Table 3.3 and the curve fit overlay of Figure 3.26 are products of partially automated curve fit estimates and engineering judgment introduced to account for reasonable values (disregarding unrealistic damping values, for example). This was the general process used for curve fitting all measurements in the presented research, whether simply driving point measurements or a full set of accelerance FRFs over a coverage area. Plots of all curve fit accelerance FRFs and summary tables of estimated frequencies and damping for NOC VII are included in Appendix F.

Figure 3.27 presents the magnitude and phase for the one driving point accelerance FRF measurement taken with the shaker located at Point 69 (mid-bay LM-45). The significant peaks of interest are at 4.80 Hz, 5.80 Hz, and 6.60 Hz, with 6.60 Hz identified as the dominant frequency (1.83% half power bandwidth estimate of damping). Table 3.4 lists the estimated frequencies and damping from a curve fit of the Point 69 driving point accelerance FRF. Again, the values are in good agreement with visually identified frequencies and damping estimate, although the 5.10 Hz frequency was not expected due to its lower magnitude accelerance.

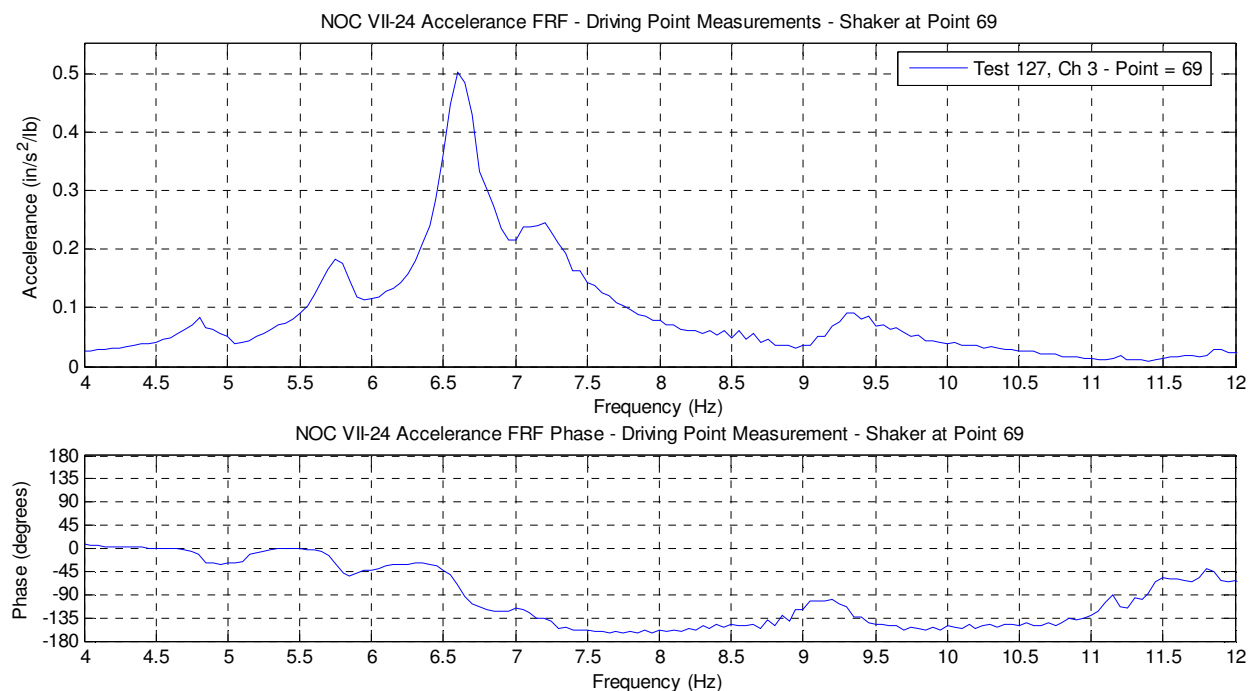


Figure 3.27: NOC VII-24 Driving Point Accelerance FRF (Point 69)

Table 3.4: NOC VII-24 Pt 69 – Driving Point Curve Fit Estimated Frequencies & Damping

Frequency (Hz)	Damping (%)
4.83	1.60
5.10	1.00
5.74	1.57
6.62	2.00
7.05	2.40
7.28	2.40

Figure 3.28 presents the magnitude and phase of the one driving point accelerance FRF measurement taken with the shaker located at Point 25 (mid-bay MN-45). The significant peaks of interest are at 4.80 Hz, 5.80 Hz, and 6.00 Hz, with 6.00 Hz identified as the dominant frequency. The 1.53% half power bandwidth estimate of damping is in good agreement with the curve fit value of 1.60% at the corresponding 6.01 Hz frequency.

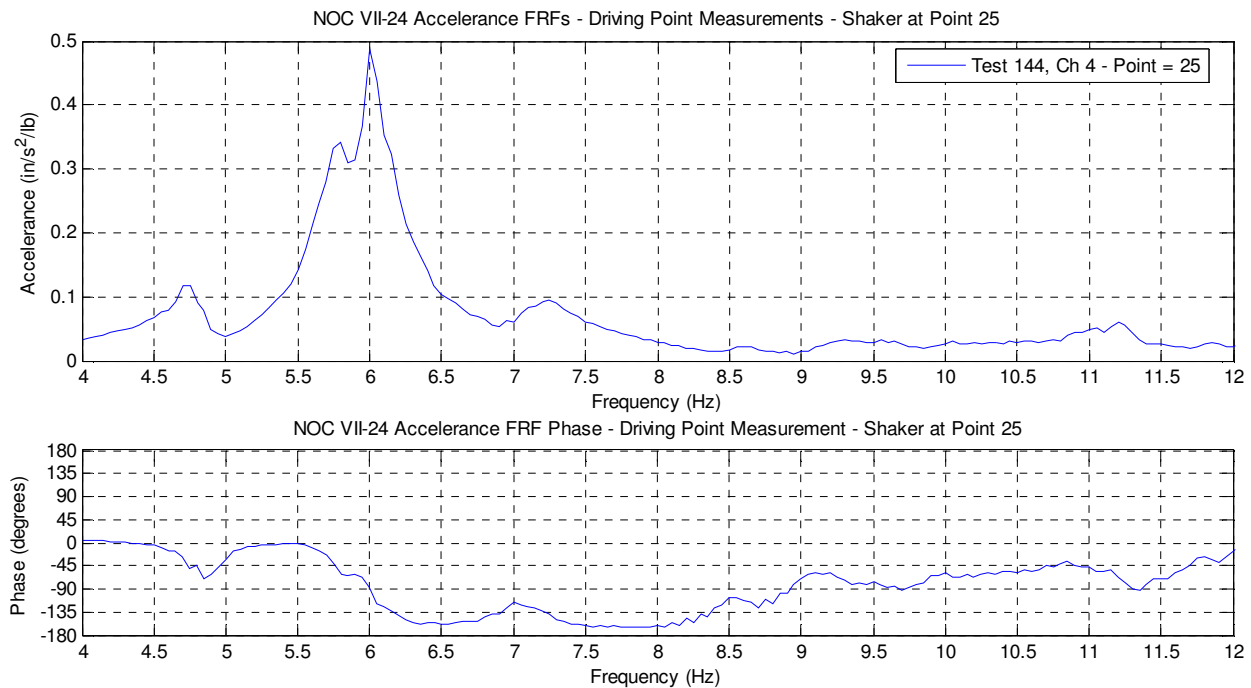


Figure 3.28: NOC VII-24 Driving Point Accelerance FRF (Point 25)

Table 3.5: NOC VII-24 Pt 25 – Driving Point Curve Fit Estimated Frequencies & Damping

Frequency (Hz)	Damping (%)
4.76	1.61
5.79	1.73
6.01	1.60
7.18	2.39

Area Coverage Curve Fit and Displayed Operating Deflection Shapes

While the MDOF curve fitting of driving point accelerance FRFs is a good method for estimating parameters of modes with a strong response at the driving point, a better method for estimating the parameters for a given mode is fitting a set of accelerance FRFs taken over an area, such as the coverage area measured while forcing at Point 73. When only a driving point measurement is available, such as for Points 69 and 25, then a curve fit of these measurements is the best available option. The set of accelerance FRFs measured by the coverage shown in Figure 3.11 from excitation at Point 73 was curve fit with the same procedure as described above, and the estimated frequencies and damping values are listed in Table 3.6. The full set of accelerance FRFs and the corresponding curve fit overlay can be found in Appendix F. When compared with the estimated parameters from curve fitting just the driving point measurements of Point 73 (Table 3.3), the values are in good agreement with the exception of a slightly higher damping ratio for the mode at 5.79 Hz and a lower frequency for the mode at 6.66 Hz.

Table 3.6: NOC VII-24 Global Curve Fit Estimated Frequencies and Damping (Point 73)

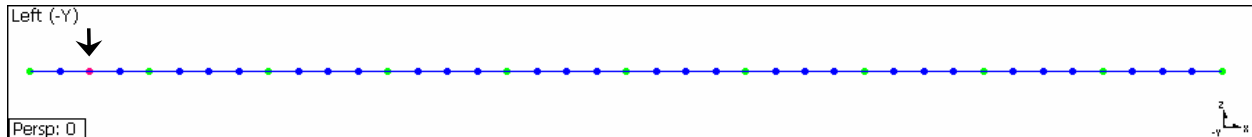
Frequency (Hz)	Damping (%)
4.58	2.00
4.82	1.60
4.91	1.80
5.09	1.00
5.79	1.60
6.66	2.22

For the purposes of displaying the shapes of the tested floor system at these six frequencies of interest, several ME'scope spatial models were constructed to animate the ODSs from the accelerance FRFs or estimated mode shapes (if desired). Two 2-D centerline models are presented to describe the response to excitation at Point 73, one along the short direction of the building and the other 10-bay span in the long direction of the building. Each of these two "slices" of coverage includes the driving point, Point 73. These two models are shown in Figures 3.29(a) and (b). While the 2-D centerline models represent the floor behavior down a strip of bays, they may not adequately represent the behavior of the rest of the floor, which exhibits two-way bending action that is out-of-plane to the displayed centerline. Thus, a 3-D surface model of the measurement coverage area is a better display of the floor's response. A model of the full coverage of the area (Figure 3.24) would be a bit unwieldy to display and difficult to interpret, so a smaller 7-bay area of coverage was created to display the shapes over

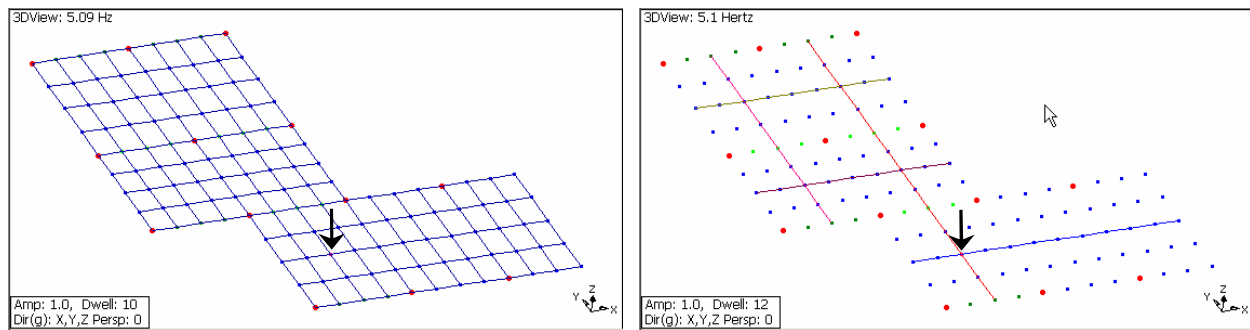
the bays in the immediate vicinity of the point of excitation, as shown in Figure 3.29(c). This area model can display the shape of response with either surface elements (left) or with line and point elements (right), which essentially represent the centerline response in 3-D rather than 2-D.



(a) ME'scope 3-Bay Centerline Model



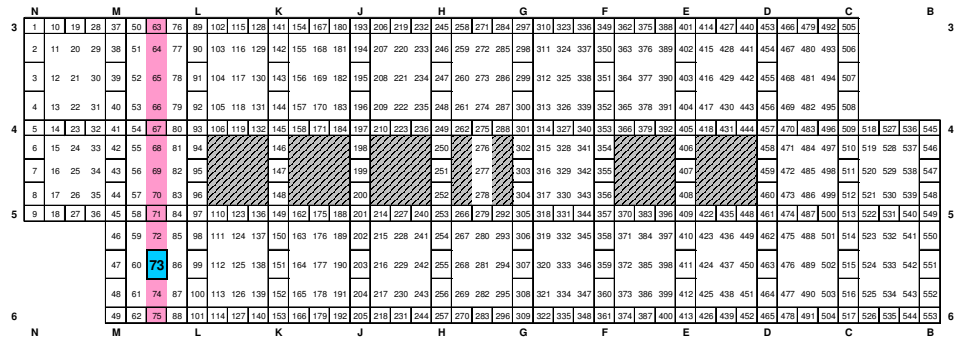
(b) ME'scope 10-Bay Centerline Model



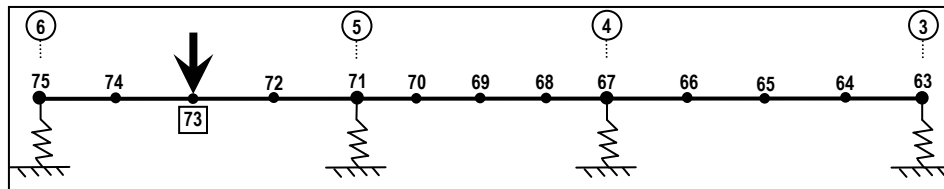
(c) End-Bay Area Model (Surface and Centerline)

Figure 3.29: NOC VII-24 ME'scope Models

3-Bay Centerline Model - As previously mentioned, the 3-bay centerline model included the driving point (Point 73) and spanned the short direction of the building, parallel to the direction of the floor framing (Figure 3.30(a)). An idealization of the centerline model is shown in Figure 3.30(b), where the floor along the centerline is represented as a continuous beam running over spring supports, which represent the girders at the ends of each bay. Besides clearly annotating the point numbers on the model, this idealization makes it a little easier to recognize familiar mode shapes along the length of the model rather than seeing it as simply a line model as shown previously in Figure 3.29(a).



(a) 3-Bay Centerline Model Coverage



(b) Idealized 3-Bay Centerline Model – Continuous Beam on Spring Supports (Girders)

Figure 3.30: NOC VII ME'scope 3-Bay Centerline Model

All operating deflection shapes are scaled by a single reference, the driving point measurement. This accelerance FRF trace is essentially the datum magnitude and phase from which all other measurements are based. With 12 different driving point measurements from excitation at Point 73 (nine of adequate quality), one had to be chosen and used as the driving point measurement for curve fitting operations and display of the shapes. The driving point measurement identified for this task was chosen for its high coherence throughout the frequency range. Additionally, one was chosen that had a magnitude and phase around the dominant peaks that were representative of the typical values for all the redundant driving point measurements. This process was repeated throughout the presented research whenever modal parameters were estimated or shapes displayed. The operating deflection shapes for each of the six frequencies identified by parameter estimation are presented in Figure 3.31 in two forms: a “static” display of the shape and a “persistent” display of the shape. The static display shows the shape at the measured phase of the driving point accelerance at the given frequency, which does not mean that all other points are at their respective maximum responses. This apparent “complexity” can be misleading, but is more a function of variation in the driving point (reference) measurement than any complex behavior of the floor system. The persistent plot is used to show the envelope of a shape which may not be fully represented by the static image. This is apparent in the ODS shown in Figure 3.31 at 5.10 Hz, the bay’s dominant frequency. Only looking at the static image

of the ODS could give the impression of very little response on the far side of the strip, however the persistent display of the shape throughout its full cycle of vibration clearly shows this is not the case.

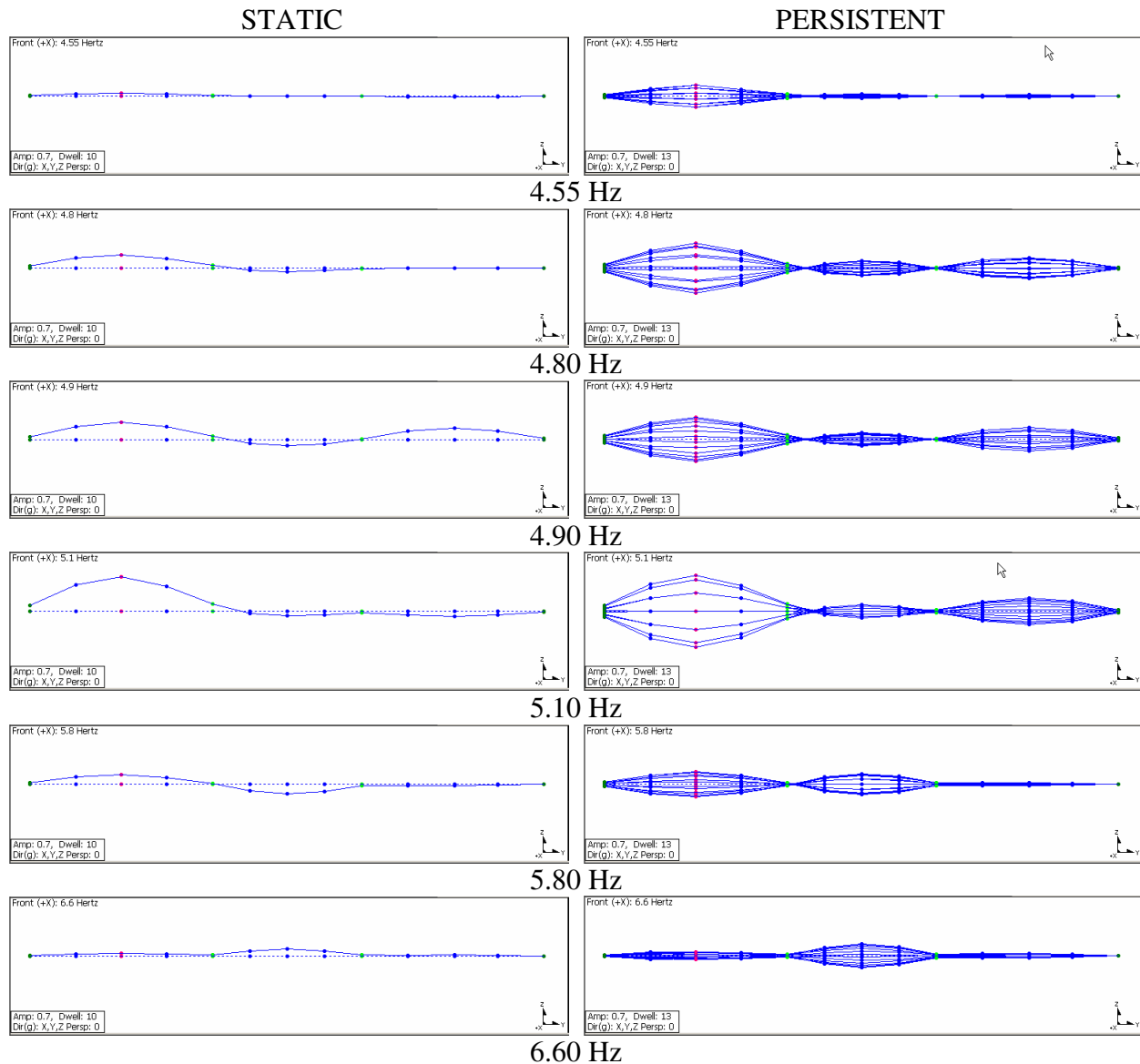
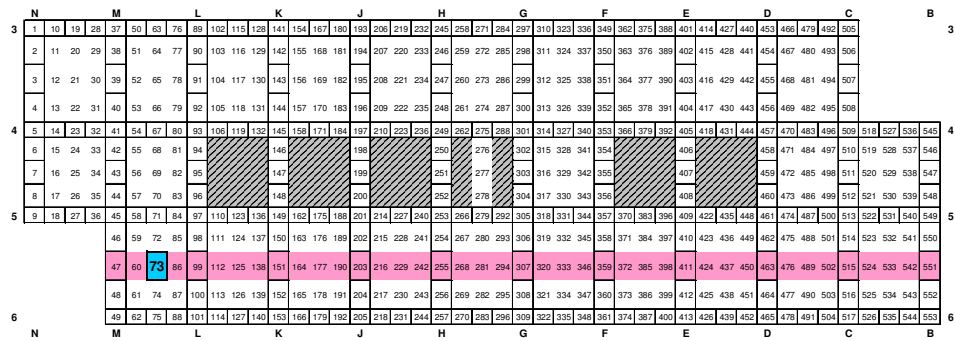


Figure 3.31: NOC VII-24 3-Bay Centerline ODSs (Forcing at Point 73)

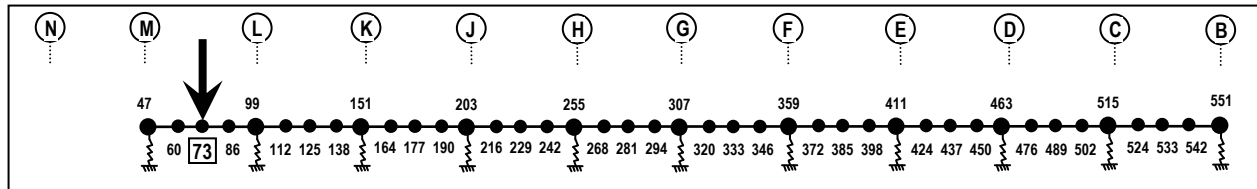
The shapes of Figure 3.31, and all future shapes shown in the presented research unless otherwise noted, are presented in “relative” scale to one another, as opposed to plotting each shape with its greatest magnitude equal to a common value. This is another advantage of the persistence plots, as weak modes are sometimes difficult to interpret at relative magnitudes, however the persistent display aids in interpretation. Additionally, this method of scaling the display allows the shapes to represent the dominance of the response at a given frequency by

plotting on a common scale. As expected, the greatest response at any one point occurs at the location of the driving point in the ODS corresponding to the identified 5.10 Hz dominant frequency.

10-Bay Centerline Model - The 10-bay centerline model included the driving point (Point 73) and spanned the long direction of the building, perpendicular to the direction of the floor framing (Figure 3.32(a)). An idealization of the system as a 10-span continuous beam on spring supports, in this case representing the stiffer beams framing between columns, is shown in Figure 3.32(b).



(a) 10-Bay Centerline Model Coverage



(b) Idealized 10-Bay Centerline - Continuous Beam on Spring Supports (inter-column beams)

Figure 3.32: NOC VII ME'scope 10-Bay Centerline Model

The shapes of the six frequencies of interest are shown in Figure 3.33. As expected, most of the response along the length of the span occurs in the immediate area around the point of excitation and at the 4.80 Hz and 5.10 Hz frequencies, the largest peaks on the FRFs. For all shapes except 5.10 Hz, the point of maximum response is at the driving point, Point 73. The 5.10 Hz ODS has a slightly larger response at the middle of the adjacent bay (Point 125, 16% larger response), although this is likely the product of the additional constraint of the excited bay. Another interesting observation from Figures 3.31 and 3.33 are the amount of response measured at the exterior boundaries of the tested bay, particularly at the 5.10 Hz dominant frequency. It is typically assumed that the exterior cladding of the building provides enough stiffness to the spandrel member that very little motion occurs at the boundary. Measurements show, however, that the response magnitude at Point 75 (the middle of the spandrel girder) was roughly 16% of

the response magnitude at the mid-bay driving point. Additionally, the response magnitude at Point 47 (the middle of the spandrel beam) is 30% of the response magnitude at the mid-bay driving point, as shown in the 10-bay centerline ODS at 5.10 Hz in Figure 3.33. One should consider, however, the measurement location at the boundary was not truly at the centerline of the spandrel girder, but 12 in. or so towards mid-bay. Regardless, the response was great enough that it should not be neglected and this behavior should be considered when developing finite element models for the floor.

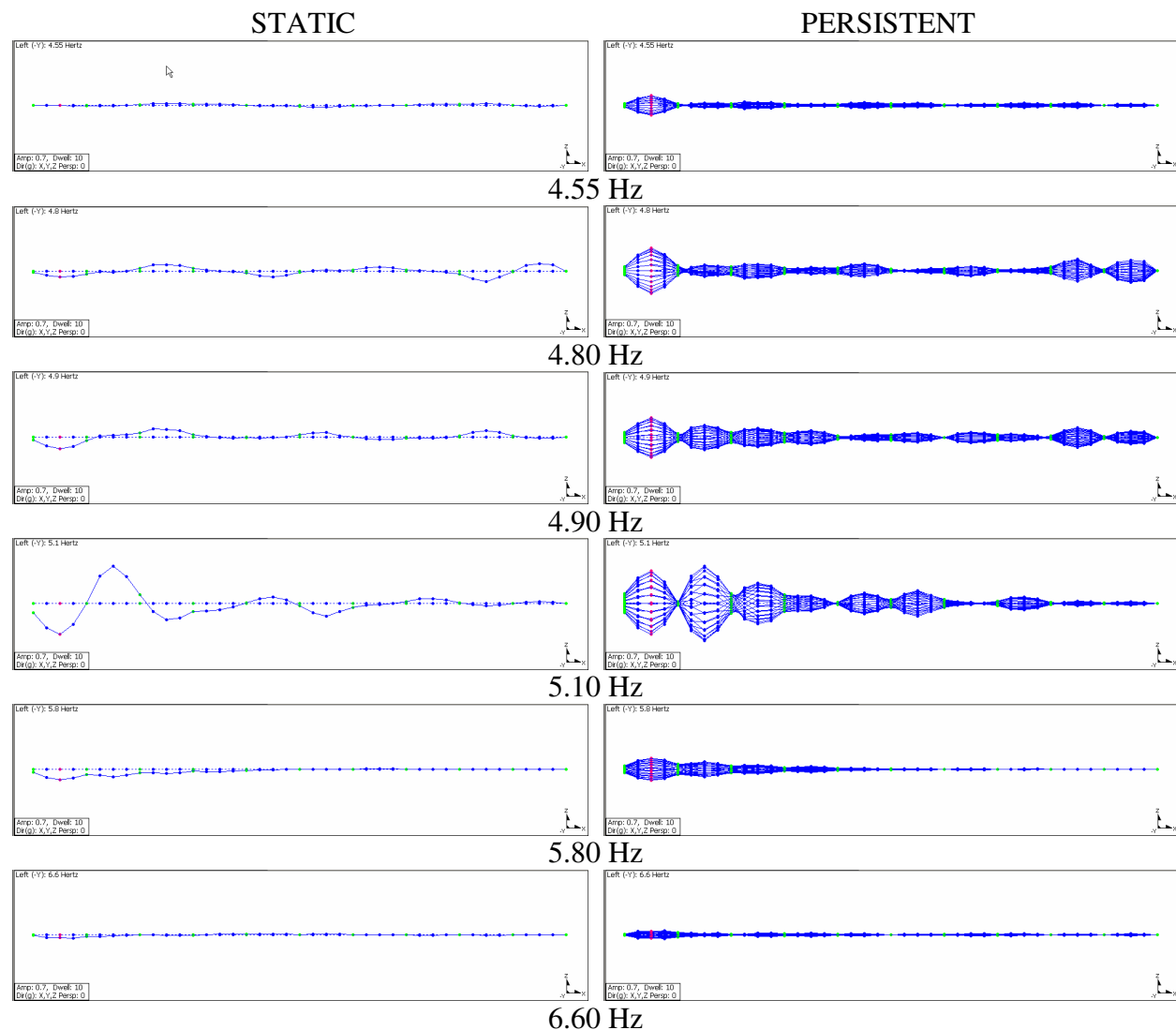


Figure 3.33: NOC VII-24 10-Bay Centerline ODSs (Forcing at Point 73)

For the ODSs at 4.80 Hz and 4.90 Hz, it is interesting to note the amount of measured response at the far end of the floor from the point of excitation, which is over 270 ft away from the shaker. Although not confirmed with any measurements on NOC VII-24, the response is

likely caused by the dominant frequencies of the end bays being at or very near 4.80-4.90 Hz. These were frequencies measured on subsequent tests of Points 21 and 65 of NOC VII-18, which share the same framing and boundary conditions.

Like the other frequencies that do not have much response, the response of the 5.80 Hz ODS is localized near the driving point, but demonstrates an interesting shape as shown at a magnified scale in Figure 3.34. Note that the response of nearly the entire system is in phase with the excitation point, which may be an indication this strip of bays acts as a one way system. Another interesting observation is the regularity of the decreasing magnitude of the shape as one goes further away from the excitation point.

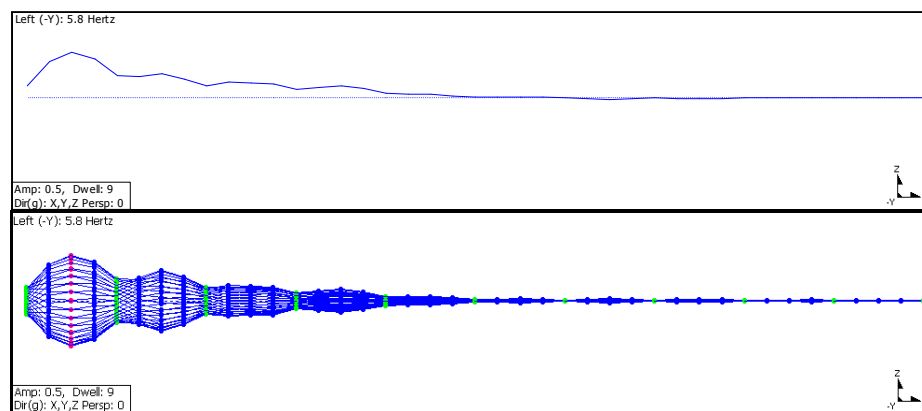


Figure 3.34: NOC VII-24 10-Bay Centerline ODS (magnified) at 5.80 Hz

End-Bay Area Model – The end-bay area model, capturing the response of the end seven bays of the floor, helps visualize the behavior over a wider area. Figure 3.35 shows the shapes of the response at the six frequencies of interest due to excitation at Point 73. From this display of the shapes, it is apparent that most of the larger amplitude response occurs in the bays perpendicular to the floor framing of the bay of excitation, following the direction of the ribs of the composite deck/slab system. This is very evident in the ODS of the 5.10 Hz dominant frequency, where the response in the adjacent bay is slightly greater than the response at the driving point, as previously mentioned.

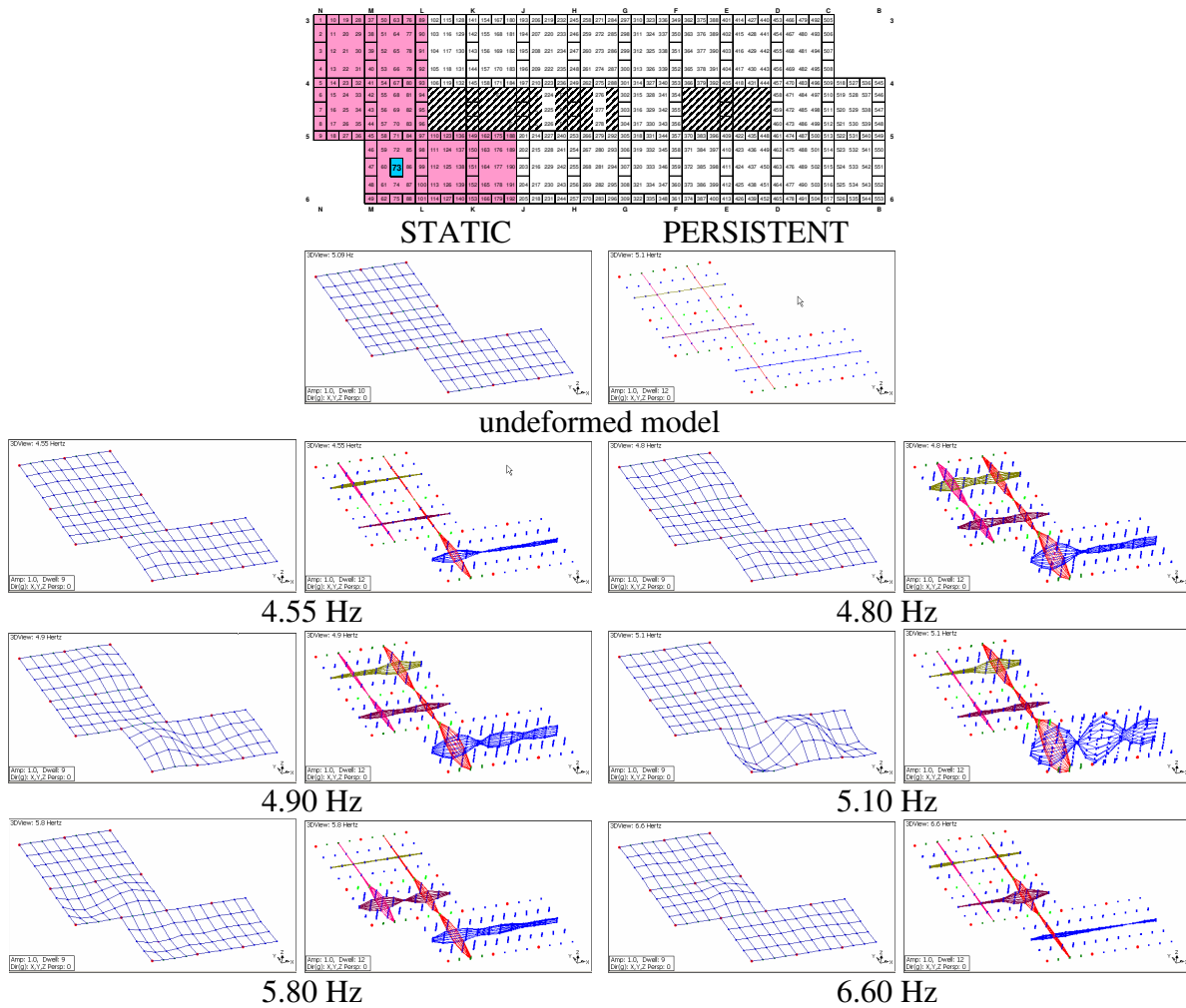


Figure 3.35: NOC VII-24 End-Bay Area ODSs (Forcing at Point 73)

Sinusoidal Measurements – A large number of steady-state sinusoidal measurements were taken at the identified dominant frequencies of each of the three excited bays. The coverage areas of these measurements were previously shown in Figure 3.11, Figure 3.12, and Figure 3.13, for Points 73, 69, and 25, respectively. Point 73 was driven at 5.05 Hz, Point 69 at 6.55 Hz, and Point 25 at 6.00 Hz. The resulting ODS shapes from these sinusoidal measurements and comparison with the shapes extracted from the accelerance FRFs are not presented here in detail for two reasons. First, only the magnitude information for the sinusoidal measurements was preserved, and not the phase information. This prevents a full comparison of the derived shapes; however a limited comparison using just the magnitudes was made. From this comparison, the magnitudes of the sinusoidally derived operating deflection shapes were in excellent agreement with the magnitudes of the chirp derived ODSs, which builds confidence in the quality of the measured accelerance FRF values. Secondly, an extensive comparison of sinusoidal

measurements and chirp derived accelerance measurements was conducted using improved techniques (preserving phase information) for NOC VII-18, and is presented in the next section.

Measured Floor Behavior - NOC VII-18 (Tested Floor #2)

A representative accelerance FRF from each of the eleven sets (locations) of driving point measurements are superimposed in Figure 3.36. Several indications of the floor's behavior can be observed from this type of plot, such as the relative magnitudes of the accelerance at the various peak frequencies, which range from 0.5-1.0 in/s²/lb of input force. One particular accelerance FRF, derived from excitation at Point 65, has a peak magnitude that is clearly larger than the others. Information such as this can be used as an indicator of the location on the floor system most susceptible to annoying levels of vibration because it is the location that will achieve the greatest level of response per lb of input force at that frequency.

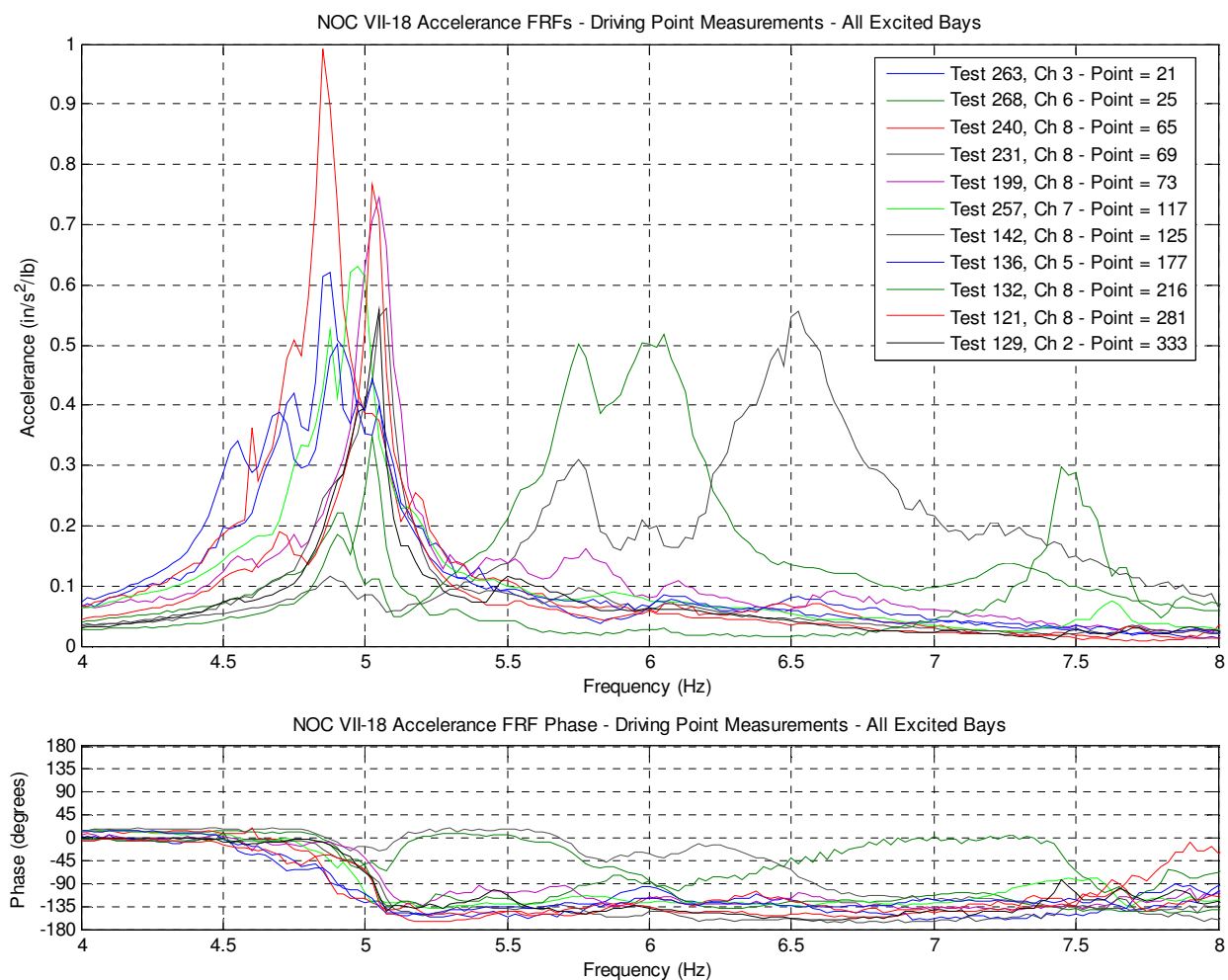


Figure 3.36: NOC VII-18 Driving Point Accelerance FRFs (All Excitation Points)

Another notable characteristic in Figure 3.36 is the location of the peak frequencies for each of the excited bays. As expected, the accelerance FRFs with higher dominant frequencies are measured within the smaller, more constrained interior bays (Point 25 and 69). For the larger exterior bays, however, the dominant frequencies are clustered in a frequency band less than 2 Hz wide, which is a common result for bays with nearly identical framing that only differ slightly by boundary conditions. It is common to see the frequency content of the dominant frequency of an adjacent bay in a driving point measurement, as shown by smaller peaks in some of the accelerance FRFs of adjacent bays in Figure 3.36. However, if adjacent bays share the same dominant frequency, then additional vibration problems can occur. Figure 3.37 shows the same representative driving point accelerance FRFs for just the six-bay strip of bays along the long exterior of NOC VII-18 (Points 73, 125, 177, 216, 281, and 333). Note that nearly all six have a dominant (or significant) peak at a frequency of 5.025-5.05 Hz. The implication of this common dominant frequency amongst adjacent bays is that a single individual walking across the bays can incite a much higher response, as a greater area of the floor is susceptible to the walking forces at this specific frequency.

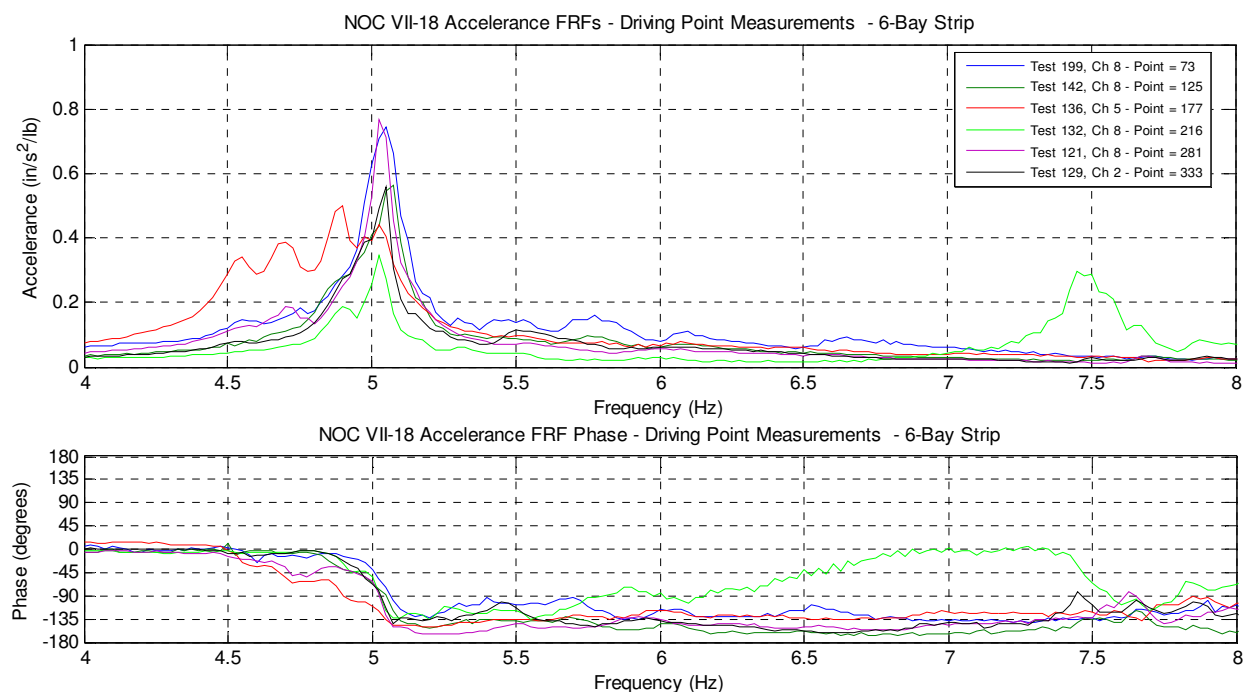


Figure 3.37: NOC VII-18 Driving Point Accelerance FRFs (6-Bay Strip)

The remainder of this section covers in more detail the experimental results from testing each of the eleven different bays of the second tested floor. The order of the discussion is based

upon the amount and detail of testing at each location, with the most extensively tested bays presented first. Results include the driving point accelerance FRFs with remarks on estimated frequency and damping, accelerance magnitude, sinusoidal measurements, operating deflection shapes for coverage areas, comparisons with locations on the floor that correspond to test locations of NOC VII-24, and other investigations including decay from resonance, linearity, and reciprocity. Large scale plots of magnitude and phase of accelerance FRFs (including coherence) for all eleven locations of excitation for NOC VII-18 are included in Appendix E, however smaller scale plots of magnitude and phase for each of the excitation locations are included here for reference and discussion.

NOC VII-18 Point 281 – The most measurements of any excitation location were taken with the shaker at Point 281 (mid-bay G/H-5-6). The magnitude and phase of a total of 61 driving point accelerance FRF measurements taken with the shaker located at Point 281 are presented in Figure 3.38. The frequencies of interest are a small peak at 4.70 Hz and a clearly dominant peak at 5.025 Hz. Note the exceptional consistency and quality of the 61 measurements that were taken over two days of testing. The average accelerance value at the dominant frequency was $0.77 \text{ in/s}^2/\text{lb}$, the second largest of any of the locations tested on NOC VII-18. This is significant because the mode with a 5.025 Hz frequency is susceptible to excitation with the second harmonic of a 2.5 steps per second walking rate. Although 2.5 steps per second is slightly faster than the upper end of walking rates, it is not unrealistic. The large magnitude of the accelerance peak at this low frequency would indicate a potential vulnerability to excessive vibration.

The half power bandwidth estimate of damping for the 5.025 Hz peak of the driving point measurements was 0.65% of critical, identical to the value estimated by MDOF curve fitting the driving point accelerance FRFs using ME'scope (Table 3.7). The 4.70 Hz peak on the driving point accelerance FRFs had a much smaller amplitude than the dominant peak, however curve fitting estimated 1.00% damping for this mode.

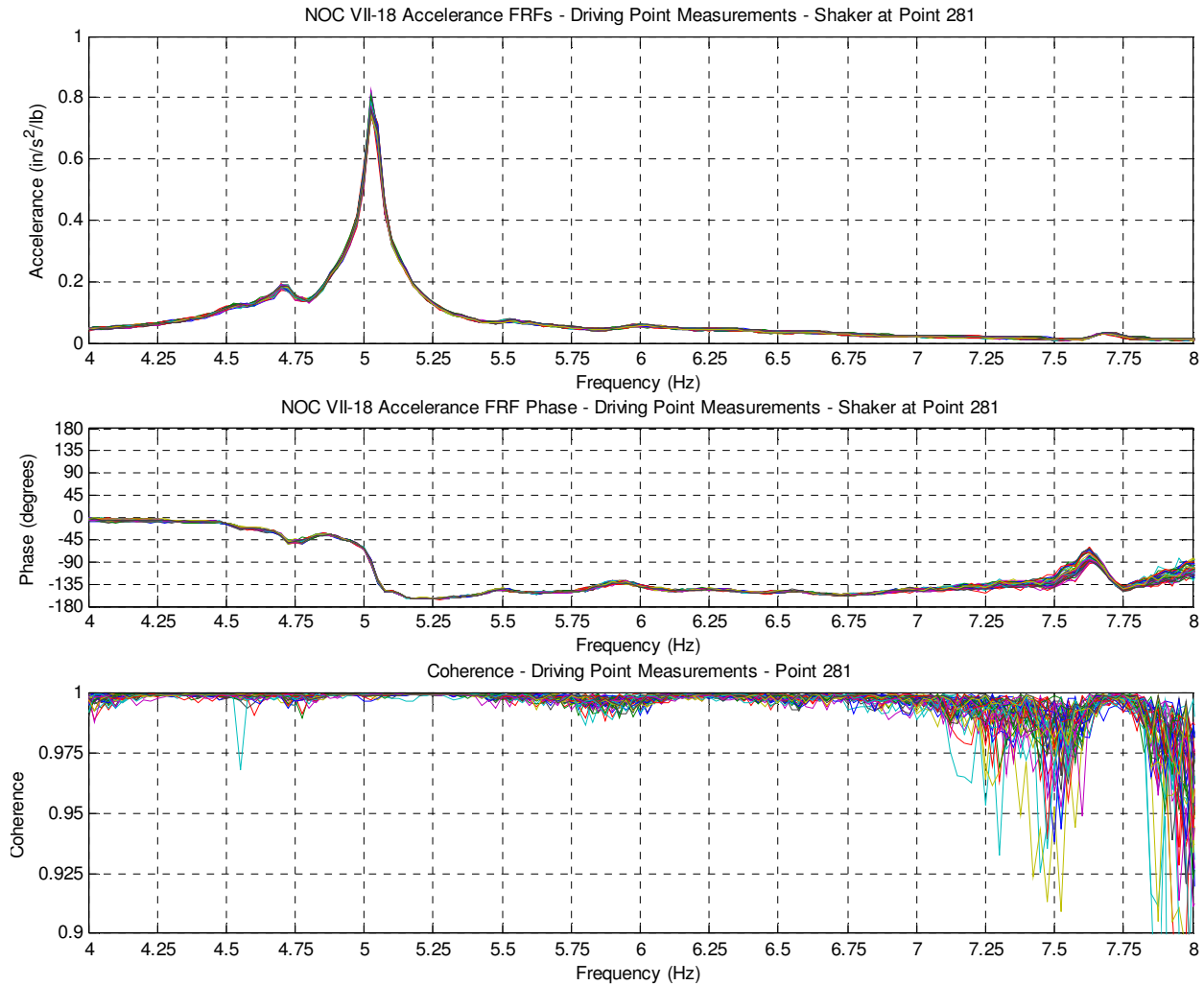


Figure 3.38: NOC VII-18 Driving Point Accelerance FRFs and Coherence (Point 281)

Table 3.7: NOC VII-18 Pt 281 –Driving Point Curve Fit Estimated Frequencies & Damping

Frequency (Hz)	Damping (%)
4.72	1.00
5.02	0.65

The curve fit frequencies were in excellent agreement with the significant and dominant frequencies manually identified from the driving point FRFs. The operating deflection shapes (ODS) for 4.70 Hz and 5.025 Hz were animated from the measured set of accelerance FRFs and are displayed in several different formats in Figures 3.39, 3.40, and 3.41. Figure 3.39 presents the animation of just the full and interior quarter points of the 10-bay strip along the length of the floor (see coverage area of Point 281 in Figure 3.16). Not included in these animated shapes are any measurements within the interior bays or end-bay centerlines. The displayed ODS at 4.70 Hz is not scaled relative to the dominant 5.025 Hz shape to illustrate the response at this

frequency of interest. The scaled shape at 4.70 Hz is difficult to visually distinguish because of its much smaller magnitude. The response shape at 4.70 Hz is interesting due to its significant response at the far end of the floor, but this is not unexpected and likely corresponds to the dominant frequencies of those end bays. The regular shape of the ODS at 5.025 Hz is interesting, as it seems the amplitude of response at this frequency is large, but it is mostly constrained to the immediate two bays on either side of Point 281.

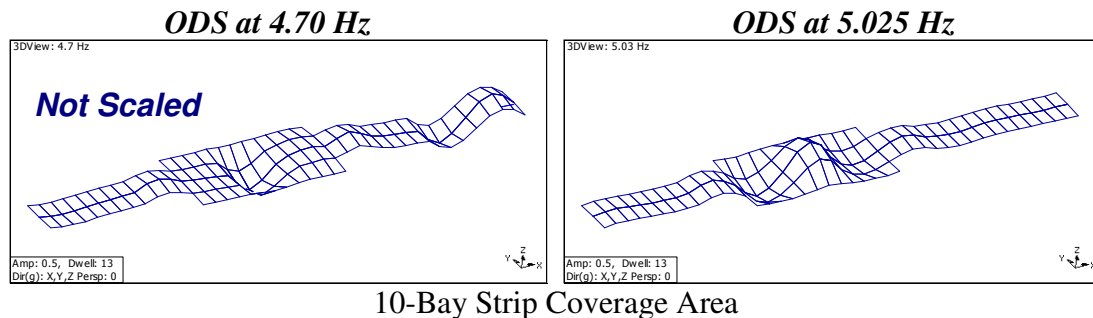


Figure 3.39: NOC VII-18 10-Bay Strip ODSs (Forcing at Point 281)

The ODSs presented in Figure 3.40 include the response at the other locations (interior bays, centerline of end bays) in addition to the previously shown measurements. The unmeasured boundaries of the bays are also displayed as fixed points (assumed zero or very little response) to enable a better visualization of the shape of response. These shapes are scaled to one another and displayed as static and persistent images as done with the previously discussed floor. Figure 3.41 includes a 2-D representation of the 10-bay centerline response to aid in interpretation.

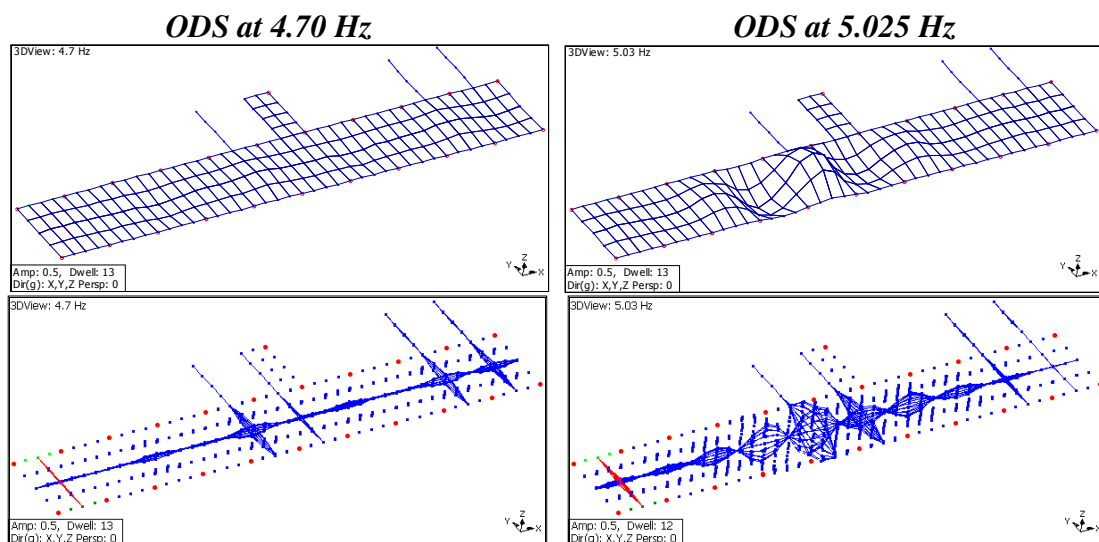


Figure 3.40: NOC VII-18 Exterior Bay ODSs (Forcing at Point 281)

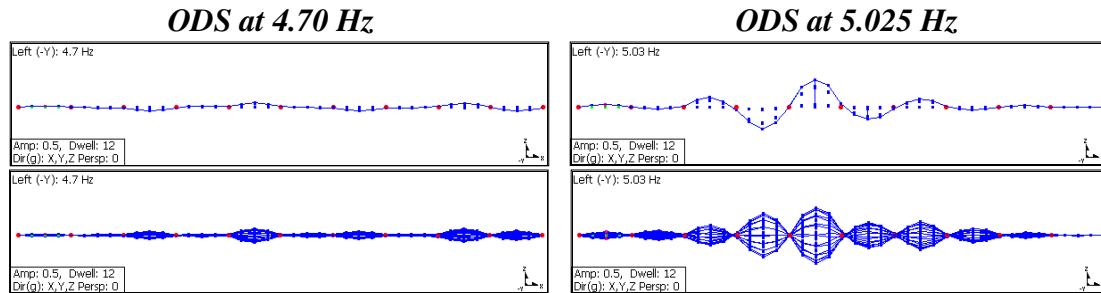


Figure 3.41: NOC VII-18 10-Bay Centerline ODSs (Forcing at Point 281)

There are several things to note about the behavior of the floor from Figure 3.40 and Figure 3.41. At the 5.025 Hz dominant frequency, the displayed shape clearly shows a regular decrease in response as you get further from the point of excitation. Additionally, there is no greater response in the coverage area than the response at the mid-bay driving point. The response at the exterior of the bay (Point 283, center of spandrel girder) was 11% of the acceleration response at the mid-bay driving point, a surprisingly large amount for an exterior boundary, however consistent with similar results from NOC VII-24. The persistent plots of Figure 3.40 show there was negligible response within certain parts of the coverage area, most notably at the interior boundaries along the full-height partition walls of the interior bays, at the interior bays that include the bank of elevators in the bay adjacent to the driving point, and along the centerlines of the end interior bays of the floor. This demonstrates the large amount of constraint these interior boundaries can provide to a floor system. As previously observed on NOC VII-24, the response is much greater perpendicular to the framing and parallel to the direction of the composite deck ribs.

A stepped sine sweep series of sinusoidal measurements was taken with the shaker at Point 281 at three different levels of excitation: 0.707 volts, 1.414 volts, and 2.0 volts. In the presented research, different levels of excitation are expressed as an output voltage, as this was the voltage output setting of the SigLab DSP unit. A higher specified output voltage corresponds to a higher level of excitation. The actual force amplitude applied to the floor by the shaker depended on the forcing frequency and the analog amplitude gain setting on the amplifier. Figure 3.42 shows the magnitude and phase of the sinusoidally derived driving point acceleration, and the markers denote the frequency increments of the sinusoidal measurements.

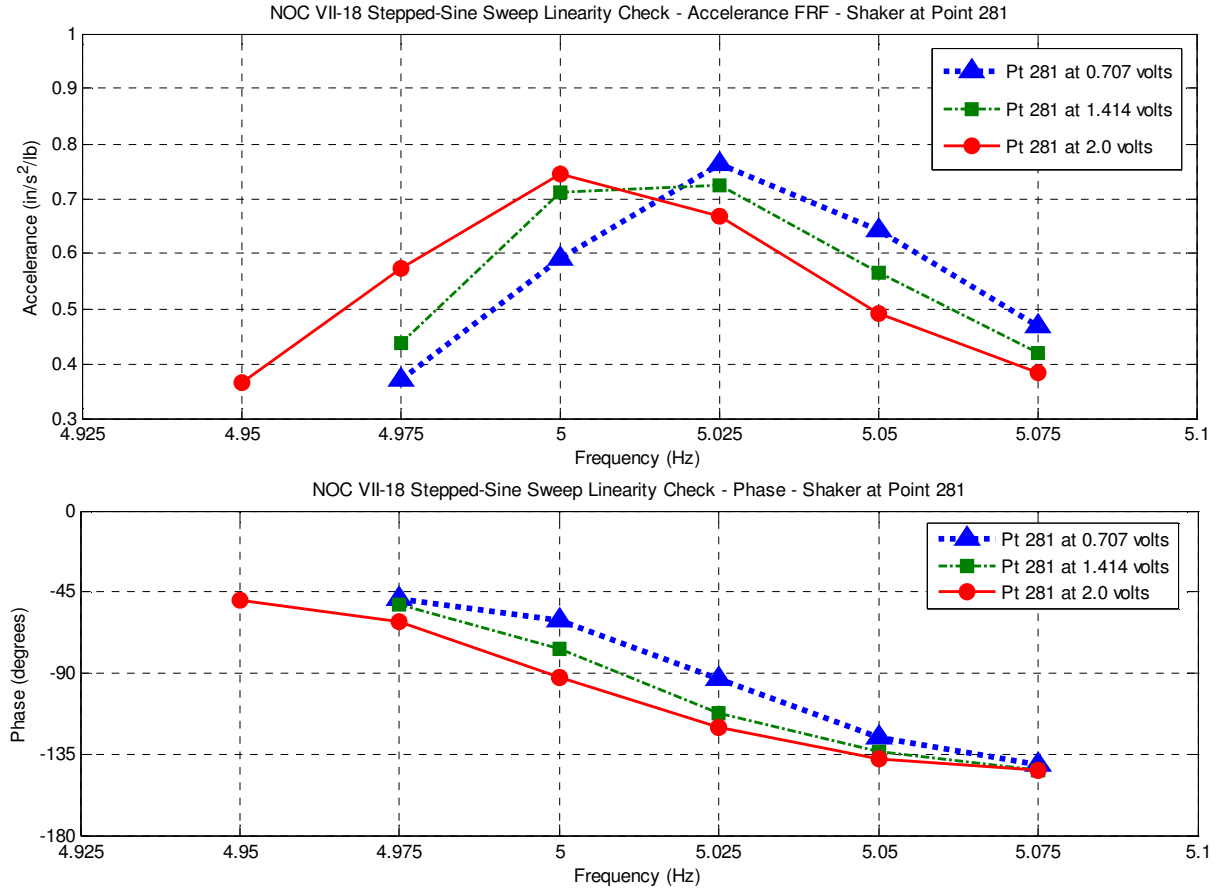


Figure 3.42: NOC VII-18 Stepped Sine Sweep Linearity Investigation (Point 281)

The plots of the three levels of excitation in Figure 3.42 indicate that increased levels of excitation cause the peak frequency of the accelerance FRF to shift slightly to the left (decrease in dominant frequency), although the shift was only one spectral line (0.025 Hz). This slight shifting of frequency is evident in both the magnitude and phase. This phenomenon was also observed on occasion when comparing the location of the peak frequency from chirp derived accelerance FRFs at different levels of excitation, as shown in Figure 3.43 for 2.0 volt, 1.0 volt, and 0.5 volt excitation levels.

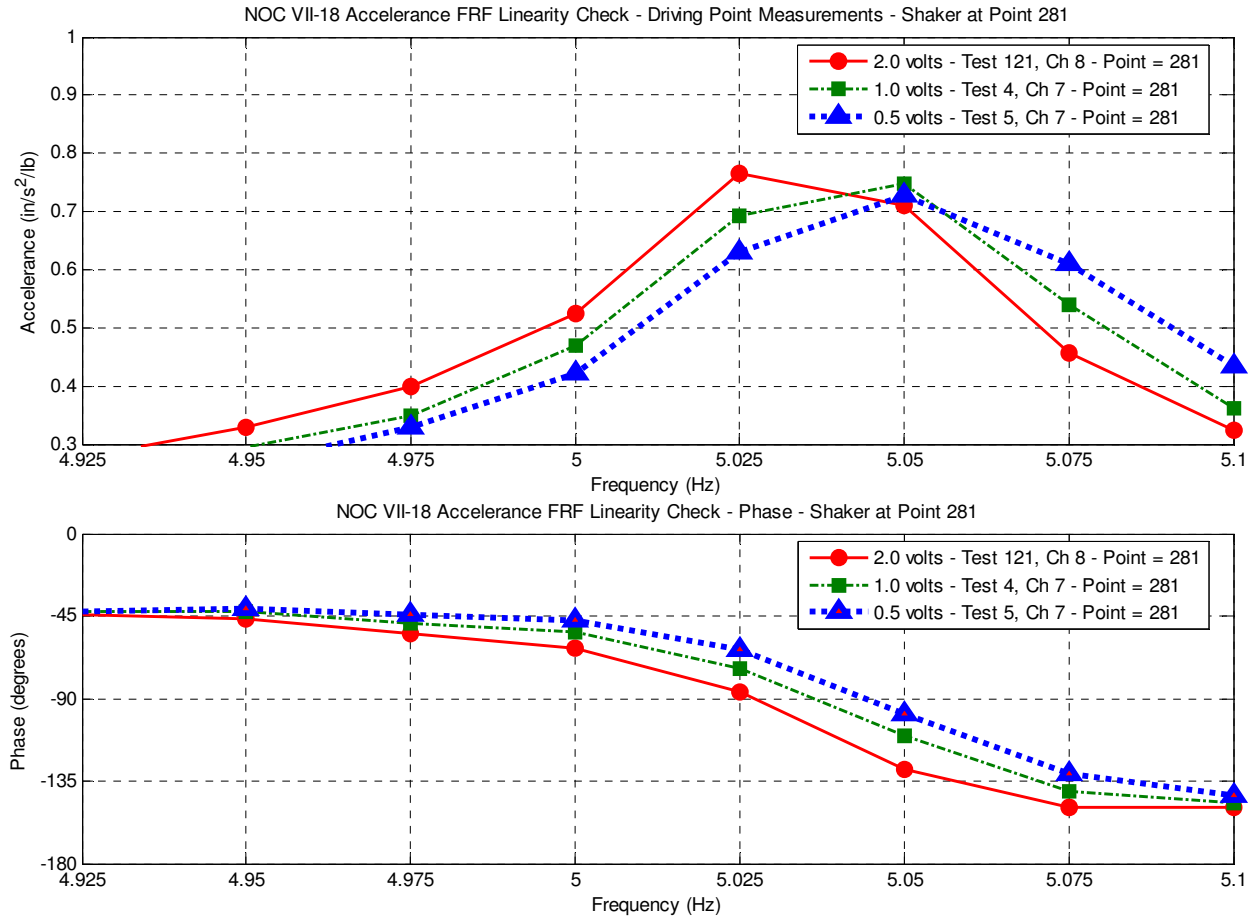


Figure 3.43: NOC VII-18 Chirp Accelerance FRF Linearity Investigation (Point 281)

One thing to note is that the magnitudes of the peaks of both linearity comparisons are relatively consistent between the three levels and it is only the location of the peak that changes. The small decrease in the location of the dominant frequency may indicate the floor system becomes slightly more flexible at higher levels of excitation. It should be noted that this phenomenon was also observed on the previously tested floor, NOC VII-24. A summary of the identified dominant frequencies and half power damping estimates from the stepped sine derived accelerance FRF peaks in Figure 3.42 and the chirp derived accelerance FRFs of Figure 3.43 are presented in Table 3.8.

Table 3.8: NOC VII-18 Parameter Estimates at Various Excitation Levels (Point 281)

General Excitation Level	Stepped Sine Sweep			Chirp Accelerance FRFs		
	Output Level (volts)	Peak Frequency (Hz)	Half-Power Damping (%)	Output Level (volts)	Peak Frequency (Hz)	Half-Power Damping (%)
High	2.0	5.00	0.77	2.0	5.025	0.65
Medium	1.414	5.025	0.77	1.0	5.05	0.69
Low	0.707	5.025	0.71	0.5	5.05	0.77

For presented sinusoidal measurements of Figure 3.42, the 0.707 volt, 1.414 volt, and 2.0 volt levels of excitation corresponded to respective force amplitudes of 15 lbs, 28 lbs, and 41 lbs at the peak frequency. Of the three levels, the 0.707 volt level agreed the most with the location of the peak frequency from a burst chirp derived accelerance FRF. The 15-lb sinusoidal force was a more realistic magnitude of steady-state excitation for floor vibration serviceability. The harmonic force component of walking computed using DG11 (Equation (1.3)) is 11.2 lbs for a floor with a 5.025 Hz resonant frequency, thus the 0.707 volt level of excitation was more appropriate. Additionally, the magnitude of the response for the 0.707 volt level was 2.9%g, but much more appropriate than the 5.0%g and 5.2%g response levels of the other two levels of excitation. The 2.9%g magnitude of response is well above the 0.5%g threshold of annoyance; however this was also a product of driving the floor exactly at its resonant frequency and large amplitudes are expected. Because the identified peak frequencies of the accelerance FRFs verified with the 0.707 volt level of sinusoidal excitation were typically the same as those identified using burst chirp excitation, the 0.707 volt excitation level was used for all steady-state excitation over the various coverage areas for Point 281 and Point 73.

A set of 5.025 Hz sinusoidal measurements was taken for the three-bay coverage area of Figure 3.17 to verify the operating deflection shapes and accelerance values obtained using burst chirp excitation were the same as those derived manually at a single frequency from steady-state excitation. Only a three-bay coverage area was captured because the smaller 0.707 volt level of excitation was used for the sinusoidal measurements and the response at large distances from the point of excitation became small (greater than two bays away). A visual display of the resulting ODSs at the dominant frequency of 5.025 Hz is presented in Figure 3.44, where the shapes are animated directly from the burst chirp derived accelerance FRFs and the sinusoidally measured accelerance values at this frequency. The differences in shape from the two types of excitation are almost visually indistinguishable.

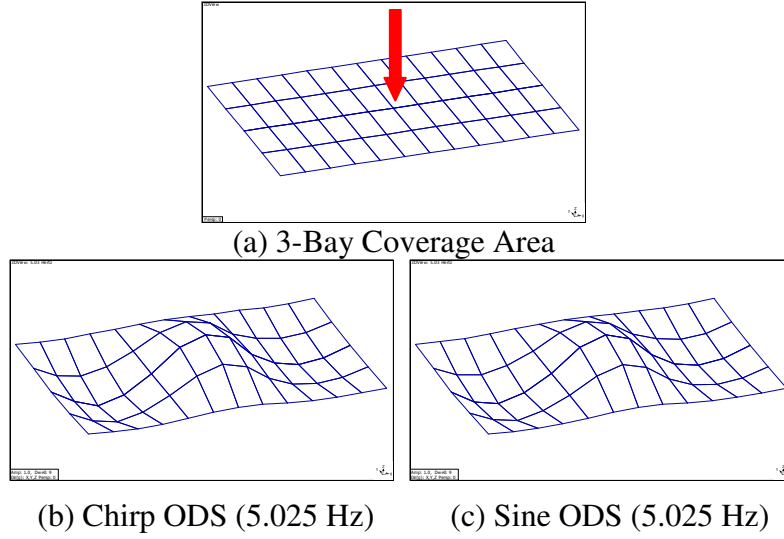


Figure 3.44: NOC VII-18 3-Bay ODS Shape Comparison (Forcing at Point 281)

Mathematically, any shapes in the form of a vector can be compared using the Modal Assurance Criterion (MAC), which provides a measure of the correlation between two shapes (Ewins 2000) and is computed using Equation (3.1).

$$MAC(i, j) = \frac{|\phi_j^T \phi_i|^2}{(\phi_j^T \phi_j)(\phi_i^T \phi_i)} \quad (3.1)$$

The MAC computation gives a real-valued scalar quantity from 0 to 1.0, with 1.0 representing perfect correlation between the two vectors and 0 indicating that the vectors are orthogonal. Nothing in Equation (3.1) prevents the shape vectors from containing complex values. A common application of the MAC function is a comparison of experimentally derived mode shapes and analytically computed shapes from FE analysis. For the chirp and sinusoidally derived shapes presented in Figure 3.44, the MAC computation gives a value of 0.989, confirming how closely correlated the two shapes are and providing a high level of confidence in the ability of the chirp derived accelerance FRFs to correctly represent the operating deflection shapes for all of the coverage areas presented in this research. A similar investigation was conducted when forcing at Point 73, with similar results, and is presented in the next section.

NOC VII-18 Point 73 – The excitation location with the second most number of measurements was Point 73 (mid-bay L/M-5/6), which corresponds with the area most covered in the previously tested floor, NOC VII-24. The magnitude and phase of 27 driving point accelerance FRF measurements taken at this location are presented in Figure 3.45. The measurements taken

at Point 73 were not as clean and consistent as those taken at Point 281, as there seemed to be a fair amount of noise in the measurements taken at this end of the floor. It is interesting to note the 5.05 Hz dominant frequency is the same as for the corresponding Point 73 of the NOC VII-24 floor (Figure 3.25), however the driving point accelerance FRFs for NOC VII-18 do not have the clearly distinguished peaks at 4.80 Hz and 4.90 Hz. Like the response at Point 281, the average accelerance value at the 5.05 Hz dominant frequency was one of the larger values measured on the NOC VII-18 floor and had a value of $0.74 \text{ in/s}^2/\text{lb}$ of input force.

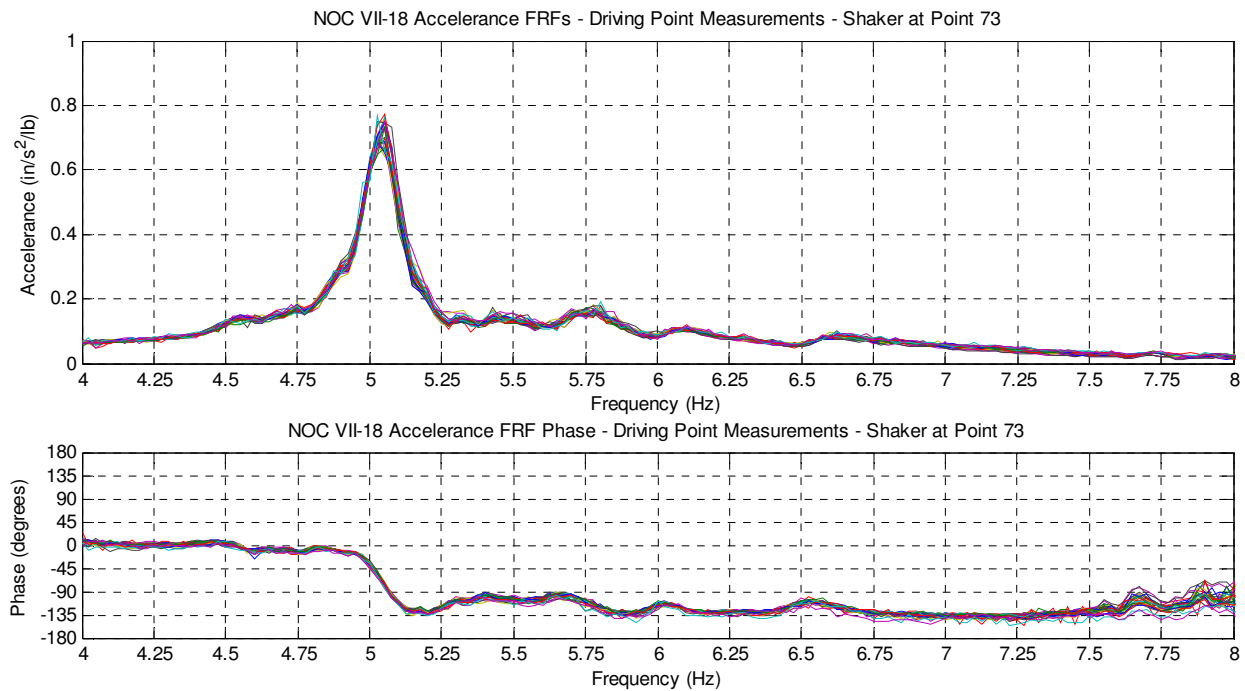


Figure 3.45: NOC VII-18 Driving Point Accelerance FRFs (Point 73)

The half power bandwidth method damping estimate for the 5.05 Hz peak of the driving point measurements was 1.13% of critical, which was slightly lower but in general agreement with corresponding estimates of damping for NOC VII-24 at this excitation location. The coverage area for excitation at Point 73 on NOC VII-18 is shown in Figure 3.19, and the estimated frequencies and damping from MDOF curve fitting of both the driving point accelerance FRFs and the area coverage accelerance FRFs are presented in Table 3.9. Although the 5.05 Hz frequency was clearly dominant, several frequencies were identified in the curve fitting process despite their weak representation. Although not represented strongly, they were included for a more accurate curve fit of the traces. The 1.15% and 1.16% estimated damping

ratios for the 5.05 Hz dominant frequency were in excellent agreement with the half power method damping estimate, which is not unexpected for such a clearly dominant mode.

Table 3.9: NOC VII-18 Pt 73 – Curve Fit Estimated Frequencies & Damping

Driving Point FRFs		All FRFs	
Frequency (Hz)	Damping (%)	Frequency (Hz)	Damping (%)
4.55	0.85	4.58	0.86
4.75	0.85	n/a	n/a
4.83	0.88	4.8	0.65
5.04	1.15	5.05	1.16
5.51	1.00	5.48	1.00
5.76	1.40	5.76	1.40
6.06	1.10	6.08	1.10
6.59	1.00	6.56	1.45

The ODS of the dominant 5.05 Hz frequency is presented in several formats: a 3-D representation of the end bay coverage area (Figure 3.46) and 2-D profiles of the superimposed centerline response of the end bays (Figure 3.47). Note that the shape is very consistent with the corresponding 5.10 Hz ODS of the previously tested NOC VII-24 (Figure 3.35), with the bulk of the response in adjacent bays that are perpendicular to the floor framing (parallel with deck ribs) and not much response in the adjacent bays parallel to the floor framing.

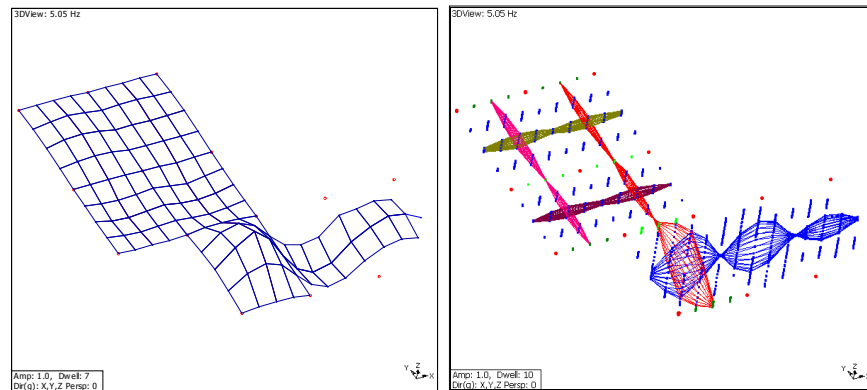


Figure 3.46: NOC VII-18 End-Bay Area ODS at 5.05 Hz (Forcing at Point 73)

The 2-D profiles of the centerline response in Figure 3.47 are a good illustration of the relative response between bays and at the boundaries of the excited bay L/M-5/6. Note that there is no greater response in any other bay than the mid-bay driving point response, which was not observed for NOC VII-24 where a slightly greater response was measured at Point 125 in the adjacent bay. The almost regular decrease in response in each successive adjacent bay in the direction of the deck ribs (Figure 3.47(a)) was also observed in the ODS at 5.025 Hz for excitation at Point 281 (Figure 3.41). As observed on NOC VII-24, the exterior boundary response was greater than anticipated. Measurements show the response at Point 75 (midspan of

spandrel girder) was approximately 9% of the response at the mid-bay driving point. For Point 47 (midspan of spandrel beam), the response was approximately 16% of the mid-bay response. Although significant for boundaries that are typically assumed rigid, they are less than those previously measured for NOC VII-24, which were 16% and 30% respectively for the spandrel girder and beam. This discrepancy is likely due to the care taken when testing NOC VII-18 to place the accelerometers as closely as possible to the centerlines of the spandrel members, and the response values for NOC VII-18 are more reliable.

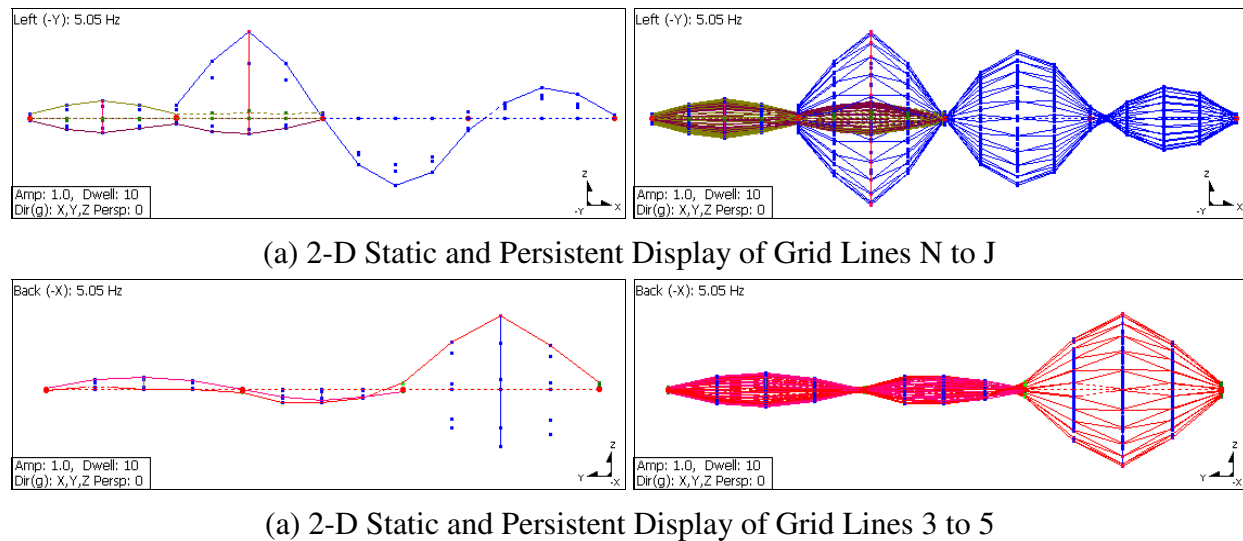


Figure 3.47: NOC VII-18 End-Bay Centerline ODS at 5.05 Hz (Forcing at Point 73)

As previously stated, the frequencies identified in the curve fitting process were not nearly as strongly represented as the 5.05 Hz dominant frequency. The scaled persistent ODSs of all the curve fit frequencies are presented in Figure 3.48 to illustrate their relative strengths and for comparison with the ODSs of the corresponding area of NOC VII-24. Only persistent plots are presented, as the small responses in some shapes were indistinguishable as a surface plot. Despite the small response, it is interesting to note the ODSs at 4.80 Hz, 5.05 Hz, 5.75 Hz, and 6.55 Hz are very similar to the ODSs of NOC VII-24 at similar frequencies (4.80 Hz, 5.10 Hz, 5.80 Hz, and 6.60 Hz) (Figure 3.35). The implication of the similarities in frequencies and shape between the two floors of identical framing (with only slightly different interior partition layout) is beneficial to floor vibration research, as it validates the assumption that similarly framed floors will behave in a relatively consistent manner. This consistency is important for developing tools to accurately predict floor behavior, such as FE modeling.

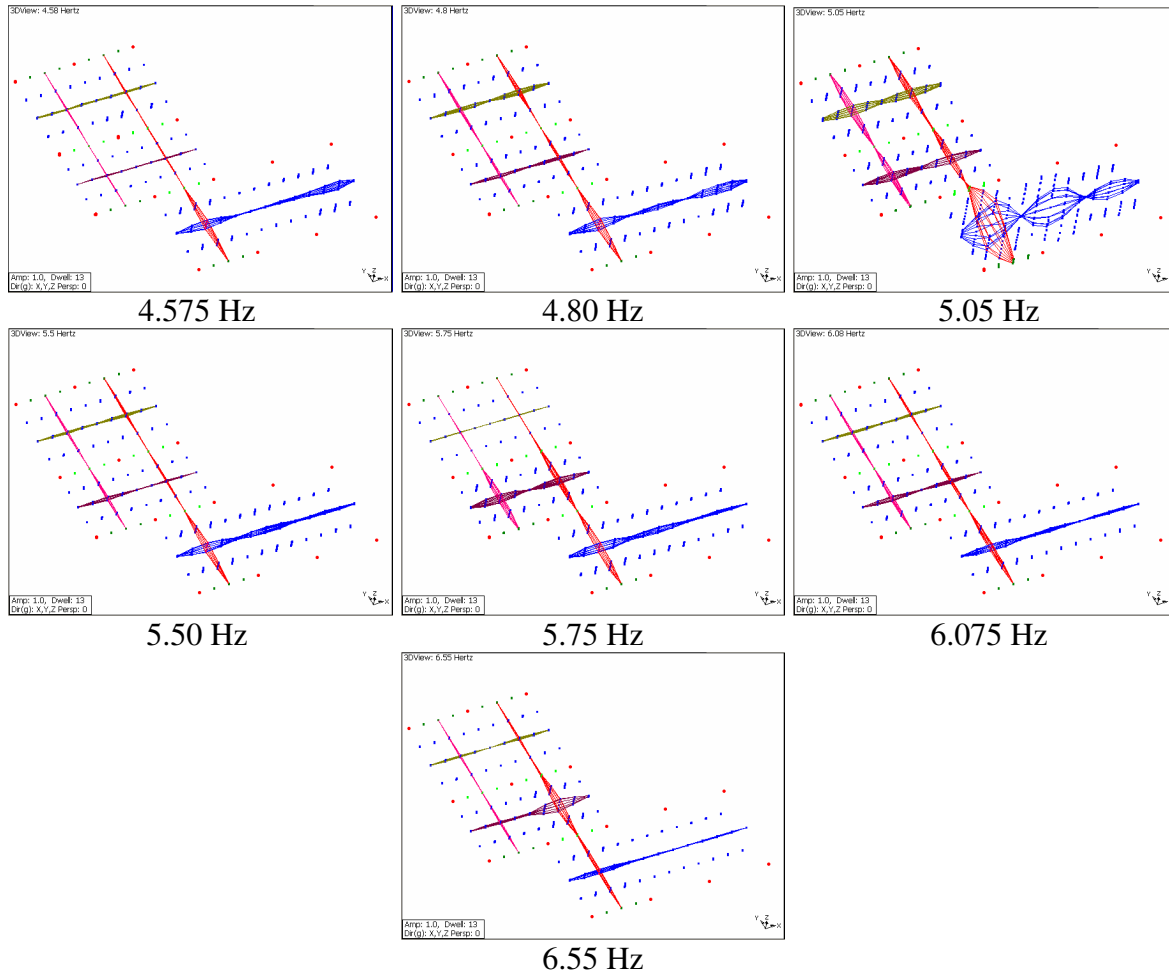


Figure 3.48: NOC VII-18 End-Bay ODSs (Forcing at Point 73)

Similar to the sinusoidal steady state investigation with the shaker at Point 281, a series of sinusoidal measurements was taken with the shaker at Point 73. A stepped sine sweep was made across the 5.05 Hz dominant frequency to verify the location of the peak and to perform a half power method estimate of damping. The half power method estimate of damping was 1.15% of critical, which agreed very well with the half power estimate of the chirp derived accelerance FRF (1.13%) and the values estimated by MDOF curve fitting (1.15% and 1.16%).

The stepped sine sweep was conducted at a higher level of excitation, 2.30 volts, which corresponded to a sinusoidal forcing amplitude of approximately 29 lbs and resulted in a steady-state driving point acceleration response of 5.5%g at its dominant frequency. The sweep indicated a peak at 5.025 Hz rather than the 5.05 Hz peak identified from the chirp FRF. Again, this is likely a product of the higher level of excitation which tends to shift the location of the peak slightly. Unfortunately, the 5.025 Hz identified frequency was used for all subsequent

sinusoidal measurements over the coverage area of Figure 3.19, although all of those measurements were taken at the much lower 0.707 volt level of excitation (force amplitude of approximately 10 lbs). The same MAC comparison was made between the operating deflection shapes from sinusoidally derived acceleration values at 5.025 Hz and the corresponding ODS from the chirp derived acceleration FRFs. Note that the ODS from 5.025 Hz was used from the acceleration FRFs rather than the identified 5.05 Hz peak. A visual display of this comparison is presented in Figure 3.49. Again, the measured shapes are virtually identical, which was confirmed by the 0.989 computed MAC value for the two, despite the much larger coverage area than the investigation for excitation at Point 281. The excellent correlation between sinusoidally derived ODS and chirp derived ODS for these two coverage areas provides a significant level of confidence in the quality of the measurements and the reliability of future shapes animated from a set of experimentally measured acceleration FRFs using the techniques employed in this research. No sinusoidal measurements were taken over a coverage area for the third tested floor because of the confidence in the shapes derived from the acceleration FRFs as a result of these investigations.

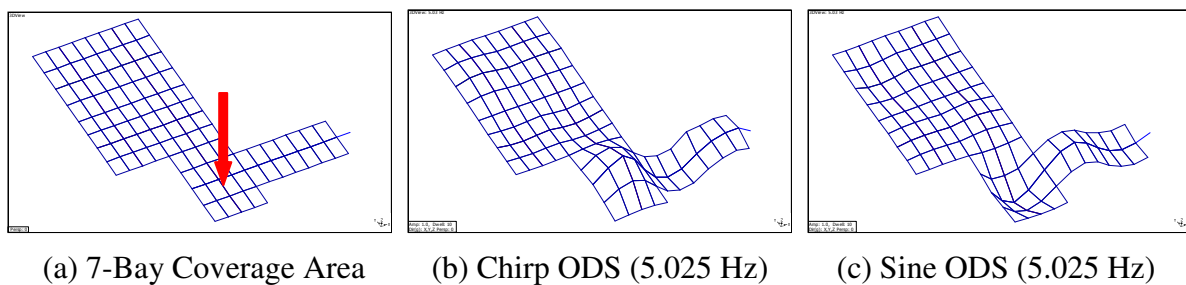


Figure 3.49: NOC VII-18 7-Bay ODS Shape Comparison (Forcing at Point 73)

NOC VII-18 Point 69 – The next location of excitation presented is with the shaker at Point 69 (mid-bay L/M-4/5), which also corresponds to one of the three excitation locations of NOC VII-24. Point 69 is the middle of an interior bay that comprises the three-bay strip that spans the short direction of the building (parallel to floor framing) and is bounded by grid lines L and M. Also included in this three-bay strip are Points 73 and 65. The magnitude and phase of 16 driving point acceleration FRF measurements taken at this location are presented in Figure 3.50. While there are several participating frequencies in these measurements, the dominant frequency is 6.55 Hz with an average acceleration magnitude of 0.56 in/s²/lb of input force. The dominant frequency of this bay is higher than at other locations on the floor because it is an interior bay with shorter spans, however the participating dominant frequencies of adjacent bays is evident in

the accelerance FRFs. Figure 3.51 plots the one driving point accelerance FRF measurement from the previously tested NOC VII-24 floor for comparison with the accelerance FRF of NOC VII-18. Again, it is interesting to note the similarity in both frequency content and magnitude of the accelerance of two different floors constructed with the same framing layout. For comparison, the dominant peak for NOC VII-24 was 6.60 Hz with a magnitude of 0.50 in/s²/lb of input force.

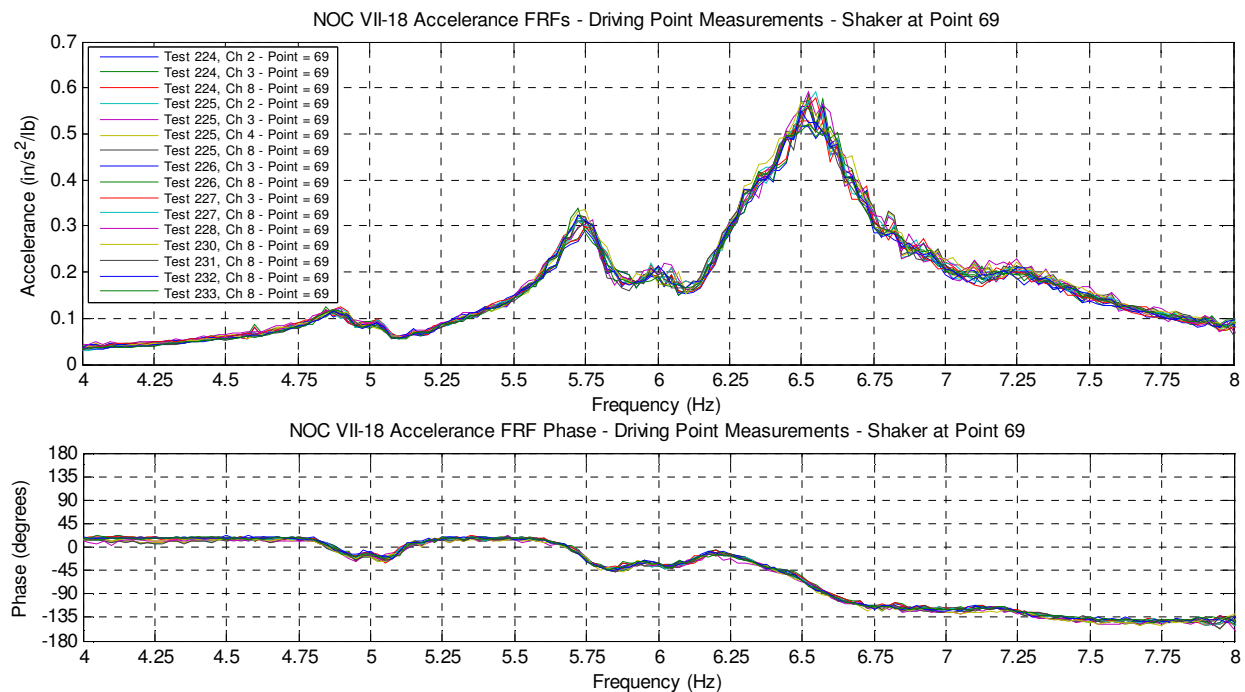


Figure 3.50: NOC VII-18 Driving Point Accelerance FRFs (Point 69)

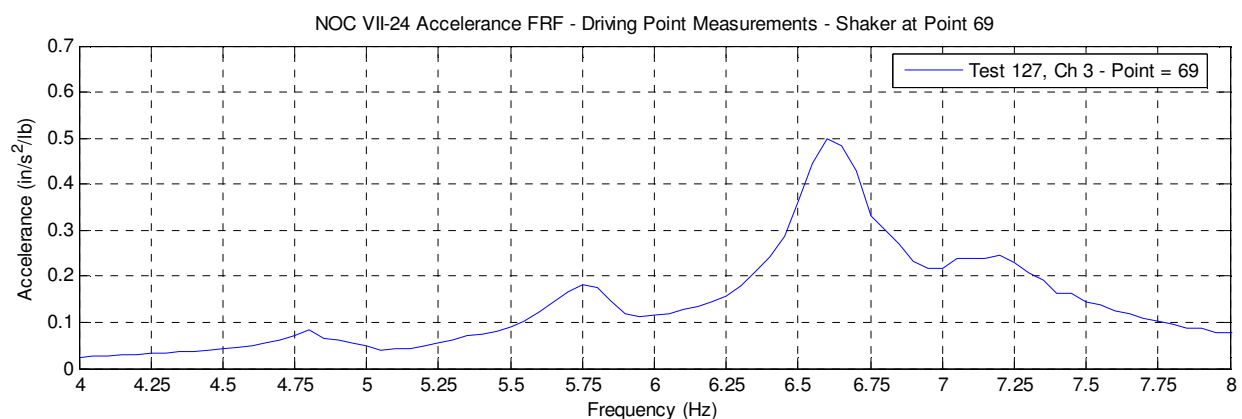


Figure 3.51: NOC VII-24 Driving Point Accelerance FRFs (Point 69)

The half power bandwidth estimate of the damping for the 6.55 Hz dominant frequency was 2.45% of critical, a level of damping considerably higher than at other locations on the floor

and slightly higher than the corresponding estimates for NOC VII-24 (1.83% half power damping estimate). The estimated frequencies and damping from MDOF curve fitting are presented in Figure 3.11, and the dominant frequency and damping ratio are in good agreement with the manual estimates. The other estimated frequencies and damping are also consistent with driving point curve fit values for Point 73, with the exception of Point 73's dominant frequency, 5.05 Hz. This discrepancy is likely due to the weak representation of that frequency in the curve fit accelerance FRFs for excitation at this location.

Table 3.10: NOC VII-18 Pt 69 – Driving Point Curve Fit Estimated Frequencies & Damping

Frequency (Hz)	Damping (%)
4.82	0.85
4.93	0.98
5.05	0.90
5.72	1.44
6.00	0.60
6.55	2.40
7.25	1.39

Although accelerance FRFs were measured for the coverage area shown in Figure 3.20(a), they are presented later for comparison of the ODSs with those derived from different points of excitation across the same coverage area. No sinusoidal measurements were taken for excitation at Point 69.

NOC VII-18 Point 65 – The next results presented are for excitation at Point 65 (mid-bay L/M-3/4). This location is at the middle of an exterior bay of the three bay strip bounded by grid lines L and M. Also included in this strip are Points 69 and 73. The magnitude and phase of 14 driving point accelerance FRFs are presented in Figure 3.52. The 4.85 Hz frequency is the lowest dominant frequency of any of the eleven tested bays on the floor. The average accelerance magnitude at the 4.85 Hz dominant frequency was 1.0 in/s²/lb of input force, the largest response magnitude of any of the tested bays on NOC VII-18. The implication of the low frequency coupled with high response is that bay L/M-3/4 is likely the most vulnerable bay for vibration serviceability issues. Other than the large dominant frequency at 4.85 Hz, several other frequencies (modes) are participating at a much smaller level as shown in Figure 3.52.

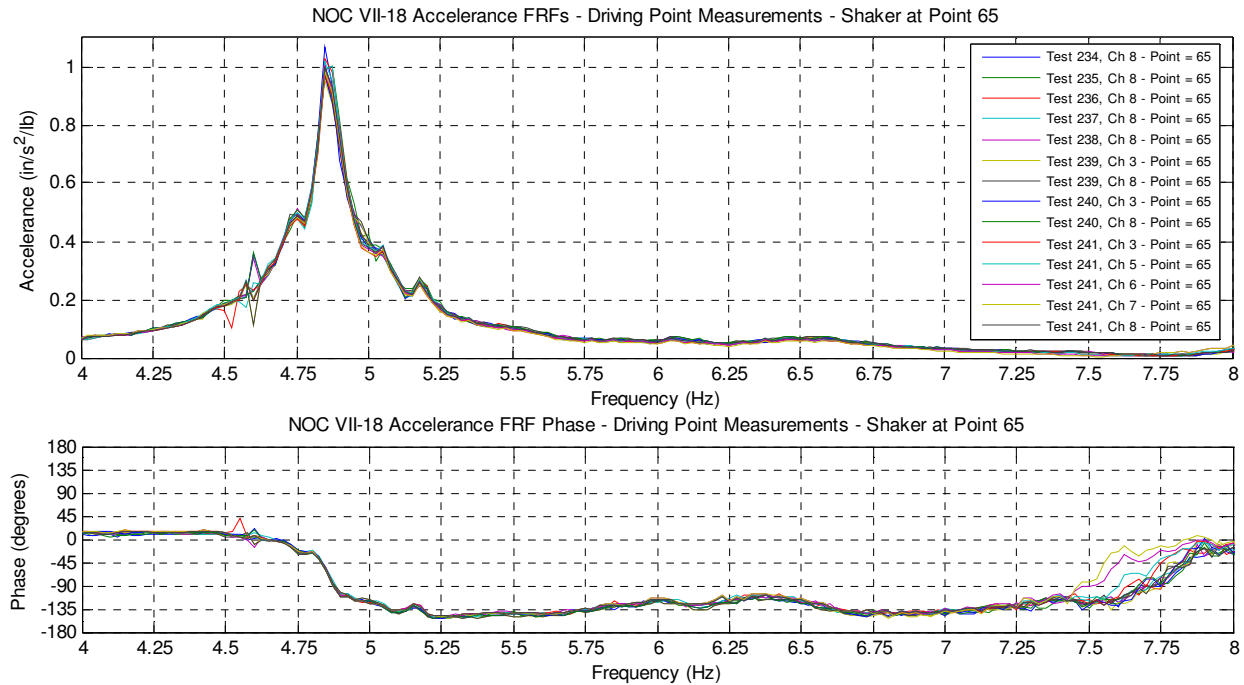


Figure 3.52: NOC VII-18 Driving Point Accelerance FRFs (Point 65)

The half power bandwidth estimate of damping at the 4.85 Hz dominant frequency was 0.88% of critical. This value is in good agreement with the MDOF curve fit frequency and damping values shown in Table 3.11, which estimates the damping ratio at 0.85% at the dominant frequency. A stepped sine sweep series of sinusoidal measurements was conducted to verify the location of the peak and to provide manual accelerance values. The stepped sine sweep identified dominant frequency was 4.875 Hz, slightly higher than the manually and curve fit estimated dominant frequency. The half power estimate of damping for these sinusoidal measurements was 0.95%, slightly higher than the estimates from other methods.

Table 3.11: NOC VII-18 Pt 65 – Driving Point Curve Fit Estimated Frequencies & Damping

Frequency (Hz)	Damping (%)
4.75	0.85
4.85	0.85
5.06	0.74
5.17	0.77

The coverage area of measured accelerance FRFs for excitation at Point 65 is shown in Figure 3.20(b). This coverage area encompassed the interior three quarter points along the three-bay strip spanning the short direction of the building. For comparison, the same area was covered while forcing at Point 69 and Point 73 (although the coverage area of Point 73 was much larger, the smaller area will be used for comparison). The purpose of this investigation was to

determine the effect on extracted shapes over a given coverage area for different locations of excitation. The 39 accelerance FRF traces that comprise the three-bay quarter point strip area are superimposed on one another in Figure 3.53 for each of the three excitation locations (Points 65, 69, and 73). Five peak frequencies of interest are highlighted in Figure 3.53 for display of the operating deflection shapes from each of the three excitation locations. These frequencies are: 4.75 Hz and 4.85 Hz from excitation at Point 65; 5.05 Hz from excitation at Point 73, and finally 5.75 Hz and 6.525 Hz from excitation at Point 69. Note that each of the identified frequencies corresponds to either a dominant or significantly participating frequency for the displayed accelerance FRFs, and not necessarily all frequencies identified from curve fitting the driving point accelerance FRFs.

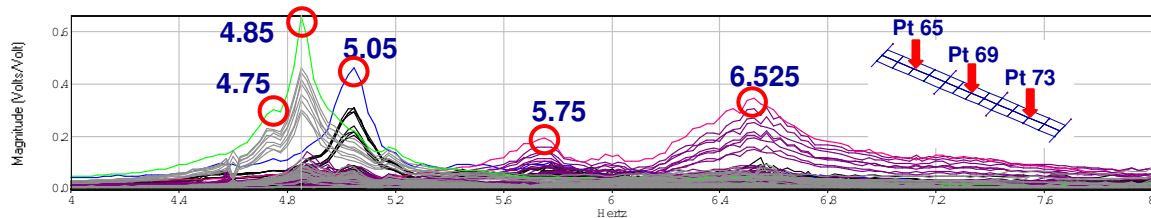


Figure 3.53: NOC VII-18 3-Bay Strip Accelerance FRFs (Multiple References)

The ODSs for each of the three points of excitation and five identified frequencies of interest are presented in 2-D profile static and persistent formats in Figure 3.54. All of the ODSs are plotted to a common scale, so the relative magnitudes of response can be displayed for comparison between frequencies and locations of excitation. Several items of interest are observed from the ODSs of Figure 3.54. First, the greatest amount of response at any of the displayed frequencies is almost exclusively at the location of the driving point, which was not entirely expected. As a result, the displayed ODSs for the same frequency at different excitation locations appear quite different in many cases. The theory behind modal analysis states the same mode shapes for a structure should be extracted no matter where the location of excitation, provided it is not on a node or nodal line. This is where the differences between mode shapes and operating deflection shapes become quite distinct. The displayed shapes are ODSs, which are dependent on frequency and location of excitation, and are not mode shapes. Thus, the presented shapes are different for the different locations of excitation. Another note of interest is the amount of response at the spandrel girder when exciting Point 65 at its 4.85 Hz dominant frequency. Consistent with previous investigations of the exterior boundaries, Point 63 (midspan of spandrel girder) had a response of approximately 11% of the mid-bay response at Point 65.

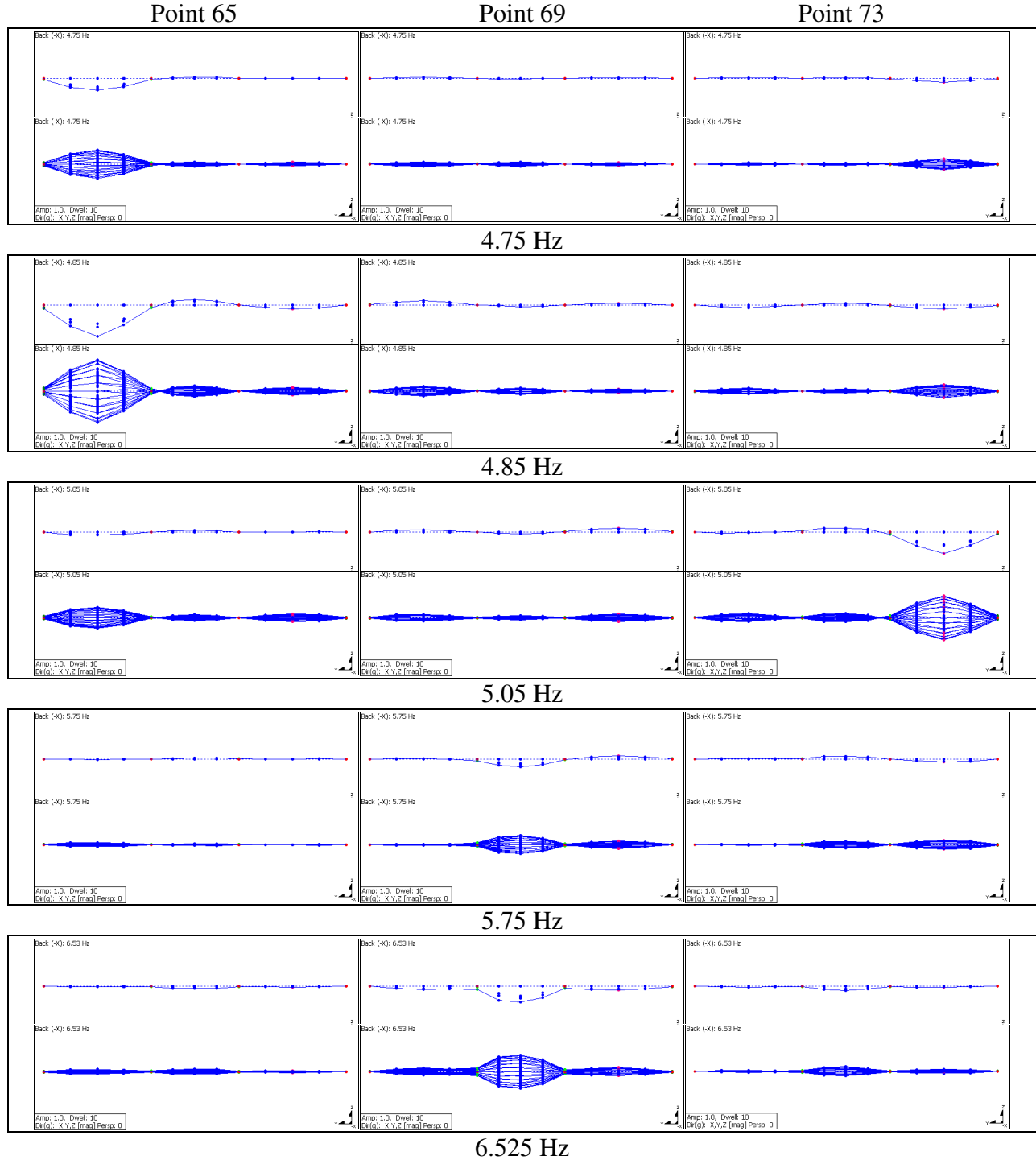


Figure 3.54: NOC VII-18 3-Bay Centerline ODSs (Multiple References)

While only one set of accelerance FRFs (i.e. one column of the accelerance FRF matrix) is required to perform MDOF curve fitting operations over the coverage area to recover the mode shapes, multiple sets of measurements can also be used to recover the mode shapes with potentially more accuracy because different locations of excitation do a better job exciting

certain modes. This is called multi-reference parameter estimation, which is similar to the previously described curve fitting process with a few more steps that provide a better estimate of the parameters. Rather than one set of accelerance FRFs imported into ME'scope, multiple sets are imported. The first step in the curve fitting process, identifying the peak frequencies, was accomplished with the Complex Mode Indicator Function (CMIF) in ME'scope. This function performs a singular value decomposition on each set of accelerance FRFs to generate a single frequency domain curve for each set (Vibrant Technology 2003). The peaks within these CMIF curves indicate resonant frequencies. Because multiple CMIF curves are produced for multiple sets of data, it is possible for a peak to exist on one CMIF curve where a mode is strongly represented and not on another CMIF curve where it is weakly represented. After identifying the frequencies and damping values in this manner, the multiple sets of FRFs are curve fit. When extracting the mode shapes for each of the curve fit frequencies, ME'scope presents a table indicating the relative mode shape strengths of curve fit modes from each of the references. Mode shape strength values range from 0 to 10, where 0 indicates no shape is present from a reference DOF, and 10 indicates a very strongly represented mode shape (very small values represent very weak shapes) (Vibrant Technologies 2003). For the multi-reference curve fitting of the three sets of accelerance FRFs in Figure 3.53, the relative shape strengths for each of the three reference DOFs are presented in Table 3.12 and the most strongly represented reference DOFs used for curve fitting are highlighted. The multi-reference curve fit estimated frequencies and damping ratios are presented in Table 3.13. These values are in good agreement with previously estimated parameters, although slightly lower.

Table 3.12: NOC VII-18 Multi-Reference Curve Fitting Shape Strengths

Mode	Frequency (Hz)	Point 65	Point 69	Point 73
1	4.76	2.4	0.5	0.3
2	4.85	5.6	1.1	0.6
3	5.05	1.1	1.1	6.2
4	5.77	0.4	2.6	1.5
5	6.54	3.2	10.0	3.0

Table 3.13: NOC VII-18 Multi-Reference Curve Fit Estimated Frequencies and Damping

Frequency (Hz)	Damping (%)
4.76	0.85
4.85	0.69
5.05	1.05
5.77	1.24
6.54	2.10

NOC VII-18 Point 25 – The following results are for the shaker located at Point 25 (mid-bay M/N-4/5), which corresponds to the last of the three excitation locations previously tested on NOC VII-24. The magnitude and phase of three driving point accelerance FRF measurements taken at this location are presented in Figure 3.55. This is a unique bay to the floor system, as it has the shorter span of an interior bay but also exterior boundaries on two sides due to the “executive corners” of the building. There are several participating frequencies in these measurements, and the two largest peaks at 5.75 Hz and 6.05 Hz have nearly equal magnitudes. These two peaks have an average accelerance magnitude around 0.51 in/s²/lb of input force. Figure 3.56 plots the one Point 25 driving point accelerance FRF measurement from NOC VII-24 for comparison with the accelerance FRF of NOC VII-18. As previously observed with the comparison of measurements at Point 69, the accelerance FRFs between the two floors are similar in both frequency content and magnitude of the accelerance, although there is slightly more participation of the 5.75 Hz frequency than previously measured on NOC VII-24. Additionally, the lowest frequency at 4.90 Hz is slightly higher than the corresponding 4.75 Hz frequency of NOC VII-24. For comparison, the dominant peak for NOC VII-24 was 6.00 Hz with a magnitude of 0.50 in/s²/lb of input force.

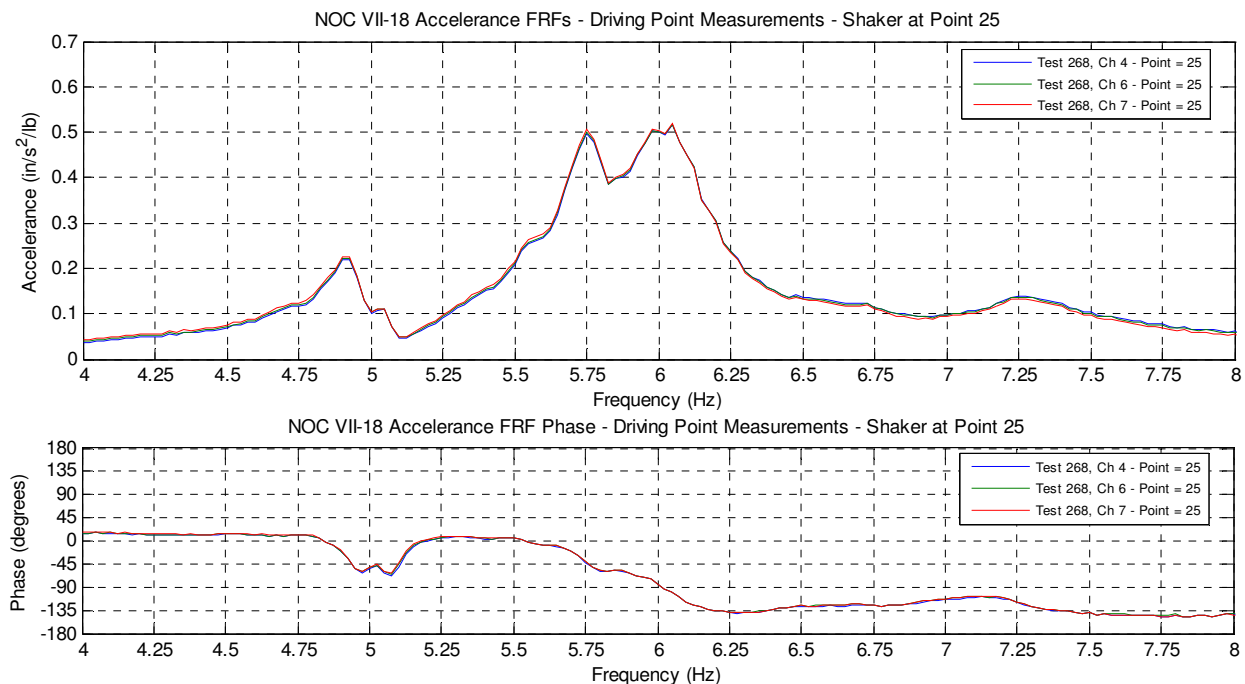


Figure 3.55: NOC VII-18 Driving Point Accelerance FRFs (Point 25)

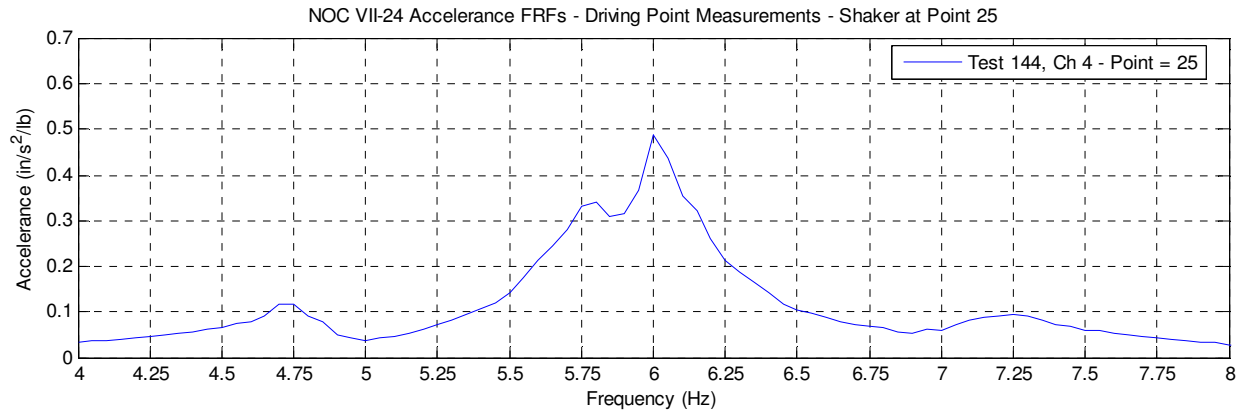


Figure 3.56: NOC VII-24 Driving Point Accelerance FRFs (Point 25)

The participation of several closely spaced modes is evident in the shape of the accelerance FRFs. There is not one clearly distinguishable peak, and attempts at a half power estimate of damping on the 6.05 Hz peak gave a high value of 2.64%. This value is unrealistic because of the obvious presence of another significantly participating mode at 5.95 Hz. MDOF curve fitting is advantageous in this situation, as it can estimate these closely spaced frequencies and damping ratios and validate the quality of the estimate with a visual curve fit. The MDOF curve fit estimated frequencies and damping for the driving point accelerance FRFs are presented in Table 3.14. The curve fit estimate of damping for the 6.05 Hz peak was 1.41% of critical, much lower than from the half power method, as anticipated. Half power damping estimates of the 4.925 Hz peak and 5.75 Hz peak gave damping ratios of 1.39% of critical for each, which are in reasonable agreement with the corresponding curve fit estimated values. As previously noted for the other interior bay containing Point 69, the damping ratio for the 5.05 Hz frequency was much lower than estimated from forcing at Point 73. Again, this discrepancy is likely due to the weak representation of that mode in these measurements.

Table 3.14: NOC VII-18 Pt 25 – Driving Point Curve Fit Estimated Frequencies & Damping

Frequency (Hz)	Damping (%)
4.81	0.85
4.94	0.99
5.05	0.73
5.74	1.28
5.96	0.90
6.05	1.41

NOC VII-18 Point 21 – The next location investigated was Point 21 (mid-bay M/N-3/4), which is an exterior corner bay. The magnitude and phase of three driving point accelerance FRFs taken at this location are presented in Figure 3.57. Several closely spaced frequencies are

participating significantly in the response of this bay. The dominant frequency is 4.875 Hz with an average accelerance magnitude of 0.63 in/s²/lb of input force, the third largest dominant response of any of the tested bays on NOC VII-18. The half power method estimate of damping at the 4.875 Hz dominant frequency was 1.36% of critical; however it is likely the presence of the closely spaced modes widens the peak of the FRF, thus providing an overestimate of the level of damping. A MDOF curve fit of the driving point accelerance FRFs is presented in Table 3.15, where more reliable estimates of damping are listed. The tabulated values are in agreement with curve fit estimates of adjacent bays at these frequencies.

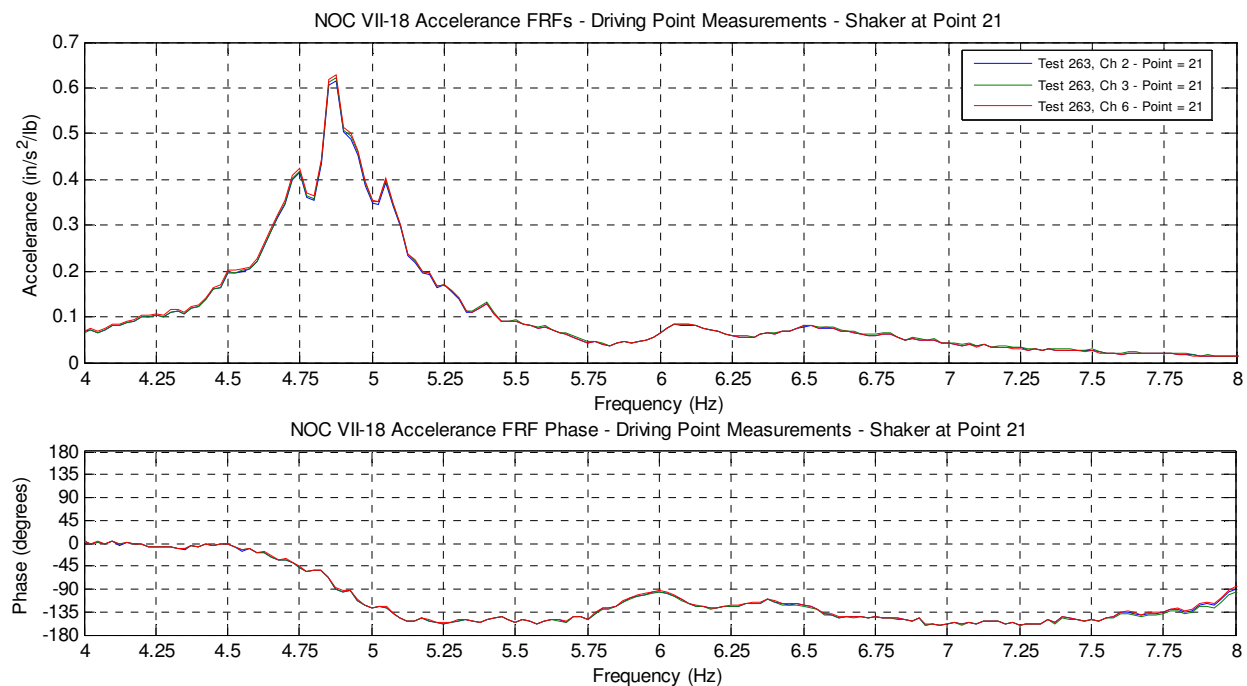


Figure 3.57: NOC VII-18 Driving Point Accelerance FRFs (Point 21)

Table 3.15: NOC VII-18 Pt 21 – Driving Point Curve Fit Estimated Frequencies & Damping

Frequency (Hz)	Damping (%)
4.74	0.85
4.87	0.85
4.95	1.00
5.06	1.10
6.05	1.19
6.58	2.21

NOC VII-18 Point 117 – The next location presented is Point 117 (mid-bay K/L-3/4), which is adjacent to the bay containing Point 65 and two bays away from Point 21 in the direction parallel to the ribs of the decking. This is noted because previous measurements showed much more participation in the response occurred in this direction rather than in the direction of the floor

framing. The magnitude and phase of the driving point accelerance FRF measurements taken at this location are shown in Figure 3.58. The dominant frequency is 4.975 Hz with an average accelerance magnitude of 0.63 in/s²/lb of input force, equal to the response of Point 21 and tied for the third largest dominant response of any of the tested bays on NOC VII-18. The half power method estimate of damping at the 4.975 Hz dominant frequency was 1.16% of critical. There is a strongly represented peak in the accelerance FRF at 4.875 Hz, which corresponds very closely to the dominant frequencies of the two adjacent bays (chirp dominant frequency of Points 21 and stepped sine sweep dominant frequency of Point 65). The MDOF curve fit estimate of damping at 4.98 Hz was 1.20%, as shown in Table 3.16, which was in very good agreement with the half power damping estimate. The 0.4% damping ratio computed for the 4.89 Hz frequency seems unreasonably low, however efforts to curve fit using a higher level of damping did not give a good curve fit overlay on the FRFs.

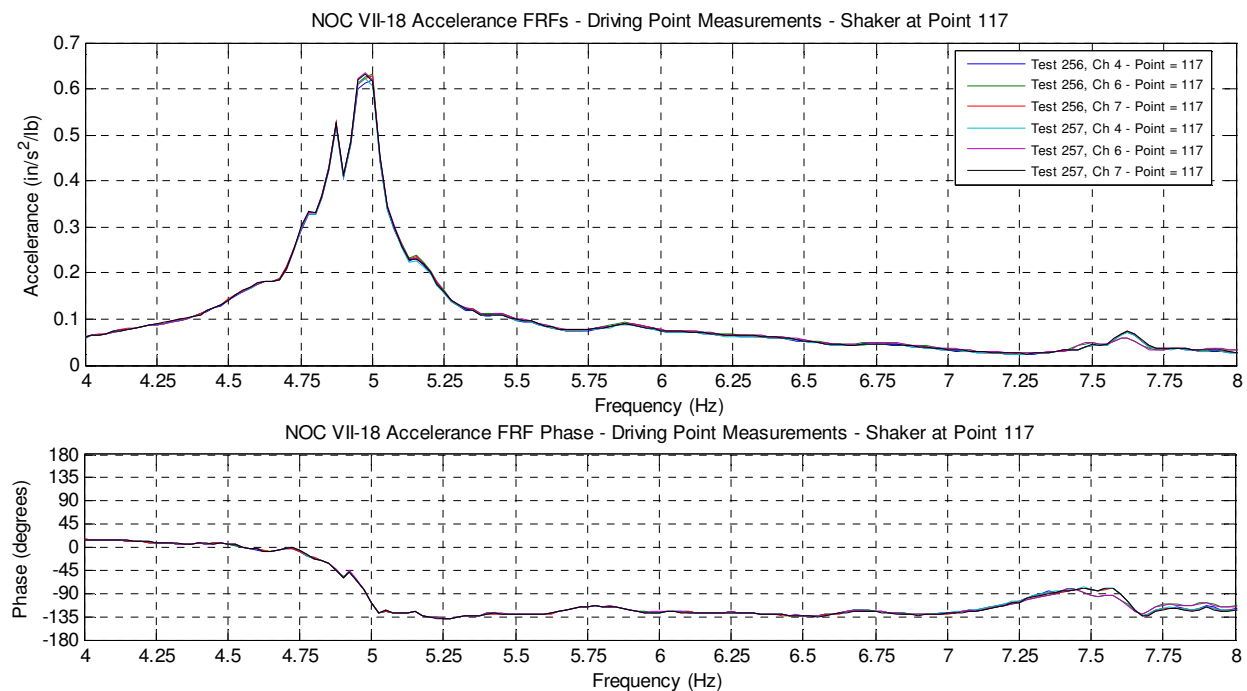


Figure 3.58: NOC VII-18 Driving Point Accelerance FRFs (Point 117)

Table 3.16: NOC VII-18 Pt 117 – Driving Point Curve Fit Estimated Frequencies & Damping

Frequency (Hz)	Damping (%)
4.74	0.85
4.89	0.40
4.98	1.20
5.15	1.00

NOC VII-18 Point 125 – Point 125 (mid-bay K/L-5/6) is located in the bay adjacent to the extensively tested bay containing Point 73 in the direction parallel to the ribs of the decking. The magnitude and phase of four driving point accelerance FRFs taken at this location are presented in Figure 3.59, which shows a dominant peak at 5.075 Hz. The accelerance at the dominant peak was 0.56 in/s²/lb of input force. The half power method estimated damping was 1.02% at the 5.075 Hz peak. While 5.075 Hz is clearly the dominant peak, several closely spaced participating frequencies make the peak of the FRF seem wider on the left side, creating the potential for overestimating the damping using the half power bandwidth method. The MDOF curve fit of the driving point accelerance FRFs shown in Table 3.17 reveal these frequencies at 4.87 Hz and 5.03 Hz. The 5.03 Hz frequency is not unexpected because of Point 125's location with respect to the bay containing Point 73, which had a dominant frequency of 5.05 Hz from chirp measurements and 5.025 Hz from stepped sine sweep measurements. The estimated damping ratio for the 5.08 Hz curve fit dominant frequency was 0.8% of critical, less than the damping ratio computed using the half power method.

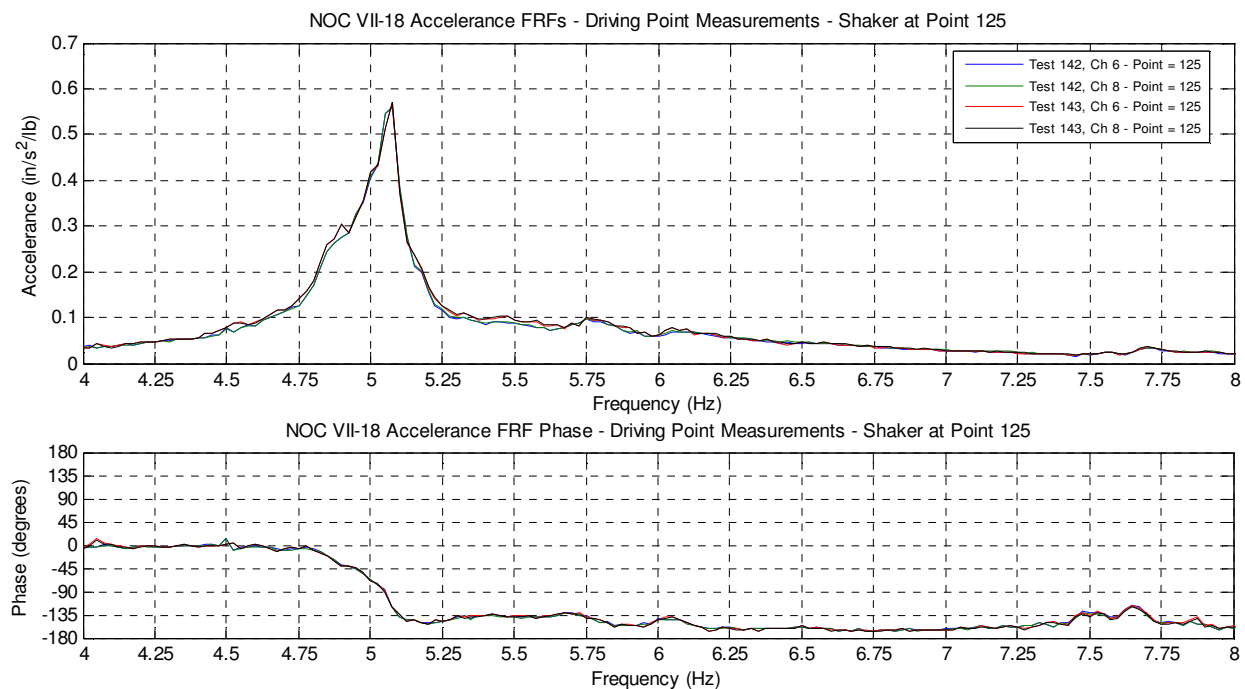


Figure 3.59: NOC VII-18 Driving Point Accelerance FRFs (Point 125)

Table 3.17: NOC VII-18 Pt 125 – Driving Point Curve Fit Estimated Frequencies & Damping

Frequency (Hz)	Damping (%)
4.87	0.86
5.03	0.90
5.08	0.80

NOC VII-18 Point 177 – The next location investigated was Point 177 (mid-bay J/K-5/6), an exterior bay located adjacent to the interior bay housing the service elevators. The magnitude and phase of the driving point accelerance FRFs taken at this location are shown in Figure 3.60. The unique accelerance FRFs for this location essentially contain four significantly participating frequencies within 0.5 Hz of one another and of nearly equal magnitude. The largest peak of the four was at 4.90 Hz with an accelerance of 0.52 in/s²/lb of input force, and the other three peaks at 4.55 Hz, 4.675 Hz, and 5.025 Hz had accelerance values ranging from 0.33-0.45 in/s²/lb. The cause of the unique response within this bay is not entirely clear, and the only difference of this bay compared to other exterior bays is its location next to the interior bay with service elevators. The participation of the 5.025 Hz frequency likely corresponds to the dominant frequencies of other bays along the exterior 10-bay strip including Point 73 and Point 281, each of which are two bays removed on either side of Point 177. As shown in Figure 3.60, a few variations to the chirp signal were made to confirm the unique accelerance FRF, namely burst chirp measurements with a 3-6 Hz sweep, to focus on the odd frequency range of the FRF. Despite this adjustment, a consistent measurement of the accelerance across this frequency range was still achieved. Because of the odd form of the accelerance FRFs, no half power estimates of damping were made, however the MDOF curve fit estimated frequencies and damping are listed in Table 3.18.

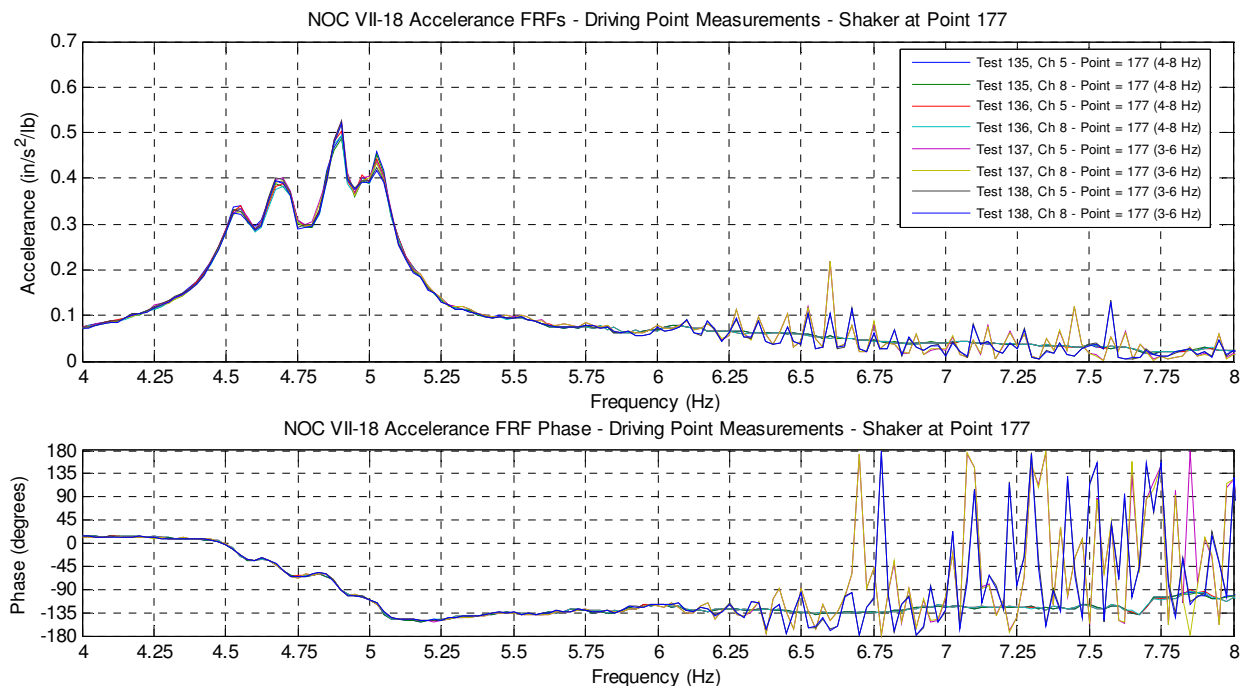


Figure 3.60: NOC VII-18 Driving Point Accelerance FRFs (Point 177)

Table 3.18: NOC VII-18 Pt 177 – Driving Point Curve Fit Estimated Frequencies & Damping

Frequency (Hz)	Damping (%)
4.53	1.55
4.68	0.90
4.89	0.87
5.03	0.90

The odd form of the accelerance FRF poses several difficulties for vibration serviceability. First, the likelihood of accurately generating a finite element model for response prediction purposes with the appropriate frequency content and participating mode shapes at this location is pretty low. Secondly, and more importantly from a serviceability standpoint, a relatively large magnitude of response (a minimum of $0.3 \text{ in/s}^2/\text{lb}$) measured across a substantial (and low) frequency range has a potentially significant vulnerability to walking excitation. The 4.5-5.1 Hz frequency range corresponds to the second harmonic of 2.25-2.55 steps per second, fast but achievable rates of walking.

NOC VII-18 Point 216 – The one location of excitation for any of the three tested floors that was not located at the middle of the tested bay was at Point 216 (quarter-bay H/J-5/6). The magnitude and phase of the two driving point accelerance FRF measurements for this test location is presented in Figure 3.61. The dominant frequency at this location was 5.025 Hz with an accelerance magnitude of $0.35 \text{ in/s}^2/\text{lb}$ of input force. While the peak magnitude was lower than for other tested bays, as expected for a non-mid-bay driving point, it still had a significant response that was roughly equal to many of the secondary peaks of other mid-bay driving point FRFs. The second peak at 7.55 Hz corresponds to the higher mode of vibration that has double curvature within the bay rather than just a concave-up or concave-down single curvature shape. The 5.025 Hz dominant frequency is the same as for the adjacent bay on one side containing Point 281, and the 4.90 Hz dominant frequency of the adjacent bay containing Point 177 is also evident in the accelerance FRFs in Figure 3.61. The half power damping estimate at the 5.025 Hz peak was 0.60% of critical, the lowest half power estimate for any of the tested bays of NOC VII-18. The MDOF curve fit frequencies and damping estimates are shown in Table 3.19, which confirm the estimated low level of damping at the dominant frequency.

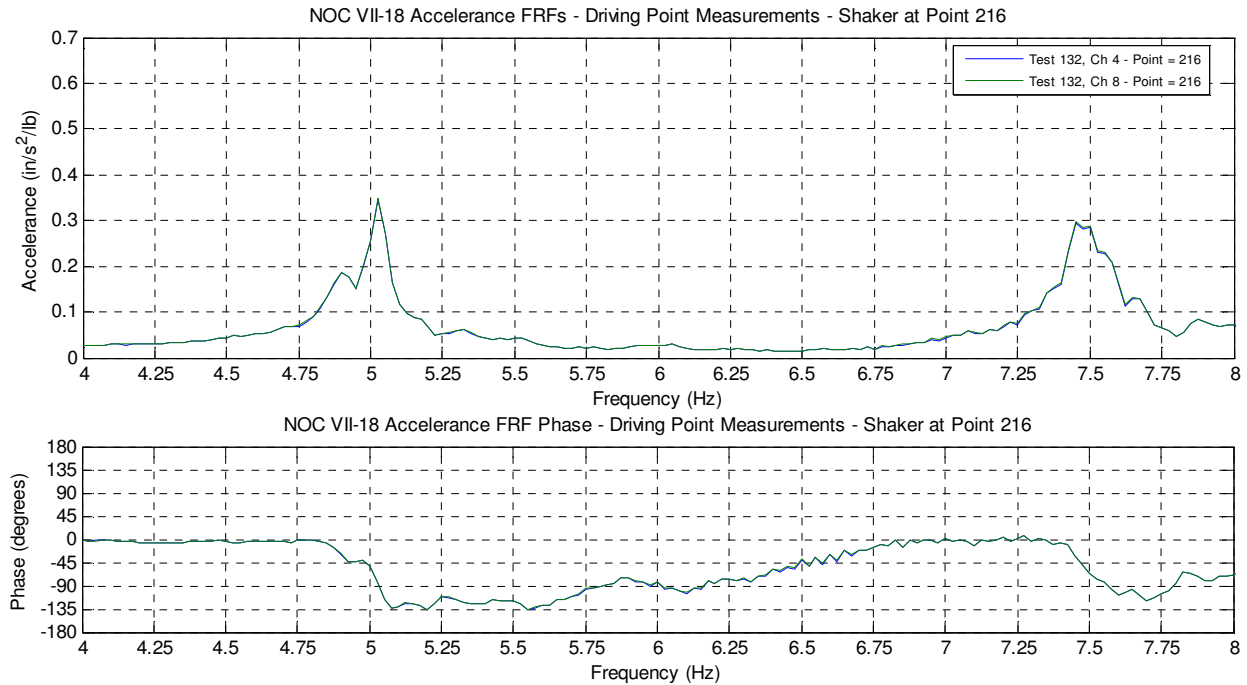


Figure 3.61: NOC VII-18 Driving Point Accelerance FRFs (Point 216)

Table 3.19: NOC VII-18 Pt 216 – Driving Point Curve Fit Estimated Frequencies & Damping

Frequency (Hz)	Damping (%)
4.91	0.67
5.03	0.62
7.44	0.90

NOC VII-18 Point 333 – The final point of excitation investigated was Point 333 (mid-bay F/G-5/6), which was in an exterior bay adjacent to the extensively tested bay containing Point 281. Also adjacent to the bay was a partially open portion of the interior bays, as shown in Figure 3.62 and previously shown in the floor layout of Figure 3.14; however the mechanical equipment for the terminated mid-rise bank of elevators below this bay made this portion of the floor have nearly negligible response.



Figure 3.62: NOC VII-18 Partially Open Bay F/G-4/5 (Adjacent to Point 333)

The magnitude and phase of the two driving point accelerance FRF measurements taken at this location are presented in Figure 3.63, which shows a dominant peak at 5.05 Hz. Oddly, the shape of the entire accelerance FRF is very similar to the driving point accelerance FRF from Point 125 for both the peak location and magnitude. The peak accelerance value for Point 333 was $0.57 \text{ in/s}^2/\text{lb}$ of input force, and the half power estimated damping was 0.72%. The MDOF curve fit frequency and damping estimates are listed in Table 3.20, which show a slightly lower estimate of damping for the corresponding 5.02 Hz peak of 0.65%. This slightly lower value was expected due to the widening of the FRF peak from closely spaced participating frequencies.

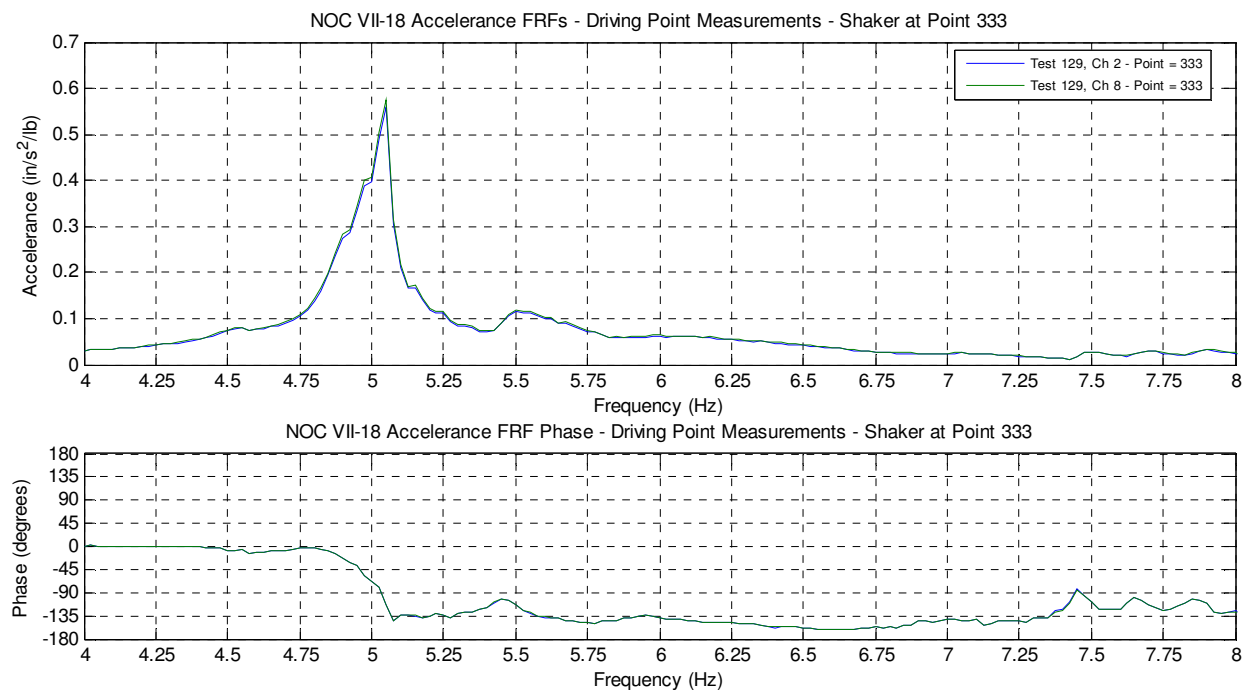


Figure 3.63: NOC VII-18 Driving Point Accelerance FRFs (Point 333)

Table 3.20: NOC VII-18 Pt 333 – Driving Point Curve Fit Estimated Frequencies & Damping

Frequency (Hz)	Damping (%)
4.84	1.30
5.02	0.65
5.05	0.60
5.48	1.01

Reciprocity of Accelerance FRF Measurements - As a check of measured data consistency, a reciprocal measurement investigation was conducted for several locations on the floor. The reciprocal measurement coverage was previously shown in Section 3.2.2, Figure 3.22, and the theory of reciprocity was previously described in Section 2.4.8. Reciprocity in modal analysis states that an accelerance FRF measured from forcing at one point while measuring the response

from another is identical to the same FRF measurement taken with the force and response locations reversed. The entirety of the measurements are not presented here, however representative measurements are presented in Figure 3.64 to illustrate the key findings of the investigation.

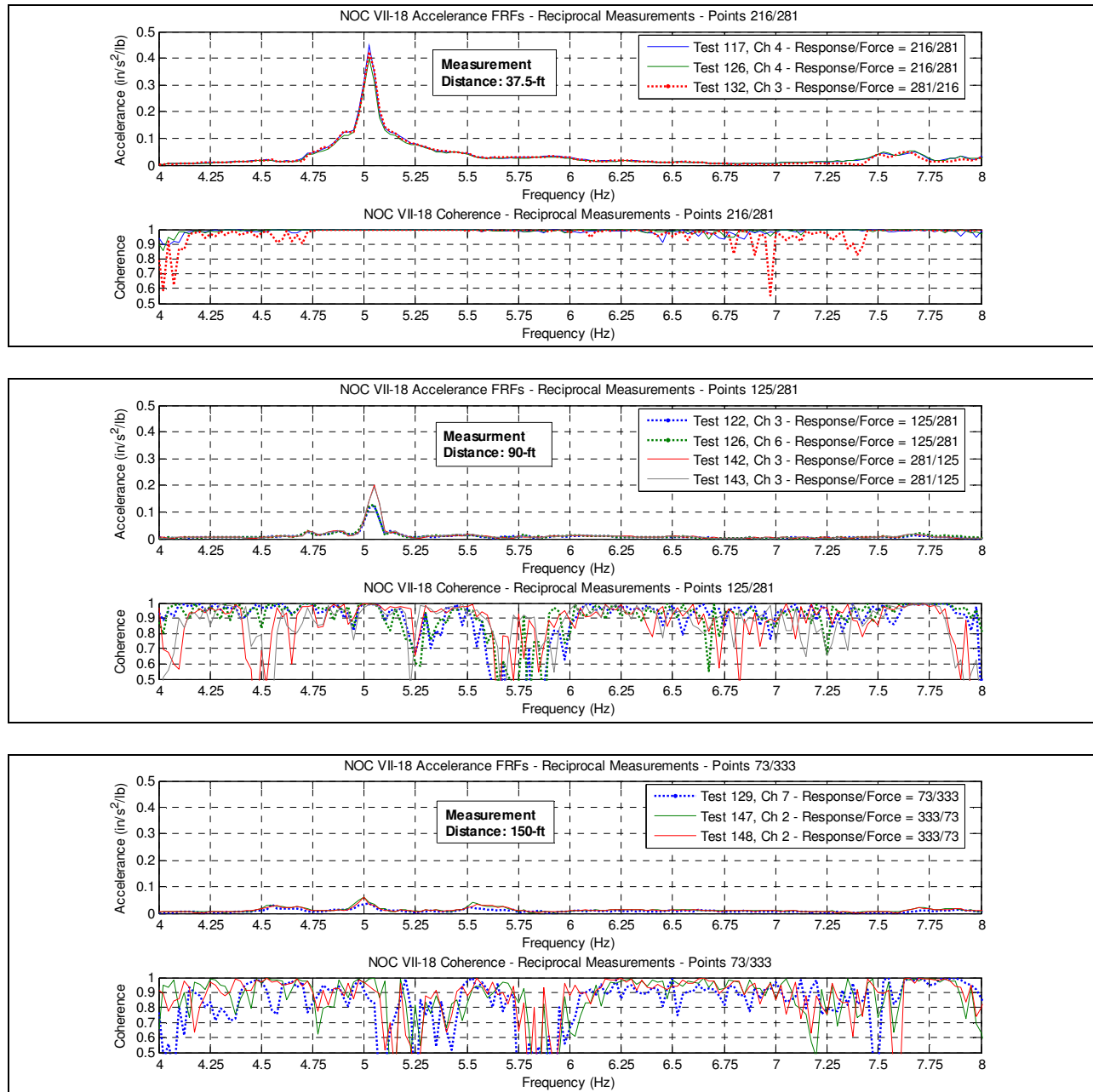


Figure 3.64: NOC VII-18 Reciprocal Accelerance FRF Comparison (Barrett et al. 2006)

Previously presented by Barrett et al. (2006), three sets of reciprocal accelerance FRFs are shown in Figure 3.64 for points on the NOC VII-18 floor at increasing distances from one another. The first set of measurements is between Points 216 and 281, separated only by one and

a quarter bays (37.5 ft). The second set of measurements is between Points 125 and 281, three bays removed (90 ft). The final set of measurements is between Points 73 and 333, five bays removed (150 ft). The quality and consistency of the measurements at a close distance is very good, indicating the floor is behaving as expected and placing faith in the high quality of the measurements and the underlying modal theory. At larger distances, however, the quality of the measurements degrades as shown by poor agreement of magnitudes of the reciprocal FRFs in the second two sets of measurements. The three sets of measurements are plotted to a common magnitude to illustrate this disagreement in reciprocal measurements at long distances is a product of much smaller response, not a gross nonlinearity of the floor. Small response translates into low signal-to-noise ratio, resulting in poorly correlated measurements as shown by the degraded coherence plots, even at peak frequencies where the response signal is strongest.

An implication of the reciprocal measurement study presented above is that the mode shapes derived from single point excitation on large floor systems may be difficult to characterize long distances away from the point of excitation. Using multiple exciters may aid in this characterization, but the approach is questionable for floor vibration serviceability analysis that focuses more on in-service behavior due to a single source of excitation. By simply increasing the level of excitation of a single actuator to generate stronger response signals at greater distances, the floor may be forced into amplitudes well outside the range that is generated by walking. The problem with this approach is it has been demonstrated that floor behavior and properties are sometimes different at higher levels of excitation.

Decay Curve Fit Damping Estimates – Section 2.4.6 was devoted to discussing the various methods for estimating damping, including an extensive discussion of the limited application of decay from resonance curve fitting as a method of estimating damping. The decay curves and decay curve fit overlays presented in that section for demonstration purposes were measurements taken at various locations on NOC VII-18 (Points 281, 21, and 125). In short, the decay from resonance curve fit method is limited by the presence of multiple contributing modes in the decay response, a property observed in the majority of the tested bays. Although driving the mid-bay of a floor sinusoidally at the dominant frequency may approximate the mode shape, it is actually placing the floor in its operating deflection shape from forcing at the location and frequency, and the resulting decay response will include contribution from any significantly participating modes. A large number of decay measurements were taken for ten of the eleven

excited bays on NOC VII-18 (all but Point 69); however the results of only a few decay curve fits are presented here because most measurements were skewed by multi-mode decay response. Although a significant number of decay measurements were taken and analyzed, the most important conclusion to be drawn from the investigation is the limited application of this method of estimating damping. The only two locations that provided reasonable single mode decay response and estimates of damping were Points 281 and 73, both of which have very dominant single peaks. The resulting decay curve fit damping estimates are presented in Table 3.21, which are in general agreement with the half power and MDOF curve fit values previously presented.

Table 3.21: NOC VII-18 Summary of Decay Curve Fit Damping Estimates

Excitation Location(s)	Type of Damping Estimate	Excitation Level (volts)	Decay Frequency (Hz)	Estimated Damping Ratio
Point 281	Decay Curve Fit from 5.025 Hz Sinusoid	0.3535	5.035	0.75%
Point 281	Decay Curve Fit from 5.025 Hz Sinusoid	0.707	5.025	0.70%
Point 281	Decay Curve Fit from 5.025 Hz Sinusoid	1.414	5.025	0.60%
Point 281	Decay Curve Fit from 5.025 Hz Sinusoid	2.30	5.025	0.60%
Point 73	Decay Curve Fit from 5.025 Hz Sinusoid	0.707	5.045	1.15%
Point 73	Decay Curve Fit from 5.025 Hz Sinusoid	1.414	5.045	1.05%
Point 73	Decay Curve Fit from 5.025 Hz Sinusoid	2.30	5.050	0.95%

For reference, a representative selection of decay measurements for NOC VII-18 and decay curve fit results for other tested bays on the floor is presented in Appendix G. It should be noted that the “upper” and “lower” curve fit values represent fitting of the upper and the lower parts of the decay curve, which may appear different due to multi-mode response. The values estimated in this manner (when different) have no relevance to the actual level of damping, and they are only presented to illustrate how multi-mode decay response can easily be misinterpreted. For bays with several participating modes, other methods for estimating damping should be used, such as the MDOF curve fitting of the driving point accelerance FRFs.

Summary of Estimated Dominant Frequencies and Damping Values – Table 3.22 provides an overall summary of the identified dominant frequencies for each of the eleven tested bays and their corresponding damping ratios and accelerance magnitudes, where applicable. The entries for Point 281 include the results from three different levels of excitation for both chirp derived accelerance FRFs and manually derived FRFs using a stepped sine sweep. All locations include the frequency and damping values from a MDOF curve fit of the driving point accelerance FRFs, and for some locations, area coverage FRFs and multi-reference accelerance FRFs.

Table 3.22: NOC VII-18 Summary of Dominant Frequency and Damping Estimates (All Bays)

Excitation Location(s)	Type of Damping Estimate	Excitation Level (volts)	Peak Frequency (Hz)	Peak Magnitude (in/s ² /lb)	Estimated Damping Ratio
Point 281	Half Power Bandwidth Method - Chirp FRF	2.0	5.025	0.74	0.65%
Point 281	Half Power Bandwidth Method - Chirp FRF	1.0	5.05	0.72	0.69%
Point 281	Half Power Bandwidth Method - Chirp FRF	0.5	5.05	0.70	0.77%
Point 281	Half Power Bandwidth Method - Stepped Sine Sweep FRF	2.0	5.00	0.71	0.77%
Point 281	Half Power Bandwidth Method - Stepped Sine Sweep FRF	1.414	5.025	0.70	0.77%
Point 281	Half Power Bandwidth Method - Stepped Sine Sweep FRF	0.707	5.025	0.73	0.71%
Point 281	MDOF Curve Fit of Driving Point FRFs	2.0	5.02	n/a	0.65%
Point 73	Half Power Bandwidth Method - Chirp FRF	2.0	5.05	0.71	1.13%
Point 73	Half Power Bandwidth Method - Stepped Sine Sweep FRF	2.30	5.025	0.69	1.15%
Point 73	MDOF Curve Fit of Driving Point FRFs	2.0	5.04	n/a	1.15%
Point 73	MDOF Curve Fit of Area Coverage FRFs	2.0	5.09	n/a	1.00%
Pt 65,69,73	Multi-Ref MDOF Curve Fit of Area Coverage FRFs	2.0	5.05	n/a	1.05%
Point 69	Half Power Bandwidth Method - Chirp FRF	2.0	6.525	0.53	2.45%
Point 69	MDOF Curve Fit of Driving Point FRFs	2.0	6.55	n/a	2.40%
Pt 65,69,73	Multi-Ref MDOF Curve Fit of Area Coverage FRFs	2.0	6.54	n/a	2.10%
Point 65	Half Power Bandwidth Method - Chirp FRF	2.0	4.85	0.95	0.88%
Point 65	Half Power Bandwidth Method - Stepped Sine Sweep FRF	0.707	4.875	0.90	0.95%
Point 65	MDOF Curve Fit of Driving Point FRFs	2.0	4.85	n/a	0.85%
Pt 65,69,73	Multi-Ref MDOF Curve Fit of Area Coverage FRFs	2.0	4.85	n/a	0.69%
Point 25	Half Power Bandwidth Method - Chirp FRF	2.0	5.75	0.48	1.39%
Point 25	MDOF Curve Fit of Driving Point FRFs	2.0	5.74	n/a	1.28%
Point 25	Half Power Bandwidth Method - Chirp FRF	2.0	6.05	0.50	2.64%
Point 25	MDOF Curve Fit of Driving Point FRFs	2.0	6.05	n/a	1.41%
Point 21	Half Power Bandwidth Method - Chirp FRF	2.0	4.875	0.60	1.36%
Point 21	MDOF Curve Fit of Driving Point FRFs	2.0	4.87	n/a	0.85%
Point 117	Half Power Bandwidth Method - Chirp FRF	2.0	4.975	0.61	1.16%
Point 117	MDOF Curve Fit of Driving Point FRFs	2.0	4.98	n/a	1.20%
Point 125	Half Power Bandwidth Method - Chirp FRF	2.0	5.075	0.54	1.02%
Point 125	MDOF Curve Fit of Driving Point FRFs	2.0	5.08	n/a	0.80%
Point 177	Half Power Bandwidth Method - Chirp FRF	2.0	4.90	0.52	n/a
Point 177	MDOF Curve Fit of Driving Point FRFs	2.0	4.89	n/a	0.87%
Point 216	Half Power Bandwidth Method - Chirp FRF	2.0	5.025	0.33	0.60%
Point 216	MDOF Curve Fit of Driving Point FRFs	2.0	5.03	n/a	0.62%
Point 333	Half Power Bandwidth Method - Chirp FRF	2.0	5.050	0.54	0.72%
Point 333	MDOF Curve Fit of Driving Point FRFs	2.0	5.05	n/a	0.60%

In general, all damping values estimated from the different methods are in good agreement with one another and ranged from 0.60% to 2.40% of critical, reasonable values for the bare condition of the floor. It is interesting to note the higher levels of damping (above 2%) were measured at higher frequencies (6.05 and 6.55 Hz) within interior bays containing Points 25 and 69. For exterior bays, which had dominant frequencies ranging from 4.85 to 5.10 Hz, the

range of estimated damping was 0.60% to 1.20%. The ranges of dominant frequencies are interesting, particularly when different locations of the floor that share the same dominant frequencies have very different damping ratios. An example of this is the 5.025-5.05 Hz dominant frequencies at Points 281 and 73, which have estimated damping values of 0.65% and 1.15% respectively (based on MDOF curve fit of driving point FRFs). A possible explanation for this is that Point 73 is a corner bay with two sides adjacent to the exterior cladding. Point 21 is also a corner bay; however it has an MDOF curve fit estimated damping value of 0.85%. The wide range of damping values for the different frequencies poses problems for finite element modeling, which requires specified damping values for any forced response analysis, and a wide range of values is difficult to accommodate. For the cases where damping values were not in agreement between half power methods and MDOF curve fitting, the half power method estimate was overestimated due to the presence of closely spaced modes, which have the effect of widening the peak of the FRF. In these situations, the values estimated using MDOF curve fitting are more reliable.

Comparison of Measured Frequencies with Predicted Frequencies from DG11 – For comparison with measured frequencies of the tested floors, Table 3.23 summarizes the predicted beam, girder, and system frequencies for NOC VII computed using DG11 procedures; the output from FloorVibe (Structural Engineers, Inc. 2004) is presented in Appendix B. Note that Bays L/M-5/6 and M/N-4/5 each bordered the exterior of the building and both were analyzed with and without considering the spandrel girder as a wall. A general exterior bay was analyzed with various assumptions of the stiffness of the exterior (spandrel) girder as well as the interior girder beneath the full-height partition wall. The points of excitation for NOC VII are also presented in Table 3.23 next to the applicable analyzed bay for comparison of predicted and measured frequencies.

Table 3.23: NOC VII - DG11 Predicted Beam/Girder/System Frequencies (Hz)

Tested Bay	Applicable Points of Excitation	Beam Panel	Left Girder Panel	Right Girder Panel	System
Bay L/M-5/6 (wall)	Pt 73, 65	4.70	9.91	wall	4.25
Bay L/M-5/6 (no wall)	Pt 73, 65	4.70	9.91	9.33	4.20
General Exterior Bay (exterior wall)	Pt 21, 117, 125, 177, 216, 281, 333	4.70	9.91	wall	4.25
General Exterior Bay (interior wall)	Pt 21, 117, 125, 177, 216, 281, 333	4.70	wall	8.48	4.11
General Exterior Bay (no walls)	Pt 21, 117, 125, 177, 216, 281, 333	4.70	9.91	8.48	4.11
Bay M/N-4/5 (wall)	Pt 69	5.70	9.56	wall	4.90
Bay M/N-4/5 (no wall)	Pt 69	5.70	9.56	8.99	4.82
Bay L/M-4/5	Pt 25	5.70	9.56	9.56	4.90

None of the DG11 predicted system frequencies in Table 3.23 matched any of the dominant frequencies identified in the driving point accelerance FRFs of the tested bays of NOC VII, and are much lower than the measured values. This discrepancy is not entirely unexpected for this tested floor, as all beams spanning between columns are larger sections than the floor beams within the bay because the floor was designed with all beam-to-column and girder-to-column connections as moment connections. Neither of these conditions is considered in the DG11 calculations and both of these conditions will cause higher frequencies.

3.3 Tested Floor #3 – VT KnowledgeWorks 2 Building, VTK2 (2nd Floor)

3.3.1 Description of Tested Floor #3

The third in-situ steel composite floor system tested was the 2nd floor of the VT KnowledgeWorks 2 building (VTK2), a two-story office building/addition under construction that is located in the Virginia Tech Corporate Research Center of Blacksburg, Virginia (Figure 3.65). This is an addition to an existing facility, the VT KnowledgeWorks building, which was completed in early 2005 and was previously investigated with the handheld analyzer in October 2004. Detailed modal testing of the first KnowledgeWorks building was not undertaken due to weather and logistical difficulties, however the framing layout of the addition is very similar to the original building and thus familiarity of the structure was an advantage. The framing layout of the tested floor is shown in Figure 3.66, and a full framing plan for the floor, including designated sections, is included in Appendix A.



Figure 3.65: VT KnowledgeWorks 2 Building (VTK2), Blacksburg, Virginia

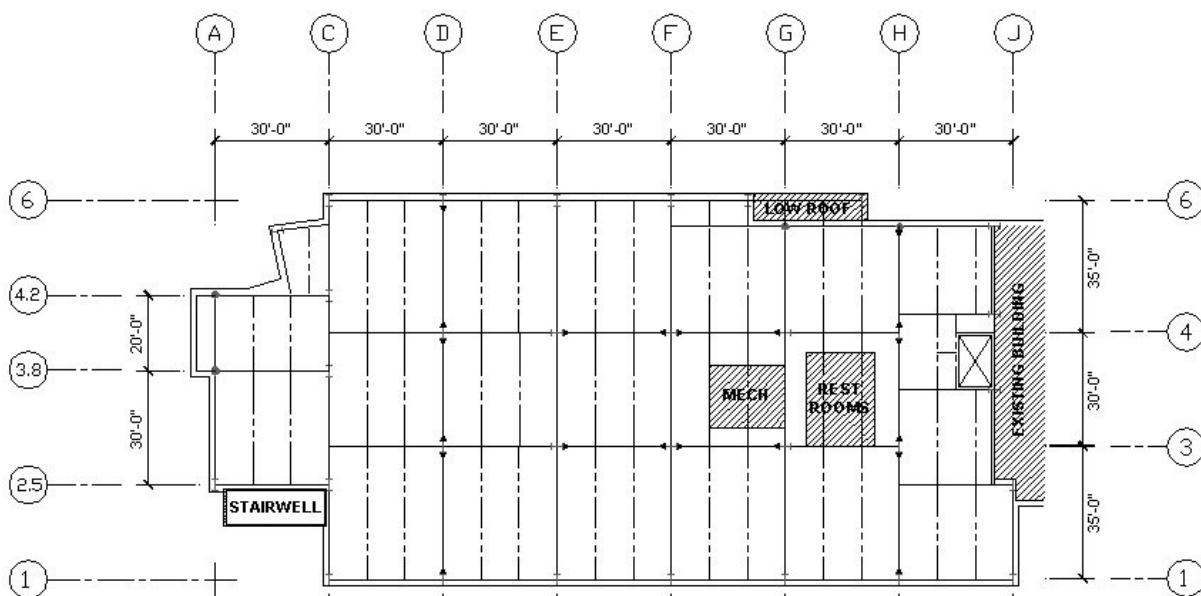


Figure 3.66: VTK2 Floor Framing Layout

The tested portion of the floor was mostly confined to the clear eleven-bay area to the left of grid line F. Although certain aspects of the floor did not make it the ideal testing candidate, such as some stacked construction materials and unfinished perimeter cladding, it was still a favorable specimen for a floor under construction. Some unique framing exists on the left end of the building as well as in the bays adjacent to the existing structure on the right end. Thus, the regular nine-bay area bounded by grid lines C and F in the long direction of the building and grid lines 1 and 6 in the short direction was the focus of the investigation. As shown in Figure 3.66, all bays are 30-ft wide, and the lengths of the three unequal span bays in the direction of the framing are 35-ft, 30-ft, and 35-ft, respectively. Moment frames run the entire width of the short direction of the building along grid lines D and H. In the long direction, moment frames run along grid lines 3 and 4 for two bays between grid lines E and G. Testing was not completely confined to the regular portion of the structure, as measurements were taken with the shaker located in the middle of the two end bays (A/C-2.5/3.8 and A/C-3.8/4.2).

The floor system was designed for composite action and consists of 3.25-in. lightweight concrete over 2-in. 18-gage LOK-Floor steel deck for a total composite depth of 5.25-in. The lightweight concrete has a specified unit weight of 115 pcf and a specified compressive strength of 3000 psi. This is a similar floor slab system to the other two previously tested floors, differing only in the specified compressive strength of the concrete. The slab/deck spans the 120-in. beam spacing and is supported by hot-rolled beams and girders. The floor beams are not continuous over the girders but are connected to the girder webs with simple shear connections. All beam-to-column and girder-to-column connections are simple shear connections with the exception of the moment frames noted above. No camber was used in the framing members, and thus there was noticeable deflection in the members beneath the finished floor. Because the finished floor is level, the resulting deflection has the effect of a greater thickness in the interior areas of a bay, making an accurate estimate of thickness (and mass) rather difficult. The site superintendent estimates the mid-bay thickness of the slab as 1-in. thicker than the 5.25-in. specified.

At the time of testing, the building was not yet completely enclosed by the exterior wall system; however it was nearly complete as shown in Figure 3.67. It is typically assumed that exterior walls provide significant edge stiffness to the floor system; however the extent to which the unfinished exterior framing provided stiffness to the tested floor was not evident without testing, specifically the edge measurements while forcing in exterior bays.



Figure 3.67: VTK2 Exterior Conditions of Tested Floor

Figure 3.68 shows the method used to attach the exterior wall framing to the tested floor. The vertical clip system used in this building (specifically the VertiClip® system) uses slide bearings at the connection points, theoretically allowing for vertical movement of the floor while still attaching the wall to the floor laterally (Figure 3.68(c)). One question addressed by dynamic testing was whether the amplitudes of vibration were large enough to overcome the friction in the connection to allow it to essentially act as a free edge. Logic dictates that the system will act with edge stiffness somewhere between a fully supported wall and a free edge. It was expected to be somewhat constrained for the levels of excitation used during testing and for floor vibration serviceability.

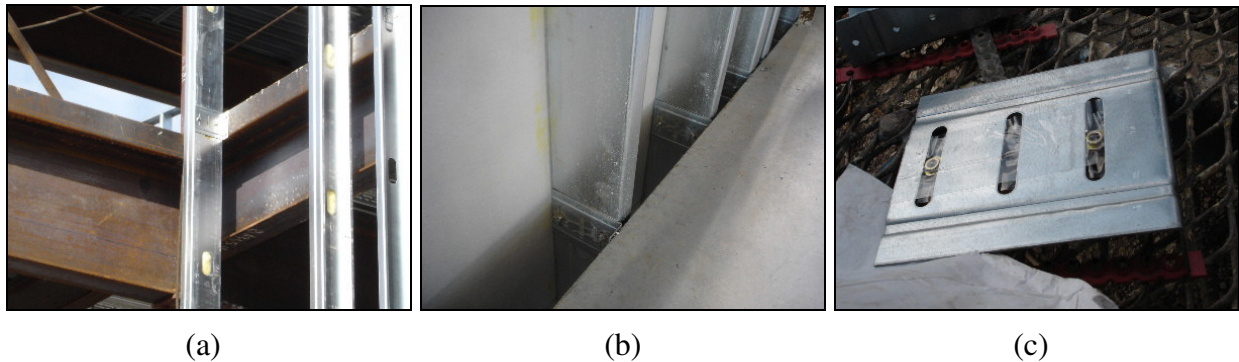


Figure 3.68: VTK2 Exterior Wall Framing Attached to Tested Floor and Vertical Clip

As shown in Figure 3.69, the end eleven bays of the floor were quite “clean” for a building under construction, although certain materials remained stacked in the tested bays that could not be removed prior to testing. Figure 3.70 shows the stacked materials present in bays C/D-1/3 and D/E-1/3 at the time of testing. A particularly large mass on the floor within the areas tested was the bundle of 700 10-ft long, ½-in. pieces of electrical conduit shown in Figure 3.70. One implication of the presence of construction materials is the effect on the frequency

and/or shape of the response, specifically because excessively heavy materials may add mass to the system without any added stiffness.



(a) Grid lines 1 and 3

(b) Grid lines 3 and 4

(c) Grid lines 4 and 6

Figure 3.69: VTK2 Surface Conditions of Tested Floor



Figure 3.70: VTK2 Stacked Construction Materials in Bays C/D-1/3 and D/E-1/3

The underside of the floor was bare with the exception of the mechanical ductwork and miscellaneous electrical conduit, both of which were still in the process of installation (Figure 3.71). The shaded areas in interior bays F/G-3/4 and G/H-3/4 shown in Figure 3.66 designate areas of the tested floor that had B-wall framing in-place during testing. The B-walls of the building enclose the electrical/mechanical rooms and restrooms, and are characterized by full floor-to-ceiling light gage steel partitions above and below the tested floor. During testing, only the light gage framing was in place, as shown in Figure 3.72. Also shown in Figure 3.72 is the connection of the ground floor framing to the underside of the tested floor, which is also a vertical clip style connection to allow vertical movement of the floor without stressing the partition walls.

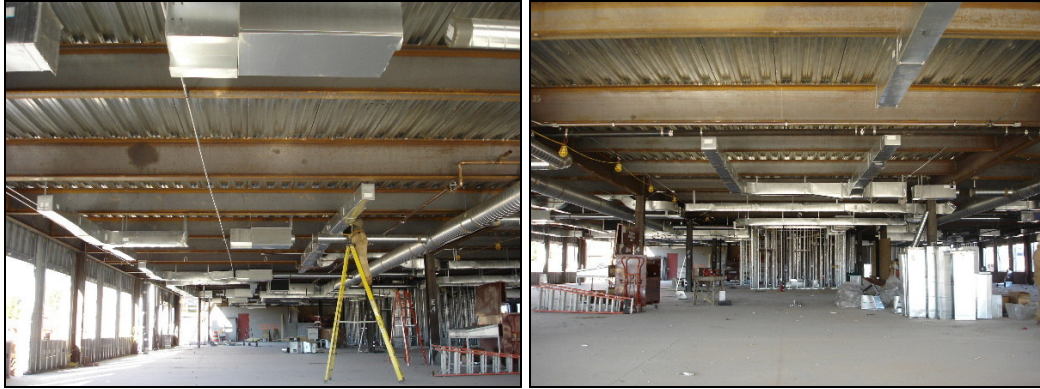


Figure 3.71: VTK2 Underside Conditions of Tested Floor



Figure 3.72: VTK2 B-Wall Partition Framing on Underside of Tested Floor

One last factor worth noting was the open condition of the building and the consequential exposure to noise. The building is located only a couple of hundred feet from a busy highway with significant traffic that was at times noticeable in the measurements. Additionally, the temperatures during testing ranged from the mid-70°s (F) in the day to the high-50°s in the evening hours. In the cooler evenings and particularly on the last day of testing, significant winds were applied to (and traveled through) the partially open building. All of these miscellaneous factors are noted, as they contribute to the level of ambient noise in the measurements and may also account for any potential change in the behavior of the structure over the time of testing.

3.3.2 Measurement Coverage of Tested Floor #3

Testing of VTK2 was accomplished over a single weekend, Friday afternoon through Sunday night. A total of 277 multi-channel measurements were taken over the two and a half days of testing. Although this was a very large number of measurements taken over a very short period of time, it was necessary to minimize the extraneous noise of construction activities and also due to the rapidly changing conditions of the floor still under construction. As with the two

previously tested floors in the NOC VII building, a quarter point test grid was used for testing to track all measurement locations. The test grid numbering scheme used for VTK2 is shown in Figure 3.73.

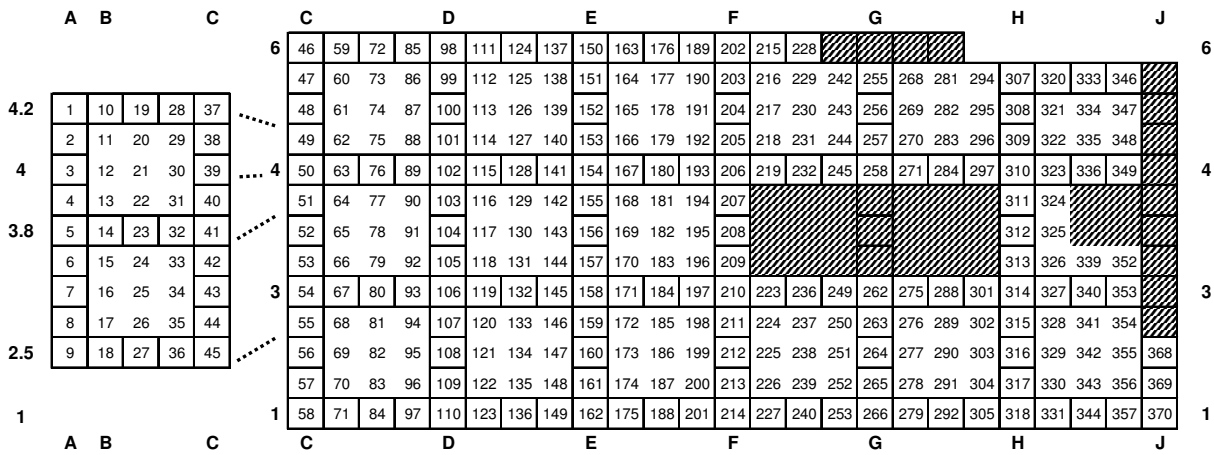


Figure 3.73: VTK2 Test Grid Point Numbers (Tested Floor #3)

The numbers designated in the framing plan of Figure 3.74 mark the 12 mid-bay locations on the floor that were subject to shaker excitation at one point or another during testing. As previously mentioned, the focus of the investigation was mainly the clear portion of the floor to the left of grid line F without interior partitions and away from the irregular geometry near the boundary of the existing building. One exception to this was Point 230 located at the middle of bay F/G-4/6, which was slightly irregular but clear of construction materials.

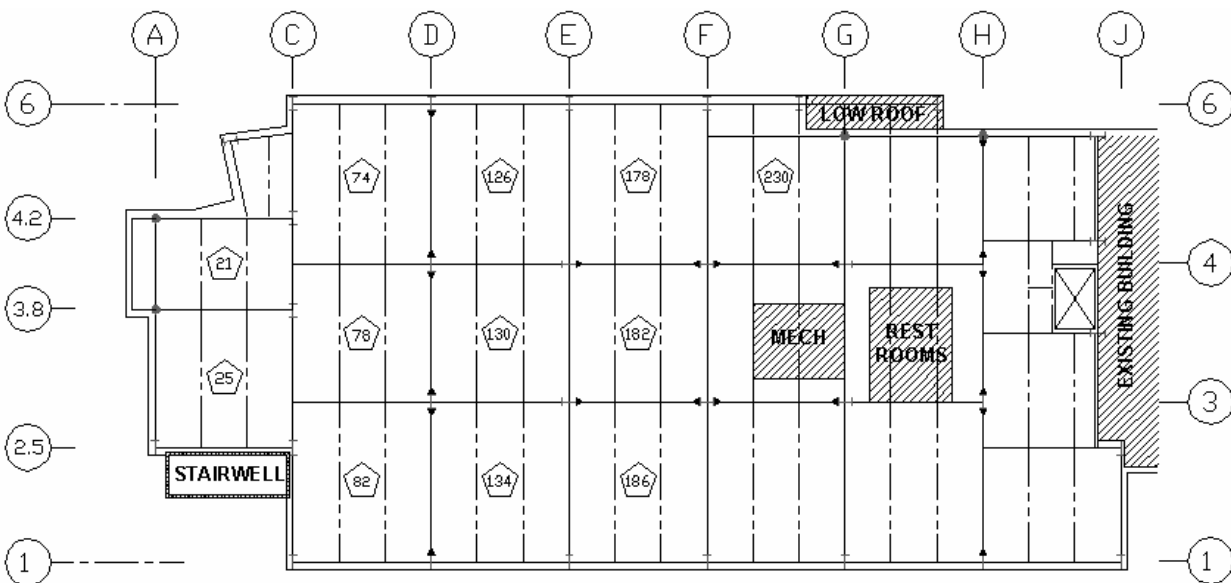


Figure 3.74: VTK2 Excitation Locations

The nine-bay area bounded by grid lines C and F in the short direction of the building and grid lines 1 and 6 in the long direction of the building was the focus of the full modal sweeps to define the mode shapes. Additional investigations measured the response from excitation at each of these nine bays as well as three other adjacent bays containing Points 21, 25, and 230. As with the previously tested floors, the full spectrum of testing was used, including burst chirp excitation to obtain the accelerance FRFs, steady-state sinusoidal measurements, and decay measurements for estimating damping. The linearity of the floor system was investigated by taking identical measurements at different levels of excitation. The spatial dissipation of energy at distances far away from the point of excitation was investigated through reciprocal measurements.

In the days prior to testing, a response-only investigation was performed using the single-channel Ono Sokki CF-1200 Handheld Analyzer (see Appendix D for these measurements). Heel drops were performed at all of the excitation locations shown in Figure 3.74 except Point 230. Based on the active frequency content of all the tested bays from this investigation, a 4-12 Hz frequency range for the burst chirp signal was deemed adequate to capture all significant response within the frequency range of interest. A summary of the test settings used for the various chirp, sine, and decay measurements is presented in Table 3.24.

Table 3.24: Summary of Test Settings and Parameters of Tested Floor #3, VTK2

Chirp Measurements:									
DSP Settings					Signal Settings				
Bandwidth	Record Length	Δf	Record Length	Δt	Chirp Type	Frequency Range	On Time	Off Time	# of Avgs
20 Hz	2048 samples	0.025 Hz	40 sec	0.01953125 sec	Burst	4-12 Hz	30-sec	15-sec	3 avgs

Sinusoidal Measurements:						
DSP Settings					Signal Settings	
Bandwidth	Record Length	Δf	Record Length	Δt	Sine Frequency	# of Avgs
20 Hz	2048 samples	0.025 Hz	40 sec	0.01953125 sec	specified	2 avgs

Decay Measurements:						
DSP Settings					Signal Settings	
Bandwidth	Record Length	Δf	Record Length	Δt	Sine Frequency	# of Avgs
20 Hz	2048 samples	0.025 Hz	40 sec	0.01953125 sec	specified	1 avg

Note that other than the different chirp frequency range, the 4-12 Hz burst chirp signal was very similar to the one used successfully for testing NOC VII-18. Because the active frequencies of the floor were a little higher than those found in NOC VII-18, the SigLab DSP

unit parameters were set to a greater bandwidth (20 Hz), however the same time record length (40-seconds) and frequency domain resolution (0.025 Hz) were maintained for quality measurements. Each of the 277 measurements was taken with the two SigLab DSP unit setup using up to eight channels (seven for the accelerometers, one for the force plate). With this setup, redundant driving point measurements were taken. The 277 measurements included 141 burst chirp signal measurements for capturing the accelerance FRFs, 106 steady-state sinusoidal measurements, 25 decay measurements, and five other measurements used for checking the calibration of the force plate

VTK2, All 12 Excitation Locations – Driving Point and Reciprocity Investigations

At each of the eleven locations highlighted in Figure 3.75, the shaker was used to perform the standard suite of driving point measurements for the excited bay, while simultaneously measuring the accelerance FRFs for the remaining 10 mid-bay positions. With the shaker and accelerometers in these mid-bay locations, the intent was to perform burst chirp measurements to get the accelerance FRFs and then perform a stepped sine sweep across dominant frequencies. The burst chirp measurements were repeated with the roving accelerometers at each of the designated bays to ensure that reciprocal FRFs were captured. Additional investigations included linearity checks (repeated measurements at different levels of excitation) and decay from steady state excitation at the dominant frequency.

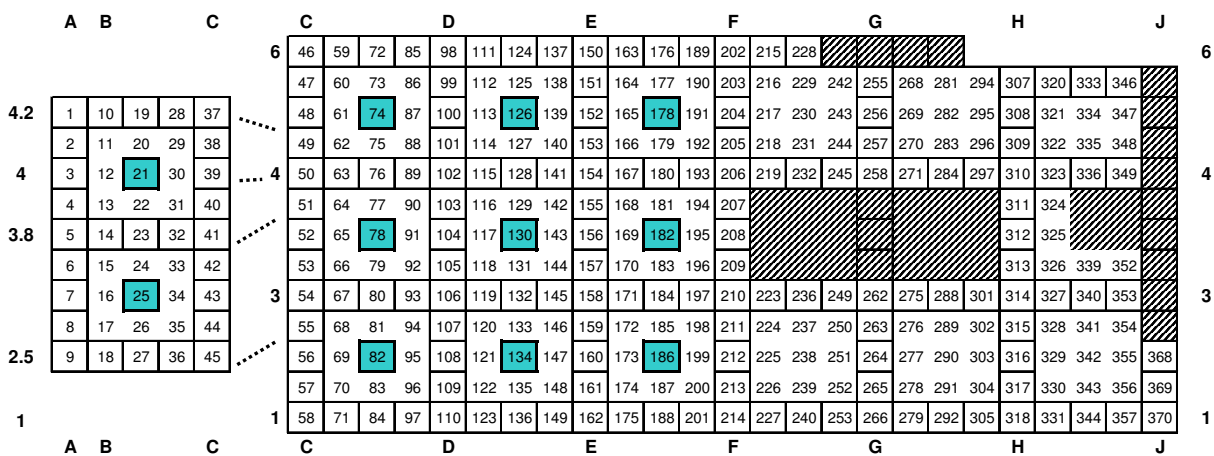


Figure 3.75: VTK2 Mid-Bay Investigations and Reciprocal Measurement Coverage

The following summarizes the extent of investigation for each of the 12 different excitation locations, including remarks on some identified dominant frequencies for the purpose of adequately describing the intent and frequency of the steady-state sinusoidal and decay

measurements. Reciprocal measurements refer to the coverage area in Figure 3.75. Unless otherwise noted, measurements described were only taken at one level of excitation.

Point 21, Mid-Bay A/C-3.8/4.2 - Measurements included driving point accelerance FRFs, reciprocal accelerance FRFs, stepped sine sweep about dominant frequency of 9.00 Hz, and decay measurements.

Point 25, Mid-Bay A/C-2.5/3.8 - Measurements included driving point accelerance FRFs at two levels of excitation, reciprocal accelerance FRFs, stepped sine sweep about dominant frequency of 6.60 Hz, and decay measurements.

Point 74, Mid-Bay C/D-4/6 - Measurements included driving point accelerance FRFs at two levels of excitation, reciprocal accelerance FRFs, stepped sine sweep about two dominant frequencies (6.975 Hz and 7.975 Hz), and decay measurements from each of the two frequencies.

Point 78, Mid-Bay C/D-3/4 - Measurements included driving point accelerance FRFs, reciprocal accelerance FRFs, stepped sine sweep about dominant frequency of 7.95 Hz, and decay measurements.

Point 82, Mid-Bay C/D-1/3 - Measurements included driving point accelerance FRFs at two levels of excitation, reciprocal accelerance FRFs, stepped sine sweep about two dominant frequencies (6.575 Hz and 8.00 Hz), and decay measurements from each of the two frequencies.

Point 126, Mid-Bay D/E-4/6 - Measurements included driving point accelerance FRFs at three levels of excitation, reciprocal accelerance FRFs, stepped sine sweep about two dominant frequencies (6.95 Hz and 7.55 Hz), and decay measurements from each of the two frequencies. Two different levels of excitation were used for the stepped sine sweep and decay measurements at the 6.95 Hz dominant frequency.

Point 130, Mid-Bay D/E-3/4 - Measurements included driving point accelerance FRFs at two levels of excitation, reciprocal accelerance FRFs, stepped sine sweep about dominant frequency of 8.00 Hz, and decay measurements.

Point 134, Mid-Bay D/E-1/3 - Measurements included driving point accelerance FRFs at two levels of excitation, reciprocal accelerance FRFs, stepped sine sweep about dominant frequency of 7.20 Hz, and decay measurements.

Point 178, Mid-Bay E/F-4/6 - Measurements included driving point accelerance FRFs at three levels of excitation, reciprocal accelerance FRFs, stepped sine sweep about dominant

frequency of 7.275 Hz, and decay measurements. Two different levels of excitation were used for the stepped sine sweep and decay measurements at the 7.275 Hz dominant frequency.

Point 182, Mid-Bay E/F-3/4 - Measurements included driving point accelerance FRFs at two levels of excitation, reciprocal accelerance FRFs, stepped sine sweep about dominant frequency of 8.20 Hz, and decay measurements.

Point 186, Mid-Bay E/F-1/3 - Measurements included driving point accelerance FRFs at two levels of excitation, reciprocal accelerance FRFs, stepped sine sweep about dominant frequency of 7.025 Hz, and decay measurements.

Point 230, Mid-Bay F/G-4/6 - This is the only location that was not included in the reciprocal measurements, however measurements did include driving point accelerance FRFs at two levels of excitation, stepped sine sweep about dominant frequency of 6.975 Hz, and decay measurements. Two different levels of excitations were used for the stepped sine sweep and decay measurements at the 6.975 Hz dominant frequency.

VTK2, Point 126 - Mid-Bay D/E-4/6 – Modal Area Coverage

To define the mode shapes over an area of the floor, the shaker was placed in the middle of bay D/E-4/6 (Point 126) with the intention of performing a full modal sweep of the nine-bay area bound by grid lines C, F, 1, and 6. The full coverage is shown in Figure 3.76. The accelerance FRFs were obtained for the 182 different locations on the floor using the 4-12 Hz burst chirp excitation signal. Figure 3.77 shows the shaker located at Point 126 for the modal sweep of the coverage area.

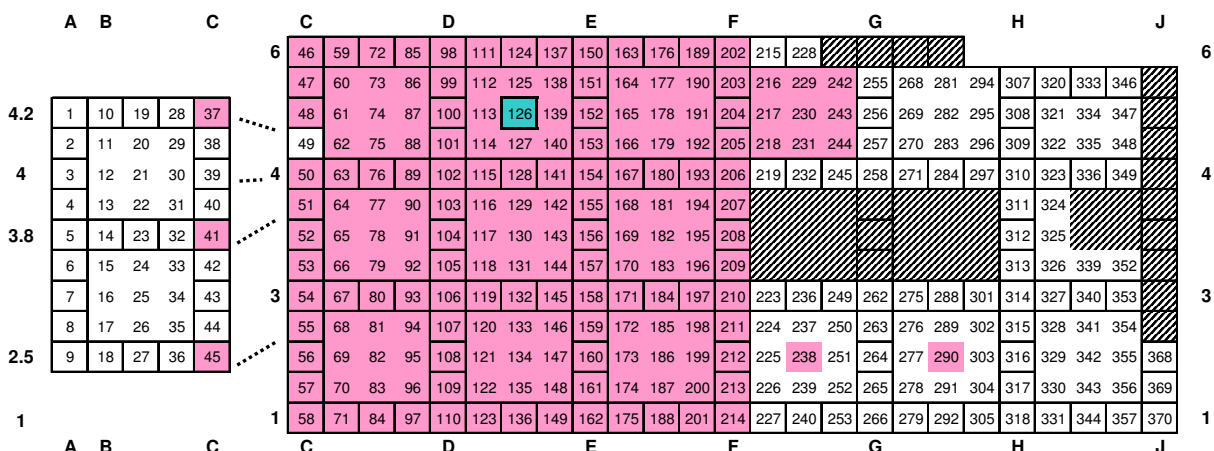


Figure 3.76: VTK2 Measurement Coverage of Modal Sweep (Forcing at Point 126)



Figure 3.77: VTK2 Shaker Located at Point 126 for Modal Sweep of 9-Bay Area

As noted in the coverage diagram of Figure 3.76, the actual column locations along grid line C (Points 37, 41, 45) and the bay's exterior quarter points were measured, with the exception of a missing measurement for Point 49. Because the measurement for column C4.2 (Point 37) was only 30-in. away from this location, it suffices for purposes of mode shape animation. While capturing the boundary response along grid line C with the channel 2, 3, and 4 accelerometers, measurement opportunities with channels 5, 6, and 7 were not wasted. Response was captured at the interior quarter points of bay F/G-4/6 and mid-bay of F/G-1/3 and G/H-1/3. With the chosen resolution and settings of the burst chirp measurements to derive the FRFs, coupled with the additional time required to move accelerometers, the full modal sweep of the coverage area took approximately four hours.

The modal sweep of the coverage area was conducted by lining the six roving accelerometers (channels 2-7) in a line across Points 98 to 163 (grid line 6 in Figure 3.76). The channel 8 accelerometer always remained with the shaker as a redundant driving point measurement. The line of accelerometers was marched down the floor (in the direction of framing, along the three-bay strip) for each subsequent measurement. Once the edge of the building was reached (grid line 1), the accelerometers were split to either side of the three bay strip that was just measured. The line of accelerometers was then marched back towards grid line 6. A few deviations were necessary to capture the edge boundary response along grid line C, which is why measurements were taken in bays other than the nine central ones. This process is only mentioned because it is possible for the pattern of testing to have an effect on the extracted mode shapes. For example, Points 163 and 176 along the exterior boundary are immediately adjacent to one another, however the accelerance FRFs were measured nearly four

hours apart, at the beginning and the end of the set of test measurements. Because only one driving point measurement is used to scale mode shapes, any change in the driving point response during this time will affect the appearance of the shapes.

VTK2, Point 134 - Mid-Bay D/E-1/3 – Modal Area Coverage

Theoretically, the mode shapes derived from forcing at one location on a structure should be the same as those derived from forcing at another location, provided neither of the forcing locations are a node of a mode. As such, an additional modal sweep of the same nine-bay area previously covered while forcing at Point 126 was conducted for a direct comparison of the resulting mode shapes. As shown in Figure 3.78, the point chosen for this task was Point 134, which was opposite Point 126 along the three-bay strip bound by grid lines D and E in the direction of framing. Like the previous modal sweep, the accelerance FRFs were obtained for the 183 different locations (including Point 49 this time) on the floor using burst chirp excitation. The time required to perform this modal sweep was also around four hours,

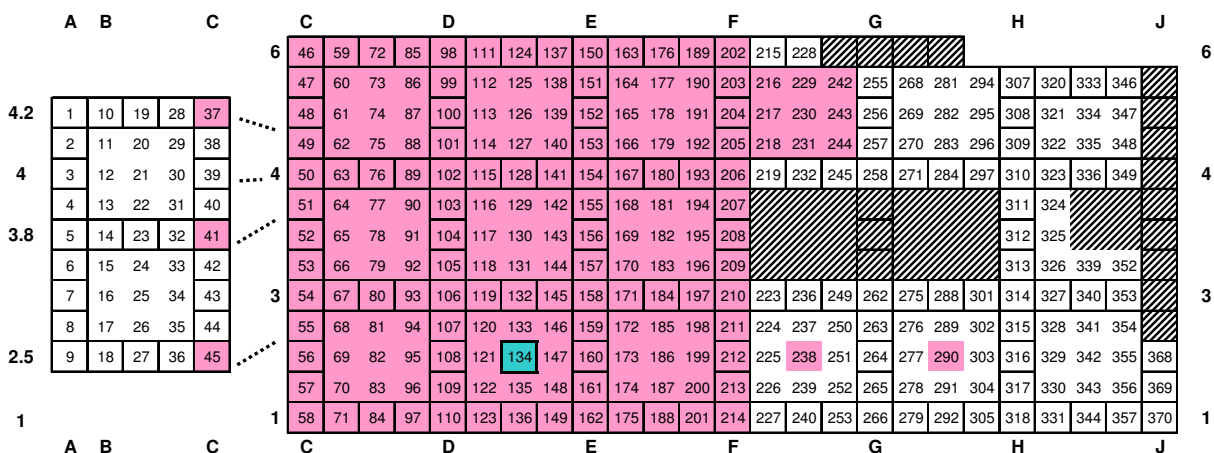


Figure 3.78: VTK2 Measurement Coverage of Modal Sweep (Forcing at Point 134)

VTK2, Point 130 - Mid-Bay D/E-3/4 – Modal Area Coverage

An additional advantage of choosing Points 126 and 134 as driving points for mode shape comparison is that a third point along the three-bay strip was also used for a modal sweep, albeit over a much smaller area, but one that was still useful for comparison. Figure 3.79 shows the coverage of modal measurements with the shaker located in the center panel of the three-bay strip, bay D/E-3/4 (Point 130). This coverage included the three interior quarter points of the three-bay strip (39 different locations), and is directly comparable to the same three-bay strip

shapes extracted from the larger coverage areas of the other two modal sweeps shown in Figure 3.76 and Figure 3.78.

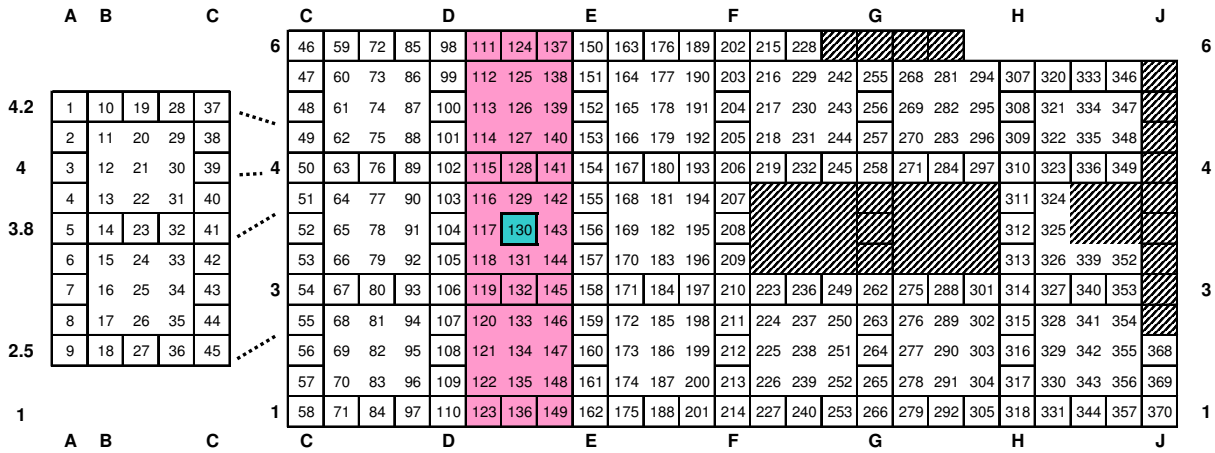


Figure 3.79: VTK2 Measurement Coverage of Modal Sweep (Forcing at Point 130)

Due to limited testing time, there were no steady-state measurements for any of the three given coverage *areas* on VTK2 (other than the mid-bay stepped sine sweep sinusoidal measurements previously mentioned). Faith must be put in the burst chirp derived accelerance FRF measurements over the given areas rather than manually derived spectral values, which is a sound assumption given the comparison of chirp and sinusoidally derived shapes of NOC VII-18 presented in Section 3.2.3. The coherence values of the measurements were closely monitored during testing to ensure good data and valid spectral values in the frequency range of interest.

3.3.3 Measured Floor Behavior – VTK2 (Tested Floor #3)

Like the presentation of measured floor behavior of NOC VII, a representative accelerance FRF from each of the twelve locations of driving point measurements on the VTK2 floor is superimposed in Figure 3.80. Again, several indications of the floor's behavior can be observed from this plot, such as the relative magnitudes of the accelerance at the various peak frequencies, which range from 0.4 to 1.30 in/s²/lb of input force. Several accelerance FRFs have substantial dominant peaks compared to the rest of the measurements (Points 21, 25, and 178). These locations had peak accelerance values between 1.20 and 1.30 in/s²/lb, and the remaining traces had peaks under 0.95 in/s²/lb. For comparison, NOC VII only had one peak much greater than the others at a magnitude of 1.0 in/s²/lb, and the remainder of that floor's excited locations had peaks less than 0.75 in/s²/lb of input force.

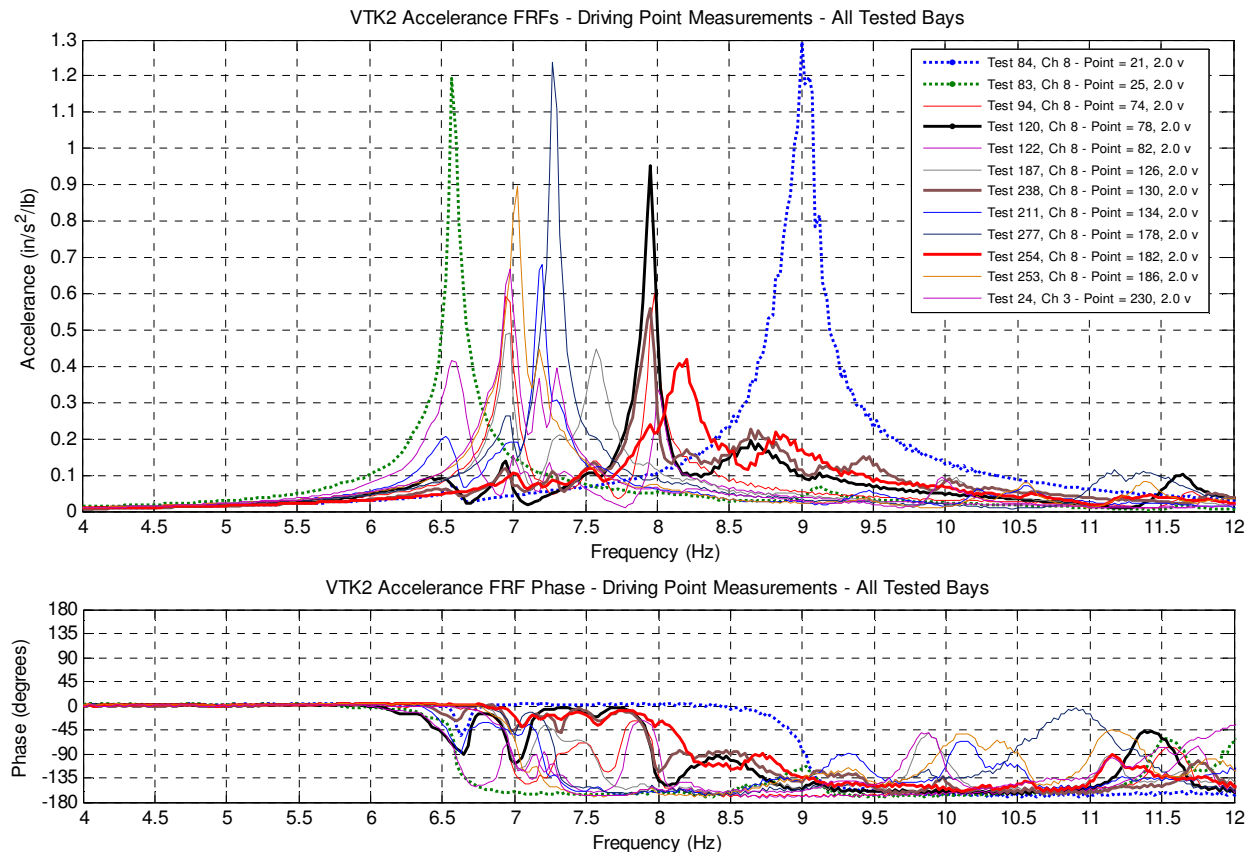
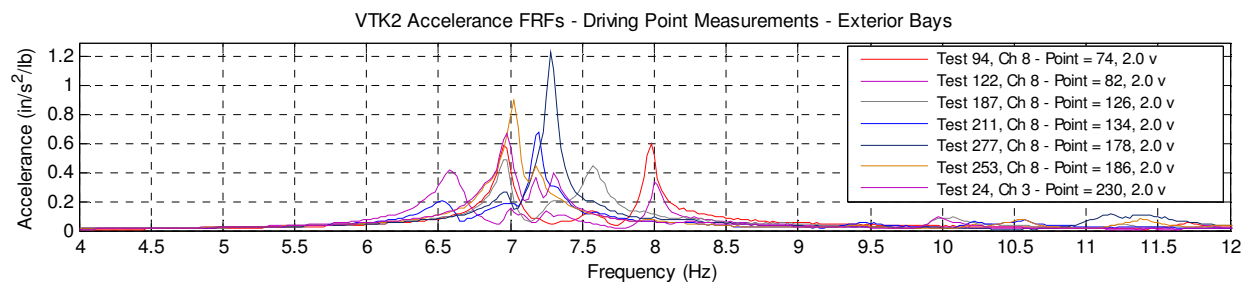


Figure 3.80: VTK2 Driving Point Accelerance FRFs (All Excitation Points)

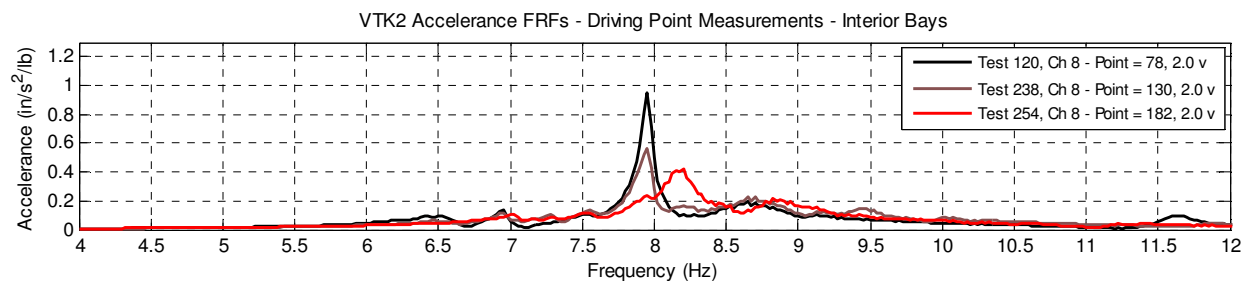
A general observation in Figure 3.80 is the clustering of peak frequencies within a relatively narrow band of frequencies (6.5-8.25 Hz) for all bays except the much smaller bay containing Point 21, which had a peak frequency of 9 Hz. This clustering was also apparent in

the previously tested NOC VII floors, however all dominant frequencies of this floor are higher. The implication of the higher frequencies, 6.55 Hz on the low end, is that the various bays of the floor would not be excited by anything other than the third or fourth harmonic of step frequency.

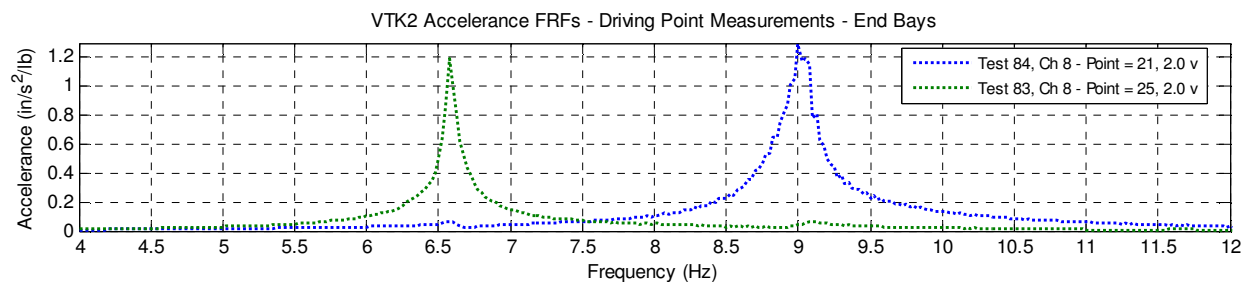
To highlight the contributing frequencies in the accelerance FRFs from different types of bays on VTK2, Figure 3.80 uses three different line types to represent exterior bays (Points 72, 82, 126, 134, 178, 186, and 230), interior bays (Points 78, 130, 182), and the two tested end bays not aligned in the same framing grid lines as the other bays of the floor (Points 21 and 25). The accelerance FRFs for the three different bay types are presented separately in Figure 3.81, which is a good illustration of the range of dominant frequencies for a given bay type and where other contributing frequencies come from.



(a) Exterior Bay Driving Point Accelerance FRFs



(b) Interior Bay Driving Point Accelerance FRFs



(c) End Bay Driving Point Accelerance FRFs

Figure 3.81: VTK2 Driving Point Accelerance FRFs (By Bay Type)

The exterior bays that have longer spans have the lower dominant frequencies and peaks in a narrow 0.30 Hz cluster between 7.0 and 7.30 Hz. However, the exterior bay FRFs also show

significant contribution from the dominant frequencies of the adjacent smaller interior bays, which have dominant frequencies ranging from 7.95 to 8.20 Hz. The two end bays containing Points 21 and 25 are also presented, with the 6.575 Hz dominant frequency of Point 25 showing up in several of the other bays' accelerance FRFs. For the exterior bay FRFs in Figure 3.81(a), the accelerance FRF derived from excitation at Point 178 has a peak magnitude that is clearly larger than the others, indicating this is the exterior bay of the floor most susceptible to annoying levels of vibration. Of the interior bays in Figure 3.81(b), Point 78 shows the greatest accelerance, however the dominant frequency is higher and the peak magnitude is less than the peak of the exterior bay containing Point 178. The two end bays shown in Figure 3.81(c), however, have the two largest magnitudes of response of any of the tested bays. This is likely a product of the unfinished condition of the bays, as the exterior cladding was not yet in place. The bay containing Point 25 also had free edges on two sides, the unclad exterior and the edge along the CMU stairwell where there were no fasteners connecting the spandrel beam and the rigid wall. As a result, the bay also had the lowest dominant frequency of any of the bays, 6.575 Hz. Although the bay containing Point 21 had the largest magnitude accelerance peak, the 9.00 Hz frequency is nearly out of the range of interest for vibration serviceability for human comfort.

The remainder of this section covers the experimental results from testing each of the twelve bays of the VTK2 floor in more detail. The order of the discussion begins with presentation of driving point accelerance FRFs for each of the twelve tested bays with remarks on estimated frequency, damping, and peak accelerance magnitude. Larger plots of magnitude and phase of the driving point accelerance FRFs (including coherence) for all locations of excitation for VTK2 are included in Appendix H, however smaller plots of magnitude and phase are included in this section for reference and discussion. Unless otherwise noted, all of the driving point measurements for VTK2 are plotted using a common scale of accelerance, 0 to 1.30 in/s²/lb, to allow a comparison of magnitudes between excitation locations. The standard level of excitation used for obtaining accelerance FRFs was 2.0 volts, however measurements were also taken at lower 1.0 volts and 0.5 volt levels for various linearity investigations. If applicable, different line types are used in the driving point accelerance FRF plots to represent different levels of excitation for the tested location. For brevity, only the identified frequencies and half power damping estimates are presented for the 2.0 volt excitation level driving point accelerance FRFs; however the tabulated results from MDOF curve fitting are for all of the

displayed the driving point accelerance FRFs, which may or may not include FRFs from different levels of excitation. The consolidated results of chirp derived FRF measurements at different levels of excitation and frequency/damping estimates from stepped sine sweep investigations are summarized in a later section. Following the driving point FRFs, the multi-reference coverage areas are presented to display operating deflection shapes and mode shapes at the frequencies of interest, as well as the results of multi-reference curve fitting of the area coverage FRFs. The ME'scope MDOF curve fitting results, including the single and multi-reference curve fit overlay, tabulated estimates of frequency and damping, and shape strength tables for coverage areas on the VTK2 floor are presented in Appendix I. Finally, other investigations are discussed including decay from resonance and reciprocity.

VTK2 Point 21 – The first location presented is excitation at Point 21 (mid-bay A/C-3.8/4.2). With a 30-ft girder span and 20-ft beam span, this was the smallest of the tested bays and was located on the end of the building (Figure 3.74). The magnitude and phase of six driving point accelerance FRFs taken at this location are presented in Figure 3.82. The dominant frequency of this bay is 9.00 Hz, the highest of all tested bays, which was expected because of its smaller size. The peak had an average accelerance magnitude of 1.29 in/s²/lb of input force.

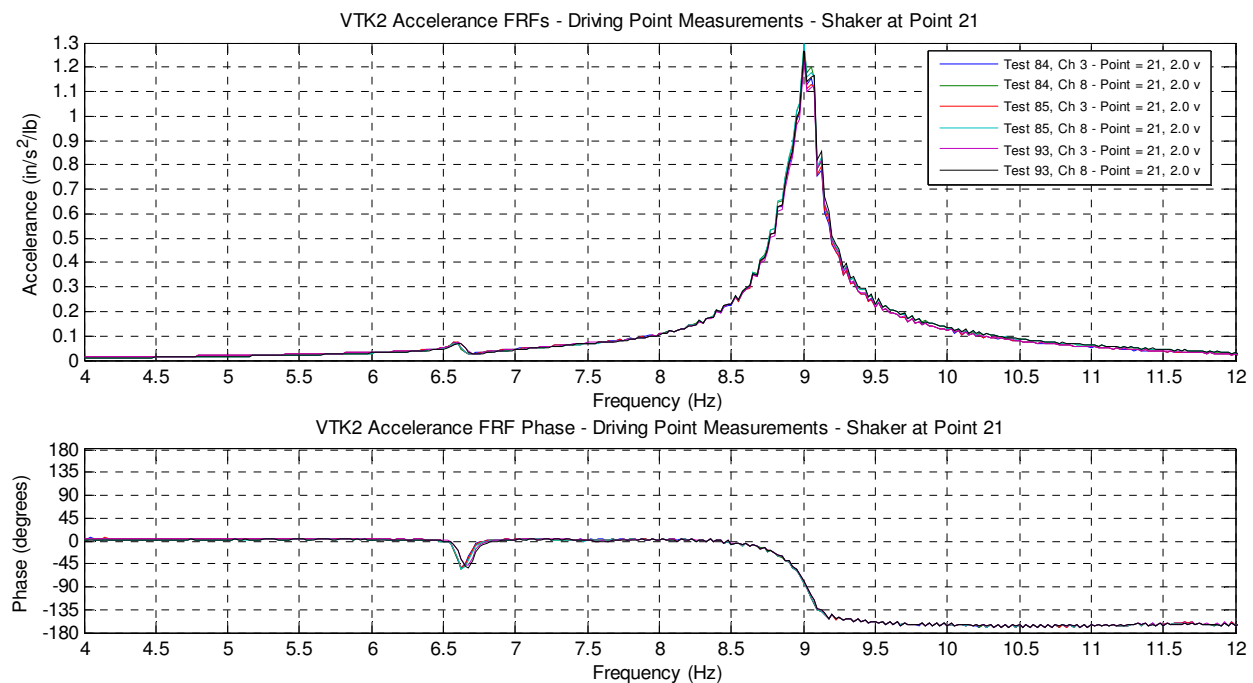


Figure 3.82: VTK2 Driving Point Accelerance FRFs (Point 21)

Although the peak of the curve was slightly degraded with a jagged appearance, a half power estimate of damping at the dominant frequency was 0.88% of critical. The estimated frequencies and damping from a MDOF curve fit of the driving point accelerance FRFs is presented in Table 3.25. The curve fit estimated 1.03% damping ratio at the dominant peak is likely a more accurate estimation of the damping at this frequency, as the MDOF curve fit was a smooth function overlaid on the jagged FRF.

Table 3.25: VTK2 Point 21 – Driving Point Curve Fit Estimated Frequencies and Damping

Frequency (Hz)	Damping (%)
6.62	0.70
9.01	1.03

VTK2 Point 25 – The next location presented is excitation at Point 25 (mid-bay A/C-2.5/3.8), the other end-bay adjacent to the smaller bay containing Point 21 (Figure 3.74). The magnitude and phase of 14 driving point accelerance FRFs taken at Point 25 are presented in Figure 3.83. In contrast to Point 21, the dominant frequency of this bay is 6.575 Hz, the lowest of all tested bays. Although the 30-ft by 30-ft bay had the same span dimensions of the interior bays of the building, its dominant frequency was much lower. This was likely the product of the free edges of the unclad bay, but more significantly, none of the edge framing members of the bay was a part of a moment frame. This was not the case for the three interior bays tested (Points 78, 130, and 182), as either an edge beam or edge girders were a part of the building’s lateral moment frames. The 6.575 Hz peak had an average accelerance magnitude of 1.20 in/s²/lb of input force and a half power estimated damping ratio of 0.53% of critical. The MDOF curve fit estimate of damping at the identified 6.59 Hz peak was 0.60%, as shown in Table 3.26, which is in very good agreement with the half power estimate.

It should be noted that the dominant frequencies of both Points 21 and 25 are present in each other’s respective accelerance FRFs and no other frequencies are noticeable. This indicates that these end two bays, which are uniquely framed within different grid lines of the rest of the building, are virtually acting as a two-bay system and not noticeably affected by the frequencies of the adjacent bays (Points 74, 78, and 82). The transmission of response is likely interrupted by the bays’ columns along grid line C, which are along the exterior beam of the other bays, and not at the corners of the panels. This observed behavior supports DG11 procedures for not including portions of the floor interrupted by columns in this manner in the floor length and floor width parameters for calculating effective panel weight participating in vibration.

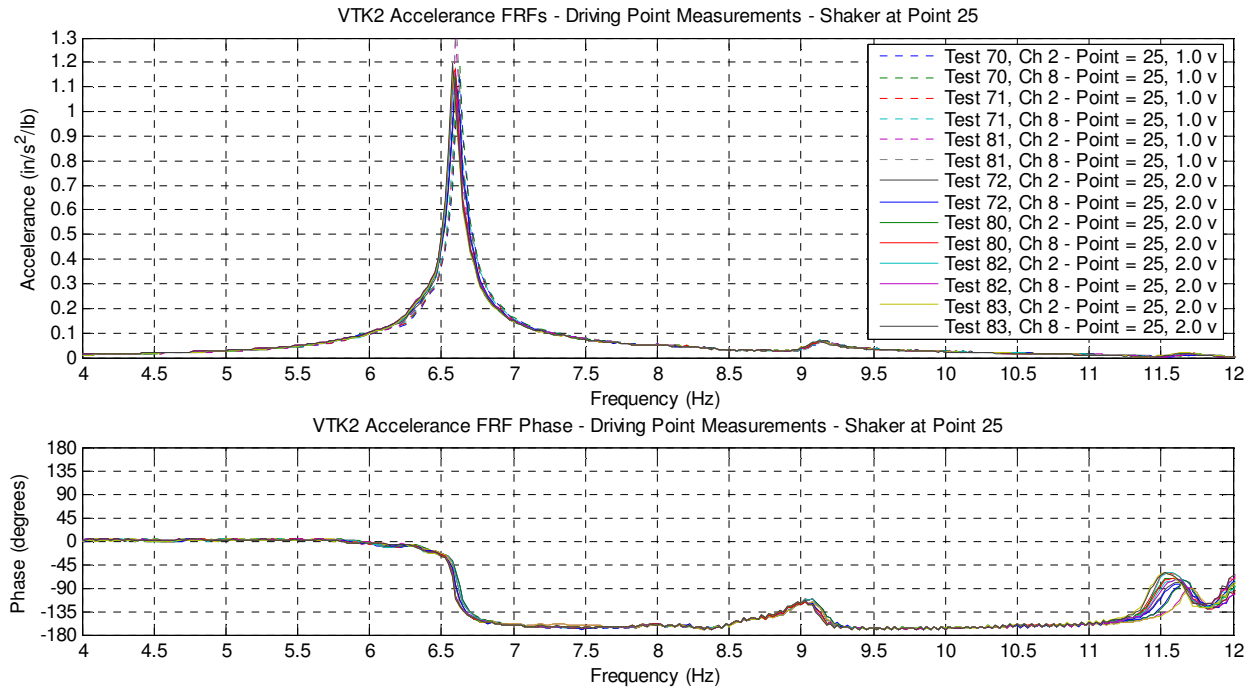


Figure 3.83: VTK2 Driving Point Accelerance FRFs (Point 25)

Table 3.26: VTK2 Point 25 – Driving Point Curve Fit Estimated Frequencies and Damping

Frequency (Hz)	Damping (%)
6.59	0.60
9.05	1.01

VTK2 Point 74 – The next location presented is excitation at Point 74 (mid-bay C/D-4/6), an exterior bay with several unique boundary conditions (Figure 3.74). The edge beam along grid line D is part of the moment frame spanning the short direction of the building. Because of the bay’s location adjacent to the end-bay containing Point 21, the bay’s interior girder actually frames into the edge beam of Point 21’s bay rather than framing into a column. The column for this corner of the bay is roughly at the three-quarter point of the edge beam. The effect this has on the behavior of the bay is increased flexibility on the interior girder boundary of the bay. Consequently, one of the lowest dominant frequencies for an exterior bay, 6.950 Hz, was measured at this location. The magnitude and phase of eight driving point accelerance FRFs taken at this location are presented in Figure 3.84. The 6.950 Hz dominant peak has an accelerance magnitude of 0.59 in/s²/lb of input force.

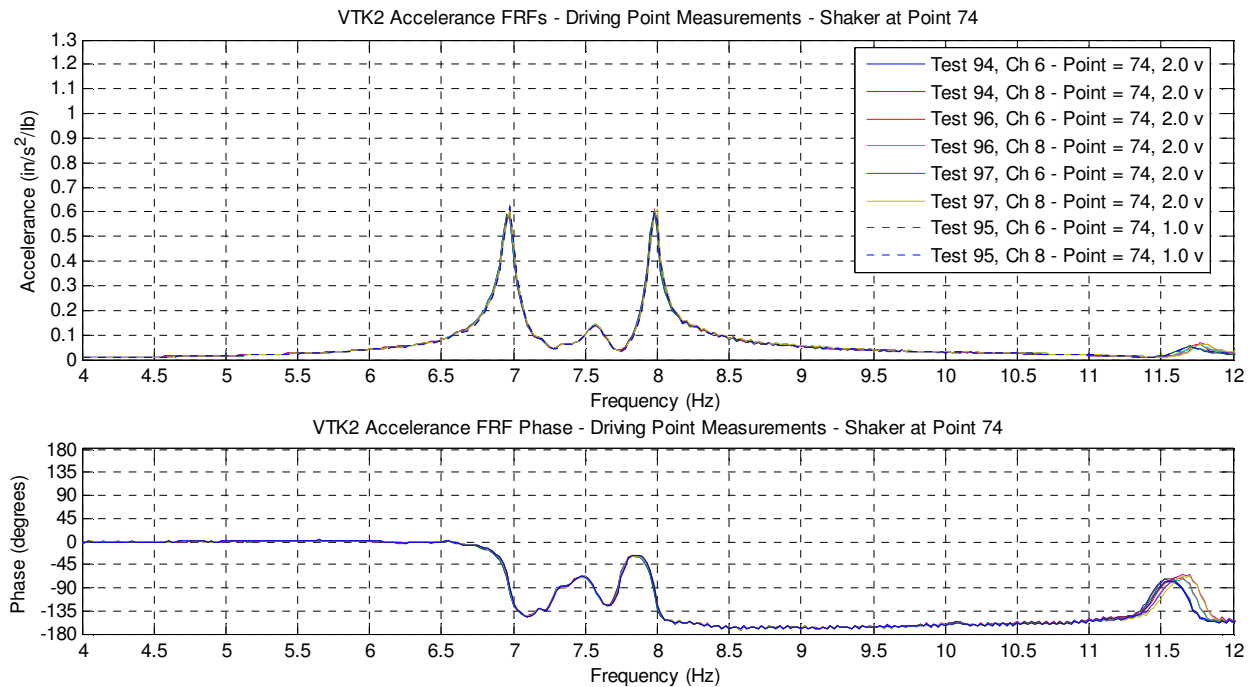


Figure 3.84: VTK2 Driving Point Accelerance FRFs (Point 74)

Another interesting property of the accelerance FRF in Figure 3.84 is the second peak frequency at 7.975 Hz, which has a magnitude nearly equal to the lower frequency peak (0.60 in/s²/lb of input force). This higher frequency peak is also a product of the interior girder framing, and corresponds with the dominant frequency of Point 78, the adjacent bay that shares this boundary. Despite nearly equal magnitudes at the peak, the lower frequency is still considered the dominant frequency because it is more susceptible to excitation from walking excitation. While the 6.950 Hz frequency could be excited by the third harmonic of a 2.32 steps per second footfall pace, the 7.975 Hz frequency could only be excited by the fourth harmonic, a considerably smaller applied force.

The half power estimate of damping at the 6.950 Hz peak dominant frequency was 0.65% of critical, which was in excellent agreement with the MDOF curve fit estimate of 0.62% shown in Table 3.27. The half power estimate of damping for the second peak at 7.975 Hz was 0.50% of critical, which is also in excellent agreement with the MDOF curve fit estimate. Included in Table 3.27 are several other identified participating frequencies and damping ratios estimated in the curve fit process, although they are much smaller in magnitude and correspond to significant or dominant frequencies of the surrounding adjacent bays.

Table 3.27: VTK2 Point 74 – Driving Point Curve Fit Estimated Frequencies and Damping

Frequency (Hz)	Damping (%)
6.97	0.62
7.16	0.44
7.36	0.50
7.59	0.91
7.97	0.46

VTK2 Point 78 – The next location presented is excitation at Point 78 (mid-bay C/D-3/4), the interior bay adjacent to the bay containing Point 74 and the two end bays (Figure 3.74). The magnitude and phase of 12 driving point accelerance FRFs taken at Point 78 are presented in Figure 3.85. Similar to the bay containing Point 74, the edge beam of the bay is part of the short direction moment frame. Additionally, the bay’s location next to the end-bays of Points 21 and 25 results in both girders framing into the edge beams of these bays rather than framing into columns. This edge condition is the likely cause for the largest measured peak response of any of the three interior bays, and the fourth largest response of any of the 12 tested bays.

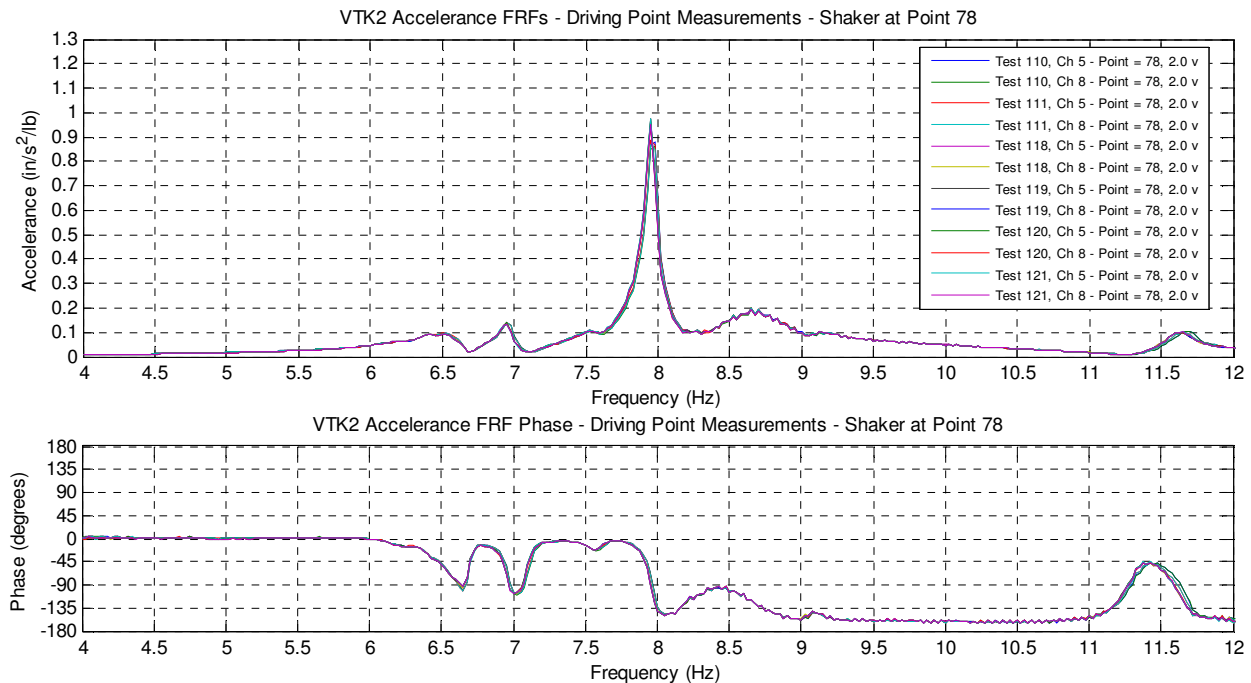


Figure 3.85: VTK2 Driving Point Accelerance FRFs (Point 78)

At the bay’s dominant frequency of 7.950 Hz, the accelerance magnitude was 0.95 in/s²/lb, and the half power estimate of damping was 0.44% of critical. This was the lowest estimated damping ratio for any of the tested bays and was in excellent agreement with the MDOF curve fit estimate of damping at this frequency (0.46%), as shown in Table 3.28 with the

other estimated frequencies and damping values for the driving point accelerance FRFs taken at Point 78.

Table 3.28: VTK2 Point 78 – Driving Point Curve Fit Estimated Frequencies and Damping

Frequency (Hz)	Damping (%)
6.61	1.05
6.95	0.69
7.52	0.90
7.95	0.46
8.64	2.17

VTK2 Point 82 – The next location presented is excitation at Point 82 (mid-bay C/D-1/3), an exterior bay within the three-bay strip bound by grid lines C and D that also include Points 74 and 78 (Figure 3.74). Like those other two bays, this bay also bordered the short direction moment frame and had a girder that framed into the edge beam of the bay containing Point 25. The magnitude and phase of ten driving point accelerance FRFs taken at Point 82 are presented in Figure 3.86, which is one of the more unique FRFs measured. Like Point 74, the accelerance FRF for Point 82 also had dual peaks. The 6.575 Hz identified dominant frequency was the lowest frequency of the exterior bays, although the 0.42 in/s²/lb accelerance magnitude at the peak was substantially smaller than that for many of the other tested bays.

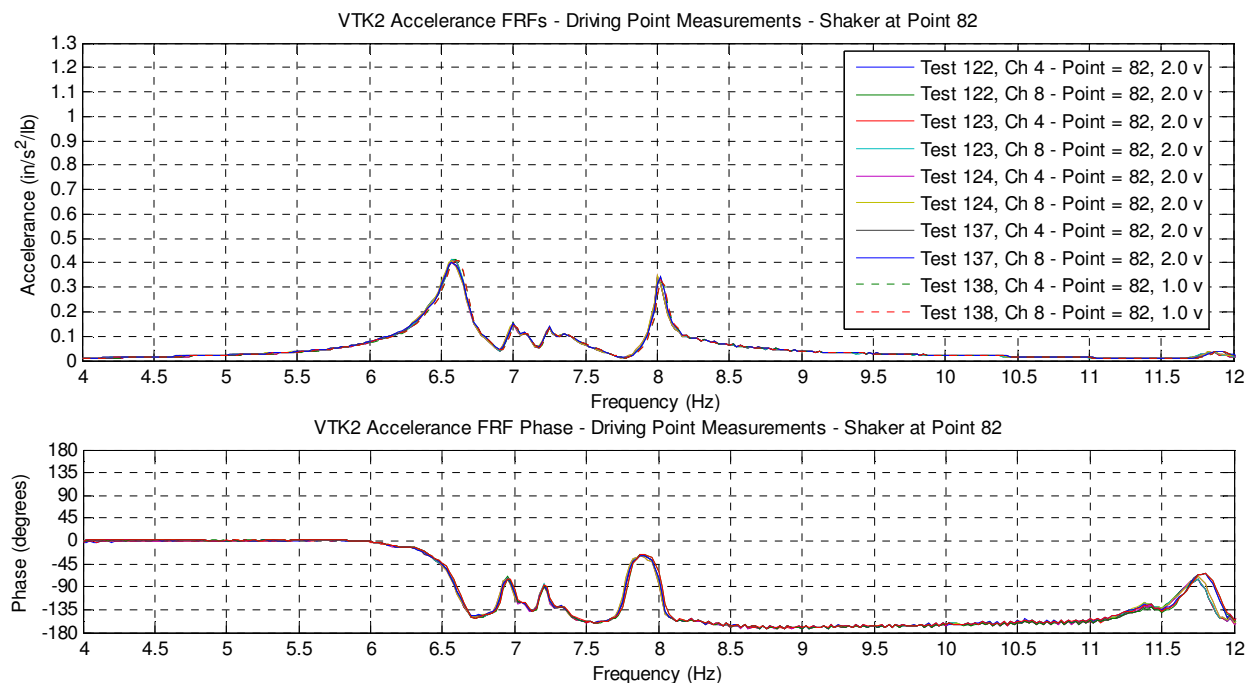


Figure 3.86: VTK2 Driving Point Accelerance FRFs (Point 82)

The half power estimated damping at the 6.575 Hz peak was 1.29% of critical, which was one of the highest damping values of any of the dominant peaks of the tested floor. However, the second peak at 8.00 Hz had an accelerance of 0.34 in/s²/lb and a half power damping estimate of 0.46%, much lower than the estimated damping at the dominant peak. The estimated frequencies and damping from an MDOF curve fit of the driving point accelerance FRFs are presented in Table 3.29. The estimated 1.19% damping at the 6.59 Hz dominant frequency is in good agreement with the half power method estimate (1.29%), as is the 0.47% estimate at the second 8.01 Hz peak. The other participating frequencies from the corresponding dominant frequencies of adjacent bays were also identified in the curve fit and are listed in Table 3.29.

Table 3.29: VTK2 Point 82 – Driving Point Curve Fit Estimated Frequencies and Damping

Frequency (Hz)	Damping (%)
6.59	1.19
6.98	0.48
7.10	0.48
7.24	0.50
7.35	0.60
8.01	0.47

VTK2 Point 126 – The next location presented is excitation at Point 126 (mid-bay D/E-4/6), an exterior bay and the point of excitation for one of the full modal sweeps over a 9-bay area of the floor. The bay containing Point 126 has a floor beam along grid line D that is part of the building’s short direction moment frame (Figure 3.74). Although part of a coverage area, the estimated parameters of the driving point measurements are presented in this section, and the area coverage operating deflection shapes and estimated modes shapes are presented in a later section. Due to the extensive investigation with the shaker in this location, several driving point accelerance FRFs are presented in this section to describe observed behavior of the floor. The magnitude and phase of twelve driving point accelerance FRFs taken at Point 126 at three different levels of excitation over multiple days are presented in Figure 3.87. The first four measurements in Figure 3.87 were taken two days prior to the remaining eight measurements. While the measurements are generally consistent between different levels of excitation, the measurements taken two days prior show a slight difference in location and magnitude of the two significant peaks around 7 Hz and 7.55 Hz (lower frequency and lower magnitude). While the differences are slight, peak magnitudes were less than 10% lower and frequencies one spectral line lower (0.025 Hz), the implication of this phenomenon is the possibility that the properties of the floor change over time.

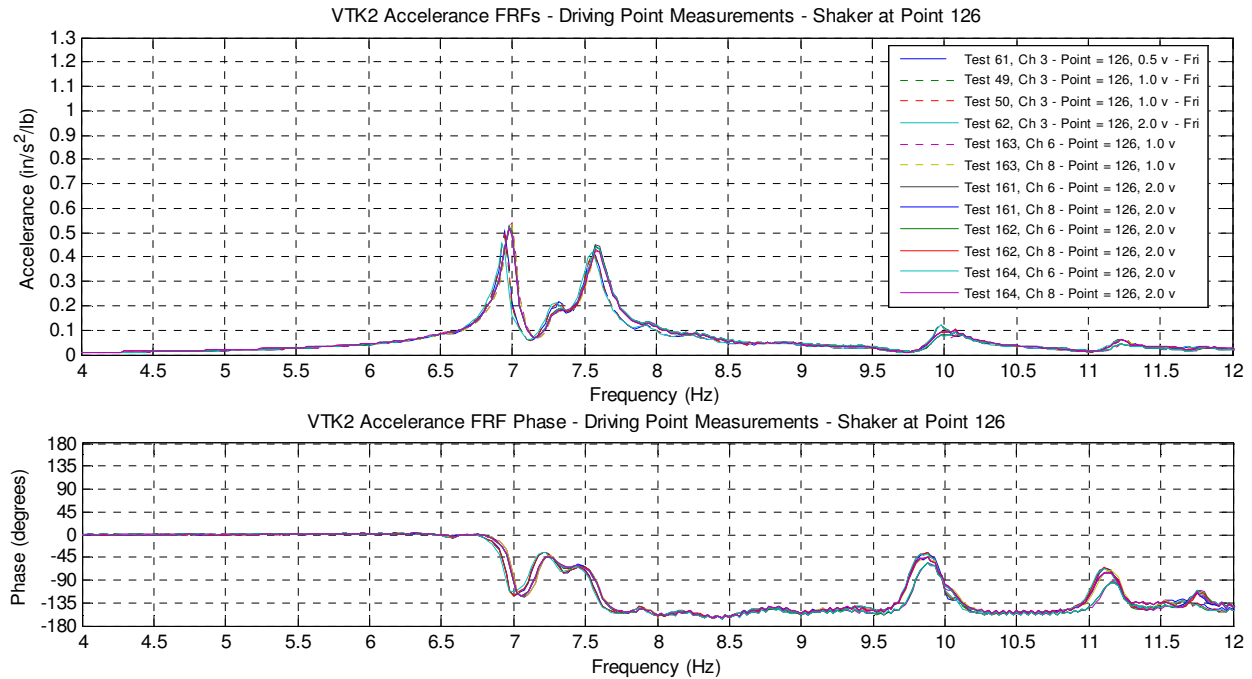


Figure 3.87: VTK2 Multiple Day Driving Point Accelerance FRFs (Point 126)

The magnitude and phase of 35 driving point accelerance FRFs taken at Point 126 during the modal coverage of a 9-bay area of VTK2 are presented in Figure 3.88. These measurements were the redundant driving point accelerance FRFs taken for each measurement while the roving accelerometers were marched across the coverage area of the floor.

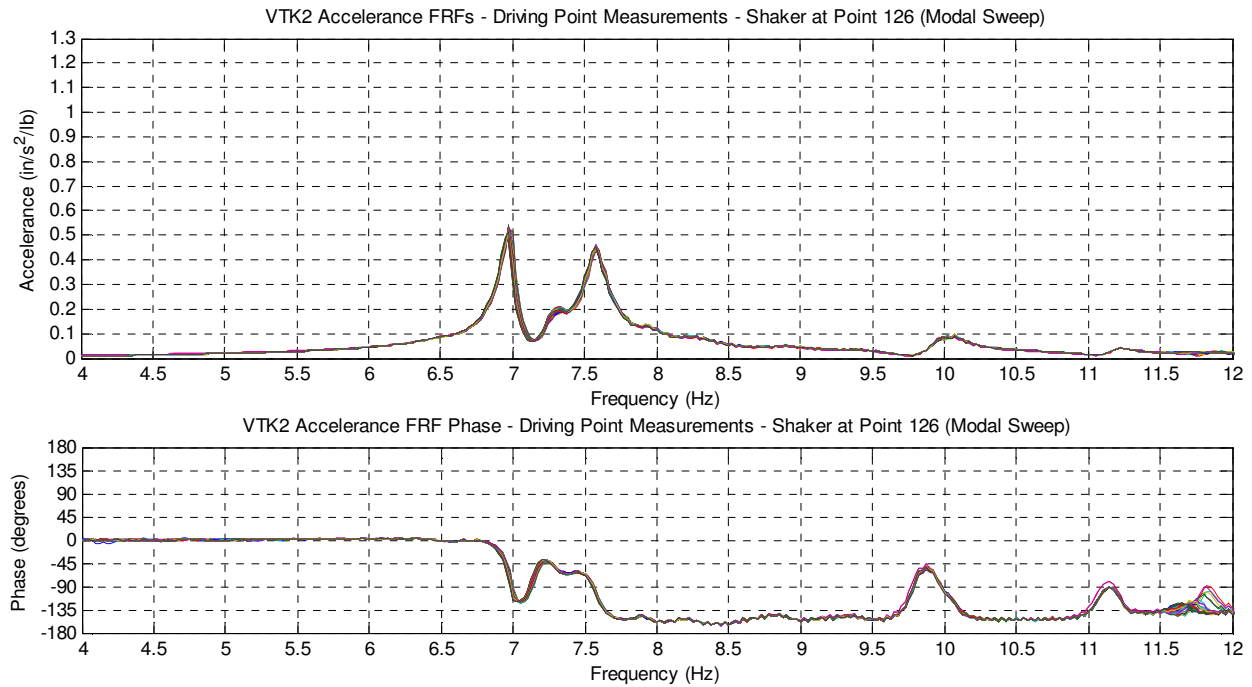


Figure 3.88: VTK2 Driving Point Accelerance FRFs (Point 126 Modal Coverage)

The dominant frequency of the dual peak accelerance FRFs for Point 126 was 6.975 Hz, with an average peak accelerance of 0.49 in/s²/lb of input force. The half power estimate of damping at the 6.975 Hz peak was 0.67% of critical. The second significant peak of the accelerance FRF was 7.575 Hz, which had a slightly lower peak accelerance of 0.45 in/s²/lb of input force and a larger half power estimate of damping of 1.04% of critical. Both of these values are in very good agreement with the estimates of frequency and damping from the MDOF curve fit of the driving point accelerance FRFs presented in Table 3.30, which were 0.60% and 0.97%, respectively.

Table 3.30: VTK2 Point 126 – Driving Point Curve Fit Estimated Frequencies and Damping

Frequency (Hz)	Damping (%)
6.98	0.60
7.33	0.98
7.58	0.97
7.92	0.70
8.22	1.20

Although the 35 driving point accelerance traces in Figure 3.88 seem relatively consistent at the plotted scale, closer inspection reveals the previously demonstrated phenomenon of changing accelerance FRFs over time. Figure 3.89 presents the magnitude and phase of the previously plotted accelerance FRFs but zoomed in on the peak frequencies to illustrate the variability in the 35 measurements. Ideally, all redundant FRFs would lay on top on one another; however this is not the case for the presented measurements. There was only a 12% difference between absolute maximum and minimum accelerance magnitude at the identified 6.975 Hz peak (which was not the peak for some of the later measurements); however there was a 33° spread in phase at the same frequency due to the slowly shifting peak frequency between the first and the last measurements. The variability in accelerance magnitude was typical for redundant measurements at all tested locations; however the variability in phase due to the shifting peaks was much more significant at this location. Only one driving point accelerance FRF is used as a reference measurement for scaling and animating the operating deflection shapes and mode shapes in ME'scope, thus a large difference in phase at the peak frequency will be quite noticeable in the animated shapes. This phase lag may mistakenly be interpreted as severe complex behavior of the floor. It should be noted the 35 accelerance FRFs presented in Figure 3.89 were taken during a modal sweep over an approximately four hour period, from 1:30pm to 4:30pm. Because the VTK2 building was not yet fully enclosed by exterior cladding or

windows, the floor was somewhat exposed to the outside conditions including wind, ambient temperature, and differential exposure of portions of the floor to the setting sun. All of these factors can change the properties of the floor slightly. Although the change in frequencies may be slight, the effect on the shifting of the peak is large enough to make a correct interpretation of the measurements difficult. This phenomenon is good justification for performing modal sweeps over a desired area in a single session to avoid the potentially significant changes in floor properties over time.

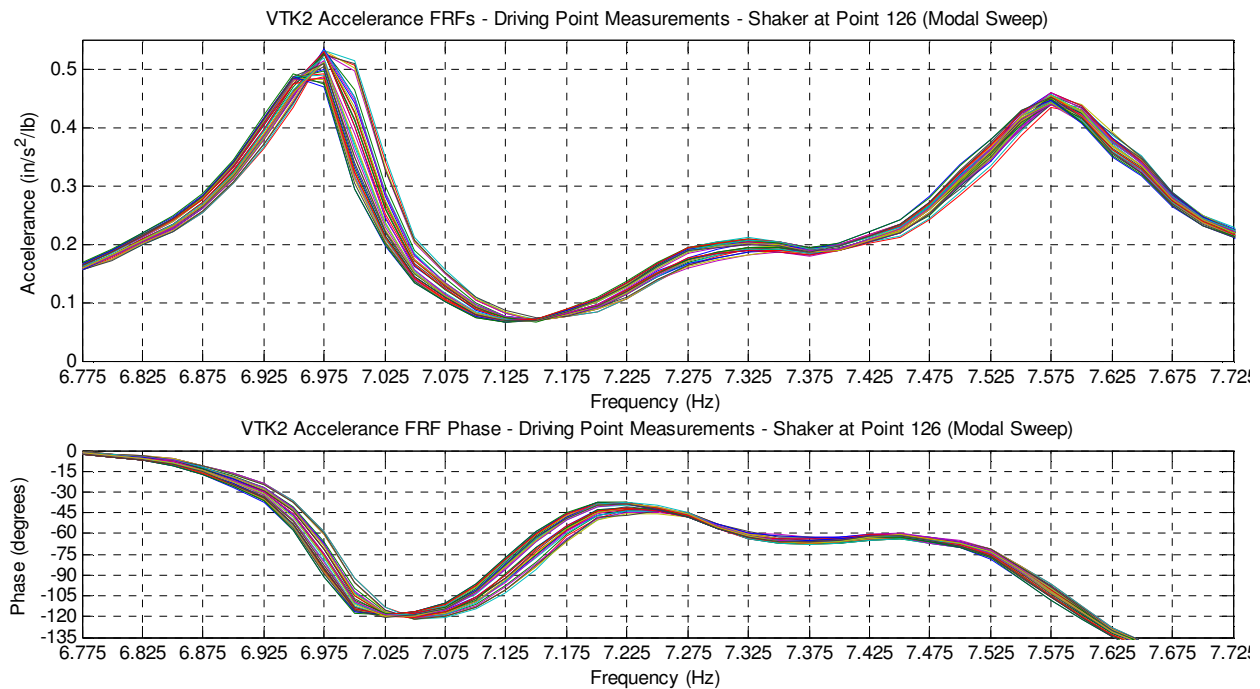


Figure 3.89: VTK2 Driving Point Accelerance FRFs (Point 126 Modal Coverage)

VTK2 Point 130 – The next location presented is excitation at Point 130 (mid-bay D/E-3/4), an interior bay and one of three points of excitation for the three-bay strip coverage area bounded by grid lines D and E (Figure 3.79). The bay containing Point 130 has a floor beam along grid line D that is part of the building’s short direction moment frame (Figure 3.74). The magnitude and phase of eight driving point accelerance FRFs taken at Point 130 during the modal sweep of the three-bay strip are presented in Figure 3.90. The presented accelerance FRFs show one dominant peak for the excitation location at 7.950 Hz, and multiple other participating frequencies of much smaller amplitudes. The average accelerance at the identified 7.950 Hz dominant peak was 0.56 in/s²/lb of input force, and the half power estimate of damping at this peak was 0.50% of critical. These estimated values were in excellent agreement with the MDOF

curve fit of the accelerance FRFs presented in Table 3.31, which also had an estimated damping value of 0.50% at 7.96 Hz.

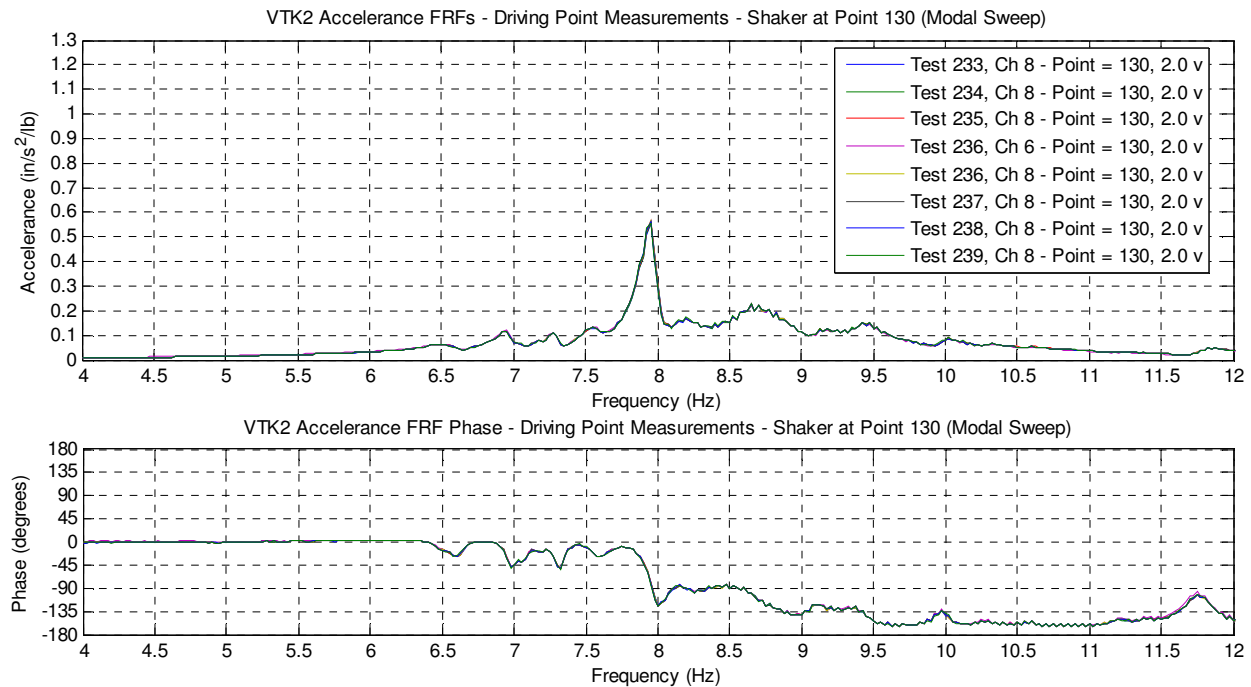


Figure 3.90: VTK2 Driving Point Accelerance FRFs (Point 130)

Table 3.31: VTK2 Point 130 – Driving Point Curve Fit Estimated Frequencies and Damping

Frequency (Hz)	Damping (%)
6.61	1.20
6.97	0.71
7.19	0.50
7.30	0.55
7.57	0.75
7.96	0.50
8.18	1.20
8.67	1.58

VTK2 Point 134 – The next location presented is excitation at Point 134 (mid-bay D/E-1/3), an exterior bay and the other point of excitation for the modal sweep over a 9-bay area of the floor. Like the respective bay on the other side of the building containing Point 126, the bay containing Point 134 has a floor beam along grid line D that is part of the building’s short direction moment frame (Figure 3.74). The magnitude and phase of 34 driving point accelerance FRF measurements taken at Point 134 during the modal sweep over the 9-bay area are presented in Figure 3.91. In contrast to the measurements over the same area taken when the shaker was located at Point 126, the 34 driving point accelerance FRFs for Point 134 were very consistent. Unlike the dual-peak FRFs of Point 126 and other similarly configured bays, the accelerance

FRFs for Point 134 have a single dominant peak frequency at 7.20 Hz, which has an average accelerance magnitude of 0.68 in/s²/lb of input force.

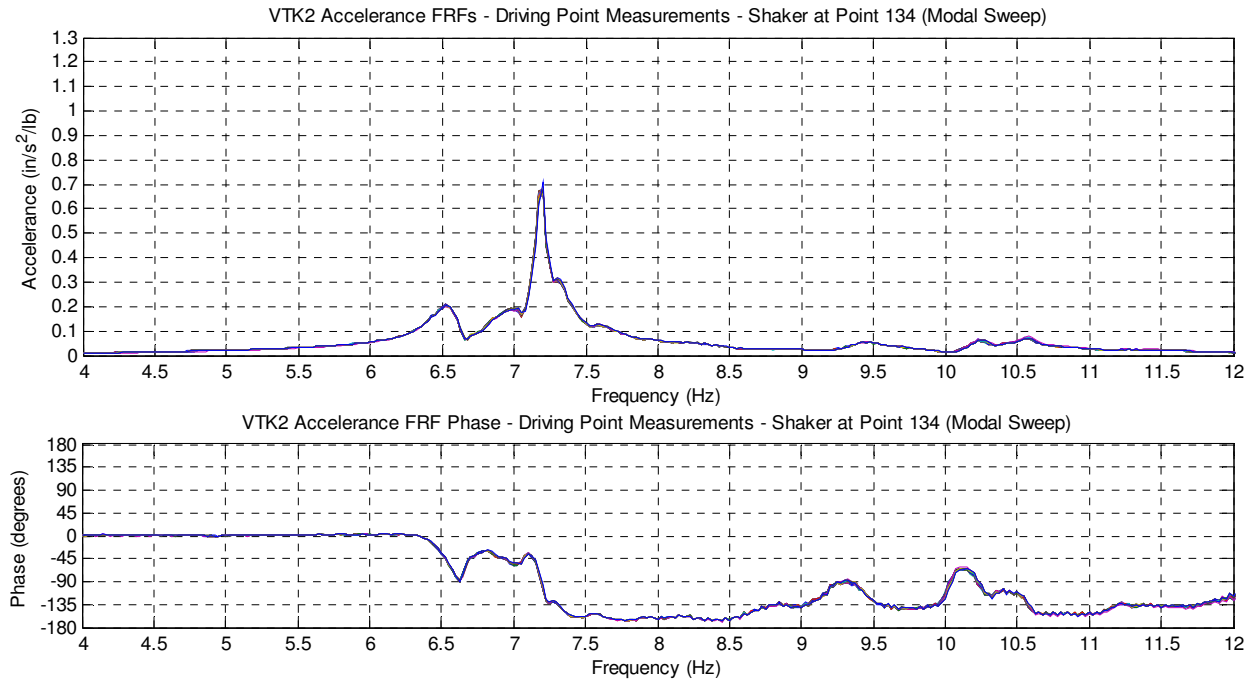


Figure 3.91: VTK2 Driving Point Accelerance FRFs (Point 134)

The half power estimate of damping at the 7.20 Hz dominant peak was 0.50% of critical, which was in excellent agreement with the estimated frequency and damping of the MDOF curve fit of the driving point accelerance FRFs presented in Figure 3.91. Another frequency of interest in the accelerance FRFs is the smaller peak at 6.57 Hz, which corresponds with the previously identified dominant frequency of the adjacent bay containing Point 82 (adjacent in a direction parallel to the direction of the deck ribs). The curve fit estimated damping for this frequency, 1.39% of critical, is also in agreement with previous half power and curve fit estimates for excitation at Point 82.

Table 3.32: VTK2 Point 134 – Driving Point Curve Fit Estimated Frequencies and Damping

Frequency (Hz)	Damping (%)
6.57	1.39
7.01	0.61
7.19	0.49
7.32	0.52
7.60	0.95

VTK2 Point 178 – The next location presented is excitation at Point 178 (mid-bay E/F-4/6), another exterior bay of the floor system, however this exterior bay’s interior girder along grid line 4 is part of the building’s long direction moment frame (Figure 3.74). The magnitude and phase of six driving point accelerance FRFs taken at Point 178 are presented in Figure 3.92. By far, this excitation location had the largest magnitude peak of all of the tested bays, with the exception of the two isolated end bays containing Points 21 and 25. The accelerance FRF for Point 178 has a clearly dominant frequency of 7.275 Hz, with an accelerance magnitude of 1.24 in/s²/lb of input force. Only one other significant frequency was obvious in the accelerance FRF, 6.975 Hz, which corresponded to the dominant frequency of the adjacent bay parallel to the deck ribs that contained Point 126. This observed cross-participation between bays adjacent to one another in the direction of the deck ribs further highlights the tendency for these types of in-situ floors to transmit vibration in this direction. The estimated frequencies and damping from a MDOF curve fit of the driving point accelerance FRFs is presented in Table 3.33, which also identified the two frequencies. The half power estimate of damping for the 7.30 Hz dominant peak was 0.49% of critical, which was in excellent agreement with the curve fit values. The curve fit estimated damping of 0.63% of critical for the 6.98 Hz frequency is also in excellent agreement with the half power and curve fit estimated damping for excitation at Point 126, which was 0.67% and 0.60%, respectively.

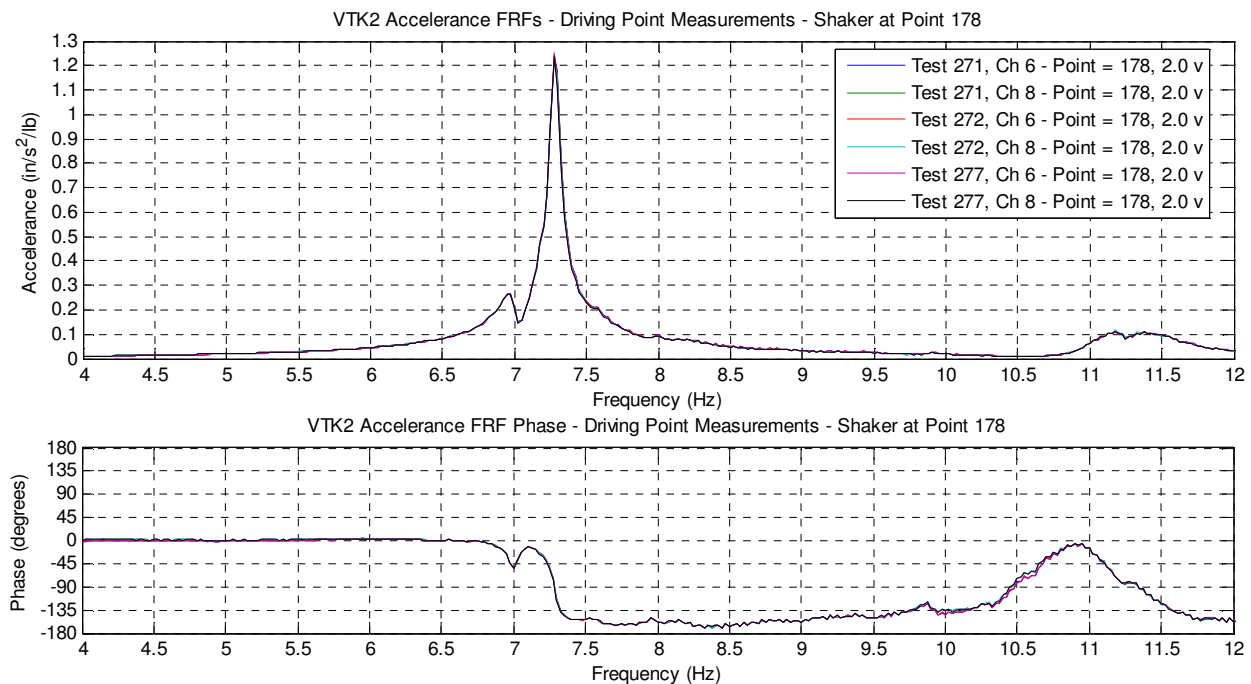


Figure 3.92: VTK2 Driving Point Accelerance FRFs (Point 178)

Table 3.33: VTK2 Point 178 – Driving Point Curve Fit Estimated Frequencies and Damping

Frequency (Hz)	Damping (%)
6.98	0.63
7.29	0.50

VTK2 Point 182 – The next location presented is excitation at Point 182 (mid-bay E/F-3/4), the last of the tested interior bays. The girders that span the bay containing Point 182 along grid line’s 3 and 4 are part of the building’s long direction moment frame (Figure 3.74), providing additional restraint along the ends of the bay. The magnitude and phase of ten driving point accelerance FRFs taken at Point 182 are presented in Figure 3.93. Similar to the adjacent interior bay containing Point 130, the presented accelerance FRFs for Point 182 show one dominant peak at 8.20 Hz and multiple other participating frequencies of much smaller amplitudes. Unlike Point 130, the 8.20 peak had a smaller amplitude of accelerance, 0.42 in/s²/lb of input force, and the width of the peak indicates a much higher level of damping. The half power estimate of damping at the dominant peak was 1.31%, the highest estimated damping value of any of the dominant peaks of the tested bays. This value was in excellent agreement with the estimated frequency and damping values from the MDOF curve fit of the accelerance FRFs presented in Table 3.34, which had an estimated damping value of 1.30% at 8.17 Hz.

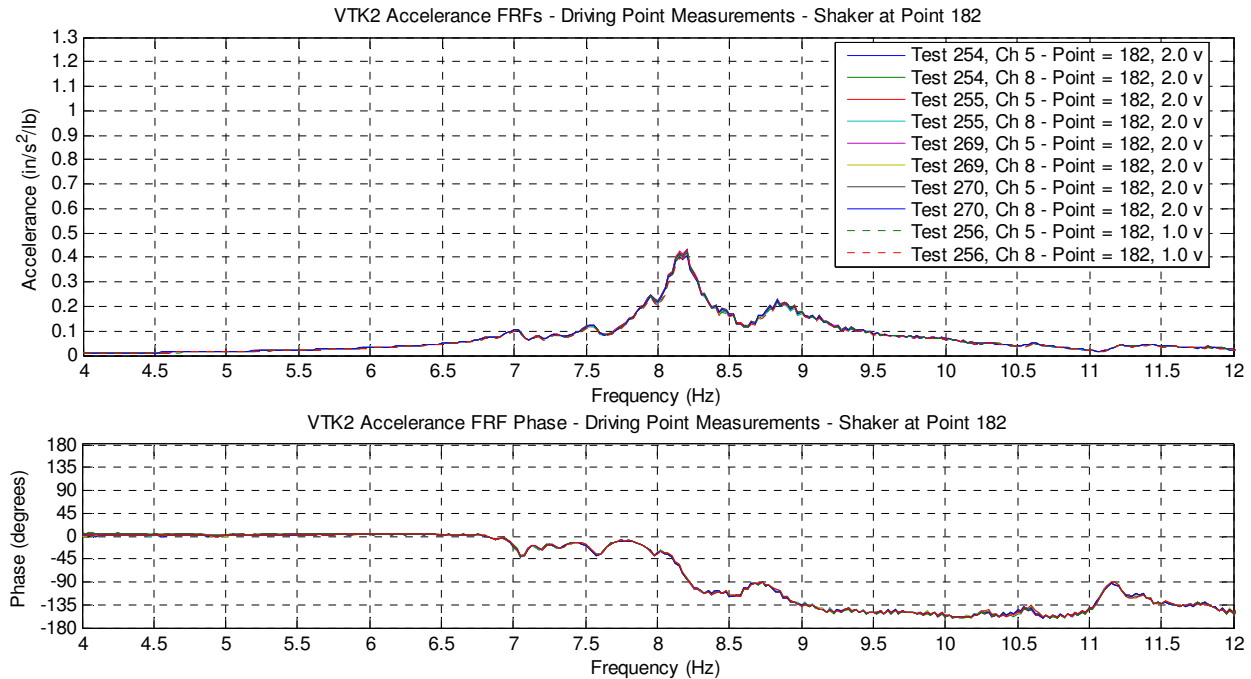


Figure 3.93: VTK2 Driving Point Accelerance FRFs (Point 182)

Table 3.34: VTK2 Point 182 – Driving Point Curve Fit Estimated Frequencies and Damping

Frequency (Hz)	Damping (%)
7.05	0.59
7.18	0.55
7.31	0.49
7.55	0.97
7.94	0.56
8.17	1.30
8.82	1.40

VTK2 Point 186 – The next location presented is excitation at Point 186 (mid-bay E/F-1/3), an exterior bay that also has its interior girder as part of the long direction moment frame (Figure 3.74). The magnitude and phase of ten driving point accelerance FRFs taken at Point 186 are presented in Figure 3.94. The identified dominant frequency of 7.025 Hz for Point 186 has the second largest peak accelerance of any of the exterior bays, 0.90 in/s²/lb of input force, second only to the bay containing Point 178. Again, the other significant peak in the FRF is at 7.175 Hz, which corresponds to the dominant frequency of the adjacent bay containing Point 134.

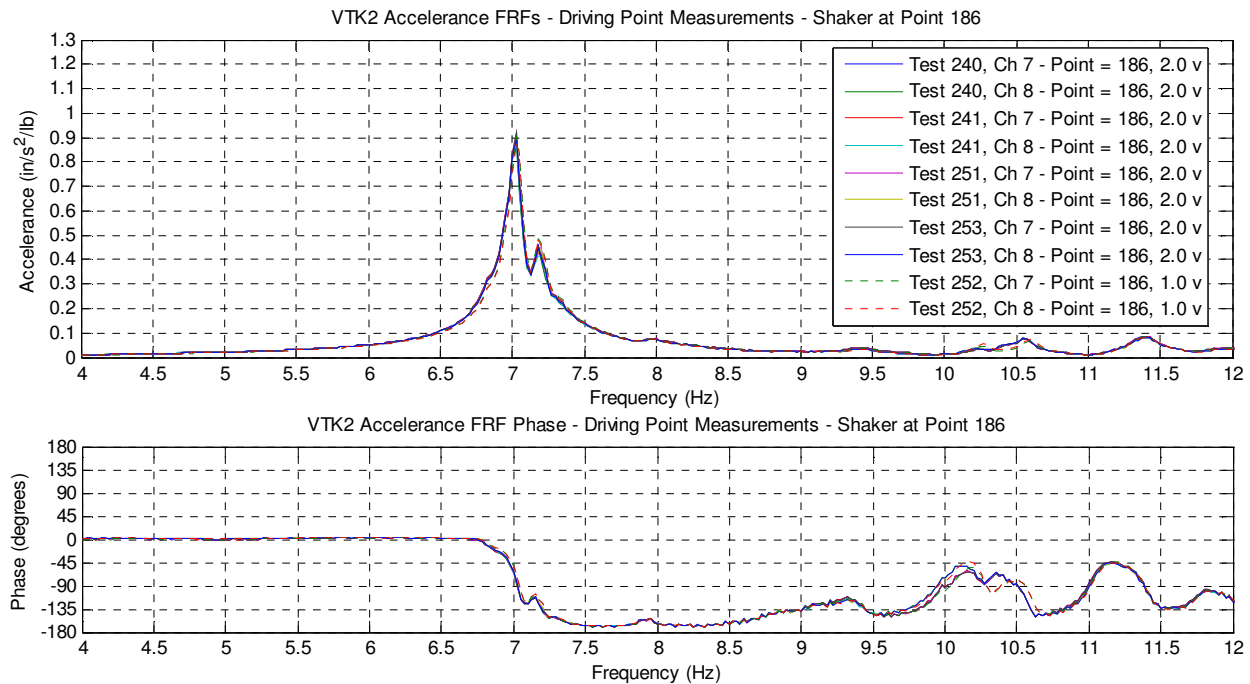


Figure 3.94: VTK2 Driving Point Accelerance FRFs (Point 186)

The half power estimate of damping for the 7.025 Hz dominant frequency was 0.64% of critical. This value was in excellent agreement with the estimated 0.65% damping ratio from a MDOF curve fit of the driving point accelerance FRFs. This value and the other estimated frequencies and damping values are shown in Table 3.35. The secondary 7.18 Hz frequency was

identified; however the estimated 0.90% damping value was considerably higher than other estimates of damping for the corresponding dominant frequency of Point 134.

Table 3.35: VTK2 Point 186 – Driving Point Curve Fit Estimated Frequencies and Damping

Frequency (Hz)	Damping (%)
7.03	0.65
7.18	0.90
7.95	0.95

VTK2 Point 230 – The final tested location presented is excitation at Point 230 (mid-bay F/G-4/6), an exterior bay with some unique framing. Like other exterior bays towards the middle of the building, this bay has its interior girder as part of the long direction moment frame; however the presence of a low roof at the edge of the building creates additional framing members towards the exterior of the bay (see framing for the bay containing Point 230 in Figure 3.74). The magnitude and phase of three driving point accelerance FRFs taken at Point 230 at lower levels of excitation than other tested bays of the floor are presented in Figure 3.95.

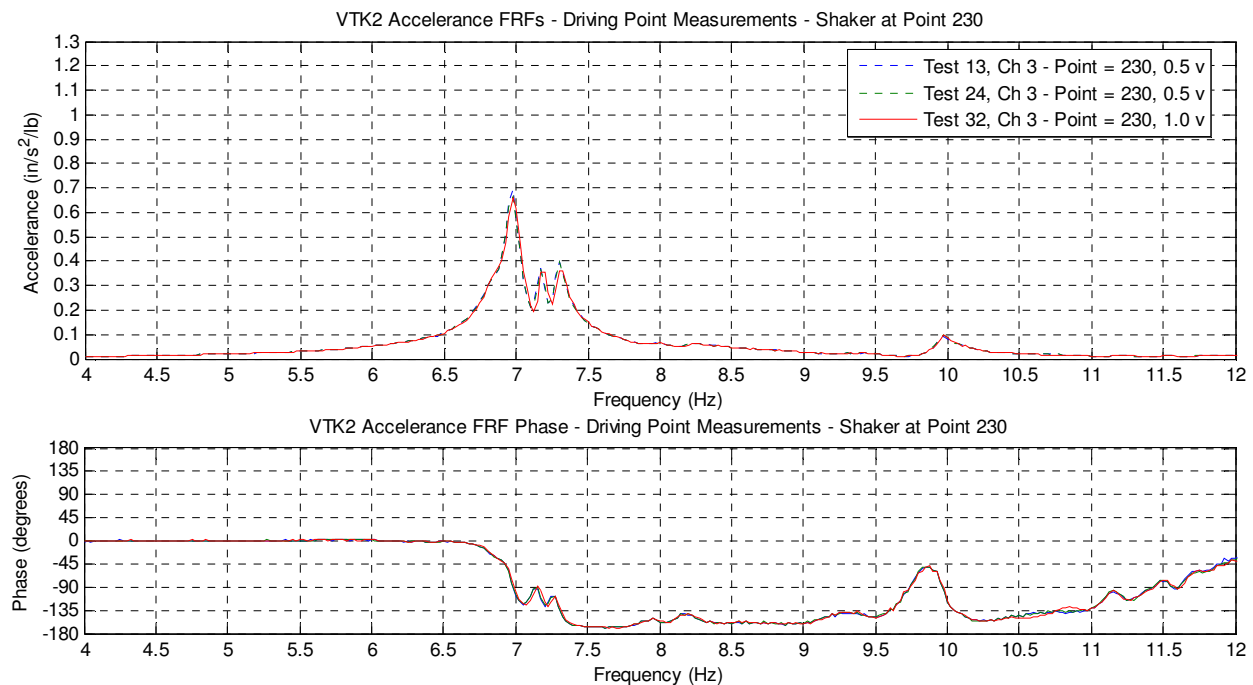


Figure 3.95: VTK2 Driving Point Accelerance FRFs (Point 230)

The driving point accelerance FRFs of Figure 3.95 are interesting, as they contain one dominant frequency at 6.975 Hz and two other significant contributing frequencies at 7.175 Hz and 7.30 Hz. The 7.30 Hz frequency undoubtedly corresponds to a contributing frequency from the adjacent bay containing Point 178, which has a dominant frequency of 7.275 Hz. Point 178

is in the bay immediately adjacent to Point 230 in the direction of the deck ribs. The identified dominant frequency of 6.975 Hz for Point 230 has a peak accelerance of 0.66 in/s²/lb of input force, and a half power estimated damping ratio of 0.74% of critical. The estimated frequencies and damping from a MDOF curve fit of the driving point accelerance FRFs are presented in Table 3.36. The 0.70% curve fit estimated damping at 6.98 Hz is in excellent agreement with the half power estimate, and the damping estimate at the 7.29 Hz contributing peak is in good agreement with its respective driving point accelerance FRF estimates (0.59% versus 0.50%).

Table 3.36: VTK2 Point 230 – Driving Point Curve Fit Estimated Frequencies and Damping

Frequency (Hz)	Damping (%)
6.98	0.70
7.18	0.60
7.29	0.59
7.96	0.95
8.22	1.28

VTK2 Multi-Reference Area Coverage Measurements and Analysis – With the shaker located at Point 126 and Point 134, accelerance FRF measurements were taken over the 9-bay coverage areas shown in Figures 3.76 and 3.78, respectively. These were the most extensive multi-reference measurements taken for any of the tested floors. A third point of excitation, Point 130, had smaller (but overlapping) measurement coverage of the three-bay strip that included the bays containing Points 126 and 134 shown in Figure 3.79. The results of this investigation are presented in this section. First, the operating deflection shapes from 9-bay coverage areas are presented for the two reference DOFs, including commentary on important observed behavior of the floors. This section is followed by the multi-reference MDOF curve fitting of these two sets of measurements, including the estimated frequencies, damping, and mode shapes. Subsets of the 9-bay area measurements for Points 126 and 134 representing the smaller three-bay strip coverage area are combined with a set of measurements from forcing at Point 130 for a similar multi-reference analysis. The operating deflection shapes and mode shapes for this three-bay strip analysis are also presented and compared with the 9-bay area coverage analyses.

9-Bay Area Coverage Accelerance FRFs and ODSs - The superimposed accelerance FRFs for the entire 9-bay coverage area from forcing at Points 126 and 134 are presented in Figure 3.96. It is interesting to note the difference in participating frequencies between the two excitation locations. Clearly one location has much greater participation at certain frequencies than the other, implying a single set of measurements over the given coverage area could result in a poor estimation of some mode shapes due to weak participation at that forcing location.

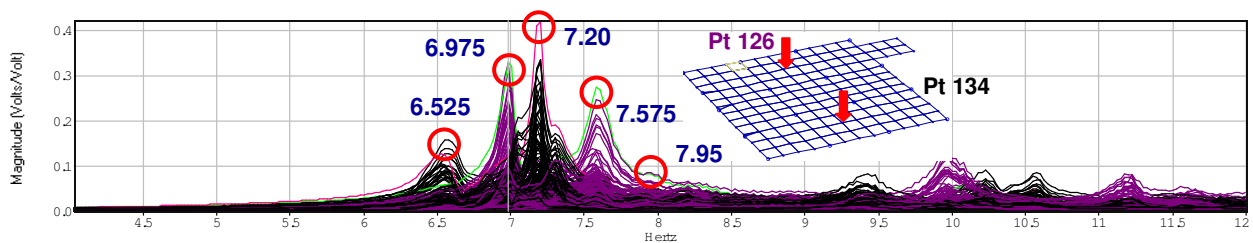


Figure 3.96: VTK2 9-Bay Area Multi-Reference FRFs (Forcing at Points 126 and 134)

The five identified frequencies in Figure 3.96 were chosen for display of the operating deflection shapes of the 9-bay coverage area to demonstrate the difference in ODSs from different points of excitation. These frequencies represent dominant and significant peaks observed in the two sets of accelerance FRFs. The 7.95 Hz frequency, while not particularly

significant in either of the two sets of acceleration FRFs, is the dominant frequency of the bay containing Point 130. The shapes at this frequency are included in this discussion for comparison with the shapes from excitation at Point 130 presented later in this section. The operating deflection shapes of the five selected frequencies are presented in Figure 3.97 in both static surface and persistent centerline format.

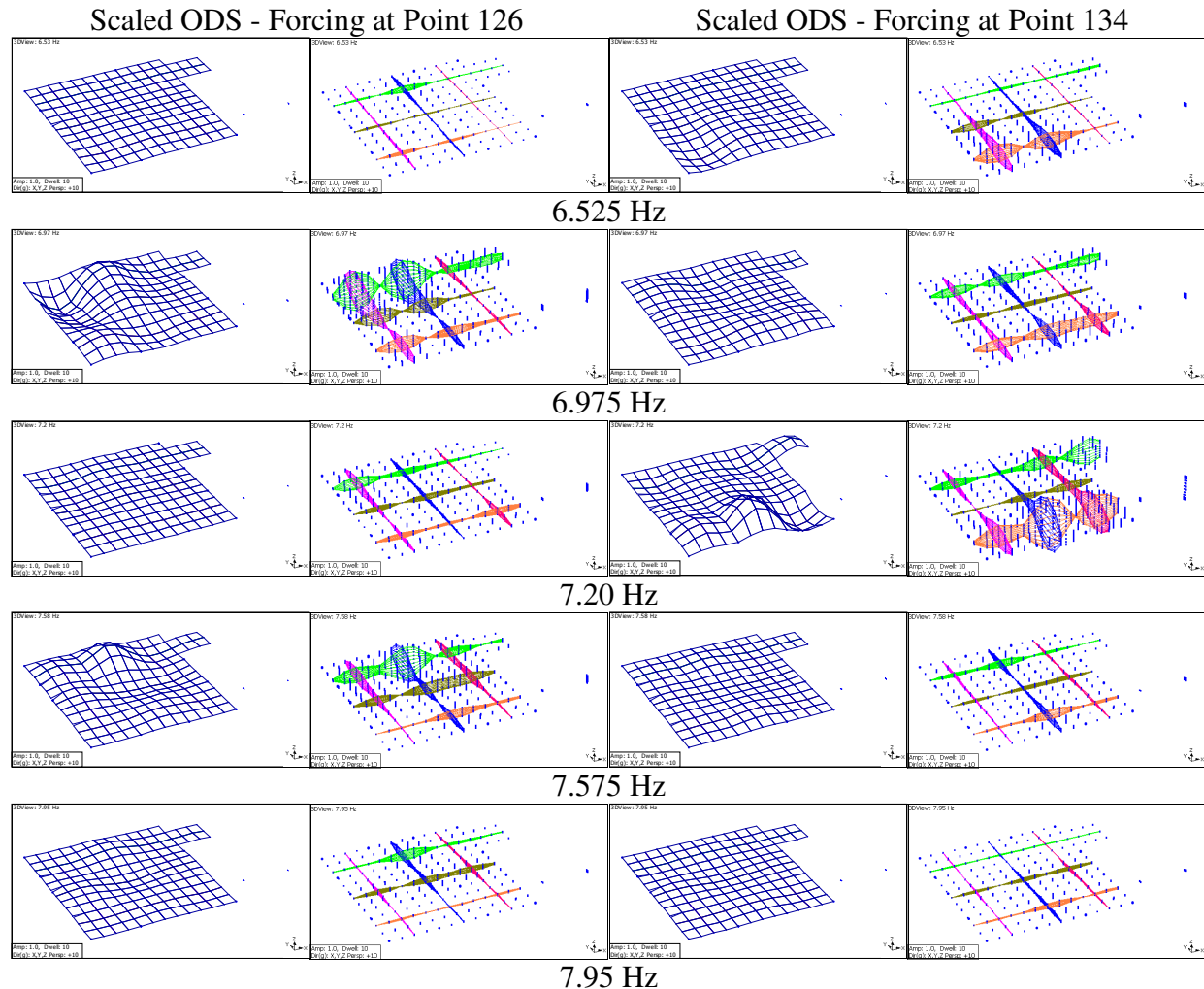


Figure 3.97: VTK2 9-Bay Area ODSs from Forcing at Points 126 and 134

The ODSs in Figure 3.97 are scaled to reflect the relative magnitude of response between shapes, which is based on the relative magnitudes of the acceleration FRFs at the chosen frequency for the particular reference. Presenting the shapes in this manner allows several comparisons. First, the scaled format indicates the magnitude of response due to forcing at a certain frequency, as well as the area of the floor participating in the response. Stated differently, this illustrates the area susceptible to vibration serviceability problems due to

walking excitation within the bay. As expected, the largest response and greatest affected area result from forcing a bay at its dominant frequency, such as 6.975 Hz for Point 126 and 7.20 Hz for Point 134. The second comparison available from the scaled format is the relative strengths of shapes derived from each driving point. The difference in the ODSs at the dominant frequencies of the two forcing locations (6.975 Hz and 7.20 Hz) highlights a common dilemma for floor vibration testing of in-situ floors. In this case, the small response from driving the floor at the other bay's dominant frequency yields a weak shape. The weaker the response at a peak frequency, the lower the reliability of a curve fit estimate of the frequency, damping, and mode shape. The implication of this is that a single reference set of measurements may not adequately excite all the frequencies of interest over a given coverage area of a floor, resulting in mode shapes that are not accounted for in the curve fit process.

The displayed ODSs of Figure 3.97 illustrate interesting behavior of the floor when driven at the significant frequencies of interest that can be useful for evaluation of vibration serviceability. Note that when the floor is driven at the dominant frequency of the bay of excitation, such as 6.975 Hz for Point 126 or 7.20 Hz for Point 134, the driving point is the location of maximum response. What is interesting for the Point 126 ODS at 6.975 Hz is that this behavior even seems to hold true despite sharing a common dominant frequency with the adjacent bay containing Point 74. Although the response at Point 74 is large, it is still roughly equal to or less than the response at the Point 126 driving point. This phenomenon was previously observed on NOC VII-18, and to a lesser extent on NOC VII-24. The important implication of this behavior for floor testing and evaluation purposes is that the driving point measurement essentially serves as an upper bound of floor response at resonance. As such, a collection of mid-bay driving point measurements may be adequate to define the participating frequency content and upper bound response magnitudes for excitation within each tested bay of a floor system.

Some additional observations can be made on the response of various portions of the floor system when driven at resonance. For the dominant frequency ODSs (6.975 Hz for Point 126 and 7.20 Hz for Point 134), there is significant response at spandrel girders. Point 124 (the midspan of the spandrel girder) had a response magnitude equal to 18% of the mid-bay response magnitude at Point 126 when the bay was driven at its 6.975 Hz dominant frequency. Similarly, Point 136 (also the midspan of the spandrel girder) had a response magnitude equal to 26% of

the mid-bay response magnitude at Point 134 when the bay was driven at its 7.20 Hz dominant frequency. This relatively large response at the spandrel members is likely a product of the slip connections installed between the slab and the exterior light gage steel framing, which provides some additional stiffness to the edge of the floor but not nearly enough to consider the exterior boundaries of the floor rigid. The various ODSs in Figure 3.97 also illustrate the generally smaller response around the members of a bay that are part of the building's moment frames.

During the modal sweeps over the 9-bay coverage area, mid-bay measurements were also taken in two non-tested bays, F/G-1/3 (Point 238) and G/H-1/3 (Point 290). The response at these locations can be seen on the right side of the ODSs of Figure 3.97. The one notable response of interest is at Point 290 for the displayed ODS at 7.20 Hz (forcing at Point 134). This point, which is three bays and 90 ft away from the point of excitation, has considerable response at 7.20 Hz. The response magnitude of this bay was 46% of the driving point response magnitude at that frequency, quite large given the distance. Although driving point measurements were not taken within this bay to verify its frequency content, the large response of this bay is likely caused by a shared 7.20 Hz dominant frequency. This conclusion is reasonable considering the bay containing Point 290 has the identical framing and nearly identical boundary conditions as the bay containing Point 134, including an edge beam that is part of the building's short direction moment frame.

Multi-Reference Area Coverage MDOF Curve Fitting and Mode Shapes – The two sets of accelerance FRFs in Figure 3.96 were curve fit using the MDOF multi-reference curve fitting techniques previously described. Eight frequencies of interest were curve fit in the process, as opposed to the five frequencies displayed as operating deflection shapes in the previous section. The relative shape strengths for each of the two reference DOFs are presented in Table 3.37 and the most strongly represented reference DOF used for curve fitting are highlighted. The multi-reference curve fit estimated frequencies and damping ratios are also presented in Table 3.37, and the corresponding curve fit mode shapes are presented in Figure 3.98 in both static surface and persistent centerline format. It is not surprising to note the reference DOF used for curve fit estimates at each frequency correspond to the set of accelerance FRFs with the strongest response at the given frequency, such as Point 126 for 6.98 Hz and 7.58 Hz, or Point 134 for 6.56 Hz and 7.20 Hz. As expected, the previous curve fit estimated

frequencies and damping from the driving point measurements of Point 126 and 134 were in excellent agreement with the values of Table 3.37.

Table 3.37: VTK2 9-Bay Area Multi-Reference Curve Fitting Shape Strengths and Estimated Frequencies and Damping

Mode	Frequency (Hz)	Point 126	Point 134	Frequency (Hz)	Damping (%)
1	6.56	2.7	9.4	6.56	1.35
2	6.98	7.8	3.9	6.98	0.56
3	7.03	10.0	8.3	7.03	0.50
4	7.19	0.9	7.8	7.19	0.45
5	7.3	2.0	3.0	7.30	0.42
6	7.58	10.0	3.4	7.58	0.94
7	7.97	1.1	0.8	7.97	0.54
8	8.21	1.7	1.2	8.21	0.67

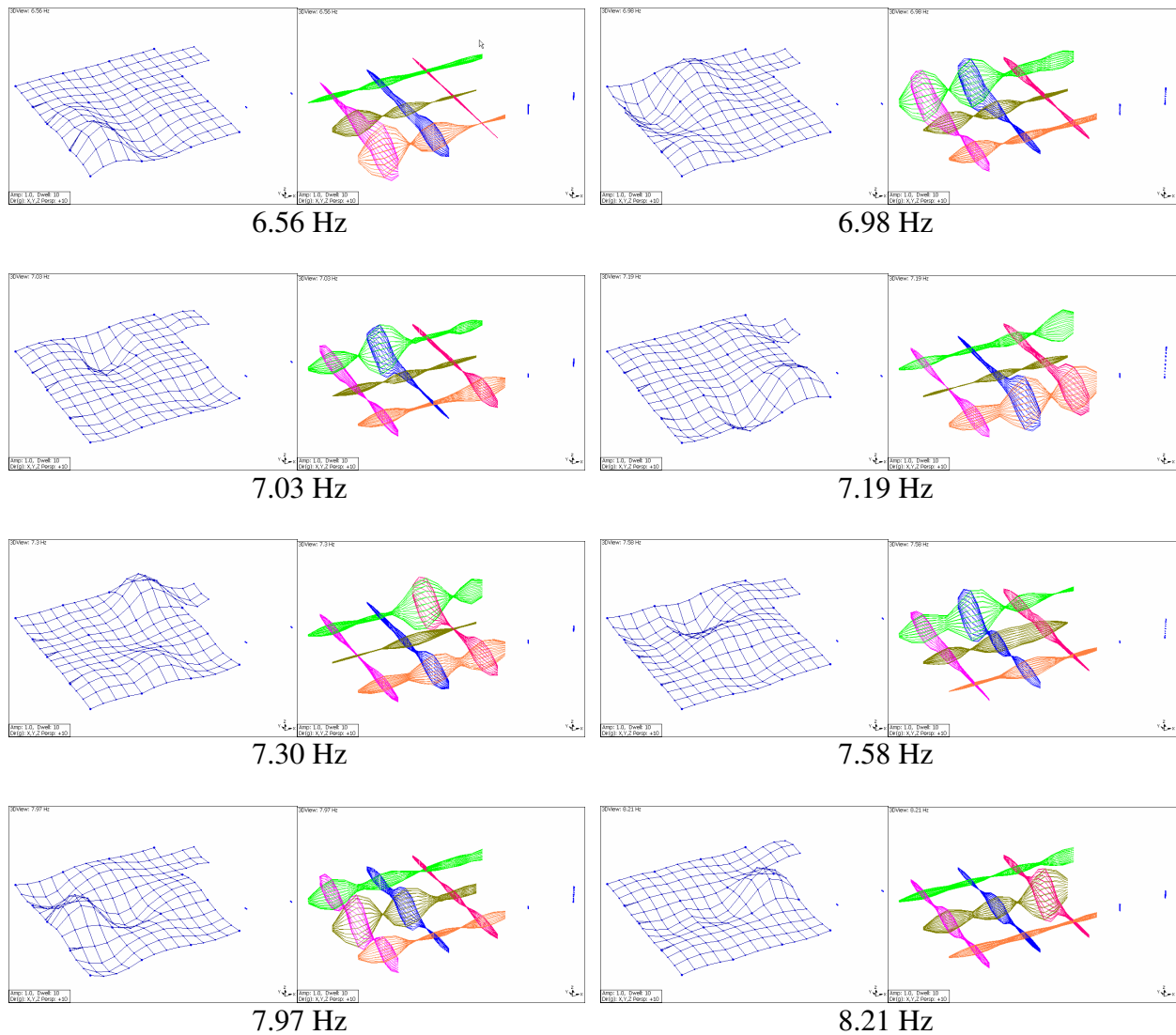


Figure 3.98: VTK2 9-Bay Area Curve Fit Mode Shapes

The amplitude of a mode shape is arbitrary. The displayed mode shapes in Figure 3.98 are all scaled to a fixed amplitude at the point of maximum response, however they could be scaled to any desired reference amplitude. Operating deflection shapes, on the other hand, have relative magnitudes as shown in the ODSs of Figure 3.97. It was previously stated that at resonance, the ODS closely approximates the mode shape if the response is dominated by a single mode. To investigate how well this holds true, four mode shapes are plotted with their respective operating deflection shapes (corresponding to the strong reference DOFs used for curve fitting) in Figure 3.99. Note that the ODSs are scaled to one another to reflect the relative magnitude of response of the floor when forcing at the denoted reference location (either Point 126 or 134), and the mode shapes are plotted to scale of the ODSs for comparison of the two shapes. It is obvious from Figure 3.99 that the strong reference-specific ODS give a very close approximation of the corresponding curve fit mode shapes.

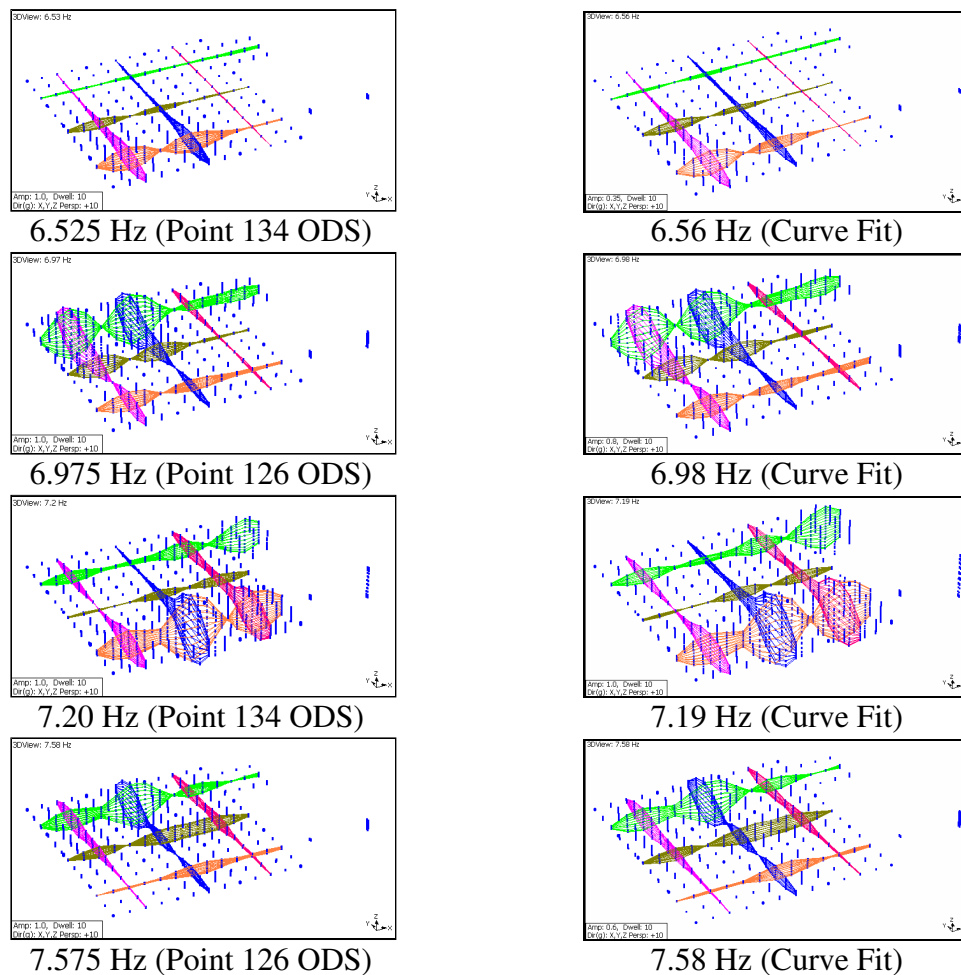


Figure 3.99: VTK2 Comparison of ODS at Strong Reference to Curve Fit Mode Shapes

The comparison made in Figure 3.99 proves that driving the floor at the anti-node (i.e. the location of maximum amplitude) and resonant frequency of a particular mode (i.e. the dominant frequency of that bay) will result in the floor vibrating in an operating deflection shape that closely approximates the mode shape. Following the same logic, the opposite must also be true. The accelerance FRFs for the 9-bay coverage area were only measured for two points of excitation, Points 126 and 134, and consequently the displayed ODSs are only valid for forcing at these two locations. However, mode shapes estimated from a set of accelerance FRFs are not dependent on excitation location. Provided the mode shapes for VTK2 shown in Figure 3.98 were accurately estimated, which is likely the case if the resonant frequencies were strongly present in one of the sets of FRFs, then they can be used to describe the response of the floor from excitation at a limited number of other locations on the floor besides Points 126 and 134. For example, the anti-node (point of maximum amplitude) of the 6.56 Hz mode shape in Figure 3.98 is at Point 82. This behavior agrees with the driving point measurements taken at Point 82 that identified its dominant frequency as 6.59 Hz. Following the argument presented above, forcing Point 82 at or very near its dominant frequency (6.59 Hz) will result in an operating deflection shape that is closely approximated by the estimated 6.56 Hz mode shape shown in Figure 3.98. This was proven true in Figure 3.99 for forcing Point 126 at 6.98 Hz and 7.58 Hz, and forcing Point 134 at 7.20 Hz. The same should hold true for forcing Point 72 at 6.98 Hz, Point 178 at 7.30 Hz, Point 82 at 7.97 Hz, and Point 182 at 8.21 Hz, all of which are anti-nodes of the respective mode shape frequencies. Furthermore, each of the frequencies for which they are anti-nodes are also the identified dominant frequencies from their respective driving point accelerance FRFs. When the arbitrary mode shape amplitude for these points of excitation are coupled with the actual peak accelerance of the respective driving point FRF, the result is a close approximation of the ODS because the response magnitude at all other locations where the shape is defined are scaled off the magnitude at the anti-node.

Three-Bay Interior Quarter Point Coverage – The superimposed accelerance FRFs for the three-bay quarter point strip coverage area from forcing at Points 126, 130, and 134 are presented in Figure 3.100. Note the FRFs for Points 126 and 134 were extracted from the previously discussed set of measurements for the 9-bay coverage area. The measurements from forcing at Point 130 provide some additional significant peaks than the previous two reference

locations, notably Point 130's identified dominant frequency of 7.95 Hz and other participating frequencies at 8.20 Hz and 8.65 Hz.

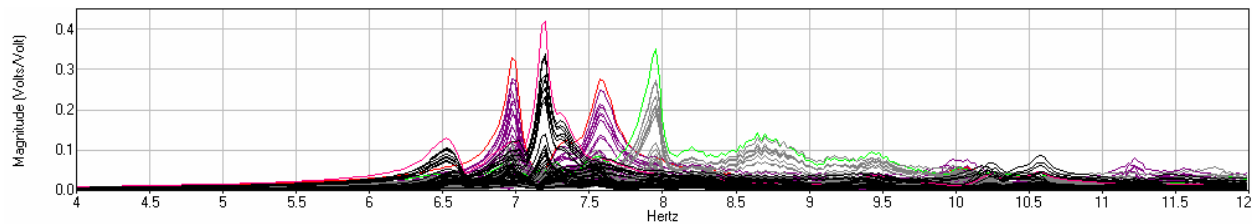


Figure 3.100: VTK2 3-Bay Strip Multi-Reference FRFs (Points 126, 130 and 134)

Using the Point 130 set of accelerance FRFs as the reference DOF, the ODS of the three-bay interior strip at the 7.95 Hz dominant frequency of Point 130 is shown to scale in Figure 3.101, which is a considerably stronger shape than either of the ODSs at this frequency measured while forcing at Points 126 or 134 (Figure 3.97). From the displayed ODS in Figure 3.101, it is obvious why there was such a weak response at the other two forcing locations, as they are very close to a node of the shape. This further highlights the need for sets of measurements (or at least mid-bay driving points) at multiple reference locations so the significantly participating modes are adequately excited to allow a more accurate estimate of their modal parameters.

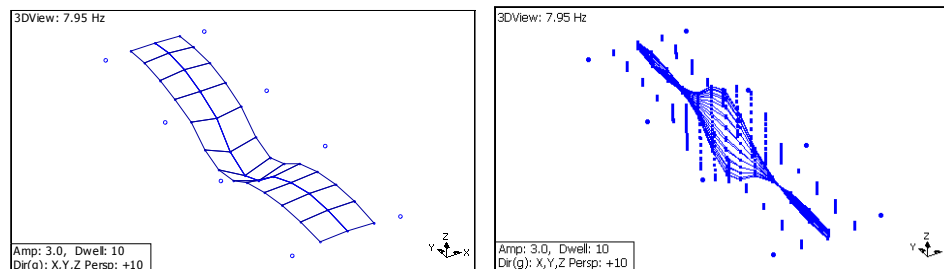


Figure 3.101: VTK2 3-Bay Strip ODS at 7.95 Hz (Forcing at Point 130)

The three sets of accelerance FRFs in Figure 3.100 were curve fit using the MDOF multi-reference curve fitting techniques, and nine frequencies of interest were curve fit in the process. The relative shape strengths for each of the three reference DOFs are presented in Table 3.38. The most strongly represented reference DOFs used for curve fitting are highlighted in the table, and the Point 130 set of measurements were used for four of the nine estimated frequencies, including the 7.96 Hz dominant frequency. The multi-reference curve fit estimated frequencies and damping ratios are also presented in Table 3.38, and they are in excellent agreement with the previous curve fit values estimated from the driving point measurements of the three different shaker locations, as well as the 9-bay multi-reference curve fit estimates.

Table 3.38: VTK2 3-Bay Area Multi-Reference Curve Fitting Shape Strengths and Estimated Frequencies and Damping

Mode	Frequency (Hz)	Point 126	Point 130	Point 134	Frequency (Hz)	Damping (%)
1	6.56	1.1	1.9	4.3	6.56	1.34
2	6.99	5.8	3.9	2.3	6.99	0.57
3	7.02	1.1	2.1	1.2	7.02	0.53
4	7.19	0.9	1.3	6.4	7.19	0.53
5	7.3	0.5	0.6	1.3	7.30	0.42
6	7.58	10.0	4.2	3.5	7.58	0.97
7	7.96	1.0	6.2	0.6	7.96	0.58
8	8.17	0.5	0.6	0.4	8.17	0.59
9	8.64	1.7	4.0	1.3	8.64	1.46

The curve fit mode shapes of the nine frequencies are presented in Figure 3.102 in a 2-D profile of the three-bay strip. The shapes are presented in both static and persistent format to highlight the absolute response of the centerline along the three-bay area. The orientation of the displayed shapes in Figure 3.102 has grid line 1 on the left side of the models and grid line 6 on the right (i.e. the bay containing Point 130 is on the left and the one containing Point 126 is on the right).

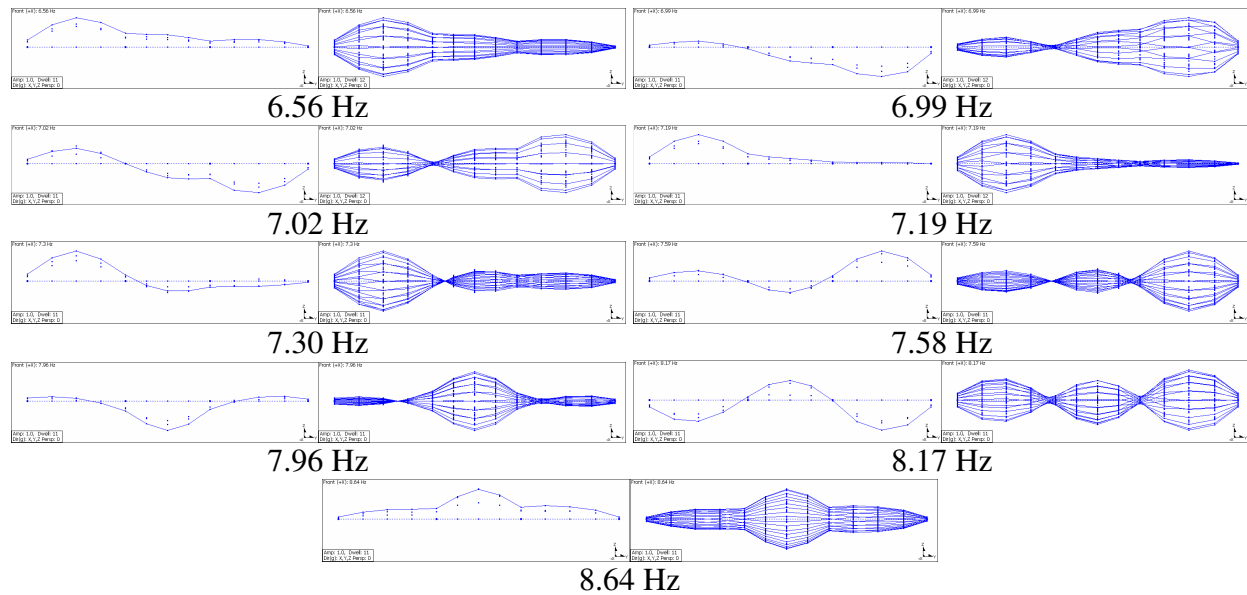


Figure 3.102: VTK2 3-Bay Strip Curve Fit Mode Shapes

For comparison, the operating deflection shapes derived from the selected curve fit references are displayed next to the curve fit mode shapes in Figure 3.103. The ODSs are presented in two forms, scaled to relative acceleration magnitude, and unscaled (or more accurately the point of maximum response within the shape is scaled to a common magnitude for all shapes) for comparison with the corresponding curve fit mode shape.

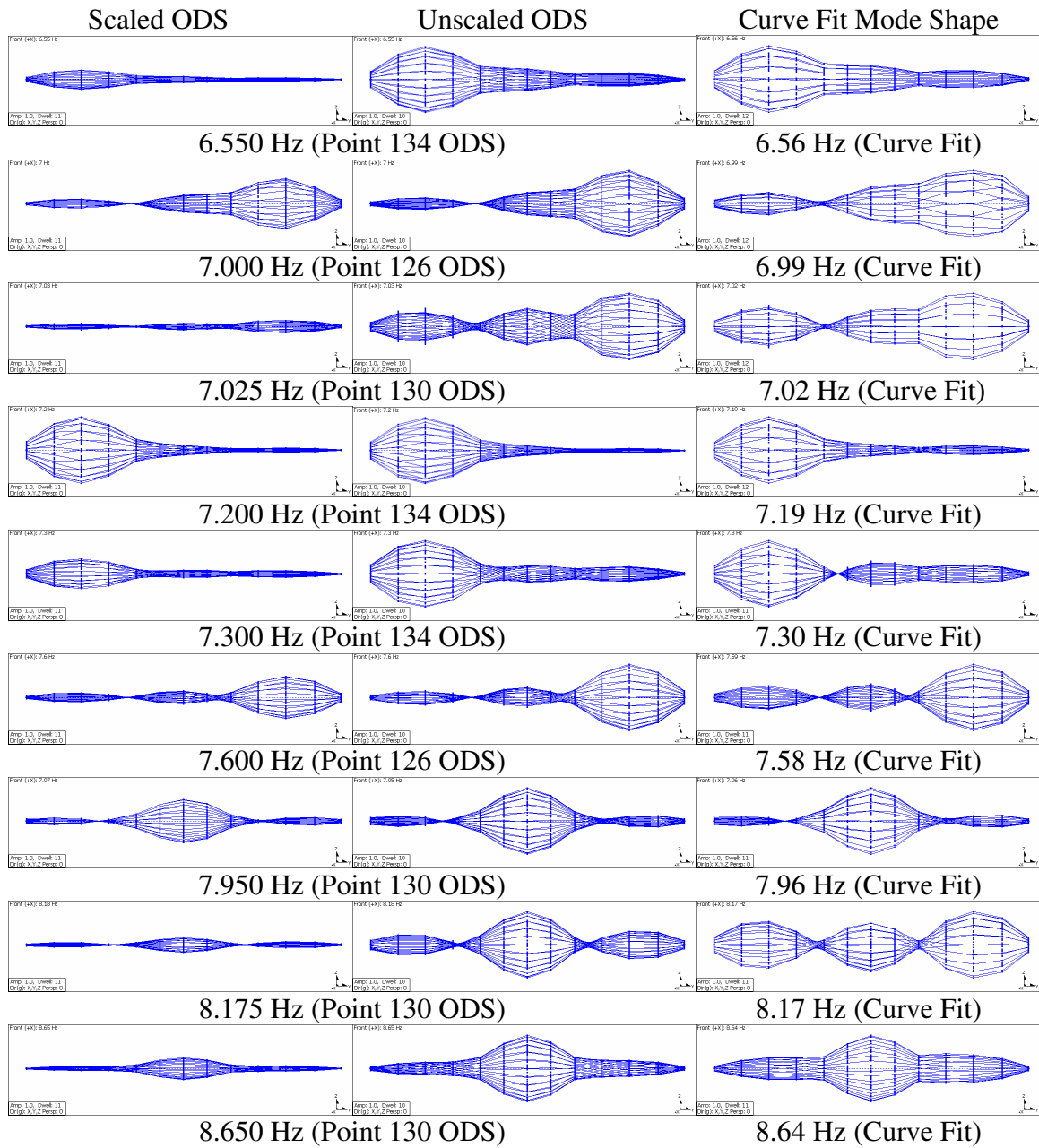


Figure 3.103: VTK2 Comparison of Reference Specific ODS & Curve Fit Mode Shapes

Again, the reference specific ODS is an excellent approximation of the curve fit mode shape, with only a few exceptions. Slight differences in the shapes are noticeable at the 6.99 Hz, 7.02 Hz, and 7.30 Hz frequencies. There is a substantial difference in the shapes for the 8.17 Hz frequency, although this was not unexpected as it was one of the most weakly represented curve fit shapes. This further highlights the need for multiple sets of measurements to ensure all

participating mode shapes in the frequency range of interest are represented with enough strength for an accurate estimation of the mode's parameters.

The 2-D profile display of the ODSs for this three-bay strip illustrates some behavior worth noting. The scaled ODSs in Figure 3.103 for 7.00 Hz (forcing at Point 126) and 7.20 Hz (forcing at Point 134) demonstrate the large spandrel girder response in the bay of excitation, which is a fairly substantial percentage of the mid-bay response. This behavior was previously described for the 9-bay area shapes. Additionally, the shapes at these frequencies show considerable response at the interior girder of the excited bay, much more than observed when testing NOC VII (Figure 3.53). The likely reason for the greater response of the girders of this three-bay strip for VTK2 is because they do not have moment connections at the columns like the corresponding members of the measured three-bay strip of NOC VII.

Overall, the MDOF curve fit estimates of frequency and damping using ME'scope were very consistent for VTK2, which was made possible by high quality measurements and extensive coverage areas. A table summarizing the estimated modal parameters for each of the curve fit sets of accelerance FRFs is presented in Table 3.39. The most notable deviations generally occurred from attempted curve fit estimates of weakly represented modes.

Table 3.39: VTK2 Consolidated Summary of Curve Fit Estimated Frequency & Damping

Frequency	9-Bay	3-Bay	Point 126	Point 130	Point 134	Point 74	Point 78	Point 82	Point 182	Point 186	Point 178	Point 230	Point 25	Point 21
6.50 Hz	6.56 1.35	6.56 1.34		6.61 1.20	6.57 1.39		6.61 1.05	6.59 1.19					6.59 0.60	6.62 0.70
	6.98 0.56	6.99 0.57	6.98 0.60	6.97 0.71		6.97 0.62	6.95 0.69	6.98 0.48			6.98 0.63	6.98 0.70		
7.00 Hz	7.03 0.50	7.02 0.53			7.01 0.61			7.10 0.48	7.05 0.59	7.03 0.65				
				7.19 0.50	7.19 0.49	7.16 0.44		7.24 0.50	7.18 0.55	7.18 0.90		7.18 0.60		
	7.19 0.45	7.19 0.53												
7.50 Hz	7.30 0.42	7.30 0.42	7.33 0.98	7.30 0.55	7.32 0.52	7.36 0.50		7.35 0.60	7.31 0.49		7.29 0.50	7.29 0.59		
							7.52 0.90		7.55 0.97					
	7.58 0.94	7.58 0.97	7.58 0.97	7.57 0.75	7.60 0.95	7.59 0.91								
8.00 Hz							7.95 0.46		7.94 0.56	7.95 0.95		7.96 0.95		
	7.97 0.54	7.96 0.58	7.92 0.70	7.96 0.50		7.97 0.46		8.01 0.47						
		8.17 0.59		8.18 1.20					8.17 1.30			8.22 1.28		
8.50 Hz	8.21 0.67		8.22 1.20											
		8.64 1.46		8.67 1.58			8.64 2.17							
									8.82 1.40					
9.00 Hz													9.05 1.01	9.01 1.03

Reciprocity of Accelerance Measurements – A reciprocity investigation similar to the one for NOC VII-18 was conducted for eleven bays of the VTK2 floor (all previously noted points of excitation except Point 230). With the shaker at one of the mid-bay locations, the accelerance FRFs were measured at the mid-bay locations of the other ten bays. This process was repeated with the shaker at each of the tested bays, resulting in a complete set of reciprocal accelerance FRFs between all tested mid-bay points. For the eleven bays tested in this manner, there were a total of 55 possible comparisons of reciprocal measurements. Although none of those reciprocal accelerance FRF measurements for VTK2 are presented here, the results of the investigation were the same as the observed behavior of NOC VII-18. To summarize, it was demonstrated that reciprocal measurements at locations of strong response, which typically corresponded to adjacent bays at shorter distances from the point of excitation, were in excellent agreement. Reciprocal accelerance FRFs with relatively small magnitudes (corresponding to weak response) did not always agree well. Again, this discrepancy is attributed to the high signal-to-noise ratio of the weak response, not an indication of a gross nonlinearity of the floor.

Decay Curve Fit Damping Estimates – Once the dominant frequency of a bay was identified from the driving point accelerance FRFs and verified with stepped sinusoidal measurements, decay-from-resonance measurements were taken and visually curve fit using the methods described in Section 2.4.6. The majority of decay measurements taken on NOC VII-18 were not conducive to decay curve fitting due to the observed “beating” effect, which is indicative of significant multi-mode decay response. For VTK2, however, the measured decay responses from steady-state excitation at the bay’s dominant frequency were much more conducive for this method of curve fitting. The decay traces and curve fit overlay for representative decay measurements are presented in Appendix J. A summary of the estimated damping ratios and decay frequencies are listed in Table 3.40 for each of the 12 tested bays. While many decay measurements were taken for the tested floor, the listed estimates were selected as representative decay traces for the respective dominant (or significant) frequencies of each excitation location. Decay measurements from two frequencies were taken for Points 74, 82, and 126 due to the dual significant peaks of their accelerance FRFs. Decay measurements from forcing at Point 126 at 6.925 Hz were taken at two different levels of excitation, which resulted in no significant difference in estimated damping ratio. In general, the estimated damping ratios for VTK2 from the decay curve fit method are in reasonable agreement with the previously presented estimated

damping values (half-power, MDOF curve fit). When the decay curve fit values listed in Table 3.40 were substantially different from the other estimated methods (“substantial” in this case defined as more than 10% different from the MDOF curve fit estimated damping ratio), the estimated damping ratios were typically lower, with the exception of the 1.15% estimated damping for Point 21, which was higher than other estimates.

Table 3.40: VTK2 Summary of Decay Curve Fit Estimates of Damping

Excitation Location(s)	Type of Damping Estimate	Excitation Level (volts)	Decay Frequency (Hz)	Estimated Damping Ratio
Point 21	Decay Curve Fit from 9.00 Hz Sinusoid	1.0	9.06	1.15%
Point 25	Decay Curve Fit from 6.575 Hz Sinusoid	1.0	6.57	0.47%
Point 74	Decay Curve Fit from 6.95 Hz Sinusoid	1.0	6.96	0.59%
Point 74	Decay Curve Fit from 7.975 Hz Sinusoid	1.0	7.97	0.48%
Point 78	Decay Curve Fit from 7.95 Hz Sinusoid	1.0	7.94	0.50%
Point 82	Decay Curve Fit from 6.575 Hz Sinusoid	1.0	6.57	1.23%
Point 82	Decay Curve Fit from 8.00 Hz Sinusoid	1.0	8.005	0.47%
Point 126	Decay Curve Fit from 6.925 Hz Sinusoid	1.0	6.935	0.54%
Point 126	Decay Curve Fit from 6.925 Hz Sinusoid	0.5	6.94	0.50%
Point 126	Decay Curve Fit from 7.55 Hz Sinusoid	1.0	7.55	0.80%
Point 130	Decay Curve Fit from 7.975 Hz Sinusoid	1.0	8.00	0.60%
Point 134	Decay Curve Fit from 7.20 Hz Sinusoid	1.0	7.19	0.50%
Point 178	Decay Curve Fit from 7.275 Hz Sinusoid	1.0	7.275	0.50%
Point 182	Decay Curve Fit from 8.175 Hz Sinusoid	1.0	8.165	1.10%
Point 186	Decay Curve Fit from 7.025 Hz Sinusoid	1.0	7.025	0.60%
Point 230	Decay Curve Fit from 6.975 Hz Sinusoid	1.0	6.96	0.63%

Summary of Estimated Dominant Frequencies and Damping Values – Table 3.41 and Table 3.42 provide an overall summary of the reported dominant frequencies for each of the 12 tested bays and their corresponding damping ratios and accelerance magnitudes. Table 3.41 provides a summary for the nine tested bays that only had driving point measurements, and Table 3.42 summarizes the three tested bays that had area coverage measurements. The manually identified dominant frequencies (i.e. visually identified peaks from the accelerance FRFs) and half-power method estimates of damping previously reported were based on driving point accelerance FRFs taken at a 2.0 volt excitation level. As described in Section 3.3.2, a variety of other measurements were taken with the shaker at each of the 12 tested locations on the floor. These measurements included additional burst chirp accelerance FRFs measured at one or more lower

levels of excitation (1.0 volt, 0.5 volts) to investigate the linearity of the response magnitude and location of the dominant peaks. The identified dominant frequencies, peak acceleration magnitudes, and half power method estimates of damping for the lower excitation level acceleration FRFs are also included in Table 3.41 and Table 3.42 for comparison with the reported values of other methods of parameter estimation.

Table 3.41: VTK2 Summary of Dominant Frequency and Damping Estimates – Part 1

Excitation Location(s)	Type of Damping Estimate	Excitation Level (volts)	Peak Frequency (Hz)	Peak Magnitude (in/s ² /lb)	Estimated Damping Ratio
Point 21	Half Power Bandwidth Method - Chirp FRF	2.0	9.000	1.29	0.88%
Point 21	Stepped Sine Sweep FRF (not enough measurements)	1.0	9.000	1.19	n/a
Point 21	MDOF Curve Fit of Driving Point FRFs	2.0	9.01	n/a	1.03%
Point 25	Half Power Bandwidth Method - Chirp FRF	2.0	6.575	1.19	0.53%
Point 25	Half Power Bandwidth Method - Chirp FRF	1.0	6.575	1.12	0.61%
Point 25	Half Power Bandwidth Method - Stepped Sine Sweep FRF	1.0	6.575	1.07	0.76%
Point 25	MDOF Curve Fit of Driving Point FRFs	2.0	6.59	n/a	0.60%
Point 74	Half Power Bandwidth Method - Chirp FRF	2.0	6.950	0.59	0.65%
Point 74	Half Power Bandwidth Method - Chirp FRF	1.0	6.975	0.62	0.59%
Point 74	Half Power Bandwidth Method - Stepped Sine Sweep FRF	1.0	6.950	0.59	0.71%
Point 74	MDOF Curve Fit of Driving Point FRFs	all	6.97	n/a	0.62%
Point 74	Half Power Bandwidth Method - Chirp FRF	2.0	7.975	0.60	0.50%
Point 74	Half Power Bandwidth Method - Chirp FRF	1.0	7.975	0.60	0.50%
Point 74	MDOF Curve Fit of Driving Point FRFs	all	7.97	n/a	0.46%
Point 78	Half Power Bandwidth Method - Chirp FRF	2.0	7.950	0.95	0.44%
Point 78	Stepped Sine Sweep FRF (not enough measurements)	1.0	7.950	0.85	n/a
Point 78	MDOF Curve Fit of Driving Point FRFs	2.0	7.95	n/a	0.46%
Point 82	Half Power Bandwidth Method - Chirp FRF	2.0	6.575	0.42	1.29%
Point 82	Half Power Bandwidth Method - Chirp FRF	1.0	6.625	0.41	1.33%
Point 82	MDOF Curve Fit of Driving Point FRFs	all	6.59	n/a	1.19%
Point 82	Half Power Bandwidth Method - Chirp FRF	2.0	8.000	0.34	0.46%
Point 82	Half Power Bandwidth Method - Chirp FRF	1.0	8.025	0.33	0.54%
Point 82	Half Power Bandwidth Method - Stepped Sine Sweep FRF	1.0	8.000	0.33	0.56%
Point 82	MDOF Curve Fit of Driving Point FRFs	all	8.01	n/a	0.47%
Point 178	Half Power Bandwidth Method - Chirp FRF	2.0	7.275	1.24	0.49%
Point 178	Half Power Bandwidth Method - Stepped Sine Sweep FRF	1.0	7.275	1.19	0.59%
Point 178	MDOF Curve Fit of Driving Point FRFs	2.0	7.29	n/a	0.50%
Point 182	Half Power Bandwidth Method - Chirp FRF	2.0	8.200	0.42	1.31%
Point 182	Half Power Bandwidth Method - Chirp FRF	1.0	8.200	0.42	1.24%
Point 182	Half Power Bandwidth Method - Stepped Sine Sweep FRF	1.0	8.175	0.39	1.33%
Point 182	MDOF Curve Fit of Driving Point FRFs	all	8.17	n/a	1.30%
Point 186	Half Power Bandwidth Method - Chirp FRF	2.0	7.025	0.90	0.64%
Point 186	Half Power Bandwidth Method - Chirp FRF	1.0	7.025	0.88	0.64%
Point 186	Half Power Bandwidth Method - Stepped Sine Sweep FRF	1.0	7.000	0.81	0.92%
Point 186	MDOF Curve Fit of Driving Point FRFs	2.0	7.03	n/a	0.65%
Point 230	Half Power Bandwidth Method - Chirp FRF	1.0	6.975	0.66	0.74%
Point 230	Half Power Bandwidth Method - Chirp FRF	0.5	6.975	0.67	0.75%
Point 230	Half Power Bandwidth Method - Stepped Sine Sweep FRF	1.0	6.950	0.70	0.72%
Point 230	Half Power Bandwidth Method - Stepped Sine Sweep FRF	0.5	6.975	0.68	0.73%
Point 230	MDOF Curve Fit of Driving Point FRFs	all	6.98	n/a	0.70%

Table 3.42: VTK2 Summary of Dominant Frequency and Damping Estimates – Part 2

Excitation Location(s)	Type of Damping Estimate	Excitation Level (volts)	Peak Frequency (Hz)	Peak Magnitude (in/s ² /lb)	Estimated Damping Ratio
Point 126	Half Power Bandwidth Method - Chirp FRF	2.0	6.975	0.49	0.67%
Point 126	Half Power Bandwidth Method - Chirp FRF	1.0	6.95	0.49	0.53%
Point 126	Half Power Bandwidth Method - Chirp FRF	0.5	6.95	0.51	0.52%
Point 126	Half Power Bandwidth Method - Stepped Sine Sweep FRF	1.0	6.925	0.43	0.65%
Point 126	Half Power Bandwidth Method - Stepped Sine Sweep FRF	0.5	6.925	0.46	0.60%
Point 126	MDOF Curve Fit of Driving Point FRFs	2.0	6.98	n/a	0.60%
Pt 126,134	Multi-Ref MDOF Curve Fit of Area Coverage FRFs	2.0	6.98	n/a	0.56%
Pt 126,130,134	Multi-Ref MDOF Curve Fit of Area Coverage FRFs	2.0	6.99	n/a	0.57%
Point 126	Half Power Bandwidth Method - Chirp FRF	2.0	7.575	0.45	1.04%
Point 126	Half Power Bandwidth Method - Chirp FRF	1.0	7.55	0.41	0.90%
Point 126	Half Power Bandwidth Method - Chirp FRF	0.5	7.55	0.42	0.89%
Point 126	MDOF Curve Fit of Driving Point FRFs	2.0	7.58	n/a	0.97%
Pt 126,134	Multi-Ref MDOF Curve Fit of Area Coverage FRFs	2.0	7.58	n/a	0.94%
Pt 126,130,134	Multi-Ref MDOF Curve Fit of Area Coverage FRFs	2.0	7.58	n/a	0.97%
Point 130	Half Power Bandwidth Method - Chirp FRF	2.0	7.950	0.56	0.63%
Point 130	Half Power Bandwidth Method - Chirp FRF	1.0	8.000	0.55	0.65%
Point 130	Half Power Bandwidth Method - Stepped Sine Sweep FRF	1.0	7.975	0.53	0.64%
Point 130	MDOF Curve Fit of Driving Point FRFs	2.0	7.96	n/a	0.50%
Pt 126,130,134	Multi-Ref MDOF Curve Fit of Area Coverage FRFs	2.0	7.96	n/a	0.58%
Point 134	Half Power Bandwidth Method - Chirp FRF	2.0	7.20	0.68	0.50%
Point 134	Half Power Bandwidth Method - Chirp FRF	1.0	7.20	0.72	0.46%
Point 134	Half Power Bandwidth Method - Stepped Sine Sweep FRF	1.0	7.20	0.64	0.66%
Point 134	MDOF Curve Fit of Driving Point FRFs	2.0	7.19	n/a	0.49%
Pt 126,134	Multi-Ref MDOF Curve Fit of Area Coverage FRFs	2.0	7.19	n/a	0.45%
Pt 126,130,134	Multi-Ref MDOF Curve Fit of Area Coverage FRFs	2.0	7.19	n/a	0.53%

In addition to burst chirp measurements at lower excitation levels, stepped sine sweep measurements were taken around the identified dominant peaks to manually verify the peak frequency, and for comparison of peak accelerance measured from steady-state rather than burst chirp excitation. Half power method estimates of damping are reported if enough sinusoidal measurements were taken on either side of the peak frequency. For some locations, the stepped sine measurements were also taken at different levels of excitation. A summary of the estimated parameters from the stepped sine sweep investigations is presented in Table 3.41 and Table 3.42

As shown in the summary tables above, VTK2 exhibited similar linearity properties as NOC VII-18 for measurements taken at various levels of excitation. The peak of the accelerance FRF was generally the same magnitude for the different levels of excitation, but higher levels of excitation tended to result in a slightly lower frequency than lower levels (shifted left). This behavior is noted in the tables for both burst chirp derived accelerance FRFs (Points 74, 82, 130) and stepped sine sweep defined accelerance peaks (Point 230) at different levels of excitation. If any difference in peak accelerance was noted, it did not vary by more than 5%. This amount of

variability in the peak magnitude was well within the bounds observed between repeated measurements at the same level of excitation.

Overall, the estimated damping values for the different methods are in excellent agreement with one another, with only a few exceptions. The MDOF curve fit damping estimates tended to follow the values estimated from the chirp derived accelerance FRFs, which was expected because these measurements were the basis of the curve fit overlay. The estimated damping values for VTK2 were typically in the range of 0.45% to 0.75% of critical, with only a few higher estimates of damping between 1.0% and 1.3%. These damping values are very low, but reasonable considering the bare condition of the floor. It is likely the unfinished perimeter of the building contributed to the lower level of damping, as fewer non-structural components were in contact with the vibrating surface in some areas. The smallest measured damping ratio was 0.44% of critical for the dominant frequency of Point 78, and the largest measured damping ratio was 1.33% for the dominant frequencies of Points 82 and 182. It is interesting to note that Point 78 is an interior bay with no exterior boundaries, which may explain the low estimated damping. Point 82, on the other hand, is an exterior corner bay. The higher level of damping for this bay may be attributed to the two exterior boundaries; however there were also stacked construction materials within the bay during testing that may have contributed a noticeable amount of damping. Point 182, an interior bay, is also the center bay of the building. The higher level of damping in this bay may be attributed to its location adjacent to bay F/G-3/4, which contained a significant area of full-height light gage steel framing (above and below floor) for a mechanical room.

When comparing the peak accelerance magnitudes and estimated damping from accelerance FRFs and stepped sine derived accelerance peaks, the values were in good agreement, however the steady-state sinusoidal measurements typically had a slightly *lower* peak accelerance magnitude and *higher* estimated damping ratio. Regardless of the method of excitation (i.e. burst chirp or stepped sine at various levels), it was found that the larger the peak accelerance magnitude, the lower the estimated damping ratio. A reasonable explanation for this trend is due to the low levels of damping and selected frequency resolution. Because the levels of damping are so low, the damping estimates are very sensitive to truncated peaks of the FRF caused by the chosen 0.025 Hz frequency resolution. A good example of a truncated peak causing a higher level of damping is the 0.92% estimated damping ratio for Point 186, which was

estimated from a stepped sine sweep across 7.00 Hz. This value was 50% higher than the other damping estimates using different methods. The peak accelerance magnitude of the sinusoidal measurement was 10% lower than the magnitude of the chirp FRF and clearly truncated, resulting in an artificially high estimate of damping. The higher the magnitude of a peak between two measurements at the same frequency, the smaller the estimated damping because the half power bandwidth is at a narrower portion of the peak.

Comparison of Measured Frequencies with Predicted Frequencies from DG11 – For comparison with measured frequencies of the tested floors, Table 3.43 summarizes the predicted beam, girder, and system frequencies for VTK2 computed using DG11 procedures; the output from FloorVibe (Structural Engineers, Inc. 2004) is presented in Appendix B. General exterior and interior bays were analyzed and the computed frequencies apply to a number of the tested bays. The exterior bay was analyzed without a wall on the spandrel girder due to the slip connection of the floor slab to the exterior cladding. Bay A/C-2.5/3.8 was analyzed with two free edges to reflect the condition of the bay when tested, which did not yet have exterior cladding. The points of excitation for VTK2 are also presented in Table 3.43 next to the applicable analyzed bay for comparison of predicted and measured frequencies.

Table 3.43: VTK2 - DG11 Predicted Beam/Girder/System Frequencies (Hz)

Tested Bay	Applicable Point(s) of Excitation	Beam Panel	Left Girder Panel	Right Girder Panel	System
General Exterior Bay (no wall)	Pt 74, 82, 126, 134, 178, 186	7.96	7.73	8.02	5.55
General Interior Bay	Pt 74, 82, 126, 134, 178, 186	7.79	7.84	7.84	5.53
Bay A/C-2.5/3.8	Pt 25	7.79	8.73	8.44	5.82
Bay A/C-3.8/4.2	Pt 21	11.68	8.55	12.20	6.90
Bay F/G-4/6	Pt 230	8.95	8.68	6.98	5.51

None of the DG11 predicted system frequencies matched any of the measured dominant frequencies of the tested bays, and are much lower than the measured values. Like NOC VII, this discrepancy is not unexpected for the tested floor due to conditions not considered in the simplified DG11 calculations. For many of the tested bays, at least one of the edge beams or girders was a part of the building's moment frames. Additionally, the edge beams that were part of the moment frame were different (stiffer) sections than the other floor beams in the bay. Neither of these conditions is considered in the DG11 calculations and both will result higher frequencies.

3.4 Summary and Implications of Observed In-situ Floor Behavior

The extensive modal testing of the in-situ floors provided valuable insight into the dynamic behavior of this type of floor system. This section summarizes the key findings noted in Sections 3.2.3 and 3.3.3 of measured in-situ behavior for the three tested floors in the presented research, including commentary on the tested floor systems' fundamental dynamic properties of frequency, damping, and mode shapes. Also included are remarks on acceleration response to sinusoidal load, display and interpretation of operating deflection shapes, linearity of the floor systems, and comments on the different methods of parameter estimation. Lastly, a reduced mid-bay testing scheme for in-situ floor systems is proposed that maximizes the investigator's ability to capture the modal properties of the floor in minimum amounts of time and measurements.

Frequency – The driving point accelerance FRF taken at a mid-bay excitation location is the most efficient and versatile measurement for characterizing the dynamic properties of an in-situ floor system, particularly the active frequency content within the bay of excitation. The driving point accelerance FRF provides immediate feedback on dominant and significantly participating frequencies within the bay, an estimate of damping can be performed using the half power bandwidth method on the peaks, and the magnitudes of the peaks relative to other measured portions of the floor provide immediate feedback on response intensity. Large multi-bay floors have many different modes of vibration, however each individual bay in a floor system is typically dominated by a single frequency, characterized as the largest peak on the driving point accelerance FRF. Although typically not the lowest (fundamental) frequency for the entire floor, the dominant frequency of each specific bay is of foremost interest for vibration serviceability because it represents the frequency that would generate the largest acceleration response per input sinusoidal force. Consequently, this dominant frequency is one of the primary targets of all methods of prediction, design, and evaluation of vibration serviceability, and therefore was one of the fundamental properties reported for each tested bay in the presented research.

Many floors, such as those in the presented research, have bays with similar (or identical) framing and only differ by slightly dissimilar boundary conditions, resulting in similar dominant frequencies. This was illustrated by superimposing representative driving point measurements from each tested bay and noting the clusters of the peak frequencies, as shown for NOC VII-18 and VTK2 in Figure 3.104. The dominant frequencies of the similarly framed exterior bays of

NOC VII all fell within a narrow cluster less than 0.5 Hz wide (4.60-5.10 Hz). Similarly, the dominant frequencies of the similarly framed exterior bays of VTK2 fell within a 1.0 Hz cluster. For comparison of dominant frequency and peak magnitude between the two tested buildings, the driving point accelerance FRFs for NOC VII-18 and VTK2 are plotted to the same scale. The two floor systems basically use the same 5.25-in. slab system and 30-ft bay width, however NOC VII-18 has longer bay lengths, resulting in lower dominant frequencies. From a serviceability standpoint, the lowest of the dominant frequencies of NOC VII-18 are vulnerable to the second harmonic of walking frequency; however the higher dominant frequencies of VTK2 would not be excited by anything but the third or fourth harmonic.

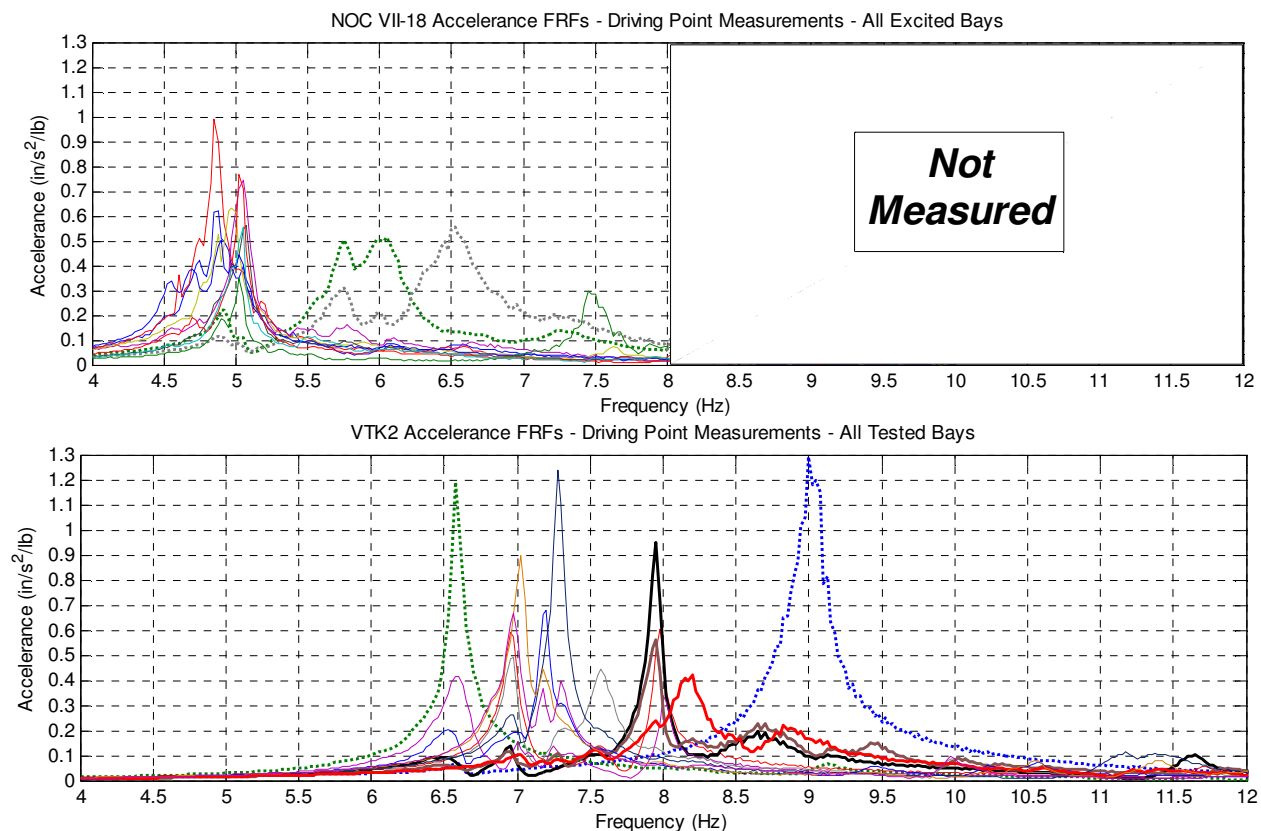


Figure 3.104: Comparison of Tested Bay's Driving Point FRFs (NOC VII-18 and VTK2)

The continuous nature of a multi-bay floor slab inevitably results in additional participating frequencies within a bay that correspond to the dominant frequencies of the surrounding bays. In some of the measured driving point accelerance FRFs, two peaks of nearly equal magnitude were present, however the lower frequency peak was still considered “dominant” because of its susceptibility to a lower harmonic of walking frequency (which translates into a larger applied force). In only one of the tested bays (NOC VII-18 Point 177,

Figure 3.60), the driving point accelerance FRF did not have one clear dominant peak, but rather a series of four (or more) closely spaced peaks between 4.55 Hz and 5.025 Hz. The overlap of these peaks resulted in a fairly substantial accelerance magnitude within this range, which has the potential for vibration serviceability problems due to the wide range of frequencies vulnerable to foot pace.

The dominant frequencies of the commonly tested bays of NOC VII's 18th and 24th floors (Points 73, 69, 25) were in excellent agreement, which was expected from their identical framing (with only slightly different interior partition layout). The agreement in frequencies (and mode shapes) is an important result, as it validates the assumption that similarly framed floors will behave in a relatively consistent manner. This consistency is a fundamental assumption for developing tools to accurately predict floor behavior, such as FE modeling.

Damping – A variety of methods for estimating damping were used in the presented research, including the half power bandwidth method on chirp and sinusoidally derived accelerance FRF peaks, MDOF curve fitting of accelerance FRFs using modal analysis software, and visual curve fitting the decay from resonance. All methods provided damping estimates that were in general agreement with one another, but the various methods also demonstrated their limitations. The half power bandwidth method applied to the peaks of the accelerance FRF was the easiest; however the presence of closely spaced modes had the tendency to widen the dominant peak, resulting in overestimated damping values. Decay curve fitting was used successfully for the measurements on VTK2, but the closely spaced modes in NOC VII-18 resulted in decay traces that were drastically skewed by the multi-mode response and not conducive to curve fitting. Using modal analysis software to perform MDOF curve fitting of the driving point FRFs or full sets of FRFs was the most reliable of the methods because of its ability to accommodate closely spaced modes, although engineering judgment was essential in the curve fitting process to validate the reasonableness of the damping estimates. In this respect, it was almost essential to already have one type of damping estimate (i.e. a manual half-power calculation) during the curve fitting as a form of parameter estimation confirmation.

In the course of performing stepped sine sweep measurements across the dominant peaks and investigating the linearity of the system from measurements at different levels of excitation, it was apparent that the larger the peak accelerance at the dominant frequency, the lower the estimated damping ratio. This trend was a clear indication of the effect of the chosen 0.025 Hz

frequency domain resolution on damping estimates, because a resonant peak truncated by poor resolution will give a larger half-power estimate of damping. This was also evident in the differences of estimated damping between the two tested floors of NOC VII. The estimated damping values of NOC VII-24 (1.0-2.0%) were generally higher than NOC VII-18 (0.60-2.4%), even though the floors were tested under nearly identical conditions. It is unlikely the actual levels of damping were different, and the discrepancy is attributed to the coarser 0.05 Hz frequency domain resolution for NOC VII-24 versus 0.025 Hz for NOC VII-18.

In general, all damping values for the tested floors were low (less than 2.5% of critical), which is reasonable considering the bare condition of the floors. NOC VII-18's estimated damping ratios ranged from 0.60% to 2.4% of critical, although 0.65-1.15% was typical. VTK2's estimated damping ratios ranged from 0.44% to 1.33% of critical, but 0.50-1.0% was typical. Although all of the measured damping values were low, there was still a wide range of damping for the various dominant frequencies of a given tested floor. This poses a significant problem for finite element analysis, which requires damping to be specified for forced response calculations. From a vibration serviceability standpoint, the range in measured values is almost moot, as the damping of the floor system will immediately change during fit out and occupancy.

NOC VII-18 had higher estimated damping ratios than VTK2, which was likely due to the finished exterior boundaries, spray-on fireproofing, and suspended sprinkler systems in NOC VII. VTK2 had unfinished boundaries in many locations, no fire proofing, and very little suspended mechanical equipment. No unilateral trend was found correlating damping with bay location, but the largest factor contributing to the damping of a bay is likely its boundaries. In several instances, corner bays had higher estimated damping ratios than other similarly framed bays, which may be a product of having two exterior boundaries.

Mode Shapes, Operating Deflection Shapes, and Multiple-Reference Testing – In the previous sections, a distinction was made in differences/relationship of mode shapes and operating deflection shapes of the tested floors. Presenting the ODSs for a floor system is advantageous for several reasons. First, the ODSs are measured forced-response shapes and vibration serviceability is a forced-response phenomenon, thus displaying the shape of a floor at its dominant frequency visually illustrates the floor's potential vulnerability to walking excitation. Secondly, the ODS closely approximates the mode shape at resonance provided it is dominated by a single mode. Lastly, the ODSs are animated directly from the measured

accelerance FRFs, thus the validity of the displayed shape is a direct result of the quality of the measurement. Mode shapes are curve fit from these FRFs, thus a poor curve fit could result in a misleading shape. Of course, having the mode shapes is equally advantageous in determining the response of the floor, as ODSs are simply the summation of the response of all modes due to excitation at a specific point.

In an effort to validate the quality of the operating deflection shapes animated from the accelerance FRFs derived from burst chirp excitation, several different coverage areas on NOC VII were tested with steady-state sinusoidal measurements. The result of the set of sinusoidal measurements was an ODS for a given frequency. Comparison of the sinusoidally derived ODS with the burst chirp derived ODS animated from the measured accelerance FRFs revealed virtually no difference in shape. The excellent correlation between the shapes derived from different methods provides a significant level of confidence in the quality of the measurements and reliability of the shapes animated from the measured sets of accelerance FRFs using the techniques employed in this research.

For coverage areas in both NOC VII and VTK2, sets of measurements were taken with the shaker in multiple locations, effectively measuring two columns of the accelerance FRF matrix. All sets of measurements were used for multi-reference parameter estimation. A common assumption for floor testing is that every mode of interest is just some combination of single curvature in all of the bays, and thus forcing at the center of one bay should excite all others. It was quickly found that even forcing at the middle of a bay, certain modes were not adequately excited for an accurate estimate of frequency and damping, let alone the mode shape. The advantage of multi-reference measurements and MDOF curve fitting is the ability to use the set of measurements from the reference that most strongly excites a particular mode, increasing the ability to accurately characterize that mode's parameters. The comparison of multi-reference operating deflection shapes for VTK2 in Section 3.3.3 is a good demonstration of the substantial difference in shapes derived from different excitation locations. It was also demonstrated that the ODS at a resonant frequency from a set of FRFs where that mode was strongly represented closely approximated the modes shape, whereas the ODS from a weakly represented set was suspect. The implications of this on the ability to accurately define all mode shapes of a floor is fairly substantial, as measurement sweeps across large areas of a floor is a formidable task to complete once, let alone multiple times for multiple points of excitation. If the goal is to

accurately identify frequencies and damping for all modes (but not the mode shapes over an area), then a set of mid-bay driving point accelerance FRFs from all bays of interest should suffice. However, if the mode shapes are of interest, coverage areas measured from multiple excitation locations are highly recommended.

General Response Behavior – The mid-bay location is the best point to locate the shaker for applying force to the floor system, as it is roughly the anti-node of response within that bay (point of maximum response) when driving at its dominant frequency. Furthermore, the ODSs presented in Sections 3.2.3 and 3.3.3 illustrate that this location is almost always the anti-node of response for the *whole floor* when excited at its dominant frequency, essentially making the driving point accelerance FRF the upper bound response for the entire floor. This upper bound has been observed even when an adjacent bay has the same/similar dominant frequency; however this is *not always* the case when driving at frequencies other than the dominant frequency of the excited bay. For example, Bay A is driven at a dominant frequency of adjacent (or perhaps even remote) Bay B, which causes a relatively larger response in Bay B than where the shaker is located in Bay A. However, when forcing Bay A at Bay B’s dominant frequency, the response in Bay B is never greater than when the shaker is in Bay B forcing at its own dominant frequency. In short, the absolute maximum response a mid-bay location feels is when the shaker is located at mid-bay and driven at the dominant frequency; no greater response can be achieved by forcing at another location. The only time this may not hold true, which only happened once for all of the tested bays, is if two adjacent bays have the same or similar dominant frequency and one of the bays is much more constrained at its boundaries (i.e. exciting a corner bay and getting a higher response in the one next to it).

The upper bound driving point response has several significant implications for vibration serviceability research. First, it validates the current practice of floor evaluation which computes the mid-bay response to some form of mid-bay excitation and assumes the vibration in other areas is never larger than the computed response. Second, it allows more efficient vibration testing because a collection of mid-bay driving point measurements may be adequate to define the participating frequency content and upper bound response magnitudes for excitation within each tested bay of a floor system. Although the mid-bay is the best location for forcing at that bay’s dominant frequency, it may not be the best location for capturing other bays’ dominant

frequencies as they may not be excited because of localized response, which was observed from the multi-reference testing previously described.

An unexpected observation from the displayed operating deflection shape was that when equal or significant response occurred in an adjacent (or remote) bay, it was typically a bay located perpendicular to floor framing in relation to the bay of excitation (i.e. response is greater in bays adjacent in the direction of the floor deck ribs rather than the direction of the floor framing). Another unexpected observation was the significant response measured in the spandrel members of the exterior boundaries of a floor, which ranged from 9-26% of the mid-bay response for both tested buildings (all three floors). This was a considerable amount of response at boundaries that are typically assumed rigid. There was actually less response observed at the interior boundaries of NOC VII along the interior bay full-height partition walls. The response within these bays and along the walls was negligible, as was the response at the columns for all tested floors. As expected, edge members of bays that were part of moment frames were considerably stiffer than other members with simple framing connections. This was apparent in the displayed operating deflection shapes, which show considerably less response along the bays' boundaries that included moment frame beams/girders.

It should be noted that the observations being made are based on the tested floors, which exist in a condition vastly different than typical in-service conditions. The reality is that in most cases, office fit out (partition walls, etc.) limits human vibration problems/concerns to the bay of excitation and the immediate adjacent/surrounding bays, and rarely across the distances measured in the tested buildings. While the observed behavior may seem anecdotal in this context, it is still important to define it for comparison/contrast with results from FE modeling

Measurement Consistency and Linearity – In general, the redundant driving point accelerance FRFs for a set of floor measurements were very consistent; however, there was some degree of variability, especially if the measurements were taken on different days or over long periods of time with changing environmental conditions (temperature). While the variability in peak magnitude was generally small, any variation in the peak frequency over time can cause problems, particularly as it pertains to the *phase* of the driving point measurement. The low level of damping creates very sharp peaks, and thus a slight shift in the location of the peak, however small, can have a drastic effect on the corresponding phase.

No significant nonlinearity was tied to level of excitation in the various linearity comparisons that were made. A detailed description of the effect of excitation level on the magnitude and location of accelerance FRF peaks was extensively described in Section 3.2.3 for Point 281 of NOC VII-18. To summarize, increasing the level of excitation generally does not affect the magnitude of the dominant peaks of the accelerance FRFs, however it does have the tendency to slightly lower the peak frequency (shift left by one or two spectral lines). This can be interpreted as a tendency for the floor to become slightly more flexible at higher levels of excitation. The *magnitudes* of the dominant peaks in FRFs were virtually the same at different levels of excitation, and when differences did occur, they were typically less than $\pm 5\%$.

There was excellent agreement between reciprocal FRFs of bays immediately adjacent to the bay of excitation, but the agreement deteriorated at locations further away from one another. Rather than a gross nonlinearity in the system, this poor agreement is much more likely a function of poor signal strength at the longer distances. This was consistently observed from the reciprocal measurement investigations in NOC VII-18 and VTK2.

Mid-Bay Floor Evaluation

The observed floor behavior, testing techniques, and modal parameter estimation can all be used to the advantage of the floor vibration researcher in the form of a reduced testing scheme consisting of a series of mid-bay measurements across the floor area of interest. An unintended byproduct of gathering sets of reciprocal measurements was acquiring mid-bay responses of all other bays on a floor while forcing at one bay. The resulting mid-bay measurements from each different shaker location essentially became reduced sets of accelerance FRFs over the entire floor, albeit for a very coarse test grid comprised of just the mid-bay points. Because the reduced mid-bay set of measurements comprise a very coarse test grid, they are generally not suitable for animation. As a set of measurements for a given reference location, however, they are still quite useful for MDOF curve fitting. As a minimum, each set of measurements will strongly excite the dominant mode of the bay of excitation, and will likely excite several others corresponding to adjacent bays. Gathering multiple sets of these measurements, one for each mid-bay shaker location, takes advantage of the multi-reference MDOF curve fitting techniques that was shown to produce the most reliable estimated parameters because the chosen reference corresponded to the set of FRFs that had the strongest shape strength for a curve fit mode. While there is no getting around a full modal sweep over an area for a detailed display of response or

extracted mode shapes, if a basic outline of the mode shape is all that is necessary, then a mid-bay analysis may work. An example of how the measurements are interpreted is presented below for a tested location on VTK2.

VTK2's Point 78 was not a location of the shaker for a modal sweep across the full coverage area of VTK2 like Points 126 and 134. With the shaker located at Point 78, the only measurements taken were driving point accelerance FRFs and roving response accelerance FRFs at the mid-bays of the 10 other tested bays. The magnitude, phase, and coherence of a set of these 11 measurements are shown in Figure 3.105. The driving point accelerance FRF for Point 78 is displayed as a thicker line for convenience. Note that at the 7.95 Hz dominant frequency, the driving point accelerance FRF is the upper bound of response (i.e. maximum accelerance).

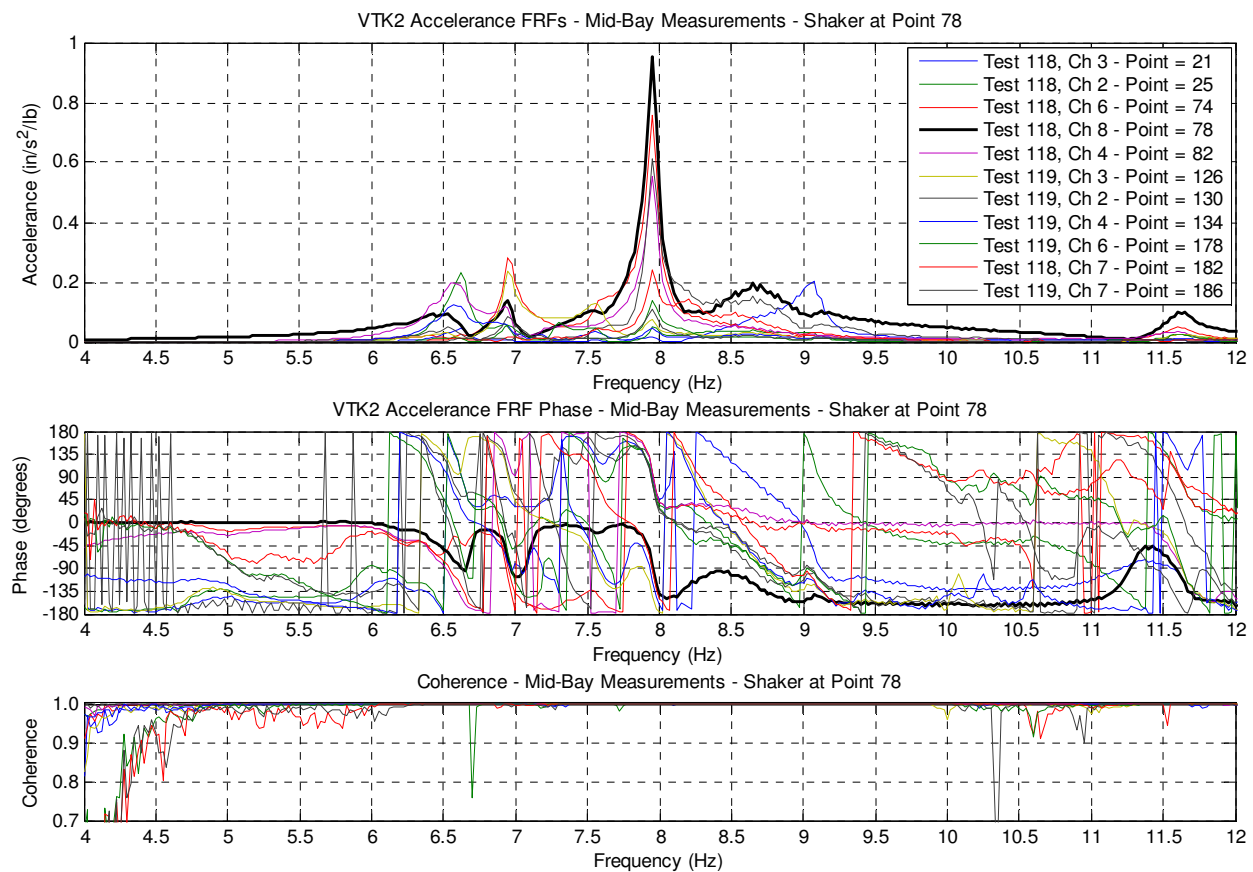


Figure 3.105: VTK2 Mid-Bay Accelerance FRFs (Forcing at Point 78)

Figure 3.106 is a closer look at the magnitude and phase of the mid-bay accelerance FRF set around the dominant peak. The accelerance magnitudes at the dominant peak literally represent the relative response magnitudes of the operating deflection shape at each of the plotted mid-bay locations. Note that Point 78 is the upper trace in the figure, there are three other bays

that are of substantial magnitude, and the remaining traces have relatively small responses at the dominant frequency. The phase indicates the relative position of the mid-bay responses to the driving point response. This shows a clear grouping of mid-bay locations that are either in-phase or out-of-phase with the driving point response. From these two pieces of information for each mid-bay location, a very rough sketch of the mode shape is presented in terms of relative response magnitude and condition of phase. For comparison with the presented mid-bay evaluation, the full coverage curve fit mode shape at this frequency is shown in Figure 3.107.

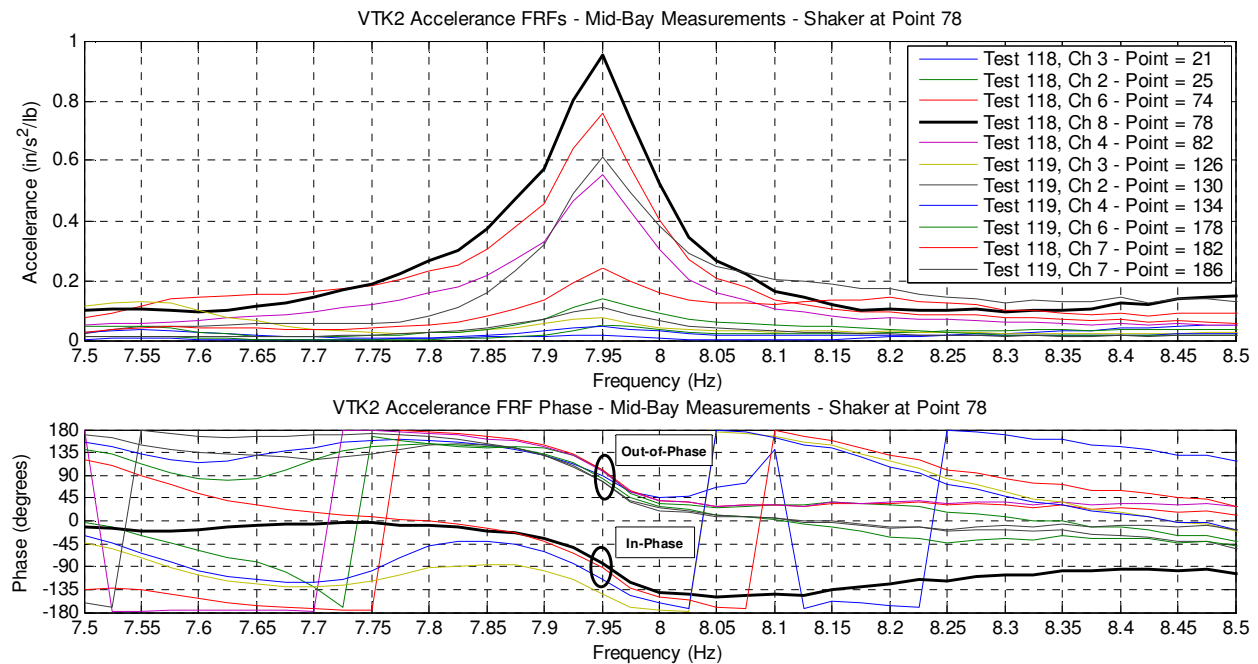


Figure 3.106: VTK2 Example Shape Evaluation Using Mid-Bay Accelerance FRFs

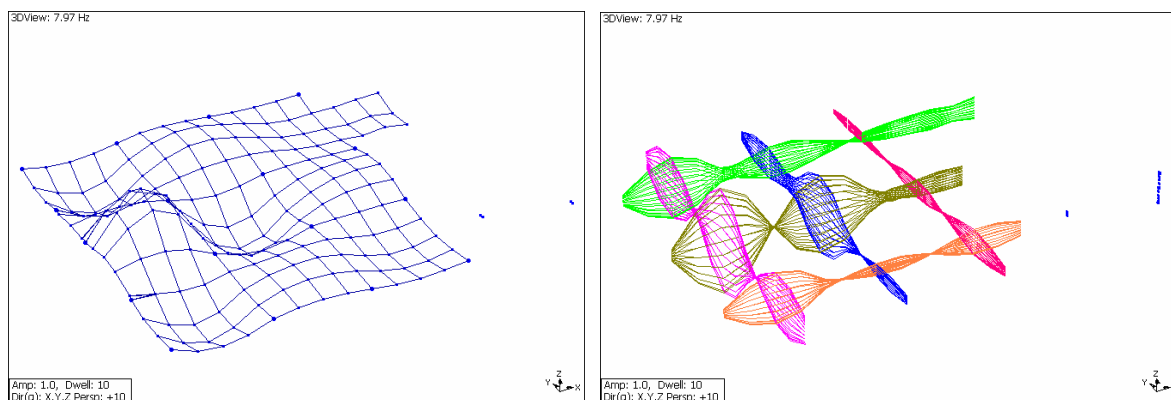


Figure 3.107: VTK2 Curve Fit Mode Shape at 7.97 Hz (Max Response at Point 78)

Note that the mode shape in Figure 3.107 was extracted from a set of measurements that was not taken while forcing at Point 78. The largest response on the shape is at Point 78, as

expected. The three other significant response locations correspond to Points 74, 82, and 130, which agree with the mid-bay interpretation of response magnitude, and all three of those locations are part of the “out-of-phase” grouping of measurements in the phase plot of Figure 3.106.

Testing in-situ floors systems is a constant compromise, and limited time is typically the key factor in the quality and quantity of the testing locations and test measurements. Unfortunately, characterizing certain behavior of a floor, such as the detailed response over a large area, requires ample time and patience. If time is very limited, the best application of the testing methods presented in this research is the proposed reduced mid-bay response analysis. The driving point accelerance FRFs alone can provide the bulk of the dynamic properties of interest very quickly. The addition of mid-bay accelerance FRFs at bays other than the location of the shaker allows a rough characterization of mode shape without the investment in time.

CHAPTER 4

FINITE ELEMENT MODELING OF COMPOSITE FLOORS FOR VIBRATION SERVICEABILITY

4.1 Finite Element Modeling of Composite Floors for Vibration Serviceability

The objective of this chapter is to present general finite element (FE) modeling techniques for composite floor systems. Methods of creating valid computational models of composite floors subjected to dynamic loads provide a tool for designers, consultants, and researchers to evaluate proposed and existing composite floor systems for serviceability. The actual method of evaluation using the computed parameters and response values is still a subject of debate, even amongst the various simplified methods for evaluating serviceability. However, without question, the ability to adequately represent the dynamic behavior of a floor system with a computational model provides many options for the development of serviceability evaluation methods because iterations of analyses on a suite of computational models is much easier than testing even a small sample size of in-situ floors.

This chapter discusses the fundamental techniques used in development of FE models of the tested in-situ floors. Although three floors were tested, only the NOC VII-18 and VTK2 floors were modeled. Only one model was developed for NOC VII, as the two different tested floors (NOC VII-24 and NOC VII-18) shared identical framing with only slightly different interior partition configurations. NOC VII-18 was the basis for comparison for the NOC VII model, as this was the most extensively tested of the two floors in the NOC VII building. The intent of the investigation was not to independently create ideal models for each individual floor using automated finite element modeling algorithms, but rather to model both floors using broad, fundamental, logical, and most importantly common/shared techniques that resulted in FE models that adequately represented the dynamic behavior of the floors. The two modeled floors were different, both in geometry and boundary conditions, thus identifying common modeling techniques that applied to both floor models builds confidence that the techniques are applicable to a variety of configurations of composite floor systems. Although three tested in-situ floors may seem to be a low number of test specimens for identification of fundamental modeling techniques, additional “samples” are intrinsic from bays of variable geometry and boundary

conditions within each floor's own assemblage. Each tested bay demonstrated unique dynamic behavior, including different dominant frequencies. Thus, the measurements from the in-situ floors presented in Chapter 3 provide an adequate sample of stiffness, geometry, and boundary conditions for identification of the FE modeling trends required to bring experimental and analytical results into agreement

Dynamic FE models of composite floor systems require adequately representing mass, stiffness, and boundaries within the model to analytically compute frequencies and mode shapes. Damping in a structure is not computed by FE analysis. For forced response computations, damping must be specified within the model, either from assumed values or based on measured estimates. Theoretically, if all of the above listed parameters are adequately represented, a forced response analysis should result in computed accelerations similar to measured acceleration response. Previous FE modeling research has had success in matching frequencies of composite floors but struggled to adequately predict the acceleration response, the most important value for vibration serviceability (Sladki 1999; Alvis 2001; Perry 2003).

The process of developing the modeling techniques described in this chapter involved creating FE models of the NOC VII and VTK2 floors and manually updating the models to bring the computed dynamic properties and acceleration response into agreement with the experimentally measured values presented in Chapter 3. In the most basic terms, floor models were created in the XY-plane with the Z-plane representing the direction of vibration. The models consisted of frame and rectangular plate area elements located in the same plane (with stiffness adjustments to represent composite behavior) and analyzed as a plane grid structure, using only UZ, RX, and RY as available degrees of freedom (DOF). UZ is the out-of-plane translational DOF, and RX and RY are the rotational DOFs about the X and Y axes, respectively. Creating an FE model of a floor system for evaluation of vibration serviceability can be summarized in six general steps:

- 1) Lay out the floor geometry using the design specified steel framing members for the beams and girders and vertical restraints at the locations of the columns.
- 2) Define area elements and materials to represent the composite slab and apply the slab area elements to the model.
- 3) Adjust model to adequately reflect mass and stiffness (mesh size and subdivision of members, additional restraints or releases, application of stiffness property modifiers to

represent composite stiffness, etc.).

- 4) Perform modal analysis on the FE model to compute the frequencies and mode shapes.
- 5) Specify damping in the model.
- 6) Apply dynamic loads and perform forced response analysis for use in evaluation of vibration serviceability.

The recommended techniques used for the above listed steps are presented first in Sections 4.1.1 and 4.1.2 using an example 8-bay floor model, followed by the application of these techniques to generate and analyze FE models for the two tested floors presented in Section 4.2.

The commercially available finite element analysis software used in the presented research was SAP2000 Nonlinear version 9.1.4 (CSI 2004). SAP2000 was used for its availability to the researcher, its dynamic finite element capability including transient time history analysis and steady-state analysis, and its popularity with practicing design engineers. The latter broadens the applicability of the presented research, as more practicing design engineers are likely familiar with performing analysis using commercial software like SAP2000 than with other FE analysis programs such as ANSYS, ABACUS, or ADINA, which are more oriented towards research. The practicing engineer's familiarity with the software is likely limited to static analysis rather than dynamic analysis, but the basic menus and commands for modeling structures for dynamic analysis are very similar.

Many of the basic techniques used for modeling composite floors in SAP2000 were based on those used by others for floor vibration research (Kitterman 1994; Rottman 1996; Beavers 1998; Sladki 1999; Alvis 2001; Perry 2003). These basic techniques were either used as-is, improved upon, disproved, or new techniques developed through comparison of the modeling results with measured in-situ floor behavior, which was generally not available when the basic techniques were originally developed. The initial discussion and application of the modeling techniques are presented in a fair amount of detail, thus Section 4.3 is a concise summary of the recommended modeling techniques. Section 4.4 presents a proposed method of evaluation for vibration serviceability using the forced response analysis results of composite floor FE models. The method combines the forced response analysis presented in this chapter with present design guidance for representing forces due to walking and the threshold of human tolerance.

represent the composite floor slab in lieu of shell elements. The in-plane forces from membrane behavior are not a factor for vibrations of composite floors. Several iterations of analysis were performed using full space frame analysis (all six available DOF) and shell area elements. The results indicated there was no significant effect on the computed frequencies, mode shapes, and response, only a significant increase in computation time. Rather than using a predefined material of concrete or steel, a user-defined material named *VIBCON* was created and assigned to the plate area elements to represent the dynamic properties of the concrete slab and metal deck. These properties included the composite slab's mass, the mass of any superimposed loads, and the dynamic stiffness of concrete ($1.35 \cdot E_c$). For both the tested/modeled floors, the same composite slab system was used, a 5.25-in. total depth slab with 18-gage 2-in. LOK-Floor steel deck. The thickness of the user-defined plate element named *SLAB* was specified as 3.25 in., equal to the depth of the concrete above the corrugated steel deck ribs. It should be noted that this method is purely a convenience to ensure adequate mass distribution using the assigned material weight and mass densities; the ramifications of this approach on representing stiffness of an orthotropic deck must be dealt with in a manner discussed in the following sections. The weight density and mass density of the user-defined material were computed using Equations (4.1) and (4.2), respectively (Beavers 1998; Sladki 1999; Perry 2003).

$$w_{material} = \left[\left(\frac{d + d_r/2}{12} \right) w_c + w_{deck} + w_d + w_l + w_{coll} \right] \left(\frac{12}{d} \right) \left(\frac{1}{1,728,000} \right) kips/in^3 \quad (4.1)$$

$$m_{material} = \frac{w_{material}}{g} = \frac{w_{material}}{386 \text{ in/s}^2} \quad kips \cdot s^2 / in^4 \quad (4.2)$$

where

d = depth of concrete above the ribs (in.)

d_r = depth of steel deck ribs (in.)

w_c = unit weight of concrete (lbs / ft³)

w_{deck} = area weight of steel decking (lbs / ft²)

w_d = superimposed dead load (lbs / ft²)

w_l = superimposed live load (lbs / ft²)

w_{coll} = superimposed collateral load (lbs / ft²)

The advantage of using this method for assigning weight and mass density is that it allows any desired superimposed dead or live load (furniture, lighting, utilities, etc.) to be included as additional mass in the computation of frequencies and mode shapes, although no superimposed loads were used in the models of the presented research due to the bare conditions of the tested floors. Because the tested floor systems had no superimposed load, only the unit weight of the concrete slab, $w_c = 115 \text{ lb/ft}^3$, and area weight of the steel deck, $w_{deck} = 2.4 \text{ lb/ft}^2$, was included in the specified mass density of the material. For the 5.25-in. composite slab of both modeled floors, the depth of the concrete above the ribs, d , is 3.25 in. and the depth of the steel deck, d_r , is 2 in.

Besides specifying weight and mass density, the constitutive properties of the user-defined material were defined per DGI1 recommendations previously described in Section 1.1.2. The modulus of elasticity of the user-defined material representing the concrete slab was taken as 1.35 times the modulus of elasticity of the concrete as “specified in current structural standards” to account for a greater stiffness of the floor slab system under dynamic loads (Murray et al. 1997). The modulus of elasticity of concrete used was based on the unit weight and compressive strength and was computed using Equation (1.6). Poisson’s ratio for the user-defined material was taken as 0.2, a typical value for concrete.

Because the FE analysis program apportions the mass of an element at each of its joints, it was important to use enough elements to properly represent the uniform distribution of mass across the slab areas and along the framing member lengths. To adequately distribute the mass of the floor, the *SLAB* area elements were appropriately meshed across their areas and the beam/girder framing members were similarly subdivided along their lengths at each mesh joint. An overly fine meshed model is computationally expensive, thus the frequencies and mode shapes of a single-bay FE model were computed at various mesh subdivisions until the first four frequencies of the model converged to within 0.01 Hz. It was found that *SLAB* area element sizes of 26 in. to 30 in. along each side gave convergent results, which corresponded to a mesh with 12 to 20 elements along a bay’s width or length, depending on the floor model and bay’s configuration. SAP2000 recommends an element aspect ratio close to unity for best results (CSI 2004), which was factored into determining the mesh and element sizes. The plate area elements representing the composite slab and the corresponding area mesh for the example 8-bay floor model are shown in Figure 4.2.

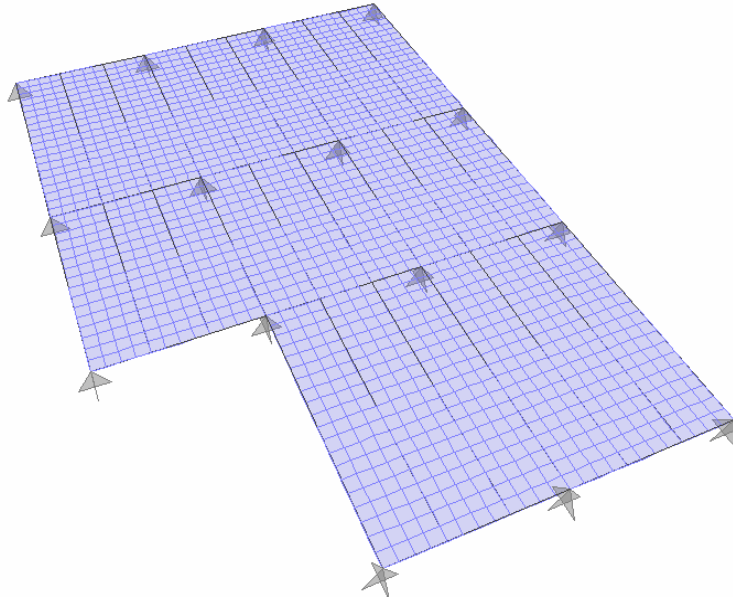


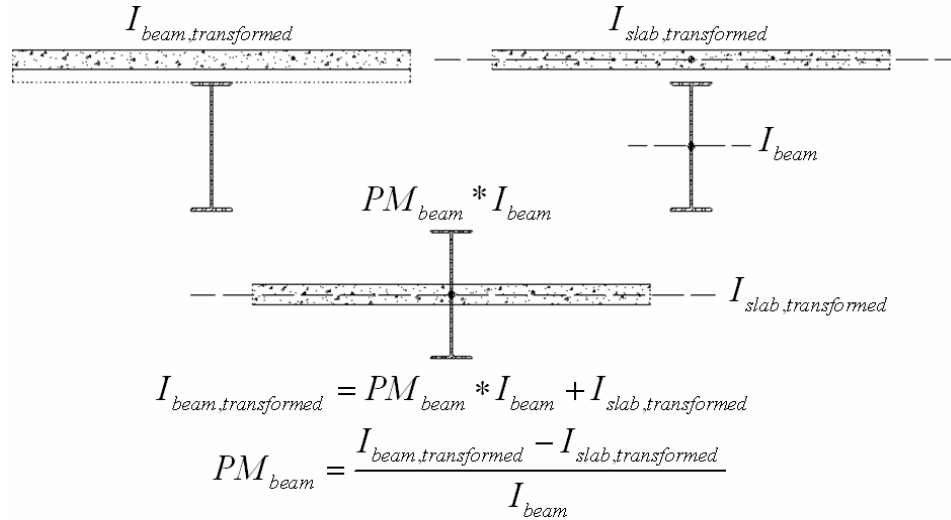
Figure 4.2: 8-Bay Floor Model Example – Plate Area Element Layout and Mesh

To ensure connectivity of the slab and framing elements and to provide the same distribution of mass along their lengths, the frame elements representing the girders and beams were auto-subdivided along their lengths corresponding with the slab mesh size. Experimental measurements were taken at quarter points of the bays of the tested floors. For convenience, the number of elements used along the length/width of a bay in the model was kept to a multiple of four to ensure a joint existed where the mode shape or response value was desired.

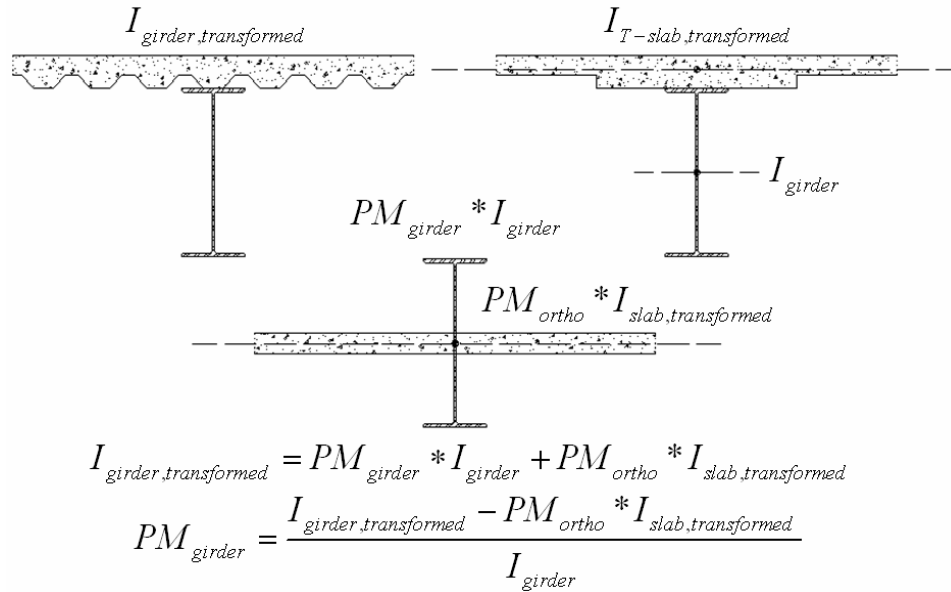
Stiffness

As previously stated in Section 1.1.2, if a slab/deck system is in continuous contact with the beams and girders, the floor system is assumed to act compositely, regardless of whether or not the floor was designed with shear connectors (Murray et al. 1997). The assumption did not have to be made for the two modeled floors, as they were both designed with composite shear studs on all beams and girders. By modeling both the area elements and the framing elements in the same plane to take advantage of the plane grid analysis, an adjustment must be made to the stiffness properties to account for the composite bending stiffness. As the first step in this adjustment, the composite transformed moment of inertia for each beam/slab and girder/slab element was computed using traditional engineering mechanics and the recommended dynamic modulus of elasticity and concrete effective width guidelines of DG11. The effective width guidelines include limitations based on beam/girder span as well as considerations for spandrel

members. Because the steel deck is oriented perpendicular to the beam framing members, the transformed moments of inertia were based on only the 3.25-in. thickness of concrete raised above the steel member, as shown in Figure 4.3(a). For girder members, where the deck is parallel to the girder span, the transformed moments of inertia were based on a T-beam approximation of the slab, as shown in Figure 4.3(b).



(a) Composite Slab on Beam (Deck Ribs Perpendicular to Member)



(b) Composite Slab on Girder (Deck Ribs Parallel to Member)

Figure 4.3: Representations of Composite Slab and Framing Members

Because the slab and framing members were modeled as separate elements, each has its own assigned moment of inertia about its own centroid, and from the plane grid modeling

choice, the centroids are located in the same XY-plane as shown in Figure 4.3(a) and (b). Thus, because the individual moments of inertia for the frame and slab elements about their own centroids are known, and the target transformed moment of inertia is also known, then a stiffness property modifier (PM) can be assigned to the strong axis moment of inertia of the frame members to represent a composite stiffness. Within SAP2000, property modifiers are multiplication factors that are applied to the desired geometric or material property of an element to increase or decrease its value. Using this approach, the sum of the transformed moment of inertia of the slab about its own neutral axis and the “modified” moment of inertia of the framing member will equal any desired target transformed moment of inertia for the composite beam/slab or girder/slab members. Identifying the strong axis stiffness property modifier to be applied to the framing member involved several steps, including computing the transformed moment of inertia for the beam/slab or girder/slab, subtracting out the computed transformed moment of inertia of the 3.25-in. slab area element about its own neutral axis, and then dividing through by the default strong axis moment of inertia of the predefined wide flange framing member. For girders, which include the deck ribs in calculations, the orthotropic stiffness property modifier on the slab must also be subtracted out so that it is not accounted for twice. An example of the computation of a transformed moment of inertia and baseline stiffness property modifier for a beam and a girder member can be found in Appendix K. It should be noted that property modifiers were computed using this method for all framing members of the modeled floors. These represent the “baseline” PM values computed and applied to the framing members. Adjustments to the stiffness PMs was the primary method for representing a different stiffness that was not considered in the composite calculations, such as spandrel or interior boundary members that may have greater stiffness due to attached exterior cladding or partition walls. The stiffness PMs used on these stiffer boundary elements are expressed as a multiple of the baseline values (e.g. 2.5 times baseline) in the presented research. The baseline computed composite stiffness property modifiers typically ranged from approximately 2.5 to 3.8 for the primary framing members of the modeled floors.

The user-defined *VIBCON* material was specified as an isotropic material, which assumes the same constitutive properties (modulus of elasticity, Poisson’s ratio) in all directions. While not an orthotropic material, the slab has an orthotropic stiffness due to the corrugated ribs. Assigning a property modifier to the girder members accounts for the composite action, however

using area elements with a constant 3.25-in. thickness (the portion of the slab above the deck ribs) does not account for the additional bending stiffness of the corrugated slab spanning the direction between beams. The strong direction moment of inertia of the 5.25-in. corrugated slab (i.e. bending includes deck ribs) is approximately three times larger than the moment of inertia of just the 3.25-in slab above the ribs, which is the effective portion resisting bending in the weak direction. To account for this, a bending stiffness property modifier of 2.88 was assigned to the *SLAB* plate area elements, which is the computed ratio of strong direction-to-weak direction moment of inertia of the concrete. As expected, applying this bending stiffness property modifier to the slab had the effect of increasing computed frequencies by 5-10%. More importantly, the effect was quite evident on the computed mode shapes, which included much more participation in bays adjacent in the direction of the deck ribs. This follows the behavior observed during experimental testing. The 2.88 ratio assigned to the slab element was also used to compute the PM for the girders, so as not to double count the orthotropic stiffness (although the bending stiffness of the slab is much smaller than the composite stiffness of the girder, so not subtracting out the 2.88 modifier has negligible effect).

As previously mentioned, the wide flange beams and girders were modeled explicitly using SAP2000's predefined steel sections rather than creating user-defined frame elements. An obvious advantage to this approach is that it more easily accommodates adjusting an existing floor model created by a design engineer for other analysis. Creating user-defined sections for a large number of framing members would be tedious, requiring the input of a wide variety of cross section properties that may or may not apply to the floor model. Although property modifiers were assigned to the strong axis moment of inertia to increase the section's bending stiffness to represent composite action, using the specified steel section kept all of the other member section properties intact and ensured the mass of the frame member was captured correctly. This approach also allows, if desired, shear deformations to be included in the computed frequencies and mode shapes. Shear deformations could be neglected simply by setting the framing members' shear area property modifiers to zero. Neglecting shear deformations essentially neglects flexibility, resulting in stiffer framing members and a 3-5% increase in computed frequencies for the floor models used in this study but no notable effect on mode shapes.

The plate elements used in the floor models of this research were the program default thin-plate elements, based on the Kirchhoff (thin-plate) formulation, which neglects transverse shear deformations. The alternative plate elements (not used) available in SAP2000 are based on the Mindlin/Reissner (thick-plate) formulation, which includes the effects of transverse shearing deformation but tends to be somewhat stiffer than the thin-plate formulation (CSI 2004). Iterations of models comparing the two plate formulations showed this to be true; however the computed frequencies were less than 1% higher for the stiffer thick-plate elements.

End Releases, Partial Fixity, and Boundary Conditions

Although modeling end and boundary conditions is a subset of representing the stiffness in a floor structure, they deserve a separate section to stress their importance as the greatest unknowns in modeling floors for evaluation of serviceability. One of the most significant modeling parameters that affected the computed frequencies and mode shapes was the stiffness of connections between beam, girders, and columns. The stiffness of beam and girder connections was handled using moment end releases and restrained DOFs in SAP2000. Moment end releases specify a pinned connection, allowing rotation between the end of the member and whatever it is connected to. When the end moment is not released, rotation between connected members is not allowed, however the joint itself is still free to rotate. Moment end releases differ from rotationally restrained DOF in that the assigned joint is not allowed to rotate when the DOF is restrained.

Intuition would suggest using a rotationally restrained DOF for members connected to columns with moment connections, however several model iterations demonstrated that this modeling technique over-restrained the models and did not allow certain mode shapes (and response in the members framing between columns) that were clearly measured during testing. Intuition may also suggest releasing the end moment of all members that are connected to columns with simple shear connections; however this provided too flexible of a system that also poorly represented mode shapes when the technique was applied to all locations with this connection type. From the presented research, the recommended configuration of beam/girder-to-column moment end releases that produced the best results for both frequency and mode shapes was releasing all end moments of members framing into column webs and *not* releasing end moments of members framing into column flanges, despite whether either connection was specified as a moment connection. It should be noted that this is a very simplified approach to

very complicated behavior of the column joint that is a function of several competing sources of stiffness, some of which are:

- Shear connections are not true pinned connections and provide rotational restraint.
- Centerline dimensions are used for the modeled geometry of all framing members and composite stiffness calculations, however members framing into column flanges can be 12-18-in. shorter (thus stiffer) based on actual clear distance.
- Although the framing members are assigned a composite moment of inertia over their full length, the actual stiffnesses at the ends are probably reduced by the perforation of the slab/deck system by the column and cracks that typically occur in the slabs over inter-column beams and girders, particularly if they are part of a moment frame (observed in the tested buildings).
- Shear connections into the webs of columns are rotationally more flexible compared to shear connections into the flange of a column. Moment end-plate weak axis connections (i.e. through the web of a column) are also rotationally flexible.
- The rotational contribution of the column will also affect the behavior of the joint for both moment and shear connected framing members.

Obviously the numerous contributions to the rotational stiffness of column joints, many of which remain unknown, are difficult and tedious to account for in a manner appropriate for the presented research. However, the competing inaccuracies of the proposed simplification resulted in models that adequately represented the behavior and response of the tested floors.

Most beams are connected to girder webs with simple shear connections, and it is generally assumed the continuity of the slab/deck over the joint provides enough continuity in the composite system that the slopes of the connecting beams on either side of girder are approximately the same. When moment end releases were applied to the ends of beams framing into girder webs, some of the computed mode shapes resulted in excessively discontinuous (i.e. kinked) mode shapes over the girder between adjacent panels due to differential rotation of the ends of the beams. Examining the experimentally measured mode shapes of the tested floors, there was often a noticeable discontinuity in the shape over the girder supports, although generally not nearly as excessive as in the full moment end-released models. It should also be noted that inspection of the tested floors showed cracks in the concrete slab over most girders and many beams spanning between columns, indicating a less-than-continuous floor slab over

these intermediate supports. The implication of this experimental observation on FE modeling is quite significant. Essentially, neither a continuous beam representation (i.e. no moment end releases for the beam members on either side of the girder web) or fully end-released beam representation may be adequate. When full moment end releases are specified, the only element providing continuity between adjacent bays across a girder is the thin 3.25-in. slab area element, which has a relatively weak bending stiffness resulting in the excessively discontinuous mode shapes. The measured behavior implies a rotational stiffness at this interface somewhere between the two representations. When specifying an end release in SAP2000, the option to include a partial fixity is available, which for moment end releases requires a value for the rotational spring in units of *kip-in/rad*. Figure 4.4 shows the example 8-bay floor model framing members with assigned releases and partial fixity designations. The columns in the example are oriented with their webs parallel to the direction of the beam framing, thus all girders have full moment end releases and the inter-column beams do not have any moment releases.

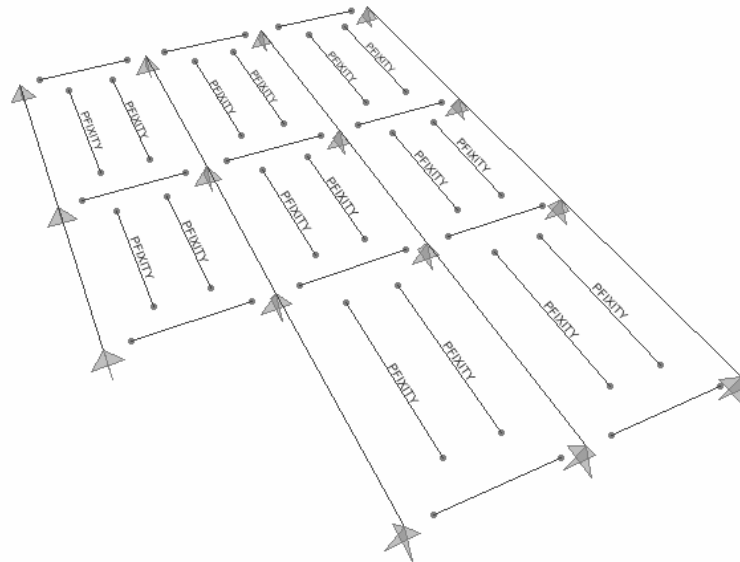


Figure 4.4: 8-Bay Floor Model Example – End-Release and Partial Fixity

Partial fixity spring values used were not based on experimental testing of the joints, instead they were determined from model iterations that produced frequencies and mode shapes that were in agreement with measured values. However, the values used *were* based on an assumed level of rotation at the end of the member that was translated into a fraction (or multiple) of EI/L for the framing member. This approach for specifying partial fixity was used for several reasons, but mainly so the rotational spring value used for any model would be based on properties of the actual framing member rather than arbitrary values. Additionally, by

specifying the rotational spring in terms of a coefficient to the frame member's baseline EI/L value, this coefficient can be used as an iteration parameter for model refinement. From iterations of the floor models in the presented research, it is recommended to use a moment end release partial fixity rotational spring value of $6EI/L$ at both ends for floor beam members that frame into girders. The $6EI/L$ value corresponds to a rotational spring at the ends of a simply supported beam under a static uniform load that responds with 25% of the rotation of a pinned-pinned supported member and 75% of the end moment of a fixed-fixed supported member under the same load. Ordered pairs of assumed moment and rotation can be used to solve for a value of the coefficient, such as $2EI/L$ for 50% end fixity or $(2/3)EI/L$ for 25% end fixity, although $6EI/L$ was used in the models of the presented research. A derivation of this method for determining rotational spring values is found in Appendix L.

The only end releases used in the presented models were the strong axis moments. Perry (2003) suggested releasing the weak axis moments at both ends of the member as well as one end of the torsional moment. The weak axis moment end releases had no effect on the computed frequencies because the floor models were analyzed as plane grid structures and the RZ rotational DOF was not used in analysis. Model iterations investigating the effect of releasing the torsional moment showed that this practice had virtually no effect on results, only changing frequencies by less than 0.001 Hz.

Like the end releases and partial fixity values, the boundary conditions of the floor models arguably had a very significant effect on the computed frequencies and damping. Boundary conditions consist of interior boundaries such as columns, interior partition walls, and the exterior spandrel members of the floor. The building's columns were modeled as pinned supports that restrained translational movement but allowed rotation. The vertical response of the columns was considered negligible because experimentally measured values from driving sinusoidally at the dominant frequency indicated the response was less than 1% of the response at the center of the bay. This small response at other frequencies was also confirmed by experimental measurements. The minimal response that was measured at the columns was more likely a function of the accelerometer being located some distance from the column centroid than an actual vertical response. Interior braced frames, such as those in the end bays of NOC VII, were also represented by pinned supports.

Generally, spandrel beams and girders were modeled with an increased stiffness modifier to represent the stiffening effect of the exterior cladding. An “increased” stiffness modifier means that a larger PM was used on the spandrel member than the original baseline PM computed based on DG11 composite section transformed moment of inertia calculations. Perry suggested using a stiffness property modifier of 1000 on the strong axis moment of inertia for spandrel beams and girders because the exterior walls and cladding sufficiently stiffen these members for floor vibration purposes (Perry 2003). Assigning stiffness property modifiers this large, the exterior boundary members essentially act like rigid walls within the model, however the experimental behavior of the tested floors proved otherwise. The measured response at these boundaries was much greater than an assumed wall (9-26% the mid-bay response), thus the suggested PM of 1000 was not used for spandrel members in the presented floor models. From model iterations comparing the spandrel member response with the mid-bay response, it is recommended to use a stiffness property modifier of 2.5 times the computed baseline PM. Another method used to stiffen the interior bays enclosed by full height partition walls was placing pin supports within the bays, essentially restraining the interior of the bay from vibration. Figure 4.5 shows the final layout of the example 8-bay floor model, including pinned supports along an interior beam to simulate cross bracing and additional pinned restraints to the slab on the interior of an enclosed bay to simulate an increased stiffness within this bay due to small mechanical rooms or elevator cores.

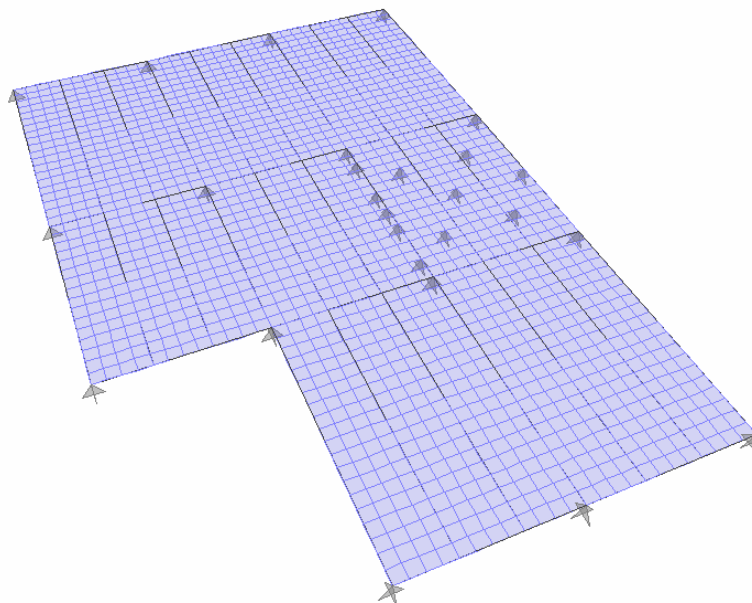


Figure 4.5: 8-Bay Floor Model Example – Pinned Supports Representing Interior Restraints

4.1.2 Dynamic Finite Element Analysis Techniques for Floor Systems

The previous section presented the first three general steps for creating an FE model of a floor system for evaluation of vibration serviceability, but the final three general steps described in this section outline the dynamic analysis of a floor's FE model for interpretation and evaluation. There are a variety of dynamic analysis case types available in SAP2000, including multi-step static, modal, response spectrum, time history, moving load, buckling, steady state, and power spectral density (CSI 2004). There are even more sub-options within each type of analysis case. Only three of these analysis case types were used and are discussed here: modal analysis, time history analysis, and steady state analysis (although modal analysis and steady state analysis are highlighted as the most important for the presented research). It should be noted that rather than describing all options and sub-options of each of the analysis cases in detail, only the relevant modeling choices (and justifications for each) are discussed. Beyond what is necessary to describe for the presented research, presentation of detailed background on the computational methods of SAP2000 is best left to the program's user manual. Additionally, the computational methods used in the research are described in as generic terms as possible so that the fundamental modeling and analysis techniques may be applied to other dynamic FE programs.

Modal Analysis

SAP2000's modal analysis of the floor's FE model computes the frequencies and mode shapes based on the assembled mass and stiffness matrices, without consideration of the presence or level of damping in the structure. The computed modes can be used as the basis for time history analysis; although the most important aspects of the modal analysis feature for evaluation of vibration serviceability are the computed dominant frequencies and the visual shapes of vibration for each of the modes. From experimental measurements, the lowest modes of a floor system generally have single curvature within bays, resulting in a concave up or concave down shape of the panel between columns. The same holds true for the FE model of a floor: the lowest computed modes are represented by single curvature within a bay, and double curvature within bays is not encountered until higher frequency modes. For a computed mode shape, just as in experimentally measured mode shapes, the response may be localized to just one bay or to several bays, generally located adjacent to one another. Again, this is a very important property for evaluation of serviceability because it links an area of the floor to a resonant frequency that

has the potential for excessive vibration due to human activities such as walking. In essence, visual inspection of the computed mode shapes highlights areas of vulnerability of a floor at their respective frequencies. The computed frequencies themselves are equally important, because the lower the frequencies of the floor, the more susceptible it is to lower harmonics of walking excitation. Using the 8-bay floor model as an example, the first six mode shapes and frequencies were computed using eigenvector modal analysis and are displayed in Figure 4.6.

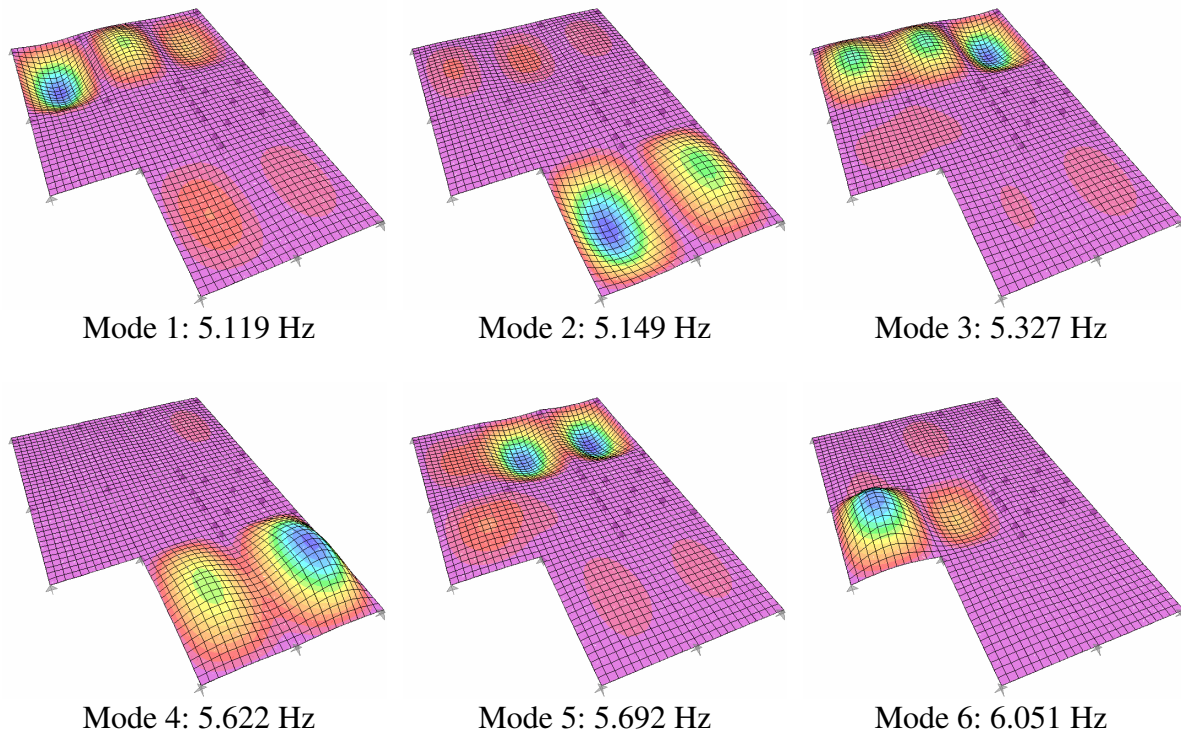


Figure 4.6: 8-Bay Floor Example – Computed Frequencies and Mode Shapes

The term “dominant” frequency is just as applicable for discussing computed frequencies as for experimentally measured frequencies. As shown for the computed mode shapes in Figure 4.6, a single bay of the floor model generally has dominant participation (as defined as the bay with the greatest response for the mode shape) at one frequency, and perhaps significant response at one or more other frequencies. For example, the bottom left bay has a dominant response in Mode 2 (5.149 Hz) and a significant response in Mode 4 (5.622 Hz) as well. It is from this observation that it can be expected any forced response analysis for loads placed within this particular bay will be dominated by contributions from these participating mode shapes. This follows experimentally measured behavior indicated by the dominant peaks (and other significant peaks) of the mid-bay driving point accelerance FRFs.

SAP2000 offers two methods of modal analysis, eigenvector analysis and Ritz-vector analysis. Eigenvector analysis determines the undamped free-vibration natural frequencies and mode shapes using only the mass and stiffness matrices to solve the generalized eigenvalue problem, whereas Ritz-vector analysis looks to compute the modes that are excited by a particular applied loading pattern (CSI 2004). Theoretically, Ritz vectors yield excellent results in dynamic analysis because they account for the spatial distribution of the loading, whereas the natural mode shapes do not. Ritz-vector analysis requires at least one starting load vector, such as an acceleration load or any of the defined load cases for the model. Several analysis iterations for both types of modal analysis were applied to the 8-bay example floor model to investigate the effect on the computed frequencies and mode shapes. The starting load vectors used for Ritz-vector analysis included the dead load of the structure from its self-weight under gravity (a logical choice) and various mid-bay point loads applied to the bays for forced response analysis. To briefly summarize the investigation, it was found that using Ritz vectors did not offer any advantage over eigenvectors for computing the frequencies and mode shapes for plane grid floor models. Depending on the number of Ritz vectors specified to be computed, the lowest computed Ritz-vector modes gave reasonable frequencies and shapes; however the higher computed modes were largely illogical. In certain cases, some lower frequency modes were only computed when a higher number of Ritz-vector modes were specified in the analysis case. In contrast, eigenvector analysis always computed the same lower modes despite the number specified in the analysis, which was advantageous for identifying how many modes were needed to cover a frequency range of interest (such as 4-12 Hz). The inconsistency of the computed mode shapes indicates the use of Ritz vectors is likely better reserved for other structure types, such as those with multi-direction mode shapes where only one direction is of interest. For example, a joist-supported footbridge with each member explicitly modeled may have “flapping” modes of the joist members and only the vertical modes of vibration are of interest. In this situation, Ritz-vectors computed using gravity dead loads as the starting load vector may be advantageous in filtering out these unnecessary modes. For the plane grid floor models in the presented research, however, the direction of vibration was never in question. Eigenvector analysis consistently produced logical mode shapes and thus it was used exclusively for the floor models in the presented research. It is recommended that a large number of modes be computed during early iterations of modal analysis of the floor model to ensure that all modes including

single curvature within all bays of interest are represented. Once these modes (and frequencies) are determined, subsequent analyses involving the modal analysis case can be scaled back in the interest of computation effort to only include the relevant modes.

Damping

As previously mentioned, eigenvector modal analysis assumes all modes computed for the structure are non-complex, hence it solves the eigenvalue problem for frequencies and mode shapes without consideration of the presence or level of damping. For computation of forced response, however, SAP2000 requires damping to be specified. SAP2000 allows the option to specify damping in several different ways, generally in the form of modal damping ratios or as Rayleigh damping (i.e. using mass and stiffness proportional coefficients), depending on the type of dynamic analysis and the methods used to solve them. Brief descriptions of how damping was specified in the analysis methods used in this research are presented in this section. The user's manual for SAP2000 gives a more detailed description of the various ways the FE software incorporates damping in its analyses (CSI 2004).

For time history analysis using modal superposition (i.e. using the computed modes from the modal analysis), modal damping may be specified as constant for all modes, specified for each mode individually, interpolated by period or frequency, or even specified as a proportional level of damping based on the mass and stiffness matrices. For time history analysis using direct integration, where computed modes are not used in the computation of the response, Rayleigh damping is used and requires specification of mass and stiffness proportional coefficients. Additional damping may be included in the response if it is also included as an assigned property of the material.

For frequency-domain response calculations, such as the steady state analysis heavily used in this research, damping is specified in terms of hysteretic damping (also known as rate-independent damping) in the form of mass and stiffness proportional damping coefficients. These coefficients may be specified as either constant hysteretic damping for all frequencies or interpolated between specified frequencies and their respective damping values. As with time history analysis, stiffness and mass proportional coefficients may also be specified for individual materials to be included in frequency-domain computations. The steady state analysis solution is solved directly without computing the modes, thus specifying modal damping directly is not an option, only hysteretic damping. However, modal damping can be approximated by specifying

the mass proportional coefficient as zero and the stiffness proportional coefficient equal to twice the modal damping ratio (i.e. use 0.02 as a stiffness proportional coefficient for a target modal damping ratio of 1%). A full derivation of this property is presented in the text by Chopra (2000).

As previously stated, damping is not a value computed by FE analysis; it is specified from experimental measurements as estimated damping values. Unfortunately, the experimentally measured values of damping for the two modeled floors varied significantly with no discernable trend based on their corresponding frequencies. Measured modal damping values for NOC VII-18 were 0.60% to 2.4% of critical for frequencies between 4.85 Hz and 6.55 Hz. For VTK2, damping values were 0.50% to 1.3% of critical for frequencies between 6.58 Hz and 8.20 Hz. This wide range of damping values for the relatively narrow range of frequencies posed a significant challenge for specifying damping in the FE models and achieving forced response analysis results that were in agreement with measured response.

For simplicity, constant damping values for all frequencies were used in all steady state analyses in the presented research. The constant damping value used for each mid-bay analysis location was the estimated damping at the dominant frequency of the corresponding experimental driving point accelerance FRF measurement. This simplification was made for the benefit of using the recommended modeling and analysis techniques for evaluation of vibration serviceability. In the absence of any measured values, which is the case for a design engineer modeling a floor that has not yet been constructed, there is no other choice but to assume a level of damping for forced response analysis. DG11 recommends several damping ratios based on the structure type and fit out (Murray et al. 1997). For bare floors with no non-structural fit out components or furnishings, such as the tested floor, it recommends a damping ratio of 1% of critical (0.01). DG11 also recommends a damping ratio of 2% for floors with few non-structural components or furnishings and 3% for floors with non-structural components, furnishings, and small demountable partitions that are found in modular office spaces. To investigate the ability of the recommended modeling techniques to adequately represent the measured response assuming no prior knowledge of measured damping values, assumed values of damping were used in analysis for each investigated location on the floor models. This resulted in two steady state analyses for each mid-bay forcing location for comparison with measured values, one using a measured damping value and one using an assumed damping value. As expected from the

wide range of measured damping values, efforts using a single assumed value of 1% for all bays investigated did not give very good results. However, based on a few observations of the measured damping in different locations of the tested floor, there was much better agreement using the following recommended damping values:

- 1% damping for typical bays
- 1.5% damping for corner bays
- 2% damping for interior bays adjacent to interior framing

Although the higher levels of damping were not always observed for corner bays or interior bays, the trends were observed in some cases and are appropriate assumptions considering the most significant source of damping for a bare floor will likely be at its boundaries, such as the friction at exterior boundaries (a corner bay has two exterior boundaries) or semi-structural interior framing. Once a floor is occupied, the addition of fit out materials will likely become the dominant source of damping, and thus a constant value for all bays should be appropriate for modeling purposes.

Time-History Analysis and Steady State Analysis

For comparison of measured acceleration response to computed values, dynamic loads were applied to the FE models for forced response analysis. The two types of forced response analysis used were time-history analysis and frequency-domain steady state analysis, the latter being the most used type of analysis in the presented research for its direct comparison with measured response values in the frequency domain. Steady state analysis also serves as the cornerstone of the proposed method of vibration serviceability evaluation presented at the end of this chapter. Each of the two types of forced response analysis requires load(s) applied spatially to the structure. Because experimental measurements of the tested floors were only taken with one shaker at the center of a tested bay, the corresponding forced response analysis was performed with a single point load located at the mid-bay location. There are several opportunities when setting up the analysis cases in SAP2000 to scale the applied loads, therefore the magnitude of the mid-bay point load was set to 1 lb to allow flexibility in later analysis. The use of a unit load also proved advantageous for comparison with measured accelerance values because the computed steady state acceleration response to sinusoidal load in in/s^2 units would also be equivalent to accelerance units of $\text{in/s}^2/\text{lb}$ of input force at the driving frequency. Figure 4.7 shows an example of the mid-bay location of the applied unit load for the 8-bay floor model.

Both the time-history analysis and frequency-domain steady state analysis examples that follow in this section refer to this driving point location as well as the computed mode shapes for the 8-bay floor model shown in Figure 4.6.

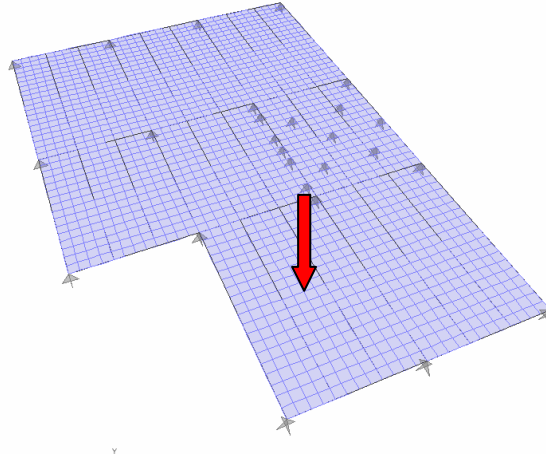


Figure 4.7: 8-Bay Floor Example – Applied Unit Load (1 lb) for Forced Response Analysis

Time-History Analysis – Time-history analysis, like its name, computes the time history response to a dynamic (time-varying) load. The dynamic equations of motion that are solved during the time-history analysis are shown in Equation (4.3) (CSI 2004):

$$\mathbf{M} \ddot{\mathbf{u}}(t) + \mathbf{C} \dot{\mathbf{u}}(t) + \mathbf{K} \mathbf{u}(t) = \mathbf{r}(t) \quad (4.3)$$

where

\mathbf{M} = diagonal mass matrix

\mathbf{C} = damping matrix

\mathbf{K} = stiffness matrix

$\ddot{\mathbf{u}}(t)$, $\dot{\mathbf{u}}(t)$, $\mathbf{u}(t)$ = joint accelerations, velocities, and displacements, respectively

$\mathbf{r}(t)$ = arbitrary applied dynamic loading

There are several options for time-history analysis. For floor models, it is recommended that linear analysis is used rather than nonlinear. This is a safe assumption, as the small amplitude vibrations do not approach yielding conditions. Two different solution methods are available to perform the time-history analysis of the equations in Equation (4.3): modal superposition using the modes computed from the modal analysis, or direct integration of the coupled equations of motion. Ideally, both methods should yield the same results, however the modal method is recommended. Modal damping is generally used for the modal time-history analysis, and it is generally much faster than direct integration, which requires damping to be

specified using mass and stiffness proportional coefficients. It should be noted that modal time-history analysis uses all modes in the specified modal analysis case, thus any number of modes can be used for computation of the time-history response, depending on modes computed in the modal analysis case. Lastly, the time-history analysis may be performed considering the applied load is either transient or periodic. A transient solution considers the load as a one-time event, thus the solution is computed assuming the structure starts from rest when the applied loading begins and includes the transient response. The periodic solution considers the load to repeat indefinitely, with the transient response damped out (CSI 2004). The periodic option is only available if modal time-history analysis is used. For the purposes of any time-history analysis for floor models, it is recommended to use transient analysis.

SAP2000 offers several types of time history functions to attach to the applied load for dynamic analysis, such as sine, cosine, ramp, or triangular functions. The ability to apply a sinusoidal load to the model and compute the acceleration response is of immediate interest for several reasons. First, the acceleration frequency response function is simply a representation of the steady state sinusoidal response at various frequencies. More importantly, driving the model sinusoidally at its resonant frequency, by definition, will generate its greatest acceleration response. Additionally, the acceleration response at the mid-bay forcing location is the quantity most often computed by the various simplified design methods for comparison with some form of serviceability criterion. How to define a sinusoidal forcing function in SAP2000 is not presented here, but can be found in the thesis by Perry (2003) or the user's manual of the FE program (CSI 2004).

To demonstrate this application of time-history analysis, the example 8-bay floor model was driven sinusoidally by the mid-bay unit load shown in Figure 4.7 at 5.149 Hz, the dominant frequency of the bay of interest (as shown by the greatest response in this bay of any of the mode shapes in Figure 4.6). A linear modal-time history analysis was performed assuming a transient time history type. The analysis included all six modes shown in Figure 4.6 that were computed using eigenvector analysis, and modal damping was input as a constant 0.95% of critical for all modes. The computed time-history of the acceleration response at the mid-bay location is shown in Figure 4.8. The acceleration response is as expected, which includes the floor starting at rest followed by a build-up to resonance (note that there is a slight transient response at the beginning of the build-up) before reaching steady state response. The magnitude of the steady state portion

of the computed acceleration response is 0.8013 in/s^2 . Because a unit load was used, it could be stated that the computed *accelerance* at the resonant frequency of 5.149 Hz was $0.8013 \text{ in/s}^2/\text{lb}$ of input force. Response in the form of accelerance is a result that could be directly compared to experimentally measured values as the applied sinusoidal loads (and thus the corresponding acceleration responses) varied for different tests and different frequencies.

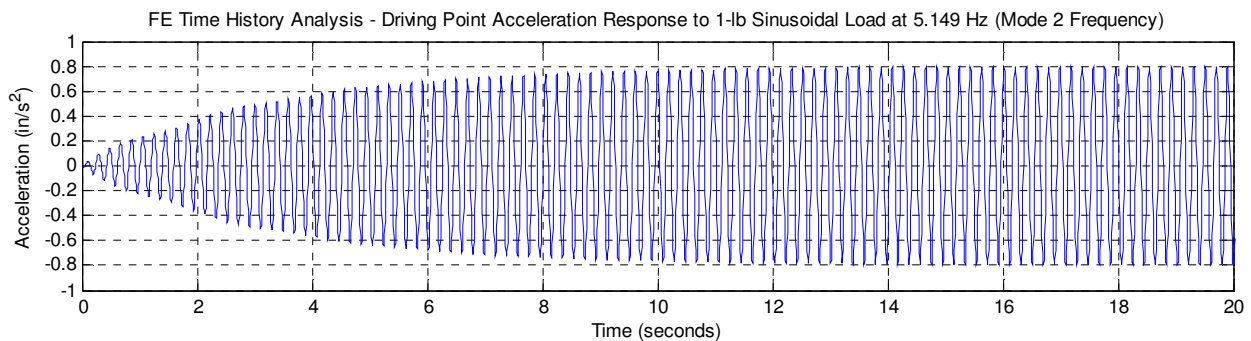


Figure 4.8: 8-Bay Floor Example – Time History Response to Sinusoidal Load

Note that the dynamic loading, $r(t)$, in Equation (4.3) is arbitrary. Besides the ability to define the above listed periodic time history functions, SAP2000 also allows the user to define any time varying load. Theoretically, the experimentally measured time-varying loads from the force time-histories of instrumented heel drops or burst chirp signals could be imported for analysis of the computed response and compared to measured response. Although a convenient feature that will likely prove useful in future research, the only dynamic functions analyzed using time-history analysis in the presented research were sinusoidal loads. While the computed acceleration response from an applied sinusoidal load is a convenient demonstration of mid-bay time-history analysis for comparison with measured values, it is a rather clumsy method for computing the accelerance because it is limited to the response at only a single frequency. Frequency-domain steady state analysis provides the most efficient method of comparison of response between measured and computed behavior.

Steady State Analysis – Frequency-domain steady state analysis computes the dynamic response to a set of harmonically varying loads (e.g. a sine and cosine function) at specified frequency increments. It seeks the steady state response, thus assuming the harmonic loading is indefinite and all transient response has damped out. Equation (4.4) shows the dynamic equations of motion that are solved in the frequency domain, for which the form of the solution is explained in greater detail in the user’s manual for SAP2000 (CSI 2004):

$$\mathbf{M} \ddot{\mathbf{u}}(t) + \mathbf{C} \dot{\mathbf{u}}(t) + \mathbf{K} \mathbf{u}(t) = \mathbf{r}(t) = \mathbf{p0} \cos(\omega t) + \mathbf{p90} \sin(\omega t) \quad (4.4)$$

where \mathbf{M} , \mathbf{C} , \mathbf{K} , $\ddot{\mathbf{u}}(t)$, $\dot{\mathbf{u}}(t)$, and $\mathbf{u}(t)$ are the same as previously defined and

$\mathbf{r}(t)$ = harmonic loading where $\mathbf{p0}$ is the in-phase (real) component

and $\mathbf{p90}$ is the 90° out-of-phase (imaginary) component

ω = the circular frequency of excitation (rad/sec)

The most important feature of Equation (4.4) is the harmonic loading that represents an in-phase and 90° out-of-phase component. This simplifies the equations to be solved in the frequency domain, but more importantly the resulting solution represents the real and imaginary components of response at each frequency increment. At each frequency increment, the real and imaginary component of response can be combined through a square root of the sum of the squares (SRSS) computation to give the magnitude of response. These quantities can also be used to determine the phase angle between the applied loading and the acceleration response. While any spatially distributed load can be used in steady state analysis (i.e. multiple point loads, distributed loads, acceleration loads, etc.), *the choice of using a unit point load at a single location for steady state analysis results in the computational equivalent of the accelerance frequency response and yields quantities directly comparable to measured accelerance FRFs.* Because steady state analysis computes the response for all degrees of freedom of the FE model, the results essentially represent a column of the accelerance FRF matrix just as a full set of experimentally measured accelerance FRFs would for a single location of excitation. This ability to compute the accelerance FRF of a floor's FE model is the most significant feature for validation of a model with respect to experimental measurements and also forms the basis for a proposed method of evaluation for vibration serviceability presented at the end of this chapter.

The application of steady state analysis is best demonstrated using the previously discussed example 8-bay floor model. For this example and comparison with the previous time-history analysis, the model was analyzed with the unit load located in the bay as shown in Figure 4.7. A target value of damping for the floor was 0.95% of critical for all modes. As previously stated, SAP2000 specifies hysteretic damping for frequency-domain calculations, thus damping must be specified as mass and stiffness proportional coefficients. It may be specified as constant hysteretic damping for all modes or interpolated hysteretic damping by frequency. For the presented example, an equivalent 0.95% modal damping for all modes was approximated by choosing constant hysteretic damping and specifying the mass proportional coefficient as 0 and

the stiffness proportional coefficient as 0.019 (see previous Damping section for details on this method). The range of frequencies to be solved was chosen to be 4 Hz to 8 Hz divided into 80 increments, resulting in a frequency resolution of the computed values of 0.05 Hz. It should be noted that the computed steady state solution is performed *directly* for all specified frequency increments, without use of the modes computed in the modal analysis case like the presented time-history analysis example. Consequently, computed values are just as susceptible to the effects of frequency resolution as experimental measurements because peak frequencies may lie between two computed/measured frequency increments. Although the modal analysis is not used directly in computing the solution, the frequencies from the modal analysis can be included as specified frequency increments to be solved during the analysis. Steady state analysis results may be presented in a variety of ways, although all are based on the computed real and imaginary components of response as shown in Figure 4.9 for the driving point location.

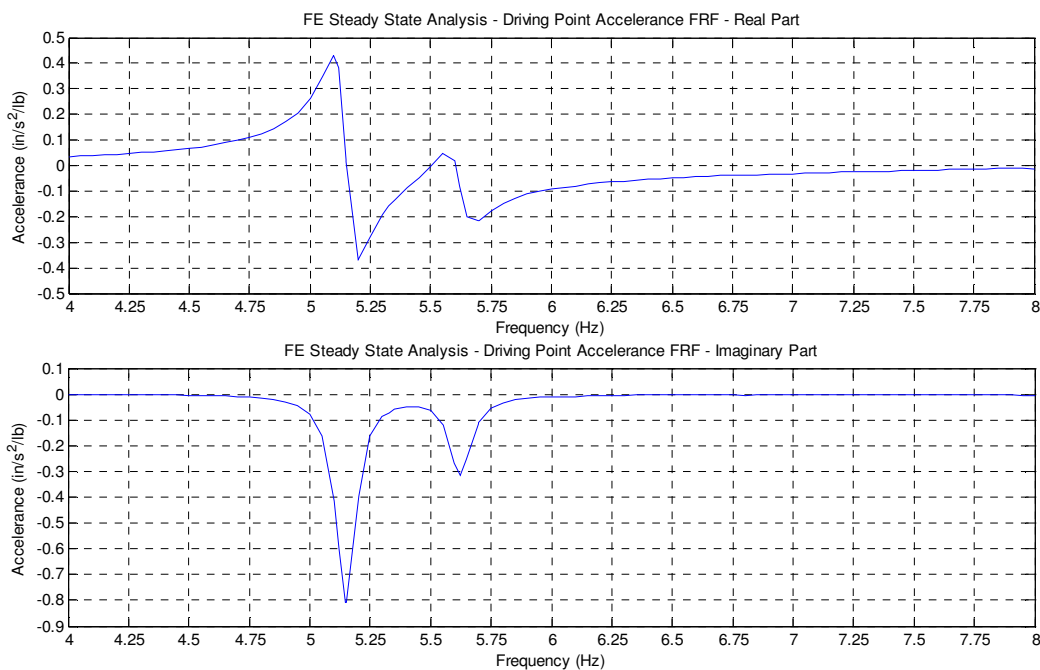


Figure 4.9: 8-Bay Floor Example – Driving Point Accelerance FRF (Real and Imaginary)

Although plotting the real and imaginary components gives valid representations of the accelerance FRFs, a more intuitive representation of the response for the presented research is given by the magnitude and phase as shown in Figure 4.10. From this representation, a few features are of immediate interest and provide valuable insight into the floor's behavior. First, there are clearly two significant peaks in the response, 5.149 Hz and 5.622 Hz, which correspond to the second and fourth modes of the 8-bay floor model as shown in Figure 4.6. Secondly, the

magnitudes of the computed response indicate both frequencies participate significantly, but the 5.149 Hz mode is clearly dominant. Lastly, the peak accelerance of the 5.149 Hz frequency was 0.8075 in/s²/lb of input force, which is in excellent agreement with the 0.8013 in/s²/lb accelerance estimated from the time-history analysis. Because steady state analysis directly solves the system of equations of motion, the results are likely to be more accurate than a modal time-history analysis that uses a finite number of modes and relies on the cumbersome method of identifying the peak amplitude of the time-history response once it achieves steady state.

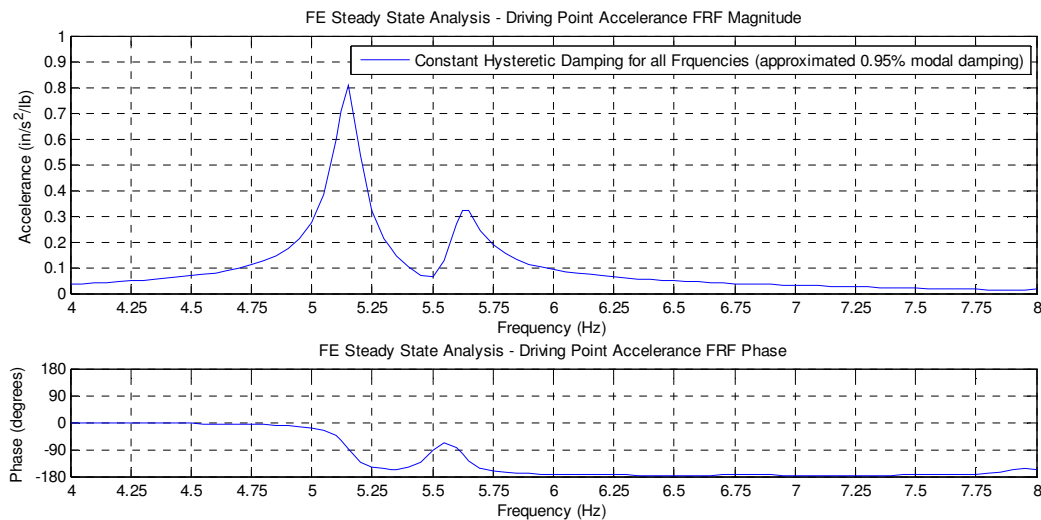


Figure 4.10: 8-Bay Floor Example – Driving Point Accelerance FRF and Phase

The computed real, imaginary, and magnitude components of response can be displayed in SAP2000 or exported for plotting in other programs, however the phase plot shown in Figure 4.10 is not internally computed by the program and was plotted by taking the inverse tangent of the imaginary component over the real. It should be noted that the computed accelerance trace shown in Figure 4.10 is only for one location on the floor, the driving point, and there are literally thousands of similar traces computed for all mass degrees of freedom in the floor model (1843 mass DOFs for the example 8-bay floor model). Like the experimental testing of in-situ floors, the driving point response is the most important computed response, however representing the response over the entire floor area is also of interest. SAP2000 allows animation of the computed response at any frequency increment (and any phase at that frequency increment). Figure 4.11 displays two animated representations of the response that are useful from a vibration serviceability standpoint. The first animated shape shown in Figure 4.11(a) is the floor response at its 5.149 Hz dominant frequency. Note that although this closely

approximates the mode shape, as a forced vibration response it is actually the computed equivalent of the operating deflection shape (ODS) at this frequency. It is plotted at a phase of 90° , as the response at resonance is almost purely defined by the imaginary component. Another useful form of the response is shown in Figure 4.11(b), which is the envelope of response that displays the absolute maximum response at any point on the floor model for any of the computed frequency increments between 4 Hz and 8 Hz. This is useful for displaying areas of the floor that are excited by the forcing location but are not readily apparent in the computed driving point accelerance FRF or the computed ODS at the dominant frequency.

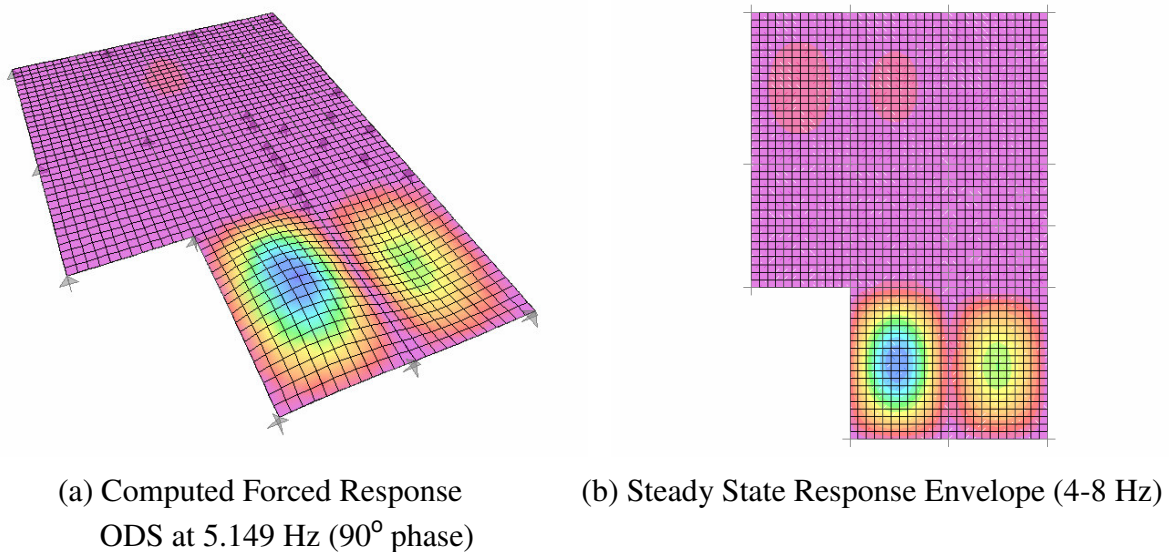


Figure 4.11: 8-Bay Floor Example – Other Representations of Response

Although a unit load is used for steady state analysis to ensure the units of response are $\text{in/s}^2/\text{lb}$, the mid-bay unit load may be scaled to any value to effectively convert the computed accelerance values to the units of choice. For example, all accelerance FRF measurements in the presented research originated in units of volts/volts from the DSP spectrum analyzers. During post-processing, calibration values were used (240 lbs/volt for the force plate and 1 g/volt for the accelerometers) to convert to accelerance units of $\text{in/s}^2/\text{lb}$. For pre-test modeling of a floor system, the unit loading could be scaled to 0.622, effectively converting all computed response values from $\text{in/s}^2/\text{lb}$ to volts/volt and allowing easy real-time comparison of measured accelerance magnitudes to pre-test FE values.

Constant hysteretic damping for all frequencies was used for the example presented above. The alternative method for specifying damping in steady state analysis is interpolated

hysteretic damping, which allows mass and stiffness proportional coefficients to be specified for any number of frequencies. To investigate the effect on the computed response using this interpolated hysteretic damping option, two analyses were run on the same 8-bay floor model. The first analysis specified 0.95% damping at the first peak (5.149 Hz) and twice as much damping, 1.80%, at the second peak (5.622 Hz). This effectively specified a linearly increasing level of damping that includes these two ordered pairs. For comparison with the constant hysteretic damping option, the second analysis specified 0.95% damping at both 4 Hz and 8 Hz, effectively specifying a constant level across the frequency range. The two computed driving point accelerance traces are plotted in Figure 4.12. As shown, nearly identical response was computed for the 5.149 Hz peak where 0.95% damping was specified for both cases. For the 5.622 Hz peak with twice as much specified damping, the response is obviously lower but not quite half the previous level of response, which would be expected. The analysis specifying constant damping using the interpolated option computed the exact same response as when constant hysteretic damping was specified. Although constant hysteretic damping was exclusively used in the presented research, the examples using the interpolated hysteretic damping option are presented for demonstration of alternative approaches to force response.

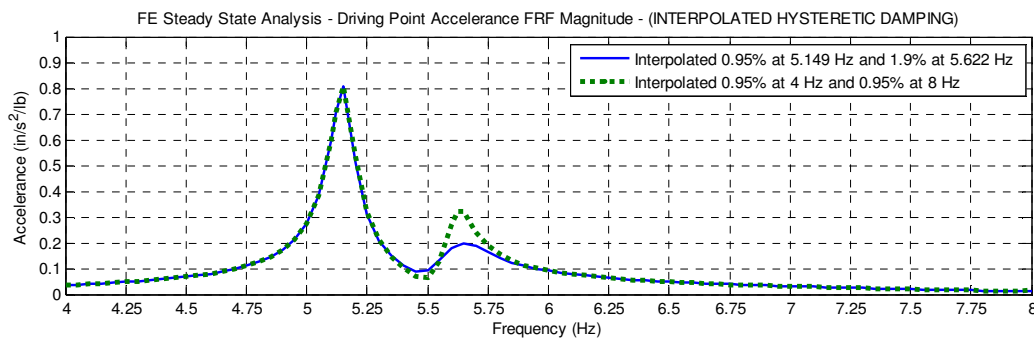


Figure 4.12: 8-Bay Floor Example – Examples Using Interpolated Hysteretic Damping

The implications of this application of FE frequency-domain steady state analysis is substantial for potential evaluation of vibration serviceability as well as experimental testing of in-situ floors. While the computed frequencies and mode shapes may provide insight into the areas of a floor that are potentially vulnerable to excitation at certain frequencies, this is only half of the information needed for evaluation of vibration serviceability, with the other half being the acceleration response in those areas at the vulnerable frequencies. The computed mid-bay driving point accelerance FRF provides all information in a single trace, with the magnitude and locations of the computed accelerance peaks representing the dominant and other significantly

participating frequencies (modes) of the bay as well as the estimated level of acceleration response. If an in-situ floor is modeled prior to experimental testing, the measured mid-bay driving point accelerance FRF can be directly compared to the computed accelerance FRF in the field for instant feedback of the validity of the pre-test FE floor model. This instant feedback may also alleviate the need for extensive modal measurements and post-processing to extract the experimentally derived mode shapes. Additionally, the experimental mid-bay floor evaluation approach described in Section 3.4 may be all that is required for validating and updating floor FE models. Using this approach, a set of experimental mid-bay driving point accelerance FRFs would indicate the participating frequencies of a bay, the accelerance at the peaks, the general mode shape if a set of mid-bay measurements were acquired, and measured estimates of damping that may differ from assumed values of the pre-test FE model.

4.2 Finite Element Analysis of Tested Floors

This section presents the finite element models of the tested floors that were generated using the techniques discussed in the previous section. It should be noted that the recommended techniques, particularly recommendations of spandrel member property modifiers, member end releases and partial fixity values, and damping used for analysis were developed during efforts to bring the results of the FE models into agreement with experimentally measured values. The FE models were developed *in parallel* so that the same techniques applied to each gave adequate results for both models. Although not presented here, certain model iterations were better at predicting frequencies and mode shapes, and other iterations were better at predicting acceleration response. This was achieved with different combinations of the above listed parameters; however the objective of the research was to identify a set of common/fundamental modeling techniques that yielded adequate results, not adjustments required to optimize an individual model unless those adjustments improved the results of both models. Thus, while the presented results may not represent the closest match of frequencies, mode shapes, and acceleration results achieved during the course of research, the promising results presented in this section demonstrate that an adequate representation of in-situ floor behavior is possible using a common set of basic modeling techniques. Although the two FE models of the tested floors were developed simultaneously, the FE model for NOC VII is presented first in Section 4.2.1, followed by the model for VTK2 in 4.2.2.

4.2.1 New Jersey Office Building, NOC VII

Two FE models are presented for the NOC VII floor. The first model represents the whole floor. A smaller model, representing a portion of the floor, was developed to address difficulties in achieving proper frequencies and mode shapes in bays along the long length of the building. Although not originally the intent of the research, the smaller model of a portion of the floor was generated using the same fundamental techniques and provided some encouraging results, highlighting an area for further research.

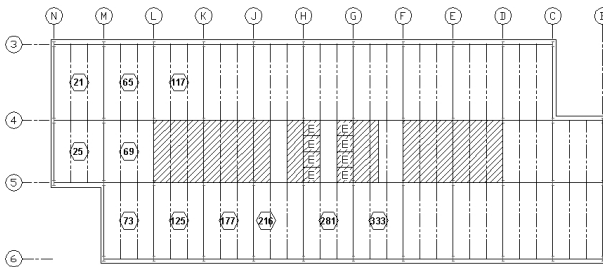
NOC VII Full Floor Model – Following the general steps previously discussed, the floor framing geometry was laid out for the full floor model with the steel framing members specified in the design drawings and pinned supports were applied at the column locations. A user-defined material (NOCVII-VIBCON) and area plate element (NOCVII-SLAB) were created to represent

the composite slab in the floor model. The input values of these user-defined parameters and the composite slab properties used in their development are presented in Table 4.1. The DG11 recommended dynamic modulus of elasticity was used ($1.35 \cdot E_c$) and the weight and mass densities of the material were computed using Equations (4.1) and (4.2). Slab details and the framing plan of the specified steel sections for NOC VII are presented in Appendix A. Plan and 3-D views of the floor model's slab and framing layout are in Figure 4.13, including the eleven locations of forced response analysis presented later in this section for comparison with experimental measurements.

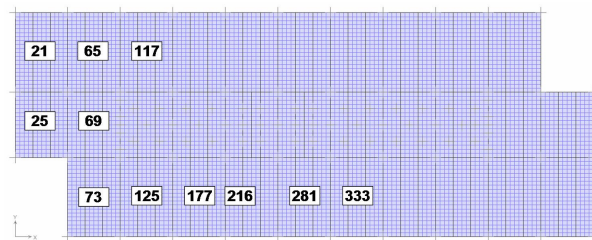
Table 4.1: NOC VII – Composite Slab Parameters & Slab Area Element/Material Properties

Overall Slab/Deck Height:	5.25 in.	Unit weight of concrete, w_c :	115 pcf
Slab height above ribs, d :	3.25 in.	Concrete compressive strength, f'_c :	4000 psi
Deck rib height, d_r :	2.00 in.	Dynamic modulus of elasticity, $1.35 \cdot E_c$:	3300 ksi
Area weight of steel deck, w_{deck} :	2.4 psf	Superimposed loads, $w_d + w_l + w_{coll}$:	0 psf

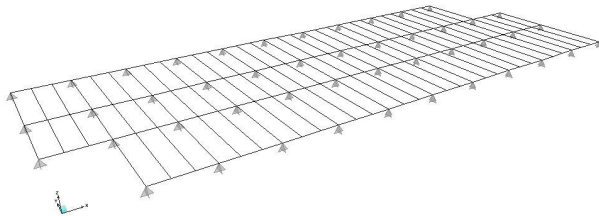
User-Defined Material Name:	NOCVII-VIBCON	User-Defined Area Section Name:	NOCVII-SLAB
Type of Material:	Isotropic	Type of Area Section:	Plate-Thin
Mass per unit Volume:	$2.3869 \times 10^{-7} \text{ k-s}^2/\text{in}^4$	Assigned Material:	NOCVII-VIBCON
Weight per unit Volume:	$9.2156 \times 10^{-5} \text{ k/in}^3$	Thickness (Membrane/Bending)	3.25 in.
Poisson's Ratio	0.2	Stiffness Modifiers:	Bending m11 = 2.88
Additional Material Damping:	None		



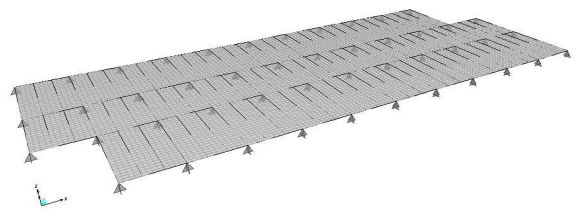
(a) NOC VII Floor Framing Layout



(b) FE Model Plan View of Framing & Slab



(b) 3-D View – Framing Only



(c) 3-D View – Framing and Slab

Figure 4.13: NOC VII – Floor Layout and Full Floor FE Model

It was found that a slab area element size of 30 in. x 28 in., which corresponds to a mesh size of 12x16 elements for interior bays and 12x20 elements for exterior bays, gave convergent

results. With this configuration, the full floor model contains over 7,000 mass degrees of freedom (UZ). With the vast number of joint numbers to track, the joints were renumbered in a manner to ease analysis of the results. Initially, all joints were automatically numbered using the features available in SAP2000, starting from 1001. The joints on the model corresponding to a measured location were manually renumbered in the pattern of Figure 3.8. (Although not required, this practice is recommended as a convenience when models are to be used in comparison with floor testing. This method simplifies identifying points of interest for extracting acceleration response from steady state analysis. Additionally, this practice is also conducive for comparing measured/computed mode shapes because the DOFs of interest are the first in the list of tabulated joint numbers and the remaining values can be discarded.)

The transformed composite moments of inertia were computed for each framing member to determine the baseline stiffness property modifiers, which ranged from 2.6 to 3.6 for NOC VII. The modifiers were computed as described in Section 4.1, and an example of this computation is presented in Appendix K. A full listing of the calculated transformed moments of inertia and their respective baseline PMs for NOC VII is found in Appendix M. The baseline values were applied as PMs to the strong axis moment of inertia for all framing members, and 2.5 times the baseline values were applied as PMs to all spandrel beams, spandrel girders, and the interior girders adjacent to bays with full height partition walls to account for the increased stiffness along these interior boundaries. Final assigned PMs are also listed in Appendix M.

Strong axis bending moment releases without any partial fixity were applied to all members framing into the webs of columns, which were limited to all girders for NOC VII. No moment releases were applied to the beam members that framed into the flanges of columns. Strong axis moment releases were applied to all beams framing into the webs of girders, and partial fixity values of $6EI/L$ (EI/L computed using properties of the beam member) were applied at both ends. Again it should be noted that the release and/or partial fixity condition of the end of a beam member framing into a spandrel girder had a negligible effect on the frequencies and mode shapes of the floor because of the minute contribution of the torsional stiffness of the spandrel girders to the stiffness of the system. Because the effect is negligible, it is recommended to include the release and partial fixity at both ends for the convenience of not having to be concerned with the local axis of the member and whether or not the correct end is

released. Figure 4.14 shows the framing layout of NOC VII, the end releases, and members with assigned partial fixities.

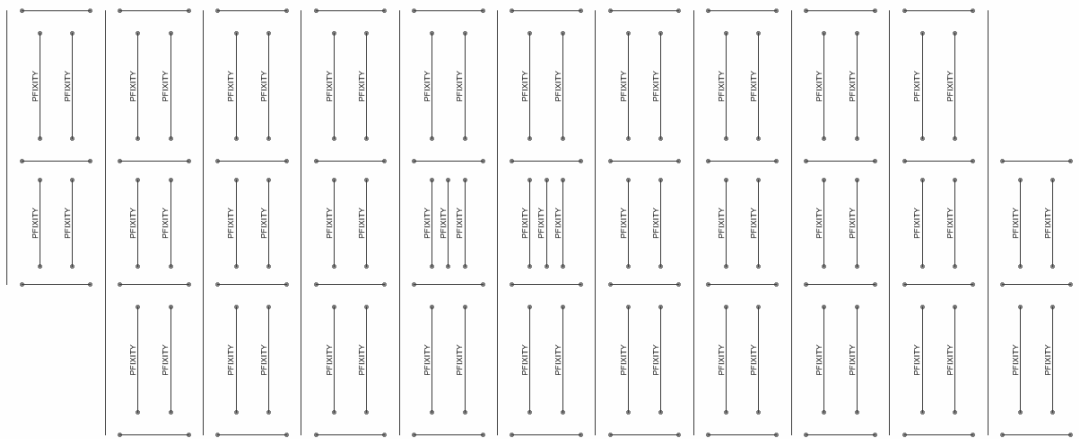


Figure 4.14: NOC VII – Full Floor Model Moment End Releases and Partial Fixities

Besides increasing the stiffness properties of the interior girders adjacent to the partition walls, additional pinned restraints were applied to the interior bays to represent elevator core framing, stairwells, restroom, mechanical room, electrical room partition walls, etc. The actual partition layout was not available, thus the layout of the pinned restraints was based on judgment. Along grid lines D and M, several pin restraints were added to represent the heavy concentrically braced frames attached to the beam members spanning between the columns. The locations of the interior pinned restraints are shown in Figure 4.15. It should be noted that the locations of these interior pins were based on judgment and may provide some degree of over-restraint that prevented the model from accurately predicting the mode shapes and frequencies of the exterior bays along the long side of the floor.

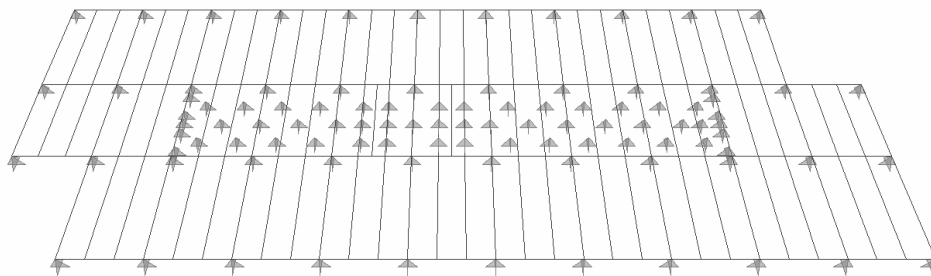


Figure 4.15: NOC VII – Full Floor Model Interior Restraints

An eigenvector modal analysis was performed on the floor model to compute the frequencies and mode shapes. The frequencies of the first 24 modes are presented in Table 4.2 and the corresponding mode shapes are presented in Figures 4.16 and 4.17.

Table 4.2: NOC VII – Computed Modes for Full Floor Model

Mode:	Frequency (Hz)	Mode:	Frequency (Hz)	Mode:	Frequency (Hz)
1	5.151	9	5.475	17	6.025
2	5.151	10	5.492	18	6.047
3	5.191	11	5.618	19	6.103
4	5.192	12	5.627	20	6.134
5	5.316	13	5.774	21	6.138
6	5.322	14	5.774	22	6.141
7	5.374	15	5.914	23	6.939
8	5.390	16	5.926	24	6.955

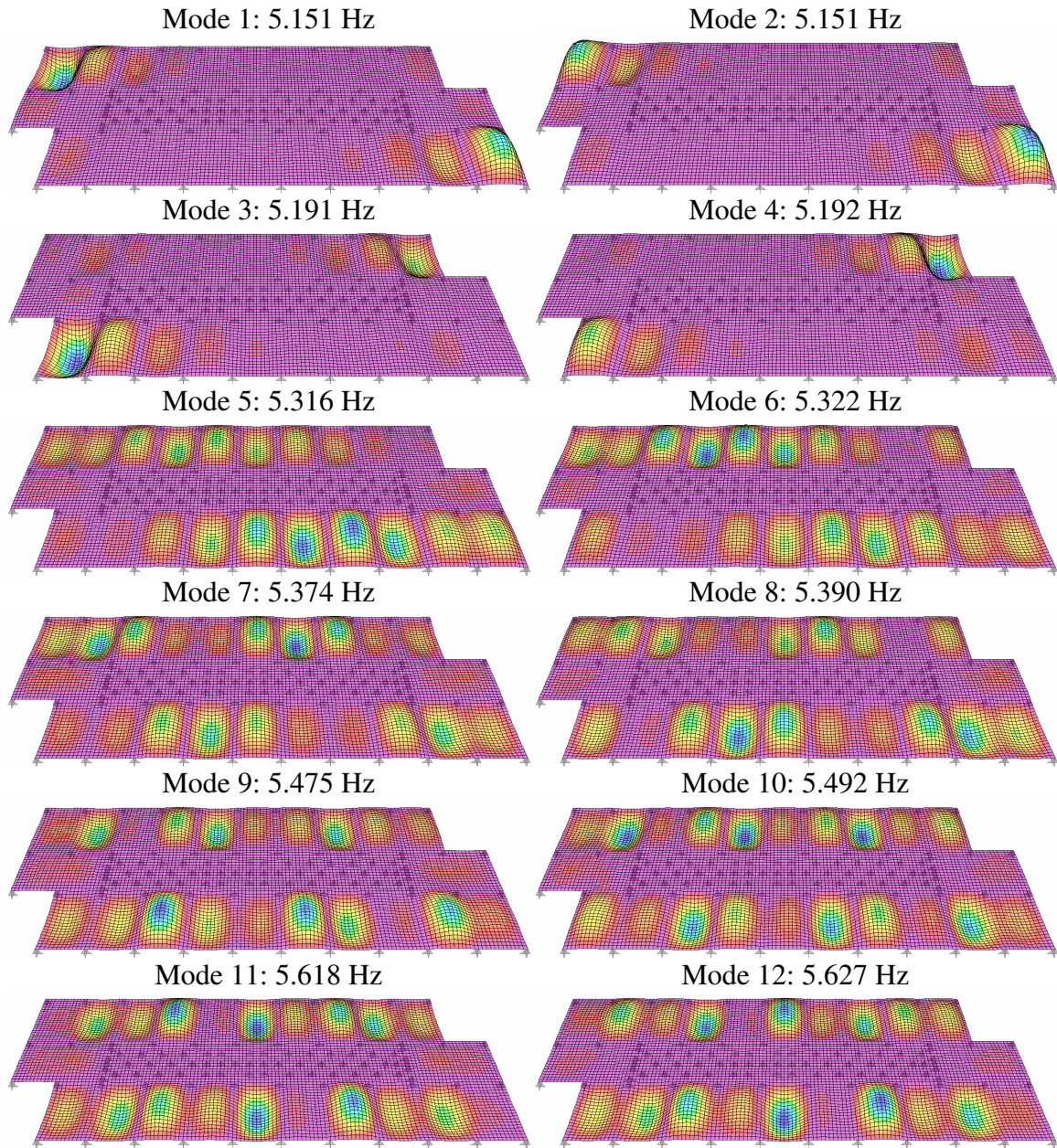


Figure 4.16: NOC VII – Full Floor Model Computed Mode Shapes (Modes 1-12)

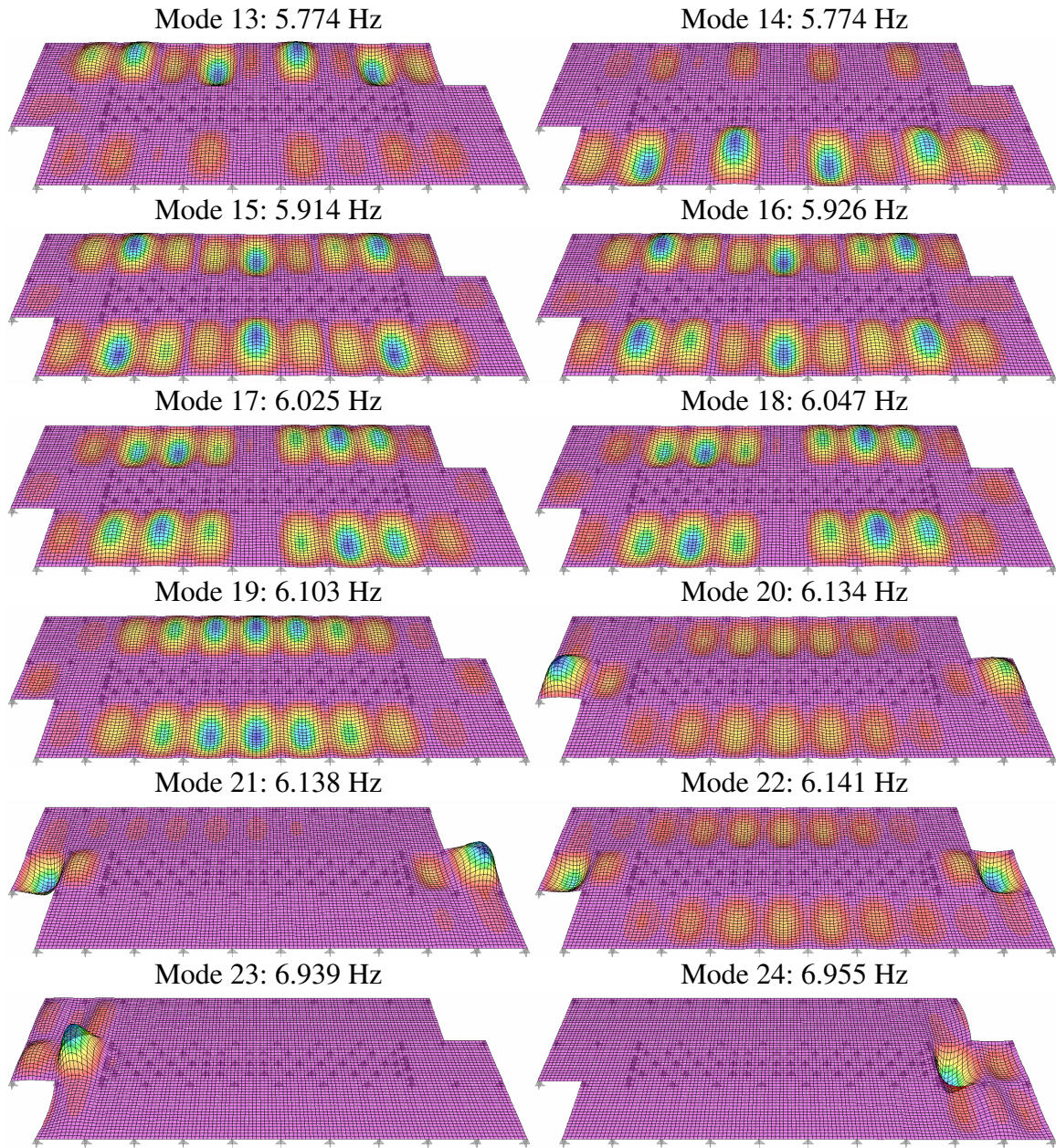


Figure 4.17: NOC VII – Full Floor Model Computed Mode Shapes (Modes 13-24)

Several iterations of the modal analysis were performed while varying the number of modes to be computed. This was accomplished to ensure that all mode shapes of interest were captured, namely the shapes that represented single curvature within a bay. It was determined that 24 modes were necessary to capture the dominant shapes of all bays; modes beyond this had double curvature within bays, which is not particularly of interest in the presented research due to comparison with mid-bay excitation locations that would likely not represent these modes well.

There are some interesting items to note in the computed mode shapes shown in Figures 4.16 and 4.17. First was the computation of “pairs” of point-symmetric mode shapes computed at nearly identical frequencies for the first 18 modes. Although not originally anticipated, this is a logical result due to the point symmetric nature of the floor framing with only slight differences in some of the interior restraints used toward the ends of the interior core of bays. Also because of this symmetry, it would be expected that the measured frequencies at the respective bays on either end of the floor will be the same or very similar, although this was not verified for the tested floor. The second observation is that certain mode shapes show a dominant response in a localized area, consistent with what was observed in experimental measurements. In particular, Modes 1, 3, 20, and 23 show clearly dominant response in the bays containing Points 21, 73, 25, and 69, respectively. These four mode shapes of the end portion of the floor that was tested are shown in Figure 4.18, along with the ODSs of the respective bay’s dominant frequency. The frequencies for these modes and their respective shapes are in good agreement with the measured frequencies of the bays (less than 6% difference in frequency).

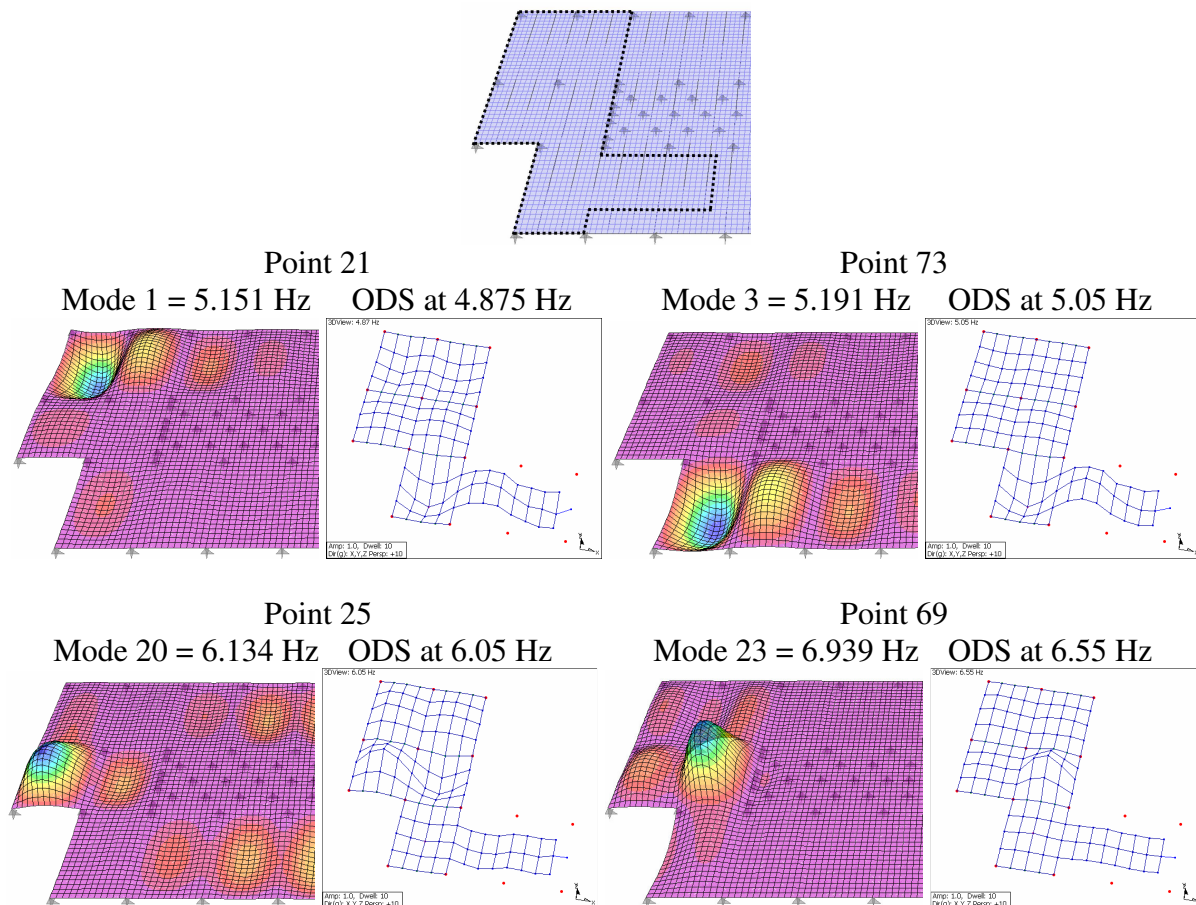


Figure 4.18: NOC VII – Full Floor Model Mode Shape and ODS Comparison

Unfortunately, there were several areas of the floor (the points of excitation other than the four listed above) that were not well represented with clearly dominant shapes, although they should be as indicated by dominant peaks in the experimentally measured driving point accelerance FRFs. Points 65 and 281 are the most notable locations with large accelerance values not well represented in the mode shapes of the model. Additionally, all excitation locations along the length of the building (Points 125, 177, 216, 281, and 333) had measured dominant frequencies of 5.025-5.05 Hz, indicating a dominant mode shape that was common to all bays along this strip. Extensive testing with the shaker located at Point 281 showed this shape to be a simple mode that alternated concavity at each bay (Figure 3.14). Examining the mode shapes for this strip of bays in Figure 4.16, Mode 5 at 5.316 Hz looks the most similar, however there are 13 other modes between 5.322 Hz and 6.103 Hz that show significant participation along this strip in various concave up or down configurations of the bays. As a result, it is likely that none of these modes will dominate the response, which is clearly not the case as indicated from experimental testing. A separate model representing this strip of bays was generated to try and isolate the response better than the full floor model and is discussed later in this section.

Although comparison of frequencies and mode shapes was a necessary step in the model validation process, the comparison of forced response analyses with experimental measurements was the final step in assessing the ability of the FE model to adequately represent the dynamic behavior of the floor system. Steady state analysis was performed on the modeled floor for the eleven different unit load locations shown in Figure 4.13(b), each corresponding to a driving point location on the floor during modal testing. These eleven locations were all at mid-bay with the exception of Point 216, which was at the quarter point of the bay along the centerline of the long direction of the floor. To correspond with the burst chirp frequency range of the experimental driving point accelerance FRFs, the steady state analyses evaluated response at increments between 4 Hz and 8 Hz with roughly a 0.05 Hz frequency resolution. Although the experimental measurements were taken with a 0.025 Hz frequency domain resolution, the FE steady state response functions generally do not require that fine a resolution, particularly because the computed modal frequencies were also included as frequency increments to ensure the peak response was captured (a luxury not afforded during experimental testing).

Steady state analysis was performed twice for each of the driving point locations. For the two analyses at each point, damping was specified as a constant value for all frequencies and was

input as either the estimated damping at the dominant frequency from experimental measurements of the bay under investigation or using the proposed damping values for a bare floor based on general bay location (1%, 1.5%, 2%). The results using the measured damping values are presented first in this section, followed by an overall summary of how well the response using an assumed level of damping was in agreement with measured response, which would be the only option for a designer modeling this floor prior to construction. The points of excitation and each of the two damping ratios used for analysis are shown in Figure 4.19.

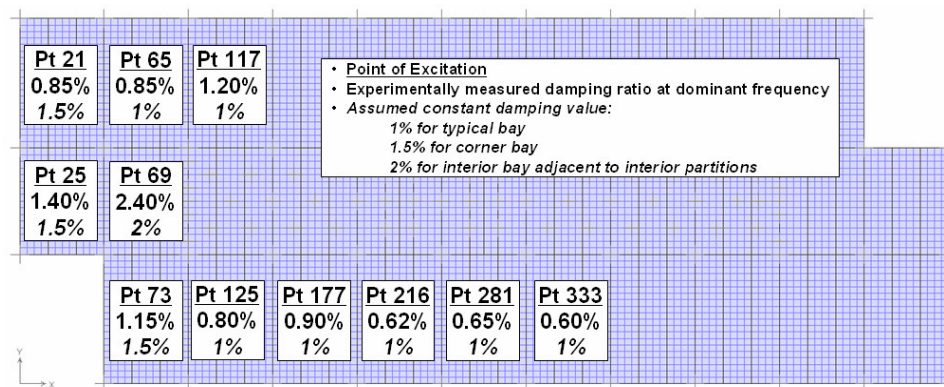


Figure 4.19: NOC VII – Constant Damping Ratios Used in Steady State Analysis

The computed driving point accelerance FRFs for each of the eleven bays are presented in Figures 4.20 and 4.21. As expected from the computed mode shapes, the FE accelerance FRFs are in better agreement with the measured accelerance FRFs for Points 21, 25, 69, and 73 as shown in the Figure 4.20. As shown in these four plots, using the measured estimates of damping did not always result in better agreement, which is particularly apparent for Point 21 where the computed response is nearly one and a half times larger than measured. This is likely a result of the dominant mode shape for Point 21 not being accurately represented by the computed shape of Mode 1. The shape for this mode is localized to a small area around the bay containing Point 21, which essentially translates into a small participating (effective) mass. An underestimation of the effective mass of that mode will result in excessively high computed acceleration response because the modal mass term is in the denominator. The same effect can be seen by the overestimated response for Point 25. It is encouraging to know, however, that an extremely localized mode results in an excessively large computed response and to recognize that it is likely a conservative estimate of response when the localized mode shape is observed from the modal analysis. The computed accelerance FRFs for Points 69 and 73 are in good agreement with the experimental FRFs.

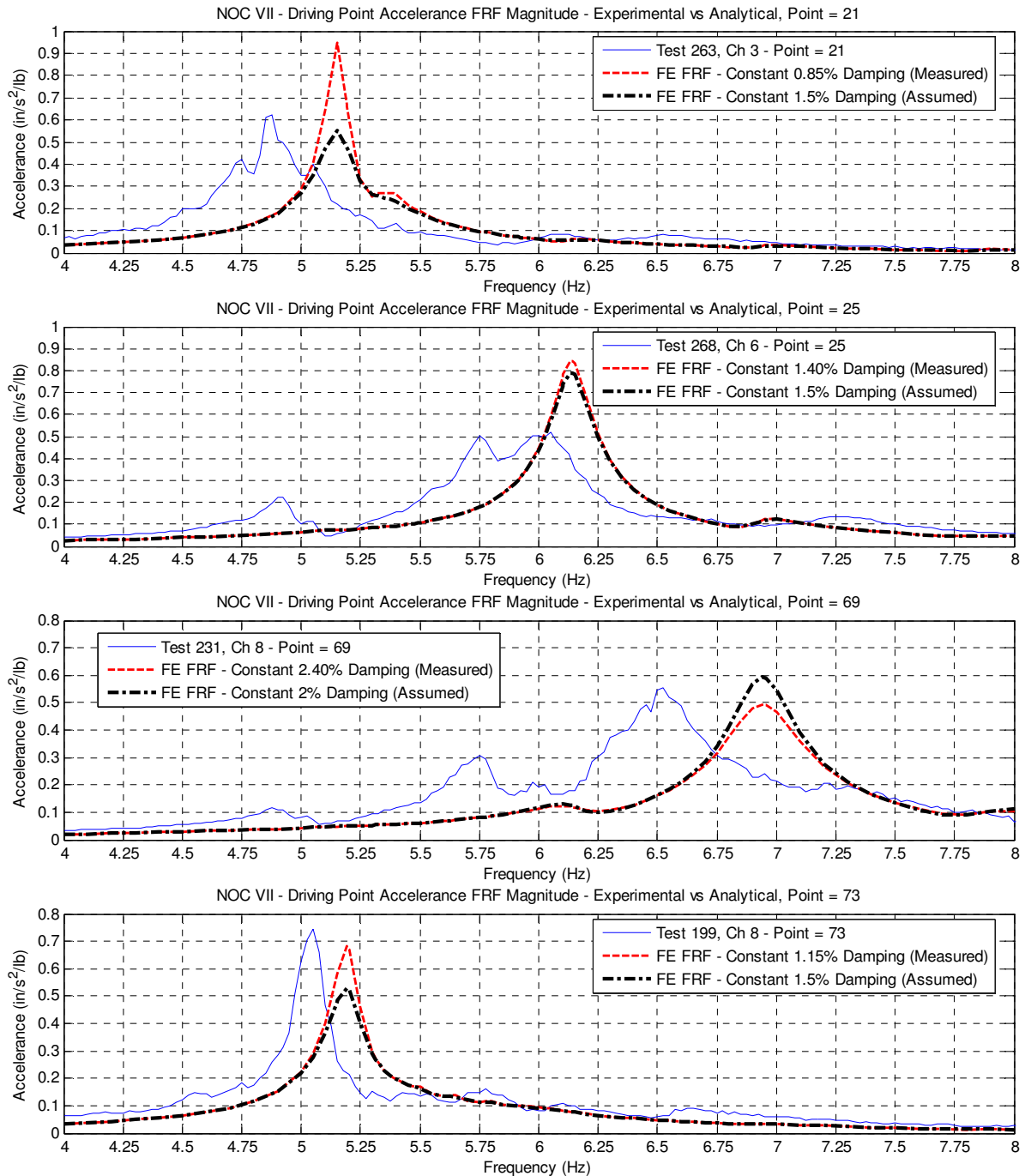


Figure 4.20: NOC VII – Full Floor Accelerance FRFs (Points 21, 25, 69, 73)

The computed accelerance FRFs for the remaining seven tested/analyzed locations were not in agreement with the measured FRFs for either magnitude or shape, as shown in Figure 4.21. The inability to match response at Points 65 and 281 with this model, which both have clearly dominant single peaks, is disappointing because they have the largest magnitudes of any of the measured locations on the floor and thus represent vulnerabilities of the floor that a

designer would strive to identify in the design phase. Again, the inability for the model to correctly represent the mode shapes of the entire strip of bays, namely a single dominant shape of alternating concavity, is the reason for the poor correlation.

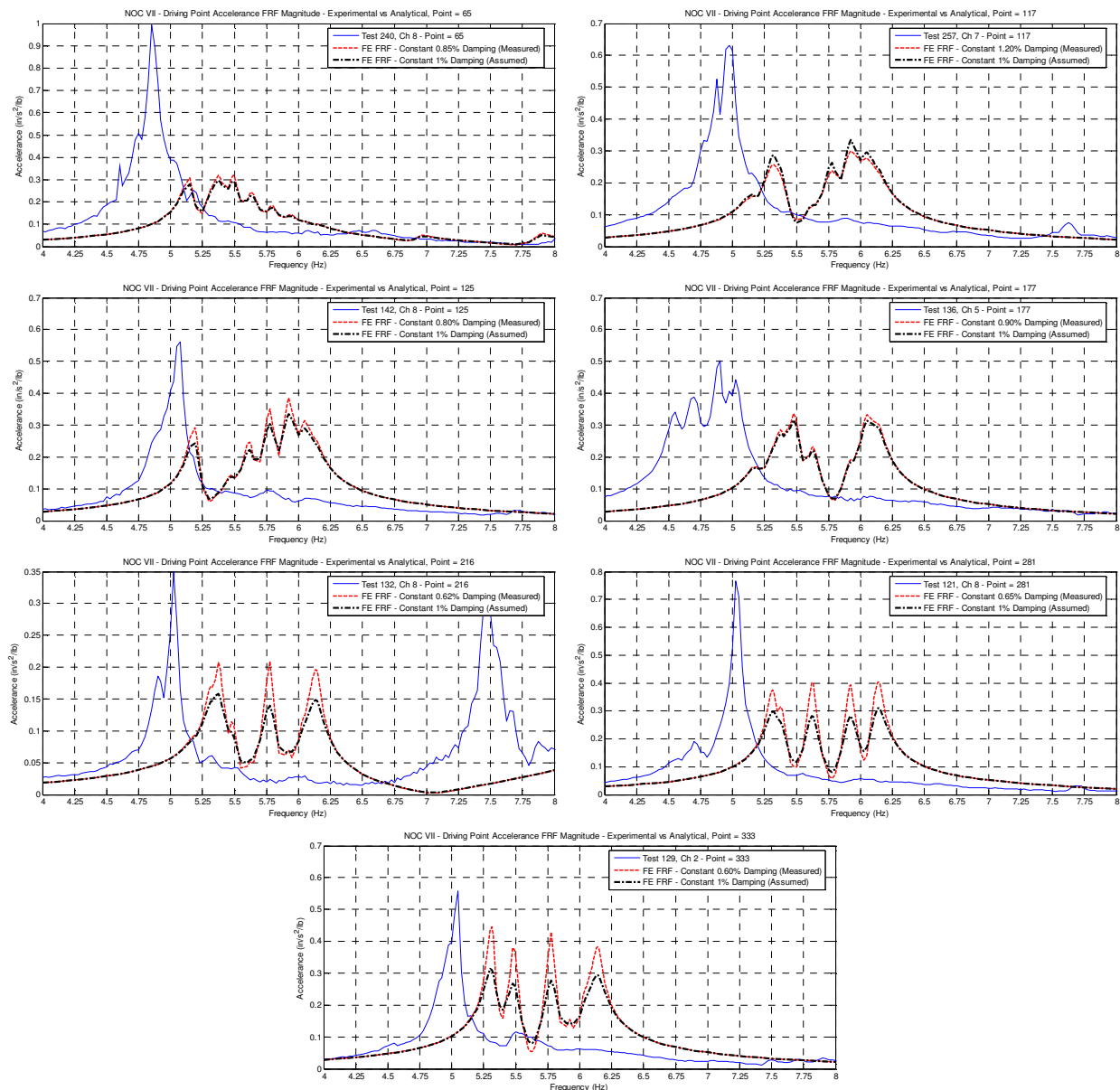


Figure 4.21: NOC VII – Full Floor Accelerance FRFs (Pts 65,117,125,177,216,281, & 333)

While the computed accelerance FRFs in Figure 4.21 did not match the measured FRFs for any level of damping, the assumed levels of damping used in the four plots of Figure 4.20 actually provided a reasonable approximation of the measured response. While notably high for Point 25 (which was true for both measured and assumed) and about 25% low for Point 73, the response was within 12% for Points 21 and 69. Overall, there seemed to be about the same

number of locations in agreement using either measured or assumed damping values. Although the computed traces are not overwhelmingly in agreement with measured values for this model, the frequencies were predicted within 6% of measured and the general shape of the acceleration FRF peaks from the different participating frequencies are represented well, including magnitude. Despite the discrepancies, this is an encouraging result for the recommended modeling techniques.

NOC VII 10-Bay Strip Model – To further investigate the bays along the length of the floor that did not agree well with measured values, a reduced model including just the 10-bay strip along the floor’s length was generated using the same recommended techniques and analyzed using the same methods as presented above. The 10-bay coverage area of the reduced FE model is shown in Figure 4.22 along with the 3-D views of the model’s framing and slab. All floor beams spanning between girders retained their end moment releases and partial fixity values, although due to the absence of members framing into the beam-to-girder joints on the other side of the girders, the effect of the partial fixity on frequencies and mode shapes was negligible.

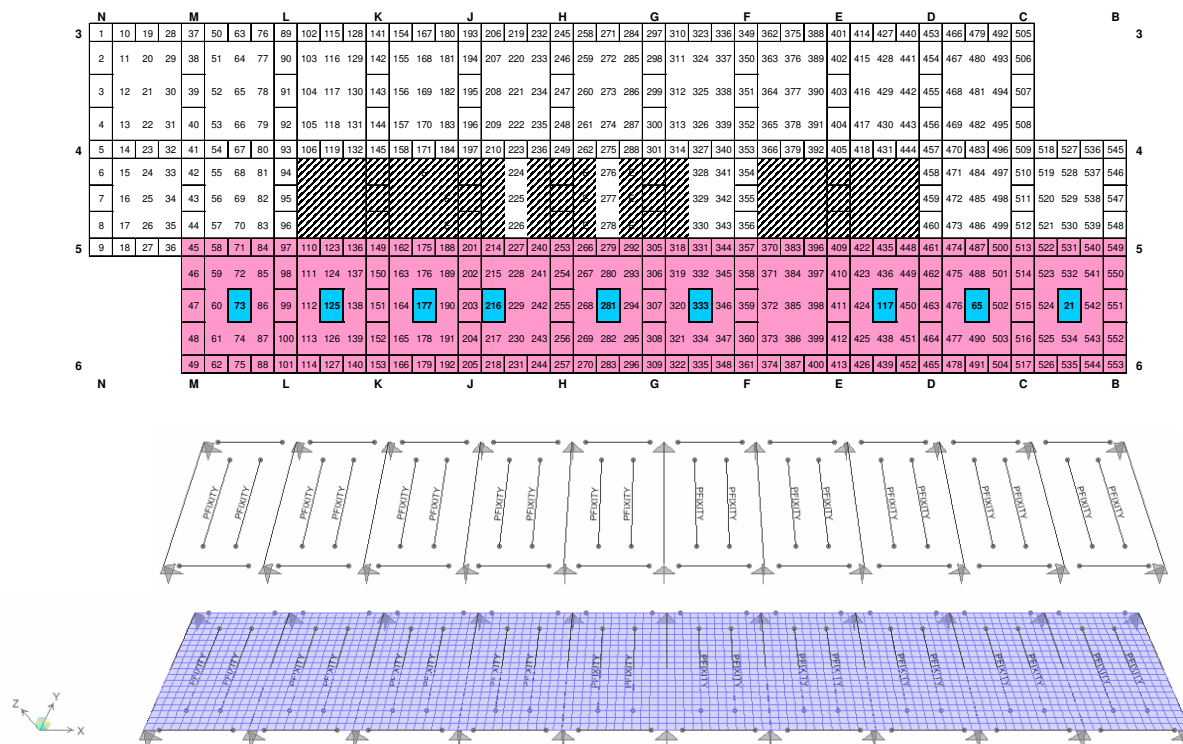


Figure 4.22: NOC VII – 10-Bay Strip FE Model

To account for the missing portions of the slab on the end bays that were adjacent to open areas of the floor (bays containing Points 73, 65, and 21 in Figure 4.22), a modeling technique

recommended by Perry (2003) was used. He recommended applying a mass property modifier of 0.5 to the girder and a strong axis moment of inertia property modifier of 0.5 times the baseline value (i.e. half mass and half composite stiffness), resulting in a member that has the same static deflection as if the adjacent bay were present. This technique was applied without any refinement to attempt to improve the results. All spandrel members (bottom, right, and left edges) retained their originally applied property modifiers, which were 2.5 times the computed baseline values. The girders that bound interior bays (i.e. girders beneath full height partition walls) also retained their respective 2.5-times-baseline stiffness property modifiers. No adjustments were made to the stiffness or mass of these interior girders to account for the missing interior bays.

The main difference of this 10-bay strip model compared to the full floor model is the absence of the highly restrained interior bays, which is probably the main contributor to the discrepancy. As expected, the computed frequencies of the 10-bay strip model were lower than their full floor model counterparts. Modal analysis of the 10-bay strip model for NOC VII computed the 16 frequencies listed in Table 4.3. It is interesting to note the first 10 computed frequencies are within 0.4 Hz of one another; however there is a 1.5 Hz gap in frequency between the 10th and 11th modes, which represents the delineation between modes with single curvature within a bay and those with double curvature. This is readily apparent in floor models with the same or very similar bay dimensions and framing members but may be less obvious in floor models that have smaller interior bays. These small interior bays tend to have higher frequencies that may be close to the double curvature modes of the larger exterior bays. The first 12 mode shapes are presented in Figure 4.23.

Table 4.3: NOC VII – Computed Modes for 10-Bay Strip Model

Mode:	Frequency (Hz)	Mode:	Frequency (Hz)
1	4.823	9	5.219
2	4.845	10	5.235
3	5.009	11	6.790
4	5.057	12	6.888
5	5.087	13	7.055
6	5.124	14	7.292
7	5.161	15	7.597
8	5.194	16	7.969

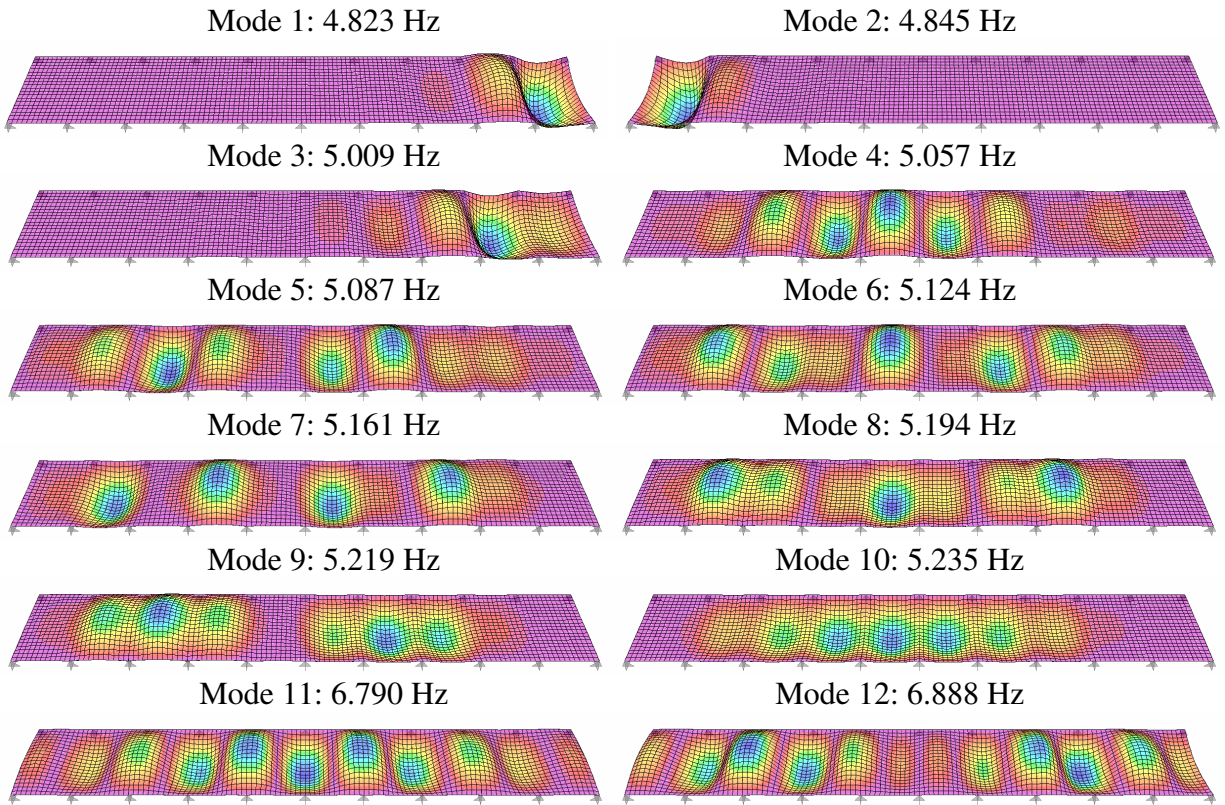


Figure 4.23: NOC VII – 10-Bay Strip Model Computed Mode Shapes

As anticipated, the lower modes show the greatest response in the “softer” areas of the floor, which are the end bays with the girders assigned lower stiffness property modifiers. As with the full floor model, the lower modes are also represented by localized response in a few adjacent bays, which would indicate large forced response values for excitations in these locations at their dominant frequencies. Unlike the full floor model, however, the frequency of the first mode shape with significant response along the middle portion of the model (Mode 4: 5.057 Hz) is very close to the measured frequencies in these bays (5.025 Hz to 5.075 Hz) and the mode shape is very similar to the measured dominant shape, as shown in Figure 4.24.

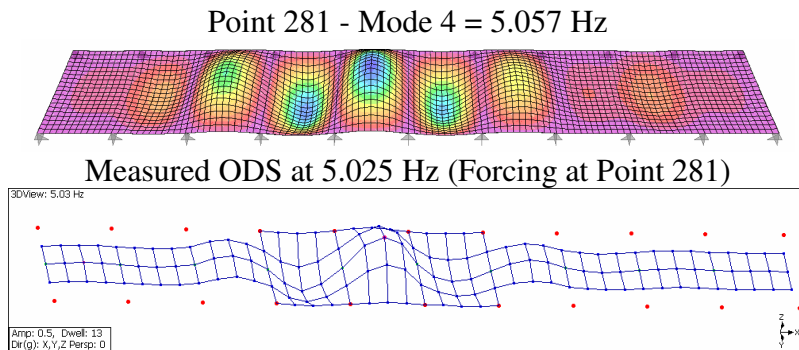


Figure 4.24: NOC VII – 10-Bay Strip Model Mode Shape and ODS Comparison (Point 281)

It should be noted that due to the point symmetric nature of the floor geometry, the mid-bay locations on the end three bays of the right side (Points 533, 489, and 437) should demonstrate the same response as the corresponding locations on the opposite corner of the building, which are Points 21, 65, and 117, respectively. Thus, unit point loads were applied to the 10-bay strip FE model and analyzed to represent these respective locations. The mode shapes with responses in these locations can also be compared with measured shapes. Figure 4.25 shows the comparison of Mode 3 with the measured ODS at the dominant frequency of Point 65. Note that the FE model was rotated to reflect its representation of Point 65 and for comparison with the ODS at the 4.875 Hz dominant frequency. Although the ODS used in the comparison was obtained by driving at Point 73, the similarity in shape is apparent by the two corresponding upper bays that are in phase (concave up). This is a promising result because this dominant response shape in the bay containing Point 65 could not be achieved in the full floor model.

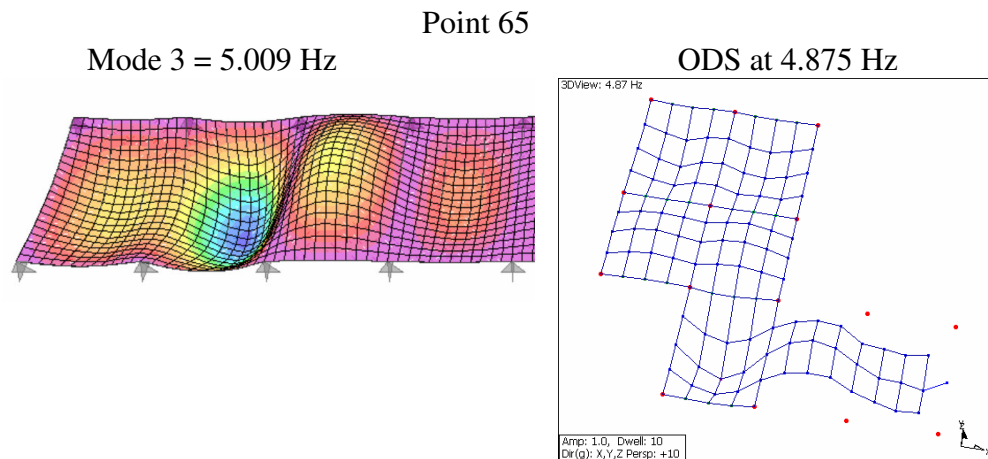


Figure 4.25: NOC VII – 10-Bay Strip Model Mode Shape and ODS Comparison (Point 65)

The computed driving point accelerance FRFs from steady state analysis of the tested bays are presented in Figure 4.26. While the strip model was expected to better represent the response of the bays in the middle of the strip, all of the analyzed bays' computed accelerance FRFs are in better agreement with the measured accelerance FRFs than the corresponding analyses of the full floor model. While the computed peak response magnitude for Point 65 was nearly 25% low using the measured value of damping (37% low for assumed level of damping), the shape of the FRF was much improved in this model. For Point 21, the computed response was essentially the same for the strip model as it was for the full floor model, which is consistent

with the observation that the mode shape is localized to the immediately adjacent bays and thus the bulk of the participating (effective) mass was not removed with the other portion of the floor.

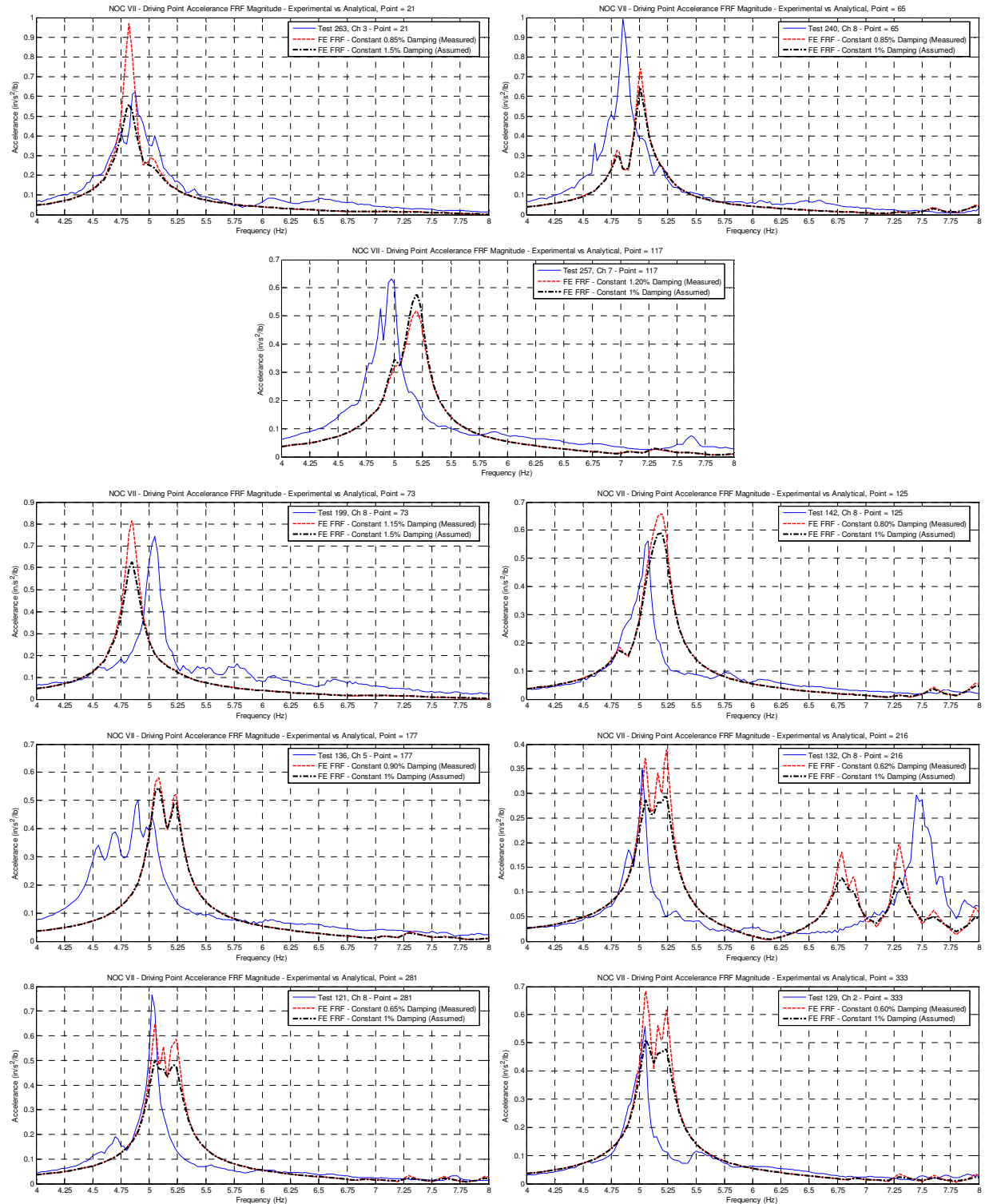


Figure 4.26: NOC VII – 10-Bay Strip Model Accelerance FRFs

The remaining analyzed locations predicted dominant frequencies within 10% of measured dominant frequencies and response magnitudes at the peaks using measured damping values to within 25%. Using an assumed level of damping, the computed peak response values were generally 10-20% low, but not unreasonable considering the smaller values of damping estimated from measurements of the bays along the interior of the strip (0.6-0.9%). It is interesting to note the ability of the model to predict the general shape of the odd multi-mode response for Point 177 and the double curvature mode measured at the higher frequencies in the FRF for Point 216, the only driving point not located at mid-bay. Overall, the reduced strip model provided some very encouraging results for both the recommended modeling techniques as well as the implication that reduced floor models can be effective in adequately predicting the response.

4.2.2 VT KnowledgeWorks 2 Building, VTK2

For the FE model of VTK2, the floor framing geometry was laid out with the steel framing members specified in the design drawings and pinned supports were applied at the column locations. Like NOC VII, a user-defined material (VTK2-VIBCON) and area plate element (VTK2-SLAB) were created to represent the composite slab in the floor model. The input values of these user-defined parameters, and the composite slab properties used in their development, are presented in Table 4.4.

Table 4.4: VTK2 – Composite Slab Parameters and Slab Area Element/Material Properties

Overall Slab/Deck Height:	5.25 in.	Unit weight of concrete, w_c :	115 pcf
Slab height above ribs, d :	3.25 in.	Concrete compressive strength, f'_c :	3000 psi
Deck rib height, d_r :	2.00 in.	Dynamic modulus of elasticity, 1.35^*E_c	2884 ksi
Area weight of steel deck, w_{deck} :	2.4 psf	Superimposed loads, $w_d + w_l + w_{coll}$:	0 psf

User-Defined Material Name:	VTK2-VIBCON	User-Defined Area Section Name:	VTK2-SLAB
Type of Material:	Isotropic	Type of Area Section:	Plate-Thin
Mass per unit Volume:	$2.3869 \times 10^{-7} \text{ k-s}^2/\text{in}^4$	Assigned Material:	VTK2-VIBCON
Weight per unit Volume:	$9.2156 \times 10^{-5} \text{ k/in}^3$	Thickness (Membrane/Bending)	3.25 in.
Poisson's Ratio	0.2	Stiffness Modifiers:	Bending m11 = 2.88
Additional Material Damping:	None		

A notable difference in the VTK2 floor from the NOC VII floor is the irregular framing in portions of the building. For both the experimentally derived mode shapes and the computed mode shapes it was found that the irregular locations of various columns and offset bays tended to localize the participation of the floor in a given mode to just a few adjacent bays. Slab details and the framing plan of the specified steel sections for VTK2 are found in Appendix A. Plan and 3-D views of the floor model's slab and framing layout are presented in Figure 4.27, including the twelve locations of forced response analysis presented later in this section for comparison with experimental measurements.

Using a slab area element size that was similar to the one used for the NOC VII model gave convergent results. This corresponded to a mesh size of 12x12 elements for interior bays (30 in. x 30 in.) and 12x16 elements (30 in. x 26.25 in.) for exterior bays. Because of the irregular geometry in some areas of the floor and the offset end bays, a few smaller rectangular elements were used in the transition areas. With this configuration, the full floor model contains nearly 3,400 mass degrees of freedom (UZ) (slightly less than half the size of the NOC VII full floor model). The joints corresponding to test locations were renumbered to the pattern shown in Figure 3.52 to ease analysis of results.

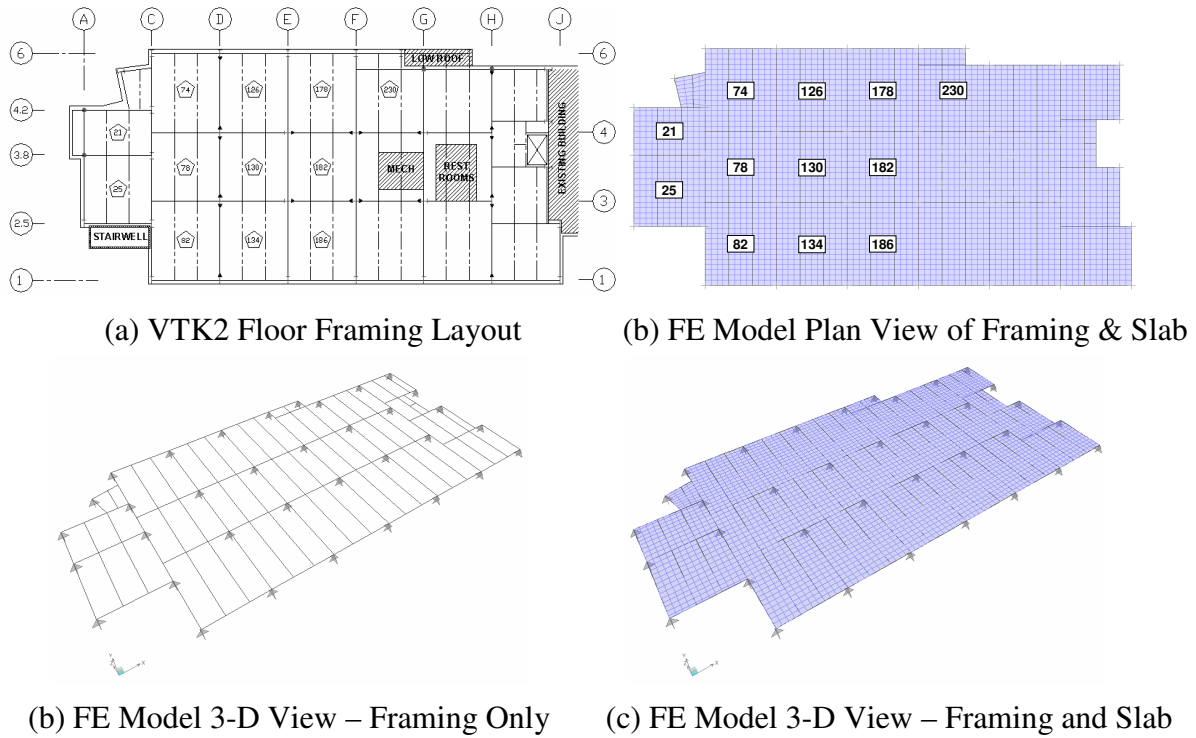


Figure 4.27: VTK2 – Floor Layout and FE Model

The transformed composite moments of inertia were computed for each framing member to determine the baseline stiffness property modifiers, which ranged from 2.5 to 3.8 for the main framing members of VTK2. A full listing of the calculated transformed moments of inertia and their respective baseline (and final) PMs is found in Appendix N. The baseline values were applied as PMs to the strong axis moment of inertia for all framing members, and 2.5 times the baseline values were applied as PMs to all spandrel beams and girders with the exception of the two spandrel members of bay A/C-2.5/3.8. This bay contained Point 25 and was in a stage of construction that essentially left it with two free edges. For this same reason, a smaller assumed damping value of 1% was used for analysis rather than the recommended 1.5% for a corner bay.

Strong axis bending moment releases without any partial fixity were applied to all members framing into the webs of columns, and no moment releases were applied to the beam members that framed into the flanges of columns. For beams framing into the webs of girders, strong axis moment releases with partial fixity values of $6EI/L$ were applied at both ends. No partial fixity values were assigned to beams framing into the webs of girders if there was not a corresponding beam framing into the other side of the beam-to-girder web connection (i.e. representing a loss of continuity and the flexibility of the unsupported girder web). Because of the irregular framing, this condition existed for several joints in the interior of the floor other

than at spandrel beams/girders. The framing layout of VTK2 showing end releases and members with assigned partial fixities is presented in Figure 4.28.

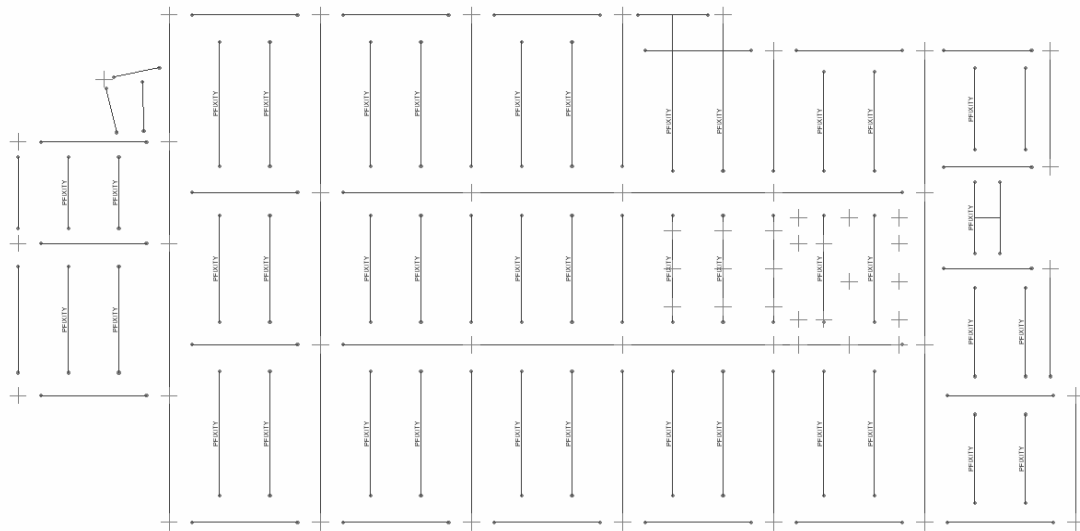


Figure 4.28: VTK2 – Moment End Releases and Partial Fixities

Additional pinned restraints were applied to two interior bays (bays F/G-3/4 and G/H-3/4 in Figure 3.45) to represent the full-height light gage steel stud framing in place above and below the floor at the time of testing (Figure 3.51). The locations of the interior pinned restraints are shown in Figure 4.29. Although the metal stud framing was connected to the underside of the floor using a clip designed to allow vertical movement, the bays with this framing were considerably stiffer. Like the stiffened behavior of the spandrel members that also had similar vertical clips at the slab edges, it is likely that the amplitudes of vibration were not enough to overcome friction at all locations and cause the increased stiffness.

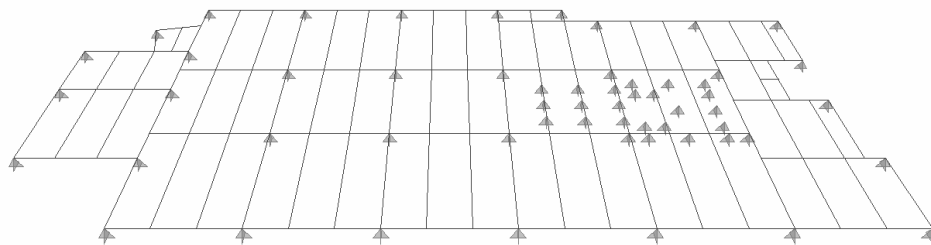


Figure 4.29: VTK2 – Interior Pinned Restraints

It should be noted that pinned supports at the interior locations shown in Figure 4.29 are likely to be much stiffer than the in-situ framing; however they were used in lieu of vertical springs, which more truly reflect the restraint condition in these areas. The use of pinned restraints was justified because formulating a vertical spring value for the light gage framing

would be impractical (and more likely inaccurate) due to variability in construction at that stage of installation and the contribution of friction at the vertical clips. The locations of these interior pins were based on judgment and the layout of the framing. It is likely they provide some degree of over-restraint in those areas that may be reflected in inaccuracies of the mode shapes and frequencies of the adjacent bays. While there is no comparison of accuracy for the untested far end of the floor, the bays most likely to be affected include Points 182 and 230.

The frequencies of the first 20 modes are presented in Table 4.5. It was determined only 20 modes were necessary to capture the dominant shapes of all bays; modes beyond this demonstrated double curvature within a bay. The 13 mode shapes that have a preponderance of participation (say that 10 times fast!) in the tested areas of the floor are presented in Figures 4.30 and 4.31.

Table 4.5: VTK2 – Computed Modes

Mode:	Frequency (Hz)	Mode:	Frequency (Hz)
1	6.535	11	7.725
2	6.689	12	7.795
3	6.772	13	8.024
4	6.867	14	8.129
5	6.870	15	8.399
6	7.055	16	8.509
7	7.200	17	8.659
8	7.295	18	8.828
9	7.307	19	8.936
10	7.387	20	9.152

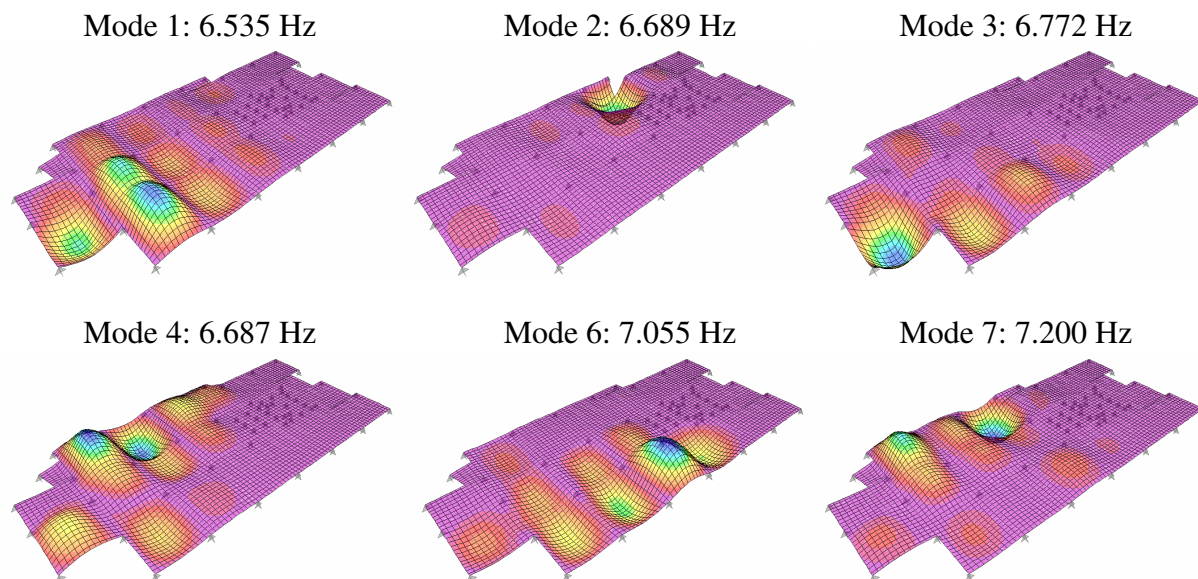


Figure 4.30: VTK2 – Computed Mode Shapes 1-7 (Tested Area of Floor)

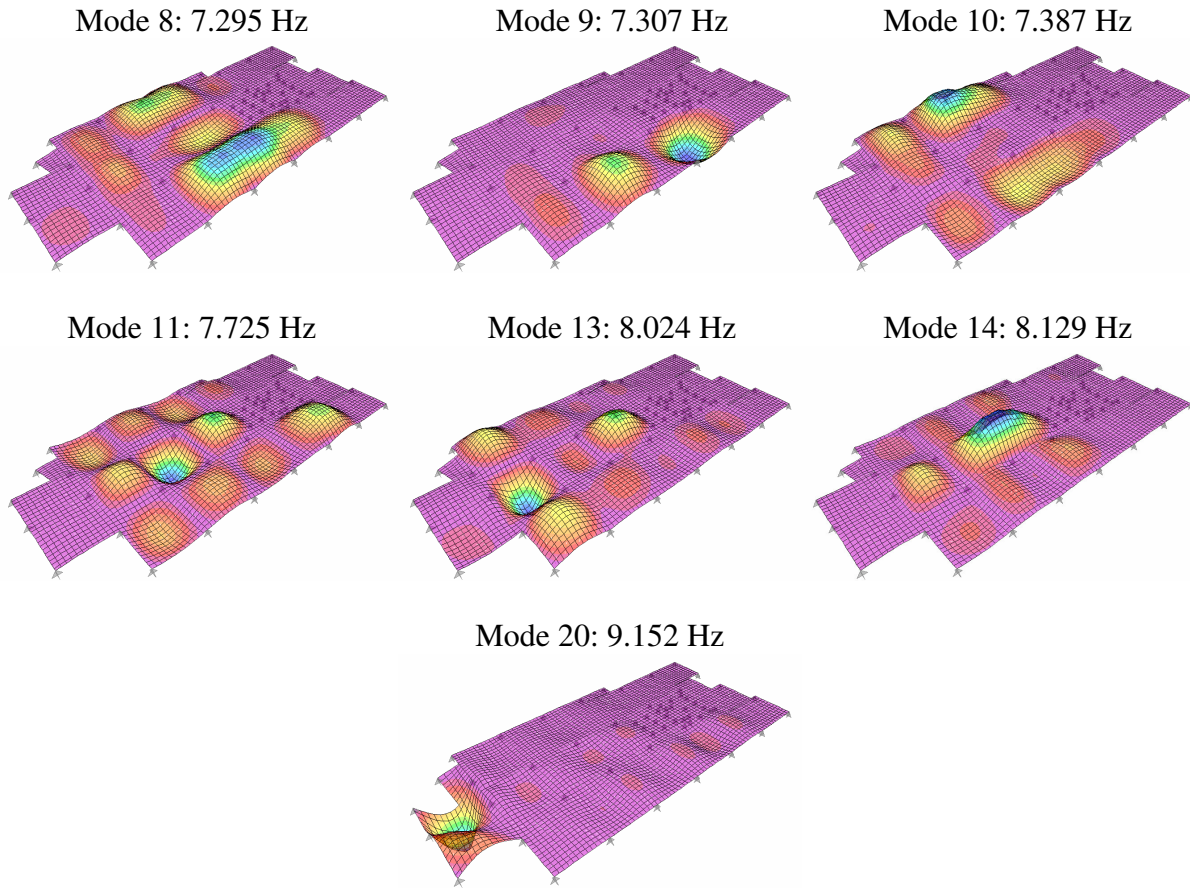


Figure 4.31: VTK2 – Computed Mode Shapes 8-20 (Tested Area of Floor)

In contrast to all but a handful of computed modes for NOC VII, it is interesting to note the localization of response within many of the modes. As previously observed in the NOC VII models, almost every mode has one or two bays with dominant participation, highlighting the dominant or significantly participating frequencies of that location of the floor. These frequencies will be significant or dominant peaks in the computed accelerance FRFs, just as they would from testing an in-situ floor. It is also evident that the irregularity of the framing and the column locations causes what could be considered “complicated” mode shapes, or mode shapes that are not necessarily intuitive or expected. However, when comparing the computed mode shapes to those measured during testing, the validity of many difficult-to-anticipate shapes was confirmed, making a strong argument for additional case studies with high quality modal testing of in-situ floors (or mid-bay testing, at the very least). Because a large area of VTK2 was tested using multiple references, the experimental data was more conducive to curve fitting and extracting quality mode shapes of multiple modes. Access to reliable extracted mode shapes (or high quality ODSs that closely resemble the mode shape near resonance) eases the comparison of

experimental data and computed mode shapes. Seven of the extracted mode shapes from in-situ testing are presented in Figure 4.32 for comparison with the respective computed mode shapes of the FE model. For reference, the area of the floor represented in the presented experimental mode shapes is shown at the top of Figure 4.32.

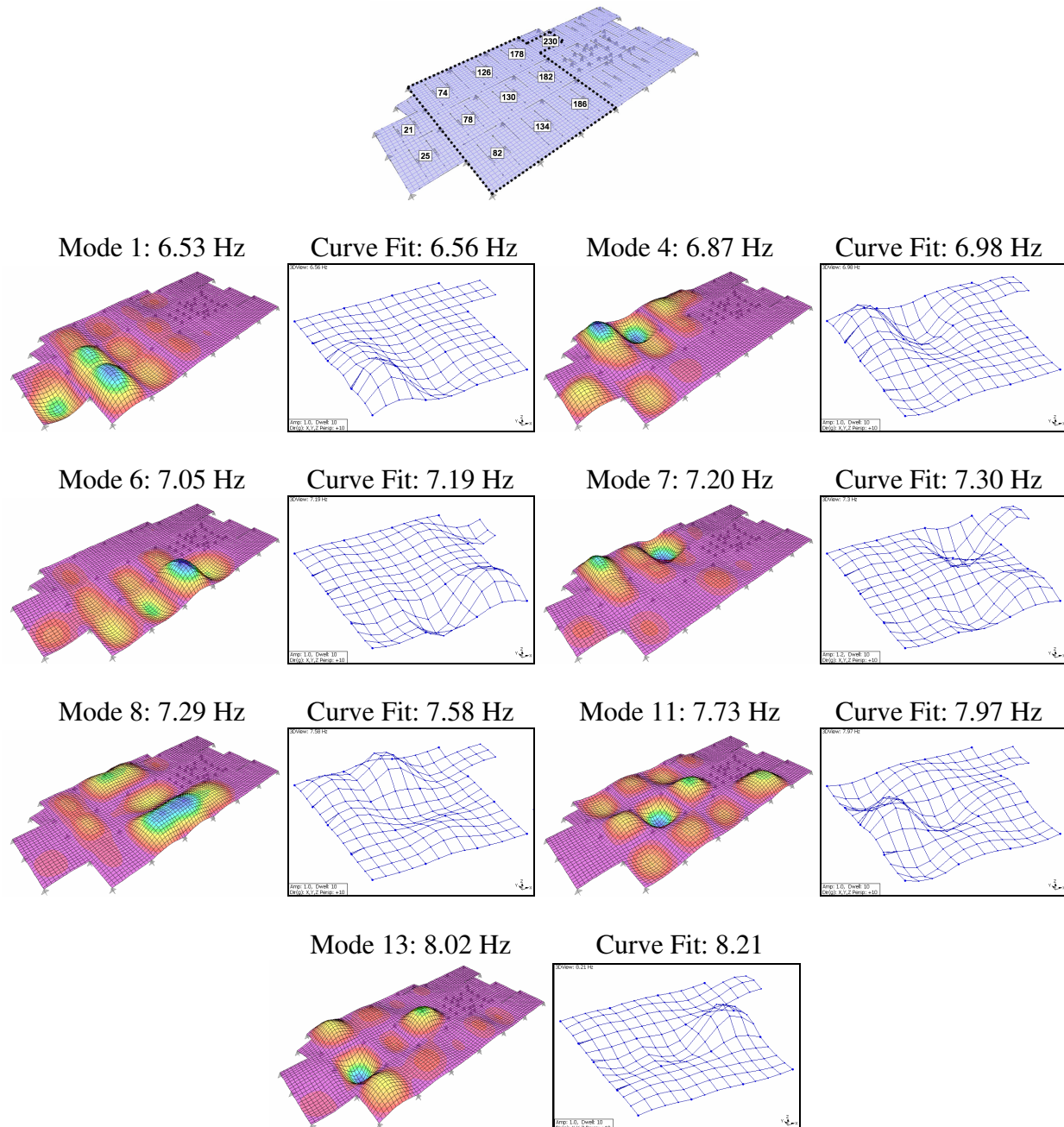


Figure 4.32: VTK2 – FE Mode Shape and Curve Fit Mode Shape Comparison

Although a numerical comparison between the computed and experimental mode shapes was not accomplished, there is exceptional agreement from visual inspection of the seven modes

compared in Figure 4.32. This is a very encouraging result given the simplified approach of many of the applied modeling techniques. Several modes were likely present in the in-situ structure but were not captured from modal testing due to either the lack of adequately exciting the mode at the forcing location or not measuring the area during the modal sweep. The three mode shapes in Figure 4.33 are the computed dominant modes at Points 25, 230, and 21. The computed modes that cannot be remarked upon due to lack of measurement of the far areas of the floor are presented in Figure 4.34.

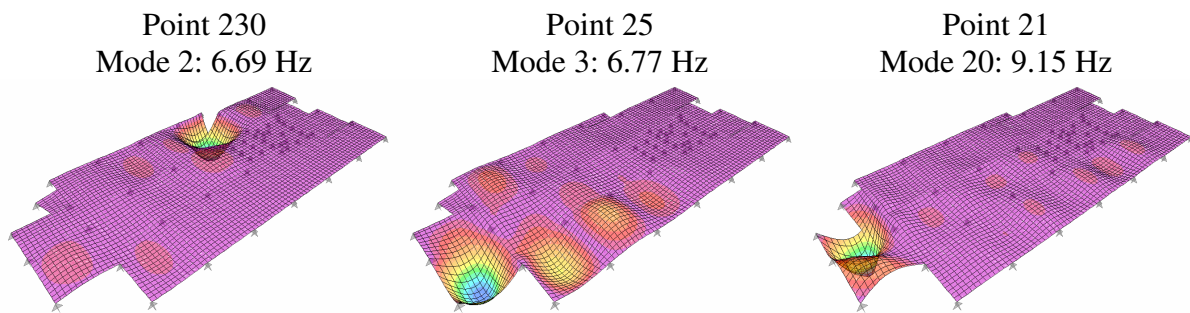


Figure 4.33: VTK2 – Dominant Mode Shapes (Points 25, 230, 21)

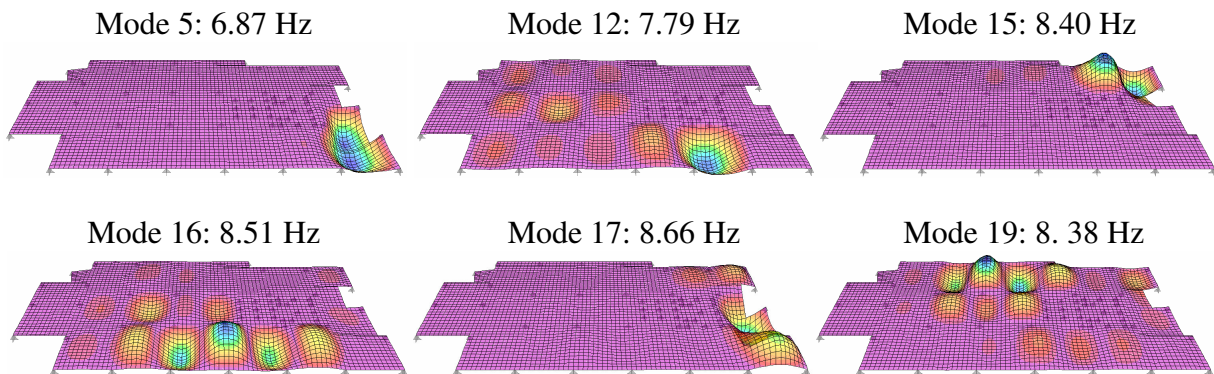


Figure 4.34: VTK2 – Computed Modes (Non-Tested Area of Floor and Double Curvature)

Steady state analysis was performed on the modeled floor for the twelve different unit load locations shown in Figure 4.27(b), each corresponding to a mid-bay driving point location on the floor during modal testing. To correspond with the burst chirp frequency range of the experimental driving point accelerance FRFs, the steady state analyses evaluated response at increments between 4 Hz and 12 Hz with roughly a 0.05 Hz frequency resolution. Steady state analysis was performed twice for each of the driving point locations. In the first analysis, constant damping was specified for all frequencies using measured estimates of damping (estimated at the dominant frequency of the tested bay) and a second analysis using the proposed

damping values for a bare floor based on general bay location (1%, 1.5%, 2%). The points of excitation and each of the two damping ratios used for analysis are shown in Figure 4.35. Note that 1% damping was used for the assumed damping analysis of Point 25. As a corner bay, 1.5% would follow the recommendations; however this bay had two sides that were essentially free edges. This is a good example of how engineering judgment must be applied at several steps in the modeling process to maximize the chances of adequately representing the in-situ behavior.

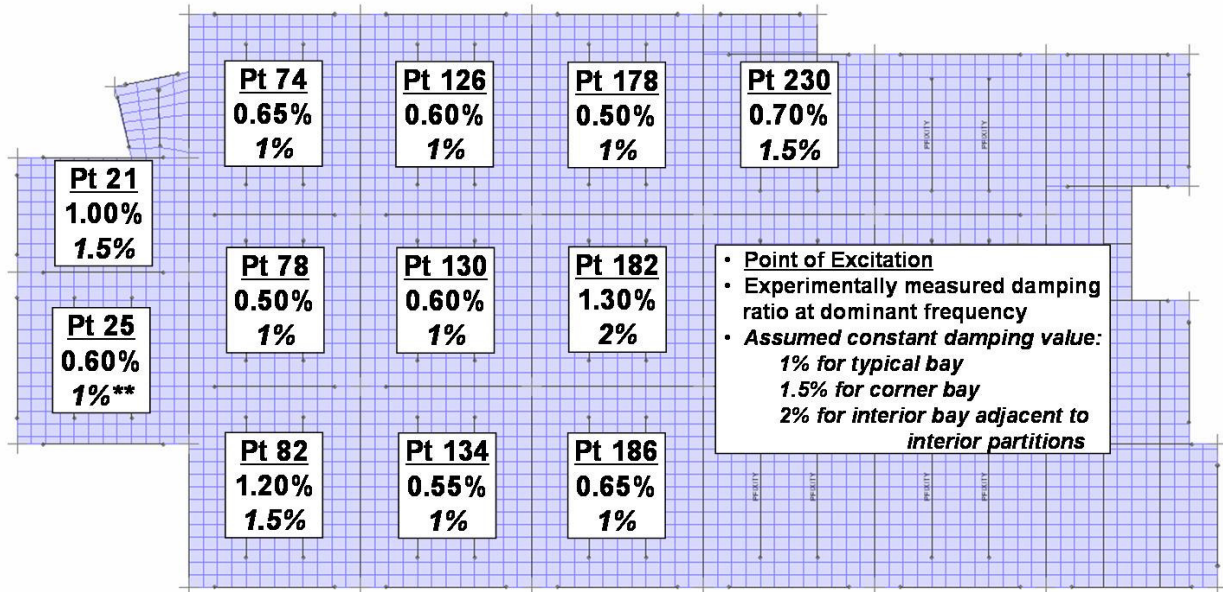


Figure 4.35: VTK2 – Constant Damping Ratios Used in Steady State Analysis

The computed driving point accelerance FRFs for each of the twelve bays analyzed are presented in Figures 4.36, 4.37, 4.38, and 4.39. The accelerance FRFs in these four figures are presented in sets of three to correspond with a three-bay strip along the short direction of the building. Although the computed FRFs are not ideal representations of the measured driving point FRFs, they provide very encouraging results for this floor model and the recommended modeling techniques. The dominant and participating frequencies of nearly all analysis locations are in good agreement with the measured frequencies, which was anticipated from the visual comparison of the computed mode shapes with the experimentally extracted modes shapes. The predicted dominant frequencies of the analyzed bays were all within 5% of the measured dominant frequencies, and half of the analyzed bays were within 1% of measured. For predicted accelerance, however, it was observed that using the measured estimates of damping did not always result in better agreement in the magnitude of the peaks of the accelerance FRFs.

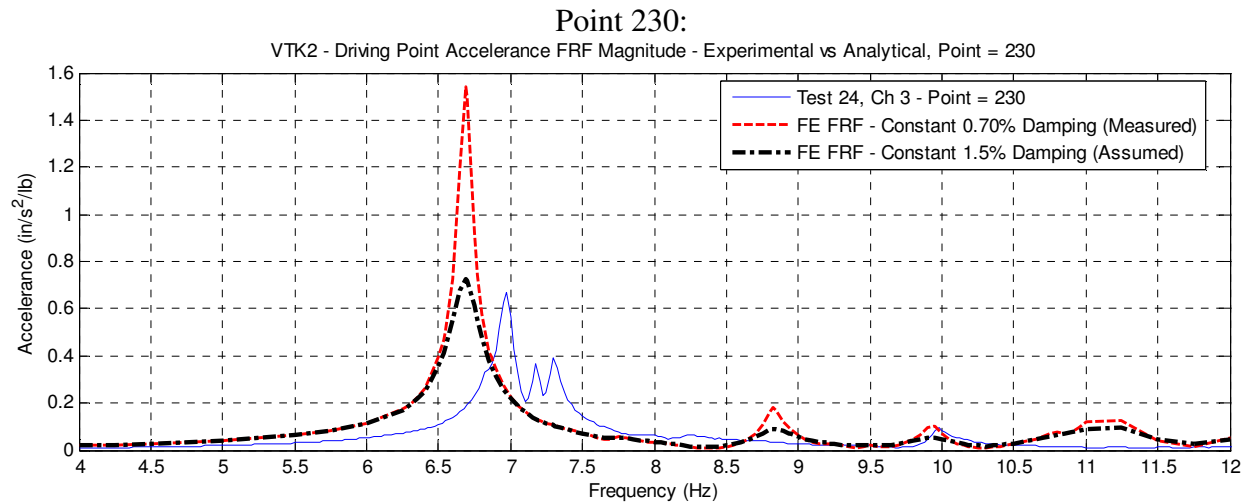
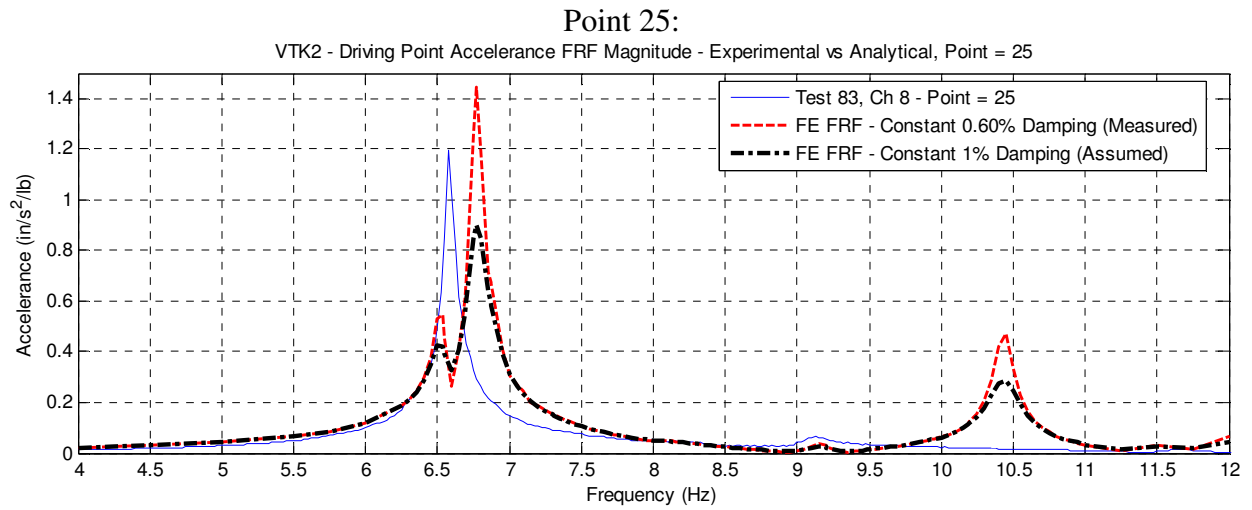
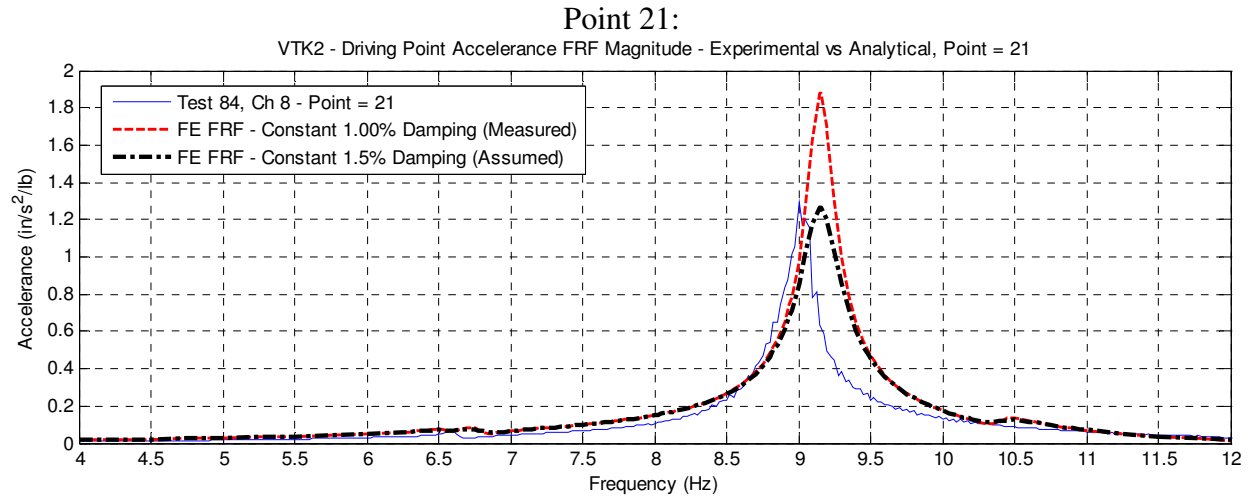


Figure 4.36: VTK2 – Accelerance FRFs (Points 21, 25, 230)

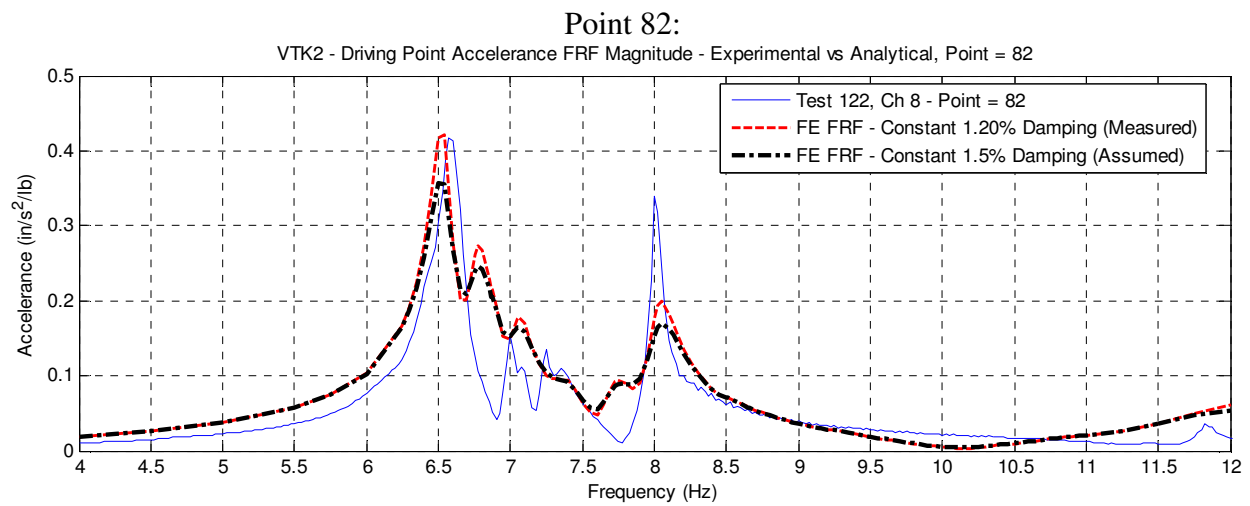
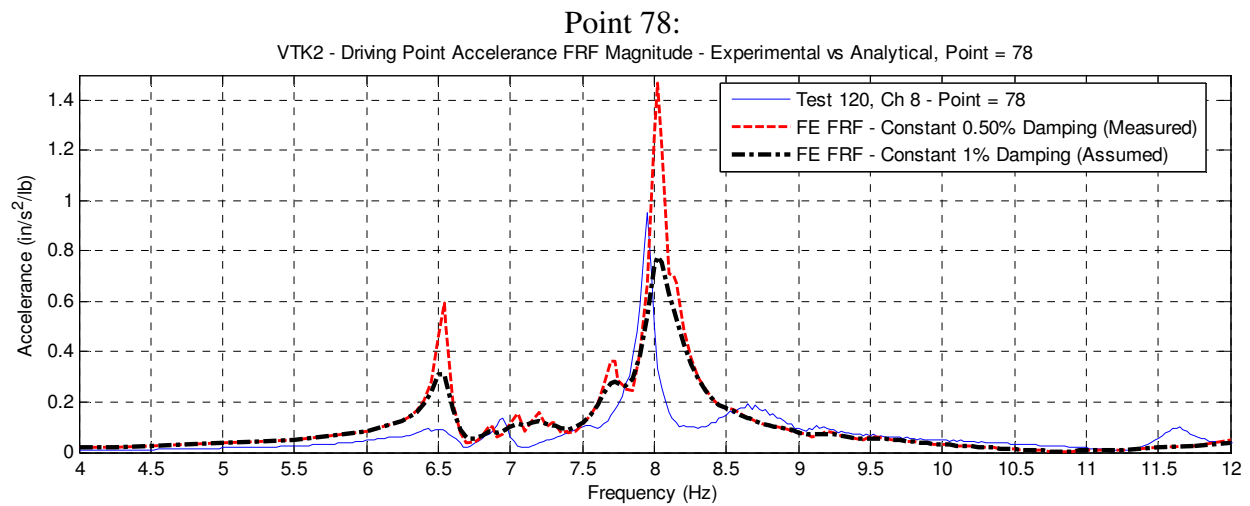
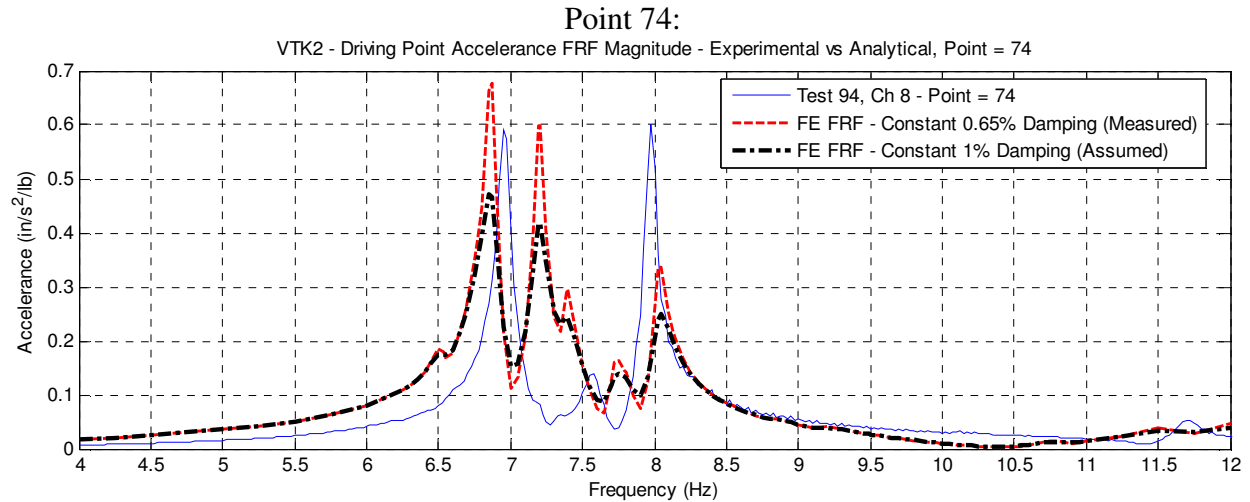


Figure 4.37: VTK2 – Accelerance FRFs (Points 74, 78, 82)

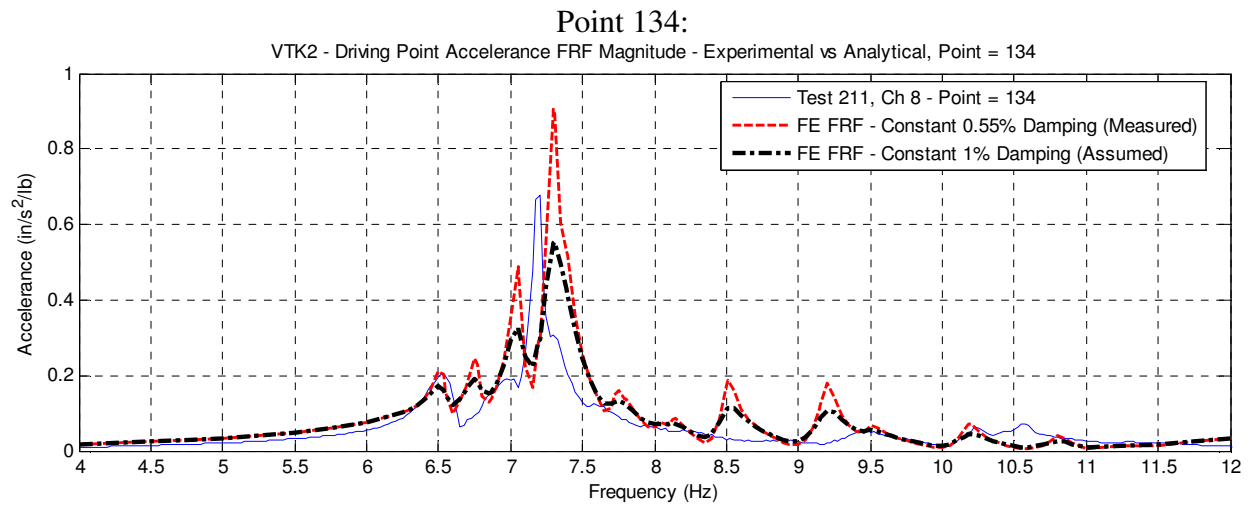
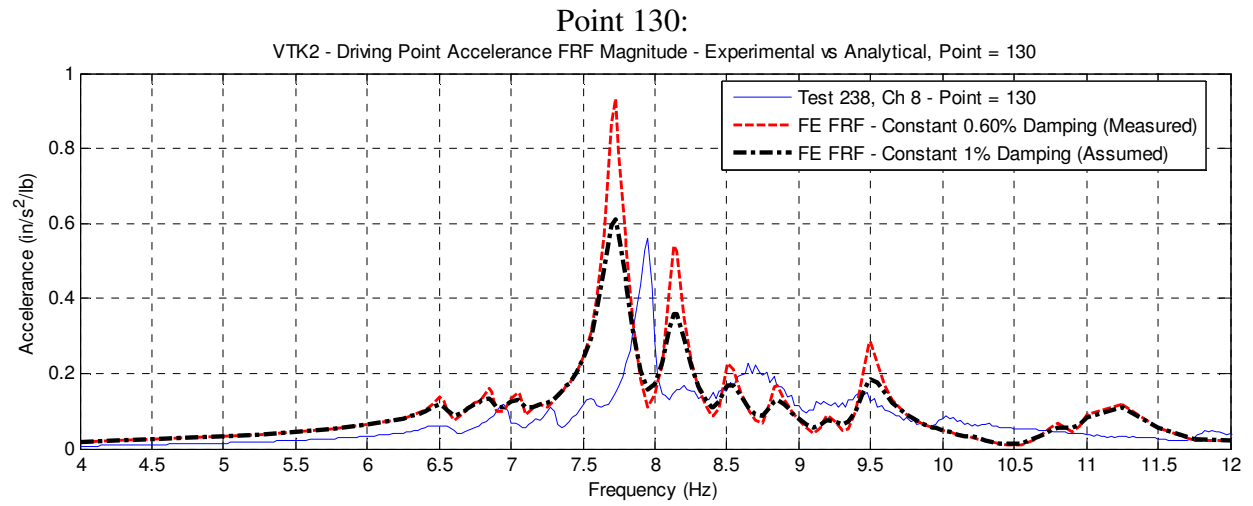
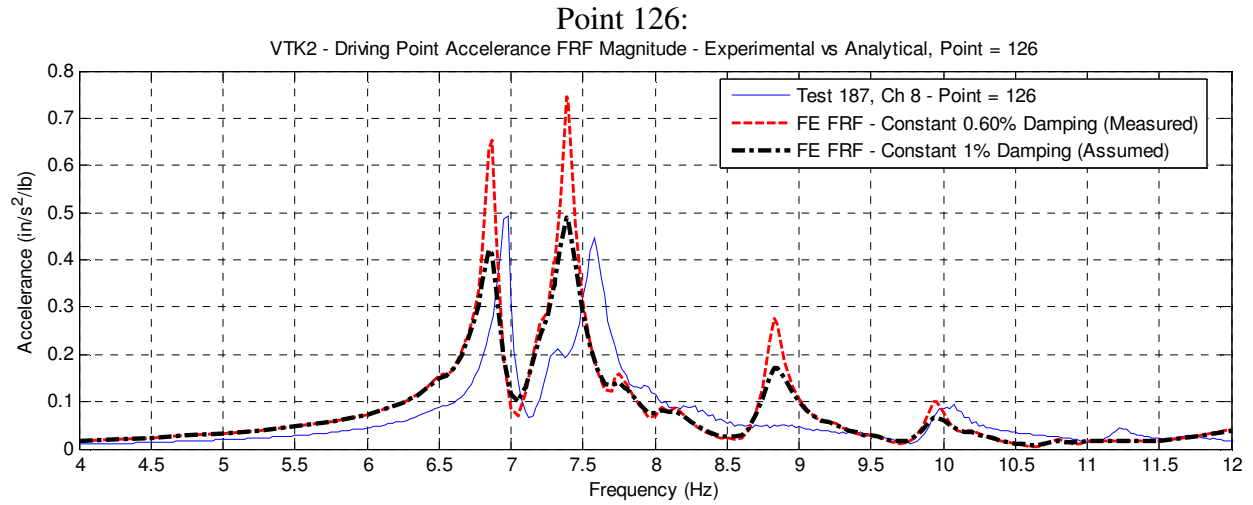


Figure 4.38: VTK2 – Accelerance FRFs (Points 126, 130, 134)

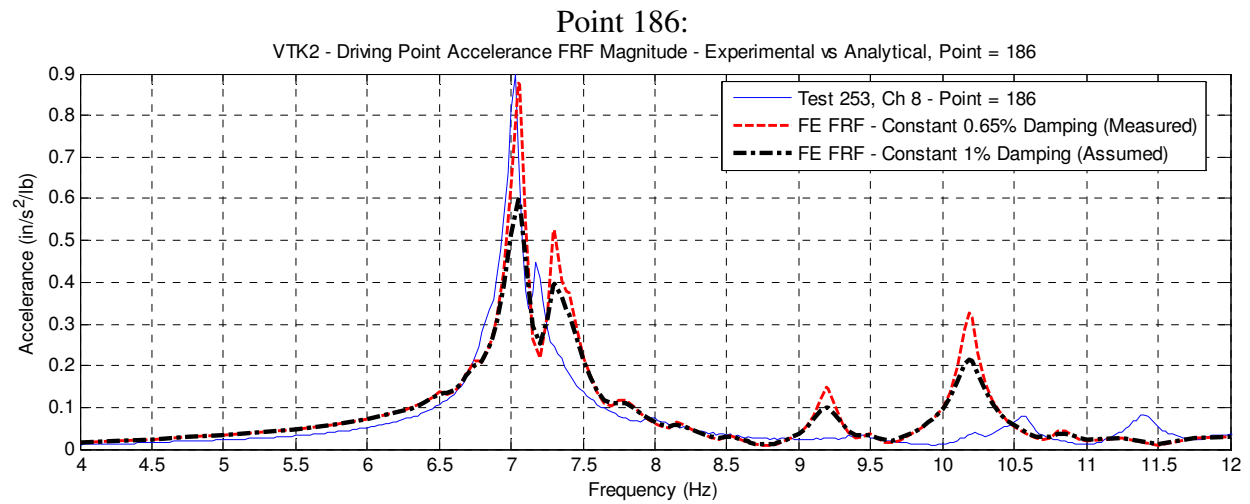
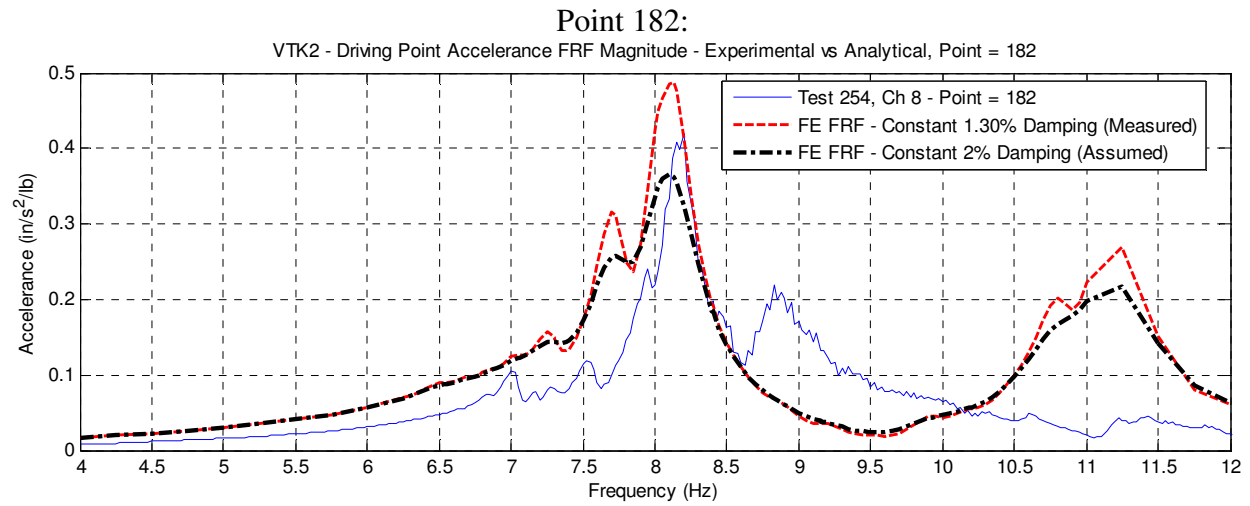
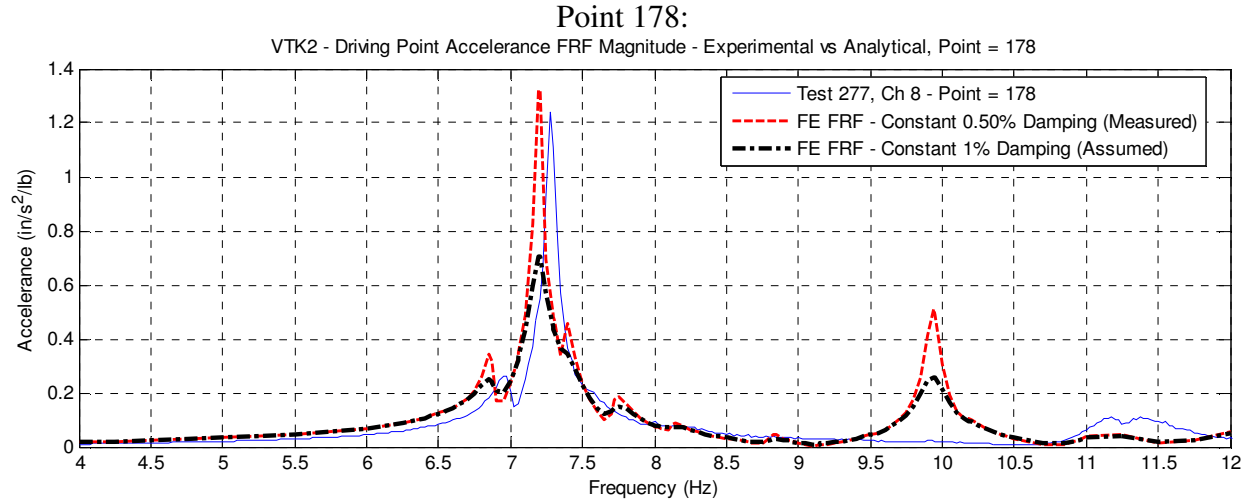


Figure 4.39: VTK2 – Accelerance FRFs (Points 178, 182, 186)

Using the measured estimates of damping, the FE steady state analyses predicted peak accelerance values (at the dominant frequency) higher than measured values in all but one of the twelve analyzed bays. Additionally, six out of the twelve bay analyses predicted a peak accelerance within 25% of measured, although the computed accelerance for three of the bay analyses exceeded the measured value by over 50%. The substantial disagreements in magnitude for these three dominant peaks are likely attributed to an overly localized response, which translates into a smaller effective mass for that mode. The effective mass of a mode is inversely proportional to the acceleration response at resonance, hence the overestimation of the peak. Using assumed values of damping in the analyses, all but one of the twelve bay analyses underestimated the peak accelerance value at the dominant frequency; however, ten of the twelve bay analyses predicted values within 25% of measured while the other two were within 50%.

Although there is admittedly room for refinement to the proposed modeling techniques, the encouraging results presented in this section demonstrate that steel composite floor systems can be modeled using a set of fundamental techniques where the resulting dynamic analyses adequately represent the behavior of an in-situ floor. Other encouraging results demonstrated that partial floor models developed with the recommended techniques can also provide a good representation of in-situ behavior. This is beneficial because creating a detailed finite element model of an entire floor system can be excessive and costly, especially if only a portion of the floor requires modeling for purposes of an adequate evaluation. The computed mid-bay accelerance FRF is the cornerstone of analysis using the FE method because of its ability to represent all important dynamic characteristics of the most vulnerable portion of a floor. It also remains an invaluable tool for validating an FE model because of its ability for direct comparison to mid-bay driving point measurements of in-situ structures.

4.3 Summary of Recommended FE Modeling Techniques for Composite Floors

This section serves as a consolidated summary of the recommended modeling techniques presented in Section 4.1 and applied to the two tested in-situ floor models in Section 4.2. The recommended techniques are presented in bullet format and follow the same order as the six *general* steps of creating an FE model of a floor system for evaluation of vibration serviceability that were presented in Section 4.1; that is,

- 1) Lay out the floor geometry using the design specified steel framing members for the beams and girders and apply vertical restraints at the location of the columns.
- 2) Define area elements and materials to represent the composite slab and apply the slab area elements to the model.
- 3) Adjust model to adequately reflect mass and stiffness (releases, restraints, PMs, etc.).
- 4) Perform modal analysis on the FE model to compute the frequencies and mode shapes.
- 5) Specify damping in the model.
- 6) Apply dynamic loads and perform forced response analysis for use in evaluation of vibration serviceability.

Mass & Materials

- Lay out the geometry of the steel floor framing in the XY-plane using the predefined frame elements in the FE program that correspond to the steel sections of the design drawings. Use centerline dimensions.
- Apply translational (vertical) restraints at all column locations.
- Create a user-defined isotropic material, and specify the modulus of elasticity to reflect the dynamic modulus of elasticity of concrete ($1.35 * E_c$ as computed by Equation (1.6)). Specify weight and mass densities of the material as computed using Equations (4.1) and (4.2) to account for the composite slab and superimposed loads, and specify a Poisson's ratio of 0.2.
- Create a user-defined thin-plate area element to represent the composite slab. Assign the user-defined concrete material to the element and input a plate thickness equal to the depth of the slab above the deck ribs. Determine the bending stiffness property modifier (PM) to represent the orthotropic stiffness of the corrugated slab by computing the ratio of strong-to-weak direction moments of inertia of the slab. Assign this PM to the appropriate plate bending moment direction (this will be based on the element's local axis).

- Apply the slab area elements to the model in the same plane as the steel framing members. Mesh the slab area elements over the floor system attempting to keep the element aspect ratio close to unity. Use at least twelve elements along the length of a bay, but slab area element sizes of 26 in. to 30 in. along each side will generally give convergent results. Using a finer mesh is acceptable but will be computationally more expensive.
- Ensure framing members are auto-subdivided along their lengths corresponding with the slab mesh size to ensure connectivity to the slab and adequate distribution of mass.

Stiffness and Boundary Conditions

- Compute the transformed composite moments of inertia for all framing members using DG11 fundamentals. Using the computed moments of inertia, calculate the respective *baseline* PMs for the framing members. When computing the PMs for members parallel to the deck ribs, account for the orthotropic bending stiffness PM assigned to the slab area elements.
- Apply the computed baseline PMs to all interior framing members and 2.5 times the baseline PMs to all spandrel members that are not free edges. Use the baseline PMs for free-edge spandrel members. Exercise engineering judgment on other members of the floor that may justify an increased stiffness PM, such as members adjacent to full-height interior partition walls or elevator cores.
- Release the strong-axis end-moment of all beams and girders framing into a column web.
- Do not assign a moment end release for any beam or girder connected to a column flange, regardless of whether it is part of a moment frame or not.
- Release the strong-axis moment in all beam-to-girder web connections that are not restrained on the other side by another member (e.g. framing into spandrel girders).
- Release the strong-axis moment and assign a partial fixity for all continuous beam-to-girder connections. Use a partial fixity rotational spring value equal to $6EI/L$, where EI/L is determined using the connecting members properties.
- Using engineering judgment, apply pinned restraints where appropriate to simulate unknown contributions of stiffness from interior partitions or interior/boundary conditions.
- In general, over-restraint of the floor using excessive numbers of interior pinned restraints, rotationally restrained degrees of freedom, or very high stiffness property modifiers does not produce good results. When in doubt, leave the model flexible in areas of unknown restraint.

Modal Analysis and Steady State Analysis

- Ensure all dynamic analysis is performed with the structure analyzed as a plane grid (UZ, RX, and RY are the available DOFs), with UZ the only translational mass DOF.
- Perform an eigenvector modal analysis to compute the frequencies and mode shapes. To determine the range of the frequencies of interest for the modeled floor, adjust the number of modes to be computed to account for all modes with single curvature within a bay.
- Apply mid-bay unit loads at all bays of interest (separate load cases for each).
- Generate separate steady state analysis cases for each bay to be evaluated and assign the respective mid-bay load case.
- Determine the frequency range of interest and the frequency increments for the steady state analysis. A frequency resolution of 0.05 Hz or finer is recommended. Include the frequencies from the modal analysis case to ensure the peak response is computed.
- Determine the assumed level of damping for each steady state analysis case based on the bay's location. Recommended levels of damping for bare floors are 1% for typical bays, 1.5% for corner bays (two exterior boundaries), and 2% for interior bays that are adjacent to interior framing. For occupied floors, assume 3% for all bays.
- For each steady state analysis case, input the assumed (or measured) level of damping as constant hysteretic damping for all frequencies. Constant modal damping is approximated by specifying the mass proportional coefficient as zero and the stiffness proportional coefficient as twice the modal damping ratio (i.e. for the assumed levels of damping for bare floors, the ratios would be 0.02, 0.03, and 0.04).
- Perform the steady state analysis and interpret the results. The most informative results are the computed driving point accelerance FRFs. Other available evaluation tools include the floor's computed operating deflection shape at resonance (very close to the computed mode shape only in actual displacement units) and envelope contour plots showing the maximum computed response at any frequency across the area of the floor.

4.4 Floor Vibration Serviceability Evaluation Using the Finite Element Method

The following section proposes a method for evaluation of vibration serviceability using the mid-bay driving point accelerance FRFs of a floor. In its most basic form, the method proposes using a *design accelerance curve* to represent a limit of vibration serviceability, and thus the peaks of an accelerance FRF for a floor must fall below the design accelerance curve to be considered acceptable. While the focus of the proposed method in this section uses the *computed* mid-bay accelerance FRFs from forced response analyses of a floor's FE model, the method is also applicable to evaluation of existing floors using *measured* mid-bay accelerance FRFs, allowing instant evaluation with field measurements. It should be noted that only the fundamental premise of the method is presented in this research, and it is neither in a final form nor validated by any case studies of floors with known serviceability problems. Efforts to identify a final form are left for future research endeavors; however the strength of the proposed method of evaluation lies in its ability to be verified with field measurements and its potential for automation within an FE program. Ideally, the form of a design accelerance threshold would be based on a database of high-quality accelerance FRFs measured from both acceptable floors and problem floors, allowing researchers to hone in on a form that is statistically significant. Unfortunately, as mentioned in Chapter 1, there is currently a very limited database of these types of measurements in the published literature, with this document possibly representing the most comprehensive listing of mid-bay driving point accelerance measurements for in-situ floors. In the absence of a significant database of measured accelerance FRFs and their corresponding subjective serviceability evaluations (human surveys of whether the floor is acceptable or unacceptable), a suggested form should be based on current practice of floor vibration evaluation. A source for this practice is the current design guidance used for serviceability evaluation. In the following section, a proposed design accelerance curve is presented based on DG11 fundamentals, although other design/evaluation methodologies are briefly discussed for reference on how their fundamentals could be adapted to develop similar design accelerance curve(s).

As mentioned in Section 1.1, the various design guidance and codes currently in use around the world address vibration serviceability in the same general manner:

- 1) Estimate the dynamic properties of the floor.
- 2) Estimate a dynamic loading to simulate the forces applied from human activities.

- 3) Compute the acceleration response of the floor for comparison with an established level of acceptability.

The two leading publications presently used for evaluation of vibration serviceability for walking excitation are the *AISC/CISC Steel Design Guide Series 11: Floor Vibrations Due to Human Activities* (Murray et al. 1997), which is used extensively in North America, and the Steel Construction Institute (SCI) *Design Guide for Vibrations of Long Span Composite Floors* (Hicks et al. 2000), which is often followed in the United Kingdom. Both publications offer simplified methods for manually computing the dynamic properties of fundamental frequency and effective mass/weight of the floor and provide recommended values of damping. Both publications recognize the complexity of representing the forces from human activities such as walking and take the approach of representing this complex loading as a Fourier series of the harmonics of footfall frequency. Lastly, using the computed properties of the floor and assumed loading, the publications compute an acceleration response to compare to acceptability criteria. For office floors, the acceptability criteria suggested by DG11 is a constant 0.005g for frequencies between 4 Hz and 8 Hz, whereas SCI allows for three different tolerance thresholds depending on a busy/general/special office occupancy condition. As discussed in Section 1.3.2, a notable difference in the two evaluation methods is in the recommended Fourier coefficients for the harmonics of step frequency. While each method recognizes a stepped nature of the dynamic load coefficients within certain frequency ranges (corresponding to the various harmonics of step frequency) DG11 offers a simplified exponentially decreasing term, $0.83\exp^{-0.35f}$, and the SCI method remains as stepped values. Young (2001) analyzed extensive footfall data and developed linear functions within each harmonic, which are still stepped in nature but with a slight upward slope. This form of the dynamic load coefficients was incorporated into more recent methods of evaluation that have been presented by Arup (Willford et al. 2006). The Arup method includes a more complex computation of acceleration response that includes the mode shape and off-resonant response in its formulation. Willford presents a reduction factor to be applied to the computed acceleration to account for not achieving full steady state response. This reduction accounts for two phenomena: an individual walks *across* the bay rather than exciting it sinusoidally at its anti-node, and a floor with a low level of damping may not undergo enough loading cycles to achieve steady state. While a similar reduction factor is included in the DG11 method of evaluation ($R=0.5$), the Arup method directly includes the bay dimensions, stride

length of an individual, and damping ratio. The computed acceleration using DG11 or SCI applies for a single fundamental frequency used in analysis and no other consideration is given for the response at (or contribution from) other frequencies. In this respect, using the accelerance FRF differs because it describes the response (and allows evaluation) over a range of frequencies and includes the contribution of other modes.

The fundamental premise of the proposed evaluation method, and its ability to represent the computed acceleration response of a floor and a level of serviceability over a range of frequencies, is the accelerance frequency response. The value of accelerance is best described by its definition as a *measured* quantity:

$$\frac{\text{Measured Accelerance}}{\text{FRF Magnitude}} = \frac{\text{measured steady state acceleration response}}{\text{measured input force}} \quad (4.5)$$

Equation (4.5) states the magnitude of the measured accelerance at a given frequency is equal to the magnitude of the measured steady state response divided by the magnitude of the input force. Because current design guidance defines a steady state acceleration limit for human comfort and estimates the applied loading from walking excitation as a steady state harmonic force, a *design* accelerance magnitude is defined:

$$\frac{\text{Design Accelerance}}{\text{FRF Magnitude}} = \frac{\text{design acceleration limit for human comfort}}{\text{design input force}} \quad (4.6)$$

Although the design acceleration limit is typically taken as a constant value over the frequency range of interest, the accelerance FRF is a function of frequency and does not require a constant acceleration threshold for all frequencies. The input force from walking excitation is generally considered a function of frequency and the magnitude of the simulated sinusoidal force is based on the harmonic of walking that will likely correspond with frequency of the floor. Thus, the design accelerance curve, $A_o(f)$, is defined in general terms as

$$A_o(f) = \frac{\text{design steady state acceleration limit}}{\text{design sinusoidal input force due to walking}} = \frac{a_o(f)}{F(f)} \quad \frac{(\text{acceleration units})}{(\text{force units})} \quad (4.7)$$

Using this form, the design accelerance curve can easily accommodate the suggested acceleration limits and effective harmonic force representation of walking excitation from DG11:

$$A_o(f) = \frac{a_o}{R\alpha_i P} = \frac{a_o}{P_o e^{-0.35f}} = \left(\frac{a_o}{P_o} \right) e^{0.35f} \quad (4.8)$$

where

$A_o(f)$ = design accelerance limit in units of acceleration per unit of input force

a_o = acceleration limit for human comfort, $0.005g$ (1.93 in/s^2) for office floors

$\alpha_i = 0.83e^{-0.35f}$ (DG11 simplified dynamic load coefficient)

P = person's weight (taken as 157 lbs for DG11)

R = reduction factor (taken as 0.5 for office floors in DG11)

$P_o = 0.83RP = (0.83)(0.5)(157 \text{ lbs}) = 65 \text{ lbs}$ when $R=0.5$ is used, otherwise $130R \text{ lbs}$

Although the variables a_o , R , and $\alpha_i P$ in the basic expression of Equation (4.8) are from DG11, they represent the general terms used in all of the evaluation methods (acceleration limit, reduction factor, and effective forcing amplitude, respectively). Using DG11 values to evaluate the expression, a final form of the design accelerance curve for a reduction factor $R = 0.5$ is:

$$A_{o,R=0.5}(f) = \frac{a_o}{R\alpha_i P} = \frac{0.005g(386 \text{ in/s}^2 / g)}{(0.5)(0.83e^{-0.35f})(157 \text{ lbs})} = \left(\frac{1.93 \text{ in/s}^2}{65 \text{ lbs}} \right) e^{0.35f} = 0.02969e^{0.35f}$$

or

$$A_{o,R=0.5}(f) \cong 0.03e^{0.35f} \left(\frac{\text{in/s}^2}{\text{lb of input force}} \right) \quad (4.9)$$

The acceleration limit a_o and forcing terms $\alpha_i P$ are based on established theories of human tolerance to vibration and the effective harmonic force due to walking, however R represents a catch-all reduction factor used to account for less-than-full steady state resonant response and because the individual walking and the individual subject to vibration are not located at the point of maximum response within a bay. The subjective nature of its suggested value means that other values of R may be considered in determining a final form of a design accelerance curve. The design accelerance curve of Equation (4.9) for $R=0.5$ is plotted in Figure 4.40 along with other values of R to illustrate the effect on using a different reduction factor.

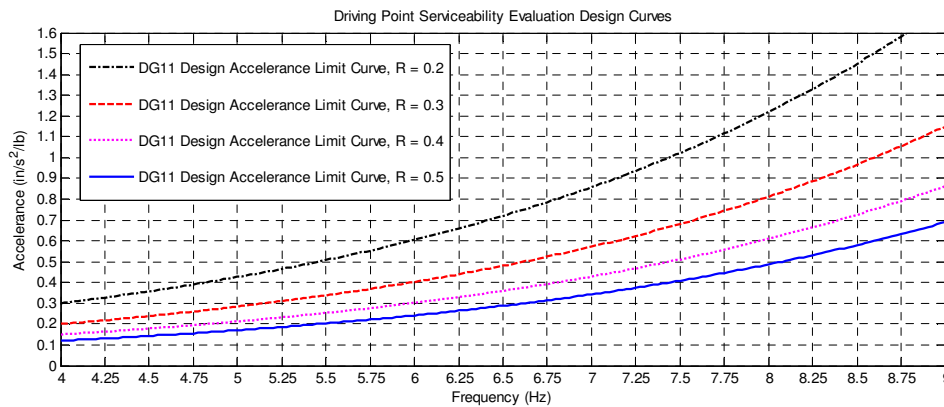


Figure 4.40: Proposed DG11 Design Accelerance Curves for Different Reduction Factors

Note that the design accelerance curves in Figure 4.40 are plotted from 4 Hz to 9 Hz, which corresponds with the lower 0.005g plateau in Figure 1.1, the figure illustrating the recommended peak accelerations for human comfort for vibrations due to human activities. The simplified dynamic load coefficient term used by DG11 makes each design accelerance curve a smooth increasing exponential. The other methods of evaluation offered by SCI and Arup use a stepped dynamic load coefficient (or stepped function with slight slope), and thus the form of the design accelerance “curve” would also be stepped. The reduction factor included in the Arup method would be computed for each analyzed bay because it is based on damping and the bay dimensions. Thus, the Arup design curves for each analyzed bay would shift up or down depending on the computed reduction factor. Although specific terms of the other methods differ from DG11, they are only highlighted to demonstrate that they are not insurmountable for developing a design accelerance curve based on the evaluation method fundamentals.

A demonstration of the proposed method for evaluation is made using the design accelerance curve for $R=0.5$ shown in Figure 4.40 and the VTK2 FE model presented in Section 4.2.2. The development and analysis of the FE model presented in that section comprise the first step in the proposed evaluation process, simply modeling the floor assuming bare conditions. This floor was modeled assuming a bare floor condition with no superimposed loads and was analyzed using the recommended damping values for a bare floor (1%, 1.5%, and 2% depending on bay type). Although the acceleration response is the critical parameter for evaluation, there are other modeling results that provide insight on the predicted performance of the floor. Modal analysis of the bare floor system indicates both frequency content of the floor as well as the general shapes of expected modes. For the bare condition VTK2 FE model, the lowest computed frequencies were 6.5-7.0 Hz, a bit high for floors that historically have shown serviceability problems. The frequencies of a floor will decrease with superimposed load, thus if the computed bare floor frequencies are initially low (4-5 Hz), this may indicate a potential problem floor early in the design process. Additionally, examining the mode shapes of the bare floor model also provides preliminary evaluation, as certain mode shapes may indicate problem areas of the floors at certain frequencies. These “soft spots” (very localized mode shapes) may result in large accelerance values at resonant frequencies due to the smaller effective mass of the mode. Performing a forced response steady state analysis of the floor at each mid-bay location will give an overall idea of the performance of that area of the floor. Analysis of the bare floor does not

have much relevance for comparison to recommended design accelerance values because it is unlikely that the floor is occupied in such a condition. The performance of the occupied condition is of the most interest for evaluation, however the computed accelerance FRFs of the bare floor (with the smaller assumed damping values) are important because they highlight dominant and significantly participating frequencies/modes. At higher levels of damping, many of these peaks will be smoothed out and difficult to distinguish. (However, on the usefulness of bare floor FE models, a bare floor is a much more likely condition for the acquisition of field measurements for validation of an FE model).

The second step in the evaluation process is to adjust the bare floor model to reflect the occupied condition. To simulate the increased load of an occupied condition, superimposed loads of 4 pounds per square foot (psf) of dead load and 6-11 psf of live load are assumed (Murray et al. 1997). This superimposed load is applied to the model by re-computing the weight and mass densities of the slab user-defined material using Equations (4.1) and (4.2). The mass density, assuming a live load of 11 psf, and the first 10 computed frequencies of the occupied floor model are listed in Table 4.6 for comparison with the mass density and frequencies of the bare floor model.

Table 4.6: FE Serviceability Evaluation Example – Change in Computed Frequencies

VTK2 Bare Floor		VTK2 Occupied	
Mass Density:		Mass Density:	
2.3869x10 ⁻⁷ k-s ² /in ⁴		3.2171x10 ⁻⁷ k-s ² /in ⁴	
Mode:	Frequency (Hz)	Mode:	Frequency (Hz)
1	6.535	1	5.699
2	6.689	2	5.828
3	6.772	3	5.901
4	6.867	4	5.983
5	6.870	5	5.991
6	7.055	6	6.155
7	7.200	7	6.281
8	7.295	8	6.358
9	7.307	9	6.371
10	7.387	10	6.442

A superimposed load is assumed to add mass to the system and not stiffness. For a typical steel composite floor, the slab will be 80-90% of a floor's mass, with the remainder belonging to the steel framing members (for the bare VTK2 model in this example, the slab elements were 86% of the floor's total mass). Thus, any increase in the mass density of the slab material to account for superimposed load will effectively be a uniform increase in the total

system mass. As a result, the shape and order of all mode shapes will not change but their respective frequencies will decrease, as will the acceleration response due to an increase in effective mass. Note this only holds true for the addition of a superimposed load. An increase in slab thickness must be accounted for in the mass *and* stiffness of the slab as well as a corresponding increase in composite stiffness of the steel framing members.

For the provided example, a forced response steady state analysis was conducted on the mass density-adjusted model at the mid-bay location of Point 82 assuming an occupied condition damping value of 3%. This location was originally analyzed with an assumed bare floor damping value of 1.5% (corner bay). A comparison of the two computed accelerance FRFs is presented in Figure 4.41. As expected, the peaks of the accelerance FRF shift to reflect the decrease in frequencies due to the applied superimposed load. The increased level of damping smoothes out all but two dominant peaks, and the peak accelerance values decrease due to both the higher damping and the increase in mass. Using DG11 as a basis for evaluation, the design accelerance curve for an office floor ($R=0.5$) is plotted along with the two computed accelerance traces. The most important comparison in Figure 4.41 is the peak magnitude of the occupied floor model's computed accelerance FRF in relation to the design accelerance curve. For this example, the peak at 5.70 Hz dominant peak is 0.17 in/s²/lb of input force, below the 0.22 in/s²/lb design curve value. Because the computed peak accelerance was less than the design accelerance curve, this bay would be considered acceptable for vibration serviceability using the proposed method of evaluation.

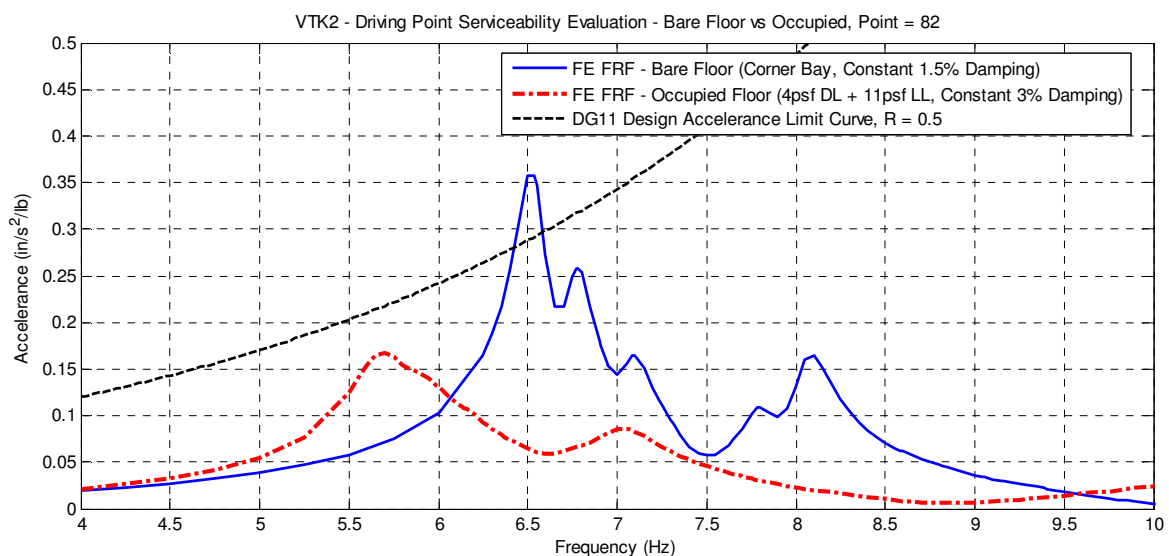
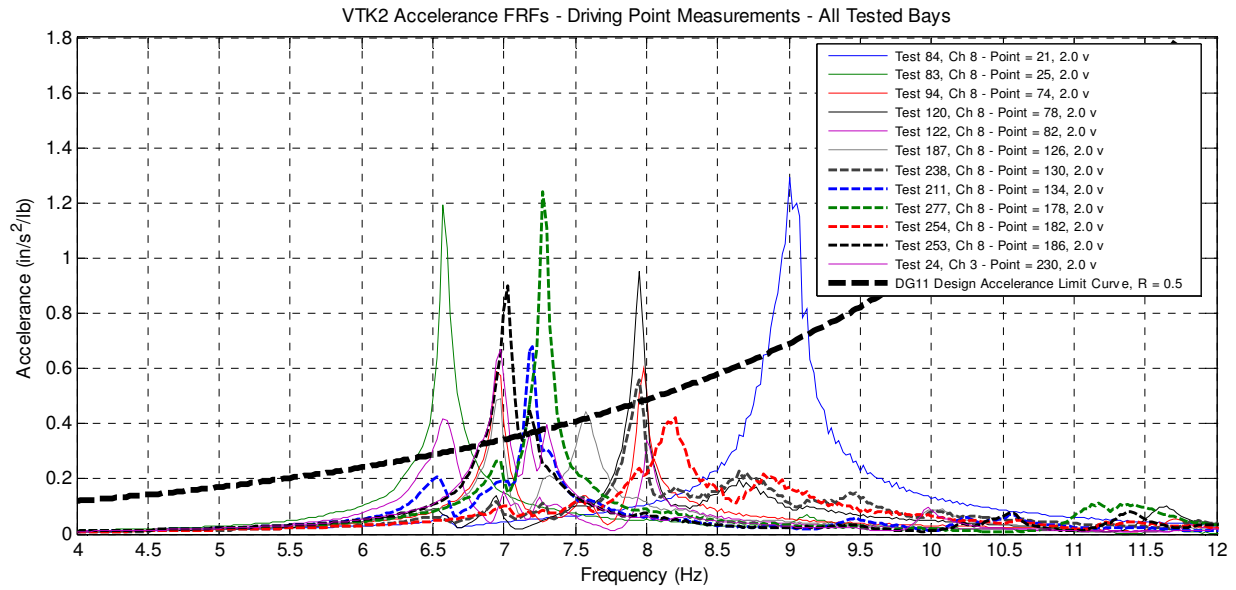


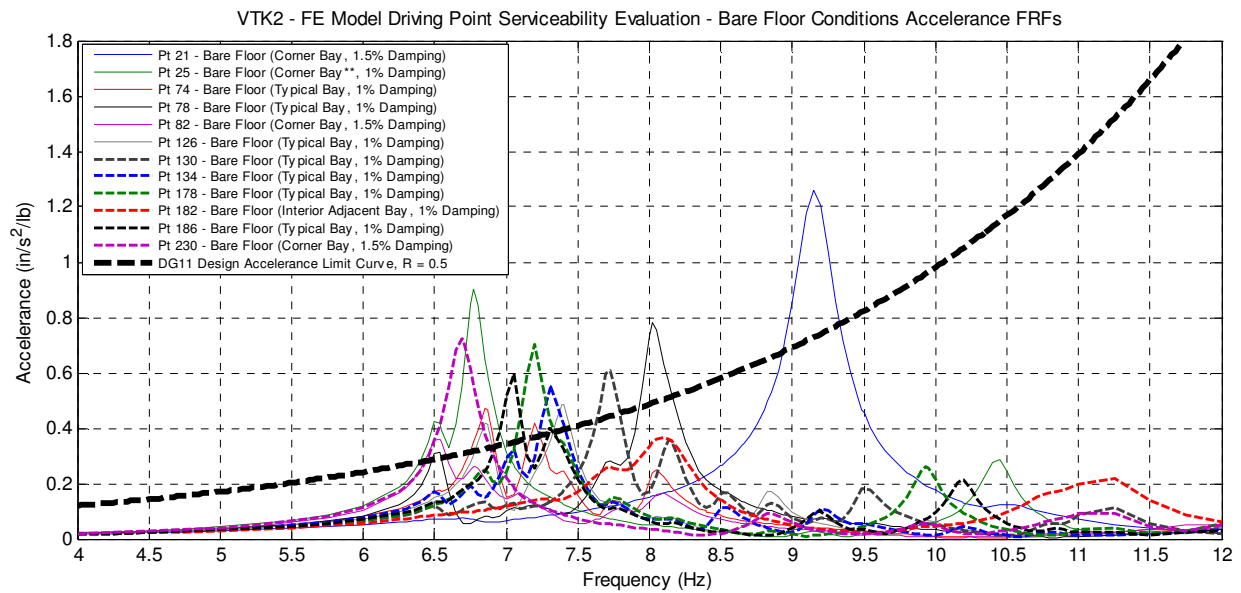
Figure 4.41: FE Serviceability Evaluation Example – Accelerance FRFs and Design Curve

Note that the comparison of this single peak accelerance value to the design accelerance curve is equivalent to the single frequency response computation of DG11 with one exception: the bay's dominant frequency and effective weight were calculated within the FE model rather than using DG11's simplified methods. The availability of the peak response of all participating modes over the frequency spectrum is advantageous, particularly if an analyzed location has multiple significant peaks, which was observed for some locations of the tested in-situ floors. Additional advantages of using the finite element method for evaluation of vibration serviceability are that the predicted frequencies of simplified methods often do not account for the effect of non-standard conditions such as different beam sizes between columns, increased stiffness at boundaries, or irregular framing that may affect the mode shapes. The effective mass estimated using these simplified procedures is also based on gross generalizations, a necessity for their broad application, whereas the FE models determine effective mass based on mode shapes that account for irregular framing or the non-standard conditions, provided they are included in the model.

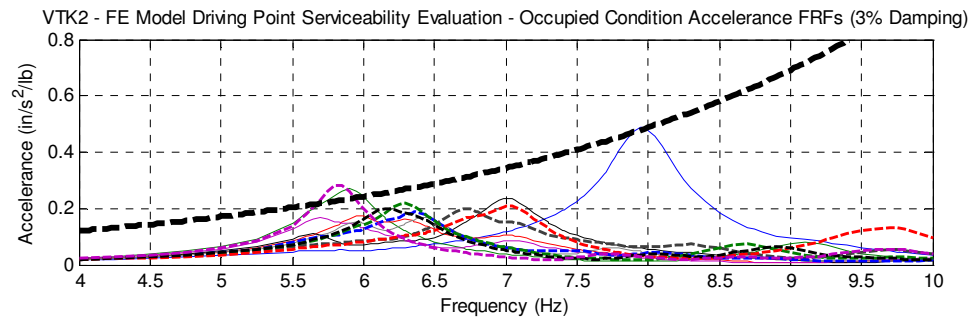
Continuing the previous evaluation example, the remaining bays of the floor were analyzed in a similar manner with steady state analyses at all mid-bay locations for comparison with the design accelerance curve. The computed accelerance FRFs for the bare floor and occupied floor FE models are presented below in Figures 4.42(b) and (c) for comparison. According to the serviceability evaluation of the occupied floor model in Figure 4.42(c), all but two bays on the floor satisfy the 0.005g serviceability limit at their respective dominant peaks. If all bays had exceeded the design curve, then a major change in the design may be warranted, however the slight overage in only a few bays may only call for some minor adjustments or may even be considered acceptable given the assumptions built into the FE model. To demonstrate the reasonableness of this example to represent in-situ floor behavior, the measured accelerance FRFs from each of the twelve analyzed bays in VTK2 are also included in Figure 4.42(a).



(a) VTK2 - Measured Mid-Bay Driving Point Accelerance FRFs (All Bays)



(b) Bare Floor FE Model Accelerance FRFs – 1%, 1.5%, 2% Damping



(c) Occupied Floor FE Model Accelerance FRFs – 3% Damping (All Bays)

Figure 4.42: FE Serviceability Evaluation Example – All Bays

Another valuable observation can be made from Figures 4.41 and 4.42 in the example. The simple comparison of the computed accelerance FRFs of an adjusted FE model is a good tool to help designers visualize the effect of design or occupancy changes on vibration performance. Using a lower damping value and decreasing the superimposed load of an existing floor system may simulate a change to a more open and lightly furnished office floor plan. Some design changes may be more tedious to address than simple occupancy-change adjustments to superimposed load and damping, adjustments to member sizes, slab thicknesses, strength or unit weight of concrete, or even the depth of steel deck can be investigated to determine their effect on vibration performance. All of the above listed items have the potential to change the frequencies and mode shapes of a floor, but sifting through a list of frequencies and looking at displayed mode shapes can easily obscure the important performance parameter, acceleration response. The computed accelerance FRF allows instant and intuitive feedback on how the design change affects vibration performance across a range of frequencies. If the computed accelerance FRFs are compared to a design accelerance curve representing a level of vibration serviceability, then the designer can make informed decisions early in the design process.

The ease of computing a design accelerance curve and the simplicity of the proposed modeling techniques and mid-bay steady state analysis presented in Sections 4.1 and 4.2 make the proposed method of evaluation for vibration serviceability a viable candidate for automation within an FE program. *It should be stressed, however, that the final form of the proposed evaluation process is not calibrated against any known problem floor case studies and should not be viewed as a replacement for current design guidance at this point.* Although the recommended FE modeling techniques demonstrated a modest ability to adequately represent measured behavior, future refinement of the modeling techniques using further testing of in-situ structures will strengthen both the accuracy of the models and the method of evaluation. DG11 seems to be a good starting point for the form of the design accelerance curve; however the final form should be based on a survey of tested in-situ floors with known subjective serviceability evaluations. Although the database of floors with high-quality accelerance measurements is very limited, an extensive database of problem floors does exist with response-only measurements and subjective evaluations. This is where a refined and accurate method for modeling floors would help define the form of the design curve, because FE models of the database of surveyed floors could be generated in lieu of high quality accelerance FRF measurements.

A final note on the proposed method is that it also serves as a simplified method of evaluating existing floors in the field. Current methods of on-site serviceability evaluation typically involve a series of heel drop or walking tests to record peak acceleration response, generally as response-only single channel measurements. A general understanding of the floor response is achieved by looking at the acceleration traces and autospectra from these excitations. Using an instrumented heel drop (Class-III Testing per Section 2.5) instantly provides a high-quality accelerance FRF that can immediately be compared to a predefined design accelerance curve.

CHAPTER 5

CONCLUSIONS AND RECOMMENDATIONS FOR FUTURE RESEARCH

5.1 Conclusions

The purpose of this research was to examine the dynamic behavior of in-situ steel composite floors and present a set of fundamental modeling techniques for generating finite element models for steel composite floor systems such that the resulting dynamic analysis yields an adequate prediction of response for evaluation of vibration serviceability. Briefly, the desired goals of the research were:

- Identify and summarize the best and recommended practices in dynamic testing of in-situ floor systems. Develop a classification system for floor vibration testing based on equipment and techniques employed, as well as the information available from each class of testing.
- Conduct extensive dynamic testing of in-situ multi-bay steel composite office floors to estimate dynamic parameters/response and to identify trends in dynamic behavior.
- Generate a set of fundamental FE modeling techniques to represent the mass, stiffness, and boundary conditions of the floor, as well as incorporating an assumed (or measured) level of damping into the model for use in dynamic response analysis.
- Propose a method for evaluation of vibration serviceability using the finite element method.

The measurement, characterization, analysis, and computation of a floor's accelerance frequency response function (FRF, the acceleration response at one location of the floor per unit of input force at another location) is the core premise linking all areas of the presented research. Chapter 2 describes best practice techniques for testing in-situ floors and acquiring high quality dynamic measurements in the form of the accelerance FRF. Chapter 3 describes the characteristics of in-situ floor behavior as a result of the experimental testing and acquisition of high quality measurements for three in-situ steel composite office floors. Chapter 4 provides recommended modeling techniques for steel composite floors based on the high quality measured data and proposes a method for evaluation of vibration serviceability based on the computed accelerance

FRF. The present chapter briefly summarizes the presented research including the notable conclusions in each of the areas of study and provides recommendations for future research in this field.

5.1.1 Dynamic Testing of In-Floor Systems

Multi-bay in-situ floors are large structures that present their own unique challenges for dynamic testing. Virtually all aspects of in-situ floor testing require compromise, and limited time available to test a floor is the leading factor in the quality and extent of test measurements. Best practice techniques for testing in-situ floors were presented that stressed efficient test methods and techniques to ensure quality measurements. The recommended approach to floor testing and best practice techniques is valid for virtually any type of in-situ floor, not just the steel composite floors of the presented research. The notable findings from this area of study are as follows:

- Various methods of excitation were described in this research, including chirp signals, instrumented heel drop, steady state sinusoid, and unreferenced measurements. The burst chirp signal using an electrodynamic shaker is recommended as the most accurate and consistent source of excitation for high quality measurements that are suitable for use in parameter estimation, operating deflection shape animation, and calibration of FE models. An instrumented heel drop may provide an inexpensive alternative to generate an accelerance FRF, however the controlled excitation and quality of measurement using an electrodynamic shaker is unparalleled.
- It is recommended to use a force transducer to measure the input force from an electrodynamic shaker rather than an accelerometer mounted to its armature, which can underestimate the measured response at its most critical values, the resonant peaks of the accelerance FRFs.
- Several methods for estimating damping were presented, including the half power bandwidth of chirp derived accelerance FRFs and sinusoidally derived accelerance FRFs, MDOF frequency domain curve fitting of the accelerance FRF using modal analysis software, and decay from resonance time domain curve fitting. All methods were in general agreement with one another, however MDOF curve fitting of the driving point accelerance FRF is recommended for its ability to deal directly with closely spaced

modes. MDOF curve fitting is the most reliable, but it still requires a fair amount of engineering judgment to confirm the validity of estimated parameters in the modal analysis software. The half power bandwidth method is very consistent; however the presence of closely spaced modes can lead to overestimation of damping. Time domain curve fitting decay from resonance is consistent for clearly dominant modes; however estimates may be misinterpreted if there are closely spaced modes with significant participation. Damping is the dynamic parameter most affected by poor frequency domain resolution, as truncated peaks in the accelerance FRF can lead to overestimates of damping.

- Although all levels of dynamic testing have various degrees of usefulness, only certain types of dynamic measurements are suitable for tasks that require high quality modal data, such as FE model calibration or detailed parameter estimation of damping and mode shapes. Section 2.5 describes a classification of floor vibration testing expressed in terms of the methods/equipment used (or required) for testing and the extent of the useful information that can be extracted from the tests. Establishing a common *Class of Floor Testing* helps prevent false expectations in the capabilities of measured data and identifies the equipment, time, and cost (in terms of analysis/testing effort) required to obtain the desired results.

5.1.2 Dynamic Behavior of In-Situ Floor Systems

Three in-situ steel composite office floors were tested in this research (NOC VII-24, NOC VII-18, and VTK2), including two nominally identical floors within the same building (identical framing, nearly identical partition wall layout). The extent of testing varied for each of the three tested floors; however accelerance FRFs were measured with an electrodynamic shaker located within 26 unique bays, providing the largest survey high-quality modal measurements on in-situ floors known to be available in the current literature. The notable findings and recommendations from this area of study are:

Frequency

- Mid-bay driving point accelerance FRFs are the most valuable and descriptive measurements from testing an in-situ floor. The driving point accelerance FRF provides immediate feedback on dominant and significantly participating frequencies within the

bay, an estimate of damping can be performed using the half power bandwidth method on the peaks, and the magnitudes of the peaks relative to other measured portions of the floor provide immediate feedback on response intensity (and indirectly the mode shape).

- The dominant frequencies of the 26 bays on the three tested floors ranged from 4.85 Hz to 9 Hz, all within the range of frequencies where humans have the lowest threshold of tolerance. The term “dominant frequency” is used to describe the frequency of the largest magnitude peak on the mid-bay accelerance FRF because it is the frequency that will generate the greatest response per unit of input force (such as from walking excitation). This term is used in lieu of “fundamental frequency,” which is typically reserved to describe the lowest frequency. When two peaks of nearly identical magnitude are present, the lower frequency peak is generally considered to be the dominant frequency because of its susceptibility to a lower harmonic of walking frequency (which translates to a larger applied force).
- The accelerance FRF measurements were consistent between the two identically framed floors tested in NOC VII (with only slightly different interior partition layout), which validates assumed consistent behavior of similarly framed floors. This consistency is a fundamental assumption for developing tools to accurately predict floor behavior, such as FE modeling.
- Because multi-bay floors generally consist of bays of similar or identical framing, they result in a narrow frequency band of the dominant frequencies. The nine exterior (similarly framed) bays of NOC VII had dominant frequencies within a 0.5 Hz band, and the seven exterior bays of VTK2 were within a 1.0 Hz band.

Damping

- Measured damping values were low (less than 2.5% of critical, many less than 1%), but the values are reasonable considering the bare condition of the tested floors.
- The measured estimates of damping varied considerably, ranging from 0.6% to 2.4% of critical for NOC VII (0.65-1.15% was typical), and 0.44% to 1.33% for VTK2 (0.5-1.0% was typical). The wide range of damping values makes it difficult to establish recommended values for damping to incorporate into FE models; however, a designer has no other choice but to use assumed damping values for forced response analysis.

- Although there was no definitive trend, some indications showed that proximity to boundaries affects the level of damping (e.g. corner bays with multiple exterior boundaries or interior bays adjacent to areas with interior partitions), which seems reasonable.
- Overall, NOC VII had higher levels of damping than VTK2, which is likely a result of spray on fireproofing, finished interior partition walls, and finished exterior boundaries.

Mode Shapes and Operating Deflection Shapes

- Because ODSs are measured forced-response shapes and vibration serviceability is a forced-response phenomenon, displaying an ODS at the dominant frequency visually illustrates the floor's potential vulnerability to walking excitation. At resonance, the ODS closely *approximates* the mode shape provided it is dominated by a single mode.
- ODSs are animated directly from measured accelerance FRFs, thus the validity of the displayed shape is a direct result of the quality of the measurements. The mode shapes are not measured; they are *estimated* from measured accelerance FRF data. Because the mode shapes are estimated from these measurements, the quality of the mode shape is also a direct result of the measurement quality. It is from this demand for quality measurements that the recommended best practice techniques were derived.
- Several measured shapes on the floors were localized to just a few bays and occasionally there was very little response in immediately adjacent bays. To investigate this phenomenon, sets of measurements were taken with the shaker in multiple locations for coverage areas in both NOC VII and VTK2. Because of the localized response, not all modes were adequately excited by forcing at a single mid-bay location. Gathering sets of measurements with the shaker at multiple locations allowed estimates of modal parameters from the set of measurements that most strongly excited a particular mode. The quality of the estimated mode shapes (and strength of the visually displayed ODSs) was significantly improved using multi-reference testing, and this approach is highly suggested if well defined mode shapes are of interest.

General Response Behavior

- The shape of a bay excited at its dominant frequency is characterized by single curvature.

- The mid-bay location is the best point for excitation because it roughly corresponds to the anti-node (point of maximum response) of the bay when driving at its dominant frequency. It was demonstrated that this location was also almost always the anti-node of response for the *whole floor* when excited at its dominant frequency, essentially making the mid-bay driving point acceleration FRF the upper bound response for the entire floor.
 - The observed upper bound response behavior validates current methods of evaluation of vibration serviceability, which compute the mid-bay response to a mid-bay excitation for comparison with acceptability criteria.
 - Additionally, it allows more efficient testing because a collection of mid-bay driving point measurements (rather than full modal testing) may be adequate to define the dominant frequencies and upper bound response for excitation within each tested bay of a floor.
- The displayed operating deflection shapes of the tested floors revealed there is generally more response in bays that are adjacent to the bay of excitation in the direction of the composite deck span than in the perpendicular direction (parallel to the floor beams).
- Significant response was measured at spandrel members of the exterior boundaries of the floor. Magnitudes of response ranged from 9-26% of the mid-bay response for both of the tested buildings, which is significant considering that such a boundary is typically assumed to be rigid.

Measurement Consistency and Linearity

- For all measurements, one or more accelerometers were located with the shaker and force plate to record redundant driving point measurements. Theoretically, these measurements should be identical, and they were very consistent in the presented research. However, slight variations can occur (due to changing environmental conditions like temperature), and redundant measurements allow the ability to recognize and account for them.
- Although the driving point measurements were very consistent in this study, it is suggested to perform a modal sweep over a coverage area as quickly as time allows, avoiding any potential changes in the condition of the floor or test set up.

- No significant nonlinearity was identified in the tested floor systems, although a larger input force (and response amplitude) had the tendency to slightly shift the dominant frequency to the left (decrease in frequency by one or two spectral lines). This can be interpreted as a tendency for the floor to become slightly more flexible at higher levels of excitation.
- There was excellent agreement between reciprocal FRFs of bays immediately adjacent to the bay of excitation, but the agreement deteriorated at locations further away (more than two bays). Rather than a gross nonlinearity in the system, this poor agreement is more likely a function of poor signal strength at the longer distances.

Mid-Bay Floor Evaluation

- A reduced mid-bay testing scheme is recommended as a time-saving alternative to modal testing over a full coverage area, provided the only desired estimates of dynamic parameters are frequencies, damping, and mid-bay acceleration response. The evaluation method requires multiple sets of accelerance FRFs to be measured with the shaker and roving accelerometers located at the centers of each of the surveyed bays.
- Forcing at the mid-bay of each of the surveyed bays ensures that all bays' dominant frequencies are adequately excited for estimates of frequency and damping. The peak accelerance of the mid-bay driving point FRF also provides the upper bound acceleration response of the floor from excitation within that bay.
- A limited description of the shape of the floor's response can be made through comparison of the relative mid-bay accelerance FRF magnitudes and phase.
- Multiple sets of measurements from different forcing locations allows multi-reference MDOF curve fitting of a small but representative set of accelerance FRFs, instilling a higher confidence in the estimated modal parameters.

5.1.3 Fundamental Modeling Techniques for Composite Floors

Using the measured in-situ behavior of the tested floors for reference, finite element (FE) models were developed for the NOC VII and VTK2 floors. The FE models for both floors were developed in parallel using a shared set of simplified FE modeling techniques. Manual FE

model updating was performed to bring the computed results into agreement with the experimentally measured results. A summary of notable results is listed here.

- Recommended fundamental FE modeling techniques for steel composite floors were presented in Section 4.1.
- The FE models for the two tested floors developed using the recommended FE modeling techniques were presented in Section 4.2.
- An abbreviated summary of the recommended techniques was presented in Section 4.3.
 - The described techniques provide recommendations for modeling mass, stiffness, and boundary conditions of steel composite floors.
 - Also included are recommendations for dynamic analysis for the purpose of evaluation of vibration serviceability. These techniques include modal analysis, representing damping in the FE model, and forced response steady state analysis over a frequency range of interest.
- Performing a steady state analysis using a *unit* point load at a single location on the FE model is the computational equivalent of measuring the accelerance FRFs for the entirety of a floor from forcing at a single driving point location with an electrodynamic shaker. Using this advantageous property, unit point loads were placed at the mid-bay locations (corresponding to experimental excitation locations) for steady state analysis. The *computed* mid-bay driving point accelerance FRFs were used for comparison with *measured* mid-bay driving point accelerance FRFs.
- Two FE models were generated for NOC VII, a full floor model and partial floor model.
 - The first FE model for NOC VII represented the entire floor and successfully captured the behavior in four of the eleven analyzed bays, but struggled to adequately represent the behavior of the floor along the long exterior strip of bays.
 - A reduced floor model containing just the ten bays along the long exterior strip was much more successful in representing the behavior of these bays. The success of a partial floor model was a particularly encouraging result as developing an FE model of an entire floor system can be costly.
 - It is likely the over-constraint of the interior bays of the floor (which was not a part of the reduced floor model) was a factor in the poor agreement of the full floor model. In these areas, vertical restraints were added to interior slab and

framing members to represent full-height partition framing, elevator cores, stairwells, etc. The exact layout within these interior bays was not known, thus engineering judgment was exercised on their placement.

- VTK2 was represented with a full floor model, although commentary and comparison of frequencies and mode shapes were not made for the portions of the floor that were not tested.
 - The VTK2 floor contains several areas of irregular framing and consequently has some unique (and non-intuitive) mode shapes. The applied FE modeling techniques were very successful in capturing the unique mode shapes at their corresponding frequencies. Predicted dominant frequencies from all twelve analyzed bays were within 5% of measured values.
- Although there is room for refinement of the techniques with further testing/modeling of in-situ floors, the presented fundamental FE modeling techniques were shown to provide adequate representations of measured floor behavior for the purposes of serviceability evaluation.
- An advantage of the recommended FE modeling techniques and method of dynamic analysis are their simplicity, making them very conducive to automation. Depending on the FE program used for modeling, the recommended techniques leave room for alternative approaches of specifying damping for forced response analysis.

5.1.4 Evaluation of Vibration Serviceability of Floor Systems

This research proposed a method for evaluating vibration serviceability of floor systems using the finite element method, which has the potential to be just as applicable to the evaluation of in-situ floors through experimental testing. The proposed method was presented in Section 4.4 and is summarized here.

- A *design accelerance curve* is proposed to represent a response threshold in the frequency domain that can be used in comparison with an acceleration response in the frequency domain (an accelerance FRF).
- Using the FE method, the proposed method of evaluation uses the *computed* mid-bay accelerance FRF as the evaluation parameter.

- Existing floors can also be evaluated through comparison of the *measured* mid-bay accelerance FRF with the design accelerance curve.
- As a proposed method, the final form of the design accelerance curve was not finalized; however, an example design accelerance curve is presented based on current serviceability guidelines, specifically DG11 limits of acceptability and effective harmonic forces due to human activities such as walking.
- Because the recommended method of evaluation is based on the mid-bay driving point accelerance FRF, it is also very conducive to automation within a FE program.
- Mid-bay driving point accelerance is a directly measured quantity (unlike walking forces), thus the final form of a design accelerance curve may be directly developed from a survey of in-situ measurements of both acceptable floors and floors with known serviceability problems.

5.2 Recommendations for Future Research

The recommended areas of future research presented in this section address several aspects of floor vibrations, including additional in-situ floor testing and refinement of FE modeling techniques. Also presented are recommendations for the calibration of the proposed *design accelerance curve* method of evaluation through further FE modeling and experimental testing of in-situ floors.

In-Situ Floor Testing

- Additional high-quality modal testing of in-situ floors fit out to all conditions of occupancy (bare floor, open office, etc.) is recommended. This includes a full modal survey over the floor area using multiple references to ensure the dominant modes of all surveyed bays are adequately excited for the purposes of MDOF curve fitting and FE model calibration.
- If the time required for a full modal sweep of the in-situ floor is not available, implement a mid-bay testing scheme as a minimum measurement survey. At the very least, this survey adds to the database of measured mid-bay accelerance FRFs.

- Perform high quality modal testing of *the same* in-situ floor at different stages of fit out, at minimum testing a floor in a bare condition and again at an occupied fit out condition to examine the change in dynamic behavior.
- In addition to mid-bay driving point measurements, test floors with the shaker located at quarter points of a bay to validate second bending mode frequencies/shapes (and confirm that these frequencies are typically out of range of the harmonics of interest and at smaller magnitudes than their mid-bay counterparts).
- Directly test specific floor components such as members between columns by placing a shaker on these areas for certain measurements. For different fixity conditions, this may give insight into their level of fixity when compared to theoretical values based on composite moment of inertia and degree of fixity (and thus frequency).
- Combine high-quality modal testing with walking tests to establish the correlation between peak accelerance values and unreferenced response-only walking tests at resonance and off resonance. Try to determine if it is possible to determine a quasi-FRF using off-resonance walking, a similar approach to stepped sine testing at frequencies near resonance.

Finite Element Modeling of In-Situ Floors

- Conduct further refinement of recommended (simplified) modeling techniques by applying automated FE model updating procedures. Potential variable parameters for iteration in the automatic update algorithms may include the partial fixity values at beam-to-girder and beam/girder-to-column web/flange connections (which, if expressed as a fraction of EI/L , provides a much more conducive variable for iteration) and/or the baseline property modifier multiplier for spandrel members.
- Conduct further investigation of reduced models of portions of a floor. Determine parameters to adequately represent the missing portion of the floor, or only consider the mode shapes localized away from these artificial boundaries as valid for the reduced models.
- Apply recommended (or refined) modeling techniques to blind testing of floors. Model an in-situ floor prior to testing using an assumed level of damping. Compute the mid-bay accelerance FRFs for the areas to be tested for immediate comparison of measurements.

Calibration of Proposed Method of Evaluation Using In-Situ Floor Accelerance FRFs

- Obtain high quality modal measurements of in-situ floors with known serviceability problems. Compare with high quality modal measurements of floors without problems and examine the data for trends in peak accelerance values. This database of measured peak accelerance values coupled with subjective serviceability evaluation should be the basis of the final form of the design accelerance curve.
- Generate FE models of the existing database of problem floors with known serviceability issues and look for trends in computed peak accelerance values.

REFERENCES

- Allen, D.E., and Murray, T.M. (1993). "Design Criterion for Vibrations Due to Walking." *AISC Engineering Journal*, 4th Qtr, 117-129.
- Alvis, S. R. (2001). "An Experimental and Analytical Investigation of Floor Vibrations." M.S. Thesis, Virginia Polytechnic Institute and State University, Blacksburg, Virginia.
- APS Dynamics, Inc. *Instruction Manual: Electro-Seis Model 400 Shaker*.
- APS Dynamics, Inc. *Instruction Manual: Dual-Mode Model 144 Amplifier*.
- Avitabile, P. (2005). "101 Ways to Extract Modal Parameters – Which is the One for Me?" Proceedings of the 23rd International Modal Analysis Conference (IMAC XXIII), Orlando, Florida.
- Bachmann, H. et al. (1995). *Vibration Problems in Structures: Practical Guidelines*. 1995. Birkhäuser Verlag, Basel.
- Band, B.S. Jr. (1996). "Several Vibration Performance Aspects of Joist and Joist-Girder Supported Floors." M.S. Thesis, Virginia Polytechnic Institute and State University, Blacksburg, Virginia.
- Barrett, A.R., Avci, O., Setareh, M., and Murray, T.M. (2006). "Observations from Vibration Testing of In-Situ Structures." Proceedings of the 2006 Structures Congress, ASCE. St. Louis, Missouri, 20 May 2006.
- Beavers, T.A. (1998). "Fundamental Natural Frequency of Steel-Joist Supported Floors." M.S. Thesis, Virginia Polytechnic Institute and State University, Blacksburg, Virginia.
- Blakeborough, A., and Williams, M.S., (2003). "Measurement of Floor Vibrations Using a Heel Drop Test." Proceedings of the Institution of Civil Engineers: *Structures and Buildings*, 156, 367-371.
- Boice, M.D. (2003). "Study to Improve the Predicted Response of Floor Systems Due To Walking." M.S. Thesis, Virginia Polytechnic Institute and State University, Blacksburg, Virginia.
- Chopra, A.K. (2001). *Dynamics of Structures: Theory and Applications to Earthquake Engineering*, 2nd Ed, Prentice Hall, Upper Saddle River, New Jersey.
- Clough, R.W. and Penzien, J. (1993). *Dynamics of Structure*, 2nd Ed, McGraw-Hill, New York, New York.

CSI (2004). “SAP2000 – Linear and Nonlinear Static and Dynamic Analysis and Design of Three-dimensional Structures – User’s Manuals.” Computers & Structures, Inc., Berkeley, California.

Dynamic Testing Agency (DTA). (1993). *Handbook on Modal Testing*. London, UK.

El-Dardiry, E., and Ji, T. (2006). “Modelling of the dynamic behaviour of profiled composite floors.” *Engineering Structures*, 20, 567-579.

El-Dardiry, E., Wahyuni, E., Ji, T., and Ellis, B.R. (2002). “Improving FE models of a long-span flat concrete floor using frequency measurements.” *Computers and Structures*, 80, 2145-2156.

Ellingwood, B. (1989). “Serviceability Guidelines for Steel Structures.” *AISC Engineering Journal*. 1st Qtr, 1-8.

Eriksson, P.E. (1994). “Vibration of Low-Frequency Floors – Dynamic Forces and Response Prediction.” Ph.D. Dissertation, Chalmers University of Technology, Göteborg, Sweden.

Ewins, D.J. (2000). *Modal Testing: Theory, Practice and Application*, 2nd Ed, Research Studies Press, Baldock, England.

Falati, S. (1999). “The Contribution of Non-Structural Components to the Overall Dynamic Behaviour of Concrete Floor Slabs.” Ph.D. Dissertation, University of Oxford, Oxford, United Kingdom.

Formenti, D. (1999). “What is the Coherence Function and How Can It Be Used to Find Measurement and Test Setup Problems?” *Sound and Vibration*, December, 2-3.

Formenti, D. (2000). “What Are the Sources of Variations in Frequency Response Function Measurements?” *Sound and Vibration*, January, 2-3.

Griffin, M.J. (1990). *Handbook of Human Vibrations*. Elsevier Press. London, England.

Hanagan, L.M. (2005). “Walking-Induced Floor Vibration Case Studies.” *Journal of Architectural Engineering*, 11(1), 14-18.

Hanagan, L.M, Raebel, C.H., and Trethewey, M.W. (2003). “Dynamic Measurements of In-Place Steel Floors to Assess Vibration Performance.” *Journal of Performance of Constructed Facilities*, ASCE, 17(3), 126-135.

Hanes, R.M. (1970). “Human Sensitivity to Whole-Body Vibration in Urban Transportation Systems: A Literature Review.” Applied Physics Laboratory, The John Hopkins University, Silver Springs, Maryland,

Hicks, S.J., Lawson, R.M., and King, C.M. (2000). “SCI RT803: Design Guide for Vibrations of Long Span Composite Floors.” Steel Construction Institute, Ascot, Great Britain.

Howard, J.N., Kaiser, M.A., and Murray, T.M. (1998). "Designing and Building a Force Plate for Measuring Input Forces in Modal Tests." Manuscript, Virginia Polytechnic Institute and State University, Blacksburg, Virginia.

Hunt, D., and Brillhart, R. (2005). "Smart Sensors, Dumb Engineers – How To Avoid Crossed Signals in Instrumentation." Proceedings of the 23rd International Modal Analysis Conference (IMAC XXIII), Orlando, Florida.

International Standards Organization, (1989). "Evaluation of Human Exposure to Whole-Body Vibration – Part 2: Human Exposure to Continuous and Shock-Induced Vibrations in Buildings (1 to 80 Hz)." International Standard ISO 2631-2.

Kerr, S.C. (1998). "Human Induced Loading on Staircases." Ph.D. Thesis, University of London, London, England.

Khoncarly, M.M.S. (1997). "Dynamic Response of Floor Systems to Footfall-Induced Vibrations." Ph.D. Dissertation, Case Western Reserve University, Cleveland, Ohio.

Kitterman, S.S. (1994). "Investigation of Several Aspects of the Vibration Characteristics of Steel Member-Supported Floors." M.S. Thesis, Virginia Polytechnic Institute and State University, Blacksburg, Virginia.

Lenzen, K.H. (1966). "Vibration of Steel Joist-Concrete Slab Floors." *AISC Engineering Journal*, 3(3), 133-136.

Mayes, R.L, and Gomez, A.J. (2005). "What's Shakin', Dude? Effective Use of Modal Shakers." Proceedings of the 23rd International Modal Analysis Conference (IMAC XXIII), Orlando, Florida.

Murray, T.M. (1975). "Design to Prevent Floor Vibrations." *AISC Engineering Journal*, 12(3), 82-87.

Murray, T.M. (1979). "Acceptability Criterion for Occupant-Induced Floor Vibrations." *Sound and Vibration*, November, 24-30.

Murray, T.M. (1991). "Building Floor Vibrations." *AISC Engineering Journal*, 28(3), 102-109.

Murray, T.M., Allen, D.E., and Ungar, E.E. (1997). "Steel Design Guide Series 11: *Floor Vibrations Due to Human Activity*." American Institute of Steel Construction (AISC), Chicago, Illinois.

Ohmart, R.D. (1968). "An Approximate Method for the Response of Stiffened Plates to Aperiodic Excitation." Studies in Engineering Mechanics, Report No. 30, The University of Kansas, Center for Research in Engineering Science, Lawrence, Kansas.

Pavic, A. and Reynolds, P (1999). "Experimental Assessment of Vibration Serviceability of Existing Office Floors Under Human-Induced Excitation." *Experimental Techniques*, September/October, 41-45.

Pavic, A., Crouch, R.S., and Waldron, P. (1995). "Experimental Validation of FE Models for Modal Analysis of a Full-Scale Prestressed Concrete Floor Structure." Proceedings of The Fifth International Conference on Reliability of Finite Element Methods for Engineering Applications, Amsterdam, The Netherlands, 319-330.

Pavic, A., Reynolds, P., Waldron, P., and Bennett, K. (2001). "Dynamic modeling of post-tensioned concrete floors using finite element analysis." *Finite Element Analysis and Design*, 37, 307-305.

Pernica, G. (1990). "Dynamic Load Factors for Pedestrian Movements and Rhythmic Exercises." *Canadian Acoustics*, 18(2), 3-18.

Pernica, G, and Allen, D.E. (1982). "Floor Vibration Measurements in a Shopping Centre." *Canadian Journal of Civil Engineering*, 9, 149-155.

Perry, J. D. (2003). "A Study of Computer Modeling Techniques to Predict the Response of Floor Systems Due to Walking." M.S. Thesis, Virginia Polytechnic Institute and State University, Blacksburg, Virginia.

Rainer, J.H., and Swallow, J.C. (1986). "Dynamic Behavior of a Gymnasium Floor." *Canadian Journal of Civil Engineering*, 13, 270-277.

Rainer, J.H., Pernica, G., and Allen, D.E. (1988). "Dynamic Loading and Response of Footbridges." *Canadian Journal of Civil Engineering*, 15, 66-71.

Reynolds, P., and Pavic, A. (2000a). "Impulse Hammer versus Shaker Excitation for the Modal Testing of Building Floors." *Experimental Techniques*, May/June, 39-44.

Reynolds, P., and Pavic, A. (2000b). "Quality Assurance Procedures for the Modal Testing of Building Floor Structures." *Experimental Techniques*, July/August, 36-41.

Reynolds, P., Pavic, A., Waldron, P. (1999). "Dynamic FE Modeling of a Multi-Storey Car Park Verified by Modal Testing." Proceedings of The 17th International Modal Analysis Conference (IMAC XVII), Kissimmee, Florida.

Richardson, M. (1997). "Is It a Mode Shape, of an Operating Deflection Shape?" *Sound and Vibration*, March, 1-11.

Ritchey, J. (2003). "Application of Magneto-Rheological Dampers in Tuned Mass Dampers for Floor Vibration Control." M.S. Thesis, Virginia Polytechnic Institute and State University, Blacksburg, Virginia.

- Rottmann, C.E. (1996). "The Use of Tuned Mass Dampers to Control Floor Vibrations." M.S. Thesis, Virginia Polytechnic Institute and State University, Blacksburg, Virginia.
- Salyards, K.A., and Hanagan, L.M. (2005). "Evaluation of a Finite Element Model for Dynamic Characteristic Prediction of a Stadium Facility." Proceedings of The 23rd International Modal Analysis Conference (IMAC XXIII), Kissimmee, Florida.
- Shope, R.L, and Murray, T.M. (1994). "Using Tuned Mass Dampers to Eliminate Annoying Floor Vibrations." Proceedings of Structures Congress XIII, ASCE, Vol I, 339-348.
- Sladki, M.J. (1999). "Prediction of Floor Vibration Response Using the Finite Element Method." M.S. Thesis, Virginia Polytechnic Institute and State University, Blacksburg, Virginia.
- Structural Engineers, Inc. (2004). "*FloorVibe v1.59*." Structural Engineers, Inc., Radford, Virginia.
- Tredgold, T. (1828). "*Elementary Principles of Carpentry*." 2nd Edition, Publisher Unknown.
- Vibrant Technology, Inc. (2003). "*ME'scopeVES Online Help*." Vibrant Technology, Inc., Scotts Valley, California.
- Warmoth, F.J. Jr. (2002). "Floor Vibrations: Girder Effective Moment of Inertia and Cost Study." M.S. Thesis, Virginia Polytechnic Institute and State University, Blacksburg, Virginia.
- Willford, M., Field, C., and Young, P. (2006). "Improved Methodologies for the Prediction of Footfall-Induced Vibration." Proceedings of the 2006 Architectural Engineering National Conference, ASCE, Omaha, Nebraska.
- Young, P. (2001). "Improved Floor Vibration Prediction Methodologies." Proceedings of Arup Vibration Seminar on Engineering for Structural Vibration – Current Developments in Research and Practice, Institution of Mechanical Engineers, London, U.K., 4 Oct 2001.

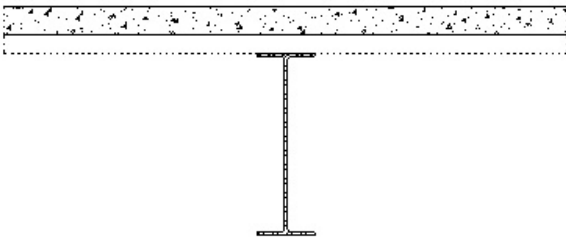
APPENDIX A

IN-SITU FLOOR FRAMING PLANS AND SLAB DETAILS

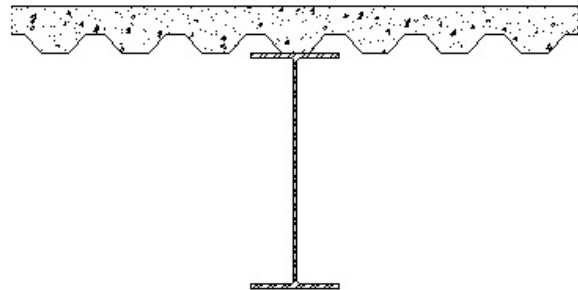
A similar slab section (5.25-in. total depth, 3.25-in. slab on 2-in. LOK-Floor steel deck) was used for both of the tested floor systems, with the only difference in the compressive strength of the concrete. Typical cross sections of the slab/deck system are shown in Figure A.1 and a representative photo of a typical cross section is shown in Figure A.2. All beams for both floors are spaced 10-ft on center. Full floor framing plans for NOC VII (both 18th and 24th floors) is shown Figure A.3 and for VTK2 in Figure A.4.



(a) 5.25" Composite Slab Cross Section



(b) Typical Beam-Slab Cross Section



(c) Typical Girder-Slab Cross Section

Figure A.1: Typical Slab Cross Section Details



Figure A.2: Typical 5.25-in. Slab on 2-in. LOK-Floor Steel Deck

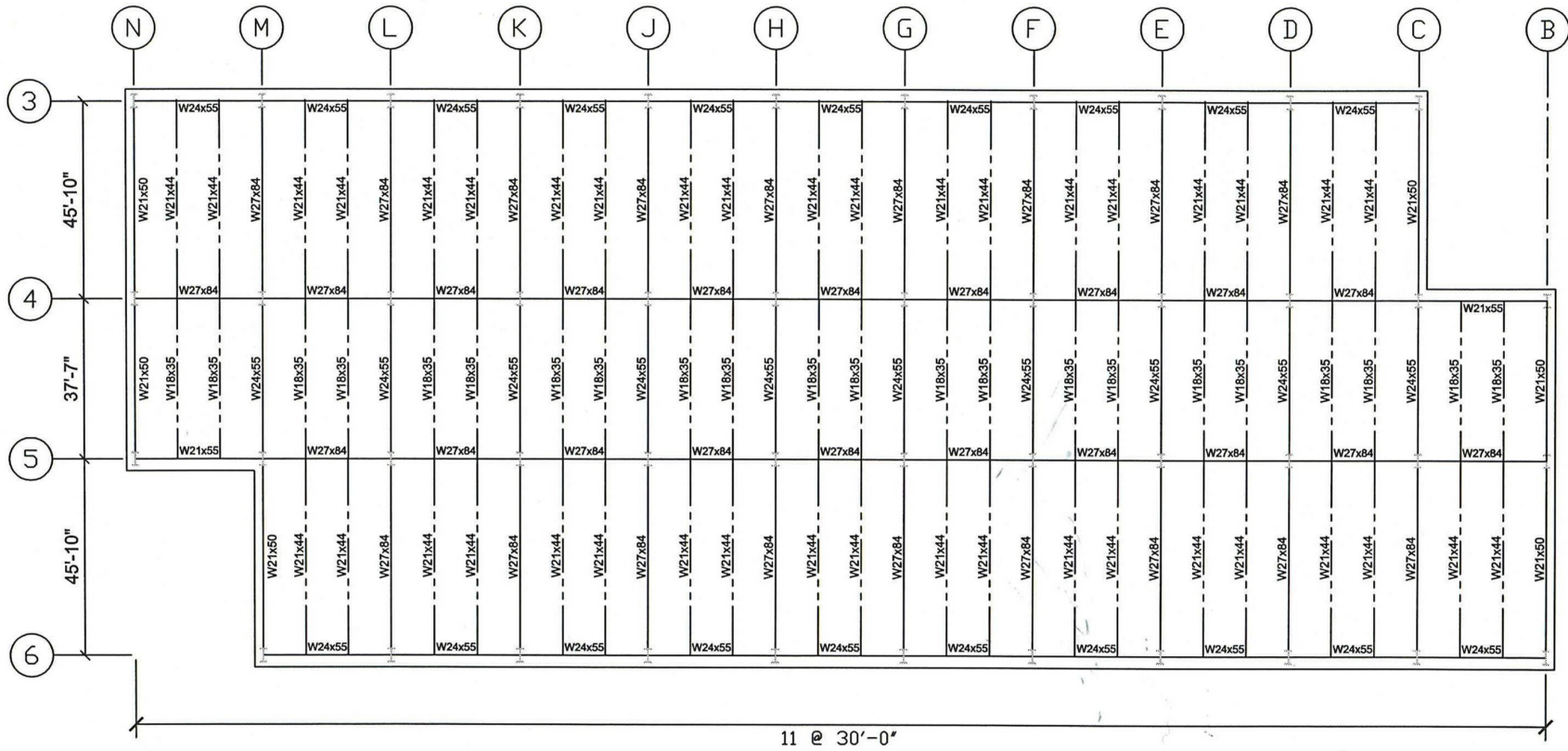


Figure A.3: NOC VII Floor Framing Plan

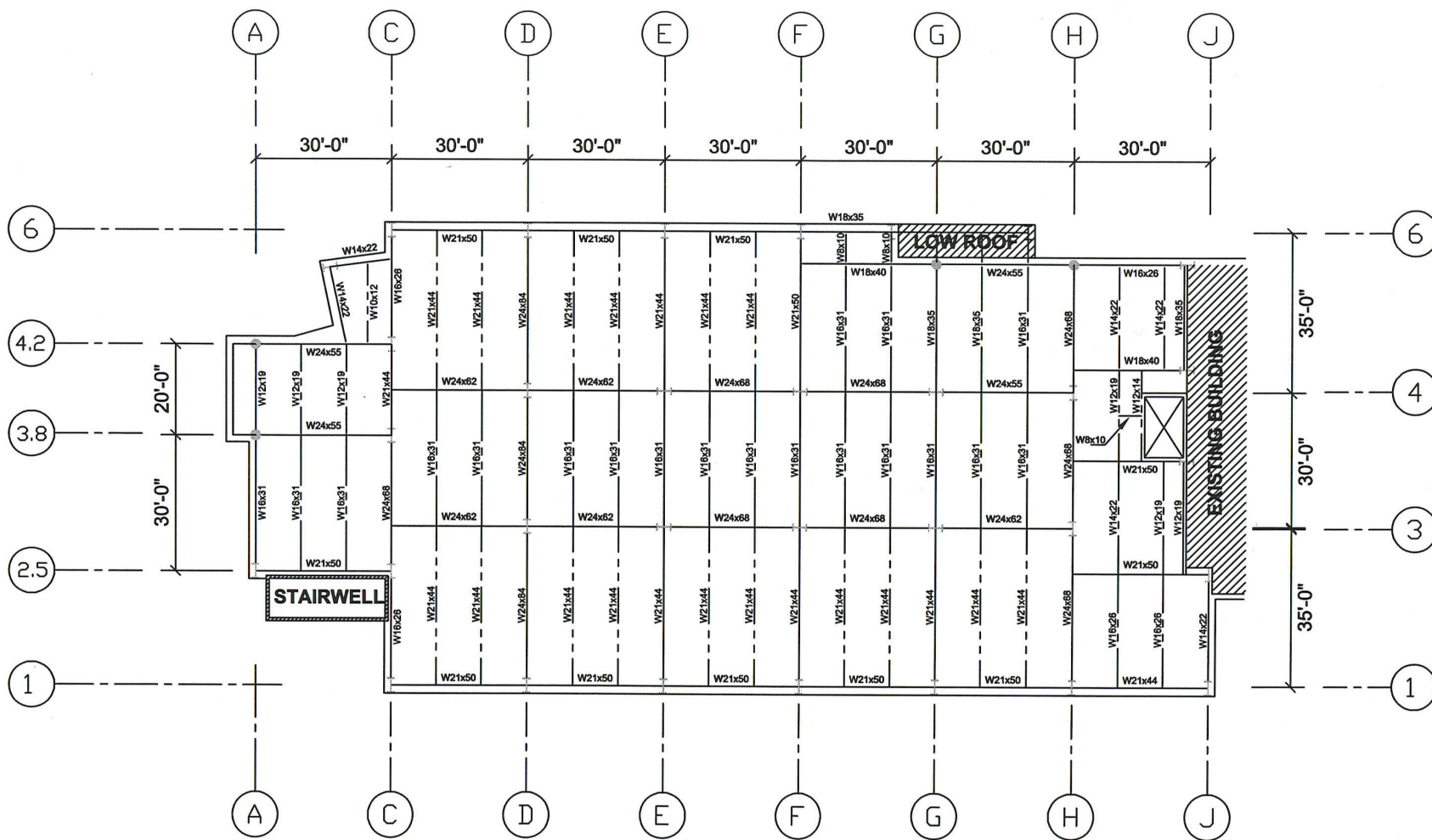


Figure A.4: VTK2 Floor Framing Plan

APPENDIX B

DESIGN GUIDE 11 ANALYSES - FLOORVIBE ANALYSIS REPORTS

The following Appendix includes FloorVibe analysis summaries using the fundamentals of Design Guide 11 for the tested in-situ floors. The DG11 method for predicting the natural frequency of a bay involves a series of calculations to estimate the frequencies of the beam and girder panels and ultimately a combination of these using Dunkerly's relationship previously shown in Equation (1.5). These computations were performed for the tested bays using the DG11 procedures incorporated in the software FloorVibe v1.59 (Structural Engineers, Inc. 2004). Without going into details of the DG11 procedure for computing frequencies, the main parameters used for these computations include the concrete slab thickness, concrete unit weight and specified compressive strength, steel deck height, superimposed loads, beam member, beam spacing, beam span, beam spans of adjacent bays, girder members on either end of the bay (including identifying walls), and girder span. From the input parameters, the procedure computes the uniform load and effective transformed moment of inertia along the beam or girder panel and computes the frequency. In bays with two different girders, the lower of the two computed frequencies are used in combination with the beam frequency in Dunkerly's equation for determining system frequency. If one side of the bay is designated a wall, that side is ignored and the remaining girder frequency is used. If both girders are designated walls, the system is considered one-way and the beam frequency is the system frequency. DG11 does not consider if an exterior beam of a bay is along a wall, if it has moment connections at the columns, or if it has different sized beams within (or on the exterior) of a bay. This is important because many of the tested bays in this research fall in one or more of these categories. In some of the presented analyses, specific bays are analyzed due to unique boundary conditions. For analysis cases that apply to the configurations of multiple bays, only one "general" analysis is presented. In other cases, certain bays are analyzed assuming different conditions at one or both ends of the bay (i.e. one end assumed a wall) and are annotated appropriately. For all of the presented analyses, damping is assumed 1% of critical and no superimposed load. To compare predicted acceleration values with a different level of damping, the results may simply be scaled by the ratio of the 1% divided by the chosen damping ratio.

NOC VII Design Guide 11 Analyses [applicable analysis for corresponding bay]:

- Bay L/M-5/6 (wall) [Point 73, 65]
- Bay L/M-5/6 (no wall) [Point 73, 65]
- General Exterior Bay with Exterior Wall [Points 21, 117, 125, 177, 216, 281, 333]
- General Exterior Bay with Interior Wall [Points 21, 117, 125, 177, 216, 281, 333]
- General Exterior Bay with No Walls [Points 21, 117, 125, 177, 216, 281, 333]
- Bay M/N-4/5 (wall) [Point 69]
- Bay M/N-4/5 (no wall) [Point 69]
- Bay L/M-4/5 [Point 25]

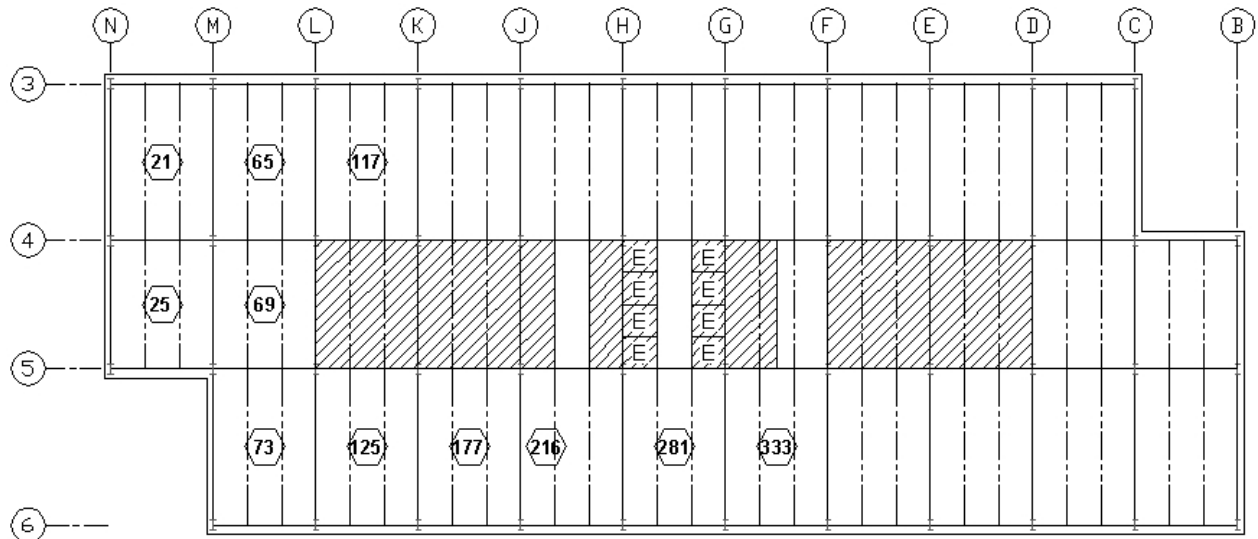


Figure B.1: NOC VII Excitation Locations (Tested Floors #1 and #2)

FloorVibe V1.59, (C)2004 by Structural Engineers, Inc.
 www.floorvibe.com
 This copy is licensed to: Anthony Barrett, Christiansburg, VA

SHEET OF
 DATE: 6/10/2001
 PAGE: 1 BY: AJ

Project ID: NOC VII, Jersey City, NJ
 Project # : DG11 Analysis
 Bay ID : L/M-5/6 (wall)

VIBRATION ANALYSIS:

Activity: Walking
 Occupancy Category: Paper Office
 Evaluation Criterion: Walking, AISC Design Guide #11, Chapter 4
 Reference: Murray, T.M., Allen, D.E. and Ungar, E.E,
 "Floor Vibrations Due To Human Activity",
 AISC Design Guide #11, June 1997

Constant Force, $P_o = 65.1b$
 Modal Damping Ratio, $\beta = 0.010$
 Acceleration Limit, $a_o/g \times 100\% = 0.50\%$
 Beams are continuous
 Girders are not continuous at columns

Evaluation: Combined mode $a_p/g = 1.25\% > 0.50\%$
 The system DOES NOT SATISFY THE CRITERION.

PARAMETER SUMMARY:

Parameter	Beam Panel	Left Girder Panel	Right Girder Panel	System
Member	W21X44	W27X84	Wall	
Uniform Load, plf	471.3	2048.6	0.0	
Effective I, in ⁴	2850.1	7894.5	0.0	
Frequency, Hz	4.70	9.91	0.00	4.25
Panel Width, ft	38.44	59.81	0.00	
Panel Weight, k	124.5	88.2	0.0	117.9

FRAMING:

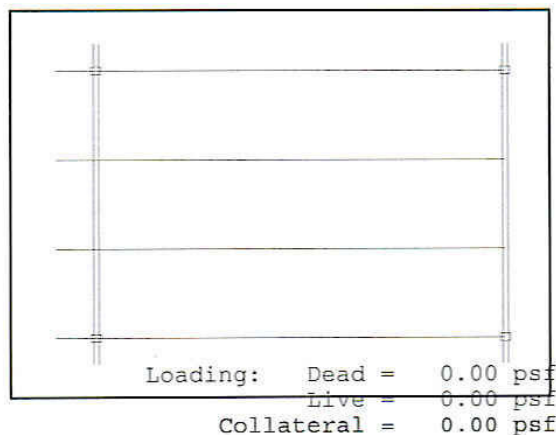
Girder Span = 30.00 ft
 Beam Spans:
 Left = 37.54 ft
 Center = 45.83 ft
 Right = 0.00 ft

Girders/Walls:
 Left -W27X84
 Right-Wall

Beam -W21X44
 3 spaces at 120.00 in

Floor Width =300.00 ft
 Floor Length=129.20 ft

Concrete: dc = 5.25 in
 f'c = 4.00 ksi
 wt. = 115.0 pcf
 Deck Height = 2.00 in



FloorVibe V1.59, (C)2004 by Structural Engineers, Inc.
 www.floorvibe.com
 This copy is licensed to: Anthony Barrett, Christiansburg, VA

SHEET OF
 DATE: 6/10/2006
 PAGE: 1 BY: ARB

Project ID: NOC VII, Jersey City, NJ
 Project # : DG11 Analysis
 Bay ID : L/M-5/6 (no wall)

VIBRATION ANALYSIS:

Activity: Walking
 Occupancy Category: Paper Office
 Evaluation Criterion: Walking, AISC Design Guide #11, Chapter 4
 Reference: Murray, T.M., Allen, D.E. and Ungar, E.E.,
 "Floor Vibrations Due To Human Activity",
 AISC Design Guide #11, June 1997

Constant Force, $P_o = 65. \text{ lb}$
 Modal Damping Ratio, $\beta = 0.010$
 Acceleration Limit, $a_o/g \times 100\% = 0.50 \%$
 Beams are continuous
 Girders are not continuous at columns

Evaluation: Combined mode $a_p/g = 1.27 \%$ > 0.50%
 The system DOES NOT SATISFY THE CRITERION.

PARAMETER SUMMARY:

Parameter	Beam Panel	Left Girder Panel	Right Girder Panel	System
Member	W21X44	W27X84	W24X55	
Uniform Load, plf	471.3	2048.6	1135.0	
Effective I, in ⁴	2850.1	7894.5	3871.3	
Frequency, Hz	4.70	9.91	9.33	4.20
Panel Width, ft	38.44	59.81	61.54	
Panel Weight, k	124.5	88.2	91.4	117.8

FRAMING:

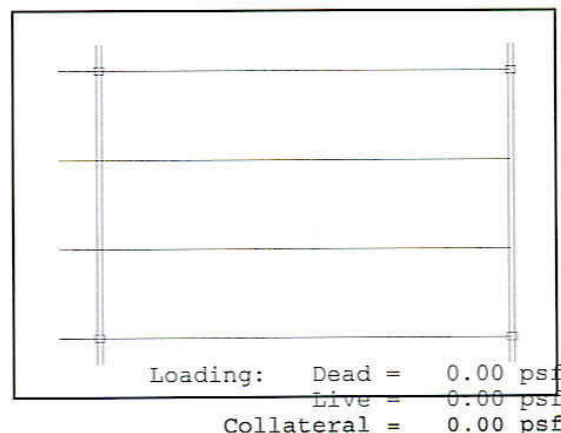
Girder Span = 30.00 ft
 Beam Spans:
 Left = 37.54 ft
 Center = 45.83 ft
 Right = 0.00 ft

Girders/Walls:
 Left -W27X84
 Right-W24X55

Beam -W21X44
 3 spaces at 120.00 in

Floor Width =300.00 ft
 Floor Length=129.20 ft

Concrete: dc = 5.25 in
 f'c = 4.00 ksi
 wt. = 115.0 pcf
 Deck Height = 2.00 in



FloorVibe V1.59, (C)2004 by Structural Engineers, Inc.
 www.floorvibe.com
 This copy is licensed to: Anthony Barrett, Christiansburg, VA

SHEET OF
 DATE: 6/10/2006
 PAGE: 1 BY: ARB

Project ID: NOC VII, Jersey City, NJ
 Project # : DG11 Analysis
 Bay ID : General Exterior Bay with Exterior Wall

VIBRATION ANALYSIS:

Activity: Walking
 Occupancy Category: Paper Office
 Evaluation Criterion: Walking, AISC Design Guide #11, Chapter 4
 Reference: Murray, T.M., Allen, D.E. and Ungar, E.E,
 "Floor Vibrations Due To Human Activity",
 AISC Design Guide #11, June 1997

Constant Force, $P_o = 65.1b$
 Modal Damping Ratio, $\beta = 0.010$
 Acceleration Limit, $a_o/g \times 100\% = 0.50 \%$
 Beams are continuous
 Girders are not continuous at columns

Evaluation: Combined mode $a_p/g = 1.34 \%$ > 0.50%
 The system DOES NOT SATISFY THE CRITERION.

PARAMETER SUMMARY:

Parameter	Beam Panel	Left Girder Panel	Right Girder Panel	System
Member	W21X44	W27X84	Wall	
Uniform Load, plf	471.3	2048.6	0.0	
Effective I, in ⁴	2850.1	7894.5	0.0	
Frequency, Hz	4.70	9.91	0.00	4.25
Panel Width, ft	38.44	30.55	0.00	
Panel Weight, k	124.5	45.0	0.0	109.9

FRAMING:

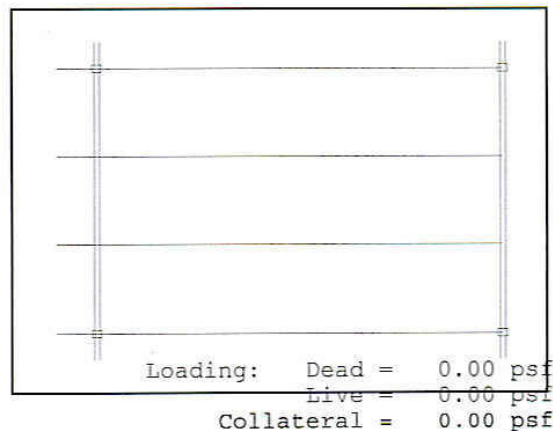
Girder Span = 30.00 ft
 Beam Spans:
 Left = 37.54 ft
 Center = 45.83 ft
 Right = 0.00 ft

Girders/Walls:
 Left -W27X84
 Right-Wall

Beam -W21X44
 3 spaces at 120.00 in

Floor Width =300.00 ft
 Floor Length= 45.83 ft

Concrete: dc = 5.25 in
 $f'_c = 4.00$ ksi
 wt. = 115.0 pcf
 Deck Height = 2.00 in



FloorVibe V1.59, (C)2004 by Structural Engineers, Inc.
 www.floorvibe.com
 This copy is licensed to: Anthony Barrett, Christiansburg, VA

SHEET OF
 DATE: 6/10/2006
 PAGE: 1 BY: ARB

Project ID: NOC VII, Jersey City, NJ
 Project # : DG11 Analysis
 Bay ID : General Exterior Bay with Interior Wall

VIBRATION ANALYSIS:

Activity: Walking
 Occupancy Category: Paper Office
 Evaluation Criterion: Walking, AISC Design Guide #11, Chapter 4
 Reference: Murray, T.M., Allen, D.E. and Ungar, E.E,
 "Floor Vibrations Due To Human Activity",
 AISC Design Guide #11, June 1997

Constant Force, $P_o = 65.1b$
 Modal Damping Ratio, $\beta = 0.010$
 Acceleration Limit, $a_o/g \times 100\% = 0.50\%$
 Beams are not continuous
 Girders are not continuous at columns

Evaluation: Combined mode $a_p/g = 2.08\% > 0.50\%$
 The system DOES NOT SATISFY THE CRITERION.

PARAMETER SUMMARY:

Parameter	Beam Panel	Left Girder Panel	Right Girder Panel	System
Member	W21X44	Wall	W21X55	
Uniform Load, plf	471.3	0.0	1135.0	
Effective I, in ⁴	2850.1	0.0	3203.1	
Frequency, Hz	4.70	0.00	8.48	4.11
Panel Width, ft	38.44	0.00	30.55	
Panel Weight, k	83.0	0.0	45.4	74.2

FRAMING:

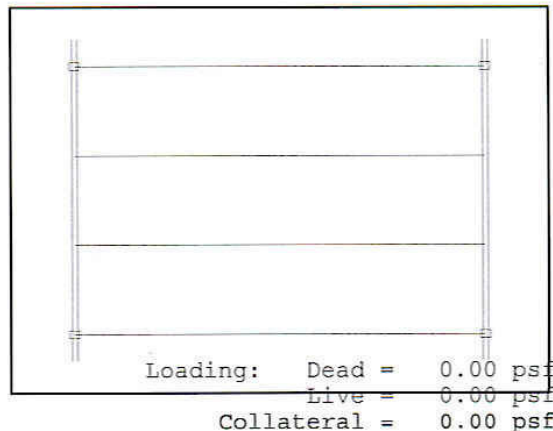
Girder Span = 30.00 ft
 Beam Spans:
 Left = 0.00 ft
 Center = 45.83 ft
 Right = 0.00 ft

Girders/Walls:
 Left -Wall
 Right-W21X55

Beam -W21X44
 3 spaces at 120.00 in

Floor Width =300.00 ft
 Floor Length= 45.83 ft

Concrete: dc = 5.25 in
 $f'_c = 4.00$ ksi
 wt. = 115.0 pcf
 Deck Height = 2.00 in



FloorVibe V1.59, (C)2004 by Structural Engineers, Inc.
www.floorvibe.com
This copy is licensed to: Anthony Barrett, Christiansburg, VA

SHEET OF
DATE: 6/10/2006
PAGE: 1 BY: ARB

Project ID: NOC VII, Jersey City, NJ
Project # : DG11 Analysis
Bay ID : General Exterior Bay with No Walls

VIBRATION ANALYSIS:

Activity: Walking
Occupancy Category: Paper Office
Evaluation Criterion: Walking, AISC Design Guide #11, Chapter 4
Reference: Murray, T.M., Allen, D.E. and Ungar, E.E,
"Floor Vibrations Due To Human Activity",
AISC Design Guide #11, June 1997

Constant Force, $P_o = 65.1b$
Modal Damping Ratio, $\beta = 0.010$
Acceleration Limit, $a_o/g \times 100\% = 0.50\%$
Beams are continuous
Girders are not continuous at columns

Evaluation: Combined mode $a_p/g = 1.46\% > 0.50\%$
The system DOES NOT SATISFY THE CRITERION.

PARAMETER SUMMARY:

Parameter	Beam Panel	Left Girder Panel	Right Girder Panel	System
Member	W21X44	W27X84	W21X55	
Uniform Load, plf	471.3	2048.6	1135.0	
Effective I, in ⁴	2850.1	7894.5	3203.1	
Frequency, Hz	4.70	9.91	8.48	4.11
Panel Width, ft	38.44	30.55	30.55	
Panel Weight, k	124.5	45.0	45.4	105.9

FRAMING:

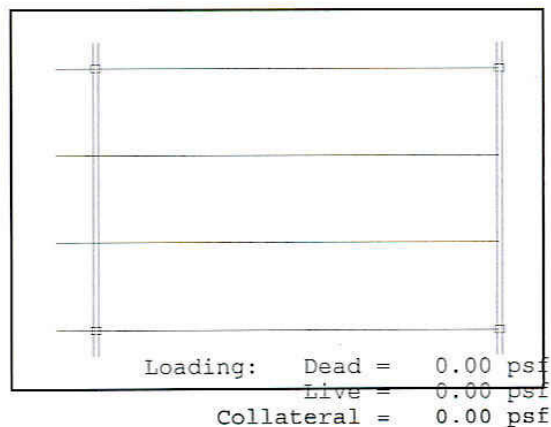
Girder Span = 30.00 ft
Beam Spans:
Left = 37.54 ft
Center = 45.83 ft
Right = 0.00 ft

Girders/Walls:
Left -W27X84
Right-W21X55

Beam -W21X44
3 spaces at 120.00 in

Floor Width =300.00 ft
Floor Length= 45.83 ft

Concrete: dc = 5.25 in
 f'_c = 4.00 ksi
wt. = 115.0 pcf
Deck Height = 2.00 in



FloorVibe V1.59, (C)2004 by Structural Engineers, Inc.
www.floorvibe.com
This copy is licensed to: Anthony Barrett, Christiansburg, VA

SHEET OF
DATE: 6/10/2006
PAGE: 1 BY: ARB

Project ID: NOC VII, Jersey City, NJ
Project # : DG11 Analysis
Bay ID : M/N-4/5 (wall)

VIBRATION ANALYSIS:

Activity: Walking
Occupancy Category: Paper Office
Evaluation Criterion: Walking, AISC Design Guide #11, Chapter 4
Reference: Murray, T.M., Allen, D.E. and Ungar, E.E.,
"Floor Vibrations Due To Human Activity",
AISC Design Guide #11, June 1997

Constant Force, $P_o = 65.1b$
Modal Damping Ratio, $\beta = 0.010$
Acceleration Limit, $a_o/g \times 100\% = 0.50\%$
Beams are continuous
Girders are not continuous at columns

Evaluation: Combined mode $a_p/g = 1.33\% > 0.50\%$
The system DOES NOT SATISFY THE CRITERION.

PARAMETER SUMMARY:

Parameter	Beam Panel	Left Girder Panel	Right Girder Panel	System
Member	W18X35	W27X84	Wall	
Uniform Load, plf	462.3	2011.1	0.0	
Effective I, in ⁴	1852.6	7894.5	0.0	
Frequency, Hz	5.70	9.56	0.00	4.90
Panel Width, ft	35.06	53.70	0.00	
Panel Weight, k	91.3	77.7	0.0	87.7

FRAMING:

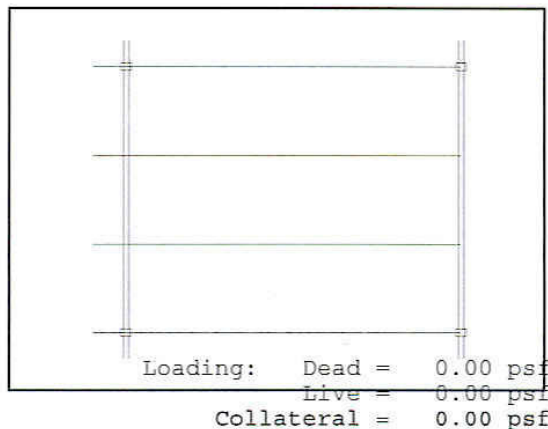
Girder Span = 30.00 ft
Beam Spans:
Left = 45.83 ft
Center = 37.54 ft
Right = 0.00 ft

Girders/Walls:
Left -W27X84
Right-Wall

Beam -W18X35
3 spaces at 120.00 in

Floor Width = 60.00 ft
Floor Length= 83.37 ft

Concrete: dc = 5.25 in
f'c = 4.00 ksi
wt. = 115.0 pcf
Deck Height = 2.00 in



FloorVibe V1.59, (C)2004 by Structural Engineers, Inc.
www.floorvibe.com
This copy is licensed to: Anthony Barrett, Christiansburg, VA

SHEET OF
DATE: 6/10/2006
PAGE: 1 BY: ARB

Project ID: NOC VII, Jersey City, NJ
Project # : DG11 Analysis
Bay ID : M/N-4/5 (no wall)

VIBRATION ANALYSIS:

Activity: Walking
Occupancy Category: Paper Office
Evaluation Criterion: Walking, AISC Design Guide #11, Chapter 4
Reference: Murray, T.M., Allen, D.E. and Ungar, E.E,
"Floor Vibrations Due To Human Activity",
AISC Design Guide #11, June 1997

Constant Force, $P_o = 65.1b$
Modal Damping Ratio, $\beta = 0.010$
Acceleration Limit, $a_o/g \times 100\% = 0.50 \%$
Beams are continuous
Girders are not continuous at columns

Evaluation: Combined mode $a_p/g = 1.36 \%$ > 0.50%
The system DOES NOT SATISFY THE CRITERION.

PARAMETER SUMMARY:

Parameter	Beam Panel	Left Girder Panel	Right Girder Panel	System
Member	W18X35	W27X84	W21X55	
Uniform Load, plf	462.3	2011.1	922.7	
Effective I, in ⁴	1852.6	7894.5	3203.1	
Frequency, Hz	5.70	9.56	8.99	4.82
Panel Width, ft	35.06	53.70	55.12	
Panel Weight, k	91.3	77.7	81.3	88.4

FRAMING:

Girder Span = 30.00 ft
Beam Spans:
Left = 45.83 ft
Center = 37.54 ft
Right = 0.00 ft

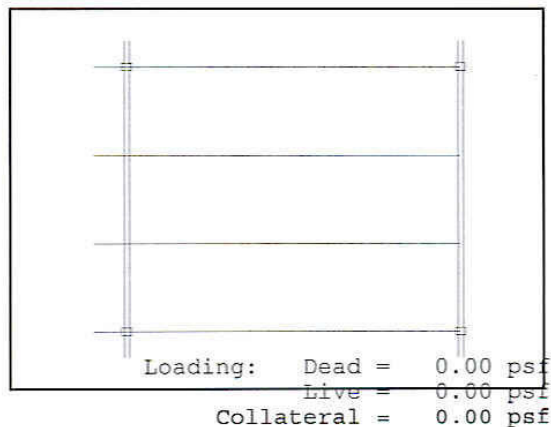
Girders/Walls:

Left -W27X84
Right-W21X55

Beam -W18X35
3 spaces at 120.00 in

Floor Width = 60.00 ft
Floor Length= 83.37 ft

Concrete: dc = 5.25 in
f'c = 4.00 ksi
wt. = 115.0 pcf
Deck Height = 2.00 in



FloorVibe V1.59, (C)2004 by Structural Engineers, Inc.
www.floorvibe.com
This copy is licensed to: Anthony Barrett, Christiansburg, VA

SHEET OF
DATE: 6/10/2006
PAGE: 1 BY: ARB

Project ID: NOC VII, Jersey City, NJ
Project # : DG11 Analysis
Bay ID : L/M-4/5

VIBRATION ANALYSIS:

Activity: Walking
Occupancy Category: Paper Office
Evaluation Criterion: Walking, AISC Design Guide #11, Chapter 4
Reference: Murray, T.M., Allen, D.E. and Ungar, E.E,
"Floor Vibrations Due To Human Activity",
AISC Design Guide #11, June 1997

Constant Force, $P_o = 65. \text{ lb}$
Modal Damping Ratio, $\beta = 0.010$
Acceleration Limit, $a_o/g \times 100\% = 0.50 \%$
Beams are continuous
Girders are not continuous at columns

Evaluation: Combined mode $a_p/g = 1.33 \%$ > 0.50%
The system DOES NOT SATISFY THE CRITERION.

PARAMETER SUMMARY:

Parameter	Beam Panel	Left Girder Panel	Right Girder Panel	System
Member	W18X35	W27X84	W27X84	
Uniform Load, plf	462.3	2011.1	2011.1	
Effective I, in ⁴	1852.6	7894.5	7894.5	
Frequency, Hz	5.70	9.56	9.56	4.90
Panel Width, ft	35.06	53.70	53.70	
Panel Weight, k	91.3	77.7	77.7	87.7

FRAMING:

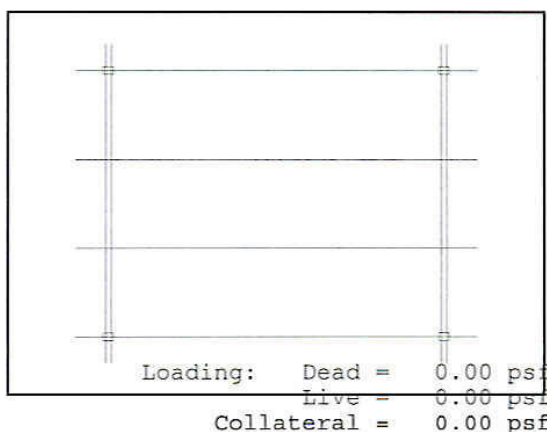
Girder Span = 30.00 ft
Beam Spans:
Left = 45.83 ft
Center = 37.54 ft
Right = 45.83 ft

Girders/Walls:
Left -W27X84
Right -W27X84

Beam -W18X35
3 spaces at 120.00 in

Floor Width = 60.00 ft
Floor Length=129.20 ft

Concrete: dc = 5.25 in
 $f'_c = 4.00 \text{ ksi}$
wt. = 115.0 pcf
Deck Height = 2.00 in



VTK2 Design Guide 11 Analyses [applicable analysis for corresponding bay]:

- General Exterior Bay (no wall) [Points 74, 82, 126, 134, 178, 186]
- General Interior Bay [Points 78, 130, 182]
- Bay A/C-2.5/3.8 [Point 25]
- Bay A/C-3.8/4.2 [Point 21]
- Bay F/G-4/6 [Point 230]

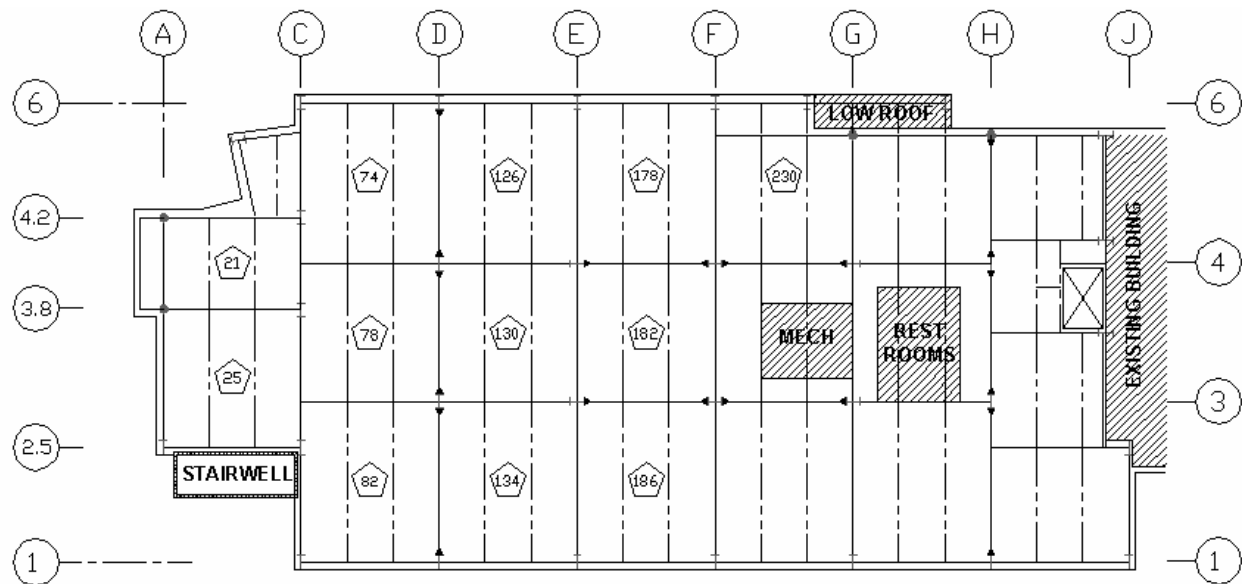


Figure B.2: VTK2 Excitation Locations (Tested Floor #3)

FloorVibe V1.59, (C)2004 by Structural Engineers, Inc.
 www.floorvibe.com
 This copy is licensed to: Anthony Barrett, Christiansburg, VA

SHEET OF
 DATE: 6/10/2006
 PAGE: 1 BY: ARB

Project ID: VT KnowledgeWorks2, Blacksburg, VA
 Project # : DG11 Analysis
 Bay ID : General Exterior Bay (no wall)

VIBRATION ANALYSIS:

Activity: Walking
 Occupancy Category: Electronic Office
 Evaluation Criterion: Walking, AISC Design Guide #11, Chapter 4
 Reference: Murray, T.M., Allen, D.E. and Ungar, E.E.,
 "Floor Vibrations Due To Human Activity",
 AISC Design Guide #11, June 1997

Constant Force, $P_o = 65. \text{ lb}$
 Modal Damping Ratio, $\beta = 0.010$
 Acceleration Limit, $a_o/g \times 100\% = 0.50 \%$
 Beams are continuous
 Girders are not continuous at columns

Evaluation: Combined mode $a_p/g = 1.14 \%$ > 0.50%
 The system DOES NOT SATISFY THE CRITERION.

PARAMETER SUMMARY:

Parameter	Beam Panel	Left Girder Panel	Right Girder Panel	System
Member	W21X44	W24X62	W21X50	
Uniform Load, plf	471.3	1593.7	874.8	
Effective I, in ⁴	2778.6	4786.8	2826.3	
Frequency, Hz	7.96	7.73	8.02	5.55
Panel Width, ft	28.50	63.29	61.85	
Panel Weight, k	70.5	93.1	92.7	82.1

FRAMING:

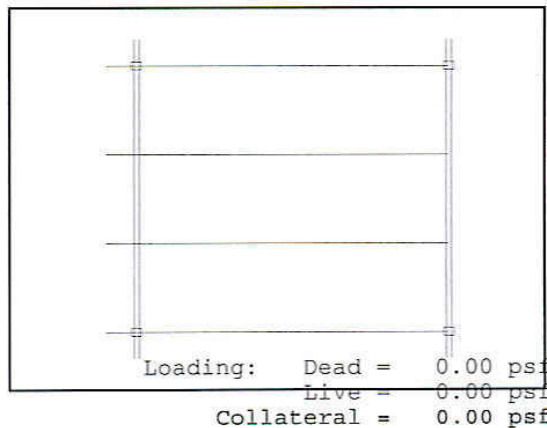
Girder Span = 30.00 ft
 Beam Spans:
 Left = 30.00 ft
 Center = 35.00 ft
 Right = 0.00 ft

Girders/Walls:
 Left -W24X62
 Right-W21X50

Beam -W21X44
 3 spaces at 120.00 in

Floor Width = 90.00 ft
 Floor Length=100.00 ft

Concrete: dc = 5.25 in
 f'c = 3.00 ksi
 wt. = 115.0 pcf
 Deck Height = 2.00 in



Project ID: VT KnowledgeWorks2, Blacksburg, VA
Project # : DG11 Analysis
Bay ID : General Interior Bay

VIBRATION ANALYSIS:

Activity: Walking
Occupancy Category: Electronic Office
Evaluation Criterion: Walking, AISC Design Guide #11, Chapter 4
Reference: Murray, T.M., Allen, D.E. and Ungar, E.E,
"Floor Vibrations Due To Human Activity",
AISC Design Guide #11, June 1997

Constant Force, $P_o = 65. \text{ lb}$
Modal Damping Ratio, $\beta = 0.010$
Acceleration Limit, $a_o/g \times 100\% = 0.50 \%$
Beams are continuous
Girders are not continuous at columns

Evaluation: Combined mode $a_p/g = 1.38 \%$ > 0.50%
The system DOES NOT SATISFY THE CRITERION.

PARAMETER SUMMARY:

Parameter	Beam Panel	Left Girder Panel	Right Girder Panel	System
Member	W16X31	W24X62	W24X62	
Uniform Load, plf	458.3	1551.4	1551.4	
Effective I, in ⁴	1399.3	4786.8	4786.8	
Frequency, Hz	7.79	7.84	7.84	5.53
Panel Width, ft	29.00	53.31	53.31	
Panel Weight, k	59.8	76.3	76.3	68.0

FRAMING:

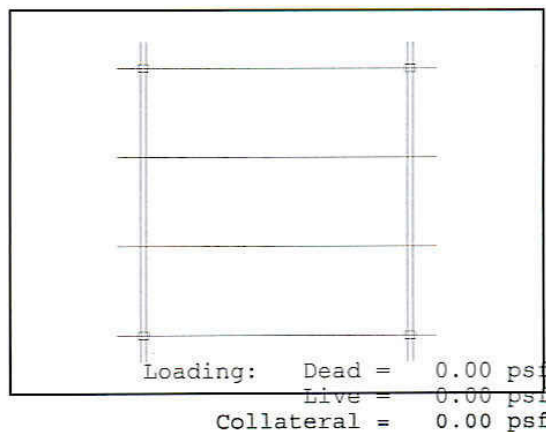
Girder Span = 30.00 ft
Beam Spans:
Left = 35.00 ft
Center = 30.00 ft
Right = 35.00 ft

Girders/Walls:
Left -W24X62
Right -W24X62

Beam -W16X31
3 spaces at 120.00 in

Floor Width = 90.00 ft
Floor Length=100.00 ft

Concrete: dc = 5.25 in
 $f'_c = 3.00 \text{ ksi}$
wt. = 115.0 pcf
Deck Height = 2.00 in



FloorVibe V1.59, (C)2004 by Structural Engineers, Inc.
 www.floorvibe.com
 This copy is licensed to: Anthony Barrett, Christiansburg, VA

SHEET OF
 DATE: 6/10/2006
 PAGE: 1 BY: ARB

Project ID: VT KnowledgeWorks2, Blacksburg, VA
 Project # : DG11 Analysis
 Bay ID : Bay A/C-2.5/3.8

VIBRATION ANALYSIS:

Activity: Walking
 Occupancy Category: Electronic Office
 Evaluation Criterion: Walking, AISC Design Guide #11, Chapter 4
 Reference: Murray, T.M., Allen, D.E. and Ungar, E.E,
 "Floor Vibrations Due To Human Activity",
 AISC Design Guide #11, June 1997

Constant Force, $P_o = 65. \text{ lb}$
 Modal Damping Ratio, $\beta = 0.010$
 Acceleration Limit, $a_o/g \times 100\% = 0.50 \%$
 Beams are not continuous
 Girders are not continuous at columns
 Mezzanine with beam and left girder parallel to open side.

Evaluation: Combined mode $a_p/g = 3.51 \%$ > 0.50%
 The system DOES NOT SATISFY THE CRITERION.

PARAMETER SUMMARY:

Parameter	Beam Panel	Left Girder Panel	Right Girder Panel	System
Member	W16X31	W21X50		
Uniform Load, plf	458.3	737.4		
Effective I, in ⁴	1399.3	2826.3		
Frequency, Hz	7.79	8.73		5.82
Panel Width, ft	14.50	20.00		
Panel Weight, k	19.9	29.5		24.2

FRAMING:

Girder Span = 30.00 ft
 Beam Spans:
 Left = 0.00 ft
 Center = 30.00 ft
 Right = 20.00 ft

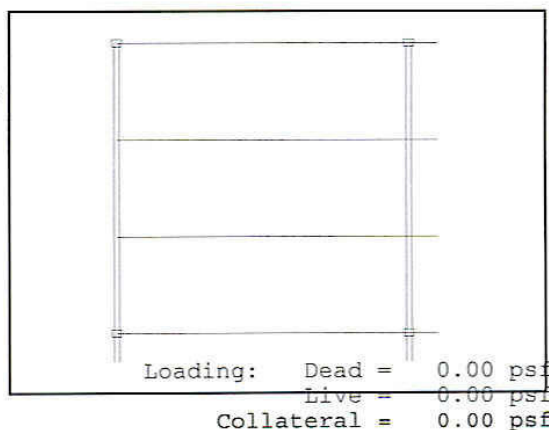
Free Edge

Girders/Walls:
 Left -W21X50
 Right -W24X55

Beam -W16X31
 3 spaces at 120.00 in

Floor Width = 60.00 ft
 Floor Length = 50.00 ft

Concrete: dc = 5.25 in
 f'c = 3.00 ksi
 wt. = 115.0 pcf
 Deck Height = 2.00 in



FloorVibe V1.59, (C)2004 by Structural Engineers, Inc.
www.floorvibe.com
This copy is licensed to: Anthony Barrett, Christiansburg, VA

SHEET OF
DATE: 6/10/2006
PAGE: 1 BY: ARB

Project ID: VT KnowledgeWorks2, Blacksburg, VA
Project # : DG11 Analysis
Bay ID : Bay A/C-3.8/4.2

VIBRATION ANALYSIS:

Activity: Walking
Occupancy Category: Electronic Office
Evaluation Criterion: Walking, AISC Design Guide #11, Chapter 4
Reference: Murray, T.M., Allen, D.E. and Ungar, E.E,
"Floor Vibrations Due To Human Activity",
AISC Design Guide #11, June 1997

Constant Force, $P_o = 65.1b$
Modal Damping Ratio, $\beta = 0.010$
Acceleration Limit, $a_o/g \times 100\% = 0.50\%$
Beams are continuous
Girders are not continuous at columns

Evaluation: Combined mode $a_p/g = 1.40\% > 0.50\%$
The system DOES NOT SATISFY THE CRITERION.

PARAMETER SUMMARY:

Parameter	Beam Panel	Left Girder Panel	Right Girder Panel	System
Member	W12X19	W24X55	W24X55	
Uniform Load, plf	446.3	1170.7	501.3	
Effective I, in ⁴	603.9	4300.0	3747.8	
Frequency, Hz	11.68	8.55	12.20	6.90
Panel Width, ft	23.85	33.33	33.33	
Panel Weight, k	31.9	46.8	50.1	41.6

FRAMING:

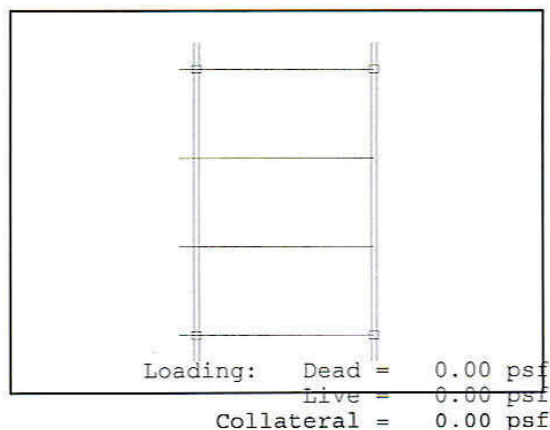
Girder Span = 30.00 ft
Beam Spans:
Left = 30.00 ft
Center = 20.00 ft
Right = 0.00 ft

Girders/Walls:
Left -W24X55
Right -W24X55

Beam -W12X19
3 spaces at 120.00 in

Floor Width = 60.00 ft
Floor Length= 50.00 ft

Concrete: dc = 5.25 in
f'c = 3.00 ksi
wt. = 115.0 pcf
Deck Height = 2.00 in



FloorVibe V1.59, (C)2004 by Structural Engineers, Inc.
www.floorvibe.com
This copy is licensed to: Anthony Barrett, Christiansburg, VA

SHEET OF
DATE: 6/10/2006
PAGE: 1 BY: ARB

Project ID: VT KnowledgeWorks2, Blacksburg, VA
Project # : DG11 Analysis
Bay ID : Bay F/G-4/6

VIBRATION ANALYSIS:

Activity: Walking
Occupancy Category: Electronic Office
Evaluation Criterion: Walking, AISC Design Guide #11, Chapter 4
Reference: Murray, T.M., Allen, D.E. and Ungar, E.E,
"Floor Vibrations Due To Human Activity",
AISC Design Guide #11, June 1997

Constant Force, $P_o = 65.1b$
Modal Damping Ratio, $\beta = 0.010$
Acceleration Limit, $a_o/g \times 100\% = 0.50 \%$
Beams are continuous
Girders are not continuous at columns

Evaluation: Combined mode $a_p/g = 2.17 \%$ > 0.50%
The system DOES NOT SATISFY THE CRITERION.

PARAMETER SUMMARY:

Parameter	Beam Panel	Left Girder Panel	Right Girder Panel	System
Member	W16X31	W24X68	W18X40	
Uniform Load, plf	458.3	1397.0	842.0	
Effective I, in ⁴	1399.3	5286.5	2063.1	
Frequency, Hz	8.95	8.68	6.98	5.51
Panel Width, ft	27.06	26.67	26.67	
Panel Weight, k	52.1	38.5	38.5	43.6

FRAMING:

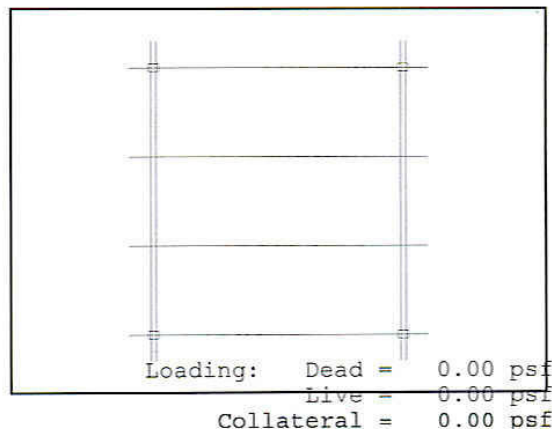
Girder Span = 30.00 ft
Beam Spans:
Left = 30.00 ft
Center = 28.00 ft
Right = 7.00 ft

Girders/Walls:
Left -W24X68
Right-W18X40

Beam -W16X31
3 spaces at 120.00 in

Floor Width =150.00 ft
Floor Length= 40.00 ft

Concrete: $d_c = 5.25$ in
 $f'_c = 3.00$ ksi
 $wt. = 115.0$ pcf
Deck Height = 2.00 in



APPENDIX C

SINGLE-CHANNEL HANDHELD ANALYZER MEASUREMENTS – NOC VII-24

The 24th floor of the NOC VII building (NOC VII-24) was investigated by Dr. Thomas M. Murray in March 2004 using a single-channel Ono Sokki CF-1200 Handheld FFT Analyzer. A variety of unreferenced measurements were taken in that investigation, including heel drops, walking parallel and perpendicular to the joists, bouncing, and decay-from-bouncing. Four select heel drop measurements are presented in this Appendix to correspond to the three testing locations on NOC VII-24 using the electrodynamic shaker. Only heel drop measurements are presented because the measured autospectra provide the best comparison to the high quality modal measurements presented in Section 3.2.3. Figure C.1 shows the location of the three points of excitation, Points 73, 69, and 25. Two heel drop measurements are presented for Point 73, a strong heel drop and a weak heel drop.

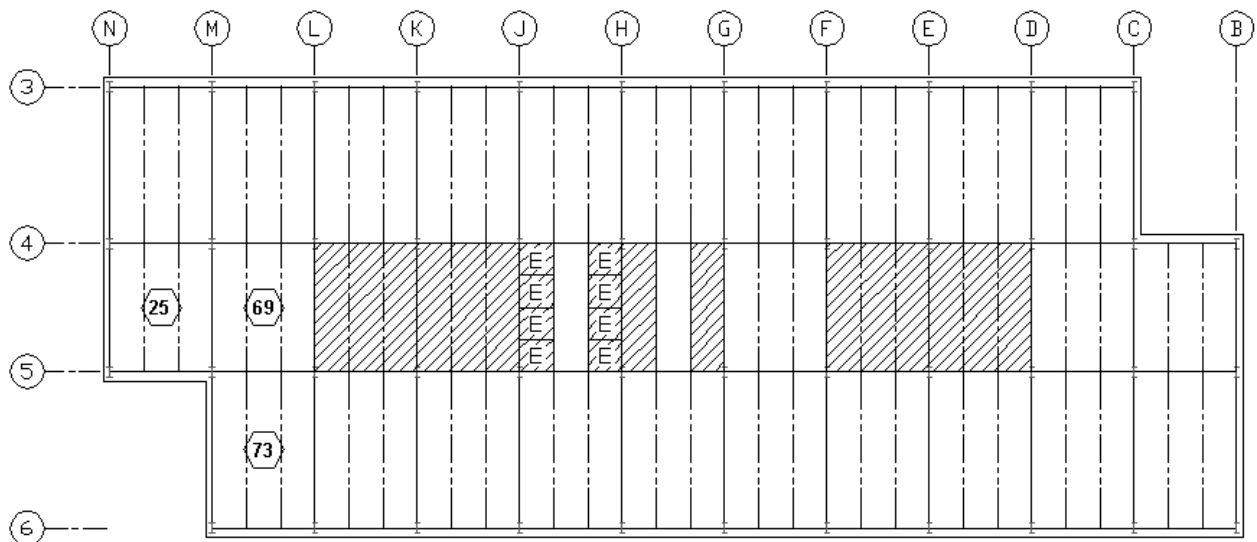
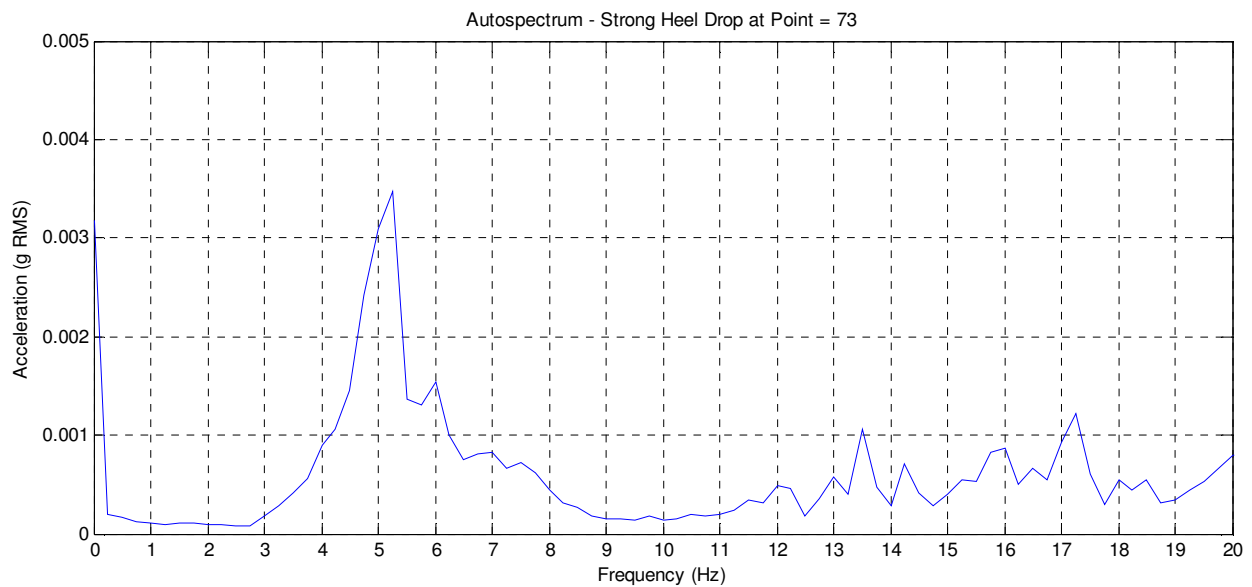
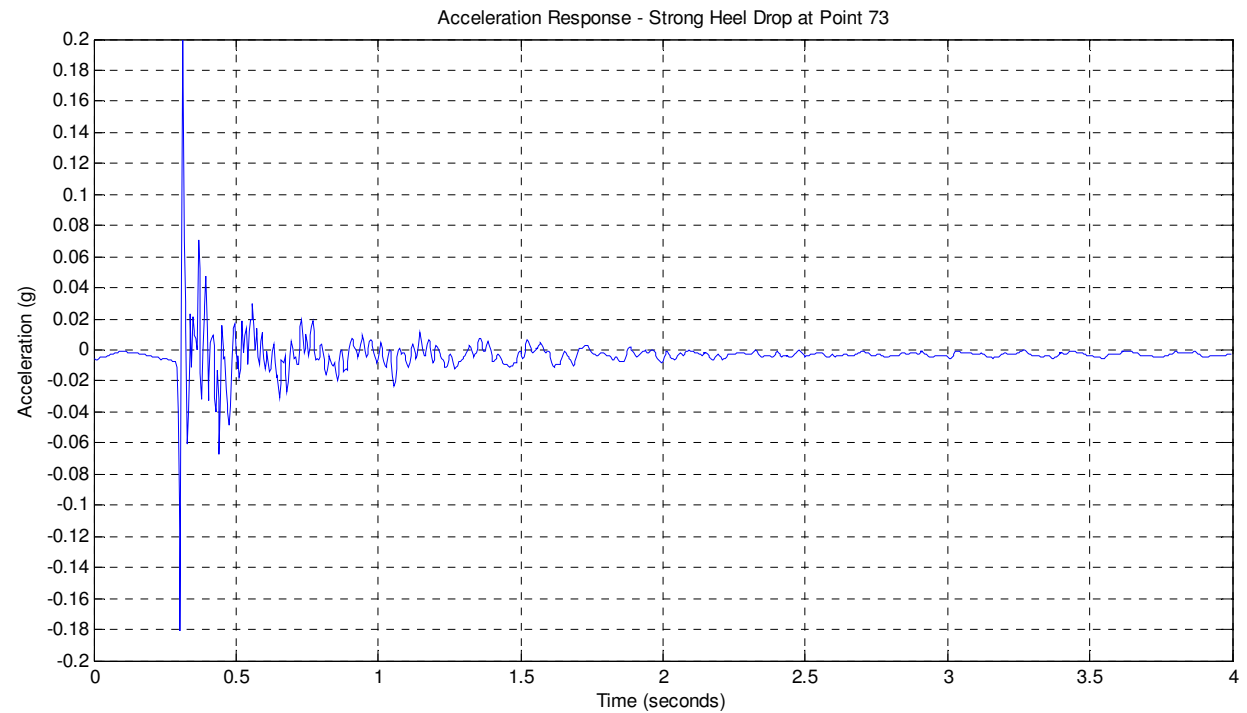


Figure C.1: NOC VII-24 Handheld Test Locations

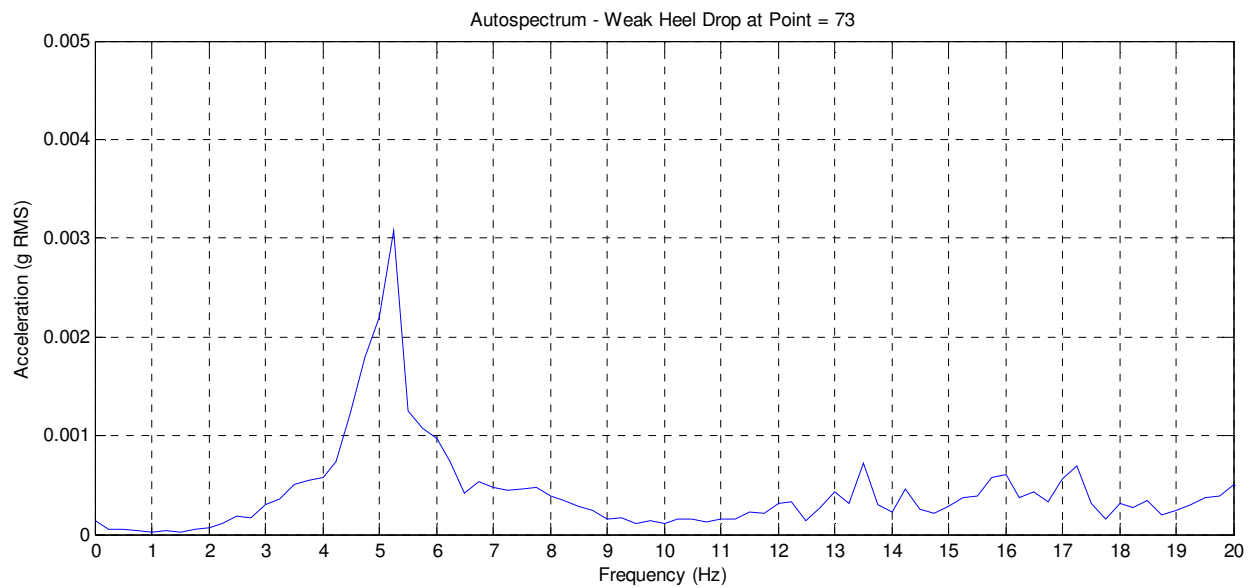
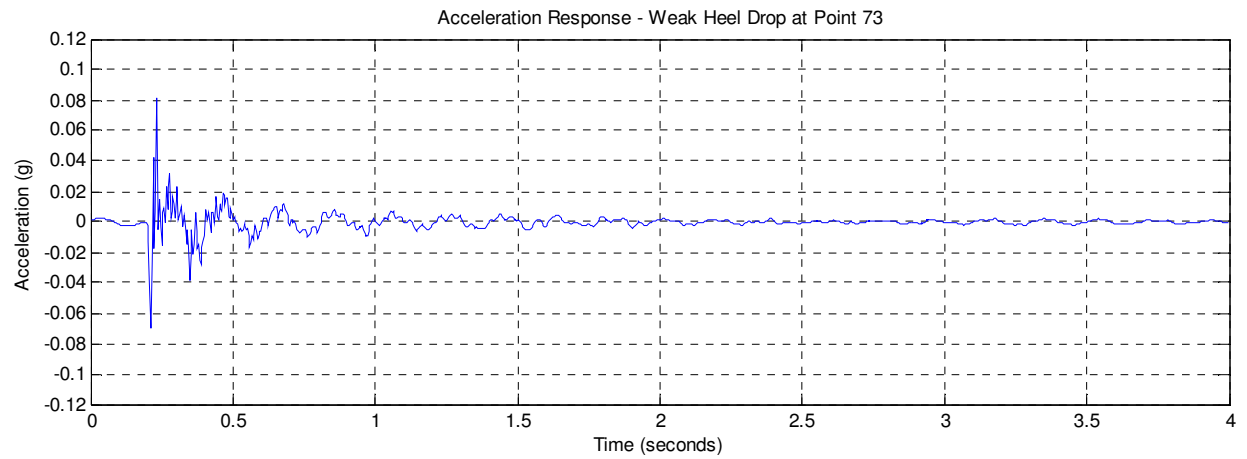
Point 73 (L/M- 5/6)
Record No.: 4-6



OVERALL	0.0178 g	
0-P:	0.313 s	20.000 %g
1ST:	5.25 Hz	0.347 %g
2ND:	29.00 Hz	0.285 %g
3RD:	37.25 Hz	0.210 %g

Figure C.2: NOC VII-24 – Unreferenced Heel Drop (Strong) at Point 73

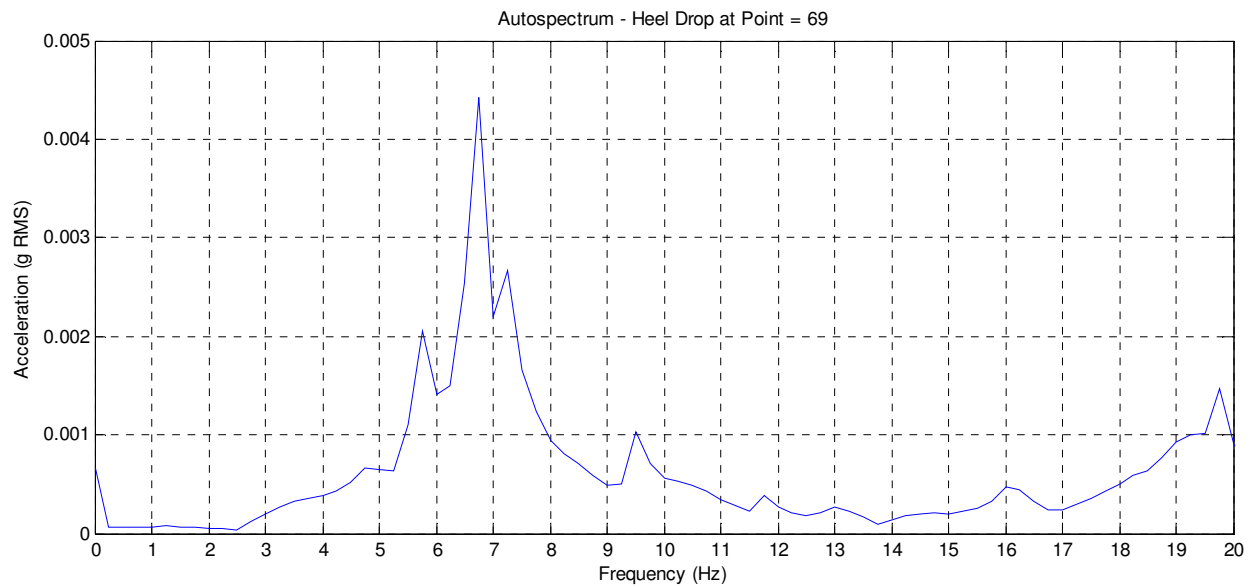
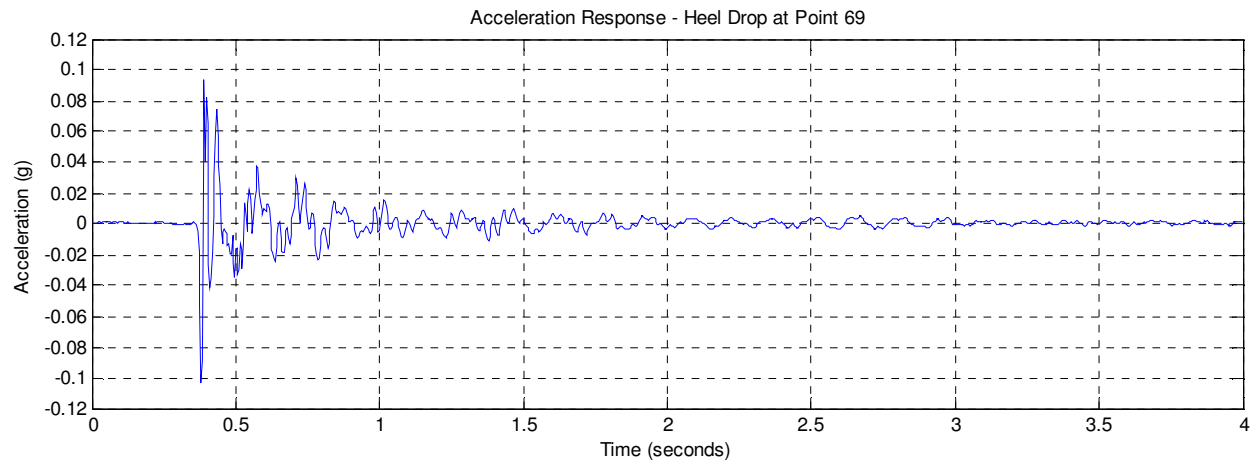
Point 73 (L/M- 5/6)
Record No.: 7-9



OVERALL	0.00827 g	
0-P:	0.231 s	8.134 %g
1ST:	5.25 Hz	0.308 %g
2ND:	29.00 Hz	0.120 %g
3RD:	22.50 Hz	0.088 %g

Figure C.3: NOC VII-24 – Unreferenced Heel Drop (Weak) at Point 73

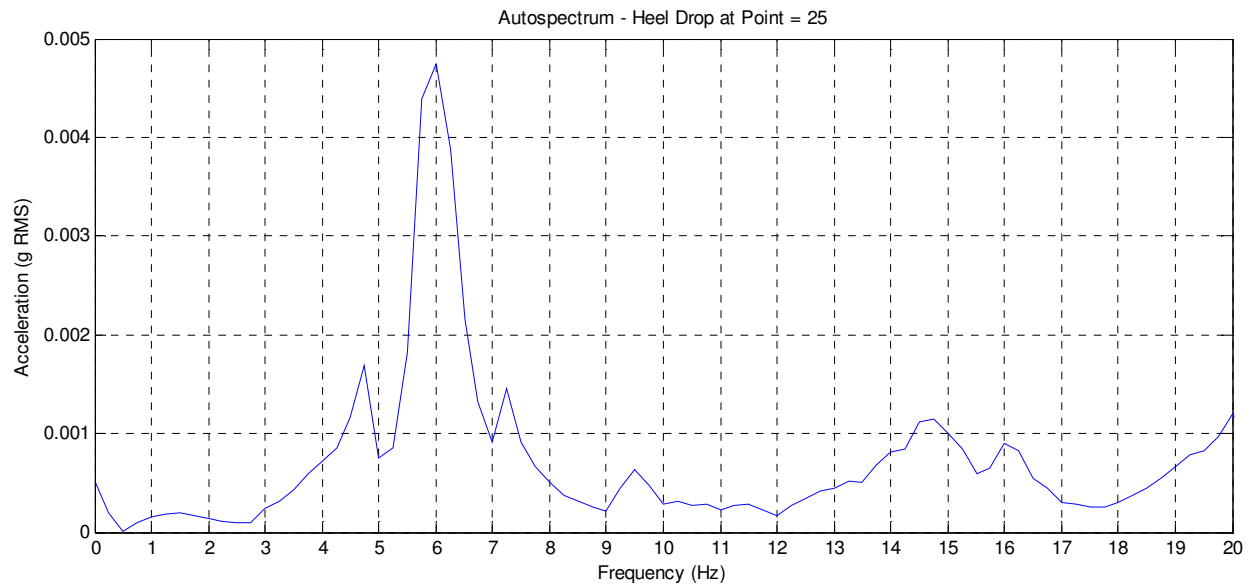
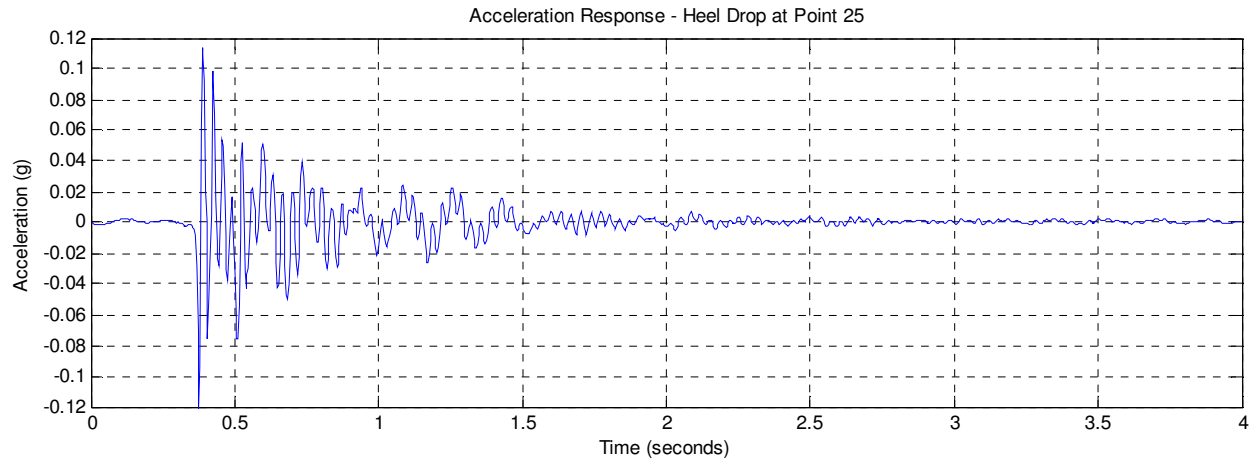
Point 69 (L/M- 4/5)
Record No.: 31-33



OVERALL	0.0138 g	
0-P:	0.391 s	9.345 %g
1ST:	6.75 Hz	0.442 %g
2ND:	7.25 Hz	0.267 %g
3RD:	27.00 Hz	0.229 %g

Figure C.4: NOC VII-24 – Unreferenced Heel Drop at Point 69

Point 25 (M/N- 4/5)
Record No.: 49-51



OVERALL	0.020 g	
0-P:	0.387 s	11.360 %g
1ST:	29.00 Hz	0.668 %g
2ND:	6.00 Hz	0.475 %g
3RD:	31.25 Hz	0.247 %g

Figure C.5: NOC VII-24 – Unreferenced Heel Drop at Point 25

APPENDIX D

SINGLE-CHANNEL HANDHELD ANALYZER MEASUREMENTS – VTK2

The 2nd floor of the VT KnowledgeWorks 2 building (VTK2) was investigated in November 2005 using a single-channel Ono Sokki CF-1200 Handheld FFT Analyzer. Heel drop measurements are presented in this Appendix to correspond to eleven locations on VTK2 tested using the electrodynamic shaker. The unreferenced measurements' autospectra provide the best comparison to the high quality modal measurements presented in Section 3.3.3. Figure D.1 shows the condition of the floor at the time of the handheld investigation, and Figure D.2 shows the location of the eleven points of excitation.



Figure D.1: VTK2 Building Condition at Time of Handheld Investigation

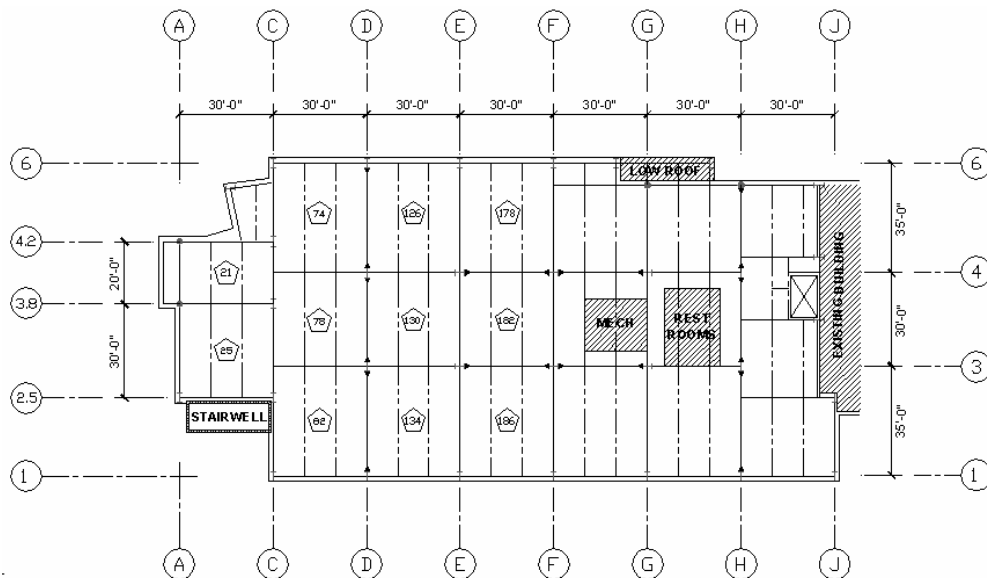


Figure D.2: VTK2 Handheld Test Locations

Point 21 (A/C-3.8/4.2)
Record No.: 67-69

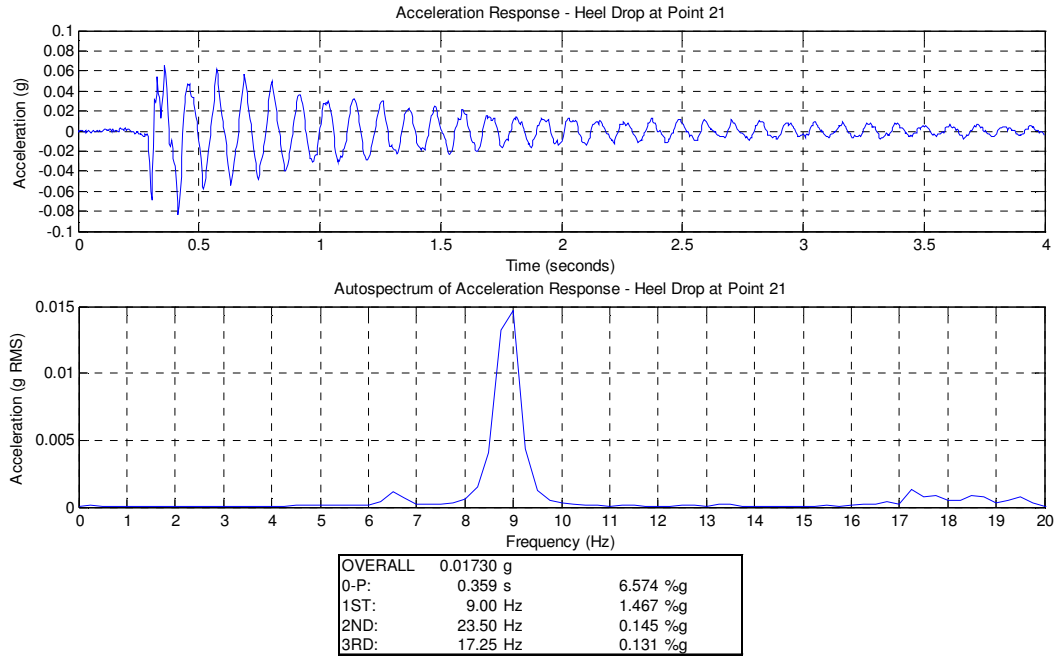


Figure D.3: VTK2 – Unreferenced Heel Drop at Point 21

Point 25 (A/C-2.5/3.8)
Record No.: 64-66

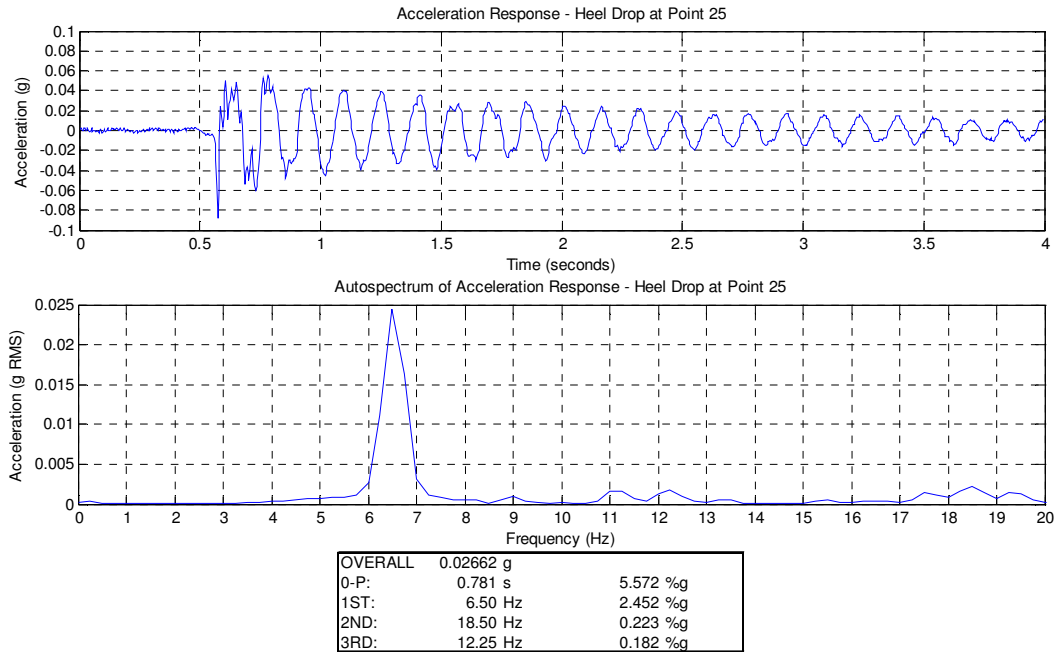


Figure D.4: VTK2 – Unreferenced Heel Drop at Point 25

Point 74 (C/D-4/6)
Record No.: 58-60

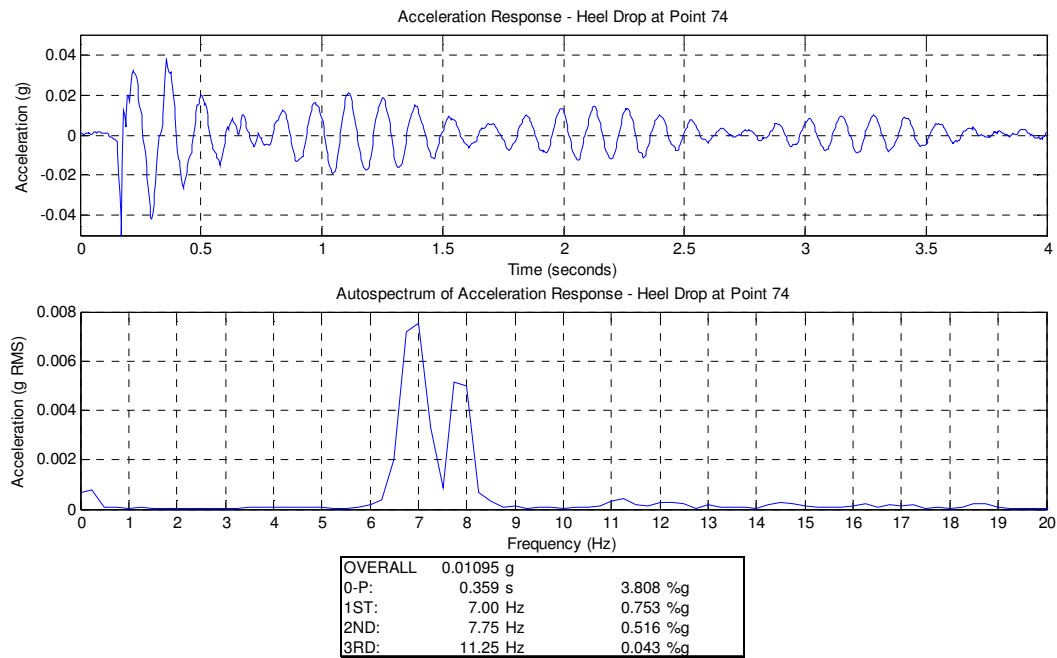


Figure D.5: VTK2 – Unreferenced Heel Drop at Point 74

Point 78 (C/D-3/4)
Record No.: 61-63

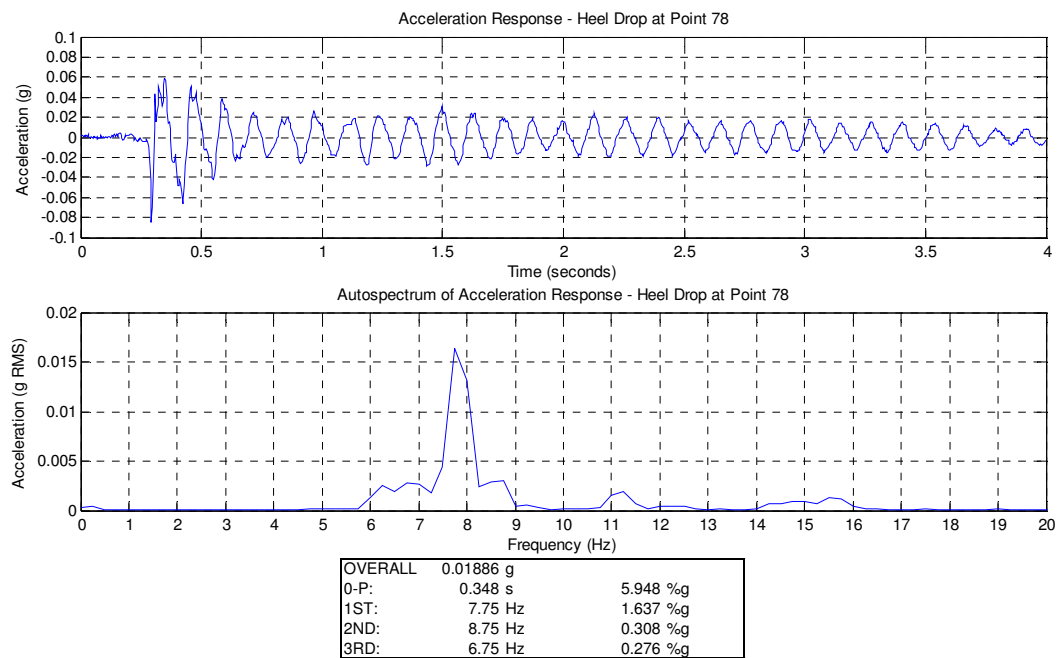


Figure D.6: VTK2 – Unreferenced Heel Drop at Point 78

Point 82 (C/D-1/3)
Record No.: 55-57

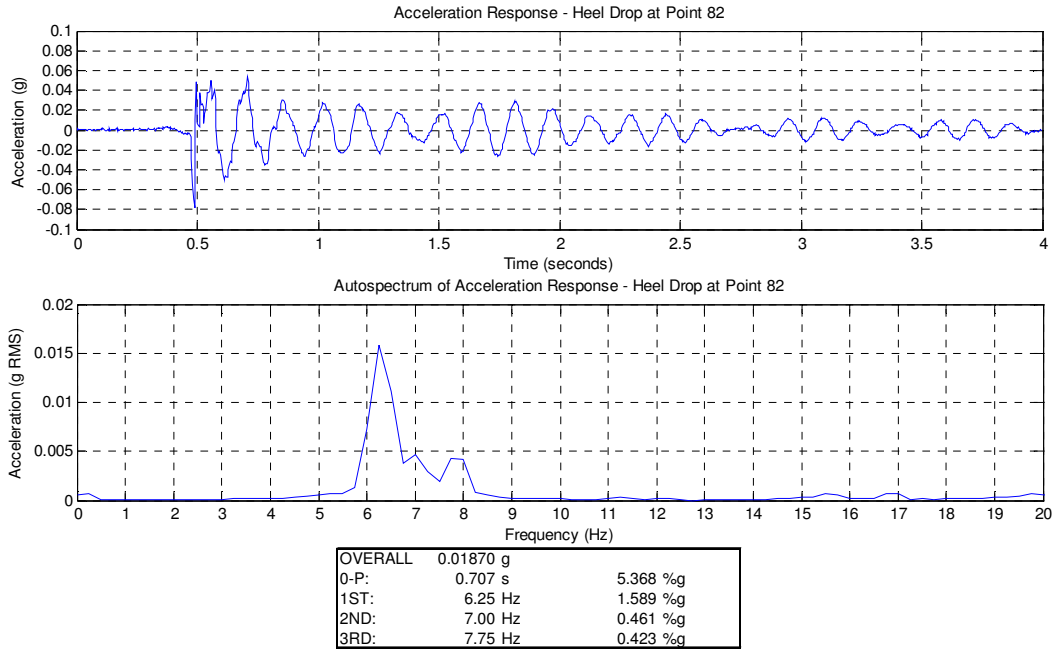


Figure D.7: VTK2 – Unreferenced Heel Drop at Point 82

Point 126 (D/E-4/6)
Record No.: 52-54

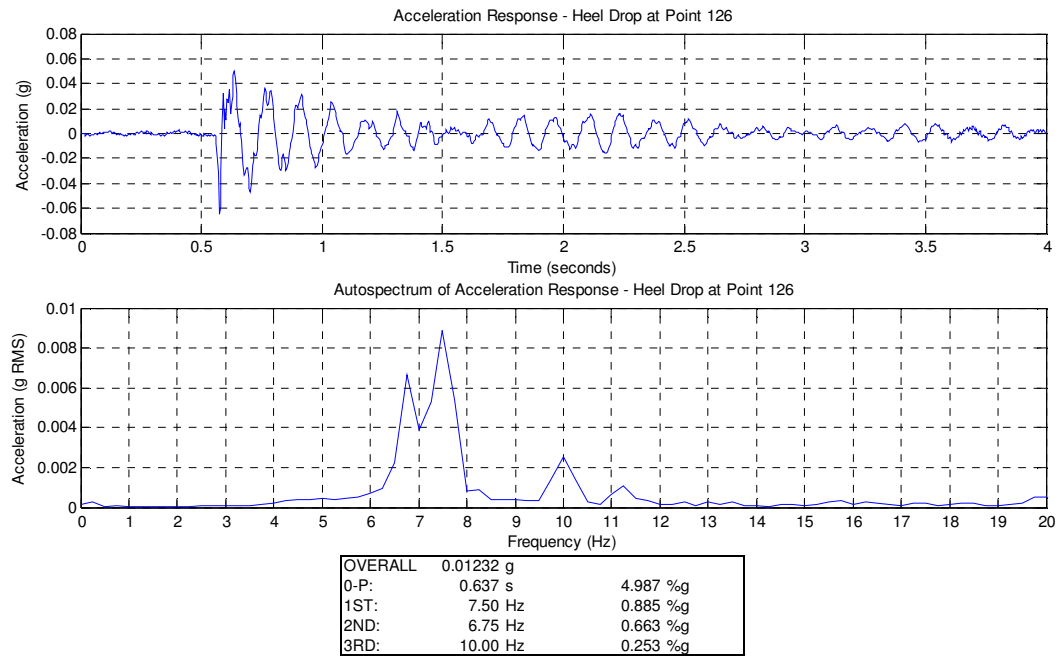


Figure D.8: VTK2 – Unreferenced Heel Drop at Point 126

Point 130 (D/E-3/4)
Record No.: 37-39

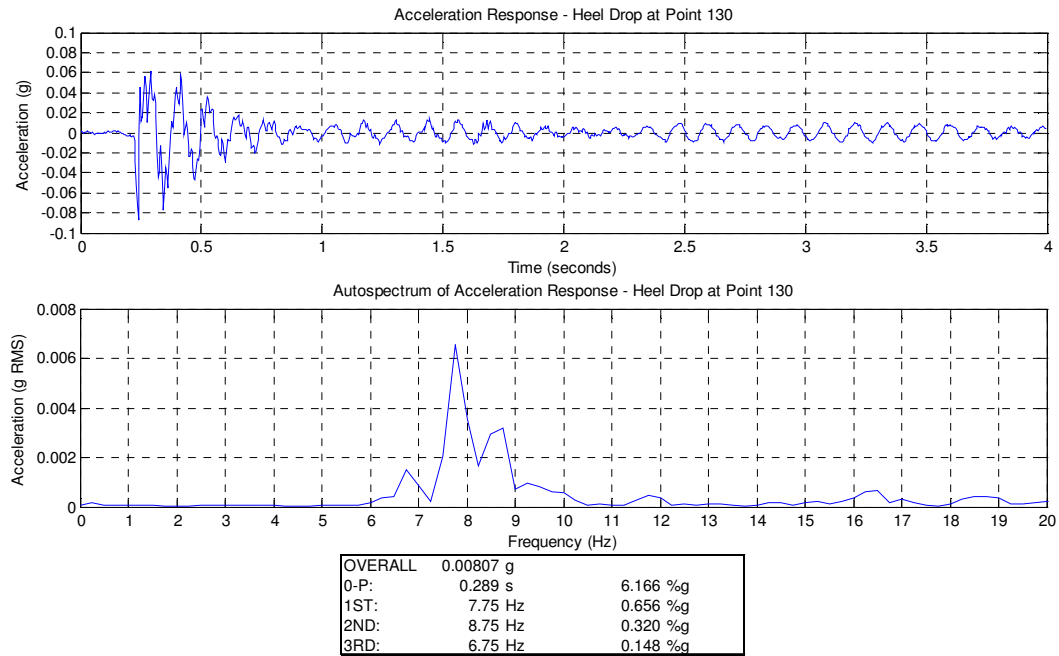


Figure D.9: VTK2 – Unreferenced Heel Drop at Point 130

Point 134 (D/E-1/3)
Record No.: 49-51

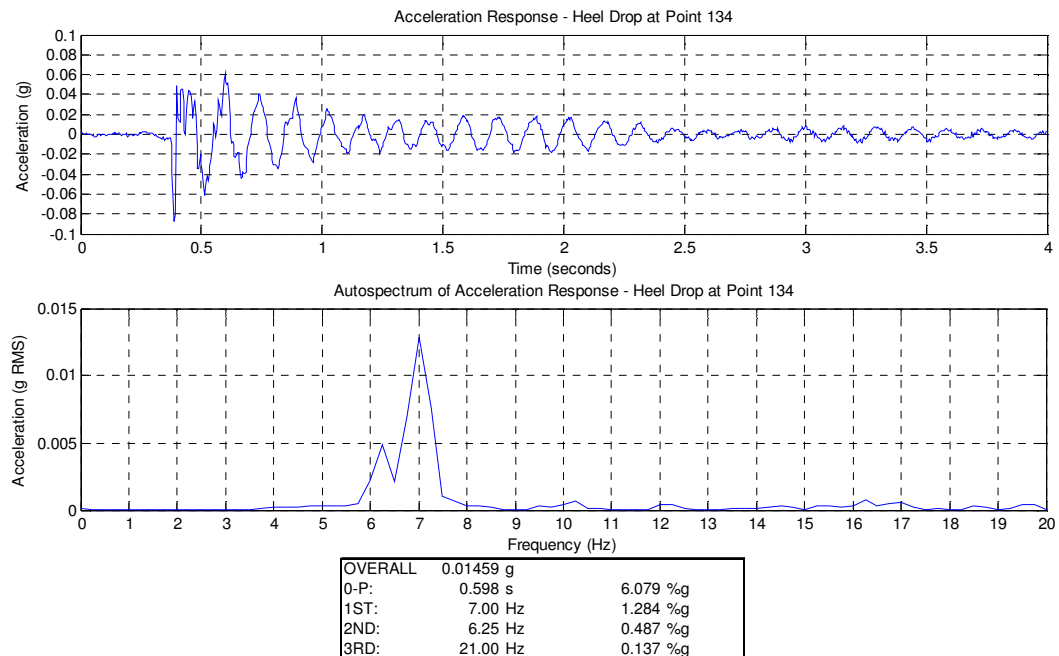


Figure D.10: VTK2 – Unreferenced Heel Drop at Point 134

Point 178 (E/F-4/6)
Record No.: 46-48

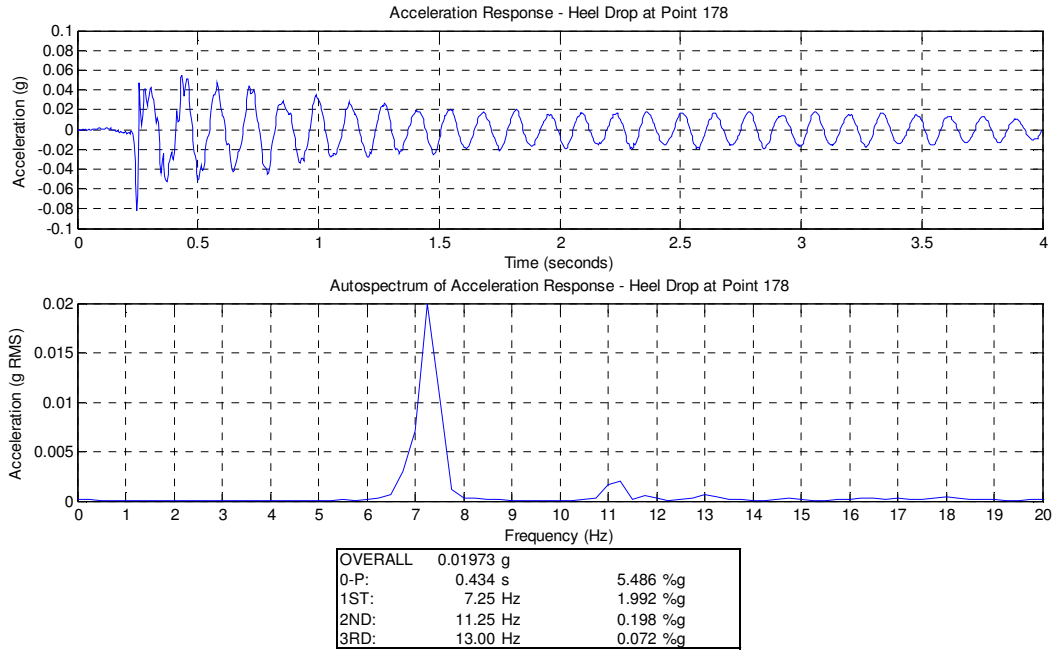


Figure D.11: VTK2 – Unreferenced Heel Drop at Point 178

Point 182 (E/F-3/4)
Record No.: 40-42

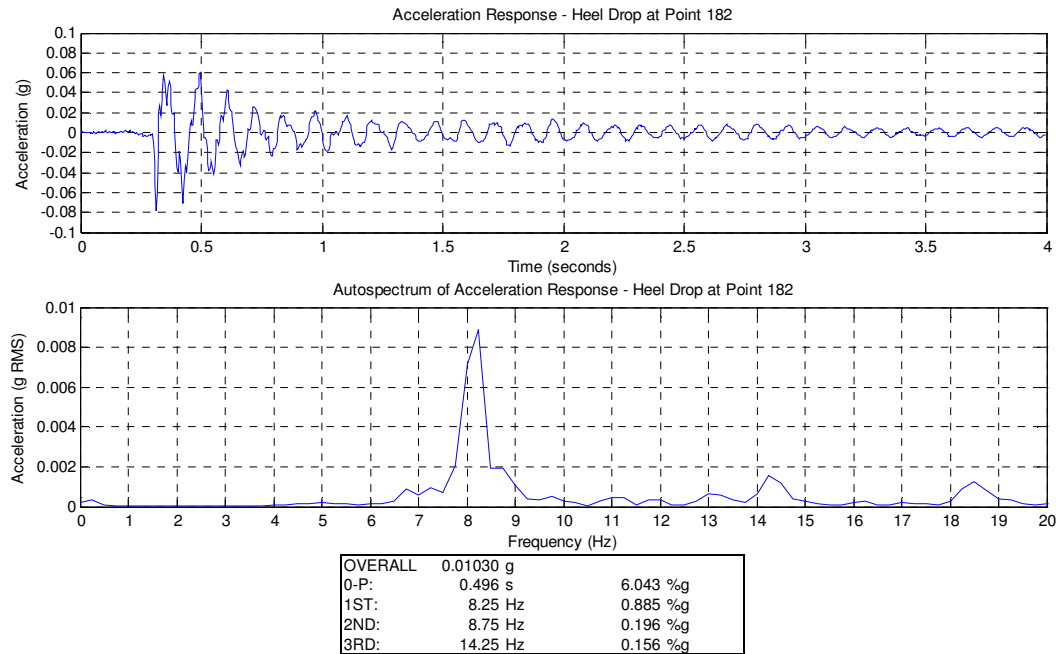


Figure D.12: VTK2 – Unreferenced Heel Drop at Point 182

Point 186 (E/F-1/3)
Record No.: 43-45

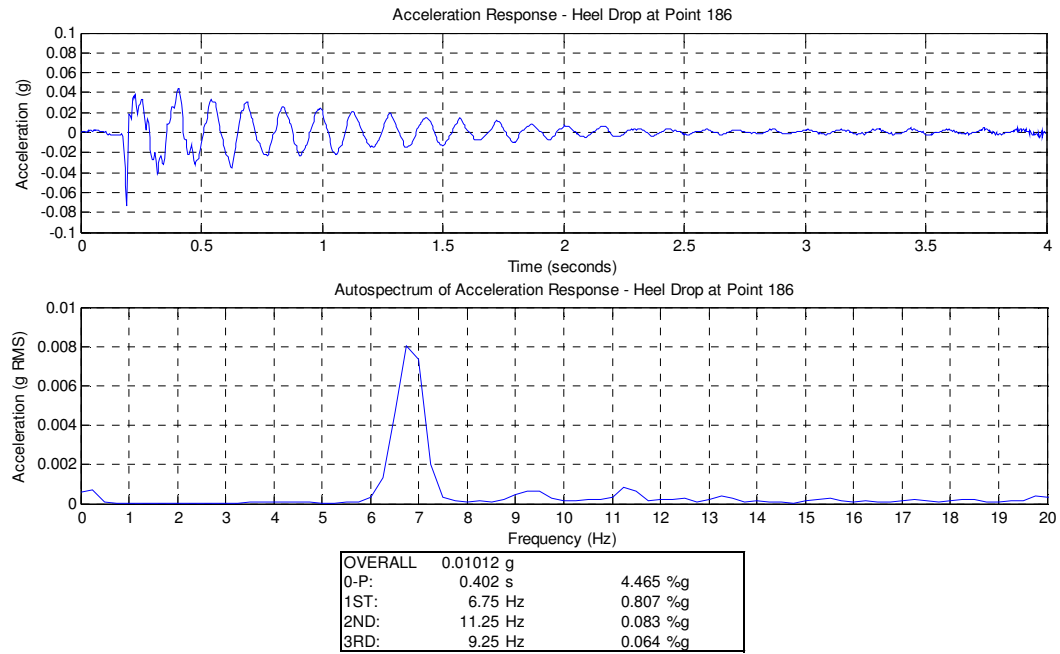


Figure D.13: VTK2 – Unreferenced Heel Drop at Point 186

APPENDIX E

DRIVING POINT ACCELERANCE FREQUENCY RESPONSE FUNCTIONS – NOC VII

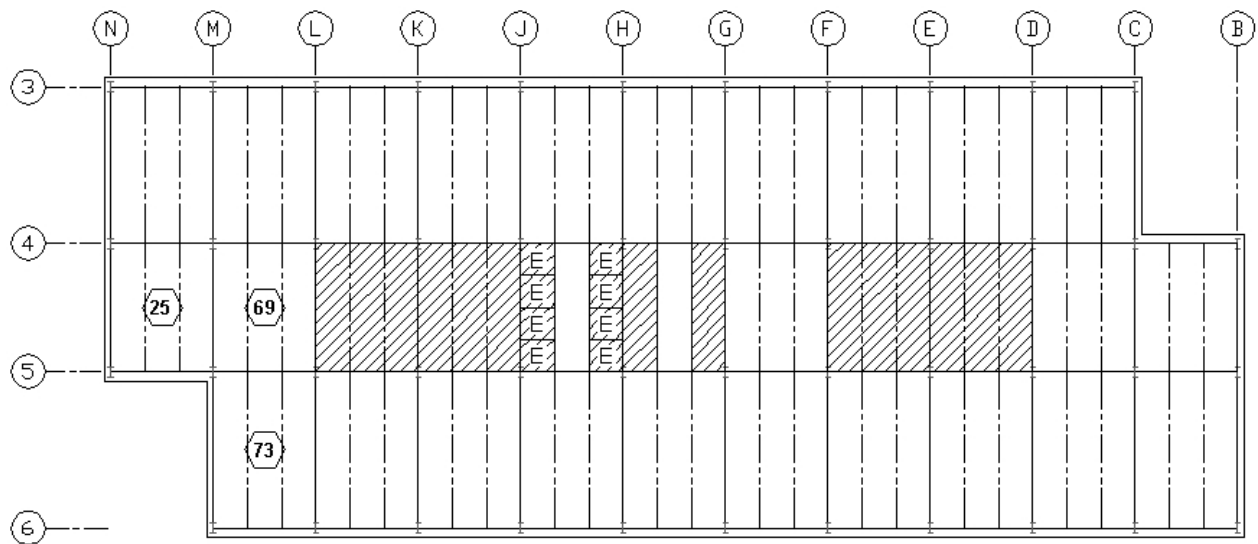


Figure E.1: NOC VII-24 Excitation Locations

Point 73 (L/M-5/6)

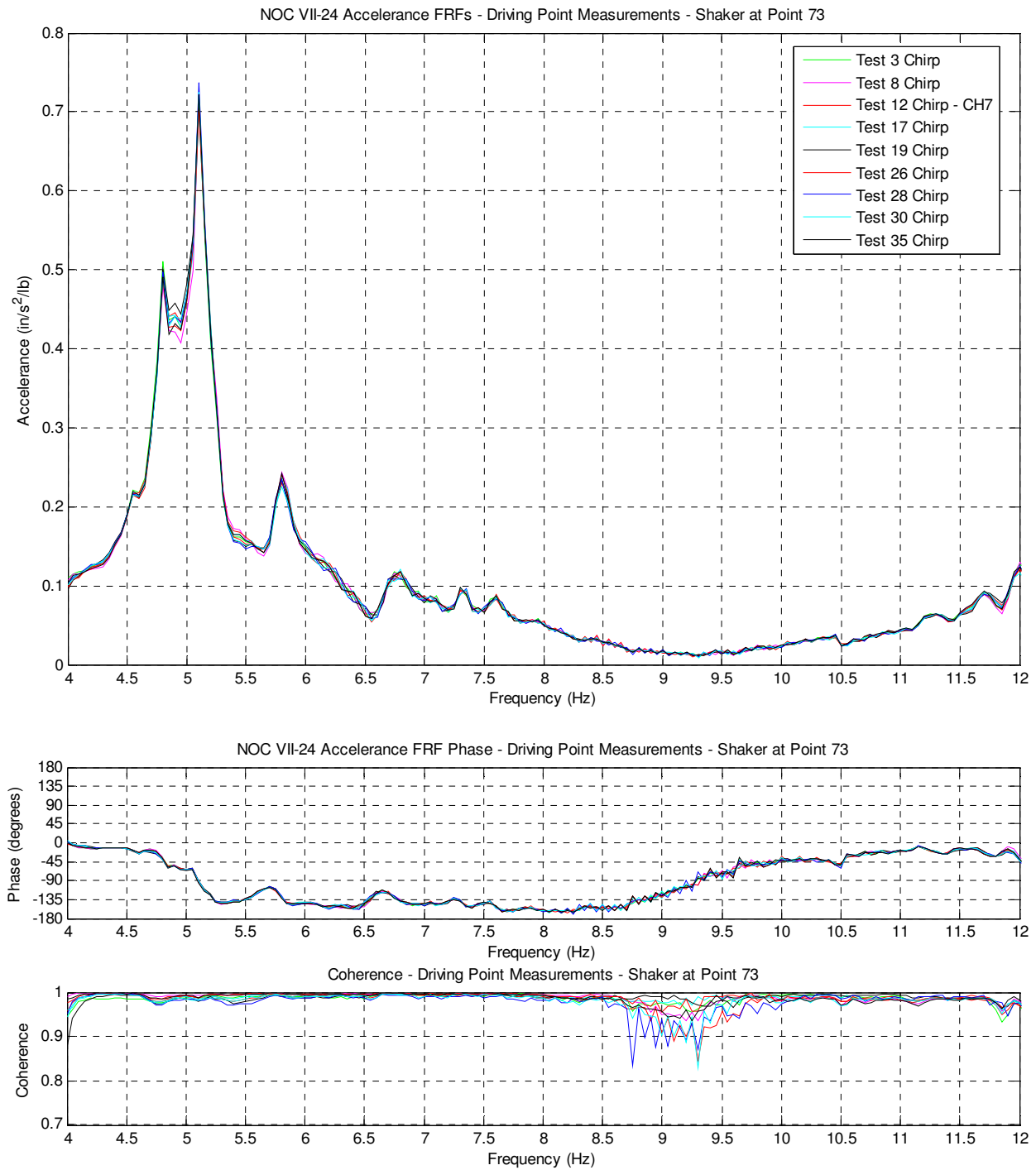


Figure E.2: NOC VII-24 Driving Point Accelerance FRF and Coherence (Point 73)

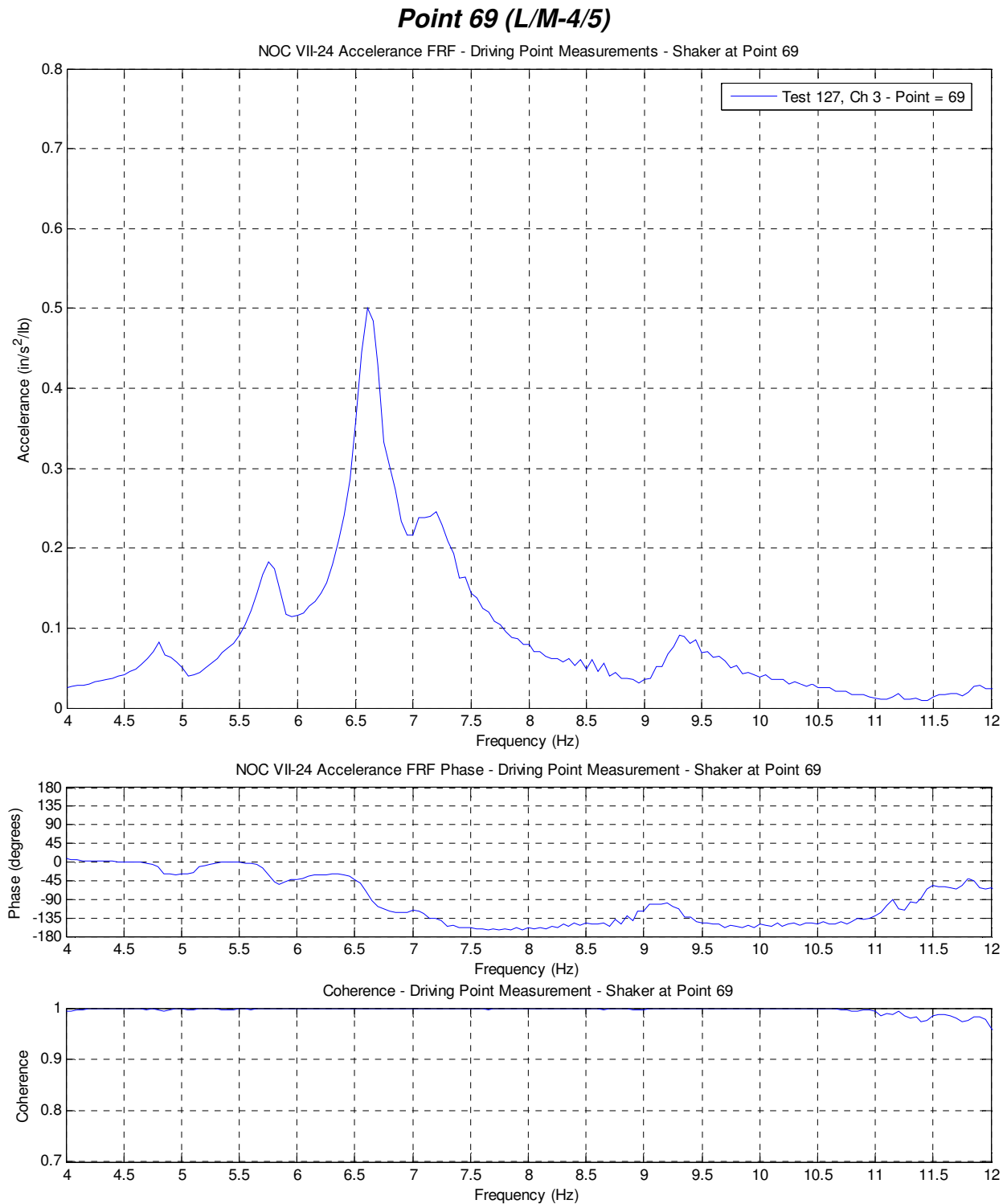


Figure E.3: NOC VII-24 Driving Point Accelerance FRF and Coherence (Point 69)

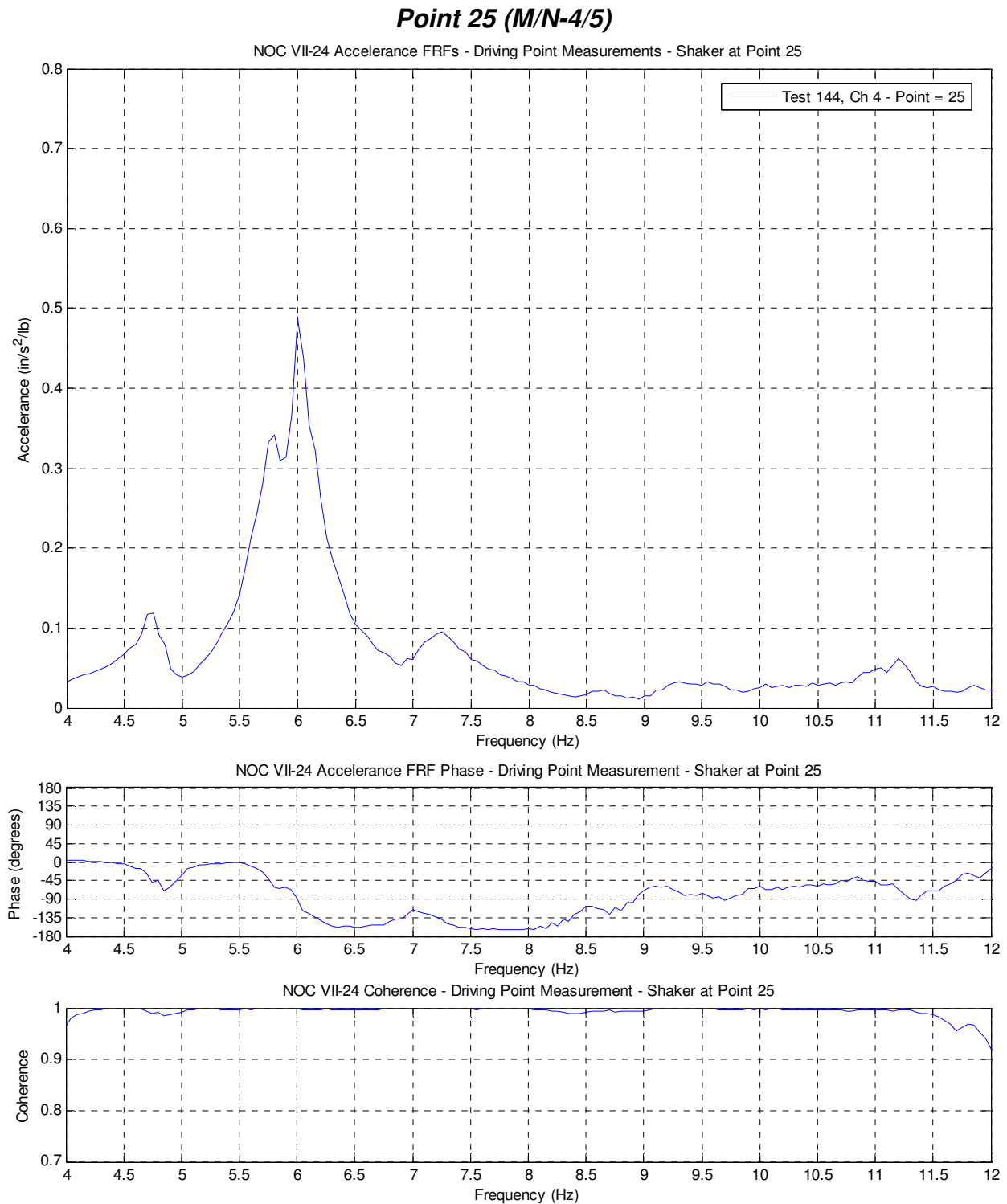


Figure E.4: NOC VII-24 Driving Point Accelerance FRF and Coherence (Point 25)

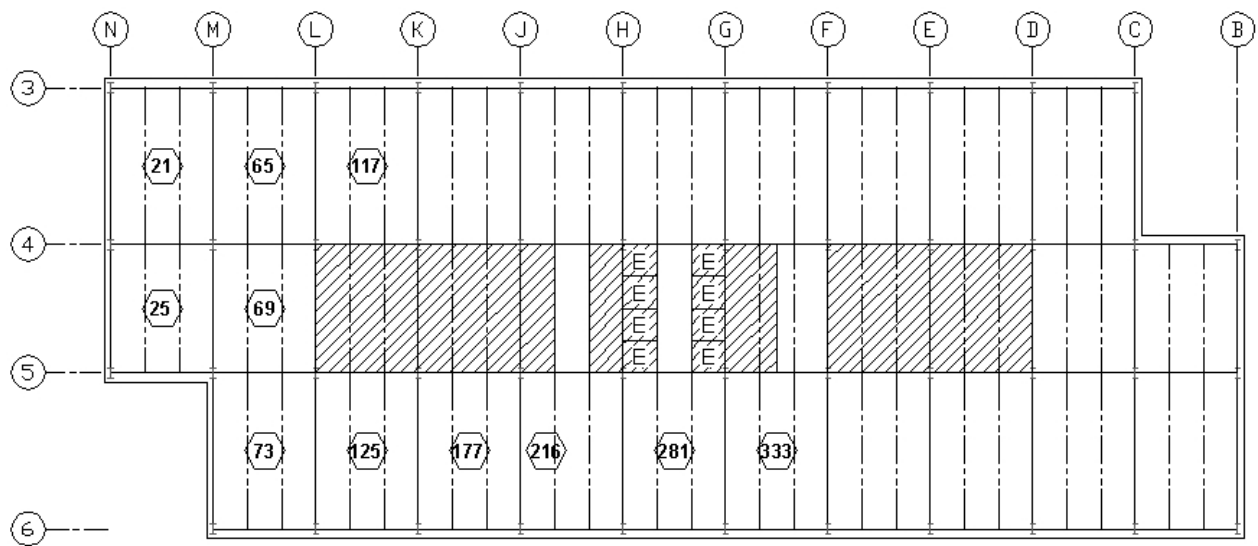


Figure E.5: NOC VII-18 Excitation Locations

Representative Accelerance FRFs - All Driving Points

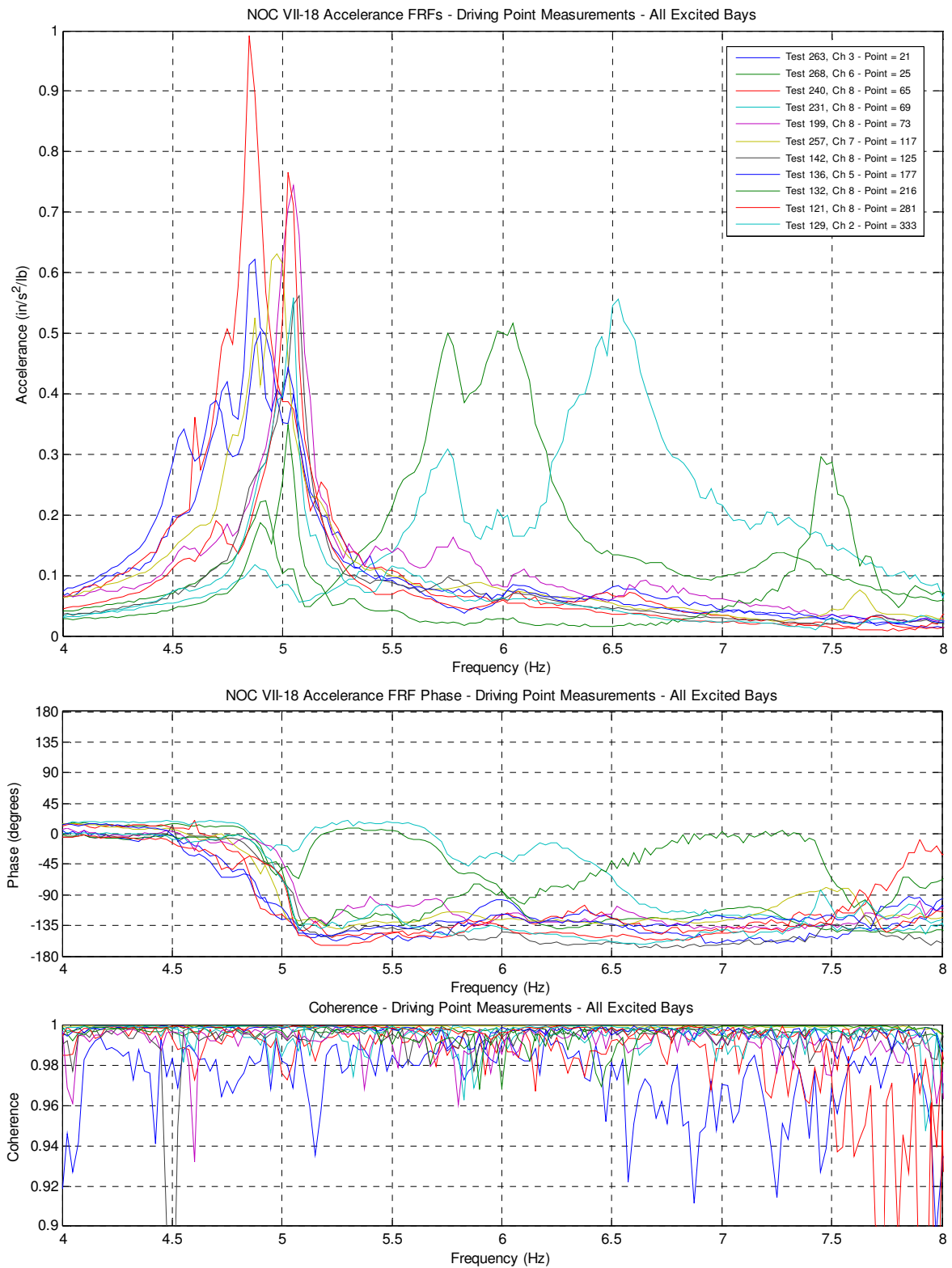
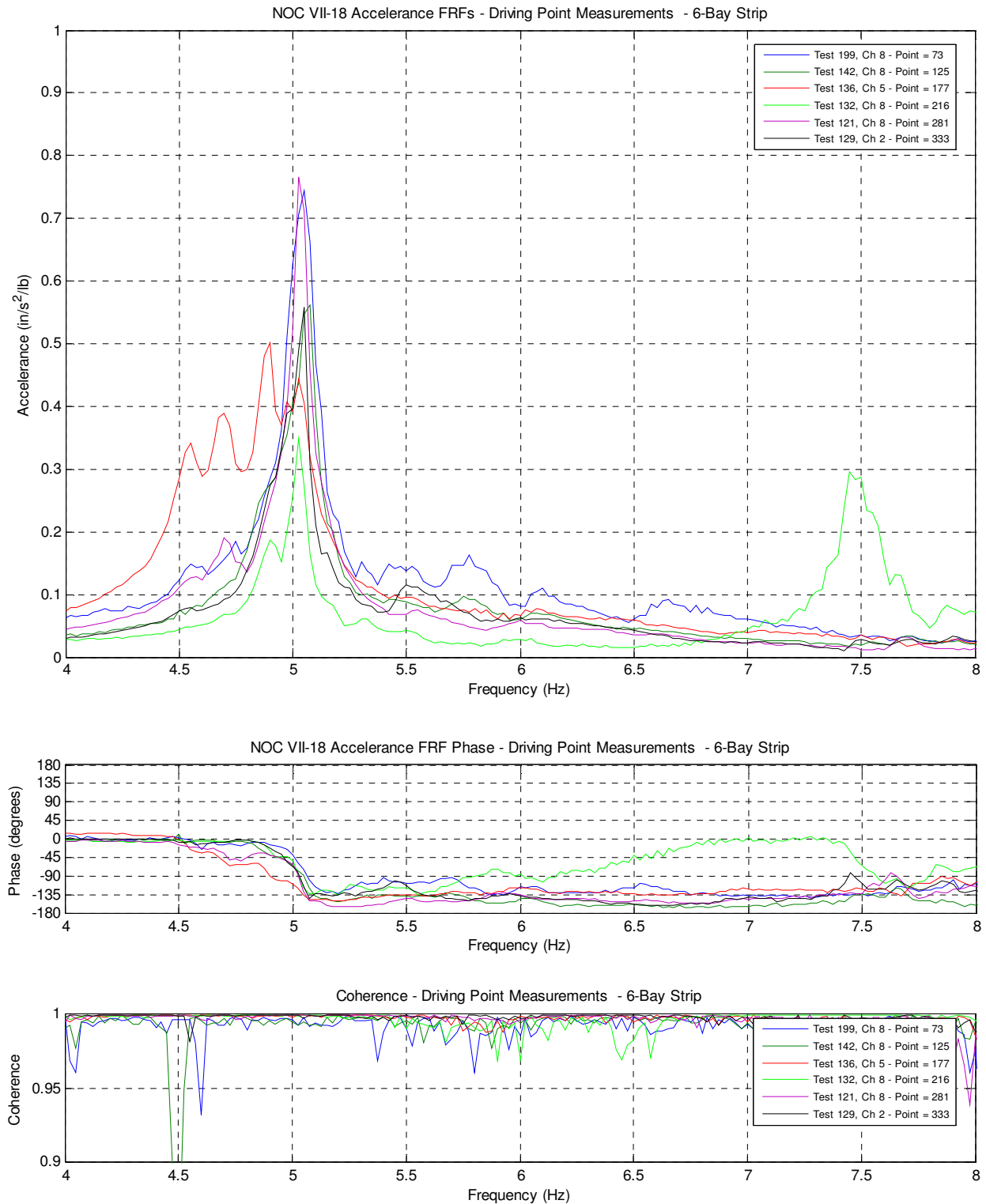


Figure E.6: NOC VII-18 Driving Point Accelerance FRFs (All Excitation Points)

Representative Accelerance FRFs – Exterior Long Strip of 6 Bays



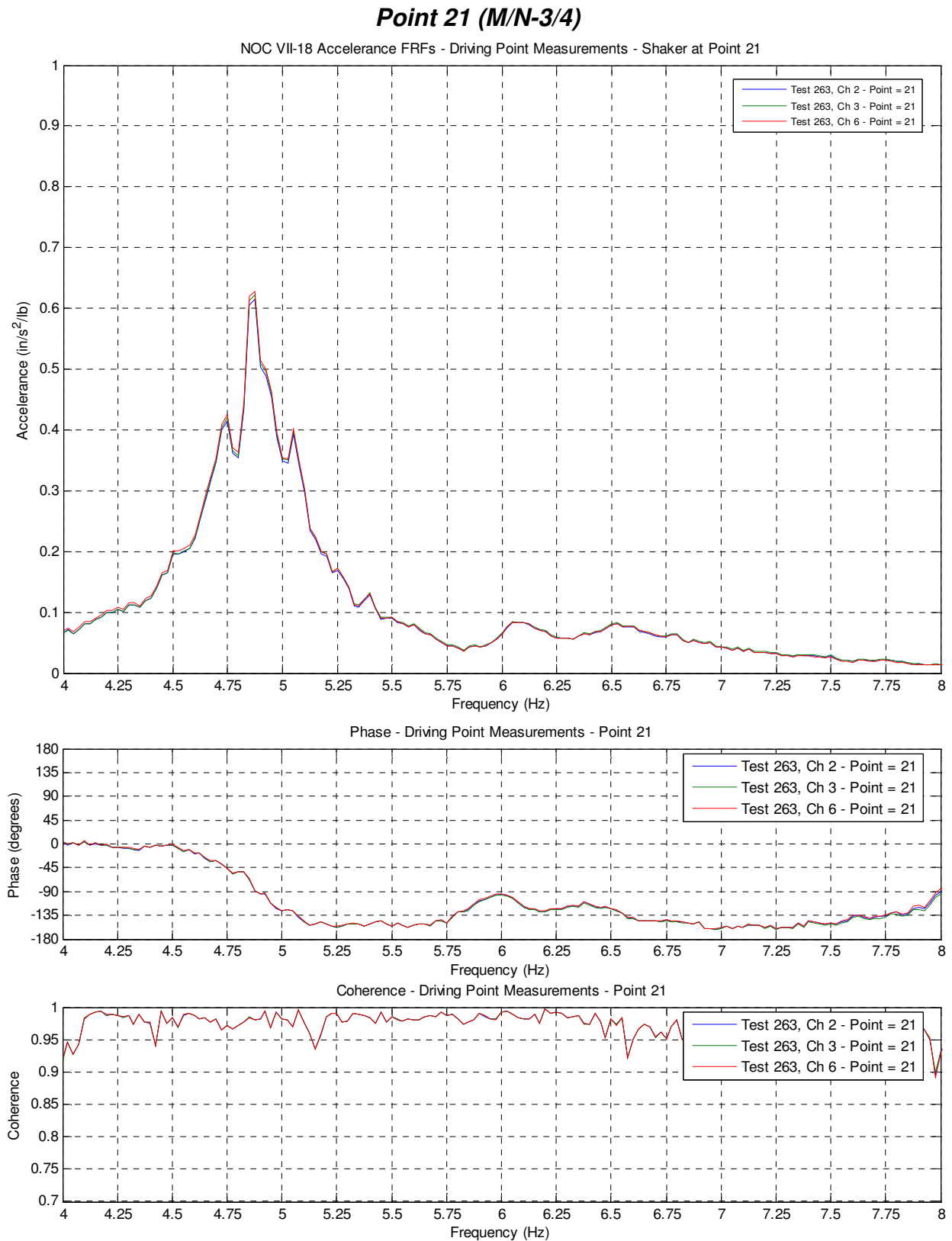


Figure E.8: NOC VII-18 Driving Point Accelerance FRF and Coherence (Point 21)

Point 25 (M/N-4/5)

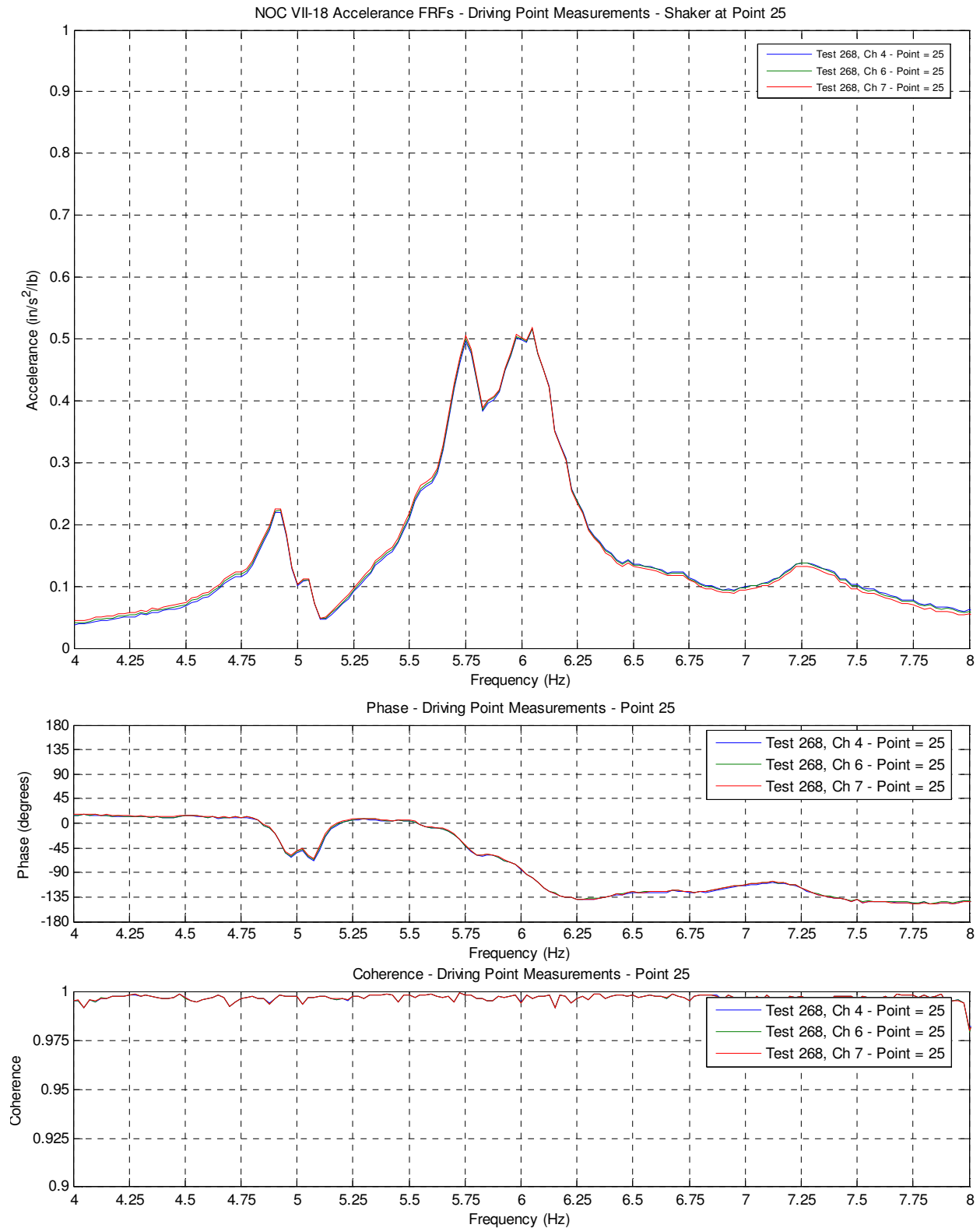


Figure E.9: NOC VII-18 Driving Point Accelerance FRF and Coherence (Point 25)

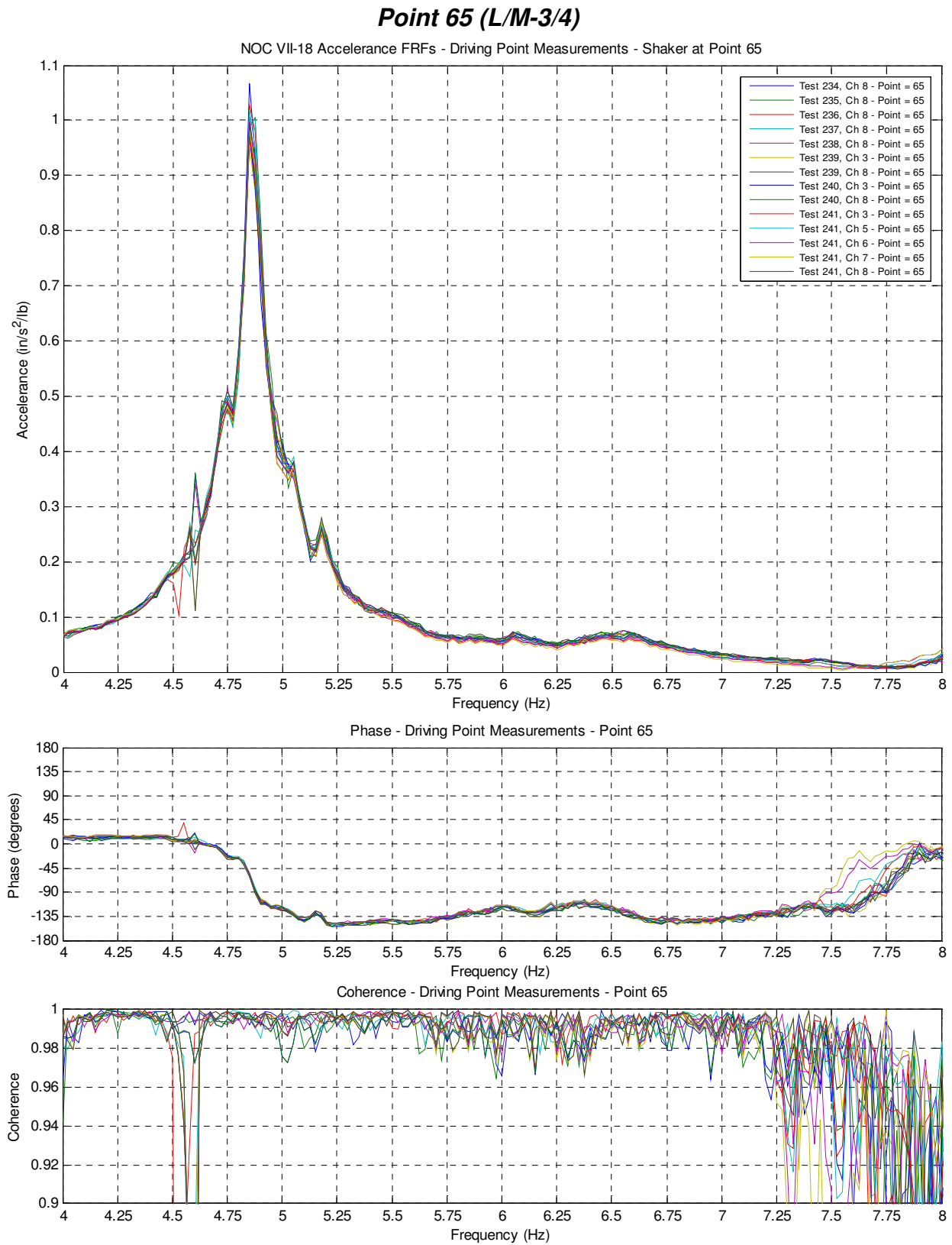


Figure E.10: NOC VII-18 Driving Point Accelerance FRF and Coherence (Point 65)

Point 69 (L/M-4/5)

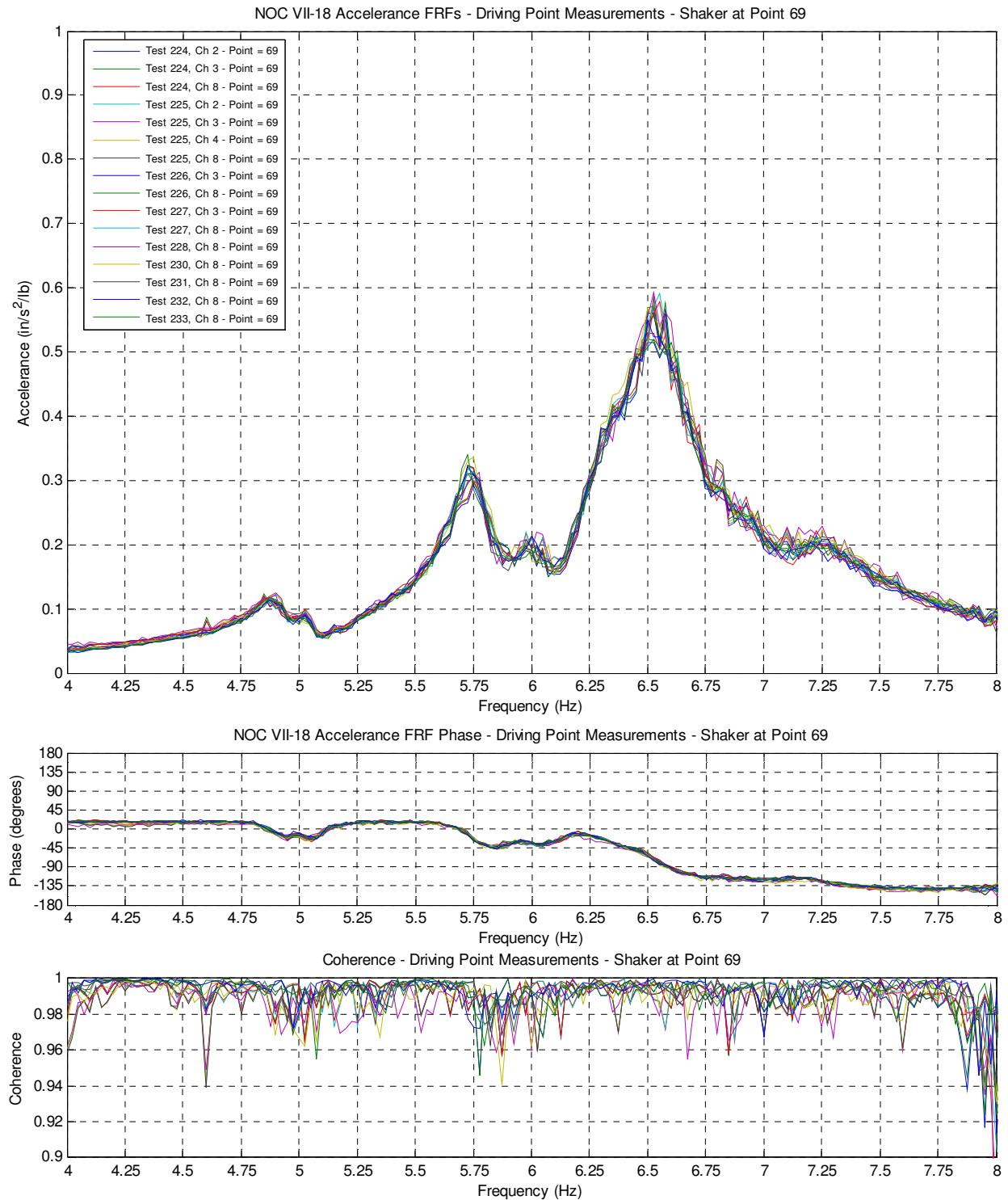


Figure E.11: NOC VII-18 Driving Point Accelerance FRF and Coherence (Point 69)

Point 73 (L/M-5/6)

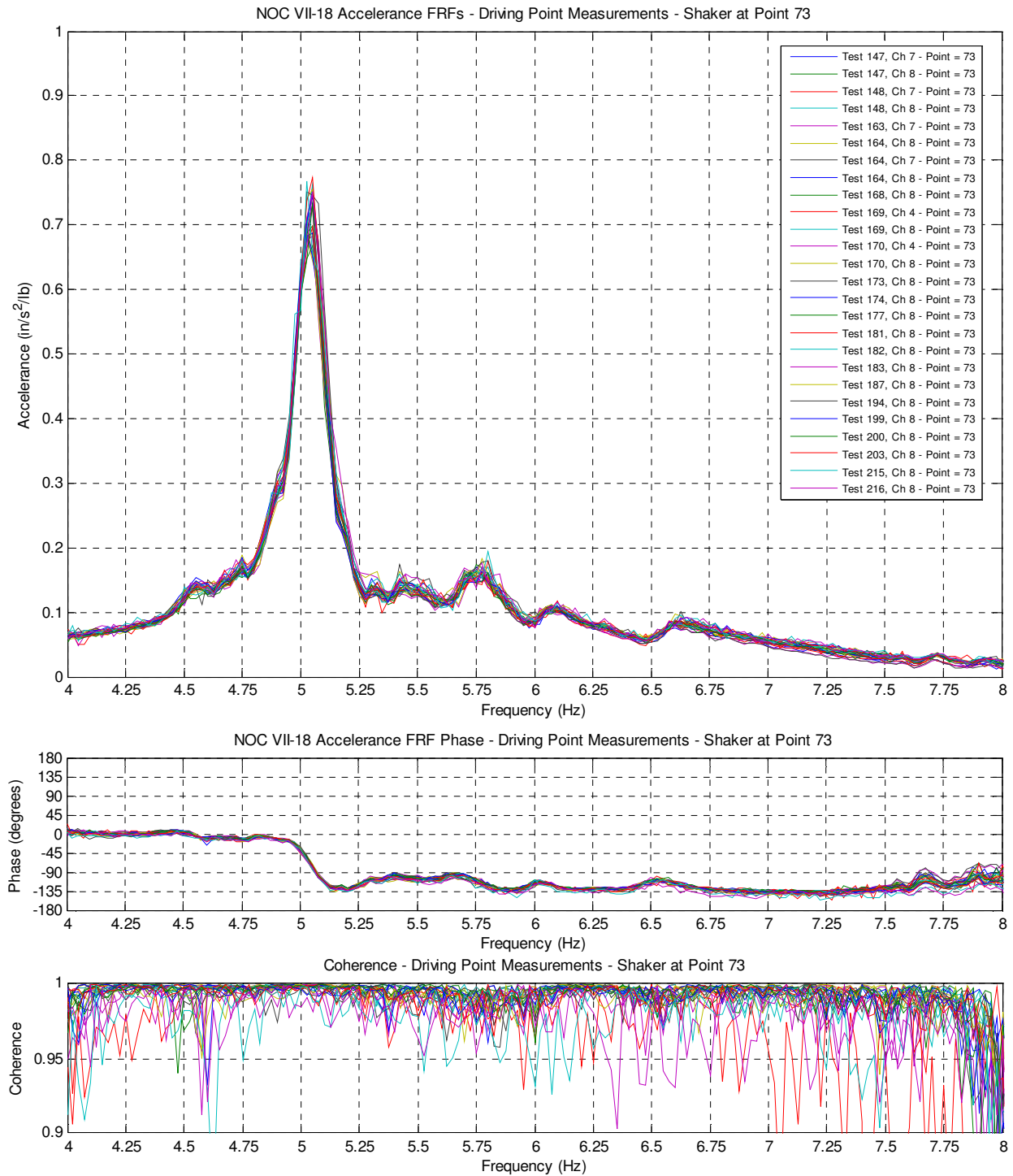


Figure E.12: NOC VII-18 Driving Point Accelerance FRF and Coherence (Point 73)

Point 117 (K/L-3/4)

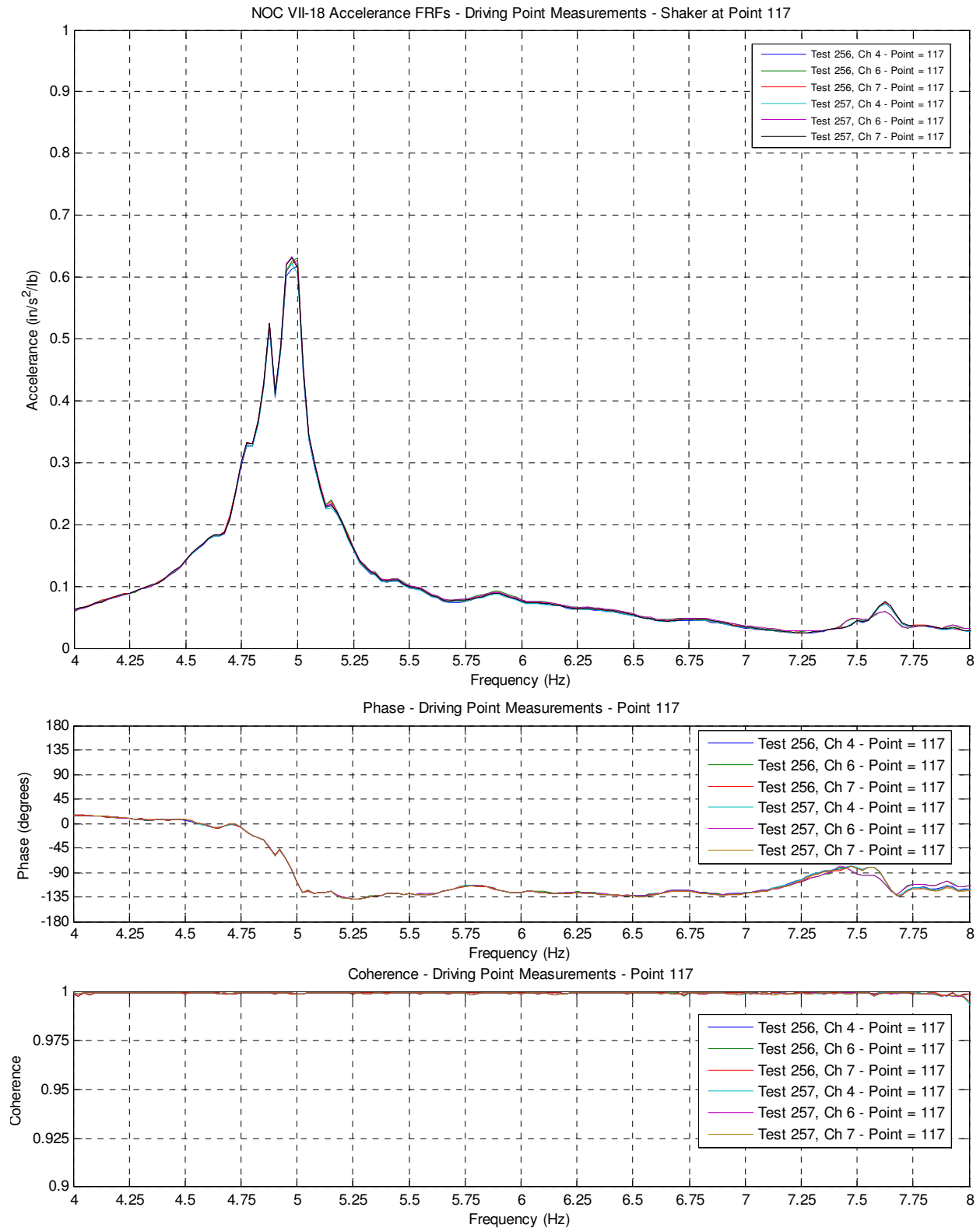


Figure E.13: NOC VII-18 Driving Point Accelerance FRF and Coherence (Point 117)

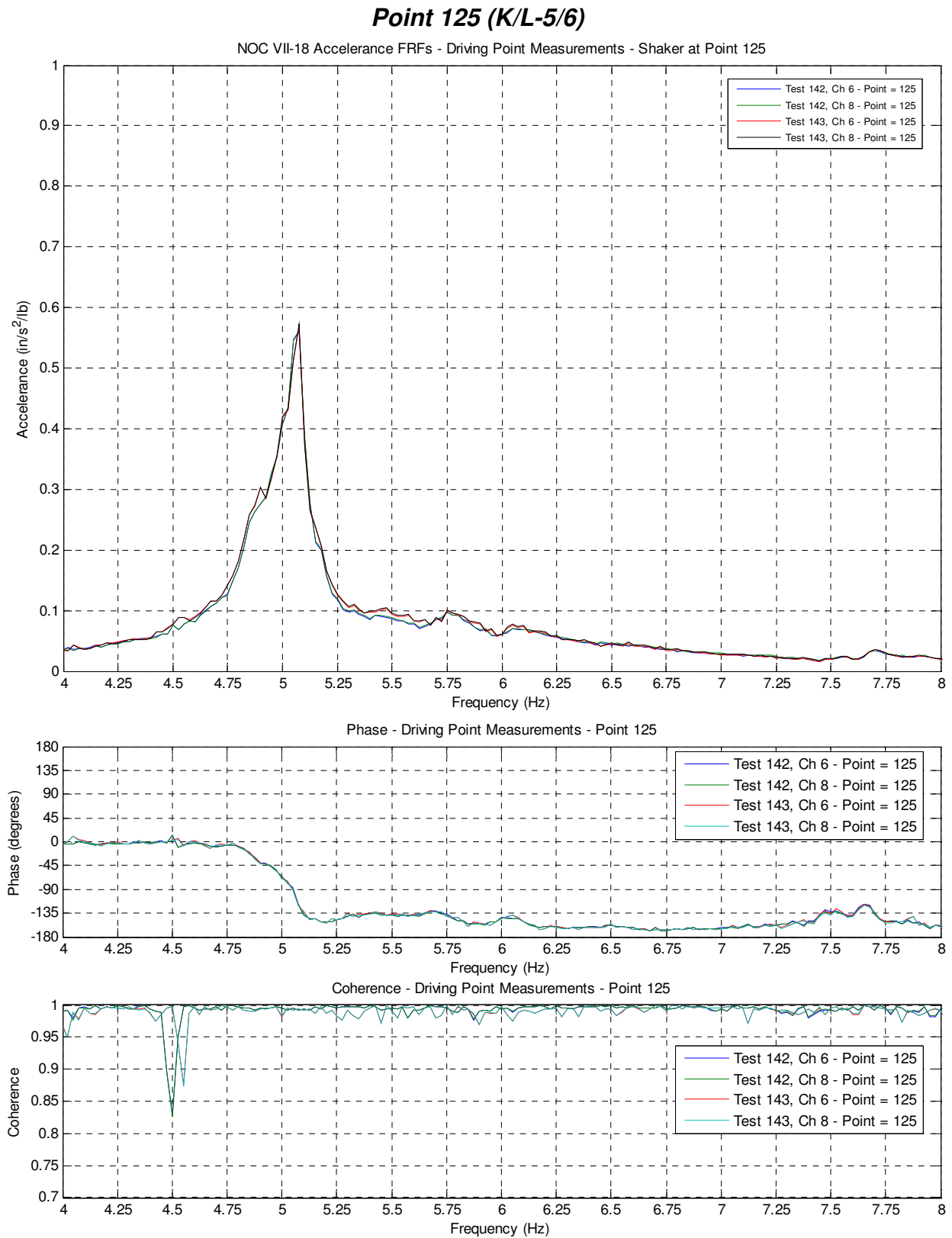


Figure E.14: NOC VII-18 Driving Point Accelerance FRF and Coherence (Point 125)

Point 177 (J/K-5/6)

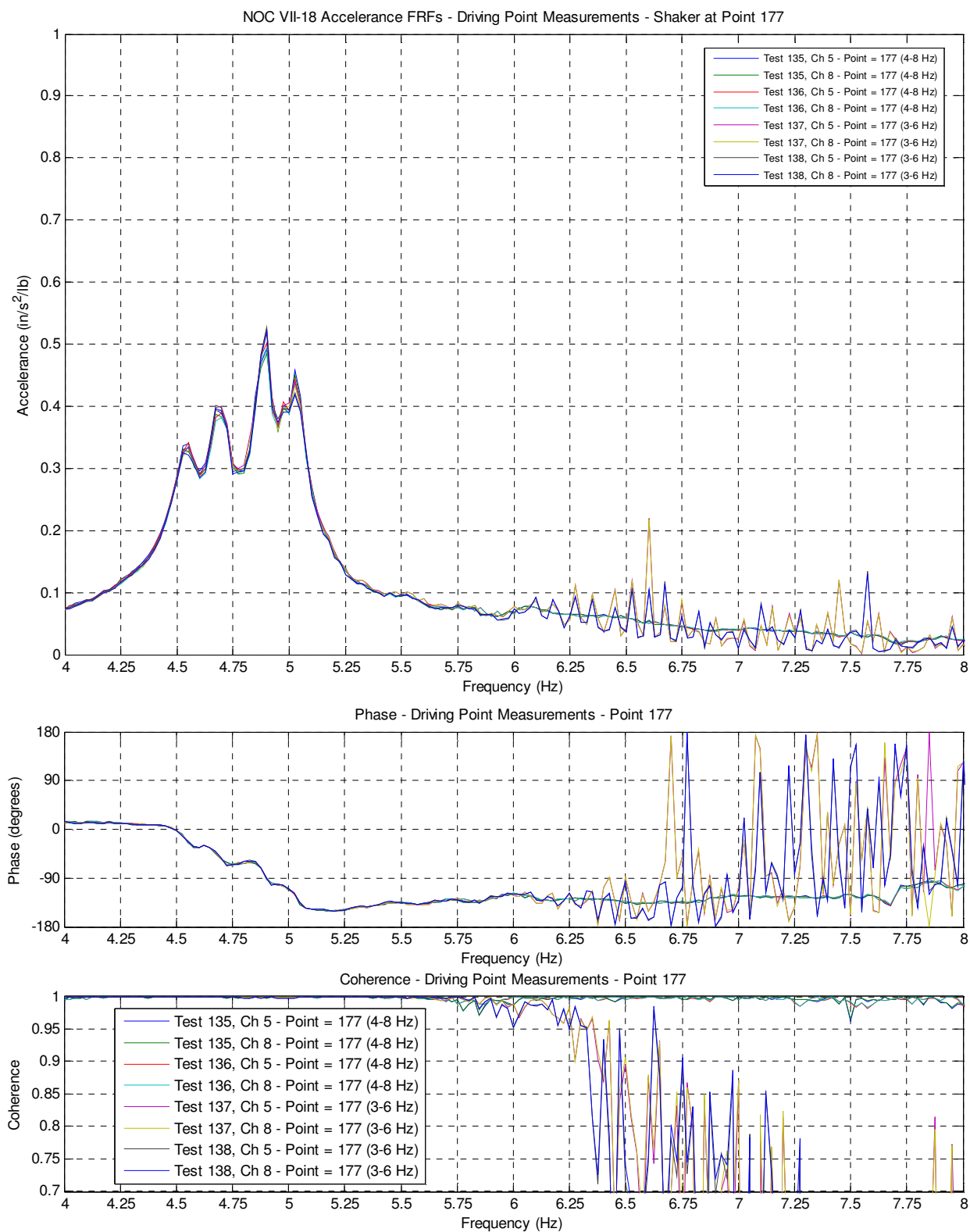


Figure E.15: NOC VII-18 Driving Point Accelerance FRF and Coherence (Point 177)

Point 216 (H/J-5/6)

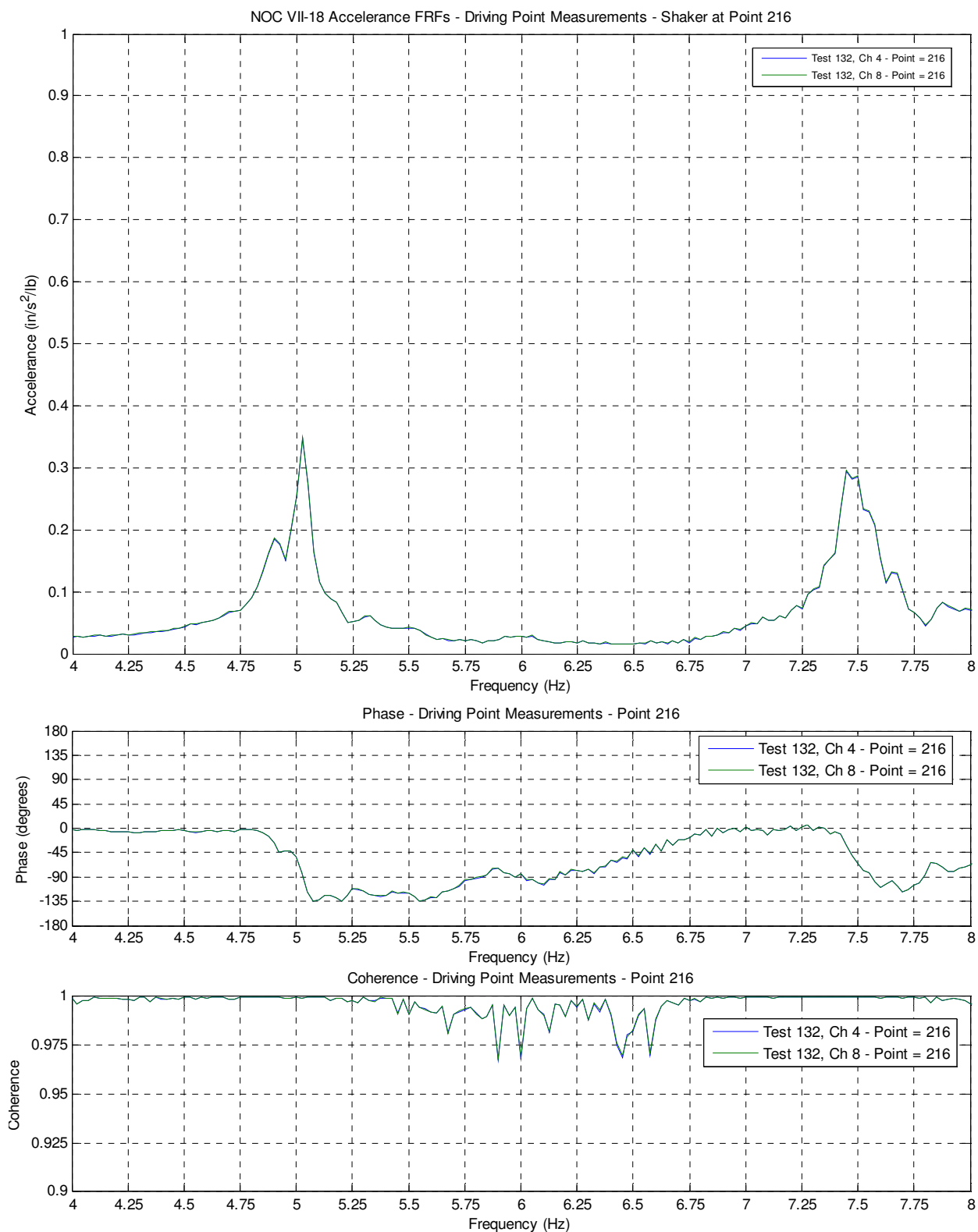


Figure E.16: NOC VII-18 Driving Point Accelerance FRF and Coherence (Point 216)

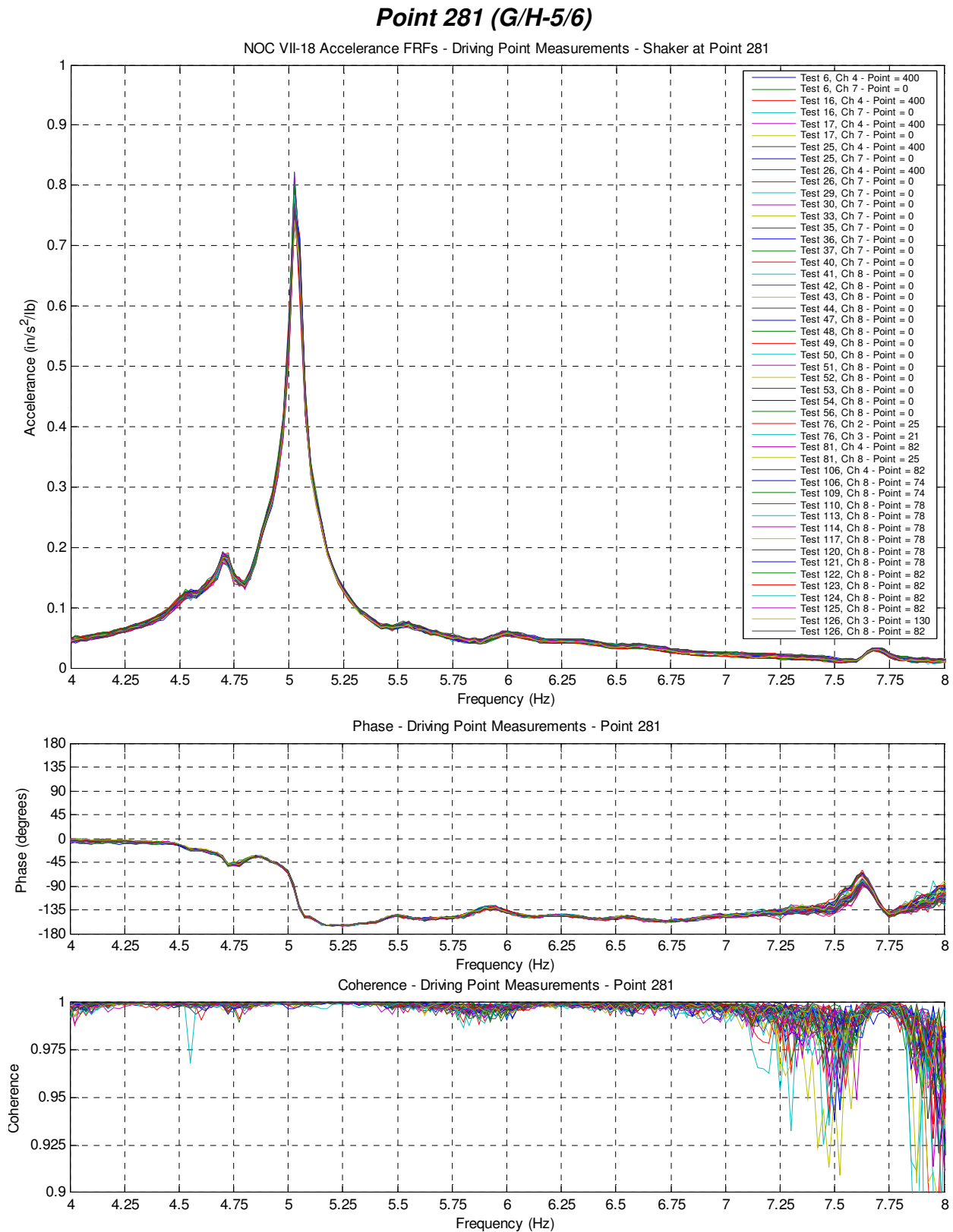


Figure E.17: NOC VII-18 Driving Point Accelerance FRF and Coherence (Point 281)

Point 333 (F/G-5/6)

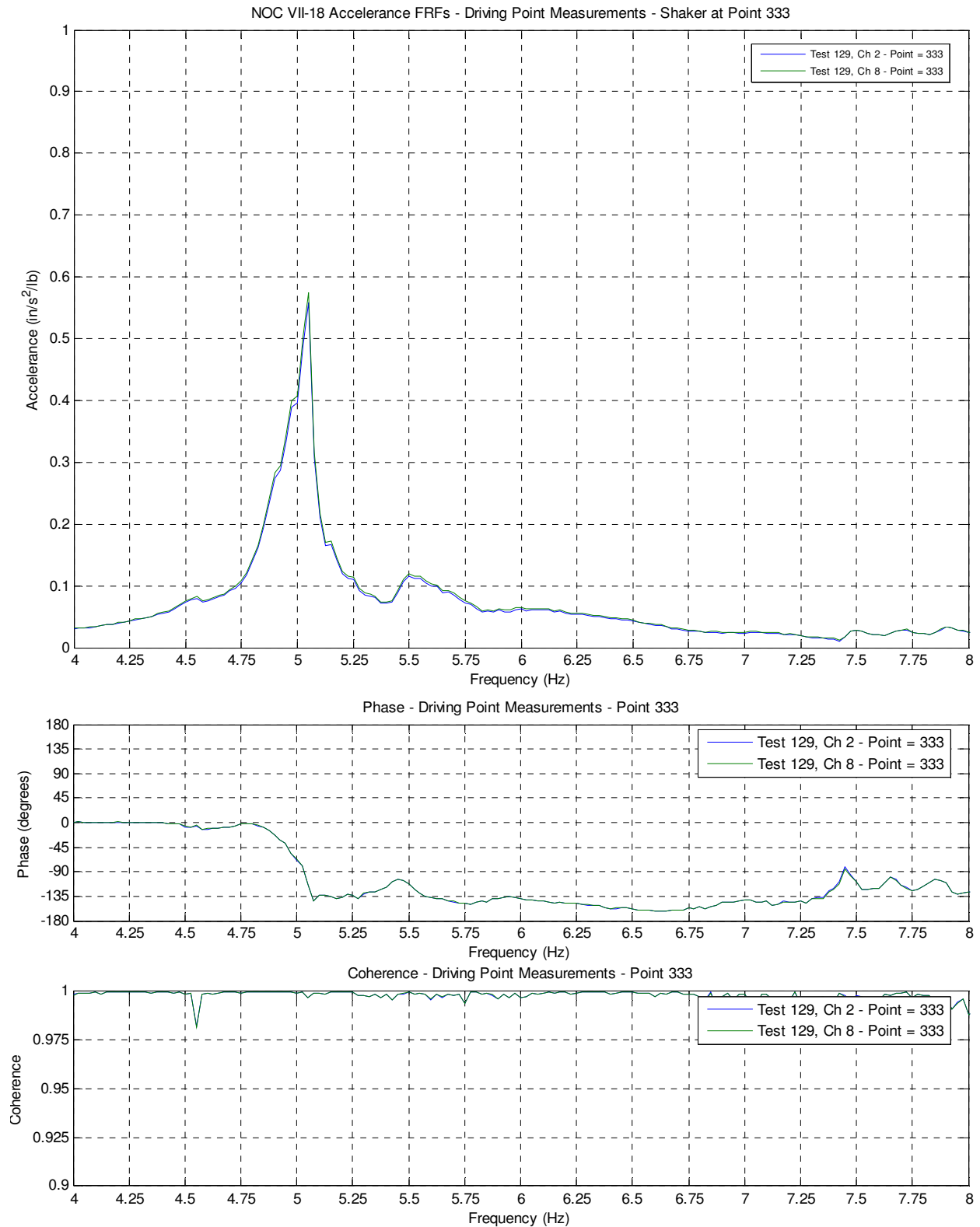


Figure E.18: NOC VII-18 Driving Point Accelerance FRF and Coherence (Point 333)

APPENDIX F

ME'SCOPEVES MODAL PARAMETER ESTIMATION – NOC VII

NOC VII-24 ME'scope Modal Parameter Estimation:

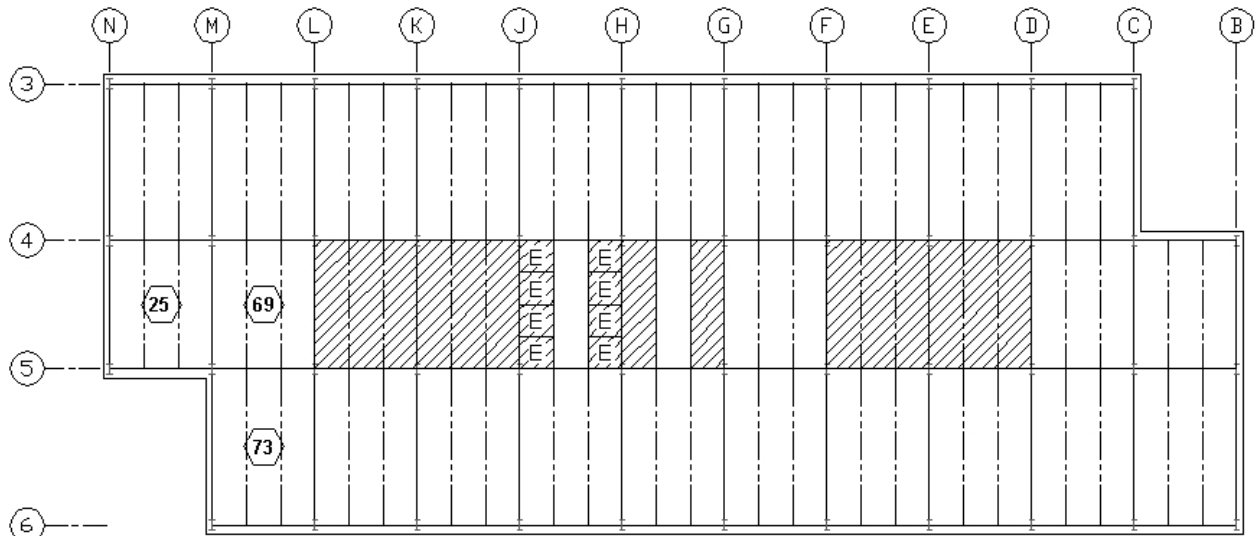
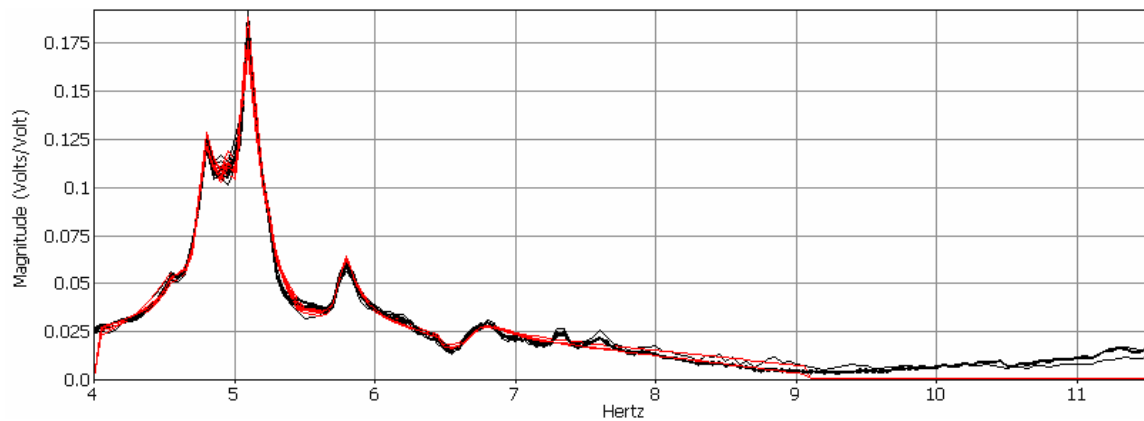


Figure F.1: NOC VII-24 Excitation Locations

NOC VII-24 Driving Point Accelerance FRF Curve Fitting:



Frequency (Hz)	Damping (%)
4.57	2.00
4.81	1.60
4.91	1.80
5.09	1.00
5.79	1.01
6.72	2.00

Figure F.2: NOC VII-24 Driving Point FRFs with Curve Fit Overlay (Point 73)

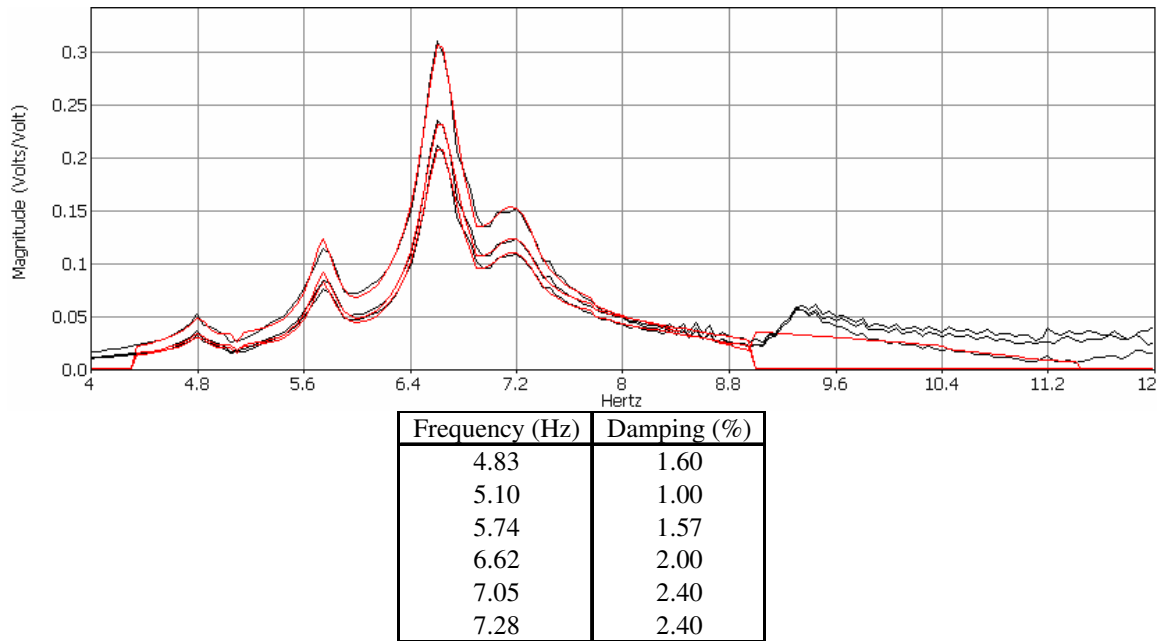


Figure F.3: NOC VII-24 Driving Point FRFs with Curve Fit Overlay (Point 69)

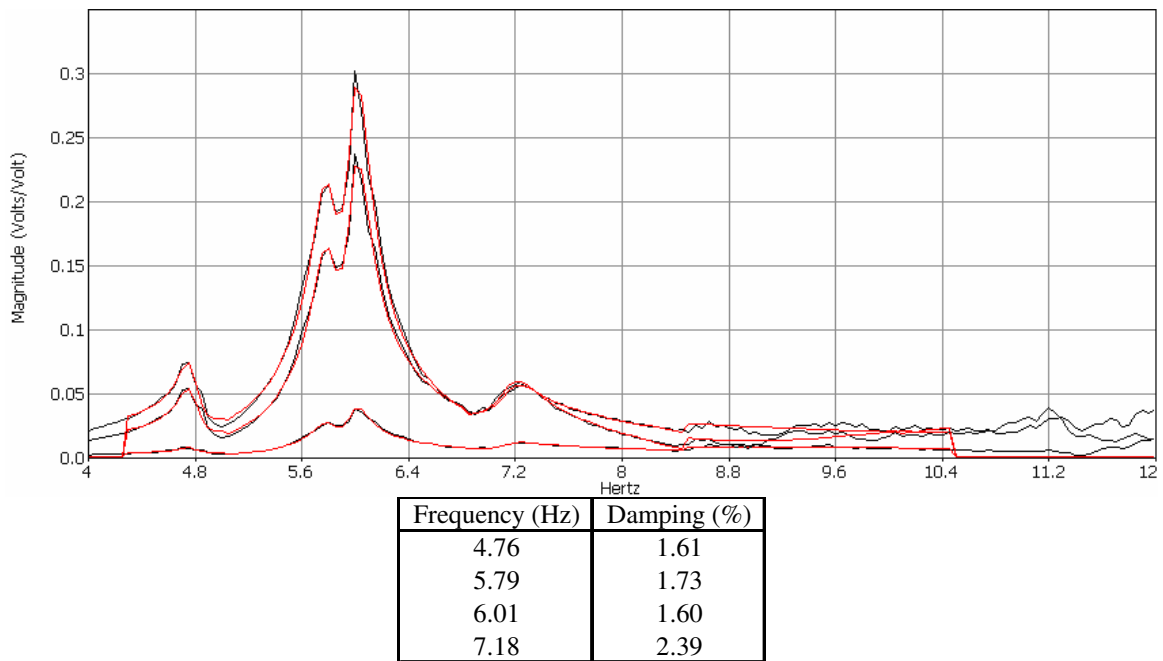


Figure F.4: NOC VII-24 Driving Point FRFs with Curve Fit Overlay (Point 25)

NOC VII-24 Curve Fit of Full Set of Accelerance FRFs:

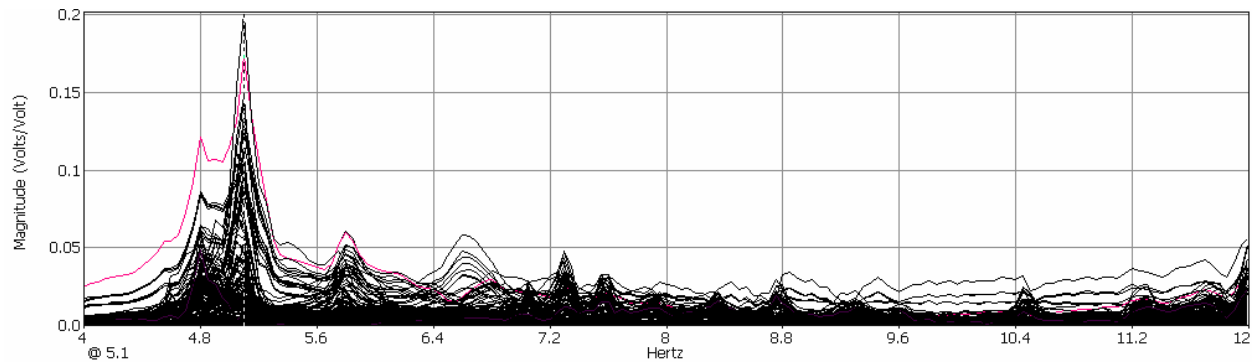
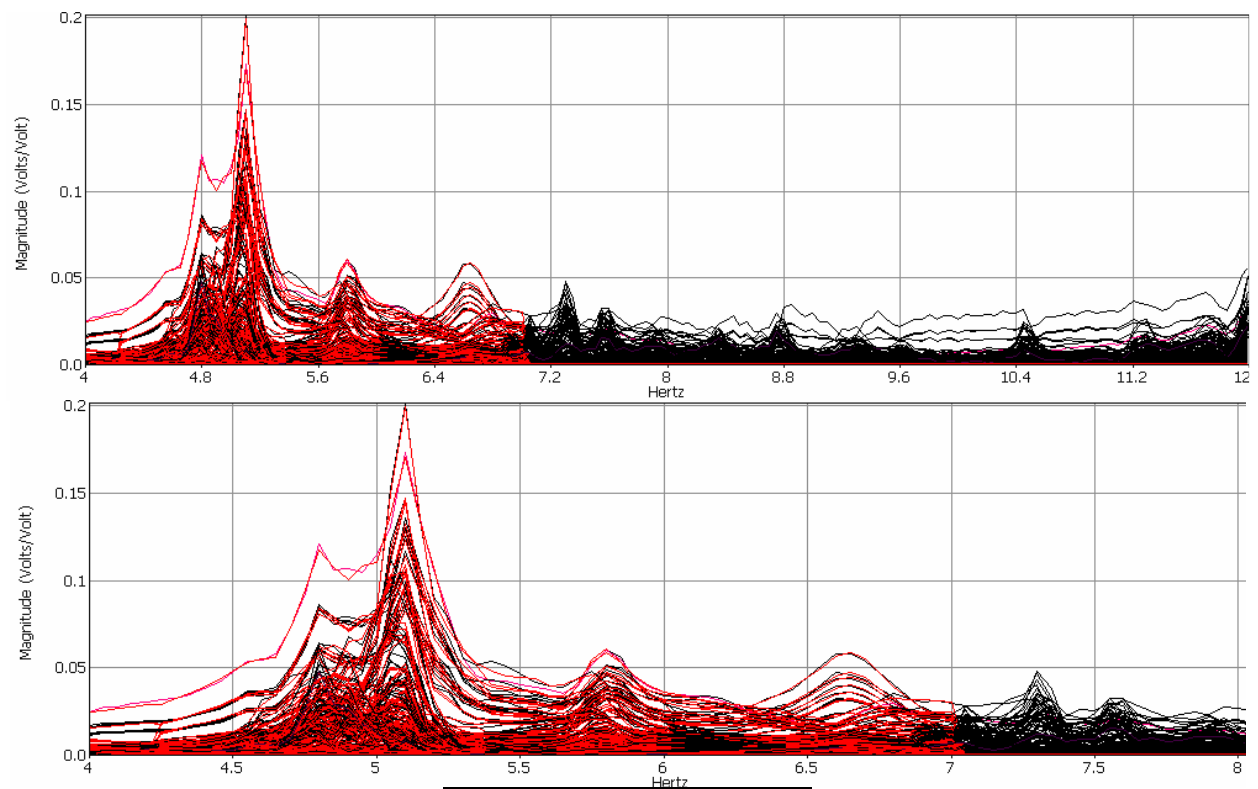
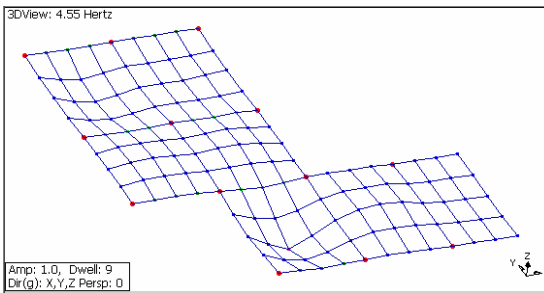
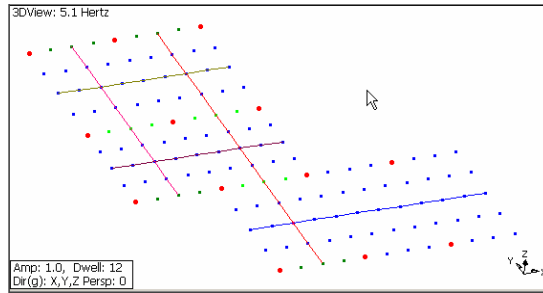
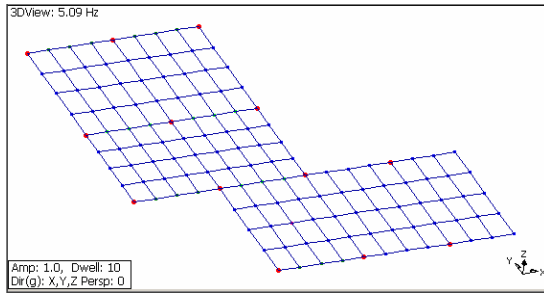
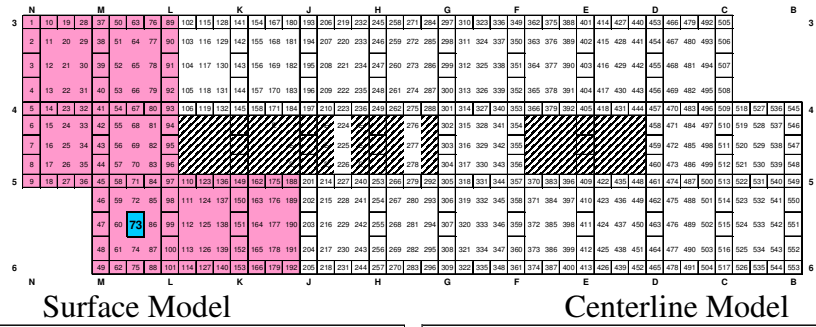


Figure F.5: NOC VII-24 All Accelerance FRFs (Point 73)

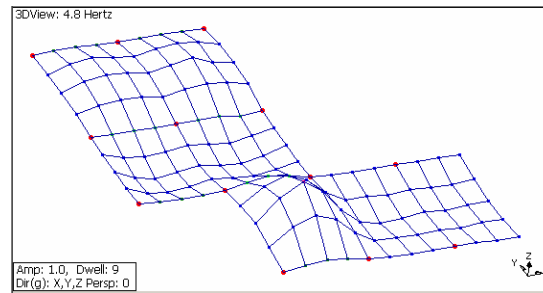


Frequency (Hz)	Damping (%)
4.58	2.00
4.82	1.60
4.91	1.80
5.09	1.00
5.79	1.60
6.66	2.22

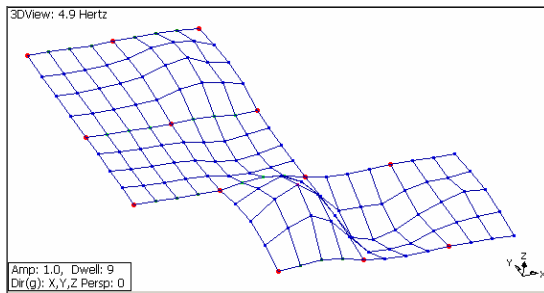
Figure F.6: NOC VII-24 All Accelerance FRFs with Curve Fit Overlay (Point 73)



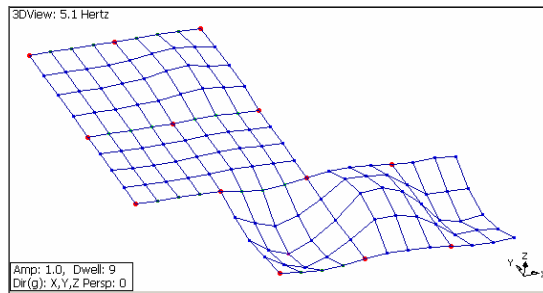
4.55 Hz



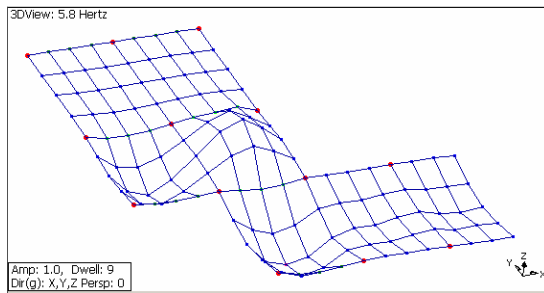
4.80 Hz



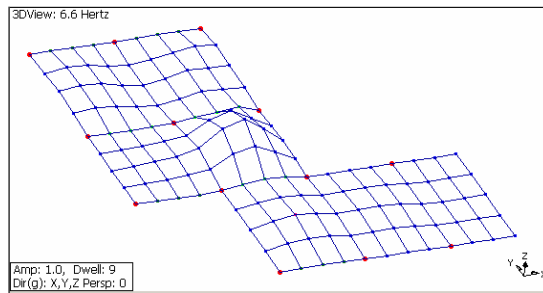
4.90 Hz



5.10 Hz



5.80 Hz



6.60 Hz

Figure F.8: NOC VII-24 *Unscaled* 10-Bay Centerline ODSs – Forcing at Point 73

NOC VII-18 ME'scope Parameter Estimation:

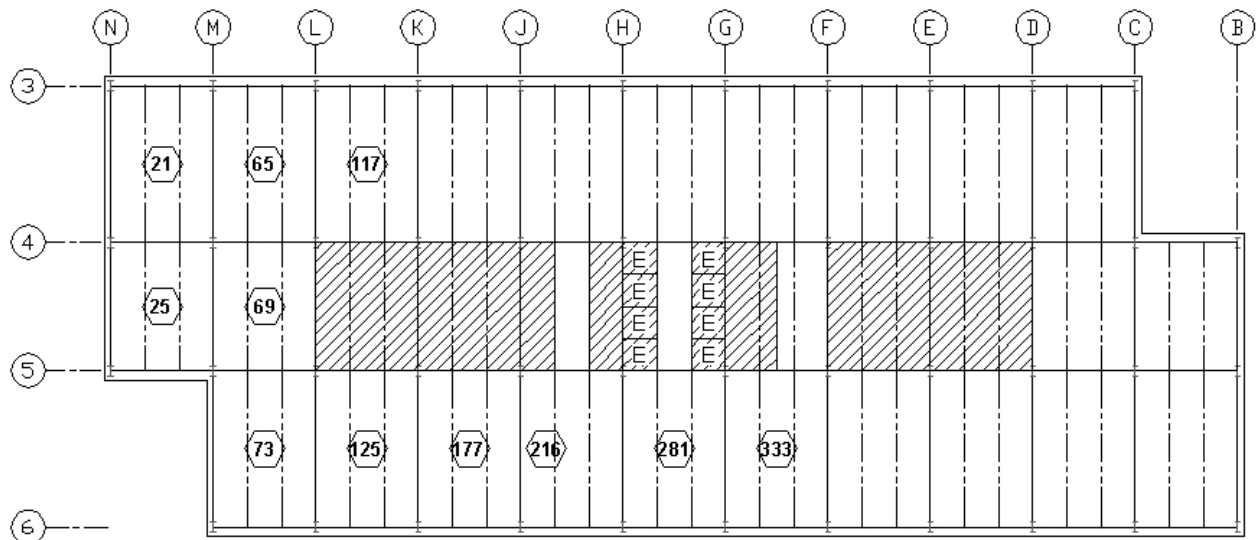


Figure F.9: NOC VII-18 Excitation Locations

NOC VII-18 Driving Point Accelerance FRF Curve Fitting:

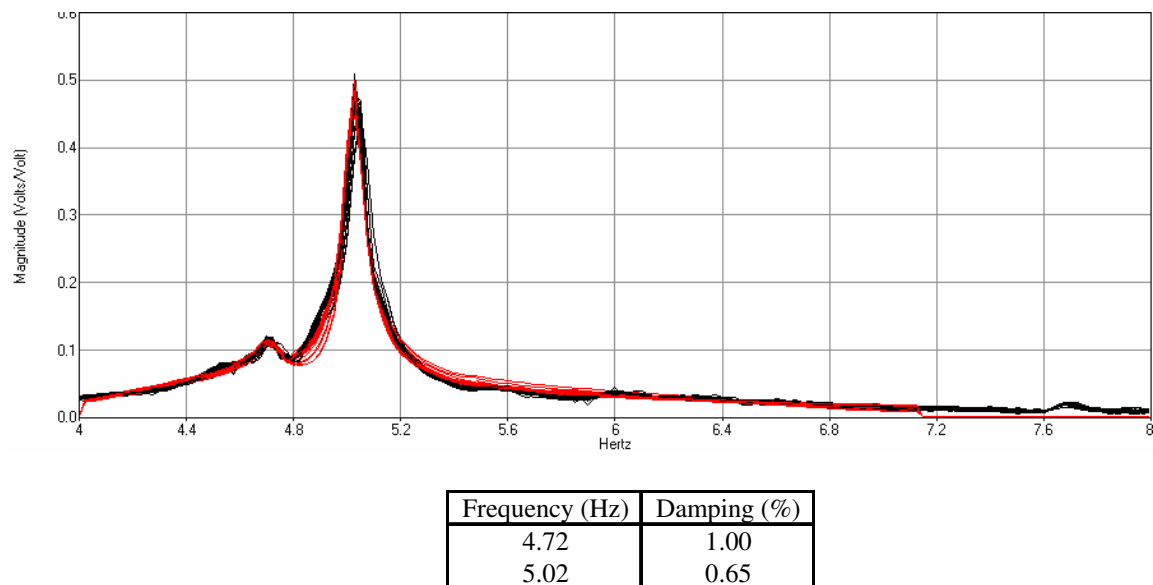


Figure F.10: NOC VII-18 Driving Point FRFs with Curve Fit Overlay (Point 281)

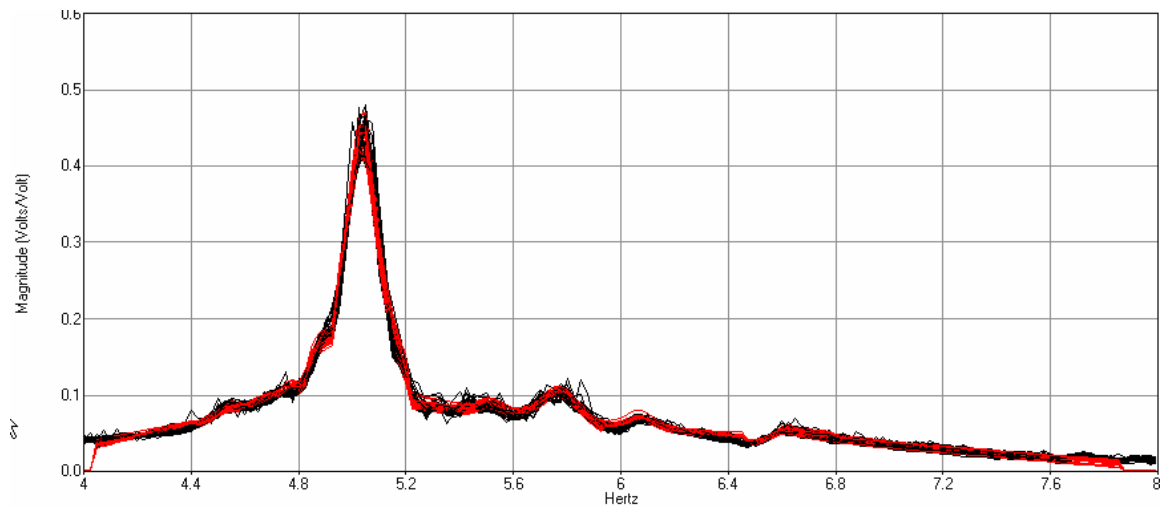


Figure F.11: NOC VII-18 Driving Point FRFs with Curve Fit Overlay (Point 73)

Driving Point FRFs		All FRFs	
Frequency (Hz)	Damping (%)	Frequency (Hz)	Damping (%)
4.55	0.85	4.58	0.86
4.75	0.85	n/a	n/a
4.83	0.88	4.8	0.65
5.04	1.15	5.05	1.16
5.51	1.00	5.48	1.00
5.76	1.40	5.76	1.40
6.06	1.10	6.08	1.10
6.59	1.00	6.56	1.45

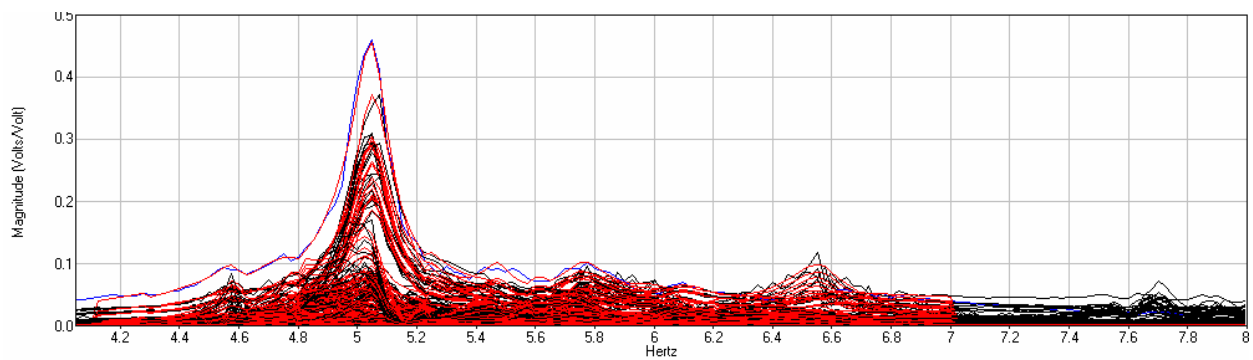


Figure F.12: NOC VII-18 All Accelerance FRFs with Curve Fit Overlay (Point 73)

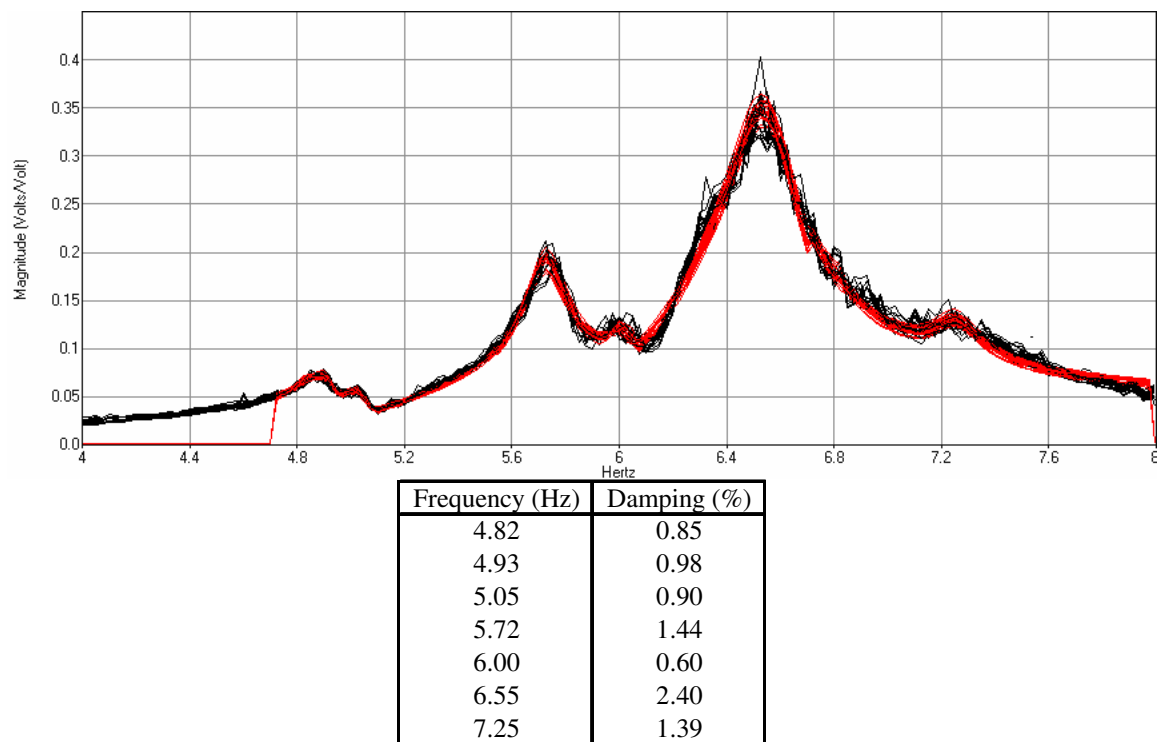


Figure F.13: NOC VII-18 Driving Point FRFs with Curve Fit Overlay (Point 69)

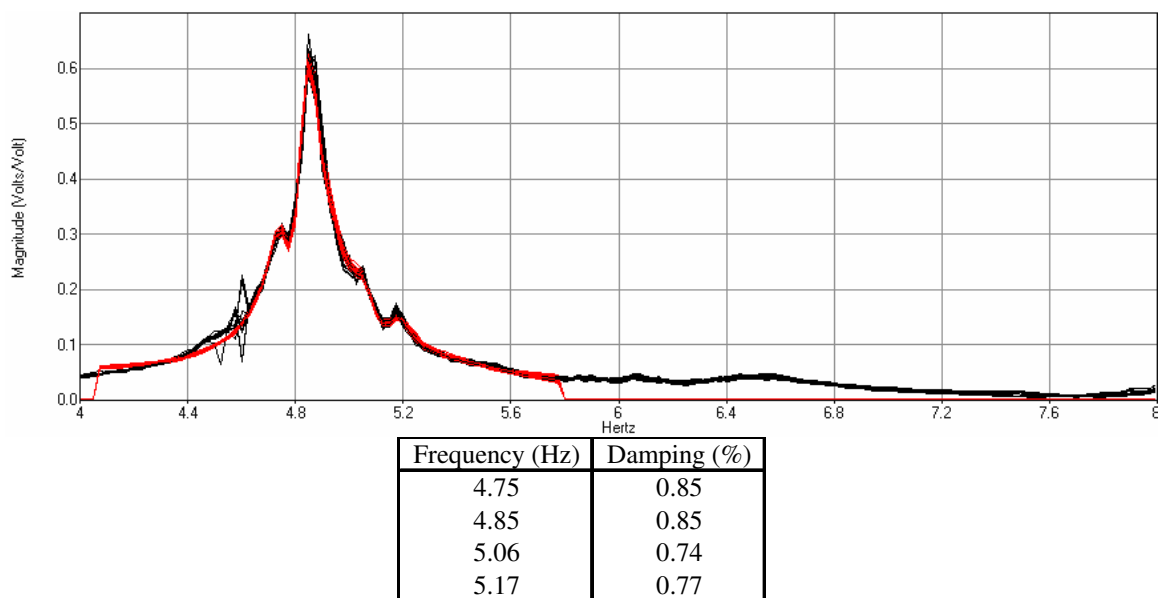
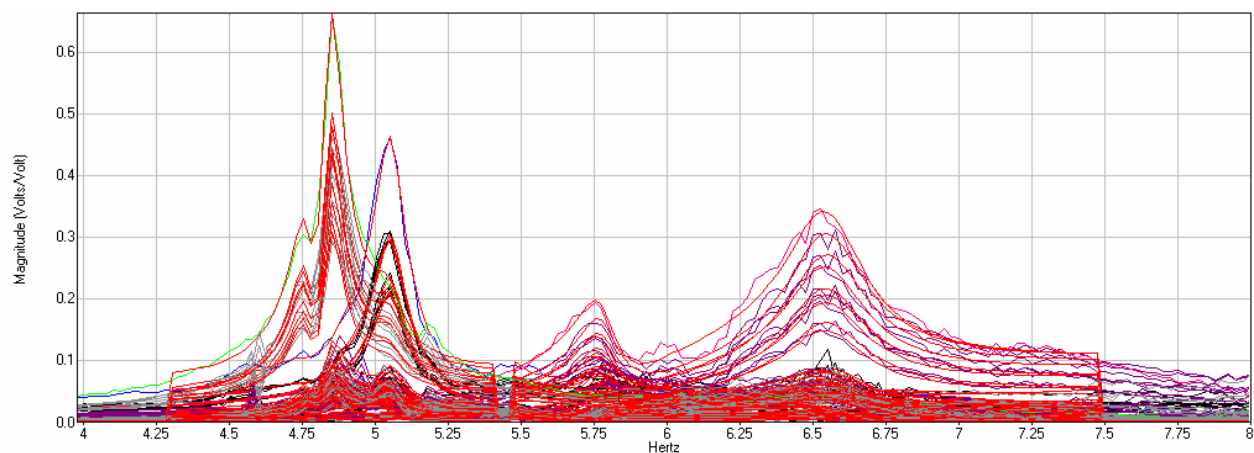
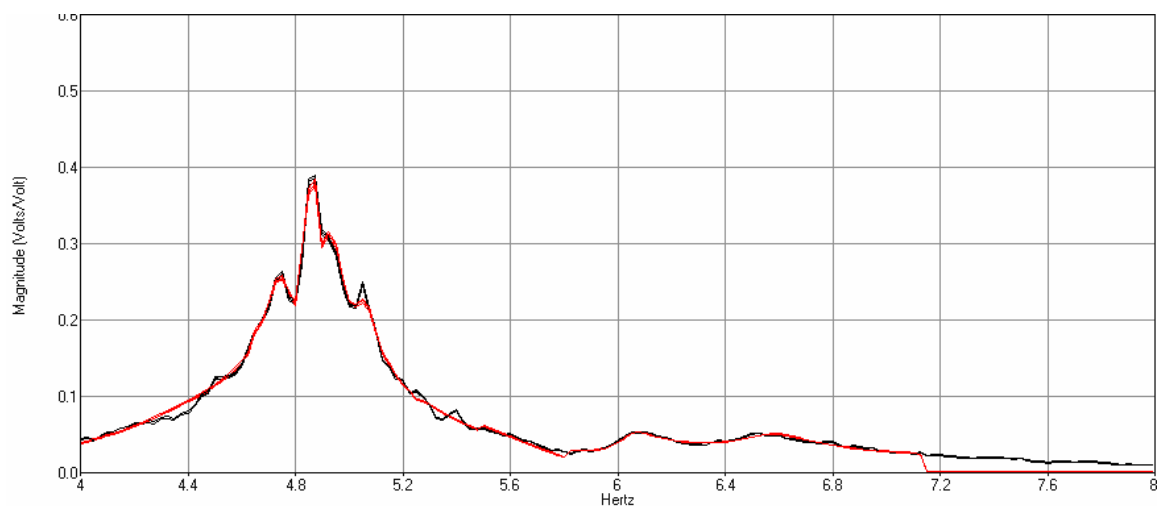


Figure F.14: NOC VII-18 Driving Point FRFs with Curve Fit Overlay (Point 65)



Mode	Frequency (Hz)	Point 65	Point 69	Point 73	Frequency (Hz)	Damping (%)
1	4.76	2.4	0.5	0.3	4.76	0.85
2	4.85	5.6	1.1	0.6	4.85	0.69
3	5.05	1.1	1.1	6.2	5.05	1.05
4	5.77	0.4	2.6	1.5	5.77	1.24
5	6.54	3.2	10.0	3.0	6.54	2.10

Figure F.15: NOC VII-18 Multi-Ref Accelerance FRFs with Curve Fit Overlay (65, 69, 73)



Frequency (Hz)	Damping (%)
4.74	0.85
4.87	0.85
4.95	1.00
5.06	1.10
6.05	1.19
6.58	2.21

Figure F.16: NOC VII-18 Driving Point FRFs with Curve Fit Overlay (Point 21)

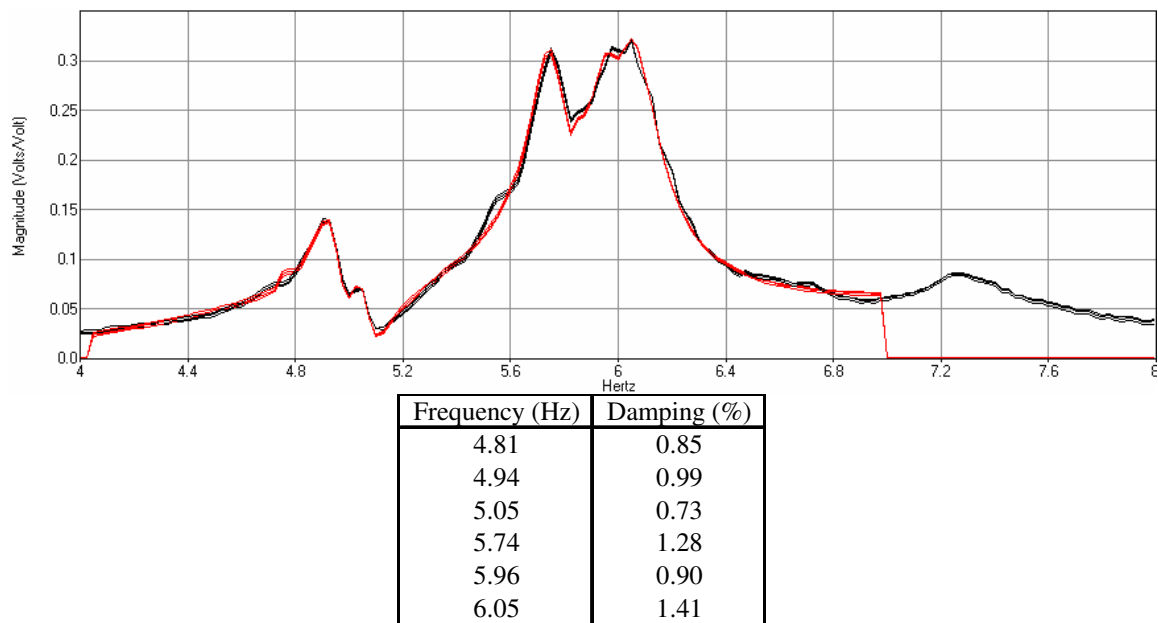


Figure F.17: NOC VII-18 Driving Point FRFs with Curve Fit Overlay (Point 25)

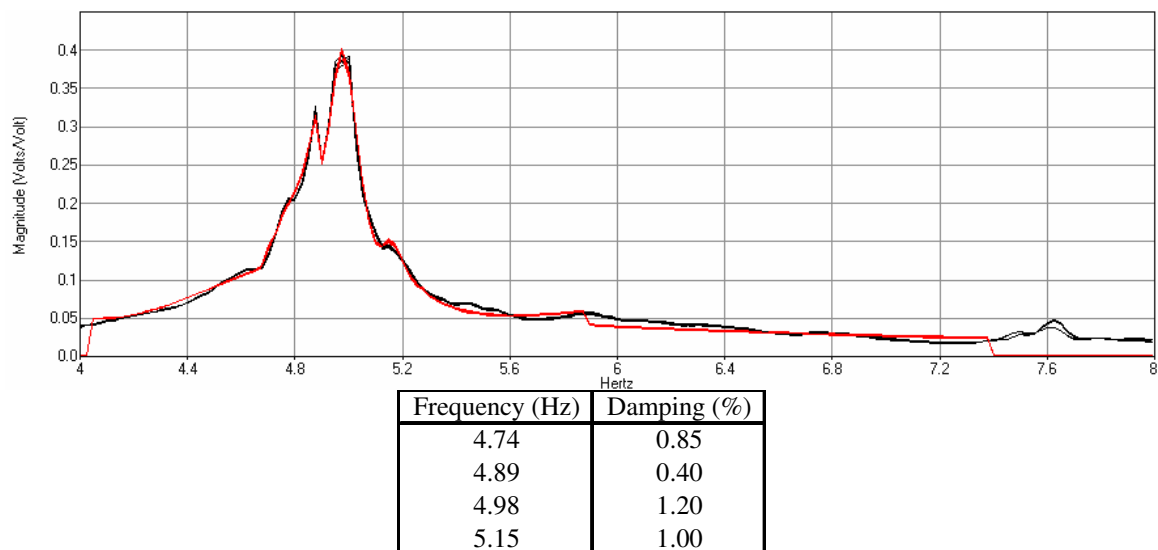


Figure F.18: NOC VII-18 Driving Point FRFs with Curve Fit Overlay (Point 117)

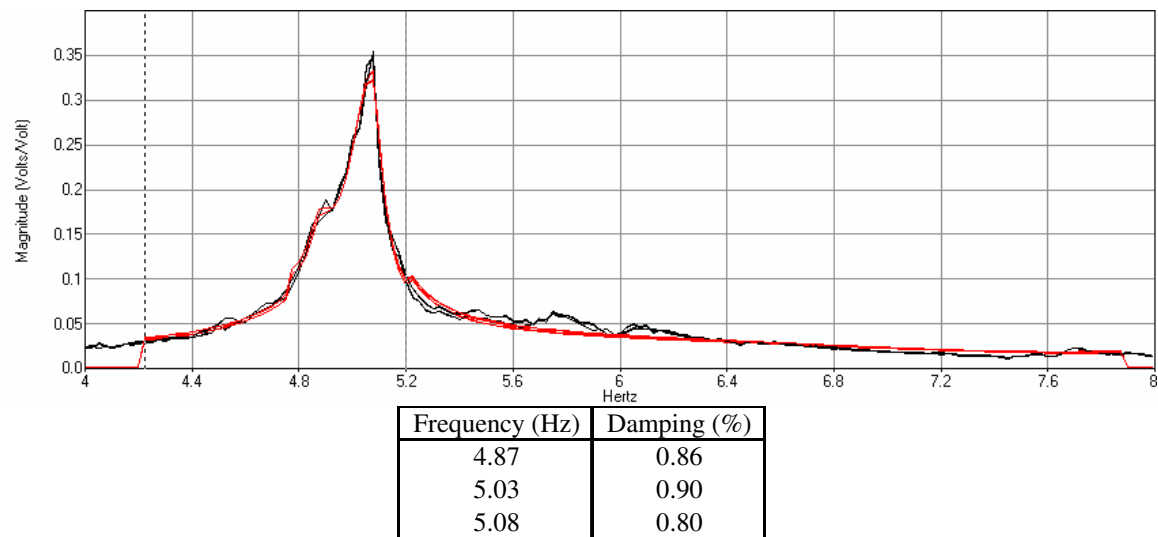


Figure F.19: NOC VII-18 Driving Point FRFs with Curve Fit Overlay (Point 125)

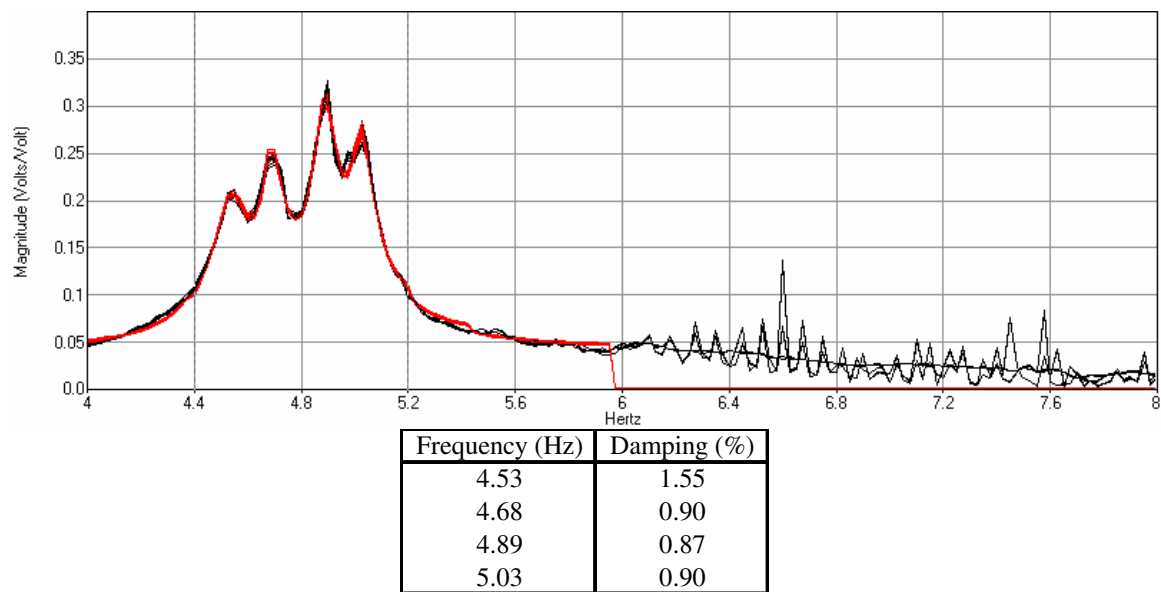


Figure F.20: NOC VII-18 Driving Point FRFs with Curve Fit Overlay (Point 177)

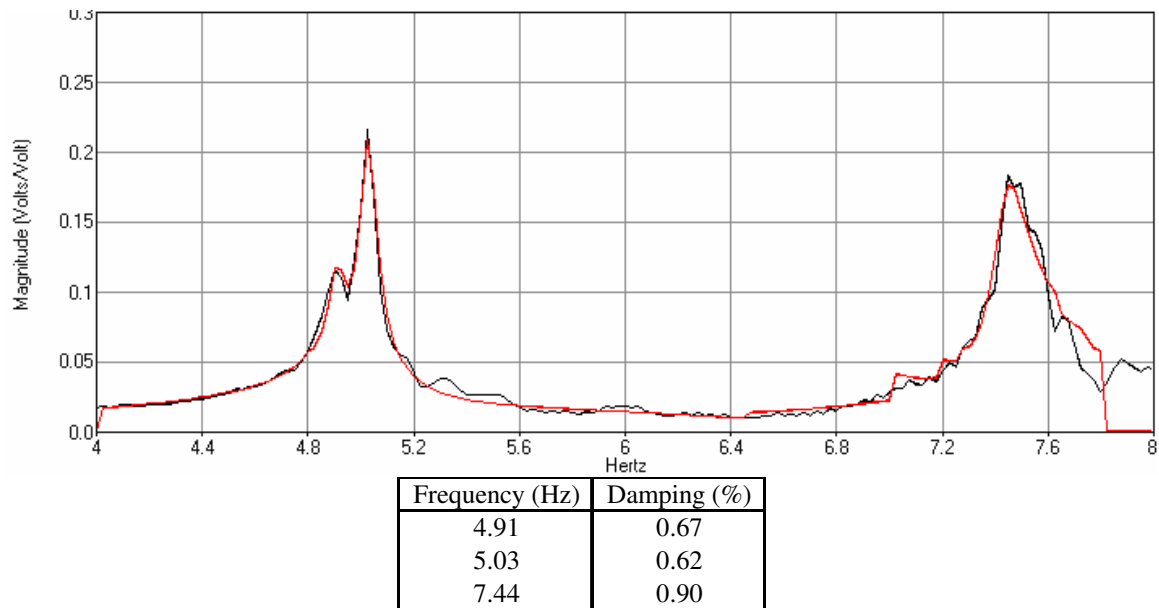


Figure F.21: NOC VII-18 Driving Point FRFs with Curve Fit Overlay (Point 216)

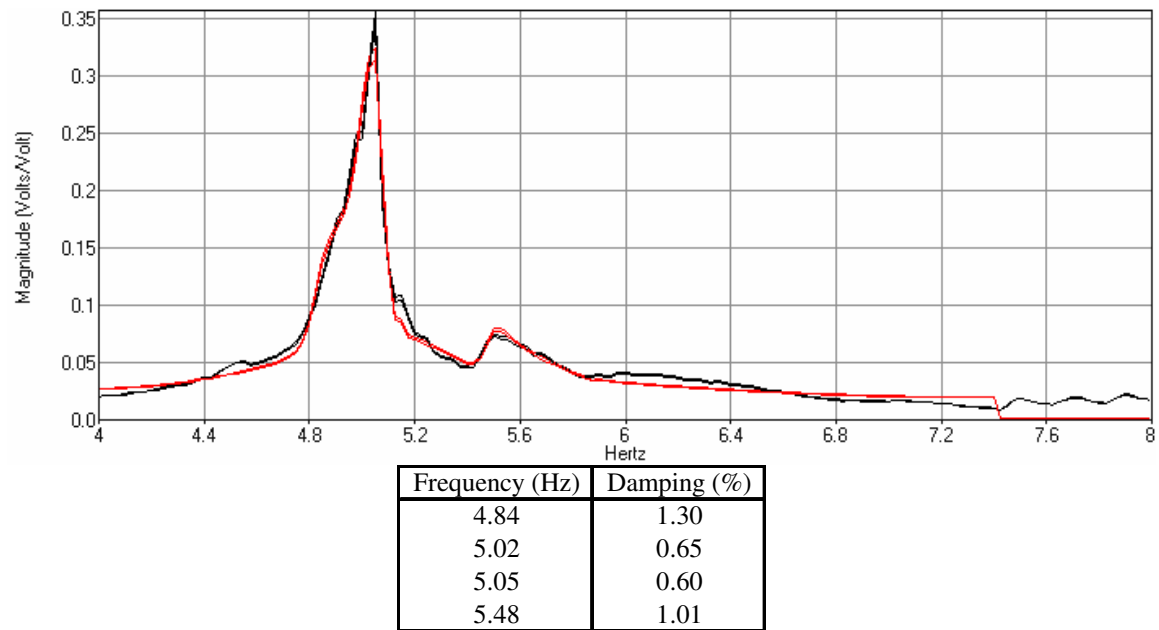


Figure F.22: NOC VII-18 Driving Point FRFs with Curve Fit Overlay (Point 333)

APPENDIX G

DECAY MEASUREMENTS AND DECAY CURVE FIT ANALYSES – NOC VII-18

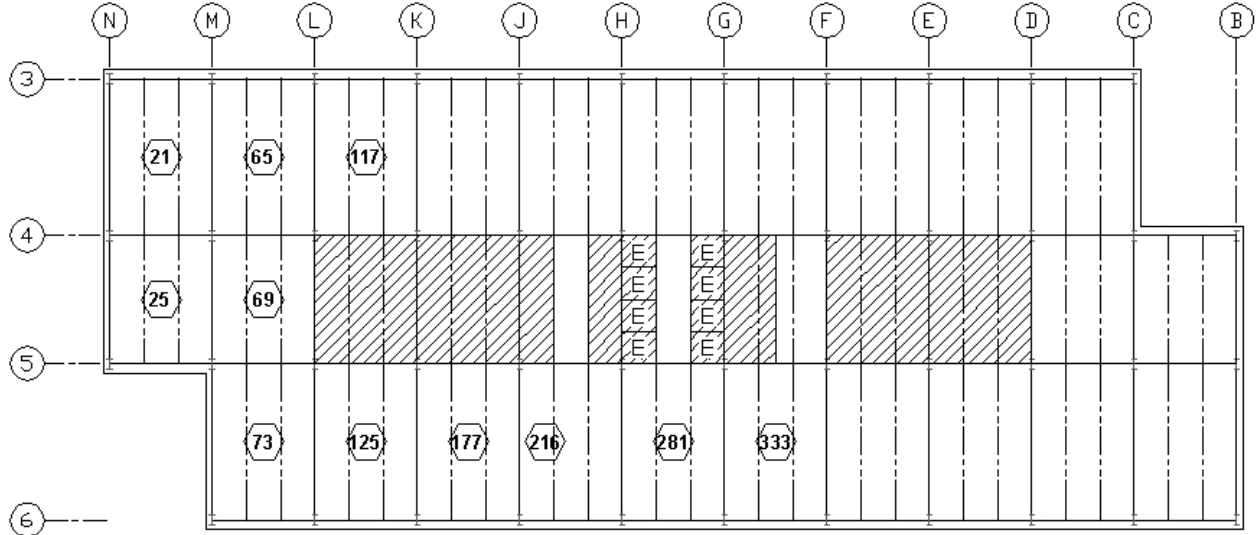
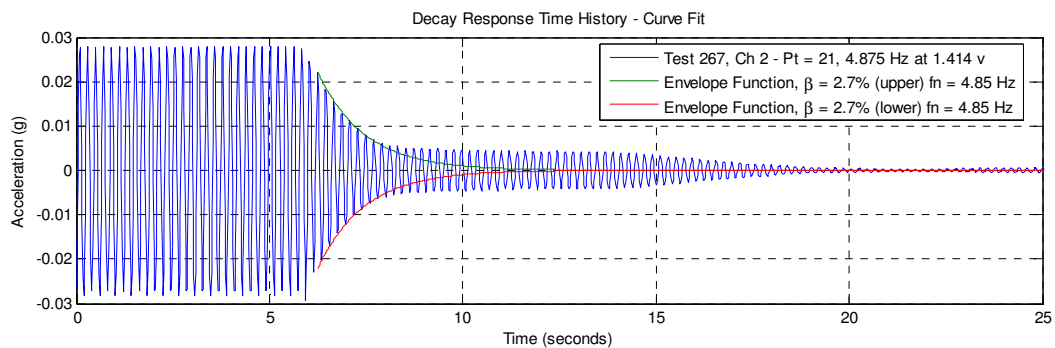
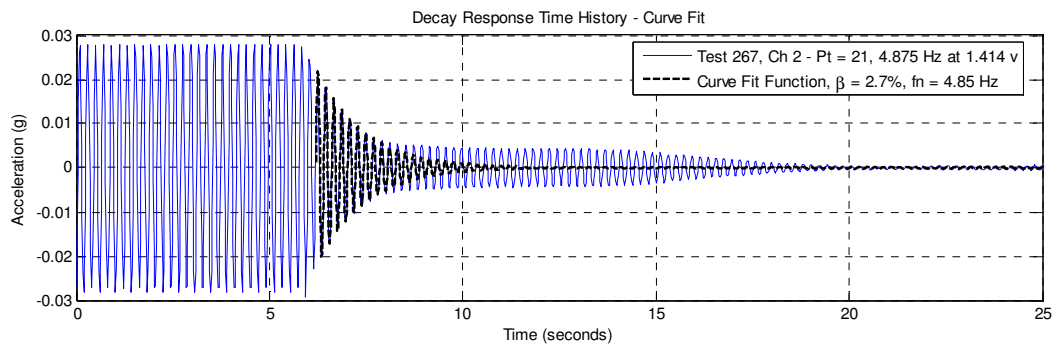
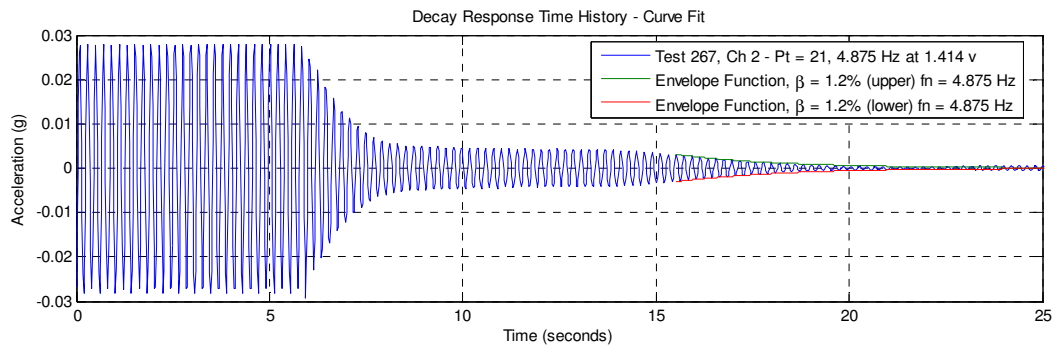
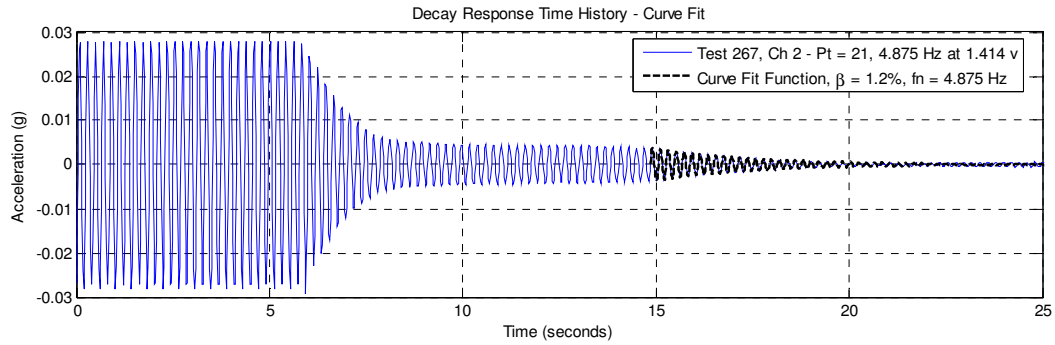


Figure G.1: NOC VII-18 Excitation Locations

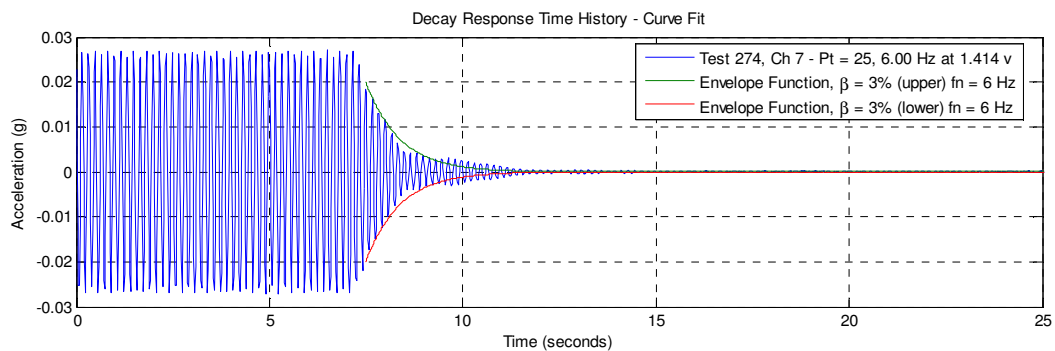
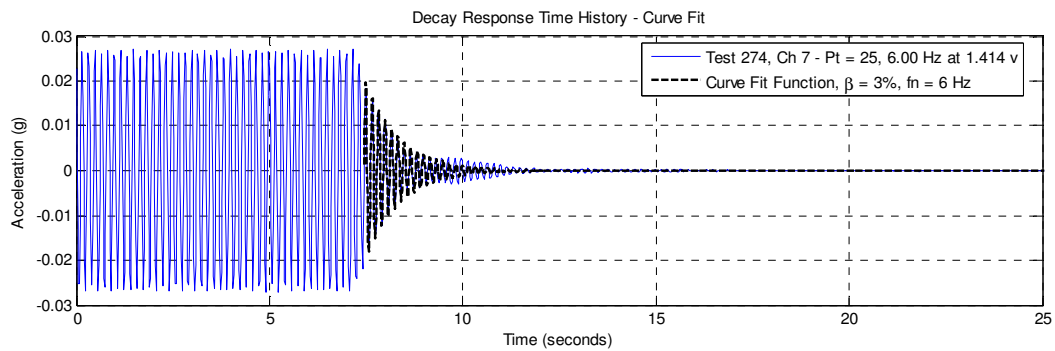
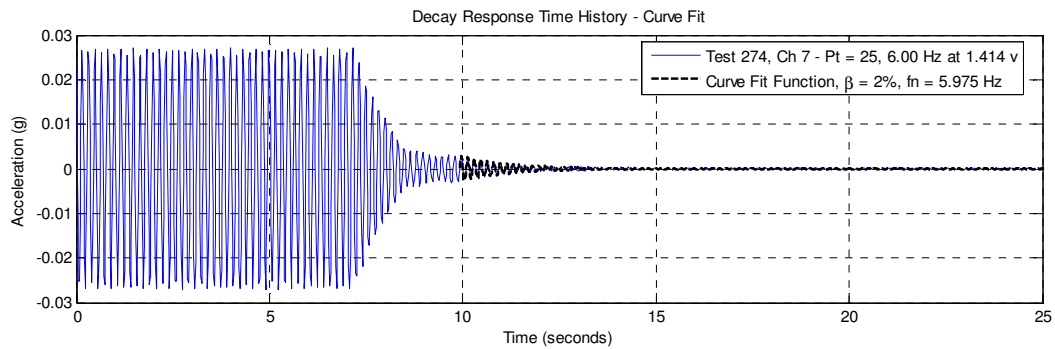
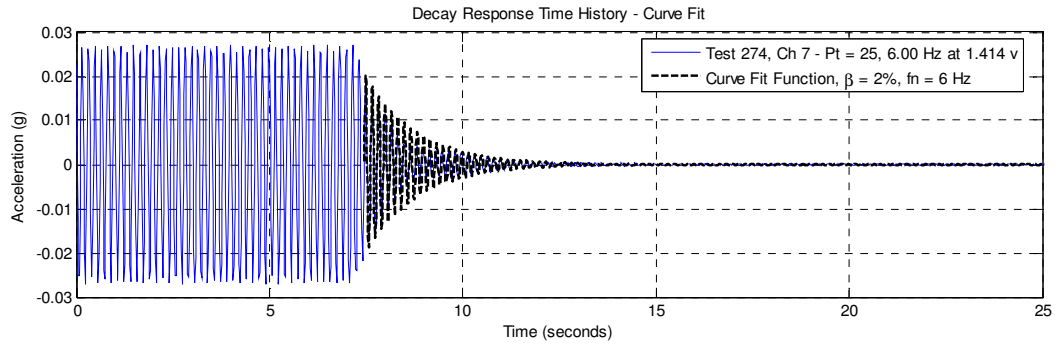
Table G.1: NOC VII-18 Summary of Decay Curve Fit Damping Estimates

Excitation Location(s)	Type of Damping Estimate	Excitation Level (volts)	Decay Frequency (Hz)	Estimated Damping Ratio	Curve Fit Portion of Decay Curve
Point 21	Decay Curve Fit Estimate from 4.875 Hz Sinusoid	1.414	4.875	1.20%	LOWER
Point 21	Decay Curve Fit Estimate from 4.875 Hz Sinusoid	1.414	4.85	2.70%	UPPER
Point 25	Decay Curve Fit Estimate from 6.00 Hz Sinusoid	1.414	5.975	2.00%	LOWER
Point 25	Decay Curve Fit Estimate from 6.00 Hz Sinusoid	1.414	6.00	3.00%	UPPER
Point 65	Decay Curve Fit Estimate from 4.875 Hz Sinusoid	0.707	4.85	0.65%	UPPER
Point 65	Decay Curve Fit Estimate from 4.875 Hz Sinusoid	1.414	4.85	0.65%	
Point 65	Decay Curve Fit Estimate from 4.875 Hz Sinusoid	3.0	4.85	0.65%	
Point 65	Decay Curve Fit Estimate from 4.875 Hz Sinusoid	3.0	4.85	0.91%	
Point 73	Decay Curve Fit Estimate from 5.025 Hz Sinusoid	0.707	5.045	1.15%	
Point 73	Decay Curve Fit Estimate from 5.025 Hz Sinusoid	1.414	5.045	1.05%	
Point 73	Decay Curve Fit Estimate from 5.025 Hz Sinusoid	2.30	5.05	0.95%	
Point 117	Decay Curve Fit Estimate from 4.975 Hz Sinusoid	1.414	4.982	0.95%	LOWER
Point 117	Decay Curve Fit Estimate from 4.975 Hz Sinusoid	1.414	4.982	1.20%	UPPER
Point 125	Decay Curve Fit Estimate from 5.05 Hz Sinusoid	2.30	5.057	0.50%	LOWER
Point 125	Decay Curve Fit Estimate from 5.05 Hz Sinusoid	2.30	5.025	1.20%	UPPER
Point 216	Decay Curve Fit Estimate from 5.025 Hz Sinusoid	2.30	5.020	0.60%	
Point 333	Decay Curve Fit Estimate from 5.05 Hz Sinusoid	2.30	5.04	0.80%	UPPER
Point 333	Decay Curve Fit Estimate from 5.05 Hz Sinusoid	2.30	5.025	0.85%	
Point 333	Decay Curve Fit Estimate from 5.05 Hz Sinusoid	2.30	5.04	0.65%	
Point 281	Decay Curve Fit Estimate from 5.025 Hz Sinusoid	0.3535	5.035	0.75%	
Point 281	Decay Curve Fit Estimate from 5.025 Hz Sinusoid	0.707	5.025	0.70%	
Point 281	Decay Curve Fit Estimate from 5.025 Hz Sinusoid	1.414	5.025	0.60%	
Point 281	Decay Curve Fit Estimate from 5.025 Hz Sinusoid	2.30	5.025	0.60%	

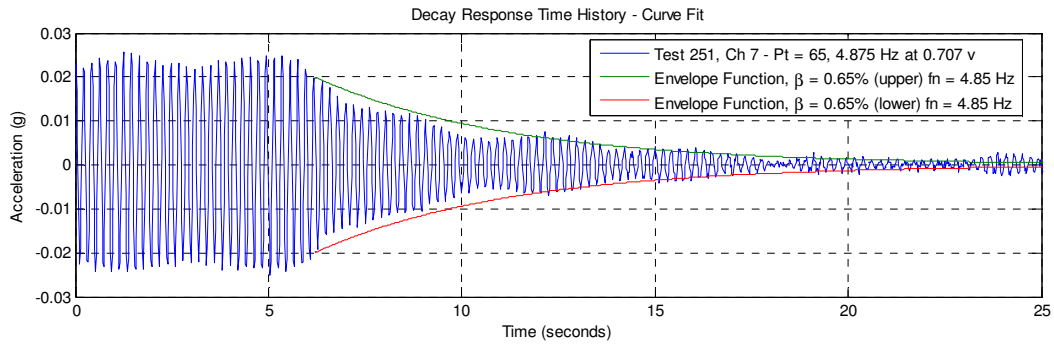
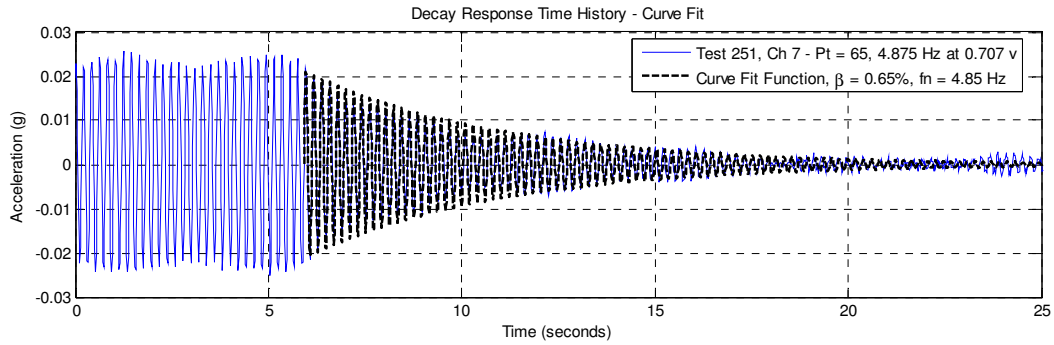
Driving Point 21 – Test 267 – Decay from Sine 4.875 Hz at 1.414 volts



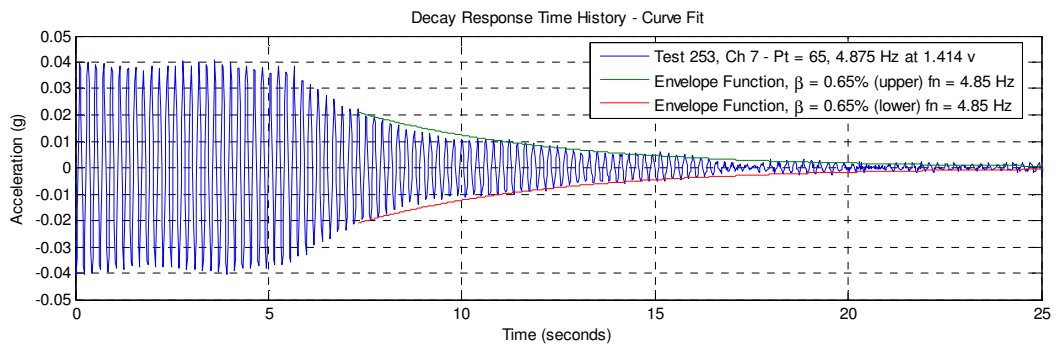
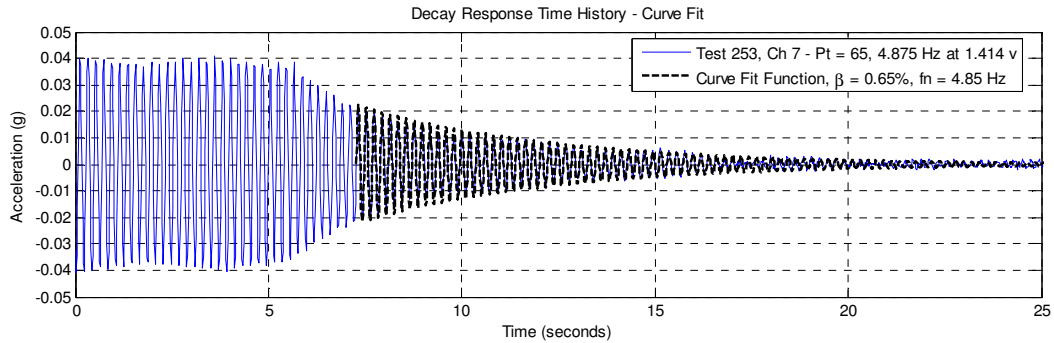
Driving Point 25 – Test 274 – Decay from Sine 6.00 Hz at 1.414 volts



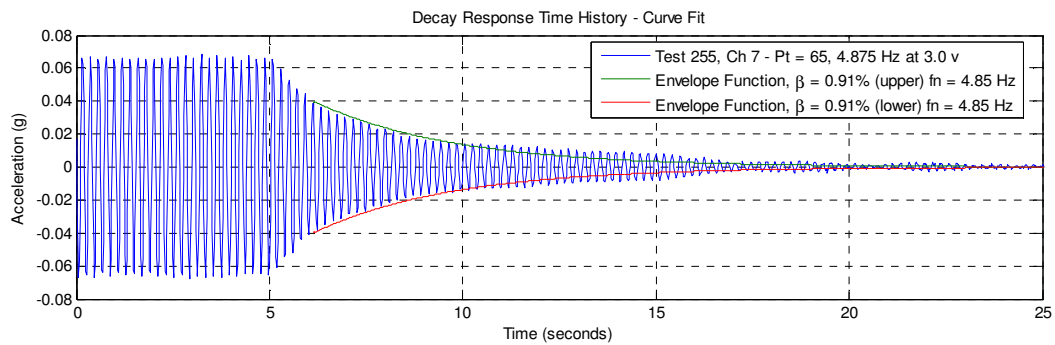
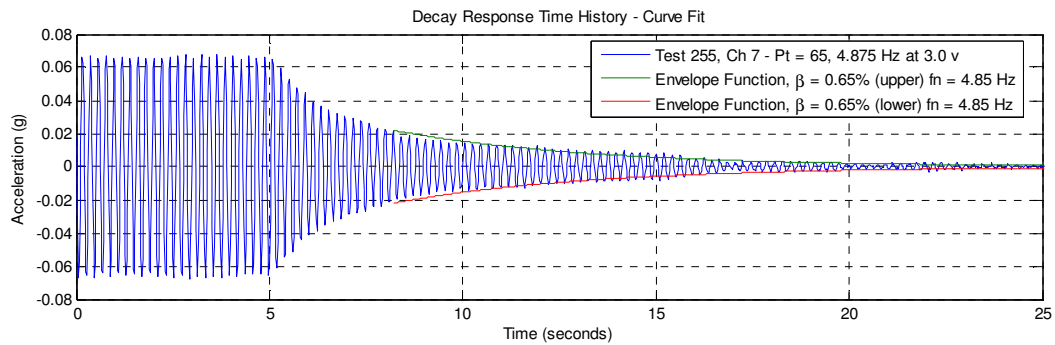
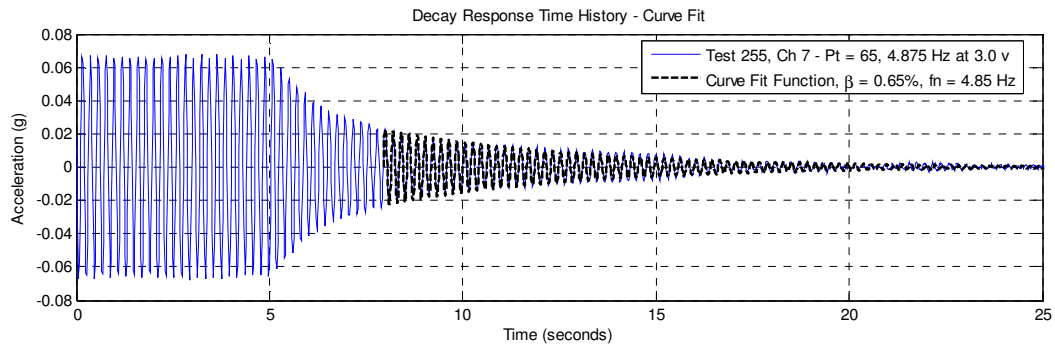
Driving Point 65 – Test 251 – Decay from Sine 4.875 Hz at 0.707 volts



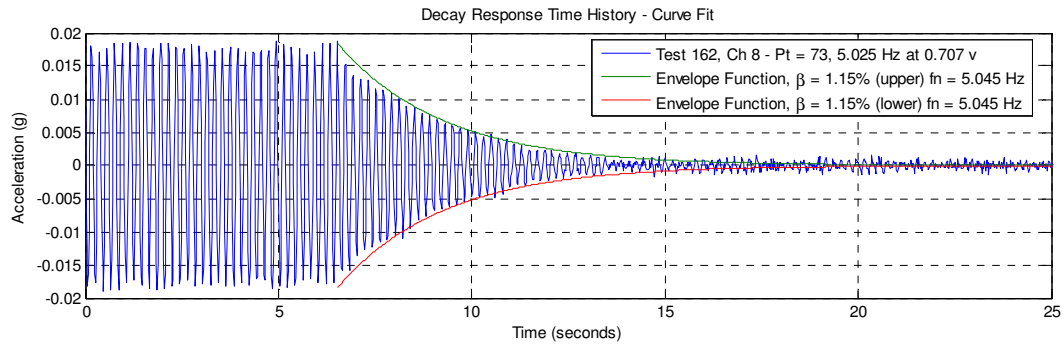
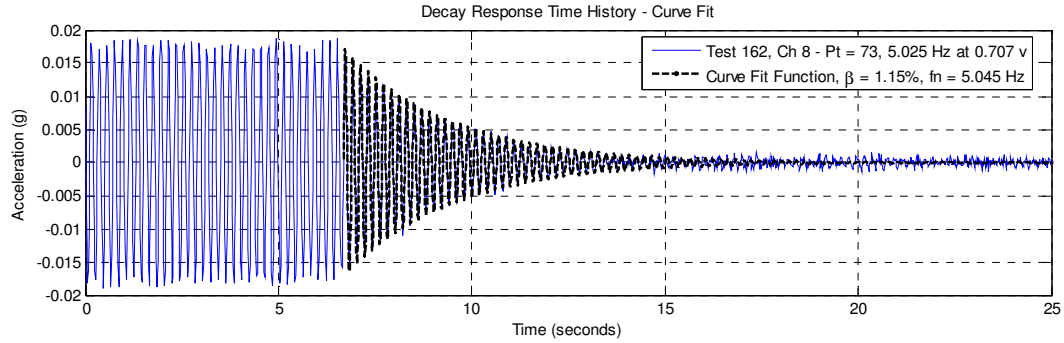
Driving Point 65 – Test 253 – Decay from Sine 4.875 Hz at 1.414 volts



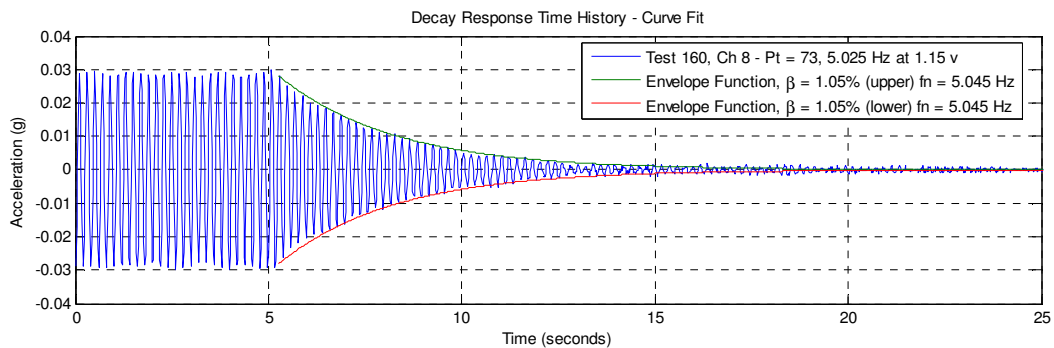
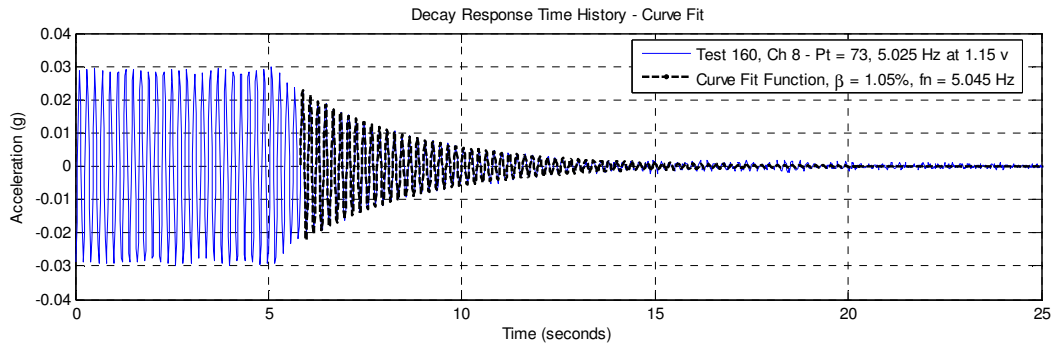
Driving Point 65 – Test 255 – Decay from Sine 4.875 Hz at 3.0 volts



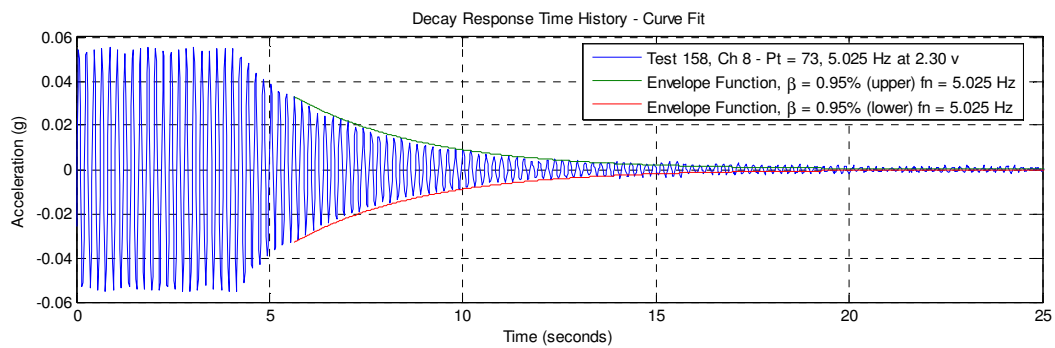
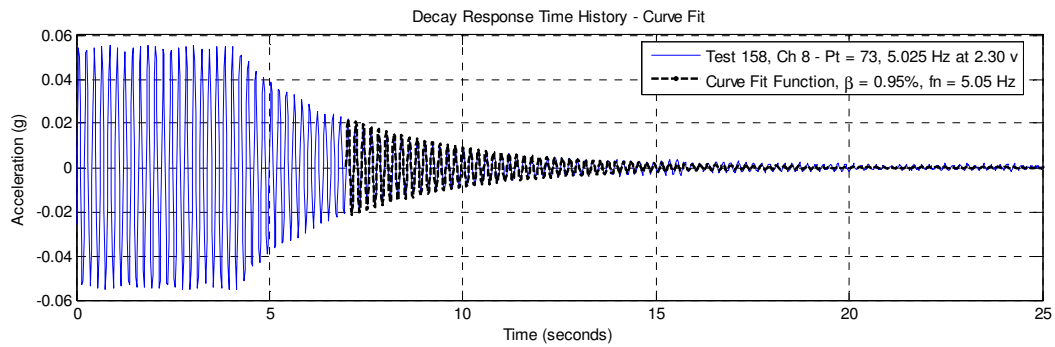
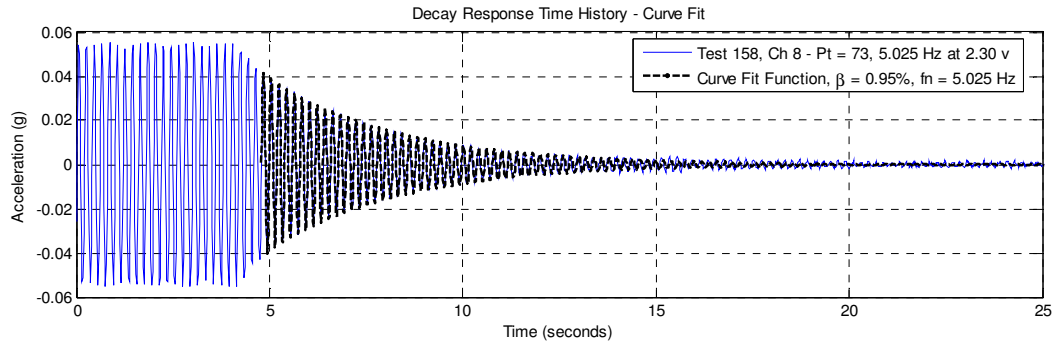
Driving Point 73 – Test 162 – Decay from Sine 5.025 Hz at 0.707 volts



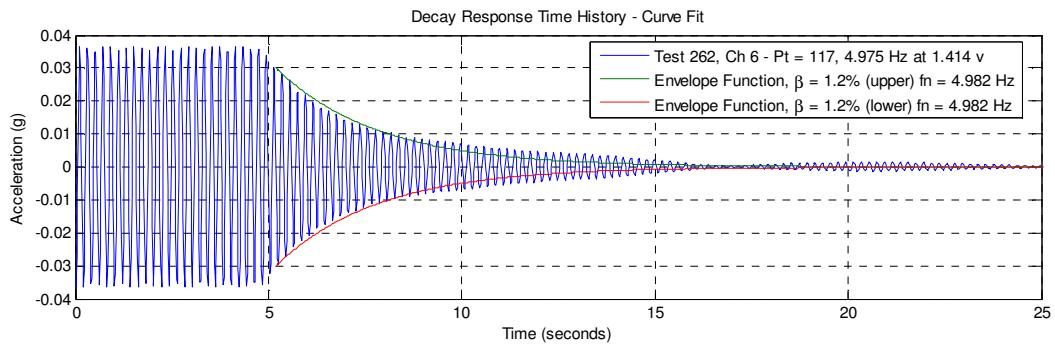
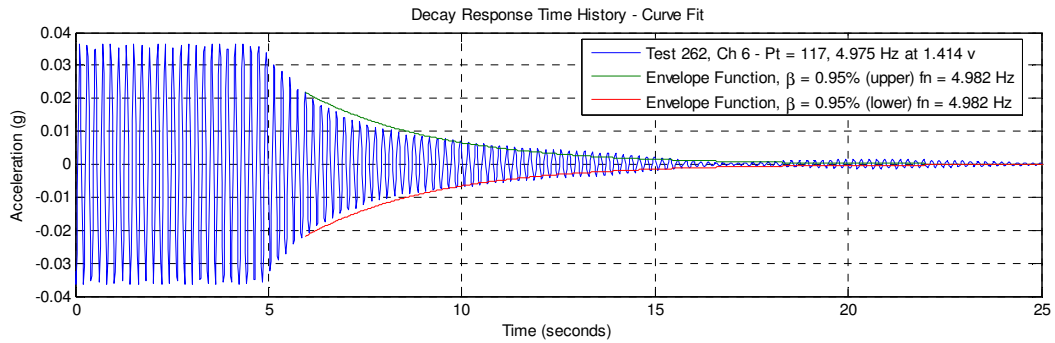
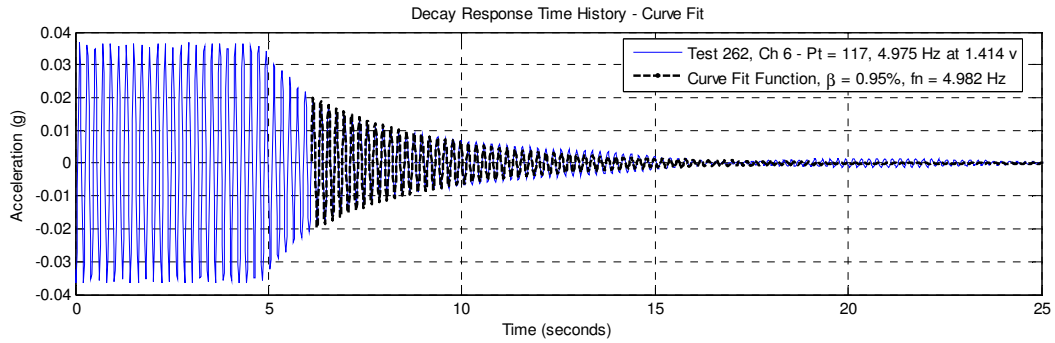
Driving Point 73 – Test 160 – Decay from Sine 5.025 Hz at 1.15 volts



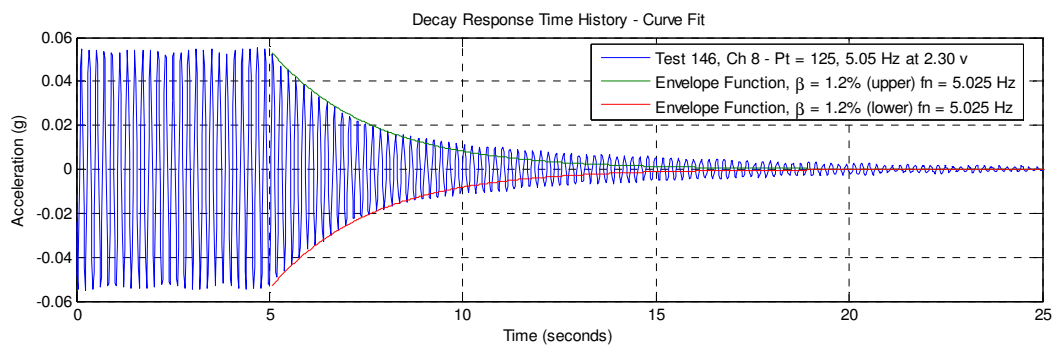
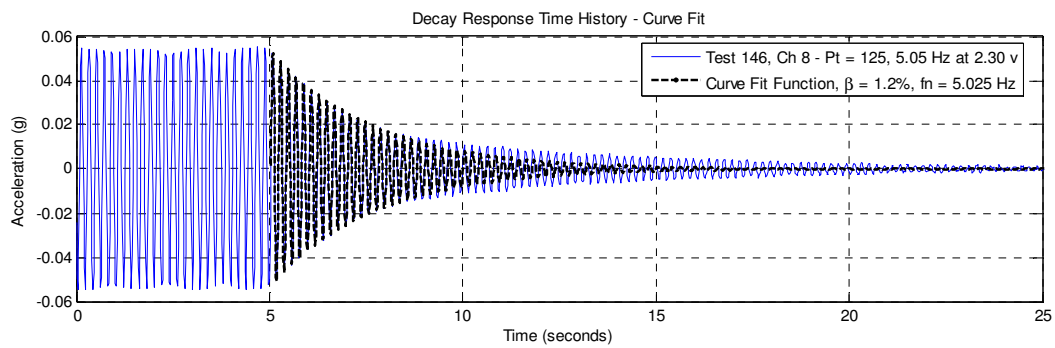
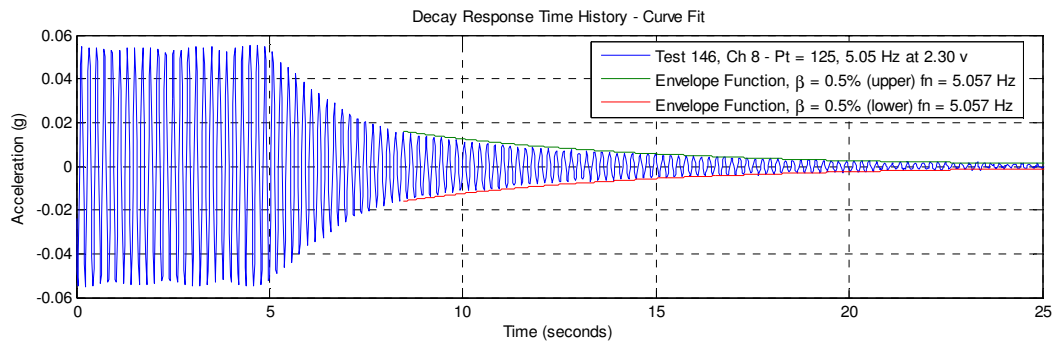
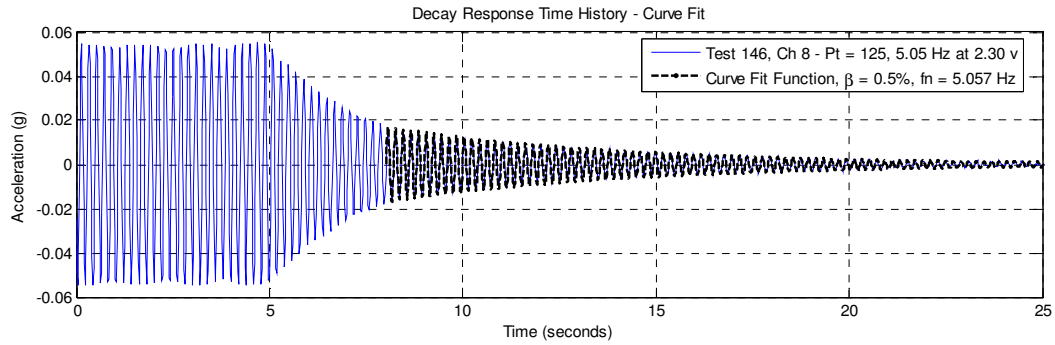
Driving Point 73 – Test 158 – Decay from Sine 5.025 Hz at 2.30 volts



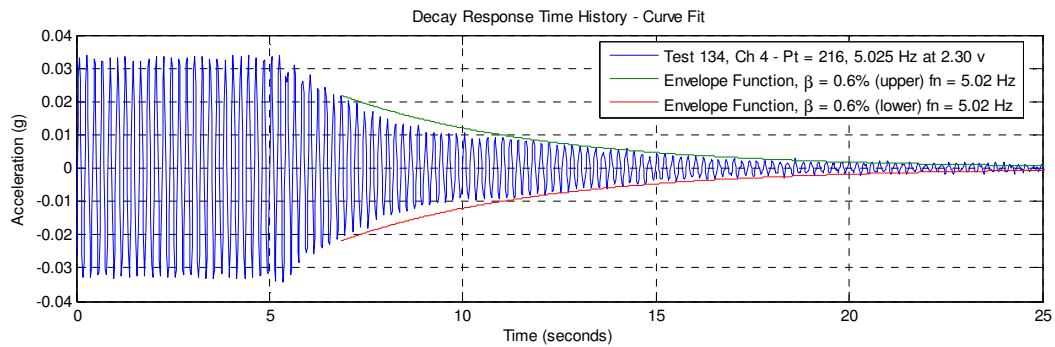
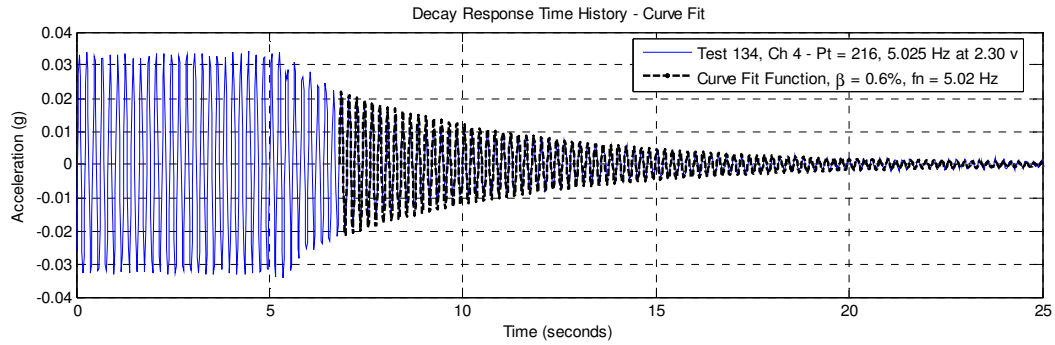
Driving Point 117 – Test 262 – Decay from Sine 4.975 Hz at 1.414 volts



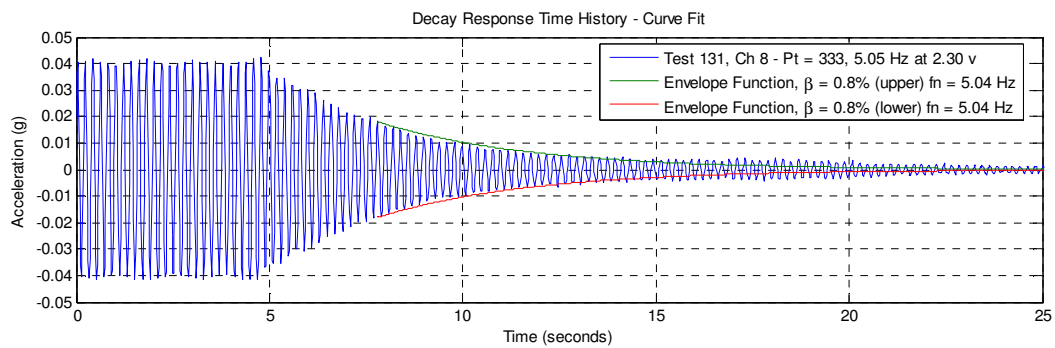
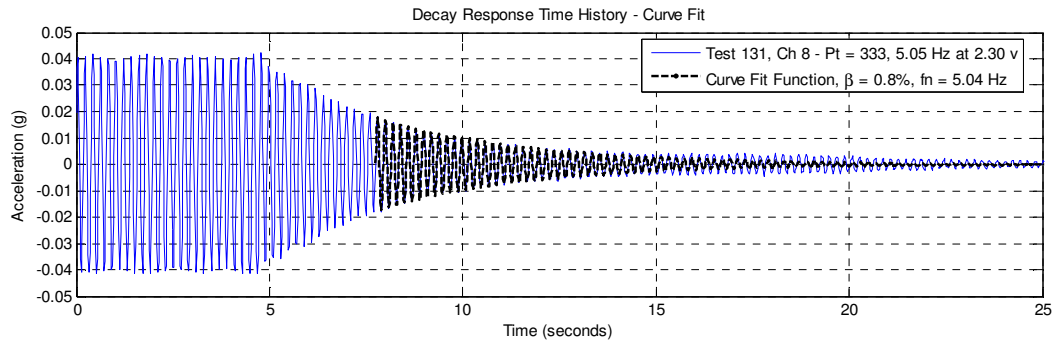
Driving Point 125 – Test 146 – Decay from Sine 5.05 Hz at 2.30 volts



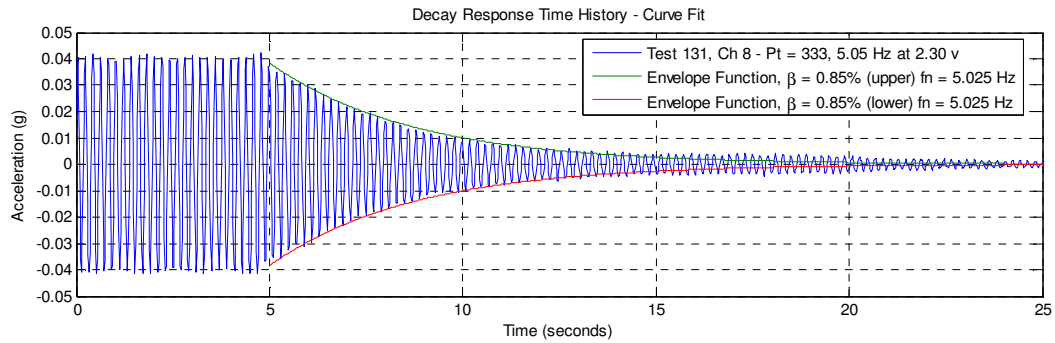
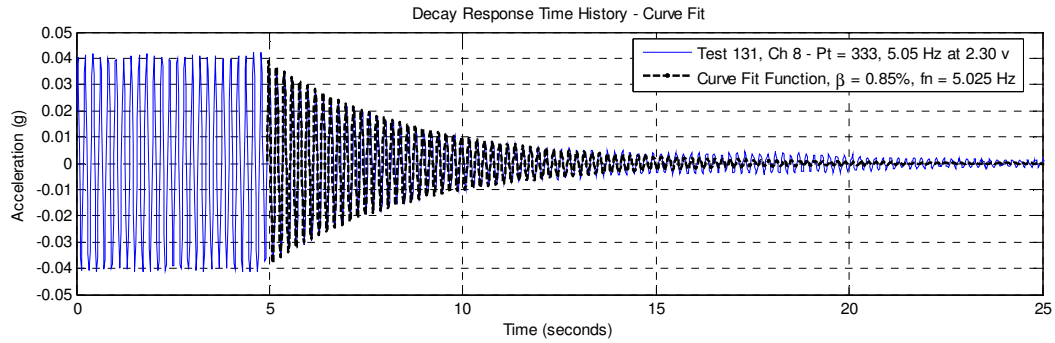
Driving Point 216 – Test 134 – Decay from Sine 5.025 Hz at 2.30 volts



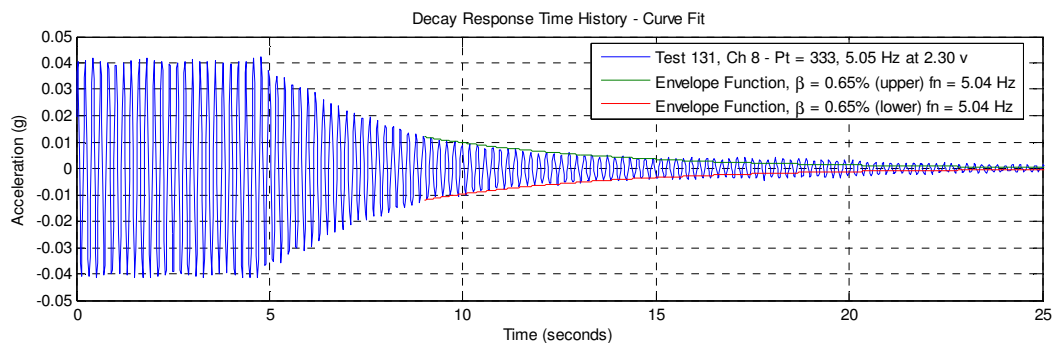
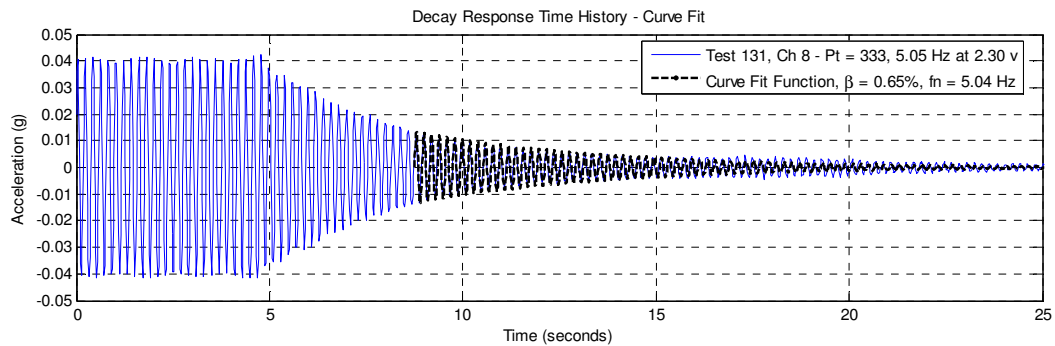
Driving Point 333 – Test 131 – Decay from Sine 5.05 Hz at 2.30 volts



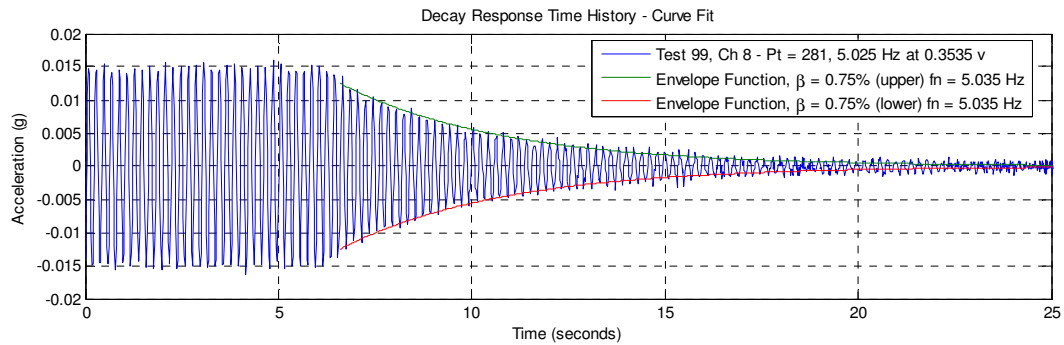
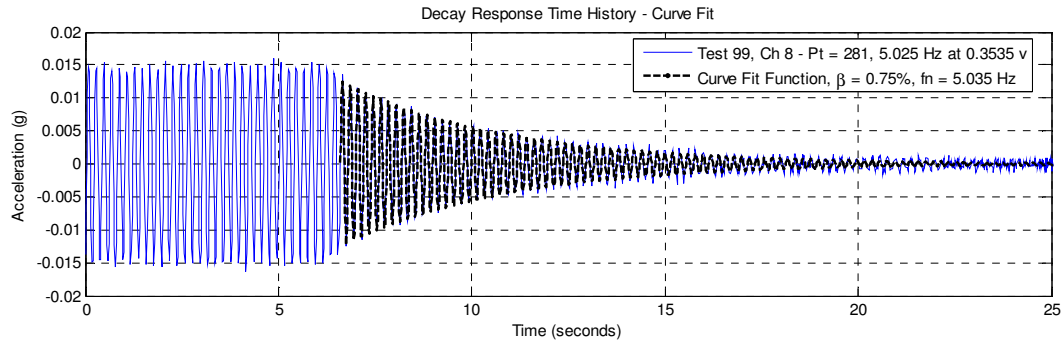
Driving Point 333 – Test 131 – Decay from Sine 5.05 Hz at 2.30 volts – UPPER



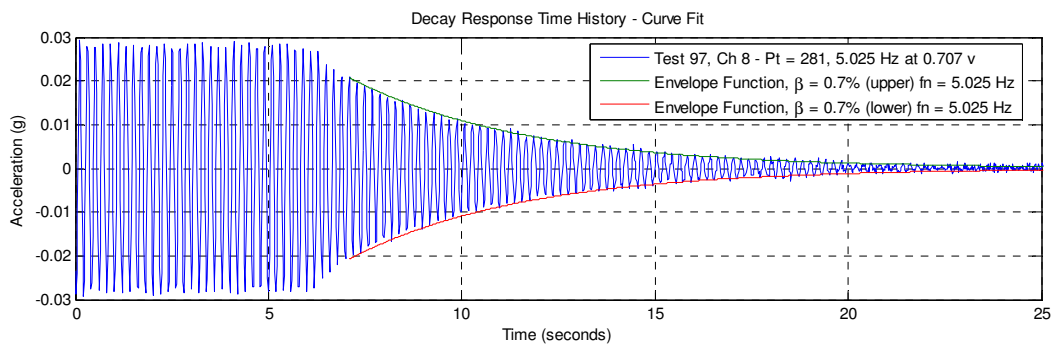
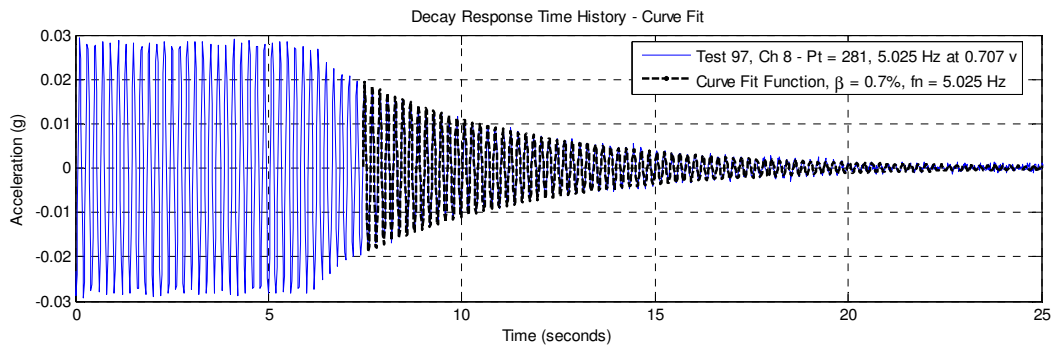
Driving Point 333 – Test 131 – Decay from Sine 5.05 Hz at 2.30 volts – LOWER



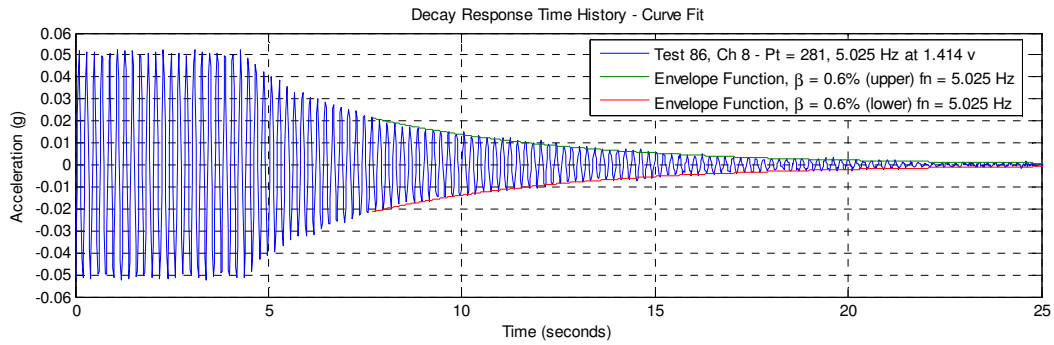
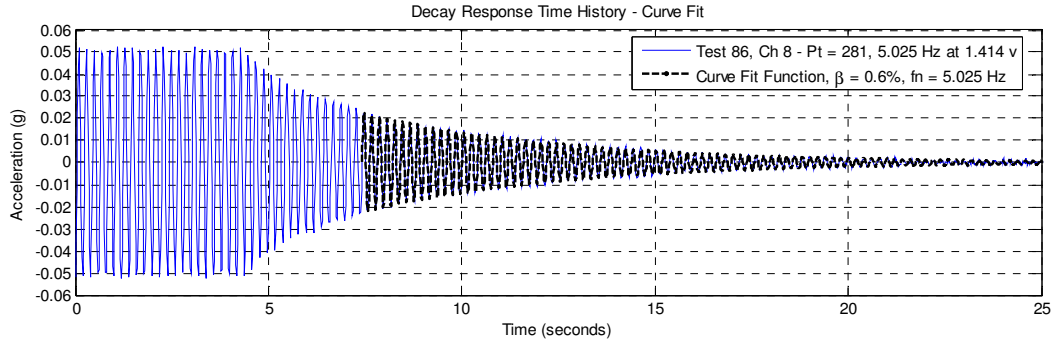
Driving Point 281 – Test 99 – Decay from Sine 5.025 Hz at 0.3535 volts



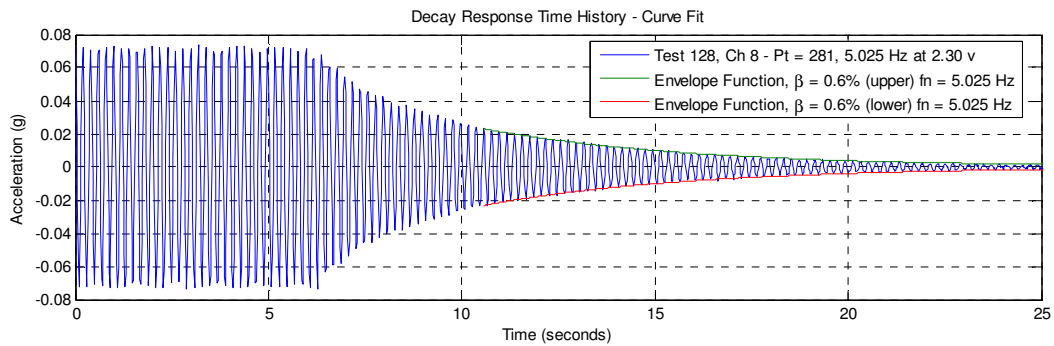
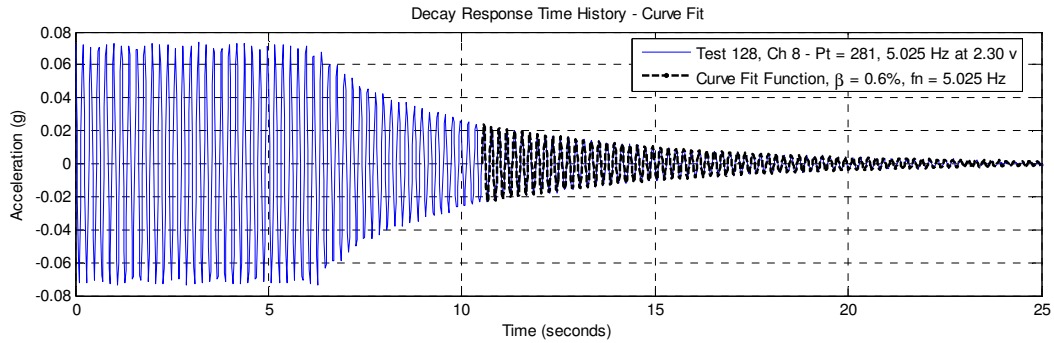
Driving Point 281 – Test 97 – Decay from Sine 5.025 Hz at 0.707 volts



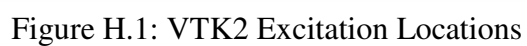
Driving Point 281 – Test 86 – Decay from Sine 5.025 Hz at 1.414 volts



Driving Point 281 – Test 128 – Decay from Sine 5.025 Hz at 2.30 volts



DRIVING POINT ACCELERANCE FREQUENCY RESPONSE FUNCTIONS – VTK2



All Representative Driving Point Measurements

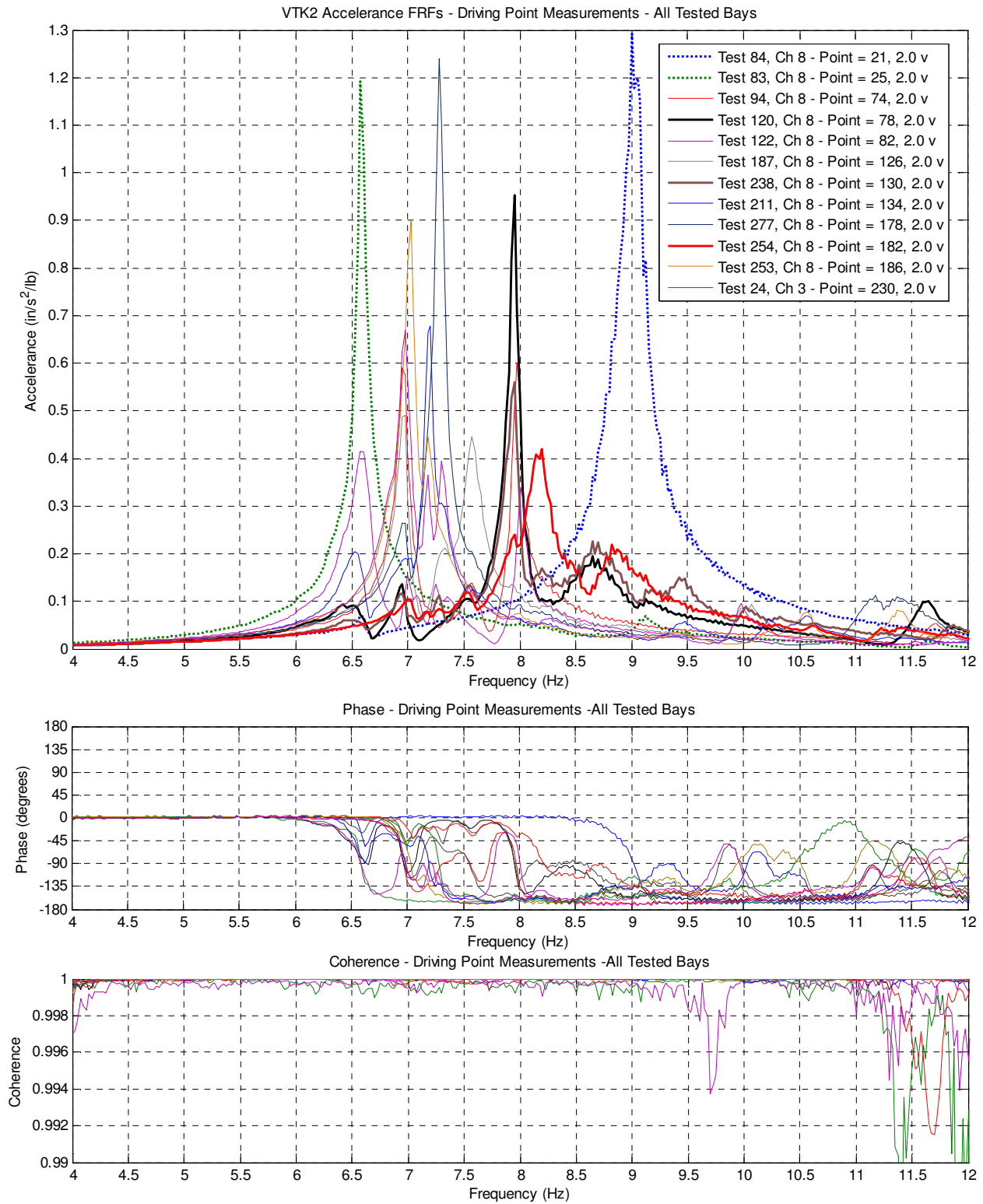


Figure H.2: VTK2 Driving Point Accelerance FRFs (All Excitation Points)

Point 21 (A/C-3.8/4.2)

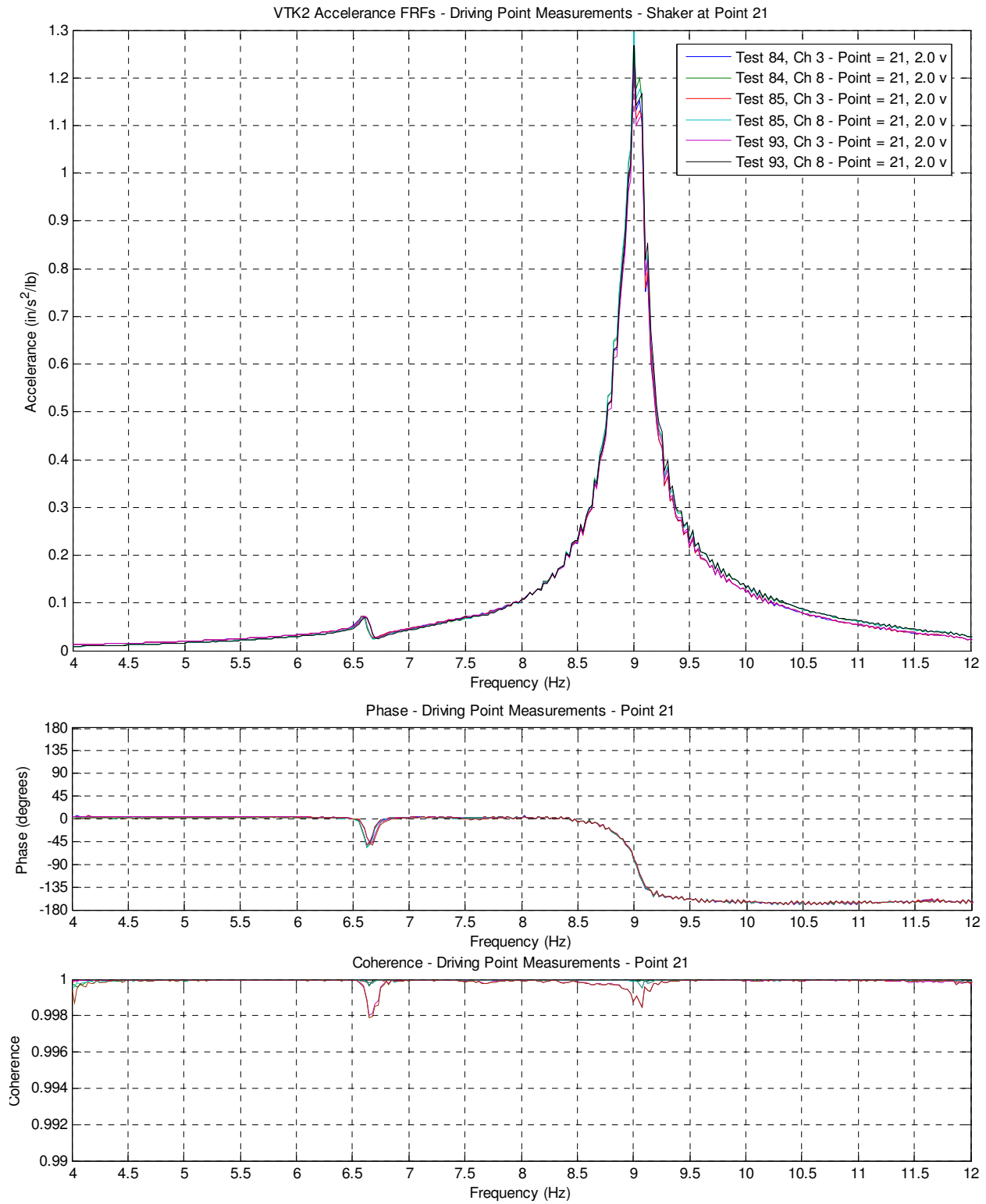


Figure H.3: VTK2 Driving Point Accelerance FRFs (Point 21)

Point 25 (A/C-2.5/3.8)

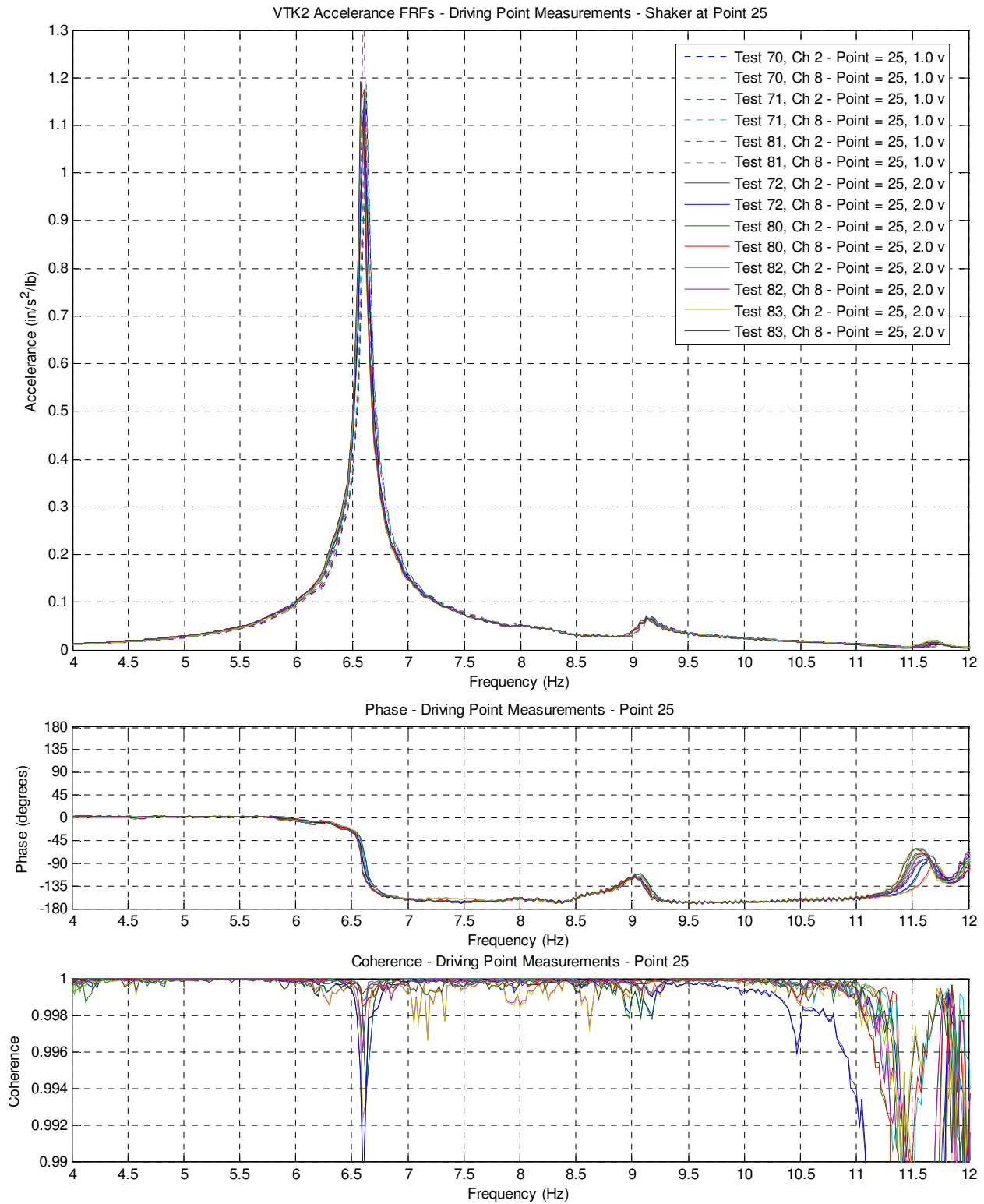


Figure H.4: VTK2 Driving Point Accelerance FRFs (Point 25)

Point 74 (C/D-4/6)

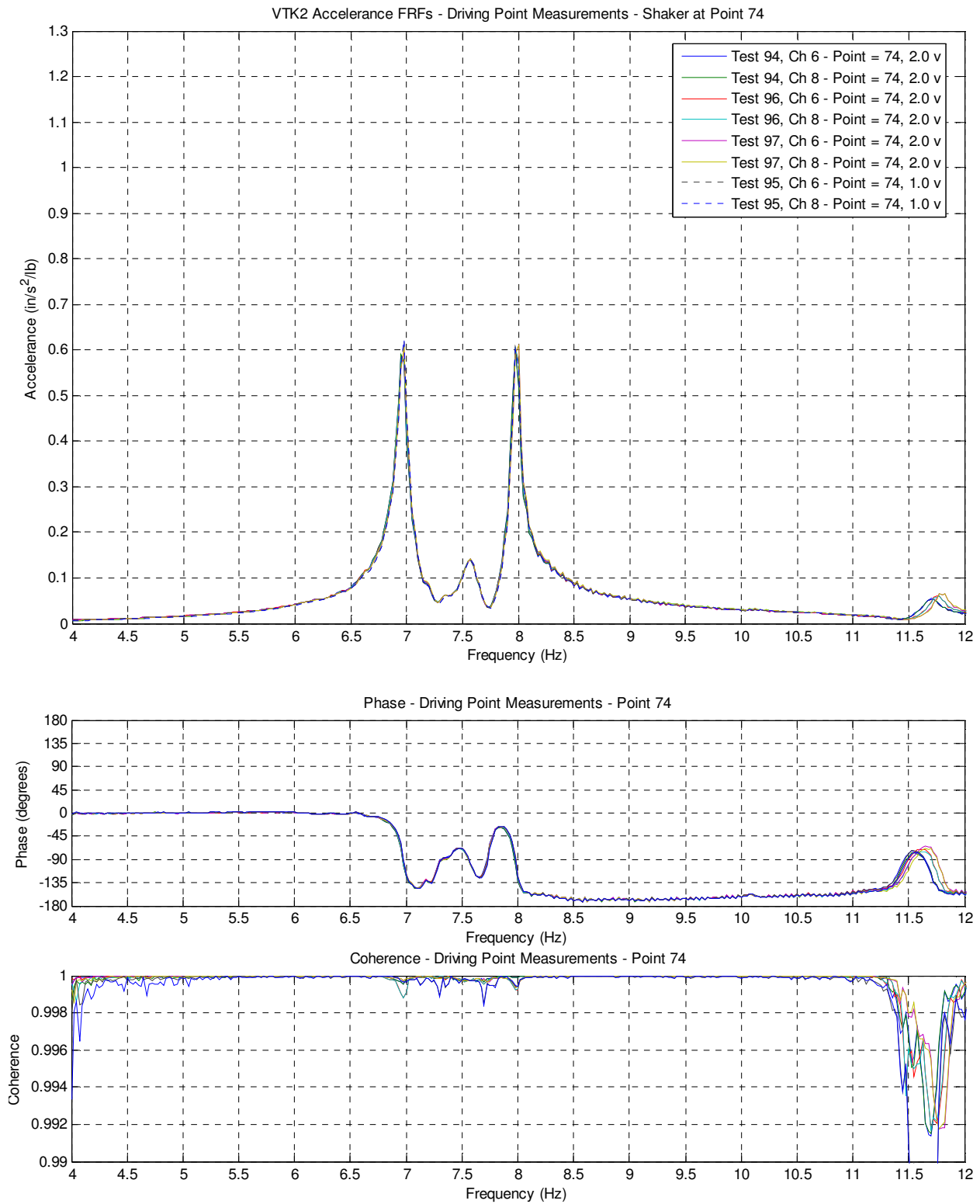


Figure H.5: VTK2 Driving Point Accelerance FRFs (Point 74)

Point 78 (C/D-3/4)

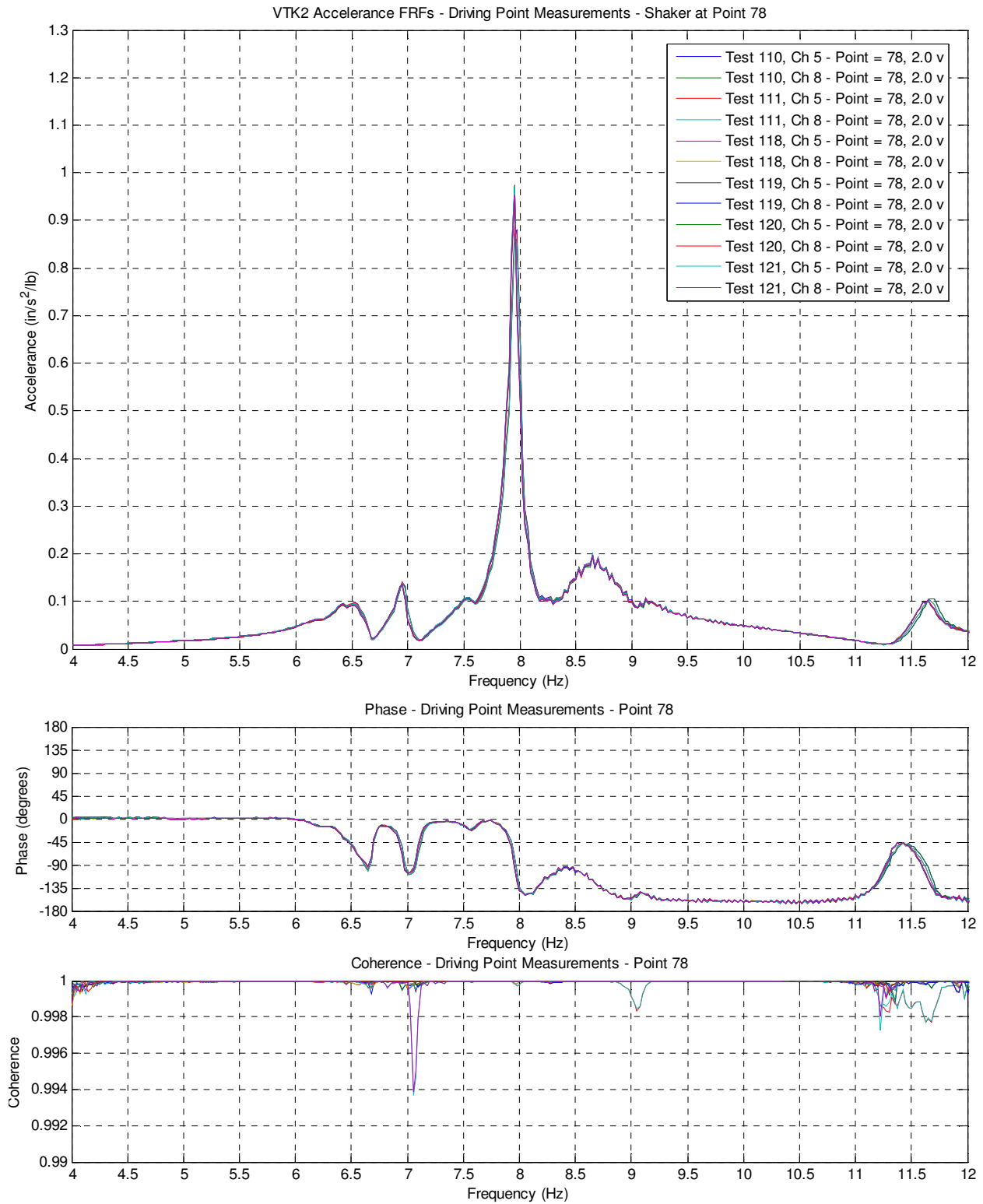


Figure H.6: VTK2 Driving Point Accelerance FRFs (Point 78)

Point 82 (C/D-1/3)

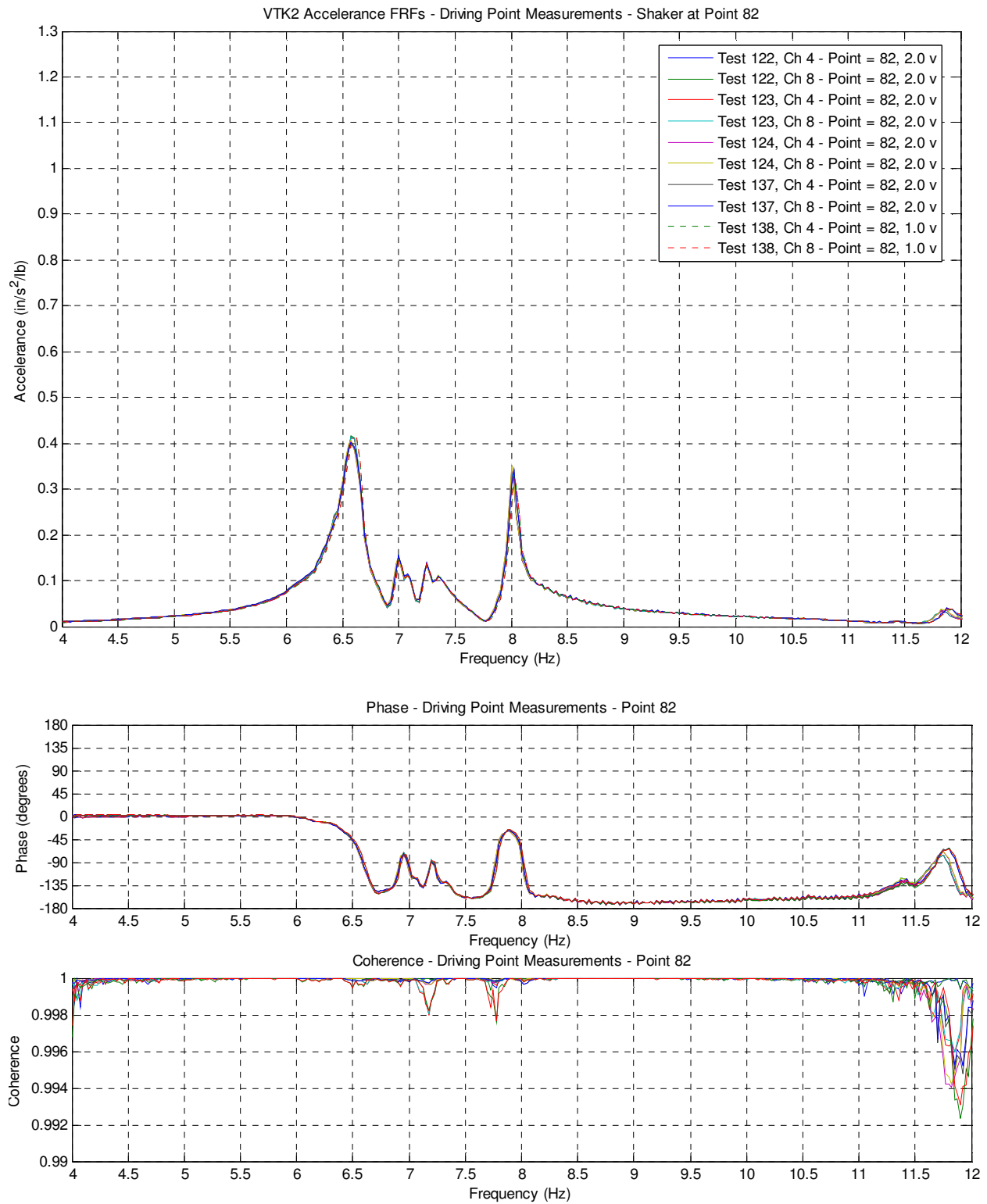


Figure H.7: VTK2 Driving Point Accelerance FRFs (Point 82)

Point 126 (D/E-4/6)
Friday and Sunday Measurements – Non-Modal Sweep

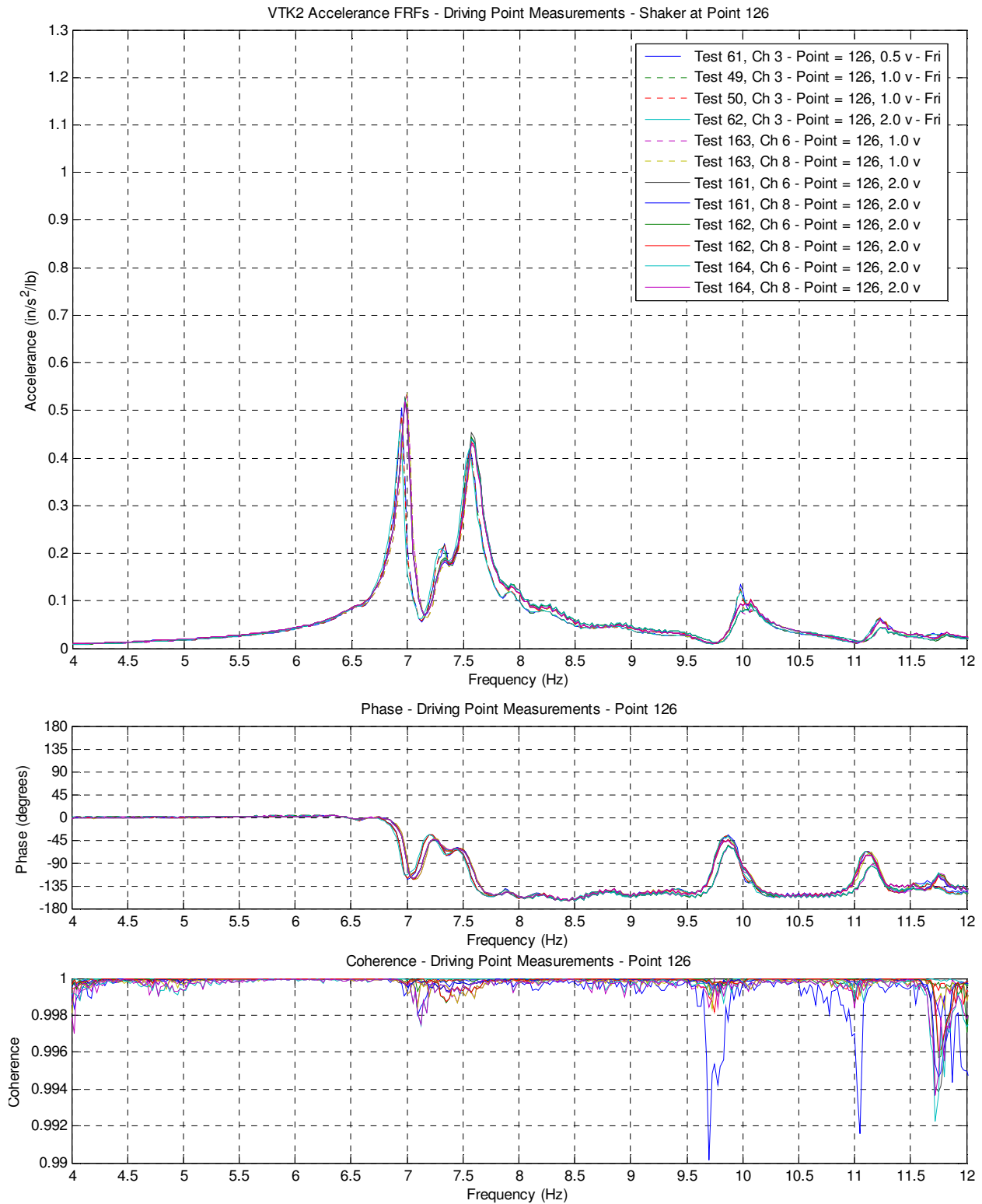


Figure H.8: VTK2 Driving Point Accelerance FRFs (Point 126 on various days)

Point 126 (D/E-4/6)
Modal Sweep (35 Traces)

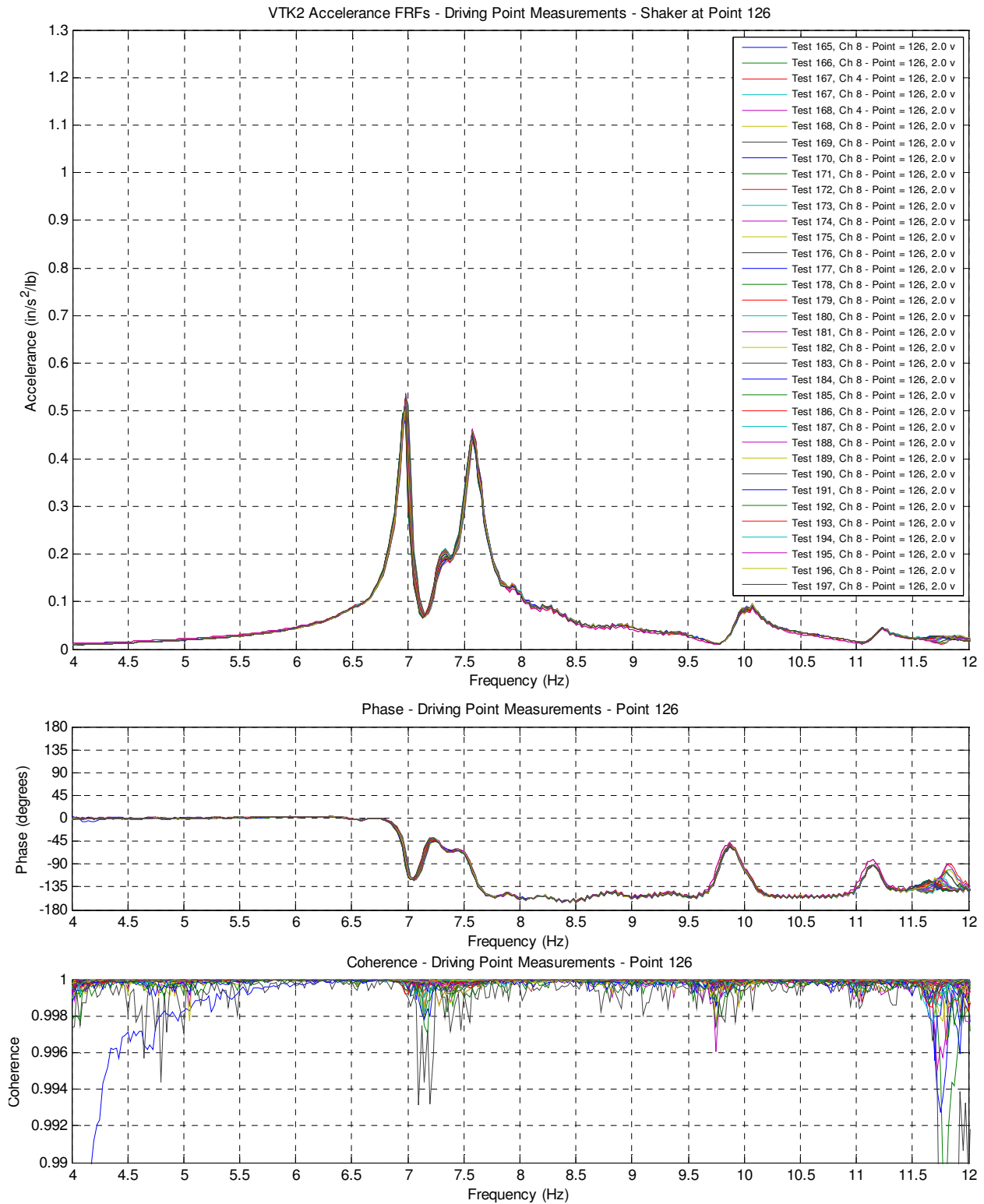


Figure H.9: VTK2 Driving Point Accelerance FRFs (Point 126)

Point 130 (D/E-3/4)
Modal Sweep (9 traces)

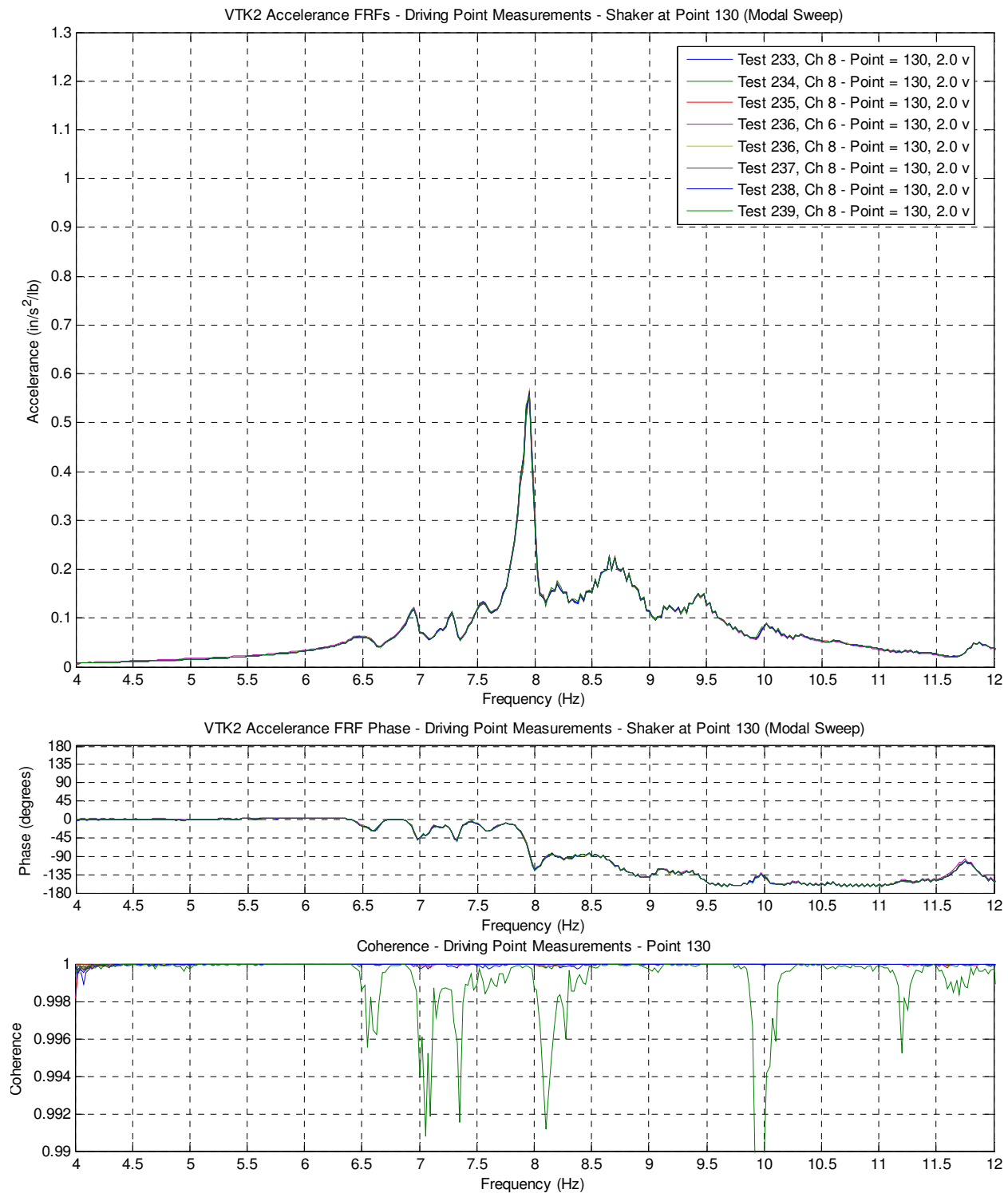


Figure H.10: VTK2 Driving Point Accelerance FRFs (Point 130)

Point 134 (D/E-1/3) **Modal Sweep (36 traces)**

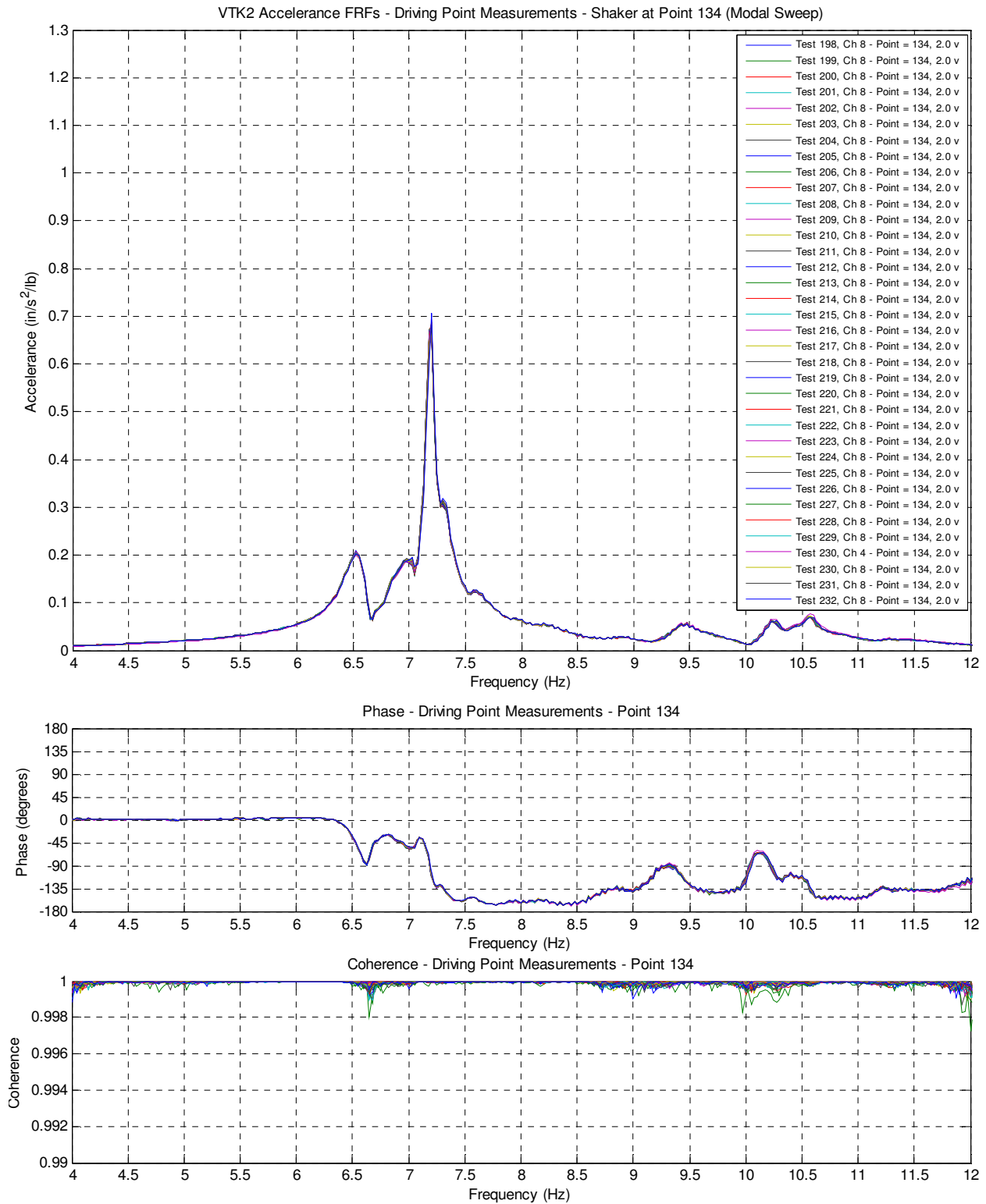


Figure H.11: VTK2 Driving Point Accelerance FRFs (Point 134)

Point 178 (E/F-4/6)

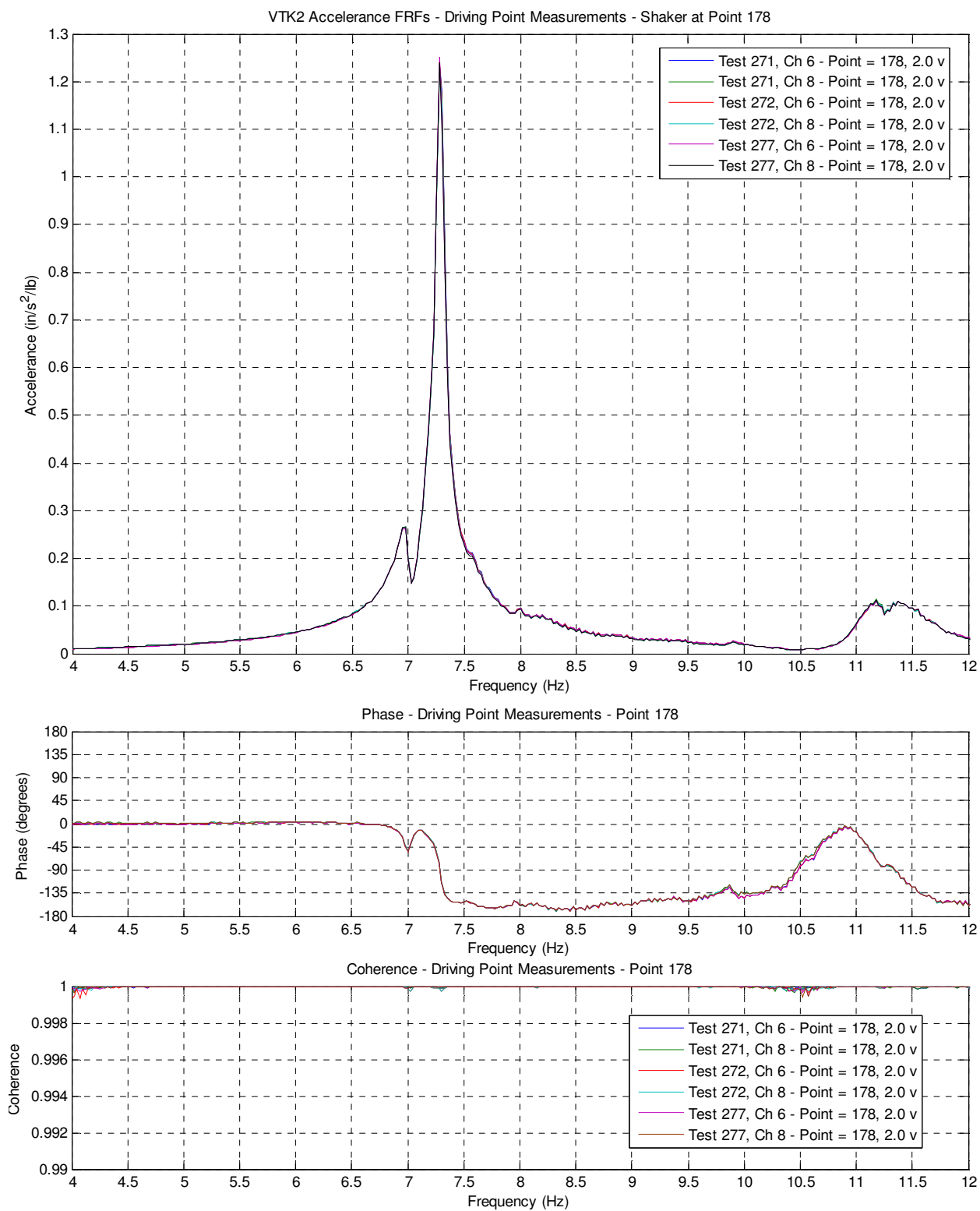


Figure H.12: VTK2 Driving Point Accelerance FRFs (Point 178)

Point 182 (E/F-3/4)

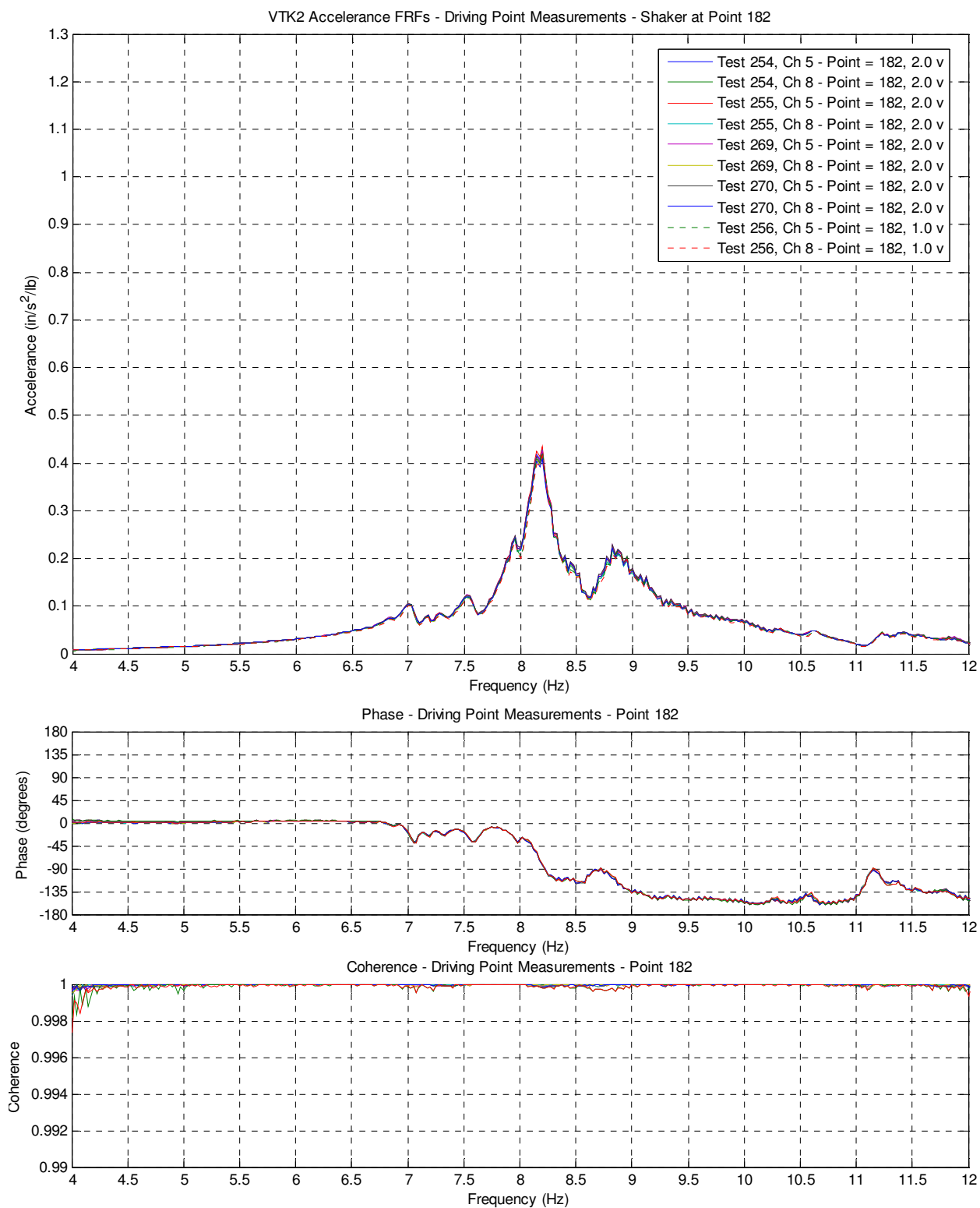


Figure H.13: VTK2 Driving Point Accelerance FRFs (Point 182)

Point 186 (E/F-1/3)

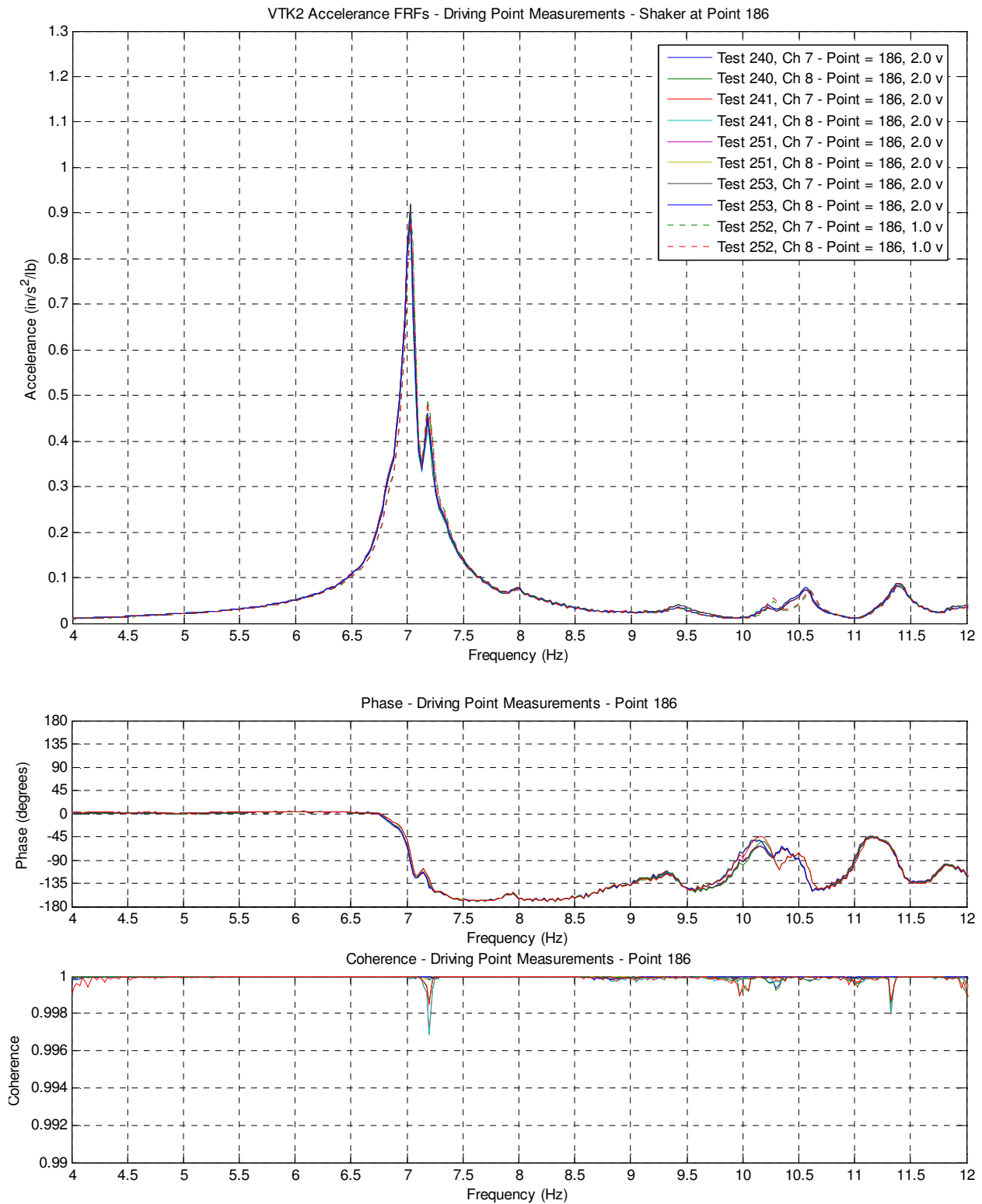


Figure H.14: VTK2 Driving Point Accelerance FRFs (Point 186)

Point 230 (F/G-4/6)

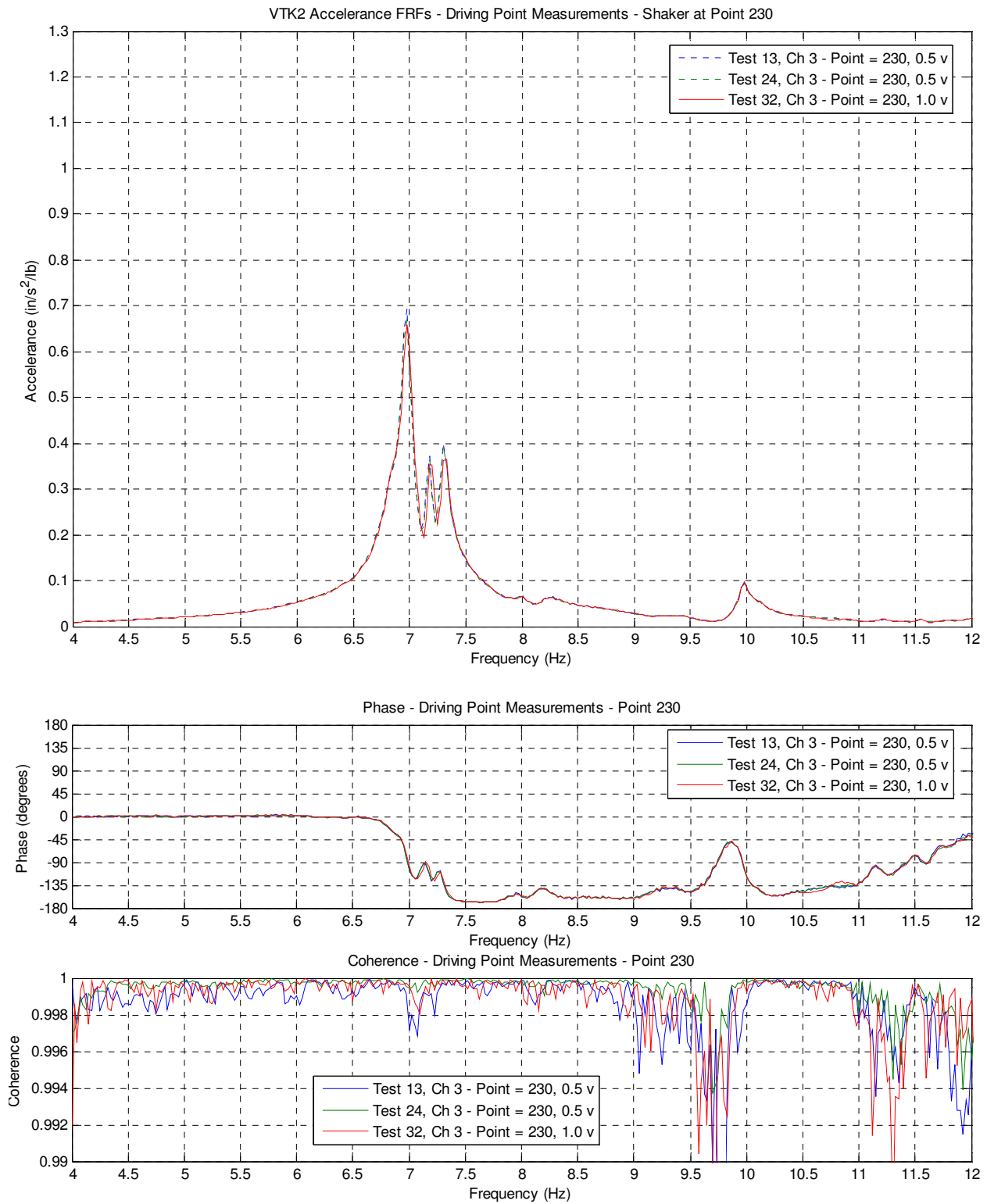


Figure H.15: VTK2 Driving Point Accelerance FRFs (Point 230)

APPENDIX I

ME'SCOPEVES MODAL PARAMETER ESTIMATION – VTK2

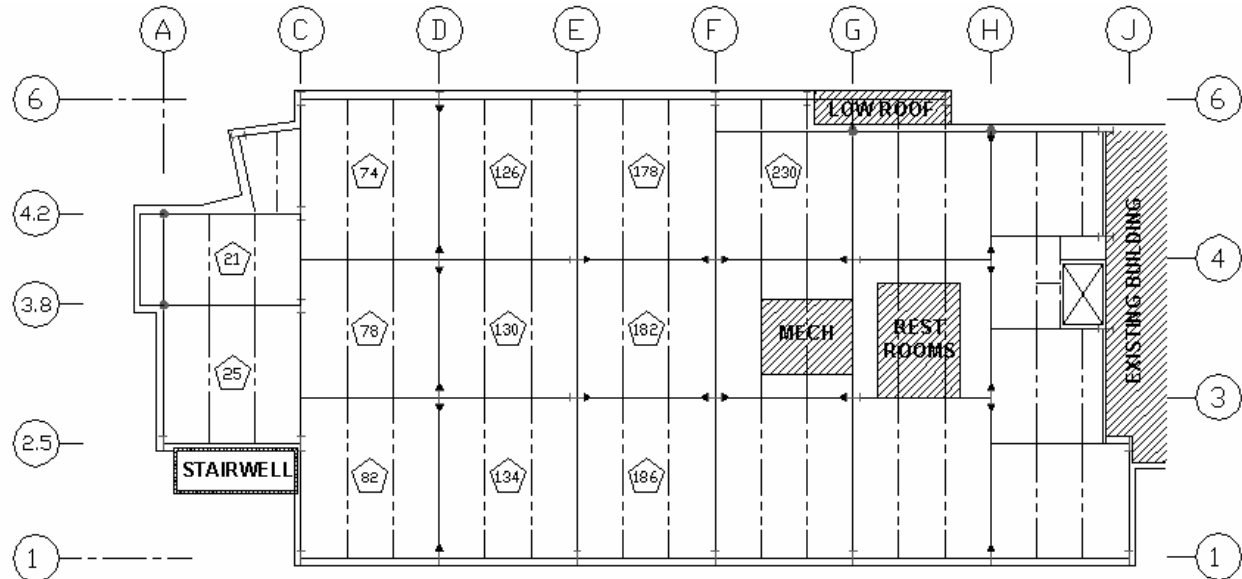
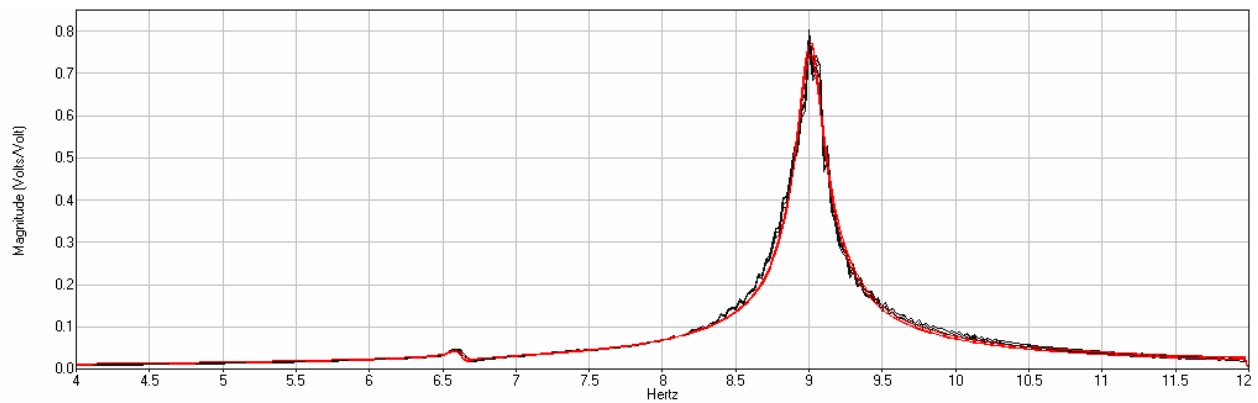


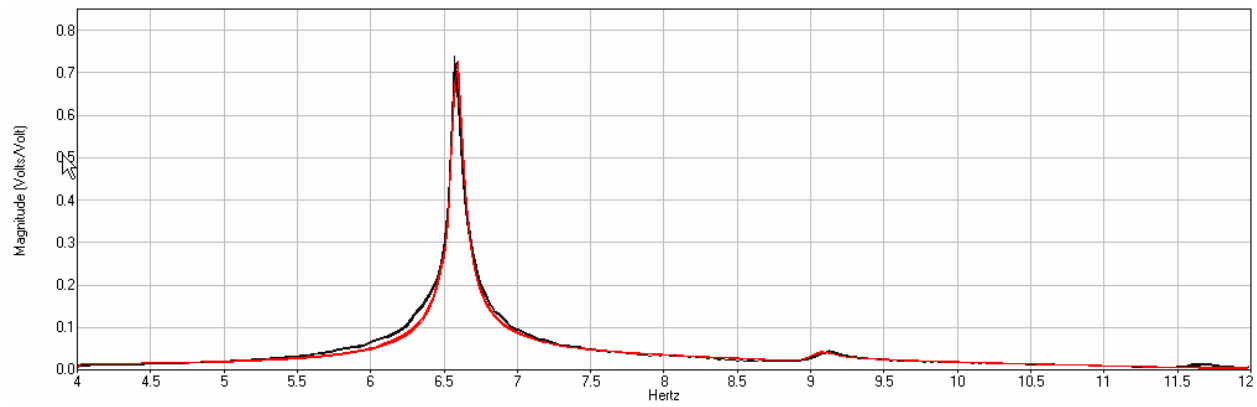
Figure I.1: VTK2 Excitation Locations

Driving Point Accelerance FRF Curve Fitting:



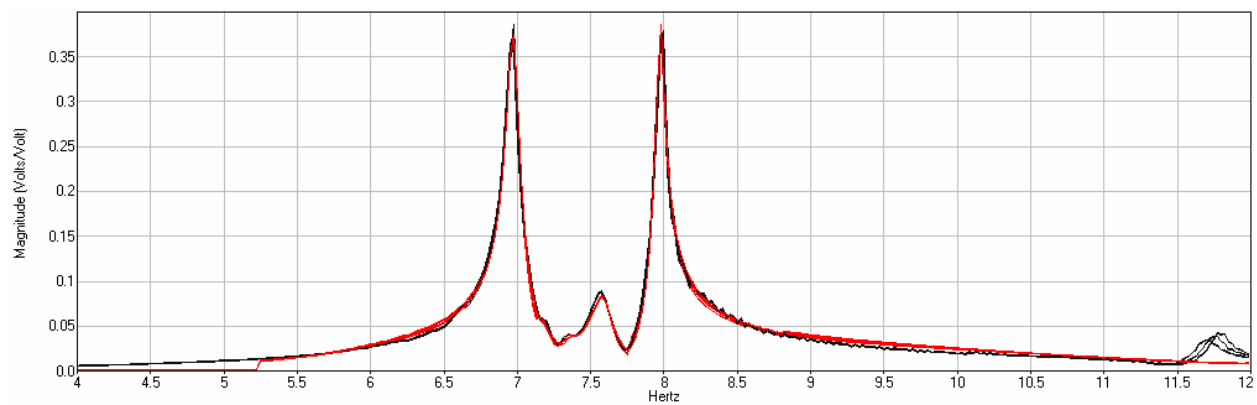
Frequency (Hz)	Damping (%)
6.62	0.70
9.01	1.03

Figure I.2: VTK2 Driving Point FRFs with Curve Fit Overlay (Point 21)



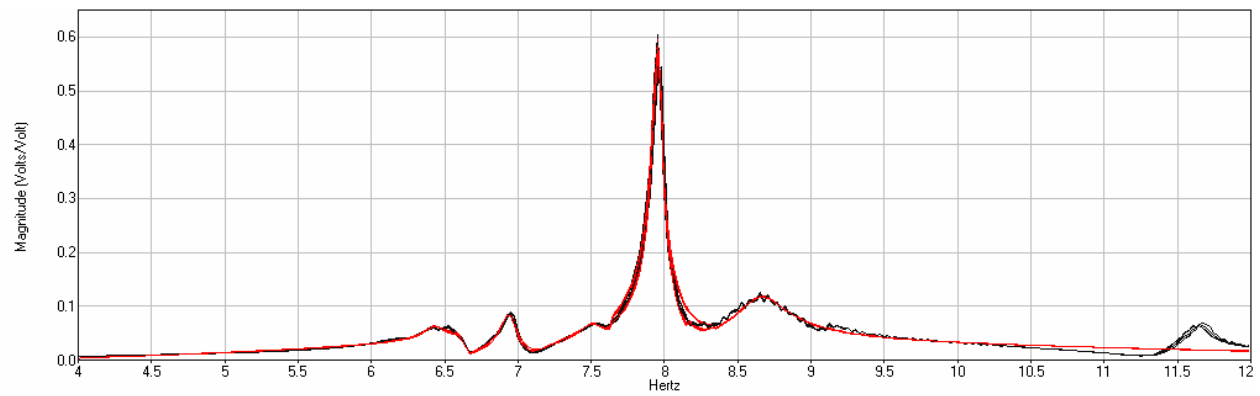
Frequency (Hz)	Damping (%)
6.59	0.60
9.05	1.01

Figure I.3: VTK2 Driving Point FRFs with Curve Fit Overlay (Point 25)



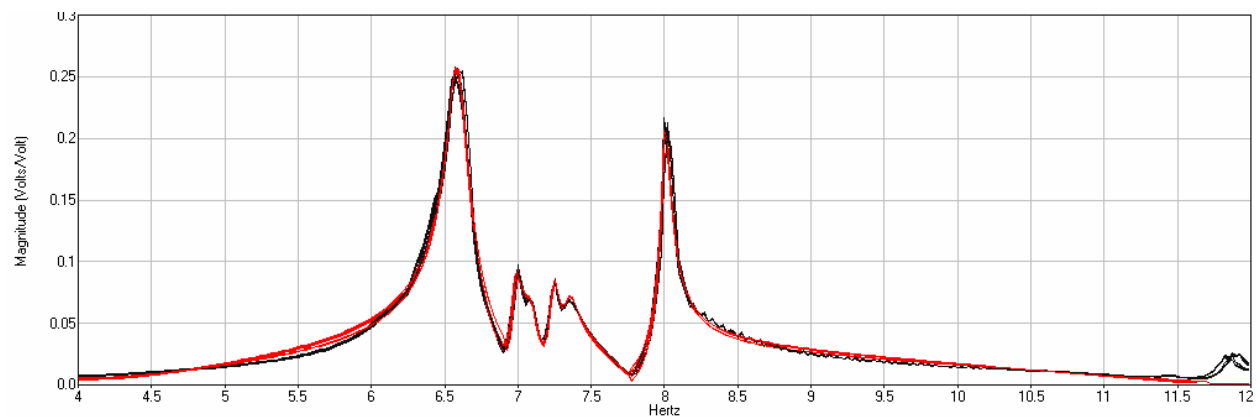
Frequency (Hz)	Damping (%)
6.97	0.62
7.16	0.44
7.36	0.50
7.59	0.91
7.97	0.46

Figure I.4: VTK2 Driving Point FRFs with Curve Fit Overlay (Point 74)



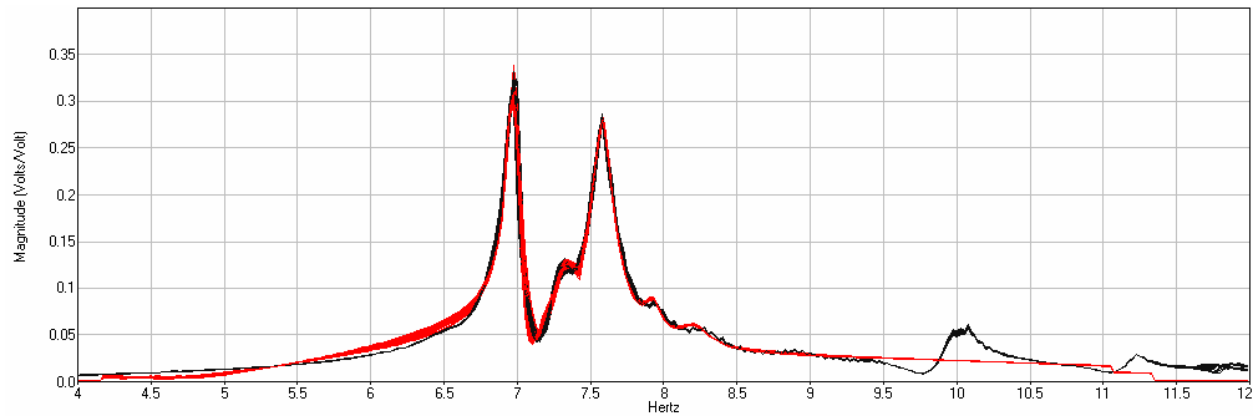
Frequency (Hz)	Damping (%)
6.61	1.05
6.95	0.69
7.52	0.90
7.95	0.46
8.64	2.17

Figure I.5: VTK2 Driving Point FRFs with Curve Fit Overlay (Point 78)



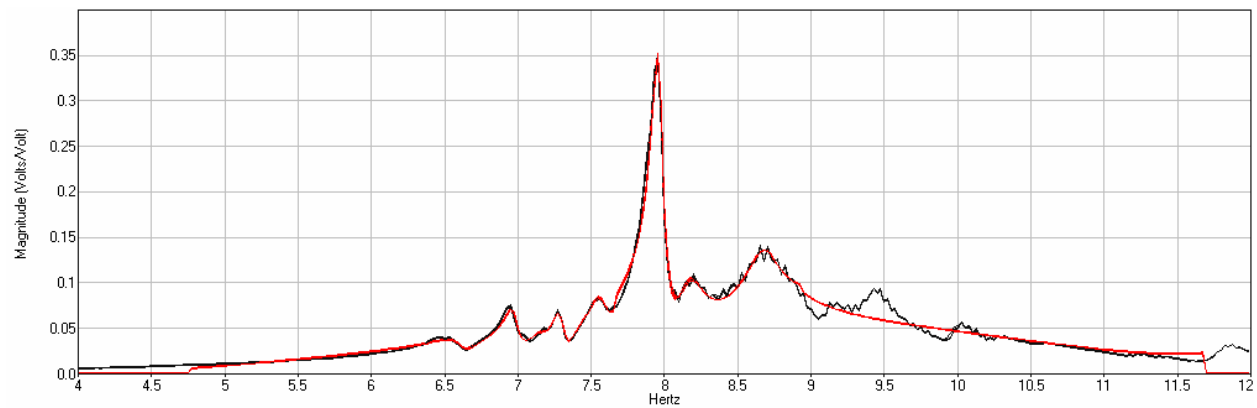
Frequency (Hz)	Damping (%)
6.59	1.19
6.98	0.48
7.10	0.48
7.24	0.50
7.35	0.60
8.01	0.47

Figure I.6: VTK2 Driving Point FRFs with Curve Fit Overlay (Point 82)



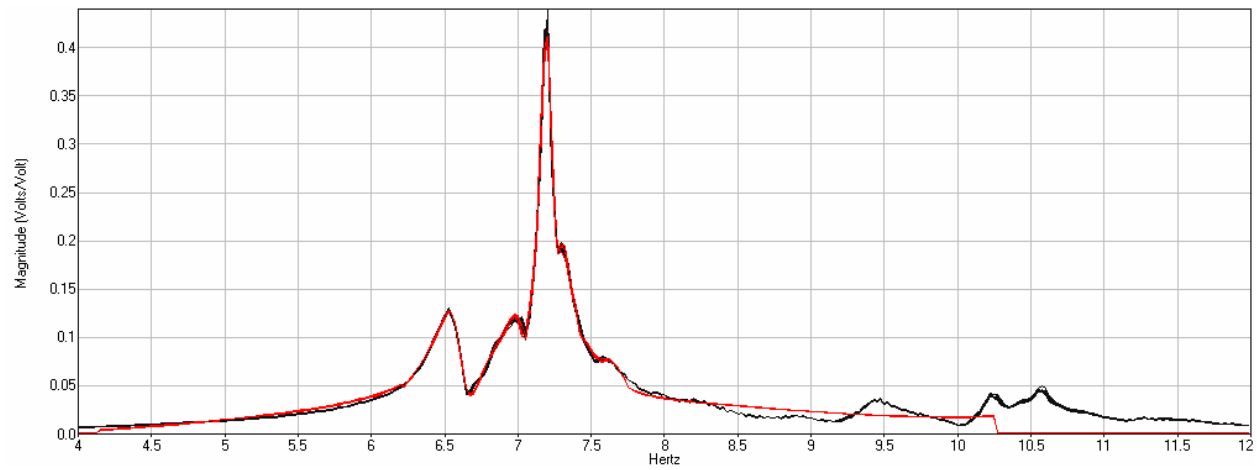
Frequency (Hz)	Damping (%)
6.98	0.60
7.33	0.98
7.58	0.97
7.92	0.70
8.22	1.20

Figure I.7: VTK2 Driving Point FRFs with Curve Fit Overlay (Point 126) - MODAL



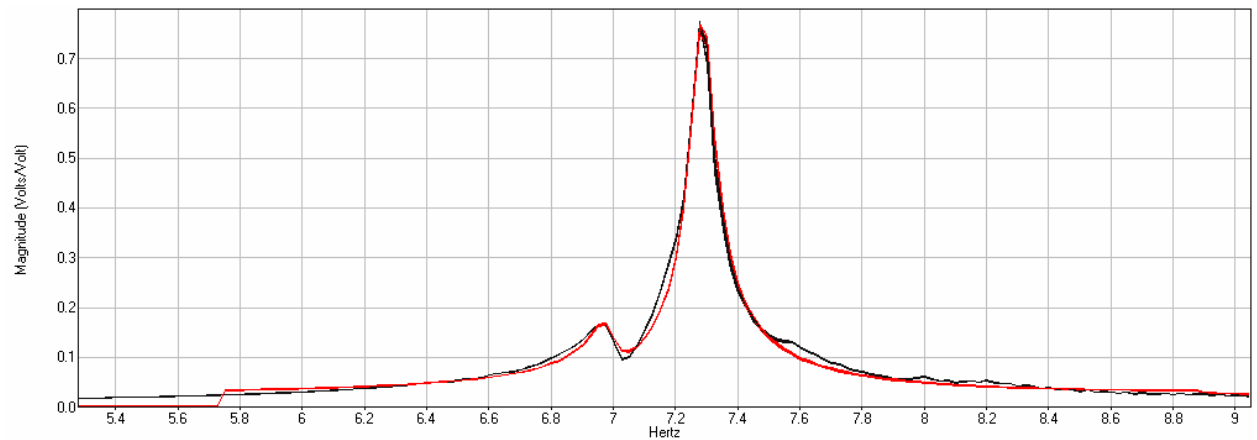
Frequency (Hz)	Damping (%)
6.61	1.20
6.97	0.71
7.19	0.50
7.30	0.55
7.57	0.75
7.96	0.50
8.18	1.20
8.67	1.58

Figure I.8: VTK2 Driving Point FRFs with Curve Fit Overlay (Point 130)



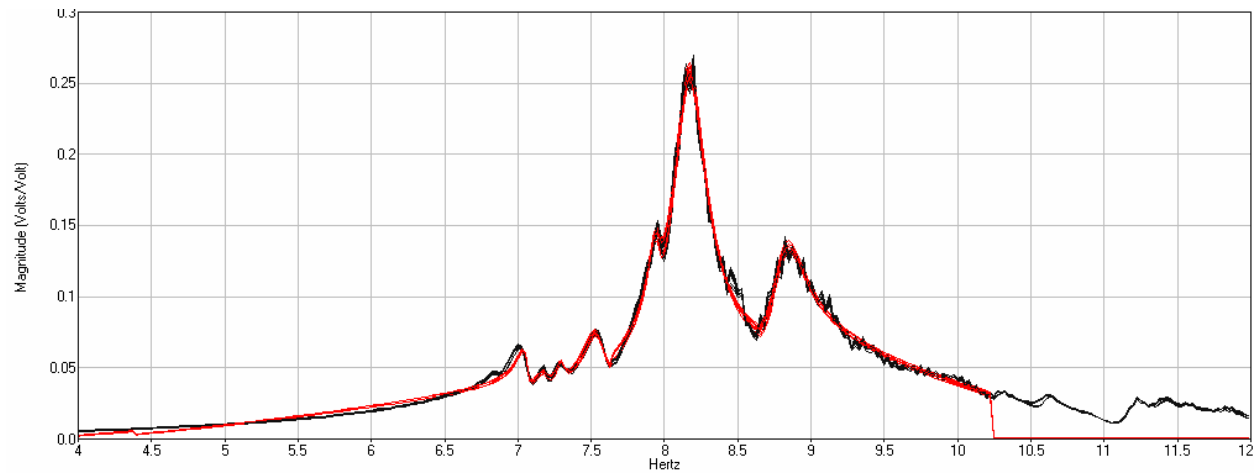
Frequency (Hz)	Damping (%)
6.57	1.39
7.01	0.61
7.19	0.49
7.32	0.52
7.60	0.95

Figure I.9: VTK2 Driving Point FRFs with Curve Fit Overlay (Point 134)



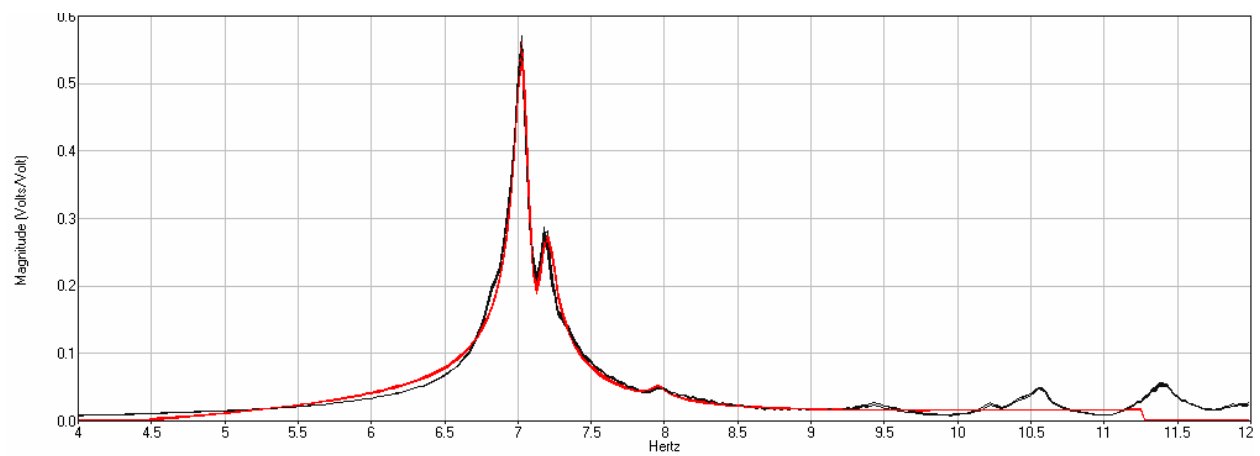
Frequency (Hz)	Damping (%)
6.98	0.63
7.29	0.50

Figure I.10: VTK2 Driving Point FRFs with Curve Fit Overlay (Point 178)



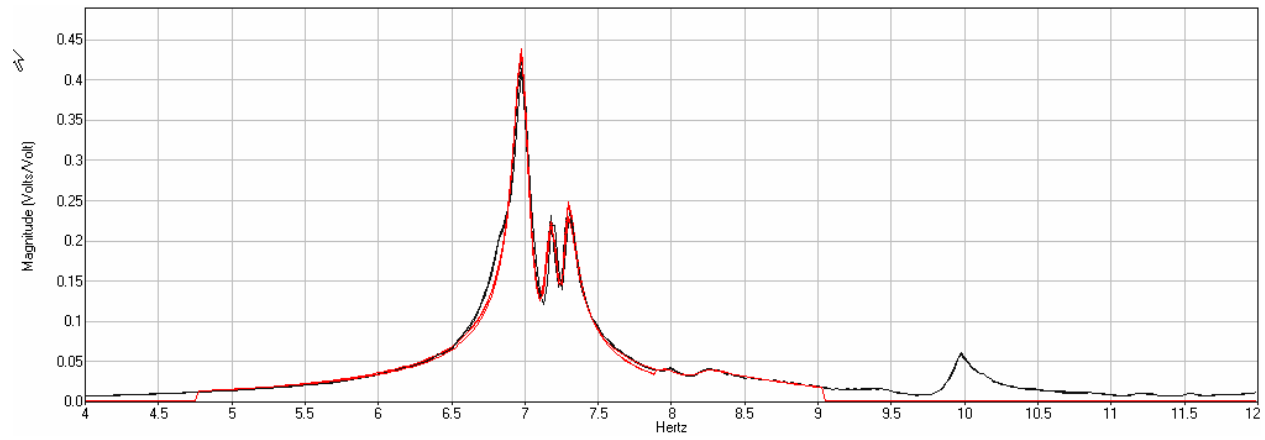
Frequency (Hz)	Damping (%)
7.05	0.59
7.18	0.55
7.31	0.49
7.55	0.97
7.94	0.56
8.17	1.30
8.82	1.40

Figure I.11: VTK2 Driving Point FRFs with Curve Fit Overlay (Point 182)



Frequency (Hz)	Damping (%)
7.03	0.65
7.18	0.90
7.95	0.95

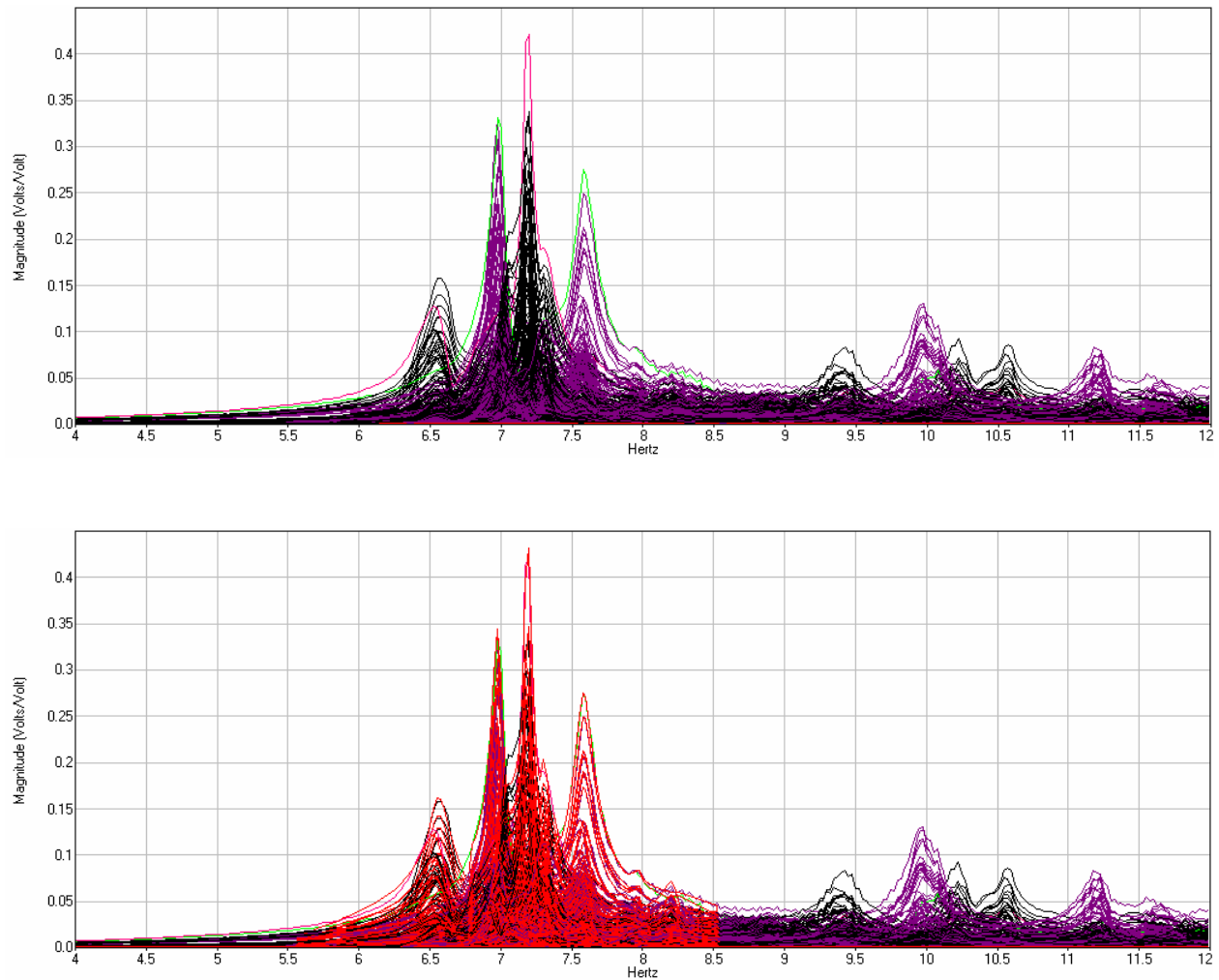
Figure I.12: VTK2 Driving Point FRFs with Curve Fit Overlay (Point 186)



Frequency (Hz)	Damping (%)
6.98	0.70
7.18	0.60
7.29	0.59
7.96	0.95
8.22	1.28

Figure I.13: VTK2 Driving Point FRFs with Curve Fit Overlay (Point 230)

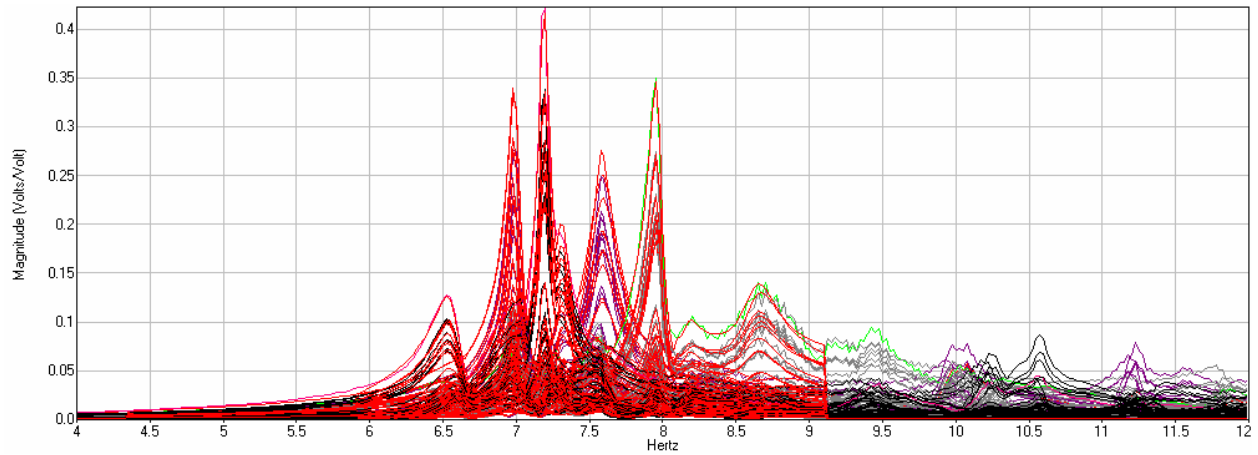
Multi-Reference Curve Fit of Full Set of Accelerance FRFs (10-Bay Area):



Mode	Frequency (Hz)	Point 126	Point 134	Frequency (Hz)	Damping (%)
1	6.56	2.7	9.4	6.56	1.35
2	6.98	7.8	3.9	6.98	0.56
3	7.03	10.0	8.3	7.03	0.50
4	7.19	0.9	7.8	7.19	0.45
5	7.3	2.0	3.0	7.30	0.42
6	7.58	10.0	3.4	7.58	0.94
7	7.97	1.1	0.8	7.97	0.54
8	8.21	1.7	1.2	8.21	0.67

Figure I.14: VTK2 10-Bay Multi-Ref Accelerance FRFs & Curve Fit Overlay (126,134)

Multi-Reference Curve Fit of Full Set of Accelerance FRFs (3-Bay Strip):



Mode	Frequency (Hz)	Point 126	Point 130	Point 134	Frequency (Hz)	Damping (%)
1	6.56	1.1	1.9	4.3	6.56	1.34
2	6.99	5.8	3.9	2.3	6.99	0.57
3	7.02	1.1	2.1	1.2	7.02	0.53
4	7.19	0.9	1.3	6.4	7.19	0.53
5	7.30	0.5	0.6	1.3	7.30	0.42
6	7.58	10.0	4.2	3.5	7.58	0.97
7	7.96	1.0	6.2	0.6	7.96	0.58
8	8.17	0.5	0.6	0.4	8.17	0.59
9	8.64	1.7	4.0	1.3	8.64	1.46

Figure I.15: VTK2 3-Bay Multi-Ref Accelerance FRFs & Curve Fit Overlay (126,130,134)

APPENDIX J

DECAY MEASUREMENTS AND DECAY CURVE FIT ANALYSES – VTK2

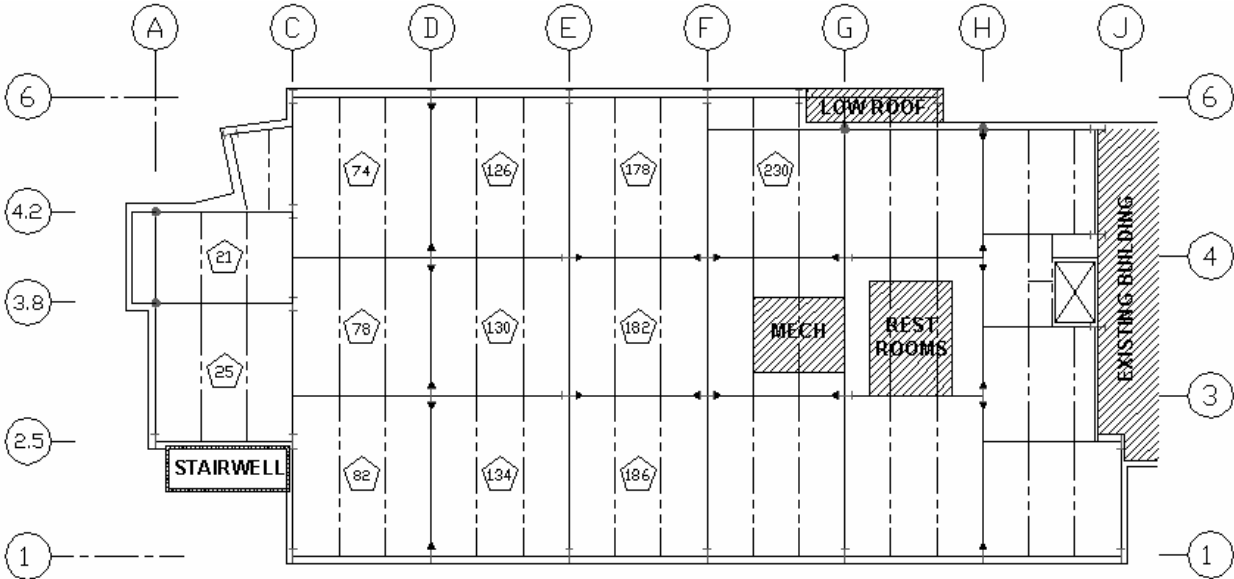
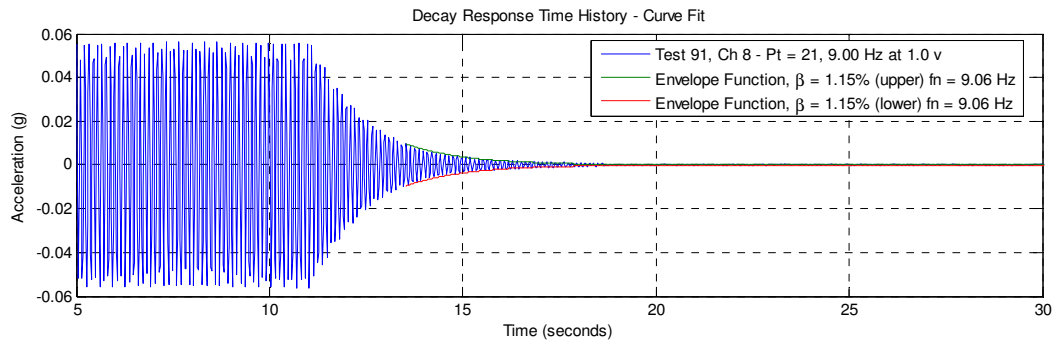
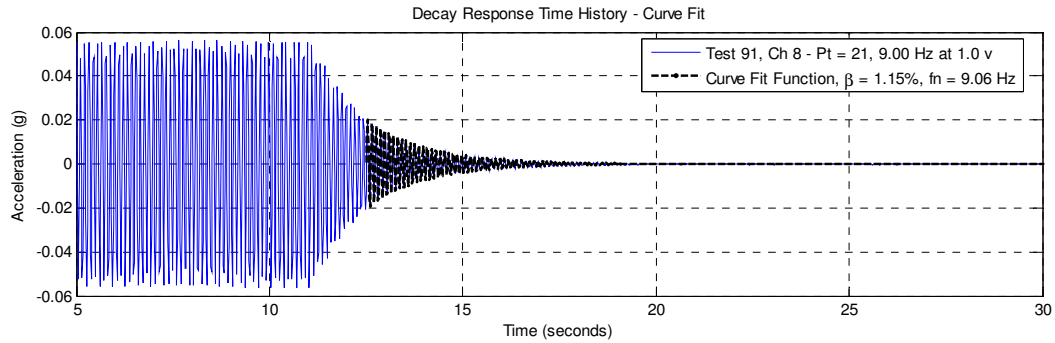


Figure J.1: VTK2 Excitation Locations

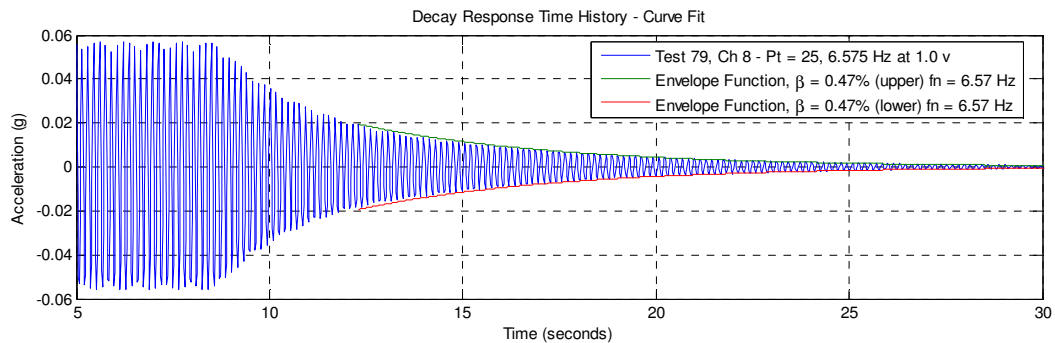
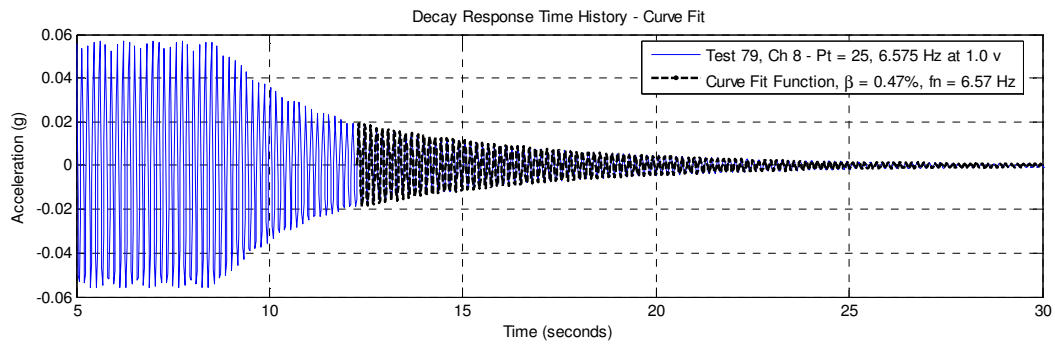
Table J.1: VTK2 Summary of Decay Curve Fit Estimates of Damping

Excitation Location(s)	Type of Damping Estimate	Excitation Level (volts)	Decay Frequency (Hz)	Estimated Damping Ratio
Point 21	Decay Curve Fit from 9.00 Hz Sinusoid	1.0	9.06	1.15%
Point 25	Decay Curve Fit from 6.575 Hz Sinusoid	1.0	6.57	0.47%
Point 74	Decay Curve Fit from 6.95 Hz Sinusoid	1.0	6.96	0.59%
Point 74	Decay Curve Fit from 7.975 Hz Sinusoid	1.0	7.97	0.48%
Point 78	Decay Curve Fit from 7.95 Hz Sinusoid	1.0	7.94	0.50%
Point 82	Decay Curve Fit from 6.575 Hz Sinusoid	1.0	6.57	1.23%
Point 82	Decay Curve Fit from 8.00 Hz Sinusoid	1.0	8.005	0.47%
Point 126	Decay Curve Fit from 6.925 Hz Sinusoid	1.0	6.935	0.54%
Point 126	Decay Curve Fit from 6.925 Hz Sinusoid	0.5	6.94	0.50%
Point 126	Decay Curve Fit from 7.55 Hz Sinusoid	1.0	7.55	0.80%
Point 130	Decay Curve Fit from 7.975 Hz Sinusoid	1.0	8.00	0.60%
Point 134	Decay Curve Fit from 7.20 Hz Sinusoid	1.0	7.19	0.50%
Point 178	Decay Curve Fit from 7.275 Hz Sinusoid	1.0	7.275	0.50%
Point 182	Decay Curve Fit from 8.175 Hz Sinusoid	1.0	8.165	1.10%
Point 186	Decay Curve Fit from 7.025 Hz Sinusoid	1.0	7.025	0.60%
Point 230	Decay Curve Fit from 6.975 Hz Sinusoid	1.0	6.96	0.63%

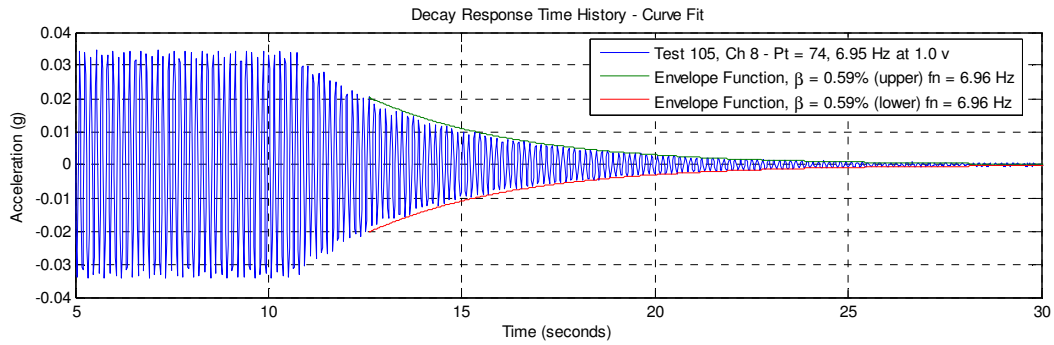
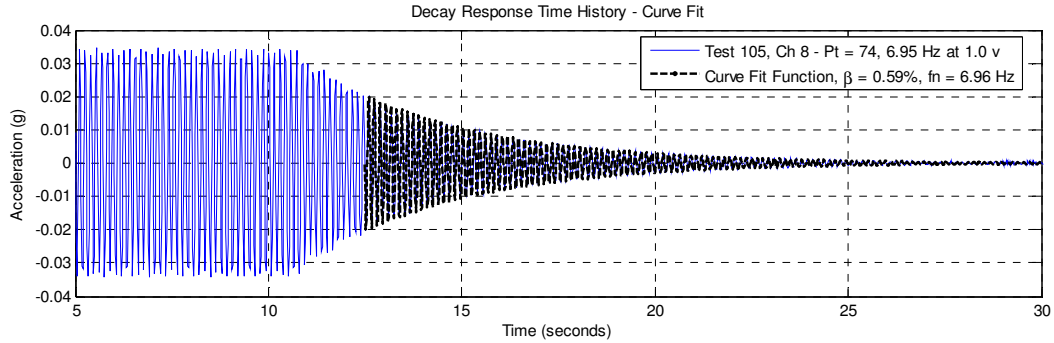
Point 21 – Test 91 – Ch 8 – Decay from Sine 9.00 Hz



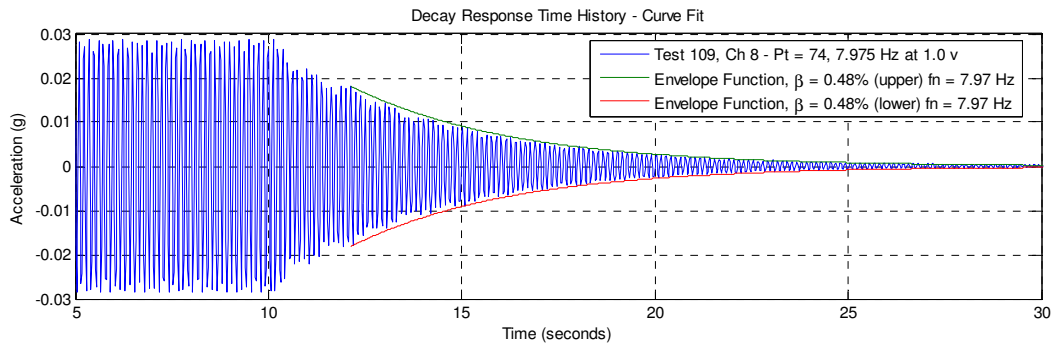
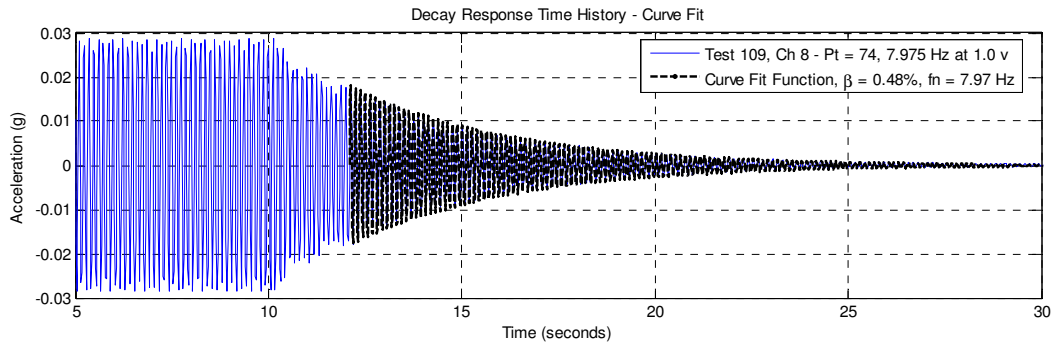
Point 25 – Test 79 – Ch 8 – Decay from Sine 6.575 Hz



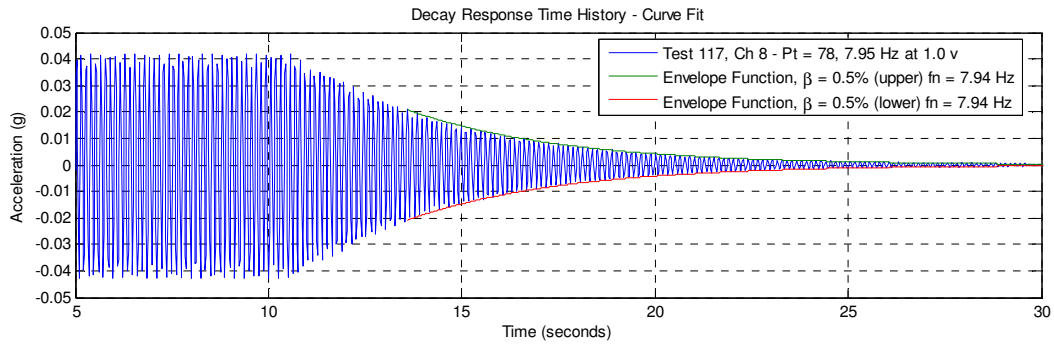
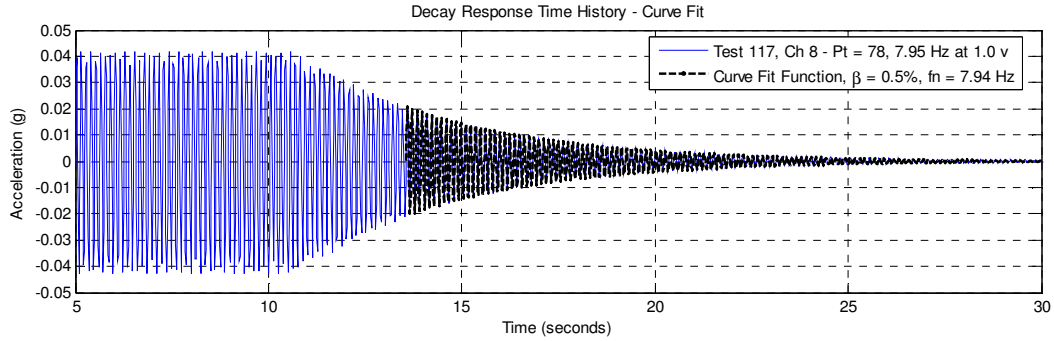
Point 74 – Test 105 – Ch 8 – Decay from Sine 6.95 Hz



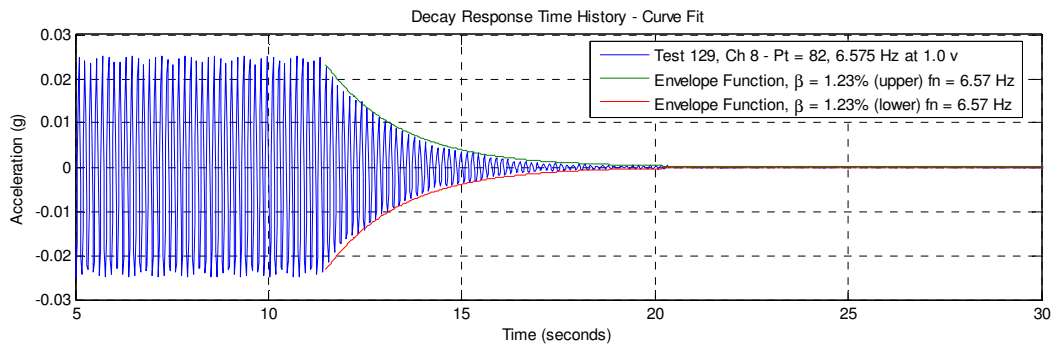
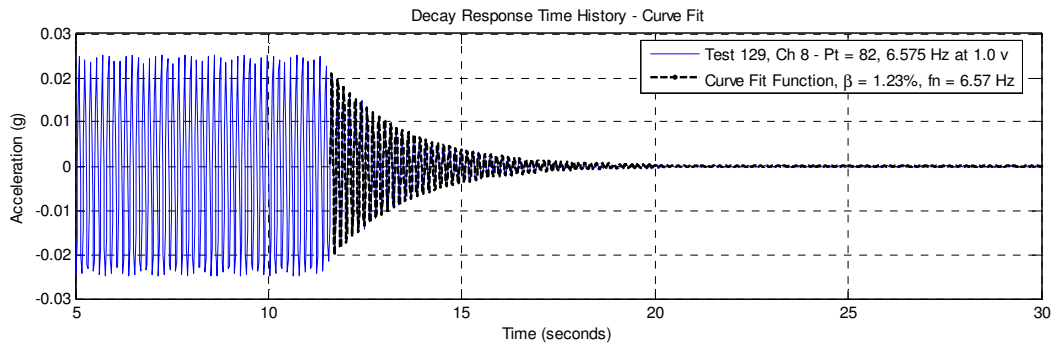
Point 74 – Test 109 – Ch 8 – Decay from Sine 7.975 Hz



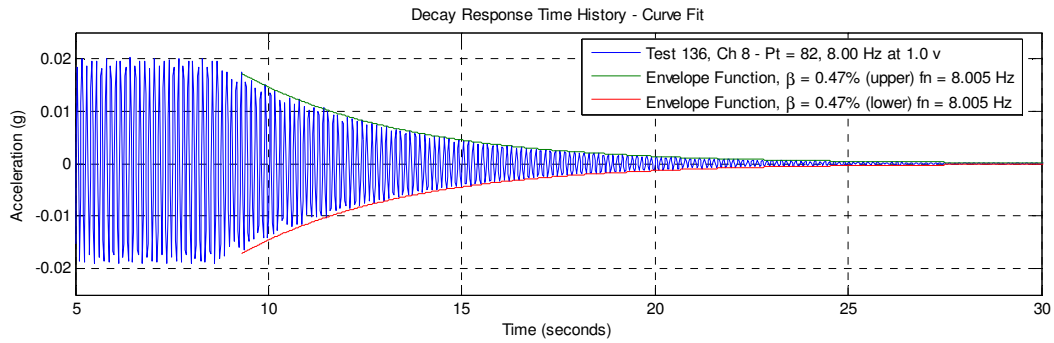
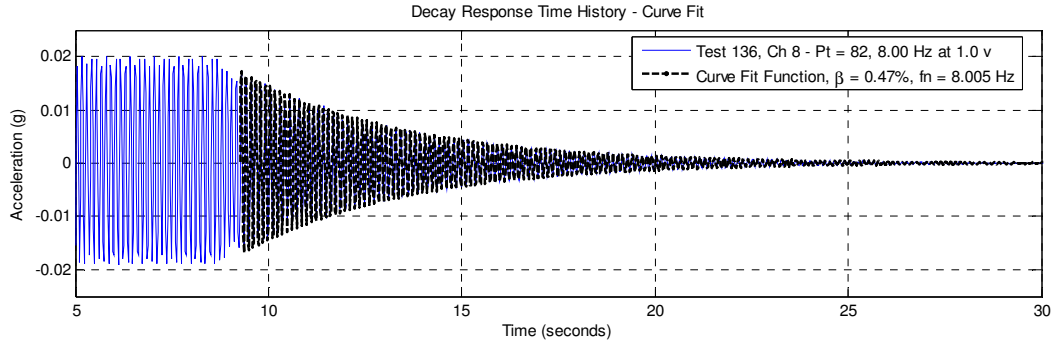
Point 78 – Test 117 – Ch 8 – Decay from Sine 7.95 Hz



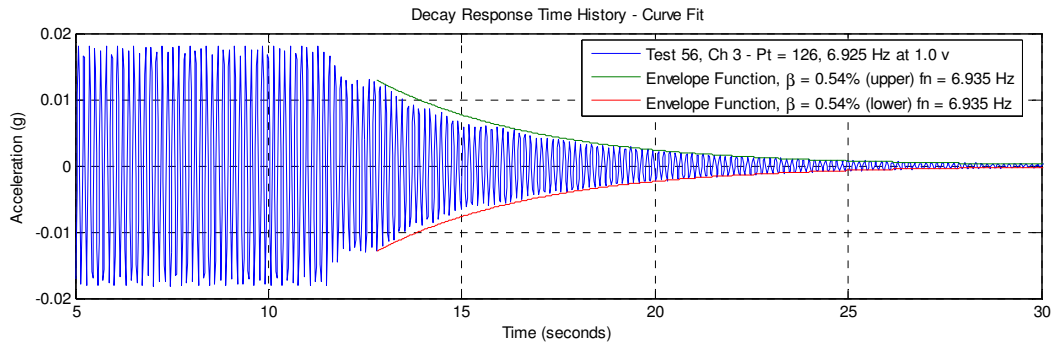
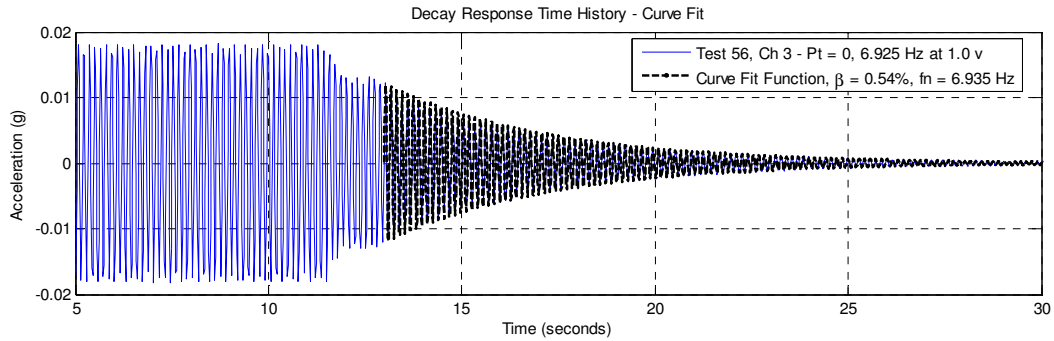
Point 82 – Test 129 – Ch 8 – Decay from Sine 6.575 Hz



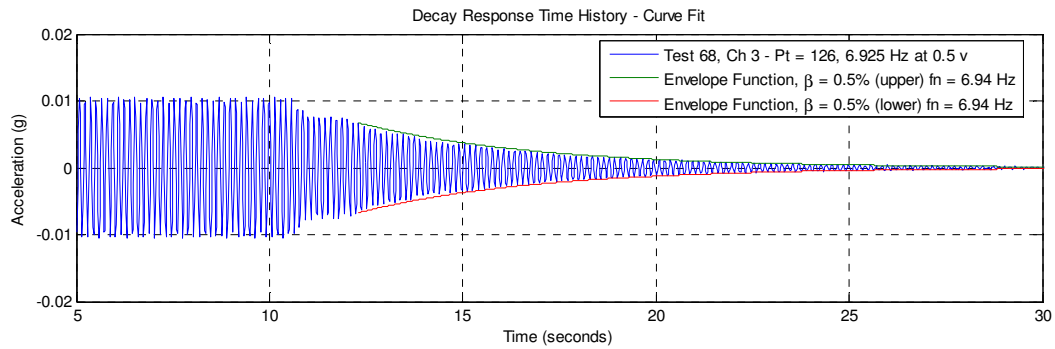
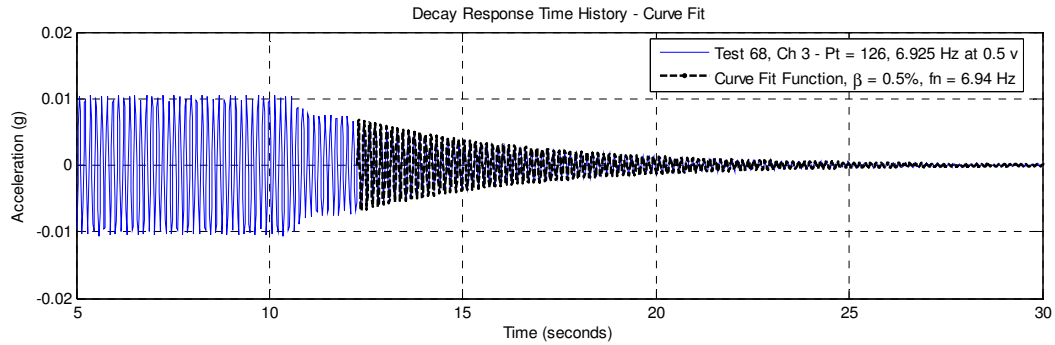
Point 82 – Test 136 – Ch 8 – Decay from Sine 8.00 Hz



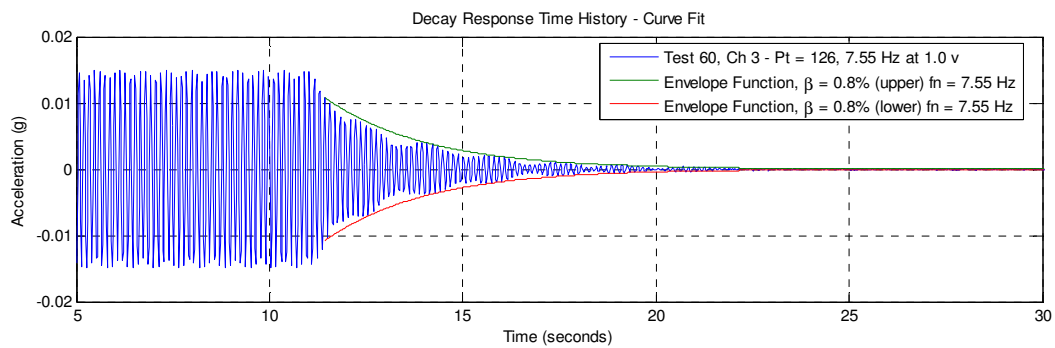
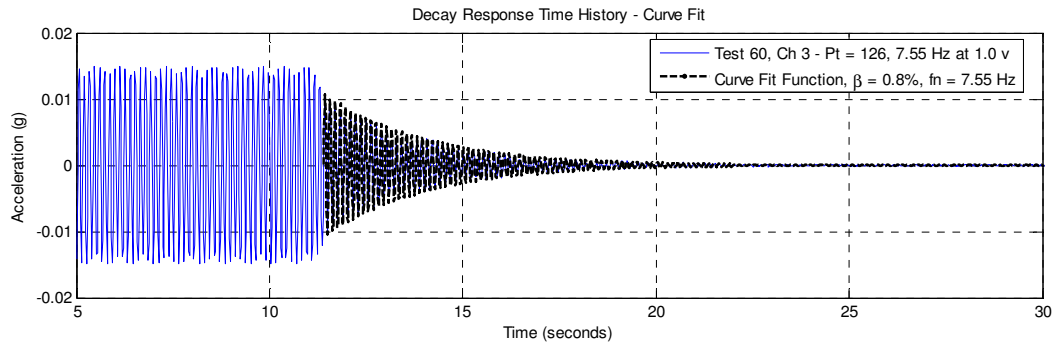
Point 126 – Test 56 – Ch 3 – Decay from Sine 6.925 Hz



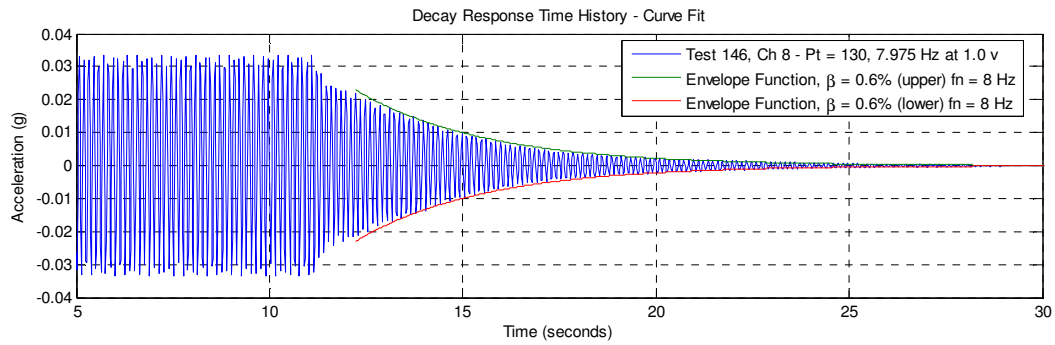
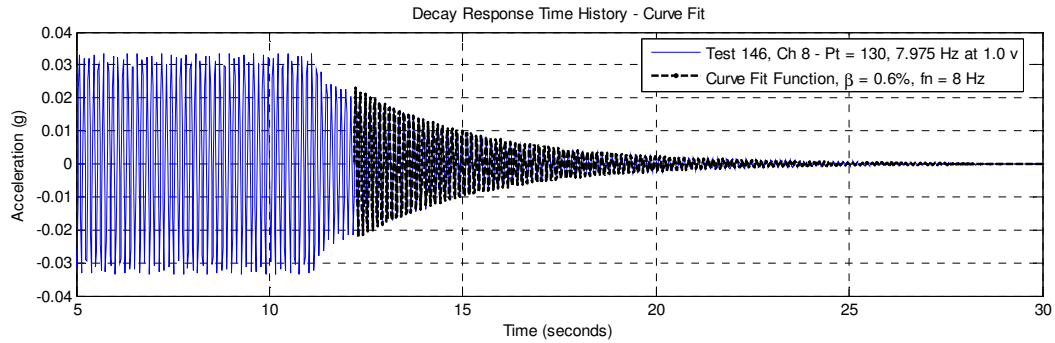
Point 126 – Test 68 – Ch 3 – Decay from Sine 6.925 Hz (0.5 v)



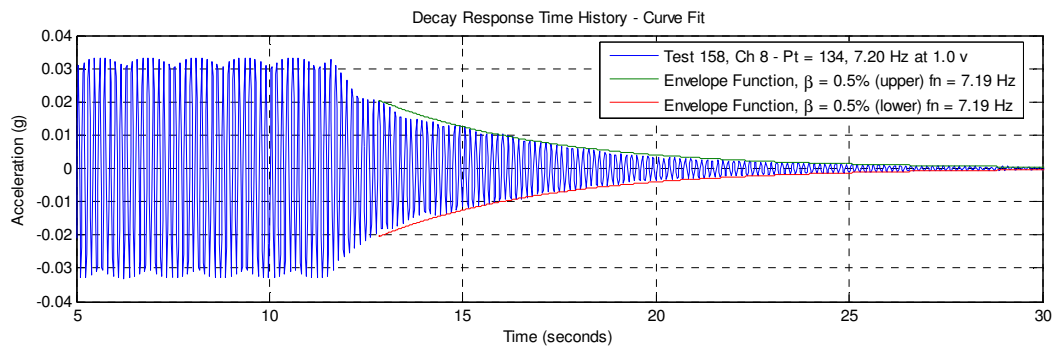
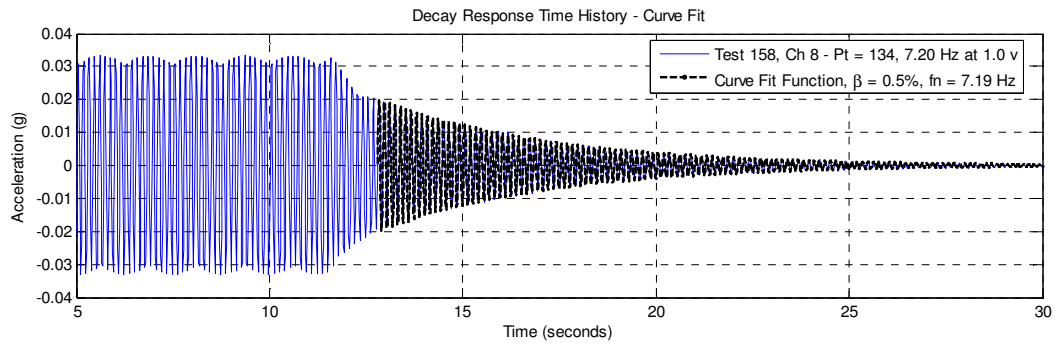
Point 126 – Test 60 – Ch 3 – Decay from Sine 7.55 Hz



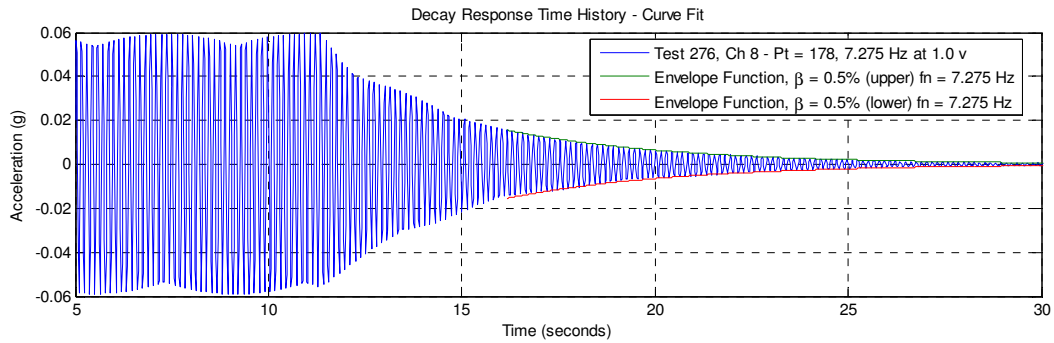
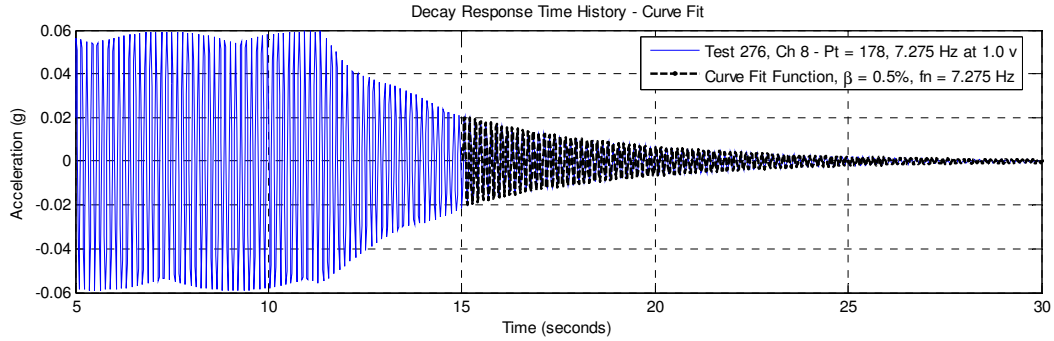
Point 130 – Test 146 – Ch 8 – Decay from Sine 7.975 Hz



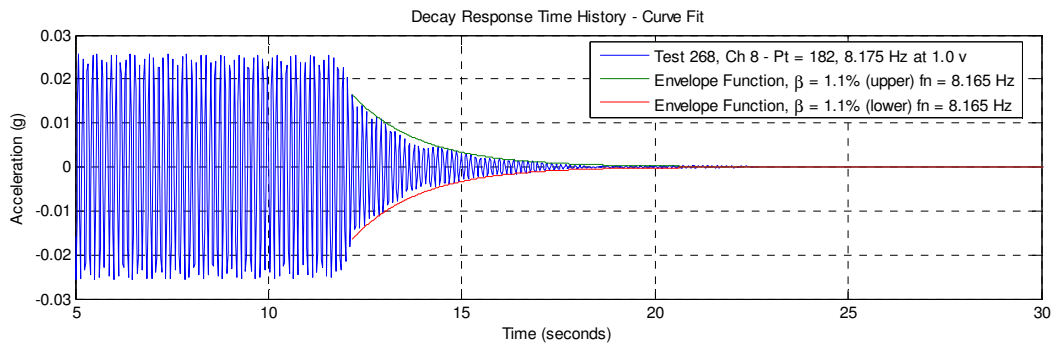
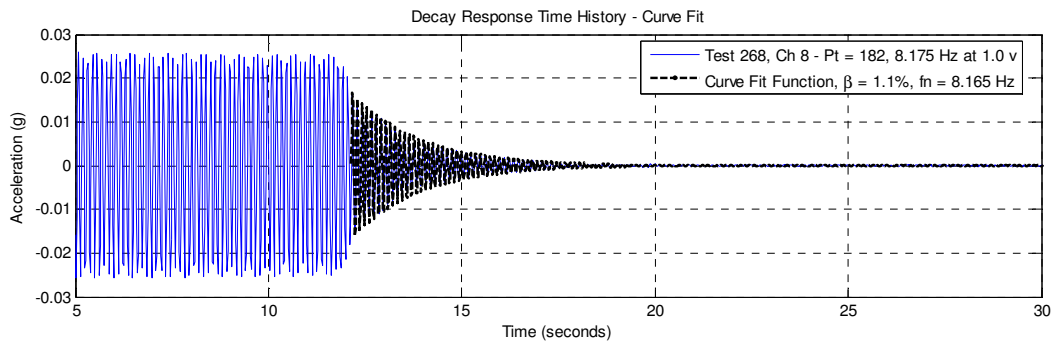
Point 134 – Test 158 – Ch 8 – Decay from Sine 7.20 Hz



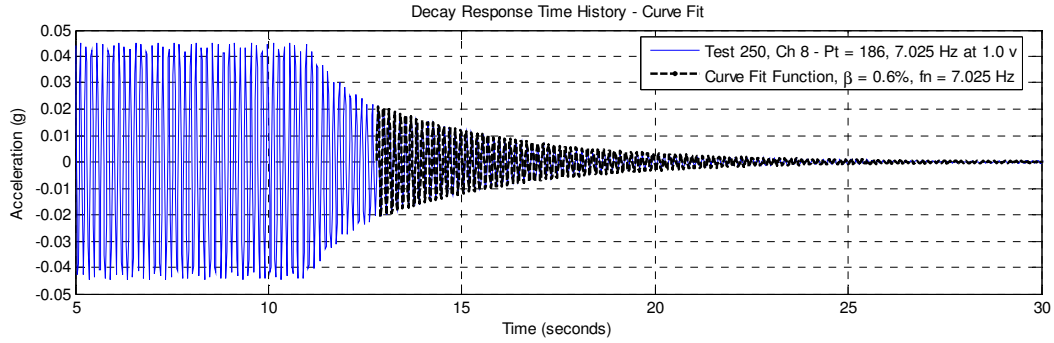
Point 178 – Test 276 – Ch 8 – Decay from Sine 7.275 Hz



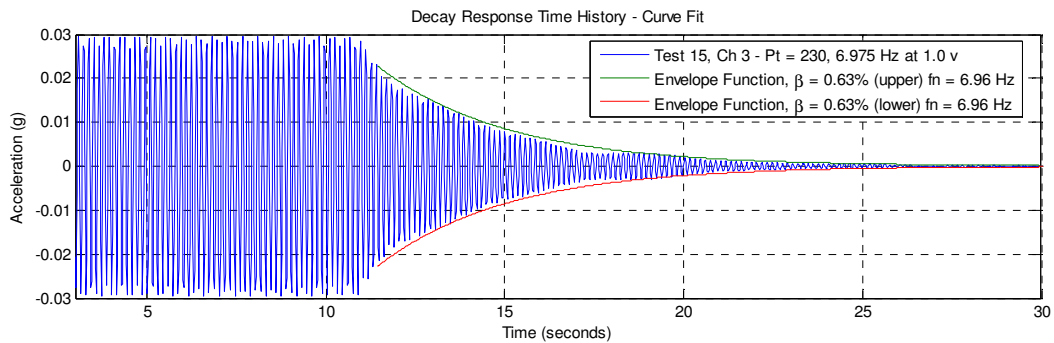
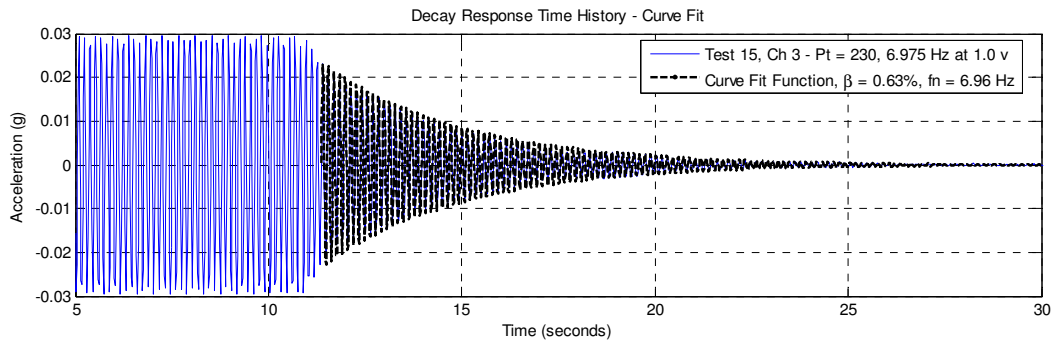
Point 182 – Test 268 – Ch 8 – Decay from Sine 8.175 Hz



Point 186 – Test 250 – Ch 8 – Decay from Sine 7.025 Hz



Point 230 – Test 15 – Ch 3 – Decay from Sine 6.975 Hz



APPENDIX K

EXAMPLE COMPOSITE SECTION CALCULATIONS

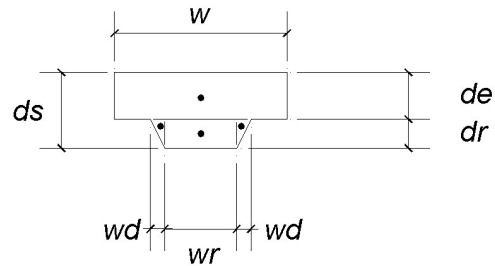
This Appendix includes example composite section and finite element property modifier calculations for the orthotropic composite deck and representative beam and girder sections.

Orthotropic Deck Moment of Inertia and Orthotropic Property Modifier Calculations:

Sloped Rib Moment of Inertia Calculation (i.e. considering the triangular sloped areas):

Note: All length units are in inches, areas in in² and moments of inertia in in⁴

$de := 3.25$ height of deck above ribs
 $dr := 2$ height of deck ribs
 $ds := de + dr$ total height of composite slab and deck
 $ds = 5.25$
 $w := 12$ one foot width of composite deck for calculation
 $wr := 5$ width of deck rib
 $wd := 1$ width of diagonal slope of deck rib



Compute areas for moment of inertia calculations:

$$Aslab := de \cdot w \quad Arib := dr \cdot wr \quad Adiag := 2 \cdot \left(\frac{1}{2} \cdot dr \cdot wd \right)$$

$$Aslab = 39 \quad Arib = 10 \quad Adiag = 2$$

$$Atot := de \cdot w + dr \cdot wr + dr \cdot wd \quad Atot = 51$$

$Aslab + Arib + Adiag = 51$ total concrete area of a one foot width of composite slab

Locate the neutral axis of the entire cross section using the areas of the slab above the deck ribs, the rectangular deck rib, and the triangular areas of the deck ribs:

$$y := \frac{Aslab \cdot \left(ds - \frac{de}{2} \right) + Arib \cdot \left(\frac{dr}{2} \right) + Adiag \cdot \left(\frac{2}{3} \cdot dr \right)}{Atot} \quad y = 3.02 \text{ from top of section}$$

Compute moments of inertia for the subdivided areas used in the calculation:

$$Islab := \frac{w \cdot de^3}{12} \quad Irib := \frac{wr \cdot dr^3}{12} \quad Idiag := 2 \cdot \frac{wd \cdot dr^3}{36}$$

$$Islab = 34.328 \quad Irib = 3.333 \quad Idiag = 0.444$$

Compute the section moment of inertia using the parallel axis theorem:

$$Icomp := Islab + Aslab \cdot \left(ds - \frac{de}{2} - y \right)^2 + Irib + Arib \cdot \left(y - \frac{dr}{2} \right)^2 + Idiag + Adiag \cdot \left(y - \frac{2}{3} \cdot dr \right)^2$$

$$Icomp = 98.875$$

Compute the ratio of the overall moment of inertia to that of just the section above the ribs to determine the orthotropic bending stiffness property multiplier:

$$PMortho := \frac{Icomp}{Islab}$$

$$PMortho = 2.88$$

Example Transformed Moment of Inertia and FE Property Modifier Calculations:

For the following example, the composite deck system used is a 5.25-in. total depth slab on 2-in. LOK-Floor steel deck (3.25-in. slab thickness above the deck ribs). All composite section computations are based on DG11 guidance, including recommendations for effective width. The concrete and deck properties and computed values needed for the example are specified below:

$$d_s = 5.25 \text{ in} = \text{total composite deck height}$$

$$d_r = 2 \text{ in} = \text{total composite deck height}$$

$$w_c = 115 \text{ pcf} = \text{specified concrete unit weight}$$

$$f'_c = 4 \text{ ksi} = \text{specified concrete strength}$$

$$1.35 * E_c = 1.35 * w_c^{1.5} \sqrt{f'_c} = 3,300 \text{ ksi} = \text{dynamic modulus of concrete (DG11)}$$

$$E_s = 29,000 \text{ ksi} = \text{modulus of elasticity of steel}$$

$$n = \frac{E_s}{1.35 * E_c} = \frac{29,000 \text{ ksi}}{3,300 \text{ ksi}} = 8.71 = \text{modular ratio (concrete-to-steel)}$$

Floor Beam Section Example (Deck Ribs Perpendicular to Member):

This example uses a typical floor beam in NOC VII, which is a W21x44 with a 45'-10" length and beam spacing of 10 ft on center:

SECTION: W21x44

$$d = 20.7 \text{ in} = \text{total depth of wide flange section}$$

$$A = 13.0 \text{ in}^2 = \text{cross section area of steel section}$$

$$I_x = 843 \text{ in}^4 = \text{strong axis moment of inertia}$$

$$L_b = 45'-10" = 550 \text{ in} = \text{beam length}$$

$$S = 10' = 120 \text{ in} = \text{beam spacing}$$

$$I_{beam,transformed} = PM_{beam} * I_{beam} + I_{slab,transformed}$$
$$PM_{beam} = \frac{I_{beam,transformed} - I_{slab,transformed}}{I_{beam}}$$

Determine effective concrete width & depth:

$$w_e = \min \left\{ \frac{S}{0.4 * L_b}, \frac{120 \text{ in}}{0.4 * 550 \text{ in}} \right\} = 120 \text{ in} = \text{effective concrete width}$$

$$d_e = 3.25 \text{ in} = \text{depth of concrete above the deck ribs}$$

Compute *transformed* concrete width and area:

$$\text{transformed concrete width} = w_e / n = (120 \text{ in}) / (8.71) = 13.78 \text{ in}$$

$$\text{transformed concrete area} = (w_e / n) \cdot d_e = (13.78 \text{ in})(3.25 \text{ in}) = 44.78 \text{ in}^2$$

Determine location of neutral axis (from bottom of steel section):

$$\bar{y} = \frac{(13.0 \text{ in}^2) \left(\frac{20.7 \text{ in}}{2} \right) + (44.78 \text{ in}^2) \left(20.7 \text{ in} + 5.25 \text{ in} - \frac{3.25 \text{ in}}{2} \right)}{(13.0 \text{ in}^2) + (44.78 \text{ in}^2)} = 21.18 \text{ in from bottom}$$

Compute transformed moment of inertia using parallel axis theorem:

$$I_{beam,transformed} = \left[(843 \text{ in}^4) + (13.0 \text{ in}^2) \left(21.18 \text{ in} - \frac{20.7 \text{ in}}{2} \right)^2 \right]$$

$$+ \left[\left(\frac{(13.78 \text{ in})(3.25 \text{ in})^3}{12} \right) + (44.78 \text{ in}^2) \left(20.7 \text{ in} + 5.25 \text{ in} - \frac{3.25 \text{ in}}{2} - 21.18 \text{ in} \right)^2 \right]$$

$$I_{beam,transformed} = \left[(843 \text{ in}^4) + (1525 \text{ in}^4) + (39 \text{ in}^4) + (443 \text{ in}^4) \right]$$

$$I_{beam,transformed} = 2850 \text{ in}^4$$

Compute the BASELINE strong axis moment of inertia property modifier for the beam

but remembering to back out the moment of inertia for the transformed slab

about its own neutral axis to ensure it is not accounted for twice:

$$I_{slab,transformed} = \left(\frac{(13.78 \text{ in})(3.25 \text{ in})^3}{12} \right) = 39 \text{ in}^4$$

$$PM_{beam} = \frac{I_{beam,transformed} - I_{slab,transformed}}{I_{x,beam}} = \frac{2850 \text{ in}^4 - 39 \text{ in}^4}{843 \text{ in}^4} = 3.334$$

Thus, this example's *baseline* stiffness property modifier is 3.334 for the beam member. Note that the above example is for an interior member with a slab on either side; however effective width limitations should also consider spandrel members and members with overhangs per DG11 guidance.

Floor Girder Section Example (T-Beam Analogy – Deck Ribs Parallel to Member):

This example uses a typical interior girder in NOC VII, which is a W27x84 with a 30-ft span, and bay's spanning 30-ft on one side and 45'-10" on the other.

SECTION: W27x84

$d = 26.7 \text{ in}$ = total depth of wide flange section

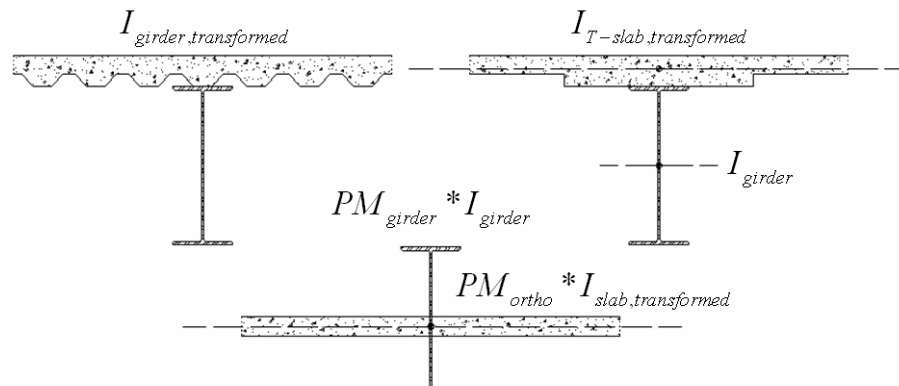
$A = 24.8 \text{ in}^2$ = cross section area of steel section

$I_x = 2850 \text{ in}^4$ = strong axis moment of inertia

$L_g = 30 \text{ ft} = 360 \text{ in}$ = girder length

$L_{b,\text{left}} = 30 \text{ ft} = 360 \text{ in}$ = left beam span

$L_{b,\text{right}} = 45'-10" = 550 \text{ in}$ = right beam span



$$I_{\text{girder,transformed}} = PM_{\text{girder}} * I_{\text{girder}} + PM_{\text{ortho}} * I_{\text{slab,transformed}}$$

$$PM_{\text{girder}} = \frac{I_{\text{girder,transformed}} - PM_{\text{ortho}} * I_{\text{slab,transformed}}}{I_{\text{girder}}}$$

Determine effective concrete width & depth of top flange and web using the T-beam analogy:

$$w_{e,\text{left}} = \min \left\{ \frac{L_{b,\text{left}}}{2}, \frac{360 \text{ in}}{2} = 180 \text{ in} \right\} = 72 \text{ in}$$

$$w_{e,\text{right}} = \min \left\{ \frac{L_{b,\text{right}}}{2}, \frac{550 \text{ in}}{2} = 275 \text{ in} \right\} = 72 \text{ in}$$

$$w_{e,\text{flange}} = 72 \text{ in} + 72 \text{ in} = 144 \text{ in} = \text{effective concrete width of top flange}$$

$$w_{e,\text{web}} = w_{e,\text{flange}} / 2 = 144 \text{ in} / 2 = 72 \text{ in} = \text{effective concrete width of web}$$

$$d_e = d_s + \frac{d_r}{2} = 3.25 \text{ in} + \frac{2 \text{ in}}{2} = 4.25 \text{ in} = \text{depth of concrete above the deck ribs}$$

Compute *transformed* concrete width and area:

$$\text{transformed concrete width (top flange)} = w_{e,flange} / n = (144 \text{ in}) / (8.71) = 16.53 \text{ in}$$

$$\text{transformed concrete area (top flange)} = (w_{e,flange} / n) \cdot d_e = (16.53 \text{ in})(3.25 \text{ in}) = 53.74 \text{ in}^2$$

$$\text{transformed concrete width (web)} = w_{e,web} / n = (72 \text{ in}) / (8.71) = 8.27 \text{ in}$$

$$\text{transformed concrete area (web)} = (w_{e,web} / n) \cdot d_r = (8.27 \text{ in})(2 \text{ in}) = 16.53 \text{ in}^2$$

Determine location of neutral axis (from bottom of steel section):

$$\bar{y} = \frac{(24.8 \text{ in}^2) \left(\frac{26.7 \text{ in}}{2} \right) + (53.74 \text{ in}^2) \left(26.7 \text{ in} + 5.25 \text{ in} - \frac{3.25 \text{ in}}{2} \right) + (16.53 \text{ in}^2) \left(26.7 \text{ in} + \frac{2 \text{ in}}{2} \right)}{(24.8 \text{ in}^2) + (53.74 \text{ in}^2) + (16.53 \text{ in}^2)}$$

$$\bar{y} = 25.44 \text{ in from bottom}$$

$$= 26.7 \text{ in} + 5.25 \text{ in} - 25.44 \text{ in} = 6.51 \text{ in from top}$$

Compute transformed moment of inertia using parallel axis theorem:

$$\begin{aligned} I_{girder,transformed} &= \left[(2850 \text{ in}^4) + (24.8 \text{ in}^2) \left(25.44 \text{ in} - \frac{26.7 \text{ in}}{2} \right)^2 \right] \\ &\quad + \left[\left(\frac{(16.53 \text{ in})(3.25 \text{ in})^3}{12} \right) + (53.74 \text{ in}^2) \left(6.51 \text{ in} - \frac{3.25 \text{ in}}{2} \right)^2 \right] \\ &\quad + \left[\left(\frac{(8.27 \text{ in})(2 \text{ in})^3}{12} \right) + (16.53 \text{ in}^2) \left(6.51 \text{ in} - 3.25 \text{ in} - \frac{2 \text{ in}}{2} \right)^2 \right] \\ I_{girder,transformed} &= \left[(2850 \text{ in}^4) + (3625 \text{ in}^4) \right] + \left[(47 \text{ in}^4) + (1282 \text{ in}^4) \right] + \left[(6 \text{ in}^4) + (84 \text{ in}^4) \right] \\ I_{girder,transformed} &= 7894 \text{ in}^4 \end{aligned}$$

Compute the BASELINE strong axis moment of inertia property modifier for the beam but remembering to back out the moment of inertia for the top flange of the transformed slab about its own neutral axis, including its orthotropic property modifier, if any, to ensure it is not accounted for twice:

$$I_{slab,transformed} = \left(\frac{(16.53 \text{ in})(3.25 \text{ in})^3}{12} \right) = 47 \text{ in}^4$$

$$PM_{ortho} = 2.88 \text{ from previous orthotropic stiffness calculations}$$

$$PM_{girder} = \frac{I_{girder,transformed} - PM_{ortho} * I_{slab,transformed}}{I_{x,beam}} = \frac{(7894 \text{ in}^4) - (2.88)(47 \text{ in}^4)}{2850 \text{ in}^4} = 2.722$$

Thus, this example's *baseline* stiffness property modifier is 2.722 for the girder.

APPENDIX L

PARTIAL FIXITY CURVE FOR ASSUMED MOMENT-ROTATION RELATIONSHIP

This Appendix includes a brief derivation of the moment-rotation based partial fixity curve used in the presented research. The relationship was based on an assumed degree of fixity expressed as a percentage of free rotation at the end of a simply supported beam under distributed load or the percentage of fixed-end moment of a fixed-fixed beam under distributed load. A 75% partial fixity would describe the end of a simply supported beam with rotational springs that attracted 75% of the fixed-end moment under a distributed load.

The fixed-end moment of a simply supported beam under a distributed load is:

$$M_{fixed} = \frac{wL^2}{12} \quad \text{where } \begin{array}{l} w = \text{uniform distributed load} \\ L = \text{length of beam} \end{array}$$

The end rotation of a simply supported beam under a distributed load is:

$$\theta_{free} = \frac{wL^3}{24EI} \quad \text{where } EI = \text{stiffness property of the beam}$$

The moment-rotation relationship for an arbitrary rotational spring is:

$$M = k_r \theta \quad \text{where } k_r = \text{arbitrary rotational spring value}$$

Solving for the rotational spring value:

$$k_r = \frac{M}{\theta}$$

Thus, with any moment and rotation pair, a rotational spring value can be established. In this research, the moment-rotation pairs used were an assumed linear relationship between a fixed end moment and a free rotation value, expressed as a percentage of fixity on either term:

$$k_r = \frac{\left(\%M_{fixed} \right) M_{fixed}}{\left(\% \theta_{free} \right) \theta_{free}}$$

The linear relationship used for the moment-rotation pairs allows the percent fixity to be expressed as a single value in terms of either fixed-end moment or free rotation:

$$\begin{aligned}
 \%M_{fixed} + \% \theta_{free} &= 1 & \text{and} & & k_r &= \frac{(\%M_{fixed}) M_{fixed}}{(\% \theta_{free}) \theta_{free}} \\
 \%M_{fixed} &= 1 - \% \theta_{free} & \text{or} & & \% \theta_{free} &= 1 - \%M_{fixed} \\
 k_r &= \frac{(1 - \% \theta_{free}) M_{fixed}}{(\% \theta_{free}) \theta_{free}} & \text{or} & & k_r &= \frac{(\%M_{fixed}) M_{fixed}}{(1 - \%M_{fixed}) \theta_{free}} \\
 k_r &= \frac{(1 - \% \theta_{free}) \left(\frac{wL^2}{12} \right)}{(\% \theta_{free}) \left(\frac{wL^3}{24EI} \right)} & \text{or} & & k_r &= \frac{(\%M_{fixed}) \left(\frac{wL^2}{12} \right)}{(1 - \%M_{fixed}) \left(\frac{wL^3}{24EI} \right)} \\
 k_r &= \underbrace{\frac{2(1 - \% \theta_{free})}{(\% \theta_{free})}}_{\alpha} \cdot \frac{EI}{L} & \text{or} & & k_r &= \underbrace{\frac{2(\%M_{fixed})}{(1 - \%M_{fixed})}}_{\alpha} \cdot \frac{EI}{L} \\
 & & & & k_r &= \alpha \cdot \frac{EI}{L} \\
 \alpha &= \frac{2(1 - \% \theta_{free})}{(\% \theta_{free})} & \text{or} & & \alpha &= \frac{2(\%M_{fixed})}{(1 - \%M_{fixed})}
 \end{aligned}$$

Similar relationships between moment and rotation can be used to determine the coefficient of the partial fixity term (i.e. the rotational spring value used at the end of the beam); however the fixed-end moment and pinned-end free rotation (and linear relationship) was used in the presented research. The partial fixity value used in the presented research was 6EI/l, which was computed assuming 75% fixed (or 25% free) as follows:

$$\begin{aligned}
 \% \theta_{free} &= 25\% = 0.25 & \%M_{fixed} &= 75\% = 0.75 \\
 k_r &= \alpha \cdot \frac{EI}{L} \\
 \alpha &= \frac{2(1 - \% \theta_{free})}{(\% \theta_{free})} & \alpha &= \frac{2(\%M_{fixed})}{(1 - \%M_{fixed})} \\
 \alpha &= \frac{2(1 - 0.25)}{(0.25)} = 6 & \alpha &= \frac{2(0.75)}{(1 - 0.75)} = 6 \\
 \therefore k_r &= \frac{6EI}{L}
 \end{aligned}$$

NOC VII – COMPOSITE SECTION CALCULATIONS & FE MODEL INPUT VALUES

[illegible]

427

NOC VII Composite Section Calculation Worksheets:

NOC VII BEAMS - Composite Section Calculations:

		B1	B2	EB1	BC1	BC2	SB1	SB2
Concrete Deck Height, ds =	in	5.25	5.25	5.25	5.25	5.25	5.25	5.25
Concrete Unit Weight, wc =	pcf	115	115	115	115	115	115	115
Concrete Strength, Fc (ksi) =	ksi	4	4	4	4	4	4	4
Deck Rib Height, dr =	in	2	2	2	2	2	2	2
Modulus of Elasticity of Steel, Es =	ksi	29,000	29,000	29,000	29,000	29,000	29,000	29,000
Ec =	ksi	2466	2466	2466	2466	2466	2466	2466
Dynamic Concrete Modulus, 1.35*Ec =	ksi	3330	3330	3330	3330	3330	3330	3330
n = Es/1.35*Ec =		8.71	8.71	8.71	8.71	8.71	8.71	8.71
Section =		W21x44	W18x35	W18x35	W27x84	W24x55	W21x50	W21x50
d =	in	20.7	17.7	17.7	26.7	23.6	20.8	20.8
A =	in ²	13	10.3	10.3	24.8	16.3	14.7	14.7
Ix =	in ⁴	843	510	510	2850	1360	984	984
Weight/length =	plf	44	35	35	84	55	50	50
Beam Spacing (ft), S =	ft	10	10	5	10	10	5	5
Beam Span (ft), Lb =	ft	45.83	37.58	37.58	45.83	37.58	45.83	37.58
Beam Spacing (in), S =	in	120	120	60	120	120	60	60
Beam Span (in), Lb =	in	550	451	451	550	451	550	451
Effective Concrete Width, S =	in	120	120	60	120	120	60	60
Effective Concrete Width, 0.4*Lb =	in	220	180	180	220	180	220	180
Effective Concrete Width, min =	in	120	120	60	120	120	60	60
Effective Concrete Depth, de, b =	in	3.25	3.25	3.25	3.25	3.25	3.25	3.25
Transformed Concrete Width =	in	13.78	13.78	6.89	13.78	13.78	6.89	6.89
Transformed Concrete Area =	in ²	44.78	44.78	22.39	44.78	44.78	22.39	22.39
Location of Neutral Axis (from bottom) =	in	21.18	18.99	17.39	24.27	23.11	18.87	18.87
Distance to Neutral Axis (above beam c.g.) =	in	10.831	10.142	8.544	10.925	11.309	8.466	8.466
Transformed Moment of Inertia, I _{b,trans} =	in ⁴	2850.1	1852.6	1627.6	7488.5	4242.7	2749.2	2749.2
		B1	B2	EB1	BC1	BC2	SB1	SB2
		W21x44	W18x35	W18x35	W27x84	W24x55	W21x50	W21x50
		39.4	39.4	19.7	39.4	39.4	19.7	19.7
Beam Modified Moment of Inertia, I ₃ * = I _{b,trans} - I _{tr,slab} =	in ⁴	2810.7	1813.2	1607.9	7449.1	4203.3	2729.5	2729.5
Beam Property Modifier, I ₃ to I ₃ * =		3.334	3.555	3.153	2.614	3.091	2.774	2.774

NOC VII GIRDERS - Composite Section Calculations:

		G1	G2	G3
Concrete Deck Height, ds =	in	5.25	5.25	5.25
Concrete Unit Weight, wc =	pcf	115	115	115
Concrete Strength, Fc (ksi) =	ksi	4	4	4
Deck Rib Height, dr =	in	2	2	2
Modulus of Elasticity of Steel, Es =	ksi	29,000	29,000	29,000
(AISC) wc*1.5*Fc*0.5 Ec =	ksi	2466	2466	2466
Dynamic Concrete Modulus, 1.35*Ec =	ksi	3330	3330	3330
n = Es/1.35*Ec =		8.71	8.71	8.71
Concrete Depth Above Rib, de =	in	3.25	3.25	3.25
		Left Beam	Left Beam	Left Beam
		B1	B1	B2
		W21x44	W21x44	W18x35
		45.83	45.83	37.58
		550.00	550.00	451.00
		Right Beam	Right Beam	Right Beam
		NONE	B2	NONE
		n/a	W18x35	n/a
		0	37.58	0
		0.00	451.00	0.00
		G1	G2	G3
		GIRDER	GIRDER	GIRDER
		W24x55	W27x84	W21x55
		23.6	26.7	20.8
		16.3	24.8	16.2
		1360	2850	1140
		55	84	55
		30	30	30
		45.83	45.83	37.58
		0	37.58	0
		360.00	360.00	360.00
		144	144	144
		72	72	72
		0	72	0
		72	144	72
		36	72	36
		4.25	4.25	4.25
		8.27	16.53	8.27
		26.87	53.74	26.87
		4.13	8.27	4.13
		8.27	16.53	8.27
		21.91	25.44	19.58
		5.31	4.88	4.85
		2.69	2.26	2.22
		10.115	12.090	9.176
		3871.3	7894.5	3203.0
		GIRDER	GIRDER	GIRDER
		G1	G2	G3
		W24x55	W27x84	W21x55
		2.88	2.88	2.88
		68.1	136.2	68.1
		3803.2	7758.3	3134.9
		2.796	2.722	2.750

NOC VII FE Model Framing Member Property Assignments:

Section							Assigned Property Modifier (I3)	End Moment Frame Release		E/I Multiplier	Partial Fixity			
Member Label:	Member Type:	Assigned Section:	Moment of Inertia, I3 (in4)	Length: (ft)	Baseline EI/L (k-in/rad)	Baseline PM I3:		PM I3 Multiplier	I-end (Yes/No)		J-end (Yes/No)	P-Fixity? (Yes/No)	I-end Kip-in/rad	J-end Kip-in/rad
B1-01	B1	W21x44	843	45.83	44,449	3.334		3.334	Yes	Yes	6EVL	Yes	266,695	266,695
B1-02	B1	W21x44	843	45.83	44,449	3.334		3.334	Yes	Yes	6EVL	Yes	266,695	266,695
B1-03	B1	W21x44	843	45.83	44,449	3.334		3.334	Yes	Yes	6EVL	Yes	266,695	266,695
B1-04	B1	W21x44	843	45.83	44,449	3.334		3.334	Yes	Yes	6EVL	Yes	266,695	266,695
B1-05	B1	W21x44	843	45.83	44,449	3.334		3.334	Yes	Yes	6EVL	Yes	266,695	266,695
B1-06	B1	W21x44	843	45.83	44,449	3.334		3.334	Yes	Yes	6EVL	Yes	266,695	266,695
B1-07	B1	W21x44	843	45.83	44,449	3.334		3.334	Yes	Yes	6EVL	Yes	266,695	266,695
B1-08	B1	W21x44	843	45.83	44,449	3.334		3.334	Yes	Yes	6EVL	Yes	266,695	266,695
B1-09	B1	W21x44	843	45.83	44,449	3.334		3.334	Yes	Yes	6EVL	Yes	266,695	266,695
B1-10	B1	W21x44	843	45.83	44,449	3.334		3.334	Yes	Yes	6EVL	Yes	266,695	266,695
B1-11	B1	W21x44	843	45.83	44,449	3.334		3.334	Yes	Yes	6EVL	Yes	266,695	266,695
B1-12	B1	W21x44	843	45.83	44,449	3.334		3.334	Yes	Yes	6EVL	Yes	266,695	266,695
B1-13	B1	W21x44	843	45.83	44,449	3.334		3.334	Yes	Yes	6EVL	Yes	266,695	266,695
B1-14	B1	W21x44	843	45.83	44,449	3.334		3.334	Yes	Yes	6EVL	Yes	266,695	266,695
B1-15	B1	W21x44	843	45.83	44,449	3.334		3.334	Yes	Yes	6EVL	Yes	266,695	266,695
B1-16	B1	W21x44	843	45.83	44,449	3.334		3.334	Yes	Yes	6EVL	Yes	266,695	266,695
B1-17	B1	W21x44	843	45.83	44,449	3.334		3.334	Yes	Yes	6EVL	Yes	266,695	266,695
B1-18	B1	W21x44	843	45.83	44,449	3.334		3.334	Yes	Yes	6EVL	Yes	266,695	266,695
B1-19	B1	W21x44	843	45.83	44,449	3.334		3.334	Yes	Yes	6EVL	Yes	266,695	266,695
B1-20	B1	W21x44	843	45.83	44,449	3.334		3.334	Yes	Yes	6EVL	Yes	266,695	266,695
B1-21	B1	W21x44	843	45.83	44,449	3.334		3.334	Yes	Yes	6EVL	Yes	266,695	266,695
B1-22	B1	W21x44	843	45.83	44,449	3.334		3.334	Yes	Yes	6EVL	Yes	266,695	266,695
B1-23	B1	W21x44	843	45.83	44,449	3.334		3.334	Yes	Yes	6EVL	Yes	266,695	266,695
B1-24	B1	W21x44	843	45.83	44,449	3.334		3.334	Yes	Yes	6EVL	Yes	266,695	266,695
B1-25	B1	W21x44	843	45.83	44,449	3.334		3.334	Yes	Yes	6EVL	Yes	266,695	266,695
B1-26	B1	W21x44	843	45.83	44,449	3.334		3.334	Yes	Yes	6EVL	Yes	266,695	266,695
B1-27	B1	W21x44	843	45.83	44,449	3.334		3.334	Yes	Yes	6EVL	Yes	266,695	266,695
B1-28	B1	W21x44	843	45.83	44,449	3.334		3.334	Yes	Yes	6EVL	Yes	266,695	266,695
B1-29	B1	W21x44	843	45.83	44,449	3.334		3.334	Yes	Yes	6EVL	Yes	266,695	266,695
B1-30	B1	W21x44	843	45.83	44,449	3.334		3.334	Yes	Yes	6EVL	Yes	266,695	266,695
B1-31	B1	W21x44	843	45.83	44,449	3.334		3.334	Yes	Yes	6EVL	Yes	266,695	266,695
B1-32	B1	W21x44	843	45.83	44,449	3.334		3.334	Yes	Yes	6EVL	Yes	266,695	266,695
B1-33	B1	W21x44	843	45.83	44,449	3.334		3.334	Yes	Yes	6EVL	Yes	266,695	266,695
B1-34	B1	W21x44	843	45.83	44,449	3.334		3.334	Yes	Yes	6EVL	Yes	266,695	266,695
B1-35	B1	W21x44	843	45.83	44,449	3.334		3.334	Yes	Yes	6EVL	Yes	266,695	266,695
B1-36	B1	W21x44	843	45.83	44,449	3.334		3.334	Yes	Yes	6EVL	Yes	266,695	266,695
B1-37	B1	W21x44	843	45.83	44,449	3.334		3.334	Yes	Yes	6EVL	Yes	266,695	266,695
B1-38	B1	W21x44	843	45.83	44,449	3.334		3.334	Yes	Yes	6EVL	Yes	266,695	266,695
B1-39	B1	W21x44	843	45.83	44,449	3.334		3.334	Yes	Yes	6EVL	Yes	266,695	266,695
B1-40	B1	W21x44	843	45.83	44,449	3.334		3.334	Yes	Yes	6EVL	Yes	266,695	266,695

Section Moment of									Assigned Property	End Moment Frame Release				Partial Fixity		
Member Label:	Member Type:	Assigned Section:	Inertia, I3 (in4)	Length: (ft)	E/I (k-in/rad)	Baseline PM I3:	PM I3 Multiplier	Modifier (I3)	i-end (Yes/No)	j-end (Yes/No)	E/I Multiplier	P-Fixity? (Yes/No)	i-end Kip-in/rad	j-end Kip-in/rad		
B2-41	B2	W18x35	510	37.58	32,794	3.555		3.555	Yes	Yes	6EVL	Yes	196,763	196,763		
B2-42	B2	W18x35	510	37.58	32,794	3.555		3.555	Yes	Yes	6EVL	Yes	196,763	196,763		
B2-43	B2	W18x35	510	37.58	32,794	3.555		3.555	Yes	Yes	6EVL	Yes	196,763	196,763		
B2-44	B2	W18x35	510	37.58	32,794	3.555		3.555	Yes	Yes	6EVL	Yes	196,763	196,763		
B2-45	B2	W18x35	510	37.58	32,794	3.555		3.555	Yes	Yes	6EVL	Yes	196,763	196,763		
B2-46	B2	W18x35	510	37.58	32,794	3.555		3.555	Yes	Yes	6EVL	Yes	196,763	196,763		
B2-47	B2	W18x35	510	37.58	32,794	3.555		3.555	Yes	Yes	6EVL	Yes	196,763	196,763		
B2-48	B2	W18x35	510	37.58	32,794	3.555		3.555	Yes	Yes	6EVL	Yes	196,763	196,763		
B2-49	B2	W18x35	510	37.58	32,794	3.555		3.555	Yes	Yes	6EVL	Yes	196,763	196,763		
B2-50	B2	W18x35	510	37.58	32,794	3.555		3.555	Yes	Yes	6EVL	Yes	196,763	196,763		
B2-51	B2	W18x35	510	37.58	32,794	3.555		3.555	Yes	Yes	6EVL	Yes	196,763	196,763		
B2-52	B2	W18x35	510	37.58	32,794	3.555		3.555	Yes	Yes	6EVL	Yes	196,763	196,763		
B2-53	B2	W18x35	510	37.58	32,794	3.555		3.555	Yes	Yes	6EVL	Yes	196,763	196,763		
B2-54	B2	W18x35	510	37.58	32,794	3.555		3.555	Yes	Yes	6EVL	Yes	196,763	196,763		
B2-55	B2	W18x35	510	37.58	32,794	3.555		3.555	Yes	Yes	6EVL	Yes	196,763	196,763		
B2-56	B2	W18x35	510	37.58	32,794	3.555		3.555	Yes	Yes	6EVL	Yes	196,763	196,763		
B2-57	B2	W18x35	510	37.58	32,794	3.555		3.555	Yes	Yes	6EVL	Yes	196,763	196,763		
B2-58	B2	W18x35	510	37.58	32,794	3.555		3.555	Yes	Yes	6EVL	Yes	196,763	196,763		
B2-59	B2	W18x35	510	37.58	32,794	3.555		3.555	Yes	Yes	6EVL	Yes	196,763	196,763		
B2-60	B2	W18x35	510	37.58	32,794	3.555		3.555	Yes	Yes	6EVL	Yes	196,763	196,763		
B2-61	B2	W18x35	510	37.58	32,794	3.555		3.555	Yes	Yes	6EVL	Yes	196,763	196,763		
B2-62	B2	W18x35	510	37.58	32,794	3.555		3.555	Yes	Yes	6EVL	Yes	196,763	196,763		
BC1-63	BC1	W27x84	2850	45.83	150,273	2.614		2.614								
BC1-64	BC1	W27x84	2850	45.83	150,273	2.614		2.614								
BC1-65	BC1	W27x84	2850	45.83	150,273	2.614		2.614								
BC1-66	BC1	W27x84	2850	45.83	150,273	2.614		2.614								
BC1-67	BC1	W27x84	2850	45.83	150,273	2.614		2.614								
BC1-68	BC1	W27x84	2850	45.83	150,273	2.614		2.614								
BC1-69	BC1	W27x84	2850	45.83	150,273	2.614		2.614								
BC1-70	BC1	W27x84	2850	45.83	150,273	2.614		2.614								
BC1-71	BC1	W27x84	2850	45.83	150,273	2.614		2.614								
BC1-72	BC1	W27x84	2850	45.83	150,273	2.614		2.614								
BC1-73	BC1	W27x84	2850	45.83	150,273	2.614		2.614								
BC1-74	BC1	W27x84	2850	45.83	150,273	2.614		2.614								
BC1-75	BC1	W27x84	2850	45.83	150,273	2.614		2.614								
BC1-76	BC1	W27x84	2850	45.83	150,273	2.614		2.614								
BC1-77	BC1	W27x84	2850	45.83	150,273	2.614		2.614								
BC1-78	BC1	W27x84	2850	45.83	150,273	2.614		2.614								
BC1-79	BC1	W27x84	2850	45.83	150,273	2.614		2.614								
BC1-80	BC1	W27x84	2850	45.83	150,273	2.614		2.614								

Member Label:	Member Type:	Assigned Section:	Section Moment of Inertia, I3 (in4)	Length: (ft)	Baseline EI/L (k-in/rad)	Baseline PM I3:	PM I3 Multiplier	Assigned Property Modifier (I3)	End Moment Frame Release		EI/L Multiplier	Partial Fixity		
									i-end (Yes/No)	j-end (Yes/No)		P-Fixity? (Yes/No)	i-end Kip-in/rad	j-end Kip-in/rad
BC2-81	BC2	W24x55	1360	37.58	87,450	3.091		3.091						
BC2-82	BC2	W24x55	1360	37.58	87,450	3.091	rigid	1000						
BC2-83	BC2	W24x55	1360	37.58	87,450	3.091	rigid	1000						
BC2-84	BC2	W24x55	1360	37.58	87,450	3.091	rigid	1000						
BC2-85	BC2	W24x55	1360	37.58	87,450	3.091	rigid	1000						
BC2-86	BC2	W24x55	1360	37.58	87,450	3.091	rigid	1000						
BC2-87	BC2	W24x55	1360	37.58	87,450	3.091	rigid	1000						
BC2-88	BC2	W24x55	1360	37.58	87,450	3.091	rigid	1000						
BC2-89	BC2	W24x55	1360	37.58	87,450	3.091	rigid	1000						
BC2-90	BC2	W24x55	1360	37.58	87,450	3.091		3.091						
EB1-97	EB1	W18x35	510	37.58	32,794	3.153		3.153						
EB1-98	EB1	W18x35	510	37.58	32,794	3.153		3.153						
SB1-91	SB1	W21x50	984	45.83	51,884	2.774	2.5*PM	7						
SB1-92	SB1	W21x50	984	45.83	51,884	2.774	2.5*PM	7						
SB1-93	SB1	W21x50	984	45.83	51,884	2.774	2.5*PM	7						
SB1-94	SB1	W21x50	984	45.83	51,884	2.774	2.5*PM	7						
SB2-95	SB2	W21x50	984	37.58	63,273	2.774	2.5*PM	7						
SB2-96	SB2	W21x50	984	37.58	63,273	2.774	2.5*PM	7						

Member Label:	Member Type:	Assigned Section:	Section Moment of Inertia, I3 (in4)	Length: (ft)	Baseline EI/L (k-in/rad)	Baseline PM I3:	PM I3 Multiplier	Assigned Property Modifier (I3)	End Moment Frame Release		EI/L Multiplier	Partial Fixity		
									i-end (Yes/No)	j-end (Yes/No)		P-Fixity? (Yes/No)	i-end Kip-in/rad	j-end Kip-in/rad
G1-01	G1	W24x55	1360	30.00	109,556	2.829	2.5*PM	6.991	Yes	Yes		No		
G1-02	G1	W24x55	1360	30.00	109,556	2.829	2.5*PM	6.991	Yes	Yes		No		
G1-03	G1	W24x55	1360	30.00	109,556	2.829	2.5*PM	6.991	Yes	Yes		No		
G1-04	G1	W24x55	1360	30.00	109,556	2.829	2.5*PM	6.991	Yes	Yes		No		
G1-05	G1	W24x55	1360	30.00	109,556	2.829	2.5*PM	6.991	Yes	Yes		No		
G1-06	G1	W24x55	1360	30.00	109,556	2.829	2.5*PM	6.991	Yes	Yes		No		
G1-07	G1	W24x55	1360	30.00	109,556	2.829	2.5*PM	6.991	Yes	Yes		No		
G1-08	G1	W24x55	1360	30.00	109,556	2.829	2.5*PM	6.991	Yes	Yes		No		
G1-09	G1	W24x55	1360	30.00	109,556	2.829	2.5*PM	6.991	Yes	Yes		No		
G1-10	G1	W24x55	1360	30.00	109,556	2.829	2.5*PM	6.991	Yes	Yes		No		
G1-11	G1	W24x55	1360	30.00	109,556	2.829	2.5*PM	6.991	Yes	Yes		No		
G1-12	G1	W24x55	1360	30.00	109,556	2.829	2.5*PM	6.991	Yes	Yes		No		
G1-13	G1	W24x55	1360	30.00	109,556	2.829	2.5*PM	6.991	Yes	Yes		No		
G1-14	G1	W24x55	1360	30.00	109,556	2.829	2.5*PM	6.991	Yes	Yes		No		
G1-15	G1	W24x55	1360	30.00	109,556	2.829	2.5*PM	6.991	Yes	Yes		No		
G1-16	G1	W24x55	1360	30.00	109,556	2.829	2.5*PM	6.991	Yes	Yes		No		
G1-17	G1	W24x55	1360	30.00	109,556	2.829	2.5*PM	6.991	Yes	Yes		No		
G1-18	G1	W24x55	1360	30.00	109,556	2.829	2.5*PM	6.991	Yes	Yes		No		
G1-19	G1	W24x55	1360	30.00	109,556	2.829	2.5*PM	6.991	Yes	Yes		No		
G1-20	G1	W24x55	1360	30.00	109,556	2.829	2.5*PM	6.991	Yes	Yes		No		
G2-21	G2	W27x84	2850	30.00	229,583	2.753		2.722	Yes	Yes		No		
G2-22	G2	W27x84	2850	30.00	229,583	2.753	2.5*PM	7	Yes	Yes		No		
G2-23	G2	W27x84	2850	30.00	229,583	2.753	2.5*PM	7	Yes	Yes		No		
G2-24	G2	W27x84	2850	30.00	229,583	2.753	2.5*PM	7	Yes	Yes		No		
G2-25	G2	W27x84	2850	30.00	229,583	2.753	2.5*PM	7	Yes	Yes		No		
G2-26	G2	W27x84	2850	30.00	229,583	2.753	2.5*PM	7	Yes	Yes		No		
G2-27	G2	W27x84	2850	30.00	229,583	2.753	2.5*PM	7	Yes	Yes		No		
G2-28	G2	W27x84	2850	30.00	229,583	2.753	2.5*PM	7	Yes	Yes		No		
G2-29	G2	W27x84	2850	30.00	229,583	2.753		2.722	Yes	Yes		No		
G2-30	G2	W27x84	2850	30.00	229,583	2.753		2.722	Yes	Yes		No		
G2-31	G2	W27x84	2850	30.00	229,583	2.753		2.722	Yes	Yes		No		
G2-32	G2	W27x84	2850	30.00	229,583	2.753		2.722	Yes	Yes		No		
G2-33	G2	W27x84	2850	30.00	229,583	2.753	2.5*PM	7	Yes	Yes		No		
G2-34	G2	W27x84	2850	30.00	229,583	2.753	2.5*PM	7	Yes	Yes		No		
G2-35	G2	W27x84	2850	30.00	229,583	2.753	2.5*PM	7	Yes	Yes		No		
G2-36	G2	W27x84	2850	30.00	229,583	2.753	2.5*PM	7	Yes	Yes		No		
G2-37	G2	W27x84	2850	30.00	229,583	2.753	2.5*PM	7	Yes	Yes		No		
G2-38	G2	W27x84	2850	30.00	229,583	2.753	2.5*PM	7	Yes	Yes		No		
G2-39	G2	W27x84	2850	30.00	229,583	2.753	2.5*PM	7	Yes	Yes		No		
G2-40	G2	W27x84	2850	30.00	229,583	2.753		2.722	Yes	Yes		No		
G3-41	G3	W21x55	1140	30.00	91,833	2.789	2.5*PM	6.875	Yes	Yes		No		
G3-42	G3	W21x55	1140	30.00	91,833	2.789	2.5*PM	6.875	Yes	Yes		No		

APPENDIX N

VTK2 – COMPOSITE SECTION CALCULATIONS & FE MODEL INPUT VALUES

This Appendix includes the computed composite transformed moments of inertia and finite element input values for the framing members in the VTK2 finite element model of Section 4.2.2. All transformed moment of inertia and property modifier values were computed using the same procedures as the example problems shown in Appendix K. Also included are a listing of member end-releases and their respective partial fixity values, if applicable. Figure N.1 shows the framing member layout and section designations.



Figure N.1: VTK2 FE Framing Member Section Designations

VTK2 BEAMS - Composite Section Calculation Worksheets (Part 1 of 2):

		B1	B2	B3	B4	B5	B6	B7	B8	B9	B10	B11	B12	B13	B14	B15	B16	B17
Concrete Deck Height, ds =	in	5.25	5.25	5.25	5.25	5.25	5.25	5.25	5.25	5.25	5.25	5.25	5.25	5.25	5.25	5.25	5.25	5.25
Concrete Unit Weight, wc =	pcf	115	115	115	115	115	115	115	115	115	115	115	115	115	115	115	115	115
Concrete Strength, f'c (ksi) =	ksi	3	3	3	3	3	3	3	3	3	3	3	3	3	3	3	3	3
Deck Rib Height, dr =	in	2	2	2	2	2	2	2	2	2	2	2	2	2	2	2	2	2
Modulus of Elasticity of Steel, Es =	ksi	29,000	29,000	29,000	29,000	29,000	29,000	29,000	29,000	29,000	29,000	29,000	29,000	29,000	29,000	29,000	29,000	29,000
(AISC) wc*1.5*f'c*0.5 Ec =	ksi	2136	2136	2136	2136	2136	2136	2136	2136	2136	2136	2136	2136	2136	2136	2136	2136	2136
Dynamic Concrete Modulus, 1.35*Ec =	ksi	2884	2884	2884	2884	2884	2884	2884	2884	2884	2884	2884	2884	2884	2884	2884	2884	2884
n = Es/1.35*Ec =		10.06	10.06	10.06	10.06	10.06	10.06	10.06	10.06	10.06	10.06	10.06	10.06	10.06	10.06	10.06	10.06	10.06
Section =		W21x44	W16x31	W24x84	W24x84	W24x68	W12x19	W21x44	W12x19	W16x31	W16x26	W16x26	W10x12	W14x22	W21x50	W16x31	W18x35	W16x26
d =	in	20.7	15.9	24.1	24.1	23.7	12.2	20.7	12.2	15.9	15.7	15.7	9.87	13.7	20.8	15.9	17.7	15.7
A =	in ²	13	9.13	24.7	24.7	20.1	5.57	13	5.57	9.13	7.68	7.68	3.54	6.49	14.7	9.13	10.3	7.68
Ix =	in ⁴	843	375	2370	2370	1830	130	843	130	375	301	301	53.8	199	984	375	510	301
Weight/length =	plf	44	31	84	84	68	19	44	19	31	26	26	12	22	50	31	35	26
Beam Spacing (ft), S =	ft	10	10	10	10	10	10	10	12	5	5	5	5	2.5	10	10	10	10
Beam Span (ft), Lb =	ft	35	30	35	30	30	20	20	20	30	25	25	14	13	35	28	28	28
Beam Spacing (in), S =	in	120	120	120	120	120	120	120	144	60	60	60	60	30	120	120	120	120
Beam Span (in), Lb =	in	420.00	360.00	420.00	360.00	360.00	240.00	240.00	240.00	360.00	300.00	300.00	168.00	156.00	420.00	336.00	336.00	336.00
Effective Concrete Width, S =	in	120	120	120	120	120	120	120	144	60	60	60	60	30	120	120	120	120
Effective Concrete Width, 0.4*Lb =	in	168	144	168	144	144	96	96	96	144	120	120	67	62	168	134	134	134
Effective Concrete Width, min =	in	120	120	120	120	120	96	96	96	60	60	60	60	30	120	120	120	120
Effective Concrete Depth, de,b =	in	3.25	3.25	3.25	3.25	3.25	3.25	3.25	3.25	3.25	3.25	3.25	3.25	3.25	3.25	3.25	3.25	3.25
Transformed Concrete Width =	in	11.93	11.93	11.93	11.93	11.93	9.55	9.55	9.55	5.97	5.97	5.97	5.97	2.98	11.93	11.93	11.93	11.93
Transformed Concrete Area =	in ²	38.78	38.78	38.78	38.78	38.78	31.02	31.02	31.02	19.39	19.39	19.39	19.39	9.69	38.78	38.78	38.78	38.78
Location of Neutral Axis (from bottom) =	in	20.82	17.32	21.63	21.63	22.04	14.34	20.20	14.34	15.82	16.07	16.07	12.17	13.12	20.57	17.32	18.71	17.43
Distance to Neutral Axis (above beam c.g.) =	in	10.466	9.369	9.576	9.576	10.192	8.245	9.848	8.245	7.870	8.219	8.219	7.238	6.275	10.170	9.369	9.857	9.578
Transformed Moment of Inertia, Ib,trans =	in ⁴	2778.6	1399.3	6111.6	6111.6	5034.4	603.9	2659.5	603.9	1223.7	1042.4	1042.4	290.2	634.1	3114.8	1399.3	1810.7	1179.2
Section =		BEAM 1	BEAM 2	BEAM 3	BEAM 4	BEAM 5	BEAM 6	BEAM 7	BEAM 8	BEAM 9	BEAM 10	BEAM 11	BEAM 12	BEAM 13	BEAM 14	BEAM 15	BEAM 16	BEAM 17
Itr,slab,b =	in ⁴	W21x44	W16x31	W24x84	W24x84	W24x68	W12x19	W21x44	W12x19	W16x31	W16x26	W16x26	W10x12	W14x22	W21x50	W16x31	W18x35	W16x26
Beam Modified Moment of Inertia, I3* = Ib,trans - Itr,slab =	in ⁴	34.1	34.1	34.1	34.1	34.1	27.3	34.1	27.3	17.1	17.1	17.1	17.1	8.5	34.1	34.1	34.1	34.1
Beam Property Modifier, I3 to I3* =		3.256	3.640	2.564	2.564	2.732	4.435	3.122	4.435	3.218	3.407	3.407	5.077	3.144	3.131	3.640	3.483	3.804

VTK2 BEAMS - Composite Section Calculation Worksheets (Part 2 of 2):

		B18	B19	B20	B21	B22	B23	B24	B25	B26	B27	B28	B29	B30	BU-1	BU-2	BU-3
Concrete Deck Height, ds =	in	5.25	5.25	5.25	5.25	5.25	5.25	5.25	5.25	5.25	5.25	5.25	5.25	5.25	5.25	5.25	5.25
Concrete Unit Weight, wc =	pcf	115	115	115	115	115	115	115	115	115	115	115	115	115	115	115	115
Concrete Strength, f'c (ksi) =	ksi	3	3	3	3	3	3	3	3	3	3	3	3	3	3	3	3
Deck Rib Height, dr =	in	2	2	2	2	2	2	2	2	2	2	2	2	2	2	2	2
Modulus of Elasticity of Steel, Es =	ksi	29,000	29,000	29,000	29,000	29,000	29,000	29,000	29,000	29,000	29,000	29,000	29,000	29,000	29,000	29,000	29,000
(AISC) wc*1.5*f'c*0.5 Ec =	ksi	2136	2136	2136	2136	2136	2136	2136	2136	2136	2136	2136	2136	2136	2136	2136	2136
Dynamic Concrete Modulus, 1.35*Ec =	ksi	2884	2884	2884	2884	2884	2884	2884	2884	2884	2884	2884	2884	2884	2884	2884	2884
n = Es/1.35*Ec =		10.06	10.06	10.06	10.06	10.06	10.06	10.06	10.06	10.06	10.06	10.06	10.06	10.06	10.06	10.06	10.06
Section =		W24x68	W24x68	W24x68	W16x26	W14x22	W14x22	W18x35	W12x19	W12x19	W14x22	W12x19	W12x19	W12x14	W8x10	W8x10	W8x10
d =	in	23.7	23.7	23.7	15.7	13.7	13.7	17.7	12.2	12.2	13.7	12.2	11.9	7.89	7.89	7.89	7.89
A =	in ²	20.1	20.1	20.1	7.68	6.49	6.49	10.3	5.57	5.57	6.49	5.57	4.16	2.96	2.96	2.96	2.96
Ix =	in ⁴	1830	1830	1830	301	199	199	510	130	130	199	130	88.6	30.8	30.8	30.8	30.8
Weight/length =	plf	68	68	68	26	22	22	35	19	19	22	19	14	10	10	10	10
Beam Spacing (ft), S =	ft	10	10	10	10	10	10	7.5	2.5	2.5	7.5	5	2.5	2.5	10	5	10
Beam Span (ft), Lb =	ft	28	30	35	25	25	23	23	20	25	25	25	20	7	7	7	5
Beam Spacing (in), S =	in	120	120	120	120	120	120	90	30	90	60	30	30	120	60	120	120
Beam Span (in), Lb =	in	336.00	360.00	420.00	300.00	300.00	276.00	276.00	240.00	300.00	300.00	300.00	240.00	84.00	84.00	60.00	60.00
Effective Concrete Width, S =	in	120	120	120	120	120	120	90	30	90	60	30	30	120	60	120	120
Effective Concrete Width, 0.4*Lb =	in	134	144	168	120	120	110	110	96	120	120	120	96	34	34	24	24
Effective Concrete Width, min =	in	120	120	120	120	120	110.4	90	30	90	60	30	30	33.6	33.6	24	24
Effective Concrete Depth, de,b =	in	3.25	3.25	3.25	3.25	3.25	3.25	3.25	3.25	3.25	3.25	3.25	3.25	3.25	3.25	3.25	3.25
Transformed Concrete Width =	in	11.93	11.93	11.93	11.93	11.93	10.98	8.95	2.98	8.95	8.95	5.97	2.98	3.34	3.34	2.39	2.39
Transformed Concrete Area =	in ²	38.78	38.78	38.78	38.78	38.78	35.68	29.08	9.69	29.08	29.08	19.39	9.69	10.86	10.86	7.76	7.76
Location of Neutral Axis (from bottom) =	in	22.04	22.04	22.04	17.43	15.82	15.71	15.41	14.90	14.26	14.26	14.70	12.28	12.65	9.89	9.89	9.42
Distance to Neutral Axis (above beam c.g.) =	in	10.192	10.192	10.192	9.578	8.973	8.863	8.564	6.049	8.162	8.162	7.848	6.176	6.700	5.948	5.948	5.479
Transformed Moment of Inertia, Ib,trans =	in ⁴	5034.4	5034.4	5034.4	1179.2	843.2	832.9	806.8	1295.8	597.7	597.7	749.6	473.1	364.0	173.6	173.6	160.4
Section =		BEAM 18	BEAM 19	BEAM 20	BEAM 21	BEAM 22	BEAM 23	BEAM 24	BEAM 25	BEAM 26	BEAM 27	BEAM 28	BEAM 29	BEAM 30	BU-1	BU-2	BU-3
Itr,slab,b =	in ⁴	W24x68	W24x68	W24x68	W16x26	W14x22	W14x22	W18x35	W12x19	W12x19	W14x22	W12x19	W12x19	W12x14	W8x10	W8x10	W8x10
Beam Modified Moment of Inertia, I3* = Ib,trans - Itr,slab =	in ⁴	34.1	34.1	34.1	34.1	34.1	31.4	25.6	8.5	25.6	25.6	17.1	8.5	8.5	9.6	9.6	6.8
Beam Property Modifier, I3 to I3* =		5000.3	5000.3	5000.3	1145.1	809.0	801.5	781.2	1287.2	572.1	572.1	732.5	464.6	355.5	164.1	164.1	153.6
		2.732	2.732	2.732	3.804	4.065	4.028	3.926	2.524	4.401	4.401	3.681	3.574	4.012	5.328	5.328	4.986

VTK2 GIRDERS - Composite Section Calculation Worksheet:

Concrete Deck Height, ds = in
 Concrete Unit Weight, wc = pcf
 Concrete Strength, f'c (ksi) = ksi
 Deck Rib Height, dr = in
 Modulus of Elasticity of Steel, Es = ksi
 (AISC) $w_c \cdot 1.5 \cdot f'_c \cdot 0.5$ Ec = ksi
 Dynamic Concrete Modulus, $1.35 \cdot E_c$ = ksi
 $n = E_s / 1.35 \cdot E_c$
 Concrete Depth Above Rib, de = in

G1	G2	G3	G4	G5	G6	G7	G8	G9	G10	G11	G12	G13	G14	G15	G16	G17
5.25	5.25	5.25	5.25	5.25	5.25	5.25	5.25	5.25	5.25	5.25	5.25	5.25	5.25	5.25	5.25	5.25
115	115	115	115	115	115	115	115	115	115	115	115	115	115	115	115	115
3	3	3	3	3	3	3	3	3	3	3	3	3	3	3	3	3
2	2	2	2	2	2	2	2	2	2	2	2	2	2	2	2	2
29,000	29,000	29,000	29,000	29,000	29,000	29,000	29,000	29,000	29,000	29,000	29,000	29,000	29,000	29,000	29,000	29,000
2136	2136	2136	2136	2136	2136	2136	2136	2136	2136	2136	2136	2136	2136	2136	2136	2136
2884	2884	2884	2884	2884	2884	2884	2884	2884	2884	2884	2884	2884	2884	2884	2884	2884
10.06	10.06	10.06	10.06	10.06	10.06	10.06	10.06	10.06	10.06	10.06	10.06	10.06	10.06	10.06	10.06	10.06
3.25	3.25	3.25	3.25	3.25	3.25	3.25	3.25	3.25	3.25	3.25	3.25	3.25	3.25	3.25	3.25	3.25

Section =
 Left Beam Span (ft), Lb = ft
 Beam Span (in), Lb = in

Left Beam	Left Beam	Left Beam	Left Beam	Left Beam	Left Beam	Left Beam	Right Beam	Left Beam	Left Beam	Left Beam	Left Beam	Left Beam	Left Beam	Left Beam	Left Beam	Left Beam
B1	B1	B1	B1	B1	B1	B1	B2	B1	B1	B1	B1	B1	B1	B1	B1	B1
W21x44	W21x44	W21x44	W16x31	W16x31	W16x31	W16x31	W12x19	W16x31	W16x31	W16x31	W16x31	W16x31	W16x31	W16x31	W16x31	W16x31
420.00	420.00	420.00	336.00	336.00	336.00	336.00	240.00	360.00	336.00	336.00	276.00	300.00	168.00	168.00	276.00	300.00

Section =
 Right Beam Span (ft), Lb = ft
 Beam Span (in), Lb = in

Right Beam	Right Beam	Right Beam	Right Beam	Right Beam	Right Beam	Right Beam	Right Beam	Right Beam	Right Beam	Right Beam	Right Beam	Right Beam	Right Beam	Right Beam	Right Beam	Right Beam
B2	B2	B2	B2	B2	B2	B2	B2	B2	B2	B2	B2	B2	B2	B2	B2	B2
NONE	W16x31	W16x31	W16x31	W16x31	W16x31	W16x31	NONE	NONE	NONE	NONE	NONE	NONE	NONE	NONE	W12x19	W14x22
0	30	30	30	30	30	30	0	0	0	0	0	0	0	0	10	0
0.00	360.00	360.00	360.00	360.00	360.00	360.00	0.00	0.00	0.00	0.00	0.00	0.00	0.00	0.00	120.00	300.00

Section =
 d = in
 A = in²
 Ix = in⁴
 Weight/length = pcf
 Girder Span, Lg = ft
 Left Beam Span, Lbl = ft
 Right Beam Span, Lbr = ft
 Girder Span, Lg = in
 0.4*Lg = in
 minimum (0.2*Lg and Lbl/2) = in
 minimum (0.2*Lg and Lbr/2) = in
 Effective Concrete Width, Top Flange = in
 Effective Concrete Width, Web = in
 Effective Concrete Deck Height, de,g = in
 Transformed Concrete Width, Top Flange = in
 Transformed Concrete Area, Top Flange = in²
 Transformed Concrete Width, Web = in
 Transformed Concrete Area, Web = in²
 Location of Neutral Axis (from bottom) = in
 Distance to Neutral Axis, Top Flange = in
 Distance to Neutral Axis, Web = in
 Distance to Neutral Axis (above girder c.g.) = in
 Transformed Moment of Inertia, Ig,trans = in⁴

G1	G2	G3	G4	G5	G6	G7	G8	G9	G10	G11	G12	G13	G14	G15	G16	G17
GIRDER	GIRDER	GIRDER	GIRDER	GIRDER	GIRDER	GIRDER	GIRDER	GIRDER	GIRDER	GIRDER	GIRDER	GIRDER	GIRDER	GIRDER	GIRDER	GIRDER
W21x50	W24x62	W24x68	W24x68	W24x55	W24x55	W24x55	W21x50	W18x40	W24x55	W16x26	W21x44	W14x22	W18x35	W18x40	W21x50	W21x50
20.8	23.7	23.7	23.7	23.6	23.6	23.6	20.8	17.9	23.6	15.7	20.7	13.7	17.7	17.9	20.8	20.8
14.7	18.3	20.1	20.1	16.3	16.3	16.3	14.7	11.8	16.3	7.68	13	6.49	10.3	11.8	14.7	14.7
984	1560	1830	1830	1360	1360	1360	984	612	1360	301	843	199	510	612	984	984
50	62	68	68	55	55	55	50	40	55	26	44	22	35	40	50	50
30	30	30	30	30	30	30	30	30	30	25	30	13	20	25	25	30
35	35	35	28	28	20	20	30	28	28	23	25	14	14	23	25	25
0	30	30	30	30	30	30	0	0	0	0	0	0	0	10	0	25
360.00	360.00	360.00	360.00	360.00	360.00	360.00	360.00	360.00	360.00	298.00	360.00	156.00	240.00	298.00	298.00	360.00
144	144	144	144	144	144	144	144	144	144	119.19984	144	62.4	96	119.19984	119.19984	144
72	72	72	72	72	72	72	72	72	72	59.59992	72	31.2	48	59.59992	59.59992	72
0	72	72	72	72	72	72	0	0	0	0	0	0	0	59.59992	0	72
72	144	144	144	144	144	144	72	72	72	59.59992	72	31.2	48	119.19984	59.59992	144
36	72	72	72	72	72	72	36	36	36	29.79996	36	15.6	24	59.59992	29.79996	72
4.25	4.25	4.25	4.25	4.25	4.25	4.25	4.25	4.25	4.25	4.25	4.25	4.25	4.25	4.25	4.25	4.25
7.16	14.32	14.32	14.32	14.32	14.32	14.32	7.16	7.16	7.16	5.93	7.16	3.10	4.77	11.85	5.93	14.32
23.27	46.54	46.54	46.54	46.54	46.54	46.54	23.27	23.27	23.27	19.26	23.27	10.08	15.51	38.52	19.26	46.54
3.58	7.16	7.16	7.16	7.16	7.16	7.16	3.58	3.58	3.58	2.96	3.58	1.55	2.39	5.93	2.96	7.16
7.16	14.32	14.32	14.32	14.32	14.32	14.32	7.16	7.16	7.16	5.93	7.16	3.10	4.77	11.85	5.93	14.32
19.44	23.27	23.02	23.02	23.48	23.48	21.44	19.44	17.57	21.44	16.17	19.71	13.46	16.71	18.64	18.87	21.20
4.99	4.05	4.31	4.31	3.75	3.75	5.78	4.99	3.96	5.78	3.15	4.62	3.87	4.61	2.89	5.56	3.23
2.36	1.43	1.68	1.68	1.12	1.12	3.16	2.36	1.33	3.16	0.53	1.99	1.24	1.99	0.26	2.93	0.60
9.040	11.422	11.168	11.168	11.679	11.679	9.642	9.040	8.616	9.642	8.320	9.359	6.606	7.864	9.688	8.466	10.799
2826.3	4786.8	5286.5	5286.5	4300.0	4300.0	3747.8	2826.3	1888.3	3747.8	1044.9	2528.7	647.9	1510.9	2079.3	2702.7	3233.5

Section =
 Othotropic Bending Stiffness Property Modifier (PMortho)=
 PMortho*trslab,g = in⁴
 Girder Modified Moment of Inertia, I3* = Ig,trans - Itr,slab,g = in⁴
 Girder Property Modifier, I3 to I3* =

GIRDER	GIRDER	GIRDER	GIRDER	GIRDER	GIRDER	GIRDER	GIRDER	GIRDER	GIRDER	GIRDER	GIRDER	GIRDER	GIRDER	GIRDER	GIRDER	GIRDER
G1	G2	G3	G4	G5	G6	G7	G8	G9	G10	G11	G12	G13	G14	G15	G16	G17
W21x50	W24x62	W24x68	W24x68	W24x55	W24x55	W24x55	W21x50	W18x40	W24x55	W16x26	W21x44	W14x22	W18x35	W18x40	W21x50	W21x50
2.88	2.88	2.88	2.88	2.88	2.88	2.88	2.88	2.88	2.88	2.88	2.88	2.88	2.88	2.88	2.88	2.88
20.5	41.0	41.0	41.0	41.0	41.0	20.5	20.5	20.5	20.5	17.0	20.5	8.9	13.7	33.9	17.0	41.0
2767.3	4668.9	5168.5	5168.5	4182.1	4182.1	3688.8	2767.3	1829.3	3688.8	996.1	2469.7	622.3	1471.5	1981.6	2653.9	3115.5
2.812	2.993	2.824	2.824	3.075	3.075	2.712	2.812	2.989	2.712	3.309	2.930	3.127	2.885	3.238	2.697	3.166

VTK2 FE Model Framing Member Property Assignments:

Member Label:	Member Type:	Assigned Section:	Section Moment of Inertia, I3 (in4)	Length: (ft)	Baseline E/I/L (k-in/rad)	Baseline PM I3:	Assigned Property Modifier (I3)	End Moment Frame Release		E/I/L Multiplier	P-Fixity? (Yes/No)	Partial Fixity	
								i-end (Yes/No)	j-end (Yes/No)			i-end Kip-in/rad	j-end Kip-in/rad
B1-1	B1	W21x44	843	35	58,207	3.256	3.256	Yes	Yes	6E/I/L	Yes	349,243	349,243
B1-2	B1	W21x44	843	35	58,207	3.256	3.256	Yes	Yes	6E/I/L	Yes	349,243	349,243
B1-3	B1	W21x44	843	35	58,207	3.256	3.256	Yes	Yes	6E/I/L	Yes	349,243	349,243
B1-4	B1	W21x44	843	35	58,207	3.256	3.256	Yes	Yes	6E/I/L	Yes	349,243	349,243
B1-5	B1	W21x44	843	35	58,207	3.256	3.256	No	Yes		No		
B1-6	B1	W21x44	843	35	58,207	3.256	3.256	Yes	Yes	6E/I/L	Yes	349,243	349,243
B1-7	B1	W21x44	843	35	58,207	3.256	3.256	Yes	Yes	6E/I/L	Yes	349,243	349,243
B1-8	B1	W21x44	843	35	58,207	3.256	3.256	Yes	No		No		
B1-9	B1	W21x44	843	35	58,207	3.256	3.256	Yes	Yes	6E/I/L	Yes	349,243	349,243
B1-10	B1	W21x44	843	35	58,207	3.256	3.256	Yes	Yes	6E/I/L	Yes	349,243	349,243
B1-11	B1	W21x44	843	35	58,207	3.256	3.256	Yes	No		No		
B1-12	B1	W21x44	843	35	58,207	3.256	3.256	Yes	Yes	6E/I/L	Yes	349,243	349,243
B1-13	B1	W21x44	843	35	58,207	3.256	3.256	Yes	Yes	6E/I/L	Yes	349,243	349,243
B1-14	B1	W21x44	843	35	58,207	3.256	3.256	Yes	Yes	6E/I/L	Yes	349,243	349,243
B1-15	B1	W21x44	843	35	58,207	3.256	3.256	Yes	Yes	6E/I/L	Yes	349,243	349,243
B1-16	B1	W21x44	843	35	58,207	3.256	3.256	Yes	Yes	6E/I/L	Yes	349,243	349,243
B1-17	B1	W21x44	843	35	58,207	3.256	3.256	Yes	Yes	6E/I/L	Yes	349,243	349,243
B1-18	B1	W21x44	843	35	58,207	3.256	3.256	No	Yes		No		
B1-19	B1	W21x44	843	35	58,207	3.256	3.256	Yes	Yes	6E/I/L	Yes	349,243	349,243
B1-20	B1	W21x44	843	35	58,207	3.256	3.256	Yes	Yes	6E/I/L	Yes	349,243	349,243

B2-21	B2	W16x31	375	30	30,208	3.640	3.640	Yes	Yes	6E/I/L	Yes	181,250	181,250
B2-22	B2	W16x31	375	30	30,208	3.640	3.640	Yes	Yes	6E/I/L	Yes	181,250	181,250
B2-23	B2	W16x31	375	30	30,208	3.640	3.640	Yes	Yes	6E/I/L	Yes	181,250	181,250
B2-24	B2	W16x31	375	30	30,208	3.640	3.640	Yes	Yes	6E/I/L	Yes	181,250	181,250
B2-25	B2	W16x31	375	30	30,208	3.640	3.640	Yes	Yes	6E/I/L	Yes	181,250	181,250
B2-26	B2	W16x31	375	30	30,208	3.640	3.640	Yes	Yes	6E/I/L	Yes	181,250	181,250
B2-27	B2	W16x31	375	30	30,208	3.640	3.640	Yes	Yes		No		
B2-28	B2	W16x31	375	30	30,208	3.640	3.640	Yes	Yes	6E/I/L	Yes	181,250	181,250
B2-29	B2	W16x31	375	30	30,208	3.640	3.640	Yes	Yes	6E/I/L	Yes	181,250	181,250
B2-30	B2	W16x31	375	30	30,208	3.640	3.640	Yes	Yes		No		
B2-31	B2	W16x31	375	30	30,208	3.640	3.640	Yes	Yes	6E/I/L	Yes	181,250	181,250
B2-32	B2	W16x31	375	30	30,208	3.640	3.640	Yes	Yes	6E/I/L	Yes	181,250	181,250
B2-33	B2	W16x31	375	30	30,208	3.640	3.640	Yes	Yes		No		
B2-34	B2	W16x31	375	30	30,208	3.640	3.640	Yes	Yes	6E/I/L	Yes	181,250	181,250
B2-35	B2	W16x31	375	30	30,208	3.640	3.640	Yes	Yes	6E/I/L	Yes	181,250	181,250

Member Label:	Member Type:	Assigned Section:	Section Moment of Inertia, I3 (in4)	Length: (ft)	Baseline E/I/L (k-in/rad)	Baseline PM I3:	Assigned Property Modifier (I3)	End Moment Frame Release		E/I/L Multiplier	P-Fixity? (Yes/No)	Partial Fixity	
								i-end (Yes/No)	j-end (Yes/No)			i-end Kip-in/rad	j-end Kip-in/rad
B3-36	B3	W24x84	2370	35	163,643	2.564	2.564						
B3-37	B3	W24x84	2370	35	163,643	2.564	2.564						
B4-38	B4	W24x84	2370	30	190,917	2.564	2.564						
B5-39	B5	W24x68	1830	30	147,417	2.732	2.732						
B6-40	B6	W12x19	130	20	15,708	4.435	4.435	Yes	Yes	6E/I/L	Yes	94,250	94,250
B6-41	B6	W12x19	130	20	15,708	4.435	4.435	Yes	Yes	6E/I/L	Yes	94,250	94,250
B7-42	B7	W21x44	843	20	101,863	3.122	3.122						
B8-43	B8	W12x19	130	20	15,708	4.435	4.435	Yes	Yes		No		
B9-44	B9	W16x31	375	30	30,208	3.218	3.218	Yes	Yes		No		
B10-45	B10	W16x26	301	25	29,097	3.407	3.407						
B11-46	B11	W16x26	301	25	29,097	3.407	3.407						
B12-47	B12	W10x12	53.8	14	9,287	5.077	5.077	Yes	Yes		No		
B13-48	B13	W14x22	199	13	36,994	3.144	3.144	Yes	Yes		No		
B14-39	B14	W21x50	984	35	67,943	3.131	3.131	No	Yes		No		
B15-50	B15	W16x31	375	28	32,366	3.640	3.640	No	Yes	6E/I/L	Yes		194,196
B15-51	B15	W16x31	375	28	32,366	3.640	3.640	No	Yes	6E/I/L	Yes		194,196
B16-52	B16	W18x35	510	28	44,018	3.483	3.483	No	Yes		No		
B16-53	B16	W18x35	510	28	44,018	3.483	3.483	Yes	Yes	6E/I/L	Yes	264,107	264,107
B17-54	B17	W16x26	301	28	25,979	3.804	3.804	Yes	Yes	6E/I/L	Yes	155,875	155,875
B18-55	B18	W24x68	1830	28	157,946	2.732	2.732						
B19-56	B19	W24x68	1830	30	147,417	2.732	2.732						
B20-57	B20	W24x68	1830	35	126,357	2.732	2.732						
B21-58	B21	W16x26	301	25	29,097	3.804	3.804	Yes	Yes	6E/I/L	Yes	174,580	174,580
B21-59	B21	W16x26	301	25	29,097	3.804	3.804	Yes	Yes	6E/I/L	Yes	174,580	174,580
B22-60	B22	W14x22	199	25	19,237	4.065	4.065	Yes	Yes	6E/I/L	Yes	115,420	115,420
B23-61	B23	W14x22	199	23	20,909	4.028	4.028	Yes	Yes	6E/I/L	Yes	125,457	125,457
B24-62	B24	W14x22	199	23	20,909	3.926	3.926	Yes	Yes		No		
B25-63	B25	W18x35	510	23	53,587	2.524	6.310						
B26-64	B26	W12x19	130	20	15,708	4.401	4.401	Yes	Yes	6E/I/L	Yes	94,250	94,250
B27-65	B27	W12x19	130	25	12,567	4.401	4.401	Yes	Yes	6E/I/L	Yes		75,400
B28-66	B28	W14x22	199	25	19,237	3.681	2.5*PM						
B29-67	B29	W12x19	130	25	12,567	3.574	2.5*PM	No	Yes		No		
B30-68	B30	W12x14	88.6	20	10,706	4.012	2.5*PM	Yes	Yes		No		

Member Label:	Member Type:	Assigned Section:	Section Moment of Inertia, I3		Length: (ft)	Baseline EI/L (k-in/rad)		Assigned Property Modifier (I3)	End Moment Frame Release		EI/L Multiplier	Partial Fixity		
			Inertia, I3 (in4)			EI/L (k-in/rad)	Baseline PM I3:		i-end (Yes/No)	j-end (Yes/No)		P-Fixity? (Yes/No)	i-end Kip-in/rad	j-end Kip-in/rad
BU-1	BU-1	W8x10	30.8	7	10,633	5.328		5.328						
BU-2	BU-2	W8x10	30.8	7	10,633	5.328		5.328						
BU-3	BU-3	W8x10	30.8	5	14,887	4.986		4.986						
G1-1	G1	W21x50	984	30	79,267	2.812	2.5*PM	7.030	Yes	Yes		No		
G1-2	G1	W21x50	984	30	79,267	2.812	2.5*PM	7.030	Yes	Yes		No		
G1-3	G1	W21x50	984	30	79,267	2.812	2.5*PM	7.030	Yes	Yes		No		
G1-4	G1	W21x50	984	30	79,267	2.812	2.5*PM	7.030	Yes	Yes		No		
G1-5	G1	W21x50	984	30	79,267	2.812	2.5*PM	7.030	Yes	Yes		No		
G1-6	G1	W21x50	984	30	79,267	2.812	2.5*PM	7.030	Yes	Yes		No		
G1-7	G1	W21x50	984	30	79,267	2.812	2.5*PM	7.030	Yes	Yes		No		
G1-8	G1	W21x50	984	30	79,267	2.812	2.5*PM	7.030	Yes	Yes		No		
G2-9	G2	W24x62	1560	30	125,667	2.993		2.993	Yes	Yes		No		
G2-10	G2	W24x62	1560	30	125,667	2.993		2.993	Yes	No		No		
G2-11	G2	W24x62	1560	30	125,667	2.993		2.993	No	Yes		No		
G2-12	G2	W24x62	1560	30	125,667	2.993		2.993	Yes	Yes		No		
G2-13	G2	W24x62	1560	30	125,667	2.993		2.993	No	Yes		No		
G3-14	G3	W24x68	1830	30	147,417	2.824		2.824						
G3-15	G3	W24x68	1830	30	147,417	2.824		2.824						
G3-16	G3	W24x68	1830	30	147,417	2.824		2.824						
G4-17	G4	W24x68	1830	30	147,417	2.824		2.824						
G5-18	G5	W24x55	1360	30	109,556	3.075		3.075	No	Yes		No		
G6-19	G6	W24x55	1360	30	109,556	3.075		3.075	Yes	Yes		No		
G7-20	G7	W24x55	1360	30	109,556	2.712		2.712	Yes	Yes		No		
G8-21	G8	W21x50	984	30	79,267	2.812		2.812	Yes	Yes		No		
G9-22	G9	W18x40	612	30	49,300	2.989		2.989	Yes	Yes		No		
G10-23	G10	W24x55	1360	30	109,556	2.712	2.5*PM	6.780	Yes	Yes		No		
G11-24	G11	W16x26	301	25	29,097	3.309	2.5*PM	8.270	Yes	Yes		No		
G12-25	G12	W21x44	843	30	67,908	2.930	2.5*PM	7.320	Yes	Yes		No		
G13-26	G13	W14x22	199	13	36,994	3.127		3.127	Yes	Yes		No		
G14-27	G14	W18x35	510	20	61,625	2.885	2.5*PM	7.210	Yes	Yes		No		
G15-28	G15	W18x40	612	25	59,160	3.238		3.238	Yes	Yes		No		
G16-29	G16	W21x50	984	25	95,120	2.697		2.697	Yes	Yes		No		
G17-30	G17	W21x50	984	30	79,267	3.166		3.166	Yes	Yes		No		

VITA

Anthony Barrett grew up in a mountain town in Colorado and pursued his undergraduate education at the United States Air Force Academy in Colorado Springs, Colorado. He played varsity basketball all four years and graduated with a BS in Civil Engineering in May 1996 before entering active duty. His first three-year assignment was in Panama City, Florida, and was followed by one year of graduate school at the University of Illinois at Urbana-Champaign, where he received an MS in Civil Engineering (Structures) in August 2000. After spending a year overseas in Honduras, he returned to Colorado Springs to join the faculty of the United States Air Force Academy's Department of Civil and Environmental Engineering as an instructor. He spent two years teaching undergraduate civil engineering before he was selected for an assignment to earn his doctorate starting in August 2003. He chose to pursue his Ph.D. at Virginia Tech to work with former USAFA Distinguished Visiting Professor Thomas M. Murray. He completed his studies in the field of floor vibrations in August 2006. He will now go where the Air Force tells him...because they have paid for every penny of his schooling since he was 17-years old.